Physics of the Solid State, Vol. 43, No. 8, 2001, pp. 1401–1419. Translated from Fizika Tverdogo Tela, Vol. 43, No. 8, 2001, pp. 1345–1362.

REVIEWS

Quantum Effects in Incipient and Low-Temperature Ferroelectrics (A Review)

O. E. Kvyatkovskiĭ

Ioffe Physicotechnical Institute, Russian Academy of Sciences, Politekhnicheskaya ul. 26, St. Petersburg, 194021 Russia

e-mail: kvyatkovskii@pop.ioffe.rssi.ru

Received December 29, 2000

Abstract—The paper discusses the theory of quantum effects in incipient and low-temperature ferroelectrics and its application to the description of some phenomena observed in $SrTiO_3$, $KTaO_3$, and solid solutions based on these compounds. Two approaches are considered, namely, the Barrett theory in the framework of the single-ion (one-sublattice) Devonshire–Slater model and the Rechester and Khmel'nitskiĭ–Shneerson theories developed in terms of a soft ferroelectric (polar TO) mode dressed by its anharmonic interaction with zero-point and thermal lattice vibrations. Consideration is given to the specific features of an isoelectronic-impurity-induced ferroelectric phase transition in incipient ferroelectrics, the theory of an isotopic-impurity-induced ferroelectric phase transition in incipient ferroelectrics, the theory of the isotopic Curie-temperature shift in low-temperature ferroelectrics, and the electric-field effect on the dielectric properties of incipient and low-temperature ferroelectrics. © *2001 MAIK "Nauka/Interperiodica".*

1. INTRODUCTION

Displacive ferroelectrics contain a group of incipient and low-temperature ferroelectrics which possess a number of specific properties at low temperatures. The best known of them are compounds of the perovskite family, such as strontium titanate $SrTiO_3$, potassium tantalate $KTaO_3$, and calcium titanate (perovskite) $CaTiO_3$ [1]. One should also class titanium dioxide (rutile) TiO_2 [2] and lead telluride PbTe with the incipient ferroelectrics [3–5]. Depending on its composition (the concentration of tin vacancies), tin telluride SnTe can be either an incipient [6] or a low-temperature ferroelectric with a phase-transition temperature dependent on vacancy concentration [7–11].

Considerable attention has been focused recently on the study of the properties of $SrTiO_3$, $KTaO_3$, and $CaTiO_3$, as well as of solid solutions based on these compounds. Of particular interest in this respect is strontium titanate, which is used to obtain promising materials for the development of microelectronics, in particular, of dynamic-memory cells [12]. The anomalous low-temperature dielectric (nearly ferroelectric) properties of strontium titanate appear to offer considerable application potential [13–15]. Under normal conditions, $SrTiO_3$ is an incipient ferroelectric. Strontium titanate exhibits anomalous dielectric properties at low temperatures [16], but it remains a paraelectric down to 0 K [16, 17] due to both quantum effects [18, 19] and the tetragonal distortion of the cubic structure below the antiferrodistortive (AFD) structural phase transition at 105 K [20].[1] To stress the significance of the quantum effects (zero-point atomic oscillations) in the paraelectric-phase stabilization at 0 K, Müller and Burkard [17] introduced the term "quantum paraelectric" for $SrTiO_3$.

Interest in the low-temperature properties of strontium titanate is also stimulated by the observation of structural, dielectric, and ultrasonic anomalies at $T = T_{q1} \cong 30$–40 K [26–31] and $T_{q2} \cong 65$ K [21, 32]. Particular interest was generated by the suggestion of the existence of a new phase in $SrTiO_3$ below 37 K [27]. While more than one conjecture has been put forward on the nature of the Müller state [29–31, 33–35], this problem still remains unclear. There are grounds to maintain that Müller's hypothesis [30] that a coherent quantum state similar to superfluidity in liquid helium occurs in $SrTiO_3$ below 37 K finds neither experimental nor theoretical confirmation and to maintain that the observed effects are of a dynamic character [31].

The dielectric properties of $SrTiO_3$ are similar to those of the paraelectric phase of real perovskite-structure ferroelectrics ($BaTiO_3$, $PbTiO_3$, $KNbO_3$) in that there is a soft polar transverse optical (TO) mode whose frequency ω_f tends to zero with decreasing temperature

[1] At T_a = 105 K, strontium titanate undergoes a second-order structural phase transition from the cubic phase with O_h^1 (*Pm3m*) symmetry to the tetragonal (nonpolar) phase with D_{4h}^{18} (*I4/mcm*) symmetry, which is accompanied by primitive-cell doubling and is associated with the condensation of a soft mode with Γ_{25} symmetry at the R point of the Brillouin zone (BZ) boundary [21–25].

1063-7834/01/4308-1401$21.00

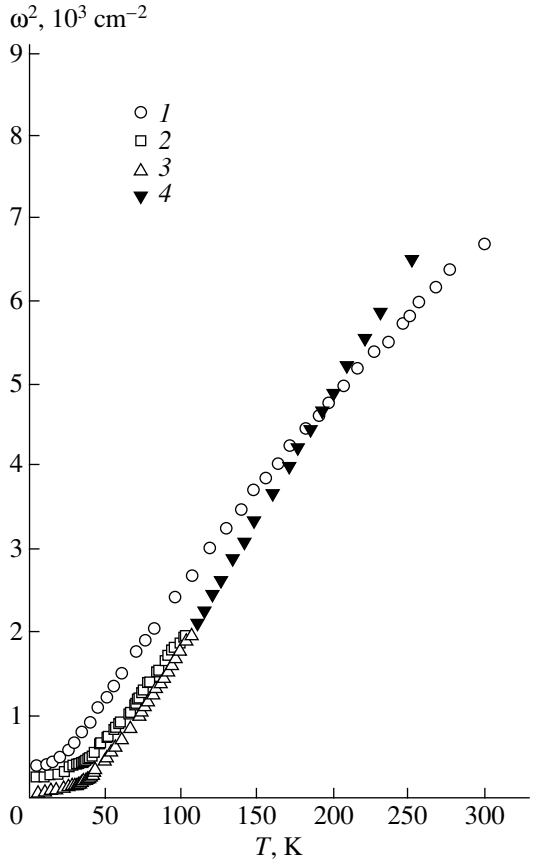

Temperature dependences of the squared frequencies of the soft FE (polar TO) mode in $KTaO_3$ [43] and $SrTiO_3$ [20]: (*1*) $\omega_f^2(T)$, F_{1u} mode in $KTaO_3$; (*2*) $\omega_{f,c}^2(T)$, A_{1u} mode in $SrTiO_3$; (*3*) $\omega_{f,a}^2(T)$, E_u mode in $SrTiO_3$; and (*4*) $\omega_f^2(T)$, F_{1u} mode in $SrTiO_3$.

[20, 36–43] and in that one observes an anomalous growth of the low-frequency permittivity ε for $T \longrightarrow 0$ K [16, 17, 32, 44–52]. The potassium tantalate $KTaO_3$, which retains cubic symmetry down to 0 K, exhibits similar but not so strongly pronounced dielectric properties. This compound also features a soft ferroelectric (FE) mode whose frequency tends to zero with decreasing temperature [43, 53–56] and exhibits an anomalous growth of ε with $T \longrightarrow 0$ K [48, 57–61].

The calcium titanate $CaTiO_3$ is a noncubic crystal below 1580 K [62], and its permittivity exhibits a behavior typical of incipient ferroelectrics at low temperatures [63–65].

Experimental data on $\varepsilon(T)$ and $\omega_f(T)$ obtained for $SrTiO_3$ and $KTaO_3$ show that both compounds are characterized by a temperature T_1 above which $\varepsilon(T)$ follows the Curie–Weiss law $B + C/(T - T_0)$ and that the squared soft-mode frequency scales linearly with temperature as $A(T - T_0)$. For $SrTiO_3$, $T_1 \approx 100$ K and $T_0 \approx 40$ K [20, 50].[2] The data on $\varepsilon(T)$ obtained for $KTaO_3$ yield $T_1 \approx 30$ K and $T_0 \approx 4 \pm 2$ K [58], and the data on $\omega_f(T)$ [43] suggest similar values of T_1 and T_0. The temperature dependences $\omega_f^2(T)$ for $SrTiO_3$ and $KTaO_3$ [20, 43] are shown graphically in the figure.

As the temperature drops below T_1, a deviation from the Curie–Weiss law is observed, namely, the growth of $\varepsilon(T)$ and falloff of $\omega_f^2(T)$ slow down. As a result, the soft FE mode remains stable down to 0 K and $\varepsilon(T)$ reaches values of $\varepsilon_a = 41900$ and $\varepsilon_c = 9380$ in $SrTiO_3$ [49] and $\varepsilon = 3800$ in $KTaO_3$ [60], while varying only slightly in the immediate vicinity of 0 K [16, 17].

A characteristic feature of displacive ferroelectrics is the anomalous behavior of the single-phonon contribution to the permittivity [66–68], which can be written as[3]

$$\varepsilon(T) = \varepsilon_r + \frac{\lambda_f}{\omega_f^2(T)}, \qquad (1)$$

where ε_r is the sum of the electronic contribution (ε_∞) and of the contributions due to the other (high-frequency) polar TO modes and λ_f is the oscillator strength of the soft polar TO mode. Equation (1) relates not only $\varepsilon(T)$ with $\omega_f^2(T)$ but also $\varepsilon(X)$ with $\omega_f^2(X)$, where X is a variable characterizing the state of the system acted upon by a static perturbation, which can be external pressure, uniform electric field, the concentration of impurity atoms (including isotopes), etc.

Theory suggests that in the situation considered here, one can neglect the dependence of the other quantities (ε_r, λ_f) on T and X [68] (for more details, see Section 2). Most available experimental data support this suggestion.

The effect of various factors on the low-temperature dielectric properties of $SrTiO_3$ and $KTaO_3$ has been dealt with in many papers. The influence of the electric field on the properties of $SrTiO_3$ was studied in [32, 45, 46, 51, 52]. Study of the effect of hydrostatic pressure on the properties of $SrTiO_3$ and $KTaO_3$ [48, 59, 60] revealed that the permittivity decreases under pressure. At the same time, it was found [49, 61, 69] that uniaxial pressure can induce an FE phase transition in these compounds. Many papers have reported on the investigation of the effect of isoelectronic impurities on the properties of $SrTiO_3$ and $KTaO_3$; they showed that even very low (but finite) concentrations of impurity atoms

[2] Viana *et al.* [50] showed that parameterization of the $\varepsilon(T)$ relation made using the Curie–Weiss law for the temperature region above $T_1 > 100$ K yields the above value of T_0, while parametrization performed at temperatures $50 < T < 100$ K leads to $T_0 = 20$ K.

[3] The thermodynamic approach based on the free energy formulates the theory in terms of force constants corresponding to the limiting TO modes (see Section 2).

are capable of transforming a solid solution into a low-temperature ferroelectric [70–85].

The influence of isotopic oxygen substitution, $^{16}O \longrightarrow {}^{18}O$, on the dielectric properties of $SrTiO_3$ was also studied [86–88]. It was found that for ^{18}O concentrations above 37%, strontium titanate becomes a low-temperature ferroelectric and that when ^{18}O is substituted completely for ^{16}O, the Curie temperature[4] T_C reaches 23 K.

These and many other phenomena observed in $SrTiO_3$ and $KTaO_3$ at low temperatures are characterized by deviations of the temperature, concentration, and other dependences from the relations predicted by classical theory. These deviations are conventionally related to the quantum effects associated with the transition from classical to quantum statistics as one approaches absolute zero. This review discusses the theory of quantum effects in incipient and low-temperature ferroelectrics and its application to the description of some phenomena observed in $SrTiO_3$, $KTaO_3$, and related solid solutions.

Section 2 considers the problems associated with general theory and the theories of quantum effects in terms of the Devonshire–Slater–Barrett single-ion (one-sublattice) model [18, 89, 90] and in terms of the soft FE (polar TO) mode dressed via the anharmonic interaction with zero-point and thermal lattice vibrations [19, 91]. Section 3 discusses specific features of the FE phase transition induced in incipient ferroelectrics by isoelectronic impurities. Section 4 deals with the theory of the isotopic-impurity-induced FE phase transition in incipient ferroelectrics and of the isotopic shift of the Curie point in low-temperature ferroelectrics. Section 5 is devoted to the electric-field effect on the dielectric properties of incipient and low-temperature ferroelectrics.

2. MICROSCOPIC THEORY

Consider the free energy $\mathcal{F}$ of a displacive ferroelectric as a function of the temperature and amplitude of the FE soft mode $\mathbf{x}_f$, which we consider to be an order parameter. The Landau expansion of $\mathcal{F}(\mathbf{x}_f)$ for a clamped crystal can be presented in the form [68][5]

$$\mathcal{F}(T, \mathbf{x}_f) = \frac{1}{2}k_f(T)\mathbf{x}_f^2 + \mathcal{F}^{ah}(\{\mathbf{x}_f\}) - v_0\mathbf{PE}, \quad (2)$$

where $k_f(T)$ is a generalized force constant corresponding to the soft mode, $\mathcal{F}^{ah}$ includes the anharmonic expansion terms, v_0 is the primitive-cell volume, and the electric polarization is given by the expression [68, 93]

$$\mathbf{P} = \frac{e}{v_0}\hat{\mathcal{Z}}(f)\mathbf{x}_f + \hat{\kappa}_\infty\mathbf{E}, \quad (3)$$

which is valid in the linear electronic-response approximation [94–96]. Equations (2) and (3) are completely equivalent to the Ginzburg–Devonshire expansion [89, 97] for a clamped crystal.

The low-frequency dielectric properties of displacive ferroelectrics are described by the single-phonon contribution to the permittivity, which, taking into account Eqs. (2) and (3), can be represented in the form (for the cubic paraelectric phase)

$$\varepsilon(T) = \varepsilon_r + \frac{\mathcal{Z}^2(f)k_v}{k_f(T)}, \quad k_v = \frac{4\pi e^2}{v_0}. \quad (4)$$

The properties of the coefficient $k_f(T)$ of the quadratic term in expansion (2), which is a generalized force constant corresponding to the soft FE (polar TO) mode, play a significant role in many phenomena associated with ferroelectric properties.

We will discuss below the structure and microscopic nature of $k_f(T)$, as well as the behavior of k_f, in the presence of various perturbations in the low-temperature domain, where the quantum effects become essential. In accordance with the general principles of the theory of lattice dynamics [68, 93], $k_f(T)$ can be represented as the sum of the harmonic force constant k_h and of the temperature-dependent anharmonic term $k_{ah}(T)$:

$$k_f(T) = k_h + k_{ah}(T). \quad (5)$$

In view of Eq. (A.5), k_h does not depend on temperature and nuclear mass, whereas k_{ah} is governed by the anharmonic interaction with zero-point and thermal lattice vibrations [68, 99, 100] and depends on the temperature and atomic mass. As follows from the experimental $\omega_f(T)$ and $\varepsilon(T)$ relations, the $k_{ah}(T)$ term is positive for soft polar TO phonon modes in crystalline dielectrics for $T \geq 0$ K.[6] One can extract the zero-point vibration contribution k_{zp} (which does not vanish in the $T \longrightarrow 0$ K limit) from the anharmonic term and, on combining it with k_h, recast $k_f(T)$ as [68]

$$k_f(T) = k_0 + \Delta k_{ah}(T), \quad (6)$$

where

$$k_0 = k_h + k_{zp}, \quad k_{zp} > 0,$$
$$\Delta k_{ah}(T > 0\text{ K}) > 0, \quad \Delta k_{ah}(0\text{ K}) = 0. \quad (7)$$

It is usually assumed that in displacive ferroelectrics, the anharmonic interaction among phonons is weak (meaning that the coupling constants are small)

[4] We understand by the Curie temperature the temperature of a real second-order ferroelectric phase transition.

[5] Vaks [68] introduces polar optical displacements through Jacobi coordinates depending on the nuclear masses. This way is no longer convenient when one considers some other problems, for instance, the isotopic effect. The approach described in the appendix, which was used in [92] for the case of zero temperature, is more adequate to our task.

[6] This property is not universal for all optical modes, because, as shown by experiments, in normal dielectrics, the temperature coefficient $\partial\omega(T)/\partial T$ is negative for optical modes and $\partial\varepsilon(T)/\partial T > 0$ [96].

Table 1. Classification of the dielectric properties of materials with respect to the magnitude of their force constants k_h, k_{zp}, and $k_0 = k_h + k_{zp}$

Class of compounds	k_h	k_{zp}	k_0
Incipient displacive FEs	$\gtrless 0$	>0	>0
	$\lvert k_h\rvert \ll k_{at}$	$\ll k_{at}$	$\ll k_{at}$
Incipient displacive FEs (quantum paraelectrics)	<0	>0	>0
	$\lvert k_h\rvert < k_{zp}$	$\ll k_{at}$	$\ll k_{at}$
Low-temperature displacive FEs	<0	>0	<0
	$k_{zp} < \lvert k_h\rvert \ll k_{at}$	$\ll k_{at}$	$\lvert k_0\rvert \ll k_{zp}$
High-temperature displacive FEs	<0	>0	<0
	$k_{zp} \ll \lvert k_h\rvert \simeq k_{at}$	$\ll k_{at}$	$\lvert k_0\rvert \approx \lvert k_h\rvert \simeq k_{at}$

[68]. For $SrTiO_3$ and $KTaO_3$, this is confirmed both by the smallness of the damping constants for the soft FE modes in these compounds [43] and by calculations of the anharmonic corrections to the soft phonon mode frequencies in $SrTiO_3$ [101]. This means that the anharmonic corrections to the force constants are small compared to the corresponding atomic estimates [68]:

$$k_{zp}, \Delta k_{ah}(T) \ll k_{at}, \quad k_{at} = \frac{e^2}{r_0^3}, \tag{8}$$

where r_0 is the minimum interatomic distance. In perovskites, $k_{at} \approx 2$ eV/Å^2 [102, 103]. In contrast to $k_{ah}(T)$, the values of the harmonic force constant k_h for the polar TO phonon modes can range from $\simeq k_{at}$ (normal dielectrics) to approximately $\simeq -k_{at}$ (high-temperature ferroelectrics).

Table 2. Harmonic force constants k_h and frequencies ω_h of the cubic phase of perovskite compounds obtained from *ab initio* calculations

Compound	k_h, eV/Å^2	ω_h, cm^{-1}
$CaTiO_3$	–2.23[a]	153i[c]
		140i[d]
$SrTiO_3$	–0.175[a]	41i[c]
$BaTiO_3$	–3.401[a]	72i[e]
		178i[c]
		219i[f]
$PbTiO_3$	–2.507[a]	125i[g]
		144i[c]
$KTaO_3$	0.48[b]	80[b]
		61i[h]
$KNbO_3$	–2.993[a]	115i[j]
		143i[c]
		203i[h]
		147i[k]
		197i[l]

Note: [a] [92], [b] [104], [c] [105], [d] [106], [e] [107], [f] [108], [g] [109], [h] [110], [j] [111], [k] [112], [l] [113].

Depending on the actual magnitude of k_h for the soft FE phonon mode, one may conceive various situations, which are shown in Table 1. For illustration, Table 2 lists the values of the force constants k_h [92, 104] and the soft FE mode frequencies calculated from first principles in the harmonic approximation [104–113] for the cubic phases of a number of perovskite-structure transition-metal oxides, which are real or incipient ferroelectrics. For all compounds (except $KTaO_3$, as follows from [104]), calculations predict an FE instability of the cubic phase at 0 K, which becomes manifest in the negative values of the force constants k_h and imaginary values of the frequencies ω_h. Note that, in all cases, except $SrTiO_3$, theory predicts a strong FE instability of the cubic phase ($k_h \simeq -k_{at}$), which should manifest itself in the existence of a high-temperature FE phase transition in these compounds. It is known that $BaTiO_3$, $PbTiO_3$, and $KNbO_3$ are high-temperature ferroelectrics, while in $CaTiO_3$, there is no FE phase transition [1].

Analysis of the experimental data on $SrTiO_3$ [20] (see Section 4) shows that, in the absence of an antiferrodistortive structural phase transition at 105 K, the soft FE mode should loose its stability at $T \approx 30$ K; this is in full agreement with the theoretical calculations (see Table 2). The tetragonal distortion of the lattice below 105 K stabilizes the soft FE mode and transforms the strontium titanate into a quantum paraelectric in the tetragonal phase. The term quantum paraelectric was introduced in [17], but the fact that the zero-point vibration contribution to $k_f(T)$ stabilizes the paraelectric phase at 0 K and is capable of suppressing the low-temperature FE phase transition predicted by classical theory was also understood by the authors of earlier works [68]. The experimental data accumulated on $\omega_f(T)$ in $KTaO_3$ [43, 53, 55, 56] show that $\lvert k_h\rvert \ll k_0$, so that this compound is an incipient ferroelectric but, perhaps, is not a quantum paraelectric or is just at the boundary of this state.

The difference between the properties of the soft FE mode in $SrTiO_3$ and $KTaO_3$ at 0 K is more important

than the purely terminological question of whether the potassium tantalate is a quantum paraelectric or not. In $SrTiO_3$, we have $\omega_0^2 = \omega_f^2(0\text{ K}) = \omega_h^2 + \omega_{zp}^2 \ll |\omega_h^2|, \omega_{zp}^2$. According to [20], in $SrTiO_3$ $\omega_{0,a} = 7.6$ cm^{-1}, $\omega_{h,a}^2 \approx -1370$ cm^{-2} (see figure), and $\omega_{zp} \approx 35.4$ cm^{-1} (the mode being considered is of E_u symmetry; for more details, see Section 4). At the same time, $KTaO_3$ features another limiting case: $|\omega_h| \ll \omega_{zp}$ and $\omega_0 \approx \omega_{zp}$. According to [43], in $KTaO_3$, $\omega_0 \approx 20$ cm^{-1} and extrapolation of the linear part of the experimental $\omega_f^2(T)$ curve yields a close-to-zero value of ω_h^2 (see figure). Thus, in $SrTiO_3$ there is nearly complete compensation of the classical (harmonic) and quantum contributions to $\omega_f^2(0\text{ K})$, whereas $\omega_f(0\text{ K})$ in $KTaO_3$ is dominated by quantum effects. This difference was shown [114, 115] to be of fundamental significance for the isotopic effect in $SrTiO_3$ and $KTaO_3$ (for more details, see Section 4).

In $CaTiO_3$, as in $SrTiO_3$, the ferroelectric instability of the cubic phase is suppressed, because below 1580 K the calcium titanate transfers from the cubic to tetragonal phase and a structural phase transition occurs at $T \approx$ 1380 K to the orthorhombic phase with space group *Pbnm* [62]. Measurements of the temperature dependence of the permittivity in the orthorhombic phase performed at temperatures from 4 to 300 K [63–65] show a behavior of $\varepsilon(T)$ typical of incipient ferroelectrics and intermediate between potassium tantalate and rutile TiO_2 [65].

The borderline state of these three perovskites, as well as of the above-mentioned IV–VI compounds and of rutile, stresses the significance of the effect of various static perturbations (hydrostatic or uniaxial pressure, substitutional impurities, isotopic substitution of the host matrix atoms, etc.) on the low-temperature properties of these materials, because even weak perturbations can convert them from incipient to real low-temperature ferroelectrics. Consider the effect of a perturbation characterized, for instance, by a variable X, on the temperature T_C of a low-temperature FE phase transition. Because T_C is a solution to the equation

$$k_f(T_C) = 0, \tag{9}$$

the $T_C(X)$ relation can be implicitly described, taking into account Eq. (6), by the equation

$$\Delta k_{ah}(T_C) = -k_0(X), \tag{10}$$

which has a physically meaningful solution for

$$k_0(X) \le 0, \quad \text{i.e., for} \quad k_h \le -k_{zp} \le 0. \tag{11}$$

Denote by X_c the solution to the equation

$$k_0(X_c) = 0. \tag{12}$$

We readily see that X_c is the critical (threshold) value of parameter X, because X_c is, at the same time, a solution to the equation $T_C(X_c) = 0$ K. Without any loss of generality, we shall assume that $\partial k_0(X)/\partial X < 0$. In view of the above, for $X > X_c$, one can recast Eq. (10) in the vicinity of $X = X_c$ in the form

$$\Delta k_{ah}(T_C) = \mathcal{H}(X - X_c), \quad \mathcal{H} = -\partial k_0/\partial X|_{X_c} > 0, \tag{13}$$

whose solution can be represented as

$$T_C = \Delta k_{ah}^{-1}(\mathcal{H}(X - X_c)) \quad \text{at} \quad X > X_c, \tag{14}$$

where $Z = \Delta k_{ah}^{-1}(Y)$ is an inverse function to $Y = \Delta k_{ah}(Z)$. Thus, the dependence of the low-temperature FE phase transition point T_C on the variable X characterizing the magnitude of a perturbation has a singularity near the threshold value X_c. Its form is uniquely determined by the temperature dependence $k_f(T)$ or $\omega_f^2(T)$ at low temperatures and, in view of Eq. (4), is related intimately to the temperature dependence of the permittivity. We consider below the character of these dependences within the single-ion model (the Devonshire–Slater–Barrett model [18, 89, 90]) and in the theory of the soft FE (polar TO) lattice vibration mode in terms of the renormalized perturbation theory in an anharmonic interaction (the Rechester and Khmel'nitskiĭ–Shneerson theories [19, 91]) and compare them with one another and with experimental data.

In most cases, perturbation primarily affects the harmonic force constant k_h. This is due to the fact that the k_h for the soft polar TO phonon mode in strongly polar ferroelectrics, to which perovskites, rutile, and the IV–VI compounds belong [102, 103, 116–118], is of a compensation nature, unlike the derivatives of k_h with respect to parameter X which characterizes the magnitude of the perturbation. As shown in [102, 119, 120], the force constant k_h of an arbitrary polar TO phonon mode is made up of contributions due to short-range interactions, k^{sr}, and dipole–dipole intercell interaction k^{dd}:[7]

$$k_h = k^{sr} + k^{dd}, \quad k^{sr} > 0, \quad k^{dd} < 0. \tag{15}$$

Each of these contributions can be found from *ab initio* calculations. It was shown [102, 103, 116–118] that each of the two contributions to k_h for the soft FE phonon mode is anomalously large (k^{sr}, $|k^{dd}| \gtrsim 10k_{at}$), while their sum k_h, as follows from calculations [92], is anomalously small for $SrTiO_3$ ($|k_h| \lesssim 0.1k_{at}$). At the same time, from general considerations, it only appears

[7] We have in mind here the part of the dipole–dipole interaction which is regular at $\mathbf{q} = 0$ and appears in TO lattice vibrations. Sometimes, this part of the dipole–dipole interaction is included in the short-range contribution [68, 140], with the long-range forces considered as relating to the interaction via the macroscopic electric field which is generated in LO lattice vibrations for $\mathbf{q} \neq 0$. Actually, this is impermissible, because the regular part of the dipole–dipole interaction also has a long-range character [93, 102, 119, 120].

reasonable to expect that, because k^{sr} and k^{dd} are of different nature, their derivatives with respect to parameter X, which characterizes the magnitude of a perturbation, not feature such a strong compensation. In section 3, we are going to use the FE phase transition induced by doping isoelectronic impurities into incipient ferroelectrics as an example to illustrate this situation in more detail.

A particular case is a quantum paraelectric with nearly complete compensation of the two above contributions to k_0, such that $k_0 \ll |k_h| \approx k_{zp}$ (this situation is realized in $SrTiO_3$). In this case, the magnitude of k_0 is strongly affected by small changes in both k_h and k_{zp}. The latter occurs in isotopic substitution for the host atoms. The harmonic force constant k_h is virtually independent of nuclear mass [93], and, in the domain where classical statistics hold, this dependence does not exist even in the most general description of interatomic interaction. Thus, the effect of isotopic substitution on $k_f(T)$ is limited to the region of fairly low temperatures, where quantum effects become essential, and is associated with the dependence of the zero-point contribution k_{zp} on the atomic mass. The corresponding theory was put forward in [114, 115] and will be discussed below in more detail.

2.1. Single-Ion Model

Consider the simplest microscopic theory of quantum effects in low-temperature and incipient ferroelectrics that provides an adequate description. The theory is based on the single-ion (one-sublattice) model used in the mean-field approximation. In the single-ion model, the atoms of all sublattices except one, for example, sublattice B, are fixed in their equilibrium positions and each atom on sublattice B behaves as an independent harmonic oscillator with a small anharmonic term added to the potential energy. The oscillators are coupled only through the mean internal electric field induced by the average displacement of sublattice B. The single-ion model was used by many authors to describe the FE phase transition in displacive ferroelectrics [18, 68, 89, 90, 121, 122]. Like all strongly simplified models, the single-ion approximation has a fairly limited applicability to real materials and yields an inaccurate description, both quantitatively and qualitatively, of some of their properties. At the same time, this model offers an understanding of the essence of the matter without recourse to complex techniques employed in renormalized perturbation theory in anharmonic interactions for the soft FE phonon mode. Within this approach, using the quantum-mechanical theory of the harmonic oscillator, Barrett [18] obtained the well-known expression for the low-frequency permittivity ε [see Eq. (22)] by generalizing the theory of Devonshire and Slater [89, 90] to the case of low temperatures. The work of Barrett was inspired to a considerable extent by the measurements of the temperature dependence of ε in $SrTiO_3$ [16] and $KTaO_3$ [57] in the 1.3- to 300-K temperature interval. These measurements revealed a deviation (a slowing down of the rise) of the temperature dependence of ε from the Curie–Weiss law for $T \lesssim 50$ K in both compounds, and in $SrTiO_3$, one observed, in addition, saturation of the $\varepsilon(T)$ dependence below 4 K.

Barrett's relation is used widely to describe the influence of quantum effects on the temperature dependence of ε_0 in low-temperature and incipient ferroelectrics [2, 17, 20, 44–46, 48, 59, 60, 65, 123], on the temperature dependence of the order parameter at low temperatures for displacive phase transitions [124], and on the dependence of the transition point T_C on pressure, impurity concentration, and other parameters characterizing the state of the system [125]. It appears of interest to discuss the results yielded by Barrett's theory for the phenomena occurring in ferroelectrics at low temperatures and to find the bounds of its applicability. The Hamiltonian in this model can be written in the form [68]

$$H = H_0 + W_{ah}, \quad H_0 = \frac{p^2}{2m} + W_h(\mathbf{u}), \tag{16}$$

$$W_h(\mathbf{u}) = \frac{a}{2}(u_1^2 + u_2^2 + u_3^2) - (V_0\bar{u} + zE)u_3 + \frac{V_0}{2}\bar{u}^2, \tag{17}$$

$$W_{ah}(\mathbf{u}) = \frac{b_1}{4}(u_1^4 + u_2^4 + u_3^4) + \frac{b_2}{2}(u_1^2u_2^2 + u_1^2u_3^2 + u_2^2u_3^2). \tag{18}$$

The free energy in the single-ion model can be presented as [18, 68, 89]

$$\mathcal{F}(T, \bar{u}, E) - \mathcal{F}_0(T) = \frac{1}{2}k_f(T)\bar{u}^2 + \frac{b_1\xi^4}{4}\bar{u}^4 - \xi z\bar{u}E, \tag{19}$$

where $\bar{\mathbf{u}} = (0, 0, \bar{u})$ is the average displacement of sublattice B and the generalized force constant $k_f(T)$ is defined by

$$k_f(T) = V_0(1 - \xi) + \xi^2 b\overline{u^2}(T), \tag{20}$$

where $b = 3b_1 + 2b_2$, $\xi = V_0/a$,

$$\overline{u^2}(T) = \frac{\hbar}{2m\Omega}\coth\frac{\hbar\Omega}{2T}, \quad \Omega = \sqrt{\frac{a}{m}}, \tag{21}$$

and m is the mass of the ferroelectrically active ion. Equations (19) and (20) directly yield the relation of

Barrett [18] for the low-frequency permittivity:

$$\varepsilon_0 - \varepsilon_\infty = \frac{C}{\frac{\hbar\Omega}{2}\coth\frac{\hbar\Omega}{2T} - T_0}. \quad (22)$$

Consider the behavior of $k_f(T)$ and $e_0(T)$ in the high- ($T \gtrsim \hbar\Omega/2$) and low- ($T \ll \hbar\Omega$) temperature domains. For $T \gtrsim \hbar\Omega/2$, one can conveniently use a high-temperature expansion in a Laurent series:

$$\frac{\hbar}{2}\coth\frac{\hbar z}{2} = \frac{1}{z} + \hbar^2\frac{z}{12} + \hbar^4\frac{z^3}{720} + \ldots \quad (23)$$

The first term in Eq. (23) does not contain the Planck constant and yields results corresponding to the classical consideration, whereas the other terms of expansion (23) are quantum corrections. At low temperatures, one can conveniently use the equality

$$\frac{1}{2}\coth\frac{z}{2} = \frac{1}{2} + \frac{1}{e^z - 1}. \quad (24)$$

Using Eqs. (23) and (24), one readily derives from Eq. (21) expressions for the mean squared amplitude of oscillations of a ferroelectrically active ion $\overline{u^2}(T)$ at high and low temperatures:

$$\overline{u^2}(T) = \begin{cases} (u^2)_{zp}\left[1 + 2\exp\left(-\frac{\hbar\Omega}{2}\right)\right], & T \ll \hbar\Omega \\ (\overline{u^2})_T\left[1 + \frac{\delta}{3} + \frac{\delta^2}{45} + \ldots\right], & T \gtrsim \hbar\Omega/2, \end{cases} \quad (25)$$

where the parameter δ is defined by

$$\delta = \frac{(\overline{u^2})_{zp}}{(\overline{u^2})_T} = \left(\frac{\hbar\Omega}{2T}\right)^2 \quad (26)$$

and

$$(\overline{u^2})_{zp} = \frac{\hbar}{2m\Omega} = \frac{\hbar}{2\sqrt{ma}}, \quad (\overline{u^2})_T = \frac{T}{a} \quad (27)$$

are the mean squared amplitudes of the zero-point and thermal oscillations of the ferroelectrically active ion, respectively. As follows from Eqs. (25) and (26), the condition for applicability of classical statistics is the inequality $\delta = (\hbar\Omega/2T)^2 \lesssim 1$.

Let us discuss the generalized force constant $k_f(T)$, which corresponds to a displacement of the sublattice of ferroelectrically active ions as a whole in a self-consistent potential, with the thermal and quantum fluctuations included. In accordance with Eq. (5), $k_f(T)$ can be represented as the sum of the harmonic force constant k_h and an anharmonic correction $k_{ah}(T)$, which, in view of Eqs. (20) and (21), are defined by the expressions

$$k_h = V_0(1 - \xi), \quad k_{ah}(T) = \xi^2 b\frac{\hbar}{2m\Omega}\coth\frac{\hbar\Omega}{2T}. \quad (28)$$

Using Eq. (24), one can extract from the anharmonic term the zero-point contribution k_{zp}, which does not vanish in the $T \longrightarrow 0$ K limit, and, on combining it with k_h, represent $k_f(T)$ in the form of Eqs. (6) and (7), where

$$k_{zp} = \frac{\hbar\xi^2 b}{2\sqrt{ma}}, \quad \Delta k_{ah}(T) = 2k_{zp}\mathcal{N}\left(\frac{\hbar\Omega}{2T}\right), \quad \mathcal{N}(x) = \frac{1}{e^x - 1}. \quad (29)$$

Taking into account Eqs. (23) and (24), one can obtain the following expressions for $k_f(T)$ for high and low temperatures:

$$k_f(T) = \begin{cases} k_0 + \xi b\frac{\hbar}{\sqrt{ma}}\exp\left(-\frac{\hbar\Omega}{T}\right), & T \ll \hbar\Omega \\ k_h + \frac{\xi b}{a}T, & T \gtrsim \hbar\Omega/2. \end{cases} \quad (30)$$

Equation (30) can be used to find the dependence of the low-temperature FE transition point T_C on the parameter X characterizing the state of the system in the vicinity of the critical (threshold) value X_c, which is a solution to Eq. (9). Recalling Eq. (14) and the definition in Eq. (13), we find that, in the Barrett model for $\mathcal{H} > 0$,

$$T_C(X) = \begin{cases} \hbar\Omega/\ln\frac{2k_{zp}}{\mathcal{H}(X - X_c)}, & X \geq X_c \\ 0, & X < X_c. \end{cases} \quad (31)$$

For $\mathcal{H} < 0$, the $T_C(X)$ dependence is described by Eq. (31), in which one should replace $\mathcal{H}$ with $|\mathcal{H}|$ and $X - X_c$ with $X_c - X$.

Thus, at high temperatures, $T \gtrsim \Omega/2$, Barrett's theory reduces to the Curie–Weiss law for $\varepsilon(T)$, while for low temperatures, $T \ll \Omega$, it predicts $\varepsilon(T)$ saturation following the law $\varepsilon(T) = \varepsilon(0\text{ K}) - A\exp(-\hbar\Omega/T)$. The behavior of the Curie temperature of the phase transition induced by a change in the X parameter characterizing the state of the system is predicted by Barrett's theory to have a logarithmic singularity described by Eq. (31) in the vicinity of the critical (threshold) value X_c. Note that the dependence in Eq. (31) is stronger than any power law of the kind of $(X - X_c)^\alpha$ with $0 < \alpha < 1$. The frequency Ω is usually treated as a fitting parameter. However, in the Barrett–Slater–Devonshire theory, this frequency has a definite microscopic meaning determined by expression (21), where, for instance, for the ABO_3 perovskites, the parameters m and a are respectively the mass of atom B and the harmonic force

constant for this atom which is governed by short-range forces). Using the results of nonempirical cluster calculations from [117], we find the parameters for $SrTiO_3$ to be a(Ti) ≅ 26 eV/Å^2, Ω(Ti) ≅ 380 cm^{-1}, and $\hbar\Omega$(Ti) ≅ 547 K; for $KTaO_3$, a(Ta) ≅ 43 eV/Å^2, Ω(Ta) ≅ 254 cm^{-1}, and $\hbar\Omega$(Ta) ≅ 366 K. These frequencies considerably exceed the frequency of the soft polar TO mode in these compounds at absolute zero. It will be shown below that, within a more adequate approach based on analysis of a system of anharmonically coupled lattice excitations (anharmonically interacting phonons), the contribution to $k_{ah}(T)$ due to the high-frequency phonon-spectrum branches, which possess a negligible dispersion, corresponds to Barrett's theory.

2.2. Theory of a Soft Ferroelectric Mode Renormalized by Anharmonic Coupling

A more adequate and consistent approach in the microscopic theory of displacive ferroelectrics is based on the concept of a soft polar TO branch of the lattice vibration spectrum which possesses dispersion and is coupled to all phonon branches as a result of lattice anharmonicity [68]. Anharmonic coupling gives rise to renormalization of the phonon frequencies and eigenvectors, to line broadening, and to a temperature dependence on these quantities. For weakly anharmonic crystals, a perturbation theory in anharmonic coupling was developed [67, 68, 126], which is based on temperature Green's functions and the corresponding diagrammatic technique [127]. The effect of quantum fluctuations on the properties of incipient and low-temperature ferroelectrics was considered in terms of this approach in [19, 68, 91, 101, 128–131].

Rechester [19] and Khmel'nitskiĭ and Shneerson [91] showed that the correlation effects in the quantum fluctuation region lead to logarithmic corrections to the results given by the Landau theory for cubic crystals, as is the case with uniaxial ferroelectrics in the region of classical fluctuations. Thus, in many problems, it is found sufficient to treat the soft polar TO mode in the self-consistent-phonon approximation, within which the infinite chain of coupled equations for quantities dressed by anharmonic interaction (vertices and self-energy parts of phonons) is cut off in the lowest approximation corresponding to the neglect of correlation effects (an analog of the Hartree–Fock approximation for electron systems). It was also shown [19, 91] that quantum effects markedly influence the temperature dependences of the soft TO mode frequency ω_f and the related quantities, e.g., ε, in the low-temperature domain. These results were confirmed subsequently by other authors [128–130]. In the book by Vaks [68], the results obtained in [19, 91] were formulated for the case of a real anisotropic dispersion law for the phonon branches, with inclusion of the possible crossing of the soft TO and acoustic TA branches. The temperature dependences of the soft polar TO mode and of the soft mode at the R point of the Brillouin zone were calculated quantitatively for $SrTiO_3$ [101].

As discussed in the beginning of this section, the generalized force constant for the soft FE (polar TO) mode $k_f(T)$, which enters the Landau free-energy expansion in Eq. (2), can be represented, in accordance with Eqs. (5), (6), and (7), as a sum of several contributions.

At a constant pressure, $\Delta k_{ah}(T)$ is a function of temperature and volume. Accordingly, this quantity can be represented as the sum of two contributions [60]:

$$\Delta k_{ah}(T) = [\Delta k(T)]_V + [\Delta k(V)]_T, \tag{32}$$

where the first term relates to a purely temperature correction associated with the heating of the body at a fixed volume corresponding to zero temperature, while the second term describes the purely volume contribution connected with thermal expansion. For a positive thermal expansion coefficient, this contribution is negative [60], and in $SrTiO_3$ and $KTaO_3$, it is substantially smaller than the purely temperature contribution [60, 101]. The variation of k_f with temperature at a constant volume can, in turn, be represented in the form [68, 132]

$$[\Delta k(T)]_V = \Delta^{(4)}_{f,f} + \Delta^{(3)}_{f,f} + \Delta^{(4)}_{f,a} + \Delta^{(3)}_{f,a} + \Delta_{f,r}, \tag{33}$$

where

$$\Delta^{(4)}_{f,f} = \frac{\hbar v_0}{2}\int_{ZB}\frac{d\mathbf{q}}{(2\pi)^3}\tilde{V}^{(4)}_{ff,ff}(0,0,\mathbf{q},-\mathbf{q})\frac{\mathcal{N}\left(\frac{\hbar\omega_f(\mathbf{q})}{T}\right)}{\omega_f(\mathbf{q})}, \tag{34}$$

$$\Delta^{(3)}_{f,f} = \hbar v_0\int_{ZB}\frac{d\mathbf{q}}{(2\pi)^3}\frac{\left|\tilde{V}^{(3)}_{f,fa}(0,\mathbf{q},-\mathbf{q})\right|^2\mathcal{N}\left(\frac{\hbar\omega_f(\mathbf{q})}{T}\right)}{\omega_f^2(\mathbf{q})-\omega_a^2(\mathbf{q})}\frac{}{\omega_f(\mathbf{q})}, \tag{35}$$

$$\Delta^{(3)}_{f,a} = -\hbar v_0\int_{ZB}\frac{d\mathbf{q}}{(2\pi)^3}\frac{\left|\tilde{V}^{(3)}_{f,fa}(0,\mathbf{q},-\mathbf{q})\right|^2\mathcal{N}\left(\frac{\hbar\omega_a(\mathbf{q})}{T}\right)}{\omega_f^2(\mathbf{q})-\omega_a^2(\mathbf{q})}\frac{}{\omega_a(\mathbf{q})}, \tag{36}$$

$$\Delta^{(4)}_{f,a} = \frac{\hbar v_0}{2}\int_{ZB}\frac{d\mathbf{q}}{(2\pi)^3}\tilde{V}^{(4)}_{ff,aa}(0,0,\mathbf{q},-\mathbf{q})\frac{\mathcal{N}\left(\frac{\hbar\omega_a(\mathbf{q})}{T}\right)}{\omega_a(\mathbf{q})}, \tag{37}$$

and $\Delta_{f,r}$ is the contribution of all other (high-frequency) phonon-spectrum branches to $[\Delta k(T)]_V$. The integration over $\mathbf{q}$ in Eqs. (34)–(37) is bounded by the Brillouin zone. The zero-point contribution k_{zp} can be obtained from the expression for $\Delta k_{ah}(T)$ by substituting 1/2 for N. Expressions for $[\Delta k(V)]_T$ and $\Delta_{f,r}$ can be found in Vaks' book [68].

In view of Eqs. (23) and (24), we find, for the high-temperature case ($T \gtrsim \hbar\omega_m/2$), that $k_{ah}(T) = AT$, where

the coefficient A is obtained from the expression for $\Delta k_{ah}(T)$ by replacing the $\mathcal{N}(x)$ function with $1/x$. It is easy to verify that ω_m is determined by the frequencies of the short-wavelength phonons of the five low-lying TO, TA, and LA branches. As follows from the experimental $\omega(\mathbf{q})$ relations for these modes in $SrTiO_3$ [133–136] and in $KTaO_3$ [137–140], $\hbar\omega_m \approx 100$–$150$ K for $SrTiO_3$ and $\hbar\omega_m \approx 50$ K for $KTaO_3$.

At low temperatures, $T \ll \hbar\omega_m$, the behavior of $k_f(T)$, $\omega_f(T)$, and, accordingly, $\varepsilon(T)$ is governed by quantum effects; these effects are described by the $\mathcal{N}(x)$ function on the right-hand sides of Eqs. (34)–(37). Because $\mathcal{N}(x) \propto \exp(-x)$ for $x \gg 1$, the low-frequency branches of the phonon spectrum exhibiting strong dispersion play an important part in the low-temperature limit $T \longrightarrow 0$ K. In normal dielectrics, only the acoustic branches exhibit such properties. Their contribution to $\Delta k_{ah}(T)$ is described by Eqs. (36) and (37) and by the corresponding terms in $[\Delta k(V)]_T$ and $\Delta_{f,r}$. For the soft polar TO mode of the phonon spectrum of incipient ferroelectrics, the existence of a frequency "window" $\omega_f \ll \omega_f(\mathbf{q}) \ll \omega_m$ at low temperatures leads to an additional contribution to the temperature dependences $k_f(T)$, $\omega_f(T)$, and $\varepsilon(T)$ given by Eqs. (34)–(36). These considerations were first put forward by Rechester [19] and Khmel'nitskiĭ and Shneerson [91]. These publications were also the first to report the temperature dependences of the various contributions to $\Delta k_{ah}(T)$ and showed that within the temperature window $\hbar\omega_f \ll T \ll \hbar\omega_m$, the contribution of self-interaction given in Eq. (34) greatly exceeds the contribution due to the acoustic branches and is dominant. For these temperatures, the region of wave vectors where $\omega_f(\mathbf{q})$ behaves as a gapless optical branch of the spectrum with an acoustic dispersion law turns out to be essential. At lower temperatures ($T \ll \hbar\omega_f$), the main contribution is due to the wave vector region in which $\omega_f(\mathbf{q}) \simeq \omega_f + s_a^2(\mathbf{n})q^2/(2\omega_f)$.

Let us first discuss the quantum effects in the temperature dependences $k_f(T)$, $\omega_f(T)$, and $\varepsilon(T)$ in incipient ferroelectrics. According to [19, 68, 91], the $\Delta_{f,f}^{(4)}(T)$, $\Delta_{f,f}^{(3)}(T)$, and $\Delta_{f,a}^{(3)}(T)$ dependences have the following form: at $\hbar\omega_f \ll T \ll \hbar\omega_m$,

$$\Delta_{f,f}^{(4)}(T) = A_{f,f}^{(4)}T^2, \quad \Delta_{f,f}^{(3)}(T) = A_{f,f}^{(3)}T^2, \quad \Delta_{f,a}^{(3)}(T) = A_{f,a}^{(3)}T^2; \tag{38}$$

in the range $T \ll \hbar\omega_f$,

$$\Delta_{f,f}^{(4)}(T) = B_{f,f}^{(4)}T^{3/2}e^{-\beta\hbar\omega_f}, \quad \Delta_{f,f}^{(3)}(T) = B_{f,f}^{(3)}T^{3/2}e^{-\beta\hbar\omega_f}, \quad \beta = 1/T, \quad \Delta_{f,a}^{(3)}(T) = B_{f,a}^{(3)}T^4. \tag{39}$$

For $T \ll \hbar\omega_m$, the temperature dependence $\Delta_{f,a}^{(4)}(T)$ has the form [19][8]

$$\Delta_{f,a}^{(4)}(T) = A_{f,a}^{(4)}T^4. \tag{40}$$

Thus, for $\hbar\omega_f \ll T \ll \hbar\omega_m$[9],

$$\Delta k_{ah}(T) = AT^2, \quad A > 0. \tag{41}$$

The T^2 scaling law described by Eq. (41) is an intermediate asymptotic dependence, which can be realized only within a limited temperature interval and with fairly stringent constraints imposed on the $\omega_f(\mathbf{q})$ relation.

Further, for $\theta_{min} \leq T \ll \hbar\omega_f$, we have

$$\Delta k_{ah}(T) = CT^4 + BT^{3/2}e^{-\beta\hbar\omega_f}, \tag{42}$$

where θ_{min} is the temperature at which the two terms on the right-hand side of Eq. (42) become equal. Finally, for very low temperatures $T \ll \theta_{min}$, we have

$$\Delta k_{ah}(T) = CT^4, \quad C = A_{f,a}^{(4)} + B_{f,a}^{(3)}. \tag{43}$$

Now, we consider the sign of the coefficient C. As follows from Eqs. (36) and (37), we have $A_{f,a}^{(4)} > 0$ and $B_{f,a}^{(3)} < 0$. Using order-of-magnitude estimates based on dimension considerations [68], it can be shown that $A_{f,a}^{(4)}/|B_{f,a}^{(3)}| \approx k_f/k_{at} \ll 1$, whence it follows that $C < 0$. This supports the result presented in [68, 91]. Thus, the temperature dependences $k_f(T)$ and $\omega_f(T)$ have a minimum and $\varepsilon(T)$, accordingly, has a maximum near 0 K. The conclusion that the coefficient C is negative (or rather that $\partial\varepsilon/\partial T$ is positive near 0 K) was drawn from thermodynamic considerations by Fröhlich in [141]. This effect, however, is rather small, even though the well-known paper of Müller and Burkard [17] reports on the presence of a weakly pronounced maximum in the $\varepsilon(T)$ curve obtained for $SrTiO_3$ at 3 K. A weakly pronounced maximum in the temperature dependence of ε for $SrTiO_3$, which shifted with increasing pressure toward higher temperatures, was also observed in [88].

Now, we consider the contribution $\Delta_{f,r}$ of the high-frequency branches of the spectrum, which is usually deemed insignificant. This contribution contains the terms described by Eqs. (34)–(37), with the $(f, \mathbf{q})$ branch on their right-hand sides replaced by one of the high-frequency branches $(r, \mathbf{q})$ of the phonon spectrum. Let us assume that an $(r, \mathbf{q})$ branch is characterized by negligible dispersion and has a frequency ω_r. One can readily verify that the contribution of such a dispersionless branch to $k_{ah}(T)$ contains terms proportional to $(\hbar/\omega_r)\coth(\hbar/\omega_r/2T)$ and similar to expression (28) for $k_{ah}(T)$ in Barrett's theory. There is a certain analogy between the approaches of Einstein and Debye in the theory of low-temperature heat capacity, on the one hand, and the Barrett–Rechester and Khmel'nitskiĭ–Shneerson approaches in the theory of low-temperature

[8] In [68, 91], this contribution was not considered.

[9] It can be shown that the ratio of corrections in Eq. (40) and in Eq. (38) is of the order of $((T/\hbar\omega_m)^2$; therefore, the T^2 scaling is dominant.

and incipient displacive ferroelectrics, on the other. The quasi-Barrett contributions of the high-frequency branches to $k_{ah}(T)$ at low temperatures are negligible compared to the corrections in Eqs. (25) and (27). At the same time, the high-frequency branch contributions give rise to quantum corrections (which depend on atomic masses) to k_f over a broader temperature region, $T \ll \hbar\omega_r$, than the low-frequency ones, because $\hbar\omega_r$ reaches values of the order of 1000 K in perovskites, for instance, for the high-frequency LO phonon branch that exhibits weak dispersion. It is possibly these quasi-Barrett contributions to $k_{ah}(T)$ that account for the isotopic effect observed in $BaTiO_3$ [142], as well as for the influence of quantum effects on the temperature of the FE phase transition in barium titanate reported in [143].

Now, we consider the temperature dependences $k_f(T)$, $\omega_f(T)$, and $\varepsilon(T)$ in the paraelectric phase of a low-temperature ferroelectric with $T_C \ll \theta_D \cong \hbar\omega_m$. At the Curie temperature defined by Eq. (9), the soft FE (polar TO) mode becomes a gapless optical mode with an acoustic dispersion law. As a result, from Eq. (41), we obtain that in a low-temperature displacive ferroelectric with $T_C \ll \theta_D \cong \hbar\omega_m$ [19, 91]

$$\Delta k_{ah}(T_C) = AT_C^2, \quad A > 0. \tag{44}$$

Thus, taking into account Eqs. (6), (9), (44), and (41), we find that in the paraelectric phase near the Curie point

$$k_f(T) = A(T^2 - T_C^2)$$
$$= \begin{cases} 2AT_C(T - T_C), & \text{for } T \longrightarrow T_C, \quad T_C > 0 \\ AT^2, & \text{for } T_C = 0. \end{cases} \tag{45}$$

Rechester [19] showed that, in the region of quantum fluctuations, the inclusion of correlation effects leads to logarithmic corrections to the results obtained by the theory of self-consistent phonons, with Eq. (45) replaced by

$$k_f(T) = A\frac{T^2 - T_C^2}{1 + 3g\ln(\theta_D^2/T^2)} \tag{46}$$
$$= \begin{cases} 2AT_C\dfrac{T - T_C}{1 + 3g\ln(\theta_D^2/T_C^2)}, & \text{for } T \longrightarrow T_C, \quad T_C > 0 \\ AT^2/\ln\dfrac{\theta_D}{T}, & \text{for } T \longrightarrow 0\ \text{K}, \quad T_C = 0, \end{cases}$$

where g is a dimensionless anharmonic coupling constant defined in [19].

With Eq. (4) for ε these results show that in the region of quantum fluctuations, the correlation effects do not affect the critical susceptibility exponent; in other words, at a low-temperature FE phase transition with $\theta_D \gg T_C > 0$, the temperature dependence of the permittivity in the paraelectric phase obeys the Curie–Weiss law [19, 91]. Quantum fluctuations become significant in the borderline case with $T_C = 0$ K [as follows from Eqs. (46) and (4), in this case, the critical susceptibility exponent is $\gamma = 2$], as well as in incipient ferroelectrics [19, 91]. Using Eq. (44), one can derive the dependence of the low-temperature FE phase transition point T_C on X, (the parameter characterizing the state of the system) in the vicinity of the critical (threshold) value X_c, which is the solution to Eq. (12).

Recalling Eq. (14) and the notation introduced in Eq. (13), we find that the theory under consideration yields, for $\mathcal{H} > 0$ [19, 91, 128–130][10],

$$T_C(X) = \begin{cases} B\sqrt{X - X_c}, & B = \sqrt{\mathcal{H}/A}, \quad \text{for } X \geq X_c \\ 0, & \text{for } X < X_c. \end{cases} \tag{47}$$

For $\mathcal{H} < 0$, the $T_C(X)$ dependence is described by Eq. (47), in which one should replace $\mathcal{H}$ with $|\mathcal{H}|$ and $X - X_c$ with $X_c - X$.

Taking into account the definition of the critical point, as well as Eqs. (46) and (4), we find that, for $T \ll \theta_D$,

$$\varepsilon(T, X_c) - \varepsilon_r = B\frac{1 + 3g\ln(\theta_D^2/T^2)}{T^2}. \tag{48}$$

The permittivity should follow such a dependence, in particular, in the solid solutions considered in Sections 3 and 4 for the compositions corresponding to the critical concentration x_c [144].

3. IMPURITY-INDUCED PHASE TRANSITION IN INCIPIENT FERROELECTRICS

Consider the important case of an FE phase transition induced in an incipient ferroelectric by isoelectronic impurities. The most well-known examples of such compounds are $Pb_{1-x}Sn_xTe$ [145], $Sr_{1-x}A_xTiO_3$ (A = Ca, Ba, Pb, Cd) [70, 75–85], $K_{1-x}Li_xTaO_3$, and $KTa_{1-x}Nb_xO_3$ [71–74]. These compounds are characterized by a critical (threshold) concentration x_c, above which they become ferroelectrics with a Curie temperature dependent on concentration as $T_C(x) = A(x - x_c)^\alpha$. For $Sr_{1-x}A_xTiO_3$ (A = Ca, Ba, Pb, Cd) and $KTa_{1-x}Nb_xO_3$, it was found that in the vicinity of x_c, i.e., for low T_C, $\alpha \cong 1/2$ [70, 71, 75–85]; this is in full agreement with the theoretical predictions for low-temperature displacive ferroelectrics in Eq. (47) [19, 91, 128–130].

However, the nature of the impurity-induced FE phase transition in perovskites remains unclear. The model of an off-center impurity ion moving in a multiwell potential is very popular. Interaction between the impurity-ion dipole moments via a soft polar TO mode can give rise both to the formation of a dipole glass phase and to the transition to the FE state [73]. This sit-

[10]The (X_c, 0 K) point is critical on the (X, T) plane, because it is here that the second-order phase transition line $T_C(X)$ described by Eq. (47) starts (or ends).

uation occurs in $K_{1-x}Li_xTaO_3$ [72, 73]. However, the applicability of this approach to the other perovskites with isoelectronic impurities considered here [146] and to $Pb_{1-x}Sn_xT$ remains questionable.

A cluster *ab initio* calculation of the potential acting upon an impurity atom was made [147] using the Hartree–Fock–Roothaan nonempirical method [148] under the assumption that the host matrix atoms are fixed in their equilibrium positions in a cubic perovskite lattice.[11] For comparison, similar calculations were also carried out for the host atom replaced by an impurity atom, as well as for an impurity atom in a like compound (for instance, for an impurity Ca in the *A* position in $SrTiO_3$, for a Sr atom in cubic $SrTiO_3$, and for a Ca atom in cubic $CaTiO_3$). Calculations performed for the compounds listed in Table 3 show that the impurity atoms and the corresponding host atoms move in a single-well, weakly anharmonic potential. The harmonic part of the potential is described by the force constant k^{sr}, whose values are given in Table 3.[12] One readily sees that the shape of the potential for impurity atoms is close to that for the corresponding host atoms and for impurity atoms in the like compound. For instance, while there is a certain softening of k^{sr} for the Ca impurity in $SrTiO_3$ compared to the force constant for Ca in $CaTiO_3$, this softening is small. Note that the relaxation in the nearest environment of an impurity atom only reduces the difference between the values of k^{sr} for the impurity atom in the unlike and like compound. The situation with the Nb impurity in $KTaO_3$ is particularly interesting. In contrast to the widespread belief that Nb in $KTaO_3$ is an off-center impurity [74], calculations reveal (Table 3) that an impurity Nb atom feels uncomfortably tight in the $KTaO_3$ lattice. Note that the values of k^{sr} for the Nb atom in $KNbO_3$ and $KTa_{1-x}Nb_xO_3$ and for the Ta atom in $KTaO_3$ exceed the atomic force constant for perovskites by more than an order of magnitude, $k_{at} = e^2/r_0^3 \approx 2$ eV/Å^2, where $r_0 \approx 2$ eV is the smallest interatomic distance in perovskites.

The neglection of quantum effects, which play an important role at impurity concentrations close to x_c, is another serious drawback of present-day theoretical approaches. The compounds under consideration can be treated as solid solutions of two isomorphic compounds [76–85]. For instance, $Sr_{1-x}A_xTiO_3$ can be represented in the form $(1-x)SrTiO_3 + xATiO_3$. Viewed from this standpoint, the approach based on describing a solid solution in first approximation as an ideal crystal with the mean values of the parameters determined by Vegard's law appears more adequate. This approach yielded [147] a simple expression for the critical concentration x_c through the parameters of the host (solvent) and the solute, which automatically takes into account the effect of the quantum fluctuations (zero-point atomic oscillations) on x_c. The derivation of the expression for x_c used in [147] is based on condition (12) for a solid solution:

$$k_{0,\,ss}(x_c) = 0, \tag{49}$$

where $k_{0,\,ss} = k_{f,\,ss}(T = 0\ \mathrm{K}) = k_{h,\,ss} + k_{zp,\,ss}$ is a generalized force constant corresponding to the FE soft mode in the paraelectric phase of the solid solution at 0 K. As follows from Eqs. (6), (7), and (10), the condition $T_C^{ss}(x_c) = 0$ for the Curie temperature of the solid solution T_C^{ss} is met simultaneously with condition (49).

Designating by k_m and k_i the force constants of the host matrix and the impurity (dissolved) component and using Vegard's law, one can write the following expression for $k_{0,\,ss}$:

$$k_{0,\,ss}(x) = (1-x)k_{0,\,m} + xk_{0,\,i}. \tag{50}$$

Equations (49) and (50) can be used to derive a nonempirical relation for x_c [147]:

$$x_c = \frac{k_{0,\,m}}{k_{0,\,m} - k_{0,\,i}}. \tag{51}$$

One can also write an expression for x_c similar to

Table 3. Force constants k^{sr} for atoms *A* and *A*' in ABO_3 and $ABO_3 : A'$ compounds with perovskite structure and for Ta atoms in $KTaO_3$ and Nb atoms in $KTaO_3 : Nb$ obtained from nonempirical cluster calculations [147]

Compound	Atom	k^{sr}, eV/Å^2	a_0, Å
$CaTiO_3$	Ca	7.6[a]	3.8367[c]
$SrTiO_3$	Sr	13.5[a]	3.9050[c]
$Sr_{1-x}Ca_xTiO_3$	Ca	6.4[a]	
$Sr_{1-x}Ba_xTiO_3$	Ba	19.4[a]	
$Sr_{1-x}Pb_xTiO_3$	Pb	8.6[a]	
$Sr_{1-x}Cd_xTiO_3$	Cd	3.6[a]	
$BaTiO_3$	Ba	15.9[a]	3.996[c]
$PbTiO_3$	Pb	6.8[a]	3.970[c]
$KTaO_3$	K	7.0[a]	3.9845[d]
	Ta	39.0	
$KTa_{1-x}Nb_xO_3$	Nb	35.3[a]	
$KNbO_3$	Nb	30.6[b]	4.0214[c]

Note: [a] [147], [b] [120]. a_0 is the lattice constant of the cubic phase from the data of [c] [1] and [d] [60].

[11] The clusters used were $[A1A_6B_8O_{12}(OH)_{24}]^{n-}$ for ABO_3 ($A1 = A$) and $ABO_3 : A'$ ($A1 = A'$) and $[B1B_6K_8O_6(OH)_{30}]^+$ for KBO_3 ($B1 = B$) and $KTaO_3 : Nb$ ($B1 = Nb$, $B = Ta$).

[12] Similar calculations performed [147] for Li atoms in $K_{1-x}Li_xTaO_3$ and for Zn atoms in $Sr_{1-x}Zn_xTiO_3$ showed these impurities to be off-central, which agrees with the experimentally established off-center position of the Li atom in $K_{1-x}Li_xTaO_3$ [72, 73].

Table 4. Critical concentration x_c for solid solutions $Sr_{1-x}A_xTiO_3$ (A = Ca, Ba, Pb) and $KTa_{1-x}Nb_xO_3$

Compound	x_c	
	experiment	theory[e]
$Sr_{1-x}Ca_xTiO_3$	0.0018[a]	0.0026–0.0032
$Sr_{1-x}Ba_xTiO_3$	0.035[b]	0.0013–0.012
$Sr_{1-x}Pb_xTiO_3$	0.0015[c]	0.0029–0.0039
$KTa_{1-x}Nb_xO_3$	0.008[d]	0.01–0.03

Note: [a] [70], [b] [76, 77, 83], [c] [79, 83], [d] [71], [e] [147].

Eq. (51) in terms of frequencies rather than of the force constants [147]:

$$x_c = \frac{\omega_{0,m}^2}{\omega_{0,m}^2 - \omega_{0,i}^2}. \quad (52)$$

Expression (52) is more convenient than Eq. (51) for calculations, because the frequencies $\omega_{0,m}$ can be measured experimentally, unlike the corresponding force constants. For $SrTiO_3$ and $KTaO_3$, this is an essential factor, because one has to take into account the contribution of zero-point vibrations in these compounds; this has still not been calculated nonempirically (unlike the contribution in the harmonic approximation).

The solid solutions under consideration are characterized by low critical concentrations, $x_c \ll 1$ (Table 4). This imposes certain constraints on the matrix and impurity parameters:

$$k_{0,i} < 0, \quad \omega_{0,i}^2 < 0$$
$$\text{and } k_{0,m} \ll |k_{0,i}|, \quad \omega_{0,m}^2 \ll |\omega_{0,i}|^2.$$

It was shown [147] that these conditions are satisfied for the solid solutions under consideration. Table 4 presents theoretical values of x_c found in [147] by using Eq. (52). The calculations made use of the experimental values of $\omega_{0,m}$ for $SrTiO_3$ and $KTaO_3$ taken from [20, 43]. To find the $\omega_{0,i}$ frequencies for the impurity component of the solid solution, the zero-point oscillation contribution to ω_f was assumed to be of approximately the same order of magnitude in all perovskites. To estimate ω_{zp}, one can take the values for $SrTiO_3$ ($\omega_{zp} \approx 35.4$ cm^{-1}) and $KTaO_3$ ($\omega_{zp} \approx 20$ cm^{-1}) presented in Section 2. Whence, taking into account the values of ω_h given in Table 2 and the equality $\omega_0^2 = \omega_h^2 + \omega_{zp}^2$, which corresponds to Eq. (7) for the force constant k_0, we obtain that, in the cubic phases of $CaTiO_3$, $BaTiO_3$, $PbTiO_3$, and $KNbO_3$, the condition $\omega_0^2 \approx \omega_h^2$ is met. Thus, for the solid solutions under consideration, one can recast Eq. (52) in the form

$$x_c \approx \frac{\omega_{0,m}^2}{|\omega_{h,i}|^2} \quad (53)$$

and use the *ab initio* calculations of $\omega_{h,i}$ given in Table 2. The last column of Table 4 contains the bounds on the theoretical estimates of x_c obtained from Eq. (53), which take into account the spread of the values of ω_h in Table 2.

Although this model is very crude, the theoretical values of the critical concentration found in [147] sufficiently approximate the experimental situation for all solid solutions except $Sr_{1-x}Ba_xTiO_3$, while somewhat overestimating x_c. This is possibly due to the neglect of the effects associated with mutual relaxation of the host and impurity lattices in the solid solution.

Consider the concentration dependence of the permittivity in the paraelectric phase of a solid solution. For concentrations near the critical value, one can write $k_{0,ss}(x) = \mathcal{H}(x_c - x)$, where $\mathcal{H} = -\partial k_{0,ss}/\partial x|_{x_c} > 0$. Recalling Eq. (4), one can present the expression for $\varepsilon(x, T)$ near $x = x_c$ in the form

$$\varepsilon(x, T) - \varepsilon_r = \frac{\mathcal{L}^2(f)k_v}{\mathcal{H}(x_c - x) + \Delta k_f(T)} = \frac{\mathcal{C}}{x_C(T) - x}, \quad (54)$$

where $\mathcal{C} = \mathcal{L}^2(f)k_v/\mathcal{H}$ and $x_C(T) = x_c + \Delta k_f(T)/\mathcal{H} \geq x_c$ is the solution to the equation $T_C(x) = T$. The expression on the right-hand side of Eq. (54) describes the concentration dependence of the permittivity in the paraelectric phase of a solid solution at constant temperature.

4. THE ISOTOPE EFFECT

The ferroelectricity induced by the oxygen isotope exchange in $SrTiO_3$ [86–88] is an interesting effect in this compound. According to [87], $SrTi(^{16}O_{1-x}{}^{18}O_x)_3$ with $x \geq x_c = 0.36$ undergoes an FE phase transition at $T_C \approx 23$ K for $x = 1$.

To understand the nature of the ferroelectricity induced by isotope exchange, one has to learn how a change in atomic mass affects the force constant corresponding to the FE soft mode. The corresponding theory of the isotope effect in displacive ferroelectrics was proposed in [114, 115]. For brevity, we will call this effect the ferroelectric isotope effect in what follows. In contrast to the vibrational frequencies, the harmonic force constants do not depend on the atomic masses in the adiabatic approximation [93]; the generalized force constants in the region where classical statistics hold are also not dependent on the atomic mass. Therefore, even without recourse to a comprehensive microscopic theory, one can maintain that the FE isotope effect is of an anharmonic and quantum nature.

According to the quantum-mechanical theory of lattice vibrations, atoms continue to move at absolute zero by performing so-called zero-point vibrations, which provide an additional contribution to the ground-state energy [93, 149]:

$$E_{zp} = \frac{\hbar}{2N}\sum_{\alpha,\,\mathbf{q}}\omega_\alpha(\mathbf{q}), \tag{55}$$

where $\omega_\alpha(\mathbf{q})$ is the frequency of the normal lattice mode $(\alpha, \mathbf{q})$. The zero-point vibration energy E_{zp} contributes, accordingly, to the atomic force constants. This contribution stabilizes the FE soft TO mode and, hence, the paraelectric phase in $SrTiO_3$ and $KTaO_3$ at 0 K. It is significant that E_{zp} depends on the atomic masses as do the phonon frequencies by which it is determined. Thus, in accordance with the theorem of Rayleigh [149], an increase in atomic mass (for instance, due to isotope substitution) results in suppression of the zero-point vibrations, i.e., to a decrease in E_{zp}. Under certain conditions, this can give rise to the onset of FE lattice instability in the paraelectric phase at 0 K and, accordingly, to a low-temperature FE phase transition. It is easy to see that this can take place only in a quantum paraelectric (the necessary condition for an isotope-exchange-induced FE phase transition to occur) and that the upper boundary for the Curie temperature of such an isotopic-impurity-induced FE transition is the Curie temperature T_0 of the phase transition that would occur in this quantum paraelectric in the absence of quantum effects in the classical limit of infinitely heavy atomic nuclei (≈40 K in $SrTiO_3$ and ≈0 K in $KTaO_3$). These considerations suggest the most probable mechanism of the isotope effect in displacive ferroelectrics, which is of an essentially different nature than the isotopic shift of the Curie temperature caused by tunneling in hydrogen-bonded ferroelectrics of the order–disorder type, such as KDP, ADP, and RDP [68, 150, 151]. However, some aspects, which are beyond the scope of purely qualitative reasoning, require comprehensive microscopic analysis of this effect. This relates to the formulation of a criterion of the isotopic-impurity-induced FE lattice instability and to the description of the dependence of the corresponding Curie temperature on the change in atomic mass and on the concentration of the heavy isotope. For instance, in view of the existence of the small parameter $[m(^{18}O) - m(^{16}O)]/m(^{16}O) = 1/8$, one might expect the Curie temperature of the FE transition in $SrTiO_3$ caused by the $^{16}O \longrightarrow {}^{18}O$ isotope substitution to be substantially lower than the limiting Curie temperature, $T_c \ll T_0 \approx 40$ K, whereas the one observed experimentally in the strontium titanate is $T_c = 23$ K [87].

We will consider a crystal containing a mixture of two isotopes with atomic masses m_0 and $m_1 = m_0 + \delta m$ and concentrations $1 - x$ and x, respectively, distributed randomly throughout the crystal volume. For most pairs of isotopes, except those of hydrogen, the condition $|\delta m| \ll m_0$ holds. Such an isotopically disordered crystal lattice is close in vibrational properties to an ordered material with an average atomic mass $m = (1 - x)m_0 + xm_1$ [152]. We are going to consider m, subsequently, as the mass of the atom involved in the FE soft TO lattice vibration.

4.1 The Criterion for Ferroelectric Instability Induced by Isotopic Exchange

Following [114, 115], we shall discuss the conditions under which an incipient ferroelectric can become a real ferroelectric as a result of a change in atomic mass δm caused by isotopic substitution. Using Eq. (10) for the Curie temperature, we find that, in order for a phase transition to occur from the paraelectric state with a mass $m = m_0$ to the ferroelectric state with $m = m_0 + \delta m$, the following inequalities must be met:

$$k_0(m_0) = k_h + k_{zp}(m_0) > 0 \tag{56}$$

and

$$k_0(m_0 + \delta m) = k_h + k_{zp}(m_0 + \delta m) < 0. \tag{57}$$

Because $k_{zp} > 0$, inequality (57) can be satisfied only for $k_h < 0$. Considered together with condition (56), this means that an isotopic-impurity-induced FE phase transition is possible only in a quantum paraelectric (the necessary condition for the transition). Inequalities (56) and (57) also directly imply the sufficient condition

$$-\frac{\partial \ln k_{zp}}{\partial \ln m}\bigg|_{m = m_0}\frac{\delta m}{m_0} > \frac{k_0}{k_{zp}}\bigg|_{m = m_0}. \tag{58}$$

In a general case, the dependence of k_{zp} on atomic mass is very complex. However, as pointed out in [114, 115], in the framework of the single-ion model and accepting certain assumptions in terms of the soft TO mode theory, this dependence can be represented in the form $k_{zp} \propto m^{-1/2}$, whence it follows that condition (58) can be recast as

$$\frac{\delta m}{2m_0} > \frac{k_0}{k_{zp}}\bigg|_{m = m_0}. \tag{59}$$

Furthermore, the right-hand side of inequality (59) can be transformed in terms of quantities that can be extracted from analyzing experimental data:

$$\frac{\delta m}{2m_0} > \frac{\omega_0^2}{\omega_{zp}^2}\bigg|_{m = m_0}, \tag{60}$$

where $\omega^2 = k/m$, $\omega_0 = \omega_f(0\text{ K})$, and $\omega_{zp}^2 = |\omega_h|^2 + \omega_0^2$. The right-hand side of inequality (60) is positive, and for most isotopes, except those of hydrogen, its left-hand side is considerably less than unity. This implies that the isotope effect under study can take place only in quantum paraelectrics with a nearly complete compensation of the harmonic and zero-point lattice vibration contributions to $\omega_f(0\text{ K})$, and only if the atoms are replaced by their heavier isotopes.

4.2 Effect of Isotope Exchange on the Curie Temperature

Following [114], we consider a low-temperature ($T_C \ll \theta_D$) FE phase transition. In view of equalities (7), (10), and (44), one can write the expression for the Curie temperature in the form

$$T_C^2 = \frac{|k_h|}{A} - \frac{k_{zp}}{A}. \quad (61)$$

It was found [114] that

$$k_{zp} = \frac{I_1}{\sqrt{m}}, \quad A = \sqrt{m} I_2, \quad (62)$$

whence one readily obtains an expression for the Curie temperature with an explicit dependence on atomic mass m [114]:

$$T_C^2 = \frac{|k_h|}{\sqrt{m} I_2} - \frac{I_1}{m I_2}. \quad (63)$$

In the case of an isotopic-impurity-induced transition, the right-hand side of Eq. (63) is nonnegative only if $m \geq m_c$, where m_c is defined by the equation $T_C(m_c) = 0$ K, whence an expression for T_C can be derived [114]:

$$T_C = Q\sqrt{\frac{m - m_c}{m_c}}, \quad Q = \sqrt{\frac{I_1}{2 m_c I_2}}. \quad (64)$$

In [114], the isotope effect was considered within the theory of the soft FE mode, using a simplified lattice Hamiltonian with one soft polar TO phonon mode (f, **q**), with self-interaction described by a fourth-order anharmonic force constant $V^{(4)}$. In the notation introduced in Eqs. (32)–(34), the equality $\Delta k_{ah}(T) = \Delta^{(4)}_{f,f}$ holds in this approximation. Assuming that $\omega_f^2(\mathbf{q})$ has an isotropic quadratic dispersion law, i.e., that $\omega_f^2(\mathbf{q}) = \omega_f^2 + c_f^2 q^2$, the expression for the coefficient Q in Eq. (64) is considerably simplified to take on the form [114]

$$Q = \frac{\sqrt{3}}{2\pi}\hbar\omega_{f,m}, \quad \omega_{f,m} = c_f q_{max}, \quad (65)$$

where $q_{max} \approx \pi/a_0$ and a_0 is the lattice constant.

Using Eqs. (39) and (31), we also obtain an expression for $T_C(x)$ in the single-ion model [114]:

$$T_C = \frac{\hbar\Omega_c}{\ln\dfrac{4m_c}{m - m_c}}, \quad \Omega_c = \Omega(m_c). \quad (66)$$

Note that Eqs. (64) and (66) for $T_C(x)$ do not contain the corresponding anharmonic constants. It can be added that the experimental relation $T_C(x)$ is approximated well by a square-root law, as in Eq. (64).

We now consider the isotope shift of the Curie point in a low-temperature displacive ferroelectric. Let the initial state with $m = m_0$ be a ferroelectric with a Curie temperature $T_{C0} \ll \theta_D$. In this case, Eq. (63) leads to a relation for the isotope shift of the Curie temperature [114]:

$$T_C(m) - T_{C0} = \left[\frac{I_1}{m_0 I_2 T_{C0}} - T_{C0}\right]\frac{m - m_0}{4m_0}. \quad (67)$$

Unlike the isotopic-impurity-induced phase transition, the isotope shift of T_C is positive, $\partial T_C/\partial m > 0$, only for $T_{C0}^2 < I_1/(m_0 I_2)$.

4.3. Application to $SrTiO_3$ and $KTaO_3$

The oxygen atoms are the lightest in these compounds. According to [104, 133, 139], the low-frequency polar TO mode in $SrTiO_3$ and $KTaO_3$ is a Slater-type mode in which the oxygen atoms have the largest relative amplitude. This permits one to use condition (60) in analyzing the possibility of an FE isotope effect in these compounds, which is associated with ^{18}O being substituted for ^{16}O [114, 115]. This condition imposes the following constraint on the parameters of the ferroelectric soft mode at 0 K in the case of complete isotope substitution:

$$\left.\frac{\omega_0^2}{\omega_{zp}^2}\right|_{^{16}O} < \frac{1}{16}. \quad (68)$$

At the same time, using the experimental data from [20, 43], we obtain [114, 115]

$$\left.\frac{\omega_0^2}{\omega_{zp}^2}\right|_{^{16}O} \approx \begin{cases} \dfrac{1}{20} & \text{for } SrTiO_3 \\ 1 & \text{for } KTaO_3. \end{cases} \quad (69)$$

Comparison of Eqs. (69) and (68) supports the possibility of an FE isotope effect in $SrTiO_3$ (this is in full agreement with experimental data [86–88]) while excluding a similar effect in $KTaO_3$ [114, 115].

Using Eqs. (64) and (65), one can estimate the Curie temperature of $SrTi(^{18}O)_3$ [114]. Taking the parameters characterizing the dispersion law for the phonon branch (f, **q**) that are quoted in Vaks' book [68], we find that $\omega_{f,m} \cong 448$ K and, hence, $T_C(^{18}O) \cong 34$ K. This value is of the same order of magnitude as the experimental Curie temperature $T_C(^{18}O) \cong 23$ K [87] and, which is essential, does not exceed the limiting value $T_0 \approx 40$ K.

In contrast to potassium tantalate, in the case of $SrTiO_3$, a question may arise as to the effect of the AFD structural transition ($T_a = 105$ K) on the low-temperature behavior of the FE soft TO mode. In the tetragonal AFD phase of $SrTiO_3$, the soft TO mode of frequency ω_f splits at the Γ point into two modes with symmetries A_{1u} and E_u and frequencies $\omega_{f,c}$ and $\omega_{f,a}$, respectively.

As the temperature decreases, the splitting $\omega_{f,c}^2 - \omega_{f,a}^2$ grows to reach 214.5 cm^{-2} at 7 K [20]; thus, only the E_u mode satisfies inequality (60). In our case, it is essential that the lattice distortion in the tetragonal phase result in a positive shift of both $\omega_{f,c}$ and $\omega_{f,a}$ with respect to ω_f such that $\omega_{f,a}^2 = \omega_f^2 + \Delta_{AFD}$. According to [20], $\omega_{f,a}^2 = 60.84$ cm^{-2} and $\Delta_{AFD} \cong 180$ cm^{-2} at 7 K, whence it follows that $\omega_f^2 \cong -119$ cm^{-2}, i.e., that the FE soft TO mode in the cubic phase is unstable near 0 K [20]. Recalling that $\omega_f^2(0\text{ K}) = \omega_h^2 + \omega_{zp}^2$ and taking into account that $\omega_f^2(T) = \omega_h^2 + \gamma T$ for $T \gtrsim \theta_D/2$, we obtain from the data presented in [20, Fig. 4] that $\omega_h^2 \cong -1386$ cm^{-2}. We finally find that $\omega_{zp}^2 \cong 1255$ cm^{-2}; it is this that yields the above estimate for ω_0^2/ω_{zp}^2 in $SrTiO_3$. The same holds for the force constants. Hence, one can write $k_{f,a} = k_f + k_{AFD} = k_{0,a} + \Delta k_{ah}$, where $k_{0,a} = k_0 + k_{AFD} = k_h + k_{zp} + k_{AFD}$. Thus, in this case, one has to replace $|k_h|$ with $|k_h| - k_{AFD}$ in expressions (61) and (63) for T_C. In principle, quantum effects can also affect k_{AFD} and, hence, k_{AFD} can produce an additional contribution to $k_{0,a}$ associated with the isotopic substitution of oxygen atoms. However, this contribution is small compared to the direct effect of the zero-point vibrations, because, in accordance with [144], quantum fluctuations exert only an insignificant effect on the phase transition occurring at 105 K in $SrTiO_3$.

The isotope effect in strontium titanate and potassium tantalate was considered theoretically in [153]. However, the nature of this effect and its criterion in terms of physically reasonable quantities rather than of fitting model parameters was not discussed qualitatively. At the same time, the quantitative results reported in [153] were obtained by a fitting procedure within an empirical nonlinear shell model which, according to [154], is physically invalid.

5. BEHAVIOR IN AN ELECTRIC FIELD

Let us discuss the effect of an electric field on the dielectric properties of an incipient ferroelectric and a low-temperature ferroelectric in the paraelectric phase. An electric field gives rise to the appearance of a maximum in the temperature dependence of the permittivity [32, 45, 46, 51, 52] and, accordingly, of a minimum in the temperature dependence of the inverse susceptibility [36, 37, 54]. The theory of this phenomenon is stated in the paper of Hegenbarth [46] for the case of a low-temperature ferroelectric ($0 \le T_C \le \theta_D$) within the model of Barrett [18] and in the book of Lines and Glass [98] for the case of a high-temperature ferroelectric ($T_C \gtrsim \theta_D$). According to [46, 98], the maxima in the $\varepsilon(T)$ curves and, hence, the minima in $\omega_f(T)$ form in strong electric fields. This statement is not correct. Thus, it might be worthwhile to consider the theory of this phenomenon in a more general context, taking into account the results reported in [19, 91, 128–130].

Choosing the electric polarization as an order parameter, we write the free energy in the form of a Ginzburg–Devonshire expansion [89, 97]:

$$\tilde{\mathcal{F}} = \frac{\mathcal{F}}{v_0} = \frac{1}{2}a(T)P^2 + \frac{1}{4}bP^4 - EP. \qquad (70)$$

The $a(T)$ and $k_f(T)$ coefficients in expansions (70) and (2) are related through [68]

$$a(T) = \frac{4\pi}{\mathscr{L}^2(f)k_v}k_f(T), \quad k_v = \frac{4\pi e^2}{v_0}. \qquad (71)$$

The condition for the minimum free energy yields

$$E = aP + bP^3, \quad \chi^{-1} = \frac{dE}{dP} = a + 3bP^2. \qquad (72)$$

In the weak-field domain (the region of linear polarization response), the following inequalities are met:

$$bP^2 \ll a, \quad E = aP \ll E_i(T) = \left(\frac{a^3}{b}\right)^{1/2}. \qquad (73)$$

For strong fields (the nonlinear polarization response region), we have

$$bP^2 \gg a, \quad E = bP^3 \gg E_i(T) = \left(\frac{a^3}{b}\right)^{1/2}. \qquad (74)$$

Let us discuss the minimum of the inverse susceptibility. Using Eq. (72), one can find an expression for $\partial\chi^{-1}/\partial T|_{E=\text{const}}$. Equating this expression to zero yields the condition for a minimum to form in the $\chi^{-1}(T)$ curve:

$$a(T_m) = 3bP^2(T_m). \qquad (75)$$

While the condition derived in [46] and [98] is similar, it is valid only for some particular cases.

A comparison of Eq. (75) with the weak- and strong-field conditions in Eqs. (73) and (74) shows that the field E in which $\varepsilon(T)$ reaches a maximum at a temperature T_m and field $E_i(T_m)$ are related through $E = 0.77E_i(T_m)$. The intermediate field is strongly dependent on temperature ($E_i \propto a^{3/2}(T) \propto \omega_f^3(T)$). For $SrTiO_3$, we have $E_i(300\text{ K}) : E_i(77\text{ K}) : E_i(7\text{ K}) \cong 1600 : 100 : 1$. Thus, for $T \ll T_m$, the field E is strong, and for $T \gg T_m$, it is weak.

Substituting Eq. (75) into the expression for $E(P)$ in Eq. (72) yields $P^2(T_m) = (E/4b)^{2/3}$, whence one obtains the equation

$$a(T_m) = \frac{3}{4}(2\sqrt{b}E)^{2/3}, \qquad (76)$$

that describes the $T_m(E)$ dependence in an implicit form. For a high-temperature ferroelectric ($T_C \gtrsim \theta_D$),

we have $a(T) = A_1(T - T_C)$, whence one derives the well-known expression for T_m [98]

$$T_m = T_C + \frac{3}{4A_1}(2\sqrt{b}E)^{2/3}. \quad (77)$$

For a low-temperature ferroelectric ($0 \le T_C \le \theta_D$), taking into account Eqs. (71) and (45), we obtain $a(T) = A_2(T^2 - T_C^2)$, whence

$$T_m = \sqrt{T_C^2 + \frac{3}{4A_2}(2\sqrt{b}E)^{2/3}}. \quad (78)$$

For an incipient ferroelectric, we use Eq. (71) and expression (41) for $k_f(T)$ to obtain, for $\hbar\omega_f \ll T_m \ll \theta_D$,

$$T_m = \sqrt{\frac{3}{4A_2}(2\sqrt{b}E)^{2/3} - T_1^2}. \quad (79)$$

For $T_m \ll \theta_{min}$, using Eq. (71) and expression (43) for $k_f(T)$, we come to

$$T_m = \left[T_2^4 - \frac{3}{4A_3}(2\sqrt{b}E)^{2/3}\right]^{1/4}. \quad (80)$$

ACKNOWLEDGMENTS

I am indebted to V.S. Vikhnin, M.E. Guzhva, V.V. Lemanov, and P.A. Markovin for numerous insightful discussions.

This study was supported by the Russian Foundation for Basic Research, project no. 00-02-16919.

APPENDIX

FREE ENERGY OF A DISPLACIVE FERROELECTRIC

The state of a displacive ferroelectric is unambiguously determined at given external conditions by a set of long-wavelength transverse optical displacements (uniform lattice displacements) $\mathbf{u}(s)$. Dropping the terms describing the interaction of optical degrees of freedom with a homogeneous strain, the free energy of a displacive ferroelectric can be represented in the form [68]

$$\frac{F}{N} = \mathcal{F}_e[\mathbf{u}(s); T] - v_0\mathbf{PE}, \quad (A.1)$$

where N is the number of primitive cells in the crystal, $\mathbf{E}$ is the electric field, and $\mathbf{P}$ is the electric polarization, which, in the linear electron response approximation, is related to $\mathbf{u}(s)$ and $\mathbf{E}$ through [68, 93]

$$P_i = \frac{e}{v_0}\sum_{sj} Z_{ij}(s)u_j(s) + \chi^{\infty}_{ij}E_j. \quad (A.2)$$

Here, v_0 is the primitive-cell volume, $Z_{ij}(s)$ is the Born effective-charge tensor for sublattice s, and χ^{∞} is the high-frequency (electronic) susceptibility. Further, we write the free energy $\mathcal{F}_e[\mathbf{u}(s); T]$ in the form of a Landau expansion [68],

$$\mathcal{F}_e[\mathbf{u}(s); T] = \frac{1}{2}\sum_{si, tj}\Phi_{ij}(st; T)u_i(s)u_j(t) + \mathcal{F}_e^{ah}[\mathbf{u}(s)], \quad (A.3)$$

by combining the terms quadratic in $\mathbf{u}(s)$ in the first term and the higher (anharmonic) terms of the expansion in $\mathcal{F}_e^{ah}$. The matrix of the $\Phi_{ij}(st; T)$ coefficients is a generalized matrix of the optical force constants of the crystal and can, in turn, be cast in the form

$$\Phi(T) = \Phi^h + \Phi^{ah}(T), \quad (A.4)$$

where the first term Φ^h is the harmonic-approximation contribution defined by

$$\Phi^h_{ij}(st) = \left.\frac{\partial^2 E}{\partial u_i(s)\partial u_j(t)}\right|_{\mathbf{u}=0}. \quad (A.5)$$

Here, E is the adiabatic potential[13] and $\Phi^{ah}(T)$ is a fluctuation term originating from the anharmonic interaction between the zero-point and thermal lattice vibrations of the crystal [68, 99, 100]. We expand the optical displacements $\mathbf{u}(s)$ in an orthonormalized basis of eigenvectors $\mathbf{w}(s; \alpha)$ of matrix Φ:

$$\mathbf{u}(s) = \sum_{\alpha} x(\alpha)\mathbf{w}(s; \alpha). \quad (A.6)$$

Using Eq. (A.6), we obtain from Eqs. (A.1)–(A.3)

$$\mathcal{F}_e[\{x\}; T] = \frac{1}{2}\sum_{\alpha} k(\alpha; T)x^2(\alpha) + \mathcal{F}_e^{ah}(\{x\}), \quad (A.7)$$

$$P_i\big|_{\mathbf{E}=0} = \frac{e}{v_0}\sum_{\alpha}\mathcal{Z}_i(\alpha)x(\alpha),$$
$$\mathcal{Z}_i(\alpha) = \sum_{sj} Z_{ij}(s)w_j(s; \alpha), \quad (A.8)$$

where $k(\alpha)$ are the eigenvalues of the generalized force-constant matrix Φ. We consider cubic crystals. In this case, the limiting optical modes (the eigenmodes of the force-constant matrix) are triply degenerate and are characterized by the mode number n and three mutually perpendicular polarizations, which can be chosen to lie along the principal crystal axes; i.e., $\alpha = (n, k)$, where

[13] By the adiabatic potential is indicated the ground-state energy of a system of atomic nuclei and electrons, which is considered a function of the coordinates of atomic nuclei under the assumption that the nuclei are classical particles (i.e., that their masses are infinite) [68, 93–96].

$k = x, y, z$ [68, 155]. In this case, $\mathscr{L}_i(nk) = \delta_{ik}\mathscr{L}(n)$ and $x(nk) = x_k(n)$. We finally come to

$$\mathscr{F}[\{\mathbf{x}\}; T] = \frac{1}{2}\sum_n k(n; T)\mathbf{x}^2(n) + \mathscr{F}^{\text{ah}}(\{\mathbf{x}\}), \quad \text{(A.9)}$$

$$\mathbf{P}|_{\mathbf{E}=0} = \frac{e}{v_0}\sum_n \mathscr{L}(n)\mathbf{x}(n). \quad \text{(A.10)}$$

If there is a soft FE mode with an anomalously small force constant $|k_f(T)| \ll k_r(T)$, where r is an index labeling the other (high-frequency) optical modes, Eqs. (A.9) and (A.10) can be recast to the form [68, 92]

$$\mathscr{F}(\mathbf{x}_f; T) = \frac{1}{2}k_f(T)\mathbf{x}_f^2 + \mathscr{F}^{\text{ah}}(\mathbf{x}_f), \quad \text{(A.11)}$$

$$\mathbf{P}|_{\mathbf{E}=0} = \frac{e}{v_0}\mathscr{L}(\text{f})\mathbf{x}_f. \quad \text{(A.12)}$$

REFERENCES

1. *Landolt-Börnstein: Numerical Data and Functional Relationships in Science and Technology*, Ed. by K.-H. Hellwege and A. M. Hellwege (Springer-Verlag, Berlin, 1981), Group III, Vol. 16a.
2. R. A. Parker, Phys. Rev. **124** (6), 1719 (1961).
3. D. D. Buss and M. A. Kinch, J. Nonmet. **1** (2), 111 (1973).
4. H. Burkhard, G. Bauer, and A. Lopez-Otero, J. Opt. Soc. Am. **67** (7), 943 (1977).
5. W. Jantsch and A. Lopez-Otero, in *Proceedings of the 13th International Conference on Physics of Semiconductors, Roma, 1976*, Ed. by F. G. Fumi, p. 487.
6. G. S. Pawley, W. Cochran, R. A. Cowley, and G. Dolling, Phys. Rev. Lett. **17** (14), 753 (1966).
7. S. I. Novikova and L. E. Shelimova, Fiz. Tverd. Tela (Leningrad) **9** (5), 1336 (1967) [Sov. Phys. Solid State **9**, 1046 (1967)].
8. L. Muldawer, J. Nonmet. **1** (3), 177 (1973).
9. K. L. I. Kobayashi, Y. Kato, Y. Katayama, and K. F. Komatsubara, Phys. Rev. Lett. **37** (12), 772 (1976).
10. S. Sugai, Y. Katayama, S. Takaoka, *et al.*, Solid State Commun. **25** (12), 407 (1977).
11. A. D. C. Grassie, J. A. Agapito, and P. Gonzales, J. Phys. C **12** (24), L925 (1979).
12. D. E. Kotecki, J. D. Baniecki, H. Chen, *et al.*, IBM J. Res. Dev. **43** (3), 367 (1999).
13. M. Lippmaa, N. Nakagama, and M. Kawasaki, Appl. Phys. Lett. **74** (23), 3543 (1999).
14. A. A. Sirenko, C. Bernhard, A. Golnik, *et al.*, Nature **404**, 373 (2000).
15. I. A. Akimov, A. A. Sirenko, A. M. Clark, *et al.*, Phys. Rev. Lett. **84** (20), 4625 (2000).
16. J. K. Hulm, Proc. Phys. Soc. London, Sect. A **63** (370A), 71 (1950).
17. K. A. Müller and H. Burkard, Phys. Rev. B **19** (7), 3593 (1979).
18. J. H. Barrett, Phys. Rev. **86** (1), 118 (1952).
19. A. B. Rechester, Zh. Éksp. Teor. Fiz. **60** (2), 782 (1971) [Sov. Phys. JETP **33**, 423 (1971)].
20. A. Yamanaka, M. Kataoka, Y. Inaba, *et al.*, Europhys. Lett. **50** (5), 688 (2000).
21. F. W. Lytle, J. Appl. Phys. **35** (7), 2212 (1964).
22. H. Unoki and T. Sakudo, J. Phys. Soc. Jpn. **23** (3), 546 (1967).
23. P. A. Fleury, J. F. Scott, and J. M. Workock, Phys. Rev. Lett. **21** (1), 16 (1968).
24. K. A. Müller, W. Berlinger, and F. Waldner, Phys. Rev. Lett. **21** (12), 814 (1968).
25. J. F. Scott, Rev. Mod. Phys. **46** (1), 83 (1974).
26. G. Sorge, E. Hegenbarth, and G. Schmidt, Phys. Status Solidi **37**, 599 (1970).
27. K. A. Müller, W. Berlinger, and E. Tosatti, Z. Phys. B **84**, 277 (1991).
28. O.-M. Nes, K. A. Müller, T. Suzuki, and F. Fossheim, Europhys. Lett. **19**, 397 (1992).
29. E. V. Balashova, V. V. Lemanov, R. Kunze, *et al.*, Ferroelectrics **183** (1–4), 75 (1996).
30. K. A. Müller, Ferroelectrics **183** (1–4), 11 (1996).
31. E. Curtens, Ferroelectrics **183** (1–4), 25 (1996).
32. R. C. Neville, B. Hoeneisen, and C. A. Mead, J. Appl. Phys. **43** (5), 2124 (1972).
33. I. M. Smolyaninov and M. D. Glinchuk, J. Korean Phys. Soc. **32**, S400 (1998).
34. V. G. Vaks, Pis'ma Zh. Éksp. Teor. Fiz. **67** (6), 399 (1998) [JETP Lett. **67**, 422 (1998)].
35. J. F. Scott, J. Phys.: Condens. Matter **11**, 8149 (1999).
36. J. M. Worlock and P. A. Fleury, Phys. Rev. Lett. **19** (20), 1176 (1967).
37. P. A. Fleury and J. M. Worlock, Phys. Rev. **174** (2), 613 (1968).
38. Y. Yamada and G. Shirane, J. Phys. Soc. Jpn. **26** (2), 396 (1969).
39. K. F. Pai, T. J. Parker, N. E. Tornberg, and R. P. Lowndes, Infrared Phys. **18**, 327 (1978).
40. D. Bäuerle, D. Wagner, M. Wöuhlecke, *et al.*, Z. Phys. B **38**, 335 (1980).
41. H. Vogt and G. Rossbroich, Phys. Rev. B **24** (6), 3086 (1981).
42. K. Inoue, N. Asai, and T. Sameshima, J. Phys. Soc. Jpn. **50** (4), 1291 (1981).
43. H. Vogt, Phys. Rev. B **51** (13), 8046 (1995).
44. H. E. Weaver, J. Phys. Chem. Solids **11** (3–4), 274 (1959).
45. E. Sawaguchi, A. Kikuchi, and Y. Kodera, J. Phys. Soc. Jpn. **17** (10), 1666 (1962).
46. E. Hegenbarth, Phys. Status Solidi **6**, 333 (1964).
47. T. Sakudo and H. Unoki, Phys. Rev. Lett. **26** (14), 851 (1971).
48. R. P. Lowndes and A. Rastogi, J. Phys. C **6** (5), 932 (1973).
49. H. Uwe and T. Sakudo, Phys. Rev. B **13** (1), 271 (1976).
50. R. Viana, P. Lunkenheimer, J. Hemberger, *et al.*, Phys. Rev. B **50** (1), 601 (1994).

51. J. Dec, W. Kleemann, and B. Westwanski, J. Phys.: Condens. Matter **11**, L379 (1999).
52. C. Ang, R. Guo, A. S. Bhalla, and L. E. Cross, J. Appl. Phys. **87** (8), 3937 (2000).
53. G. Shirane, R. Nathans, and V. J. Minkiewicz, Phys. Rev. **157** (2), 396 (1967).
54. P. A. Fleury, Phys. Rev. Lett. **18**, 665 (1967).
55. C. H. Perry and N. E. Tornberg, Phys. Rev. **183** (2), 595 (1969).
56. H. Vogt and H. Uwe, Phys. Rev. B **29**, 1030 (1984).
57. J. K. Hulm, B. T. Matthias, and E. A. Long, Phys. Rev. **79** (5), 885 (1950).
58. S. H. Wemple, Phys. Rev. **137** (5A), 1575 (1965).
59. W. R. Abel, Phys. Rev. B **4** (8), 2696 (1971).
60. G. A. Samara and B. Morosin, Phys. Rev. B **8** (3), 1256 (1973).
61. H. Uwe and T. Sakudo, J. Phys. Soc. Jpn. **38** (1), 183 (1975).
62. B. J. Kennedy, C. J. Howard, and B. C. Chakoumakos, J. Phys.: Condens. Matter **11** (6), 1479 (1999).
63. A. Linz and K. Herrington, J. Chem. Phys. **28** (5), 824 (1958).
64. L.-S. Kim, M. Itoh, and T. Nakamura, J. Solid State Chem. **101**, 77 (1992).
65. V. V. Lemanov, A. V. Sotnikov, E. P. Smirnova, *et al.*, Solid State Commun. **110**, 611 (1999).
66. W. Cochran, Phys. Rev. Lett. **3** (9), 412 (1959); Adv. Phys. **9** (36), 387 (1960).
67. R. A. Cowley, Adv. Phys. **12** (48), 421 (1963).
68. V. G. Vaks, *Introduction to the Microscopic Theory of Ferroelectrics* (Nauka, Moscow, 1973).
69. W. J. Burke and R. J. Pressley, Solid State Commun. **9** (3), 191 (1971).
70. J. G. Bednorz and K. A. Müller, Phys. Rev. Lett. **52** (25), 2289 (1984).
71. U. T. Höchli, H. E. Weibel, and L. A. Boatner, Phys. Rev. Lett. **39** (18), 1158 (1977).
72. U. T. Höchli, K. Knorr, and A. Loidl, Adv. Phys. **39** (5), 405 (1990).
73. B. E. Vugmeister and M. D. Glinchuk, Rev. Mod. Phys. **62** (4), 993 (1990).
74. O. Hanske-Petitpierre, Y. Yacoby, J. Mustre de Leon, *et al.*, Phys. Rev. B **44** (13), 6700 (1991).
75. W. Kleemann, Int. J. Mod. Phys. **7** (13), 2469 (1993).
76. V. V. Lemanov, E. P. Smirnova, and E. A. Tarakanov, Fiz. Tverd. Tela (St. Petersburg) **37** (8), 2476 (1995) [Phys. Solid State **37**, 1356 (1995)].
77. V. V. Lemanov, E. P. Smirnova, and E. A. Tarakanov, Phys. Rev. B **54**, 3151 (1996).
78. P. A. Markovin, V. V. Lemanov, O. Yu. Korshunov, and W. Kleemann, Ferroelectrics **199**, 121 (1997).
79. V. V. Lemanov, E. P. Smirnova, and E. A. Tarakanov, Fiz. Tverd. Tela (St. Petersburg) **39**, 714 (1997) [Phys. Solid State **39**, 628 (1997)].
80. V. V. Lemanov, Fiz. Tverd. Tela (St. Petersburg) **39** (9), 1645 (1997) [Phys. Solid State **39**, 1468 (1997)].
81. P. A. Markovin, V. V. Lemanov, M. E. Guzhva, *et al.*, Ferroelectrics **184**, 269 (1996).
82. M. E. Guzhva, V. V. Lemanov, P. A. Markovin, and T. A. Shuplygina, Ferroelectrics **218**, 93 (1998).
83. V. V. Lemanov, Ferroelectrics **226**, 133 (1999).
84. V. V. Lemanov, in *Defects and Surface-Induced Effects in Advanced Perovskites* (Kluwer, Amsterdam, 2000), p. 329.
85. V. V. Lemanov, Ferroelectrics (2001) (in press).
86. M. Itoh, R. Wang, Y. Inaguma, *et al.*, Phys. Rev. Lett. **82** (17), 3540 (1999).
87. M. Itoh, R. Wang, and T. Nakamura, Appl. Phys. Lett. **76** (2), 221 (2000).
88. R. Wang, N. Sakamoto, and M. Itoh, Phys. Rev. B **62** (6), R3577 (2000).
89. A. F. Devonshire, Philos. Mag. **40**, 1040 (1949); Adv. Phys. **3** (10), 85 (1954).
90. J. C. Slater, Phys. Rev. **78** (6), 748 (1950).
91. D. E. Khmel'nitskiĭ and V. L. Shneerson, Fiz. Tverd. Tela (Leningrad) **13** (3), 832 (1971) [Sov. Phys. Solid State **13**, 687 (1971)].
92. R. D. King-Smith and D. Vanderbilt, Phys. Rev. B **49**, 5828 (1994).
93. M. Born and K. Huang, *Dynamical Theory of Crystal Lattices* (Clarendon, Oxford, 1954; Inostrannaya Literatura, Moscow, 1958).
94. L. J. Sham, Phys. Rev. **188** (3), 1431 (1969).
95. R. M. Pick, M. H. Cohen, and R. M. Martin, Phys. Rev. B **1** (2), 910 (1970).
96. O. E. Kvyatkovskiĭ and E. G. Maksimov, Usp. Fiz. Nauk **154** (1), 3 (1988) [Sov. Phys. Usp. **31**, 1 (1988)].
97. V. L. Ginzburg, Zh. Éksp. Teor. Fiz. **15** (12), 739 (1945); **19** (1), 36 (1949); Usp. Fiz. Nauk **38** (4), 490 (1949).
98. M. E. Lines and A. M. Glass, *Principles and Applications of Ferroelectrics and Related Materials* (Oxford Univ. Press, Oxford, 1977; Mir, Moscow, 1981).
99. P. C. Kwok and P. B. Miller, Phys. Rev. **151** (2), 387 (1966).
100. V. G. Vaks, Zh. Éksp. Teor. Fiz. **54** (3), 910 (1968) [Sov. Phys. JETP **27**, 486 (1968)].
101. A. D. Bruce and R. A. Cowley, J. Phys. C **6**, 2422 (1973).
102. O. E. Kvyatkovskiĭ, Fiz. Tverd. Tela (St. Petersburg) **35** (8), 2154 (1993) [Phys. Solid State **35**, 1071 (1993)].
103. O. E. Kvyatkovskiĭ, Fiz. Tverd. Tela (St. Petersburg) **39** (4), 687 (1997) [Phys. Solid State **39**, 602 (1997)].
104. D. J. Singh, Phys. Rev. B **53** (1), 176 (1996).
105. W. Zhong, R. D. King-Smith, and D. Vanderbilt, Phys. Rev. Lett. **72** (22), 3618 (1994).
106. E. Cockayne and B. P. Burton, Phys. Rev. B **62** (6), 3735 (2000).
107. R. E. Cohen and H. Krakauer, Phys. Rev. B **42** (10), 6416 (1990).
108. P. H. Ghosez, X. Gonze, and J.-P. Michenaud, Ferroelectrics **206**, 205 (1998).
109. R. E. Cohen and H. Krakauer, Ferroelectrics **136**, 65 (1992).
110. A. V. Postnikov, T. Newmann, and G. Borstel, Phys. Rev. B **50** (2), 758 (1994).

111. D. J. Singh and L. L. Boyer, Ferroelectrics **136**, 95 (1992).
112. R. Yu and H. Krakauer, Phys. Rev. Lett. **74** (20), 4067 (1995).
113. C.-Z. Wang, R. Yu, and H. Krakauer, Phys. Rev. B **54** (16), 11161 (1996).
114. O. E. Kvyatkovskii, Solid State Commun. **117** (8), 455 (2001).
115. O. E. Kvyatkovskii, Ferroelectrics (2001) (in press).
116. O. E. Kvyatkovskii, Ferroelectrics **153** (1–4), 201 (1994).
117. O. E. Kvyatkovskiĭ and B. F. Shchegolev, Izv. Akad. Nauk, Ser. Fiz. **64** (6), 1060 (2000).
118. O. E. Kvyatkovskiĭ, Fiz. Tverd. Tela (Leningrad) **28** (4), 983 (1986) [Sov. Phys. Solid State **28**, 548 (1986)].
119. O. E. Kvyatkovskiĭ, Fiz. Tverd. Tela (Leningrad) **27** (9), 2673 (1985) [Sov. Phys. Solid State **27**, 1603 (1985)].
120. O. E. Kvyatkovskii, Ferroelectrics **237**, 33 (2000).
121. H. Shmidt, Phys. Rev. **156** (2), 552 (1967).
122. M. E. Lines, Phys. Rev. **177** (2), 797 (1969); **177** (2), 812 (1969); **177** (2), 819 (1969).
123. J. Dec and W. Kleemann, Solid State Commun. **106** (10), 695 (1998).
124. E. K. H. Salje, B. Wruck, and H. Thomas, Z. Phys. B **82**, 399 (1991).
125. S. A. Hayward and E. K. H. Salje, J. Phys.: Condens. Matter **10** (6), 1421 (1998).
126. A. A. Maradudin and A. E. Fein, Phys. Rev. **128** (6), 2589 (1962).
127. A. A. Abrikosov, L. P. Gor'kov, and I. E. Dzyaloshinskii, *Methods of Quantum Field Theory in Statistical Physics* (Fizmatgiz, Moscow, 1962; Prentice-Hall, Englewood Cliffs, 1963).
128. R. Oppermann and H. Thomas, Z. Phys. B **22** (4), 387 (1975).
129. T. Schneider, H. Beck, and E. Stoll, Phys. Rev. B **13** (3), 1123 (1976).
130. R. Morf, T. Schneider, and E. Stoll, Phys. Rev. B **16** (1), 462 (1977).
131. A. S. Chaves, F. C. S. Barreto, and L. A. A. Ribeiro, Phys. Rev. Lett. **37**, 618 (1976).
132. B. D. Silverman and R. I. Joseph, Phys. Rev. **129** (5), 2062 (1963).
133. R. A. Cowley, Phys. Rev. **134** (4A), 981 (1964).
134. W. G. Stirling, J. Phys. C **5**, 2711 (1972).
135. M. Iizumi, K. Gesi, and J. Harada, J. Phys. C **6**, 3021 (1973).
136. W. G. Stirling and R. Currat, J. Phys. C **9**, L519 (1976).
137. J. D. Axe, J. Harada, and G. Shirane, Phys. Rev. B **1** (3), 1227 (1970).
138. R. Cómes and G. Shirane, Phys. Rev. B **5** (5), 1886 (1972).
139. C. H. Perry, R. Currat, H. Buhay, *et al.*, Phys. Rev. B **39** (12), 8666 (1989).
140. E. Farhi, A. K. Tagantsev, R. Currat, *et al.*, Eur. Phys. J. B **15**, 615 (2000).
141. H. Frölich, in *Theory of Dielectrics* (Clarendon, Oxford, 1949), p. 9.
142. T. Hidaka and K. Oka, Phys. Rev. B **35** (16), 8502 (1987).
143. W. Zhong and D. Vanderbilt, Phys. Rev. B **53** (9), 5047 (1996).
144. D. Rytz, U. T. Höchli, and H. Bilz, Phys. Rev. B **22** (1), 359 (1980).
145. K.-P. Möllman, K. H. Herrman, and R. Enderlein, Physica B **117–118**, 582 (1983).
146. V. S. Vikhnin, P. A. Markovin, V. V. Lemanov, and W. Kleemann, J. Korean Phys. Soc. **32**, S583 (1998).
147. O. E. Kvyatkovskiĭ, Fiz. Tverd. Tela (St. Petersburg) **43**, (2001) (in press) [Phys. Solid State **43**, (2001) (in press)].
148. C. C. J. Roothaan, Rev. Mod. Phys. **23**, 69 (1951).
149. A. A. Maradudin, E. W. Montroll, and G. H. Weiss, in *Solid State Physics*, Suppl. 3 (Academic Press, New York, 1963; Mir, Moscow, 1965).
150. F. Jona and G. Shirane, *Ferroelectric Crystals* (Pergamon, Oxford, 1962; Mir, Moscow, 1965).
151. R. Blinc, J. Phys. Chem. Solids **13**, 204 (1960).
152. A. A. Maradudin and G. H. Weiss, J. Chem. Phys. **29**, 631 (1958).
153. A. Bussmann-Holder, H. Büttner, and A. R. Bishop, J. Phys.: Condens. Matter **12**, L115 (2000).
154. R. E. Cohen, Ferroelectrics **150**, 1 (1993).
155. H. Poulet and J.-P. Mathieu, *Spectres de vibration et symétrie des cristaux* (Gordon and Breach, Paris, 1970; Mir, Moscow, 1973).

Translated by G. Skrebtsov

Physics of the Solid State, Vol. 43, No. 8, 2001, pp. 1420–1425. Translated from Fizika Tverdogo Tela, Vol. 43, No. 8, 2001, pp. 1363–1368.

METALS AND SUPERCONDUCTORS

Electronic Structure of Yb, Ag, and Cu in the Heavy-Fermion System $YbCu_{5-x}Ag_x$

V. A. Shaburov*, A. E. Sovestnov*, Yu. P. Smirnov*, A. V. Tyunis*, and A. V. Golubkov**

** Konstantinov Petersburg Institute of Nuclear Physics, Russian Academy of Sciences, Gatchina, Leningrad oblast, 188350 Russia*
e-mail: asovest@mail.pnpi.spb.ru

*** Ioffe Physicotechnical Institute, Russian Academy of Sciences, Politekhnicheskaya ul. 26, St. Petersburg, 194021 Russia*

Received December 19, 2000; in final form, January 18, 2001

Abstract—The method of shifts of x-ray diffraction lines is used to study the electronic structure (the populations of 4*f* states in Yb, 5*s* states in Ag, and 4*s* states in Cu) in the heavy-fermion system $YbCu_{5-x}Ag_x$ ($0 \le x \le 1$, $T = 300$ K for Cu and Ag and 77, 300, and 1000 K for Yb). In the cubic phase ($AuBe_5$-type structure), Yb is shown to exist in the state with a noninteger valence whose magnitude is independent of the composition and is equal to $\bar{m}_{cub} = 2.91 \pm 0.01$. At $x < 0.125$, in the two-phase region (a mixture of cubic $AuBe_5$-type and hexagonal $CaCu_5$-type phases), the magnitude of m decreases with decreasing x. Based on the experimental values of m in the cubic and hexagonal phases in the two-phase region, the valence of Yb in the hexagonal phase was found to be $\bar{m}_{hex} = 2.71 \pm 0.04$. With increasing temperature in the range of 77–1000 K, a linear decrease in m for the samples from the cubic-phase field and a linear increase in m for the samples from the two-phase field is observed. At $T = 1000$ K, the valence of Yb in the cubic and hexagonal phases is virtually the same: $m_{cub} = 2.83 \pm 0.02$ and $m_{mix} = 2.78 \pm 0.02$. The cubic phase exhibits a composition-independent increase in the population of 5*s* states of Ag (in comparison with the metal) $\overline{\Delta n}_{5s}(\text{Ag}) = 0.69 \pm 0.07$ electron/atom and a simultaneous linear increase in Δn_{4s}(Cu) from about 0.1 electron/atom for $x = 1$ to about 0.3 electron/atom for $x = 0.2$. The difference in the behavior of the effects of Δn_s for Cu and Ag is explained by the specific features of the crystal structure of $YbCu_{5-x}Ag_x$. It follows from the analysis of microscopic and macroscopic properties that $YbCu_{5-x}Ag_x$ is a system with an intermediate valence and, correspondingly, the increase in the effective mass of electrons in it is related to the shift of the 4*f*-electron level to the Fermi level (delocalization). The effect of the increase in the population of *s* states in the partners of Yb is explained by the fact that, upon the transition into the state with an intermediate valence, the 4*f* electron of Yb is hybridized with *s* electrons of neighboring atoms of Ag and Cu rather than with the electrons of Yb itself. © *2001 MAIK "Nauka/Interperiodica".*

1. INTRODUCTION

The population of the 4*f* shell of a rare-earth atom in systems with heavy fermions is a fundamental characteristic of this state when we consider the problem of its formation. The mechanism of the appearance of a band of "heavy" electrons at the Fermi level is still to be clarified. It is not clear whether this is related to the shift of the *f* level toward the Fermi level (in this case, the *f* electrons become delocalized and the width of the band is determined directly by the *f*–*sd* hybridization [1]) or with collective processes, when the *f* level still lies relatively deep and the electron properties near the Fermi level can be determined by collective effects such as the Kondo effect, i.e., the resonance scattering of conduction electrons by localized magnetic moments of the *f* centers [2]. To a certain extent, the problem as to in which state (localized or delocalized) an *f* electron is in the crystal can be clarified by determining the electronic structure (the population of the *f* shell) of Yb. In the first case, the number of *f* electrons should be integral; in the second case, it should be fractional.

Among the heavy-fermion systems based on rare-earth elements, cerium- and ytterbium-containing systems are most common. Previously, using the method of displacements of x-ray lines (see, e.g., [3, 4]), we investigated the electronic structure of Ce in classical heavy-fermion systems $CeAl_3$, $CeCu_2Si_2$, and $CeCu_6$, as well as in $CeCu_4Al$ that had a record value of the coefficient of electronic heat capacity $\gamma = 2800$ mJ/(mol K^2) [5]. It was shown that in all the compounds studied, the valence of Ce has a nearly integer value $\bar{m}_{Ce} = 3.011 \pm 0.002$. On the other hand, according to L_{III} spectroscopy data [6] for a number of intermetallic compounds of Yb (which later were identified as heavy-fermion systems, e.g., $YbCu_2Si_2$, $YbPd_2Si_2$, YbCuAl, etc.), noninteger values such as $m \approx 2.8$–2.9 have also been observed. A noninteger value of m was also observed in $YbIn_{1-x}Ag_xCu_4$ [7]. It followed from an analysis of macroscopic and micro-

scopic properties that $YbIn_{1-x}Ag_xCu_4$ is a system with an intermediate (fluctuating) valence ($\bar{m} = 2.91 \pm 0.01$) and the existence of heavy electrons was explained by the hybridization of 4*f* electrons of Yb with *s* electrons of its partners, mainly of In and Ag and to a lesser extent of Cu. The observed difference in the valence properties of Ce and Yb appears to be a consequence of the dual nature of the 4*f* electrons (localized–delocalized) in heavy-fermion systems.

In this work, we studied the electronic structure, i.e., the population of 4*f* states of Yb, 5*s* states of Ag, and 4*s* states of Cu, in the $YbCu_{5-x}Ag_x$ system ($0 \le x \le 1$, T = 300 K for Ag and Cu and 77, 300, and 1000 K for Yb) using the method of displacements of x-ray lines. This system is genetically linked to a related system $YbIn_{1-x}Ag_xCu_4$ investigated in our previous works; it has the same crystal structure ($AuBe_5$) in a wide composition range (x = 0.125–1), a moderate value of the coefficient of electronic heat capacity (γ = 210 mJ/(mol K^2) for $YbAgCu_4$ and 460 mJ/(mol K^2) for $YbCu_{4.875}Ag_{0.125}$), and belongs to the class of Yb-based heavy-fermion systems. The macroscopic properties of $YbCu_{5-x}Ag_x$ (crystal structure, magnetic susceptibility, electrical resistivity, heat capacity, etc.) have been investigated in much detail [8]. At the same time, there are no direct microscopic data on the electronic structure of both Yb and its surroundings, although these are of importance for determining the mechanism of the formation of the heavy-fermion state. Along with the similarity, there is observed a sufficiently interesting difference in the structural properties between $YbIn_{1-x}Ag_xCu_4$ and $YbCu_{5-x}Ag_x$. In the first system, the cubic crystal structure (of the $AuBe_5$ type) exists in the whole composition range (x = 0–1), whereas in the second system, this structure is only retained to x_0 = 0.125. In the range of $x \le 0.125$, a hexagonal phase (with a structure of the $CaCu_5$ type) appears and coexists with the cubic phase up to x = 0 ($YbCu_5$). Based on magnetic data [8, 9], it is assumed that Yb is divalent in the hexagonal phase and is trivalent in the cubic phase; it is, therefore, of interest to investigate the electron nature of the structural ($AuBe_5 \longrightarrow CaCu_5$) transition using a direct microscopic method.

2. RESULTS AND DISCUSSION

The polycrystalline samples of $YbCu_{5-x}Ag_x$ were synthesized from stoichiometric mixtures of pure metals (Yb of double distillation; Ag and Cu of high purity). The smelting was performed in tantalum crucibles under vacuum with subsequent annealing at a temperature of 700°C. The samples with x = 0.2–1.0 were single-phase and had a cubic crystal structure (*C*15*b* or $AuBe_5$ type). The concentration dependence of the lattice parameter $a(x)$ at room temperature agrees well with the data of [8] (Fig. 1). The composition (x) was controlled by x-ray fluorescent analysis. Samples with

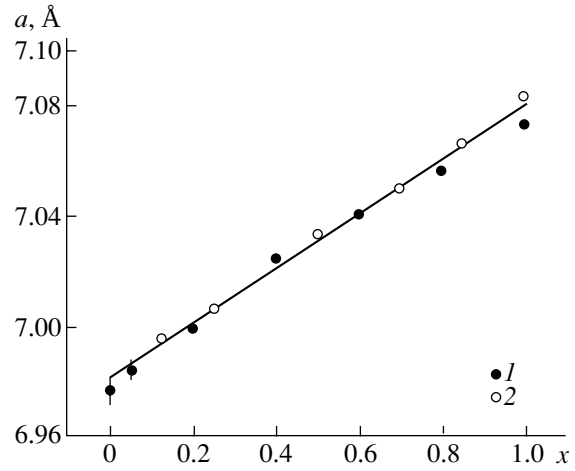

Fig. 1. Variation of the lattice parameter of $YbCu_{5-x}Ag_x$ in the cubic phase ($AuBe_5$-type structure) as a function of the composition: (*1*) our data and (*2*) data taken from [8].

$x < 0.2$ consisted of a mixture of cubic ($AuBe_5$) and hexagonal ($CaCu_5$) phases whose concentrations (as determined using a standard FULL PROF program) proved to be equal to $C_{cub} = 27 \pm 4\%$ and $C_{hex} = 73 \pm 4\%$ for x = 0, and $C_{cub} = 33 \pm 4\%$ and $C_{hex} = 67 \pm 4\%$ for x = 0.05. The lattice parameters of the hexagonal phase were virtually the same for both samples (x = 0 and 0.05); their weighted mean values $\bar{a}$ = 4.995 Å and c = 4.124 Å agree well with the values given in [8, 10].

The displacements of the $K\alpha_1$ lines of Yb, Ag, and Cu were measured on a special x-ray crystal-diffraction spectrometer by the Koshua method. The fluorescent radiation was excited in the sample using an RAP-150/300 commercial x-ray tube (I = 10 mA, U = 150 kV). The samples for room-temperature experiments were wafers pressed of a mixture of fine powders of the substance to be investigated and a filler (polyethylene). In experiments at 77 K, low-temperature liquid-nitrogen cryostats were used; for high-temperature experiments, vacuum chambers made of quartz and equipped with thin plane-parallel polished windows and an external heater were employed. The experimental scheme and measurement procedure were described in detail in previous works (see, e.g., [3, 11]).

2.1. Ytterbium

As is well-known, the valence of rare-earth elements is unambiguously related to the population of the 4*f* shell: $m = Z_{Ln} - Z_{Xe} - n_{4f}$, where Z_{Ln} and Z_{Xe} are the atomic numbers of a lanthanide (*Ln*) and xenon, respectively, and n_{4f} is the population of the 4*f* shell. Changes in n_{4f} lead to anomalously large (in comparison with the effects of 6*s*(*p*) and 5*d* electrons) changes in the energy (large displacements) of the emission *K* lines of the rare-earth elements under consideration

Experimental displacements (ΔE) of the $K\alpha_1$ lines of Yb, Ag, and Cu in $YbCu_{5-x}Ag_x$ with metallic Yb, Ag, and Cu used as the standards (T is the measurement temperature)

x	T, K	ΔE (Yb), meV	ΔE (Ag), meV	ΔE (Cu), meV
0	77	–387 ± 17	–	–
	300	–428 ± 5	–	–19 ± 6
	1000	–454 ± 14	–	–
0.05	300	–471 ± 6	–	–
0.2	300	–550 ± 6	–43 ± 7	–31 ± 6
0.4	77	–524 ± 18	–	–
	300	–520 ± 6	–35 ± 6	–18 ± 6
	1000	–468 ± 18	–	–
0.6	300	–542 ± 6	–53 ± 7	–21 ± 6
0.8	300	–526 ± 6	–38 ± 7	–22 ± 6
1.0	77	–543 ± 23	–	–
	300	–528 ± 6	–39 ± 7	–8 ± 2
	1000	–495 ± 12	–	–
Yb_2O_3		–583 ± 5	–	–
AgCl		–	122 ± 5	–
CuCl		–	–	164 ± 5

Note: In the bottom of the table, experimental shifts of the $K\alpha_1$ lines for ionic compounds are given.

($\left|\Delta E^{4f}_{K\alpha_{1,2}}\right| \approx 500$–$600$ meV, $\left|\Delta E^{4f}_{K\beta_{1,3}}\right| \approx 1500$–$1700$ meV, $\left|\Delta E^{6s(p),5d}_{K\alpha,\beta}\right| \approx 20$–$80$ meV) [4]. This makes the method of displacements of x-ray diffraction lines a sufficiently sensitive technique suitable to the investigation of processes related to a rearrangement of the 4*f* shell (changes in the valence).

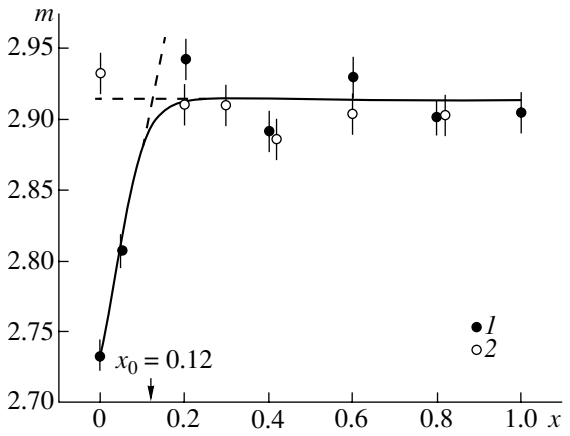

Fig. 2. Variation of the Yb valence in (*1*) $YbCu_{5-x}Ag_x$ and (*2*) $YbIn_{1-x}Ag_xCu_4$ [7] as a function of the composition at room temperature (hereafter, the errors that are indicated are statistical). x_0 is the boundary of transition from the single-phase to the two-phase region in $YbCu_{5-x}Ag_x$.

The experimental values of the displacements of the $K\alpha_1$ line of Yb in $YbCu_{5-x}Ag_x$ with respect to a divalent standard (metallic Yb) are given in the table. The sign and the anomalously large magnitudes of the effects unambiguously indicate a decrease in the number of 4*f* electrons (an increase in the valence) of Yb. The difference between the numbers of 4*f* electrons in the compound and in the standard was determined as $\Delta n_{4f}(x, T) = \Delta E(x, T)/\Delta E(Yb^{3+} - Yb^{2+})$, where $\Delta E(x, T)$ is the experimental line shift and $\Delta E(Yb^{3+} - Yb^{2+})$ is the calibration displacement corresponding to a shift of the $K\alpha_1$ line of Yb upon a decrease in the population of the 4*f* shell by unity. It is obvious that the valence of Yb in the sample studied is $m = m_{st} + \Delta n_{4f} = 2 + \Delta n_{4f}$. The calibration displacement was measured for the pair Yb_2O_3–Yb_{met} and is equal to $\Delta E(Yb^{3+} - Yb^{2+}) = -583 \pm 5$ meV. The dependence of the valence of Yb on the composition at room temperature is given in Fig. 2. In the field of the cubic phase ($x = 0.2$–1.0), the Yb valence is virtually constant and has a noninteger value $\bar{m}_{cub} = 2.91 \pm 0.01$ coinciding with the Yb valence in $YbIn_{1-x}Ag_xCu_4$ ($\bar{m} = 2.91 \pm 0.01$ [7]). In the region of $x < 0.2$, in which the cubic and hexagonal phases coexist, the Yb valence decreases. Based on the experimental values of m for the cubic phase ($x > 0.2$) and for a mixture of phases ($x = 0$ and 0.05) and on the concentrations of the hexagonal and cubic phases, the Yb valence in the hexagonal phase was determined to be $\bar{m}_{hex} = 2.71 \pm 0.04$. Note that a linear extrapolation of $m(x)$ for the compositions from the two-phase region ($x < 0.2$) meets the straight line $\bar{m}_{cub}$ at the point $x = 0.12 \pm 0.02$, which agrees well with the value $x_0 = 0.125$ that was obtained in macroscopic experiments [8] for the boundary of transition from the single-phase to the two-phase region.

The noninteger values of the valence of *f* atoms are characteristic of a specific class of rare-earth and actinide compounds with an intermediate (fluctuating) valence. The noninteger value $m = 2.91$ in $YbCu_{5-x}Ag_x$ differs only a little from the value of 3 which is normal for Yb. However, even this small difference leads to fundamentally different conclusions in choosing the mechanism responsible for the heavy-fermion state (*f–sd* hybridization or collective processes of the Kondo-effect type). The expected valence of Yb in the intermediate-valence state was quantitatively estimated on the basis of the phenomenological model of interconfiguration fluctuations [12, 13], in which the state of intermediate valence is considered as a resonance (fluctuations) between energetically close initial ($4f^n$) and final ($4f^{n-1} + e$) states of the 4*f* electron. The probability for an *f* atom to be found in the state f^{n-1} is determined by the Boltzmann-type distribution

$$P(f^{n-1}) = \left[1 + \frac{M_n}{M_{n-1}} \exp\frac{E_{ex}}{T + \Gamma}\right]^{-1}, \qquad (1)$$

where $E_{ex} = E_{n-1} - E_n$ is the difference of the energies of the $4f^n$ and $4f^{n-1}$ configurations, M_n and M_{n-1} are the statistic weights of these states, and Γ is the energy of Anderson hybridization of the 4*f* electron with an electron of the conduction band (the width of the 4*f* level). The intermediate-valence state is realized if $|E_{ex}| \le \Gamma$. In the assumption that fluctuations of the 4*f* electron of Yb in $YbCu_{5-x}Ag_x$ from site to site occur only between coinciding (degenerate) energy levels ($E_{ex} \approx 0$) (Anderson-type transition [14]), the probability of an Yb^{3+} state arising is determined only by the statistic weights of the Yb^{2+} ($J = 0$, $M_n = 1$) and Yb^{3+} ($J = 7/2$, $M_{n-1} = 8$) states and is equal to $P(Yb^{3+}) = M_{n-1}/(M_{n-1} + M_n) = 8/9$, which corresponds to the value $m = 2.89$; this agrees satisfactorily (for such a simple model) with our experimental value 2.91 ± 0.01.

The identification of the intermediate-valence state by only the sign if *m* is integer or noninteger is insufficient. The noninteger valence also takes place in mixed-valence compounds, when the ions of different valences occupy inequivalent positions in the crystal lattice (as, e.g., in Eu_3O_4).

As indirect evidence of the occurrence of an intermediate-valence state in the cubic phase of $YbCu_{5-x}Ag_x$, the results of high-temperature experiments can be considered. Figure 3 displays the temperature dependences of the valence of Yb in $YbCu_{5-x}Ag_x$ for samples with $x = 0.4$ and 1. It is seen that *m* decreases with increasing temperature; the course of the $m(T)$ curve in $YbCu_{5-x}Ag_x$ is virtually the same as in the previously investigated system $YbIn_{1-x}Ag_xCu_4$. The decrease in *m* with increasing temperature in $YbIn_{1-x}Ag_xCu_4$ was explained in the assumption of the dependence of E_{ex} on *T* (theory admits such a possibility in principle [15]). Earlier, the effect of decreasing the valence of a rare-earth element at a high temperature in classical systems with intermediate valence was observed for a wide class of intermetallic compounds of cerium [16, 17] and europium [18] using the method of x-ray line displacements and Mössbauer spectroscopy for Eu compounds [19, 20]. The temperature dependences $m(T)$ for coinciding objects ($EuCu_2Si_2$, $EuRh_2$, $Eu(Ni_{1-x}Cu_x)_5$) exhibit good agreement between both methods.

Thus, the totality of the above-considered microscopic and macroscopic properties of $YbCu_{5-x}Ag_x$ in the cubic phase ($x = 0.2$–1) and the fact that Yb atoms occupy equivalent positions in the crystal lattice suggest that this system is a system with an intermediate (fluctuating) valence and, correspondingly, the appearance of a heavy electron in it is a result of *f–sd* hybridization upon the transition of an 4*f* electron into the intermediate-valence state.

The differences in the behavior of the Yb valence in the cubic and mixed phases (Fig. 3) can be explained by two probable mechanisms: (i) it follows from Eq. (1) that the probability of occurrence of Yb in the trivalent state $P(3+)$ can either increase or decrease with increasing temperature depending on the sign of E_{ex}; (ii) with increasing temperature, a smooth structural phase transition from the hexagonal to cubic phase occurs, and at 1000 K, the $YbCu_{5-x}Ag_x$ system becomes single-phase over the whole region of *x* from 0 to 1. At $T = 1000$ K, the Yb valence in the cubic phase $YbCu_{5-x}Ag_x$ is virtually coincident with its valence in the mixed phase: $m_{cub} = 2.83 \pm 0.02$, $m_{mix} = 2.78 \pm 0.02$. The choice of one of the two variants given above can be made on the basis of phase analysis in the high-temperature region.

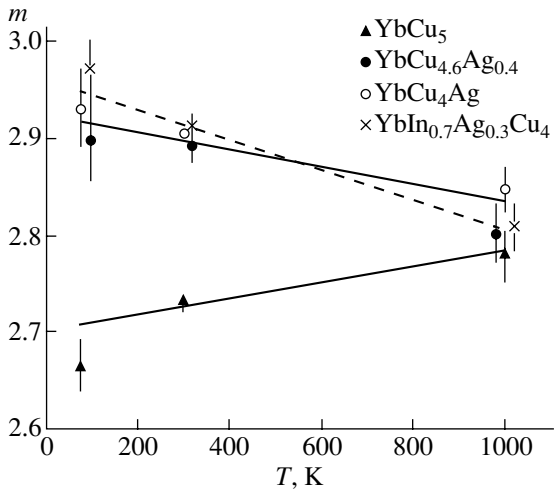

Fig. 3. Temperature dependences of the Yb valence in $YbCu_{5-x}Ag_x$ for single-phase ($YbCu_{4.6}Ag_{0.4}$ and $YbCu_4Ag$) and two-phase ($YbCu_5$) samples and the data for $YbIn_{0.7}Ag_{0.3}Cu_4$ taken from [7].

2.2. Silver and Copper

One of the key (and virtually uninvestigated) questions in the problem of intermediate valence (and, correspondingly, heavy fermions) is the question of what are the centers at which the *f–sd* hybridization occurs. We supposed in [7] that upon the transition into the intermediate-valence state, the 4*f* electron is mainly hybridized with 5*s* electrons of In and Ag and, to a lesser extent, with 4*s* electrons of Cu.

The question of what are the centers at which the *f–sd* hybridization occurs was also studied in this work. To this end, we determined the populations of the outer *s* states of Ag and Cu from the displacements of their $K\alpha_1$ lines. The shifts of the $K\alpha_1$ lines of Ag and Cu are given in the table. For all $YbCu_{5-x}Ag_x$ compositions that were studied in this work, negative displacements relative to the corresponding metals are observed. As was shown in our previous work [21], a removal of valence *s* (*p*) electrons from an atom in heavy elements leads to positive displacements of the $K\alpha_1$ lines (quantitatively, the effects of *s* and *p* electrons are virtually identical). The magnitudes of the effects $\Delta E_{K\alpha_1} = E_{ion} - E_{met}$ for the ionic compounds of Yb, Ag, and Cu are illustrated

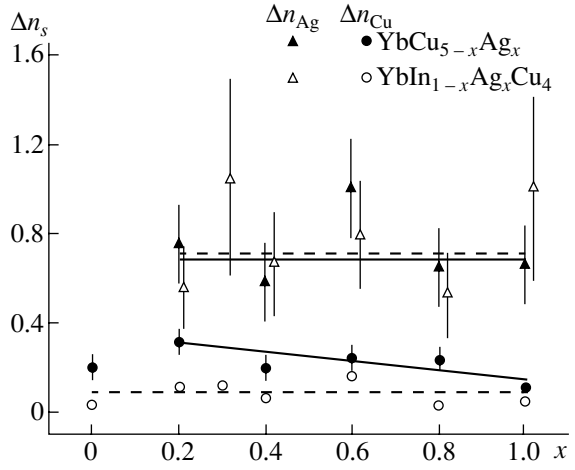

Fig. 4. Variation of the change in the population of 5*s* states of Ag and 4*s* states of Cu in $YbCu_{5-x}Ag_x$ as a function of the composition at room temperature and the data for Δn_s for $YbIn_{1-x}Ag_xCu_4$ taken from [7].

in the table. The nonzero negative values of the displacements of the $K\alpha_1$ lines of Ag and Cu in $YbCu_{5-x}Ag_x$ imply that the populations of the outer *s* (*p*) states of Ag and Cu increase upon the transition from the metallic state into the intermediate-valence state.

The populations of the 5*s* states of Ag and of the 4*s* states of Cu were determined from the experimental displacements of the $K\alpha_1$ lines and Dirac–Fock atomic calculations. For each sample of $YbCu_{5-x}Ag_x$, we found the magnitude of Δn_s from the equation

$$\Delta E_{\text{calc}}(\Delta n_s) = \Delta E^M(x), \qquad (2)$$

where M = Ag or Cu, $\Delta E_{\text{calc}}(\Delta n_s)$ are the calculated displacements, $\Delta E^M(x)$ are the experimental displacements, and Δn_s is the difference between the numbers of 5*s* (4*s*) electrons of Ag (Cu) in $YbCu_{5-x}Ag_x$ and in the metallic standard (the electron configurations of Ag and Cu are $4d^{10}5s^1$ and $3d^{10}4s^1$, respectively). The results are shown in Fig. 4, from which it follows that the magnitudes of $\Delta n(x)$ for Ag are virtually independent of the composition, and their weighted mean value $\overline{\Delta n}_{5s} = 0.69 \pm 0.07$ electron/atom agrees well with the value $\overline{\Delta n}_{5s} = 0.71 \pm 0.09$ electron/atom for $YbIn_{1-x}Ag_xCu_4$.

An increase in the population of the 5*s* states of Ag and 4*s* states of Cu in $YbCu_{5-x}Ag_x$ can be explained (as this was made for $YbIn_{1-x}Ag_xCu_4$ in our previous work [7]) by the hybridization of 4*f* electrons of Yb with conduction electrons of neighboring atoms of Ag and Cu. The variant in which the 4*f* electron fluctuates between the states of neighboring atoms of Yb should not, in principle, lead to changes in the electronic structure of silver and copper. In $YbIn_{1-x}Ag_xCu_4$, the total increase in the population $\overline{\Delta n}_\Sigma$(Ag, In, Cu) = 1.0 ± 0.1 electron/atom is nearly coincident with the decrease in the population of the 4*f* shell of Yb in the intermediate-valence state $\overline{\Delta n}_{4f} = 0.91 \pm 0.01$ electron/atom; the balance $\Delta n_f \approx \Delta n_\Sigma \approx 1$ is independent of the composition and is ensured mainly by Ag and In and, to a lesser extent, by four atoms of copper.[1]

The situation is different in $YbCu_{5-x}Ag_x$. Here, an increase in the population of 5*s* states of Ag coincides with Δn_s(Ag) in $YbIn_{1-x}Ag_xCu_4$ and independent of the composition (Fig. 4); however, the total number of silver atoms decreases because of the copper substitution and, correspondingly, $x\Delta n_s$(Ag) decreases from ~0.7 electron/atom at $x = 1$ to ~0.14 electron/atom at $x = 0.2$. The valence of Yb is also independent of the composition ($\overline{\Delta n}_{4f} = 0.91$ electron/atom), although it should decrease if the hybridization of the 4*f* electron occurs mainly at Ag atoms (as in $YbIn_{1-x}Ag_xCu_4$). We suppose that as the concentration of Ag decreases in $YbCu_{5-x}Ag_x$, copper atoms (which ensure the constancy of the Yb valence with decreasing x) begin to play a significant role in the mechanism of *f*–*s* hybridization. It is seen from Fig. 3 that the population of 4*s* states increases with decreasing Ag concentration and the magnitude of Δn_{4s}(Cu) at $x = 0.2$ is greater by a factor of about 3 than that in $YbIn_{1-x}Ag_xCu_4$.

The difference in the behavior of the effects of Δn_{4s} for Cu in $YbIn_{1-x}Ag_xCu_4$ and $YbCu_{5-x}Ag_x$ can be explained by the specific features of the crystal structure of these compounds. The unit cell of Yb(In, Ag)Cu_4 consists of two sublattices: a sublattice of (Yb, In, Ag) atoms, as in the $MgCu_2$-type Laves phases of rare-earth elements, and a sublattice of Cu atoms, which is formed by tetrahedra of four copper atoms [22]. It is assumed that the atoms of the first sublattice are strongly bound with one another and weakly bound with the atoms of the second sublattice [23]; therefore, the exchange by electrons in the process of hybridization is mainly determined by the atoms of the first sublattice (Yb, Ag, In).

The unit cell of $YbCu_{5-x}Ag_x$ in the cubic phase also consists, as in the case of YB(In, Ag)Cu_4, of two sublattices: a sublattice formed by the rare-earth element (as in $MgCu_2$-type Laves phases) and a copper sublattice, with the difference that in the first sublattice there is a fifth copper atom (Cu*), which, like In in Yb(In, Ag)Cu_4, compensates the loss of Ag and ensures that Δn_{4f} is independent of the composition upon *f*–*s* hybridization. The change in the total population $\overline{\Delta n}_\Sigma$(Ag, In, Cu*) increases from 1.2 ± 0.2 electron/atom for $x = 1$ to 1.6 ± 0.2 electron/atom for $x = 0.2$. The excess $\Delta n_\Sigma > \Delta n_{4f}$ can be due to an additional transfer of outer valence 6*s* and 5*d* electrons of Yb onto the Cu* atoms in the first

[1] In Yb(In, Ag)Cu_4, the weighted mean $\overline{\Delta n}_s$(Ag) ≈ $\overline{\Delta n}_s$(In) ≈ 0.7 electron/atom is independent of x [7] and the number of copper atoms is constant; therefore, the relation $\Delta n_{4f} \approx \Delta n_\Sigma \approx 1$ electron/atom will always be fulfilled.

sublattice. We observed such an effect in the Laves phases $CeRu_2$, $CeRh_2$, and $CeOs_2$ [17].

An increase in the coefficient of electronic heat capacity γ in $YbCu_{5-x}Ag_x$ with decreasing x was explained in [8] by an increase in the chemical contraction that arises as smaller Cu atoms substitute for Ag in the crystal lattice.[2] When describing the mechanism of *f–sd* hybridization in intermediate-valence and heavy-fermion systems, it is commonly accepted (see, e.g., [25]) that, along with the size factor (chemical contraction in this case), an important role belongs to the electronic structure of the components of the compound (electronic factor). It follows from our data that the total change in the population of 5*s* (4*s*) states Δn_Σ increases with increasing concentration of Cu from ~1.2 electron/atom for $x = 1$ to ~1.6 electron/atom for $x = 0.2$ and correlates with increasing the coefficient of heat capacity from ~250 to ~460 mJ/(mol K^2) [8]. An analysis of the quantities Δn_s(Ag, Cu) reveals those atoms that lead to an increase in Δn_Σ with increasing copper concentration and corresponds to an increase in γ. As is shown above, the growth in Δn_Σ with increasing copper concentration is determined by the fifth copper atom (Cu*).

ACKNOWLEDGMENTS

This work was supported in part by the Russian Foundation for Basic Research, project no. 99-02-16633. The work on the synthesis of the samples to be studied performed by one of us (A.V.G.) was supported in part by the Russian Foundation for Basic Research, project no. 99-02-18078. We are grateful to E.G. Andreev for his assistance in experiments and P.L Sokolova for assistance in preparing the paper.

REFERENCES

1. O. W. Overhauser and J. Appel, Phys. Rev. B **31** (1), 193 (1985).
2. A. M. Tsvelick and P. W. Wiegmann, Adv. Phys. **32** (4), 453 (1983).
3. O. I. Sumbaev, in *Modern Physics in Chemistry* (Academic, New York, 1977), Vol. 1, p. 33.
4. O. I. Sumbaev, Usp. Fiz. Nauk **124** (2), 281 (1978) [Sov. Phys. Usp. **21**, 141 (1978)].
5. V. A. Shaburov, Yu. P. Smirnov, A. E. Sovestnov, *et al.*, Fiz. Tverd. Tela (St. Petersburg) **38** (3), 954 (1996) [Phys. Solid State **38**, 530 (1996)].
6. J. Röhler, in *Handbook on the Physics and Chemistry of Rare Earths*, Ed. by K. A. Gschneidner, Jr. and L. Eyring (North-Holland, Amsterdam, 1987), Vol. 10, p. 453.
7. V. A. Shaburov, A. E. Sovestnov, Yu. P. Smirnov, *et al.*, Fiz. Tverd. Tela (St. Petersburg) **42** (7), 1164 (2000) [Phys. Solid State **42**, 1199 (2000)].
8. N. Tsujii, J. He, K. Yoshimura, *et al.*, Phys. Rev. B **55** (2), 1032 (1997).
9. A. Iandelli and A. Palenzona, J. Less-Common Met. **25**, 333 (1971).
10. E. I. Gladyshevskiĭ and O. I. Bodak, *Crystal Chemistry of Intermetallic Compounds of Rare-Earth Metals* (Vishcha Shkola, Lvov, 1982).
11. Yu. P. Smirnov, A. E. Sovestnov, G. I. Terekhov, *et al.*, Zh. Éksp. Teor. Fiz. **93** (2), 692 (1987) [Sov. Phys. JETP **66**, 391 (1987)].
12. B. C. Sales and D. K. Wohlleben, Phys. Rev. Lett. **35** (18), 1240 (1975).
13. L. L. Hirst, Phys. Rev. B **15** (1), 1 (1977).
14. P. W. Anderson, Phys. Rev. **109** (5), 1492 (1958).
15. D. K. Wohlleben, J. Phys. (Paris) **37**, C4-321 (1976).
16. V. A. Shaburov, Yu. P. Smirnov, A. E. Sovestnov, and A. V. Tyunis, Pis'ma Zh. Éksp. Teor. Fiz. **41** (5), 213 (1985) [JETP Lett. **41**, 259 (1985)].
17. Yu. P. Smirnov, A. E. Sovestnov, A. V. Tyunis, and V. A. Shaburov, Fiz. Tverd. Tela (St. Petersburg) **40** (8), 1397 (1998) [Phys. Solid State **40**, 1269 (1998)].
18. M. N. Groshev, V. I. Petrova, Yu. P. Smirnov, *et al.*, Fiz. Tverd. Tela (Leningrad) **29** (4), 1035 (1987) [Sov. Phys. Solid State **29**, 592 (1987)].
19. F. Scherzberg, Ch. Sauer, U. Köbler, and W. Zinn, Solid State Commun. **49** (11), 1027 (1984).
20. E. R. Bauminger, D. Froindlich, I. Nowik, and S. Ofer, Phys. Rev. Lett. **30** (21), 1053 (1973).
21. E. V. Perovich, Yu. P. Smirnov, A. I. Grushko, *et al.*, Zh. Éksp. Teor. Fiz. **61** (5), 1756 (1971) [Sov. Phys. JETP **34**, 935 (1971)].
22. M. Yu. Teslyuk, in *Metallic Compounds with Laves Phase Structures* (Nauka, Moscow, 1969), p. 13.
23. H. R. Kirchmayer and C. A. Poldy, in *Handbook on the Physics and Chemistry of Rare Earths*, Ed. by K. A. Gschneidner and L. Eyring (North-Holland, Amsterdam, 1978; Metallurgiya, Moscow, 1982).
24. W. B. Pearson, *Crystal Chemistry and Physics of Metals and Alloys* (Wiley, New York, 1972; Mir, Moscow, 1977).
25. D. I. Khomskiĭ, *Unusual Electrons in Crystals (Intermediate Valence and Heavy Fermions)* (Znanie, Moscow, 1987).

Translated by S. Gorin

[2] Although the metallic radii of Ag and Cu atoms differ significantly (~12%) [24], the change in the lattice parameter of $YbCu_{5-x}Ag_x$ is only ~1% (Fig. 1). The weak sensitivity of the lattice parameter to the size of Ag and Cu atoms is explained by the fact that the lattice parameter is mainly determined by the size of atoms of the second sublattice, whereas the substitution of Cu atoms for Ag occurs in the first sublattice [24].

Physics of the Solid State, Vol. 43, No. 8, 2001, pp. 1426–1432. Translated from Fizika Tverdogo Tela, Vol. 43, No. 8, 2001, pp. 1369–1375.

SEMICONDUCTORS AND DIELECTRICS

Effect of Electric Field on the Optical Absorption of Amorphous Molecular Semiconductors Doped with Polymethine Dyes

N. A. Davidenko*, N. A. Derevyanko, A. A. Ishchenko**, and V. A. Pavlov***

** Shevchenko National University, Vladimirskaya ul. 64, Kiev, 01033 Ukraine*

*** Institute of Organic Chemistry, National Academy of Sciences of Ukraine, Murmanskaya ul. 5, Kiev, 02094 Ukraine*

Received October 18, 2000

Abstract—The effect of a dc electric field on the evolution of the electronic absorption spectra of poly(*N*-epoxypropylcarbazole) (PEPC), poly(styrene) (PS), and poly(vinyl butyral) (PVB) films doped with methine dyes is investigated. It is revealed that these spectra in the absorption range of the dye undergo transformations depending on the dipole moment and the symmetry of the π-electron structure of dye molecules. The inference is made that the electron density in the dye molecule is redistributed in an external electric field. This redistribution gives rise to the electric field–induced anisotropy in the spatial distribution function of photogenerated electron–hole pairs in amorphous molecular semiconductors. *© 2001 MAIK "Nauka/Interperiodica".*

1. INTRODUCTION

Amorphous molecular semiconductors based on photoconducting polymers doped with organic compounds possess photoconducting properties in the visible and near-IR spectral ranges, because dopant molecules can serve not only as optical absorption centers but also as charge carrier photogeneration centers. At present, amorphous molecular semiconductors based on poly(*N*-vinylcarbazole) and poly(*N*-epoxypropylcarbazole) (PEPC) are the most well investigated and find practical use. It is well known that, in these semiconductors, the photoconduction process in the absorption range of photogeneration centers involves two stages [1, 2]. At the first stage, the absorption of a photon by a molecule of the photogeneration center leads to the transfer of a positive charge (hole) from this molecule to a carbazole group of the polymer and to the formation of a bound electron–hole pair. At the second stage, the electron–hole pair either annihilates or dissociates. The probability of dissociating the electron–hole pair increases with an increase in the external electric field strength E and the temperature T. The electron–hole pair dissociation is theoretically described within the Onsager model for the probability of separating two charged particles in an isotropic medium [3]. In high fields E, the probability of dissociating an electron–hole pair in the Onsager model coincides with the probability calculated in the framework of the Pool–Frenkel one-dimensional model [2]. Note that, in the range $1 \times 10^7 < E < 1 \times 10^8$ V/m, the theoretical relationship for electron–hole pair dissociation is consistent with the analytical expression that was empirically obtained from experimental data on the photocurrent j in amorphous molecular semiconductors. Since the photocurrent j is directly proportional to the quantum yield η of charge carrier photogeneration, it is assumed that

$$j \sim \eta \sim \eta_0 \exp(-(W_{0ph} - \beta E^{1/2}))(T^{-1} - T_0^{-1})/k, \quad (1)$$

where η_0 is the quantum yield of electron–hole pair generation; W_{0ph} is the activation energy of photogeneration, which is equal to the energy of Coulomb attraction between a hole and an electron in the photogenerated electron–hole pair; β is the Pool–Frenkel constant; k is the Boltzmann constant; and T_0 is the characteristic temperature, which, for PEPC-based films, is equal to 490 ± 20 K. From relationship (1), it follows that the η and j quantities increase with an increase in the field E and, at $E > (W_{0ph}/\beta)^2$, they should be independent of E. However, this is not necessarily observed in experiments. An increase in the field $E > (W_{0ph}/\beta)^2$ to prebreakdown electric field strengths frequently leads to an increase in j. The observed deviation of the experimental dependences $\eta(E)$ and $j(E)$ from relationship (1) at high fields can be explained by at least three factors.

First, an electron–hole pair is formed from a photogeneration center molecule in excited states with different lifetimes. The external electric field contributes the probability of ionizing excited molecules [4, 5] owing to the decrease in the potential barrier for the transfer of a charge carrier from the photogeneration center to the adjacent molecules. This mechanism of increase in the quantum yield of electron–hole pair photogeneration in an external electric field was studied earlier for PEPC-based amorphous molecular semiconductor films doped with intramolecular charge-transfer complexes [6] and ionic dyes [7].

Second, amorphous molecular semiconductors contain organic molecules with an inhomogeneous distribution of charges over the molecular structure, which

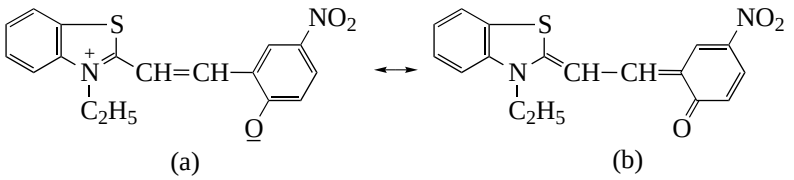

1

Fig. 1. Structural formulas of merocyanine *1* in (a) the ground and (b) excited states.

produce electric inhomogeneities in the bulk of amorphous molecular semiconductors. These inhomogeneities can be responsible for trapping of nonequilibrium carriers. The external electric field decreases the binding energy between charge carriers and electric inhomogeneity regions, which manifests itself in an increase in the photoconductivity with an increase in E. This mechanism of trapped carrier release under the action of an electric field was previously investigated in PEPC-based amorphous molecular semiconductor films doped with intramolecular charge-transfer complexes [8, 9] and ionic [10] and intraionic dyes [11].

Third, relationship (1) involves the quantum yield η_0 of electron–hole pair photogeneration as a multiplier. In the photogeneration models for isotropic amorphous molecular semiconductors, this quantity is assumed to be independent of the strength and direction of an external electric field. This implies that the direction of escape of a charge carrier from an excited photogeneration center in the course of electron–hole pair formation should be independent of external factors and that the spatial distribution of photogenerated electron–hole pairs over the distances between charges in electron–hole pairs can be described by a spherical function. However, photogeneration center molecules with large dipole moments should exhibit a strong anisotropy of the probability of intramolecular and intermolecular electron transitions. In an external electric field, the probability of intermolecular electron transitions from these molecules should depend on the molecular orientation with respect to the field. Moreover, in the case when dipole molecule moments can rotate in an external electric field E and its strength increases, the spatial distribution of electron–hole pairs over the distances between charges cannot be considered a spherical function. We can expect an increase in the probability of generating electron–hole pairs whose dipole moment is oppositely aligned with the direction of the electric field lines. These electron–hole pairs have the highest dissociation probability. This circumstance should result in an increase in η_0 with an increase in E. The discussed mechanism of electron–hole pair photogeneration under the influence of an electric field in amorphous molecular semiconductors is similar to the Freédericksz effect, which is well understood for liquid crystals [12, 13]. However, the experimental verification and investigation of this mechanism for amorphous molecular semiconductors have received little attention in the literature.

The specific features of the influence of an external electric field on the spatial distribution of photogenerated electron–hole pairs in doped amorphous molecular semiconductors can be experimentally investigated using spectroscopic techniques, specifically by analyzing the effect of an electric field on photoabsorption and photoluminescence. The purpose of the present work was to elucidate how the external electric field affects the optical absorption spectra of amorphous molecular semiconductors doped by organic dyes with different charge distributions.

2. SAMPLES AND EXPERIMENTAL TECHNIQUE

For this purpose, PEPC-based amorphous molecular semiconductors doped with polymethine dyes were chosen as the objects of investigation. Polymethine dyes can serve as efficient centers of charge carrier photogeneration in PEPC [7]. Owing to the features of their molecular structure, the distribution and magnitude of the charge state in these dyes can be varied in a controlled manner [14]. According to these characteristics, dyes can be divided into three groups.

The first group contains intraionic dyes with a strong localization of positive and negative charges at terminal parts of the chromophore in the ground state [15]. A representative example of these dyes is merocyanine *1*. The structural formulas of its molecule are depicted in Fig. 1. Merocyanine in the ground state has a bipolar structure. The absorption of a photon brings about the transfer of an excess electron density from the oxygen atom to the positively charged benzothiazole heterocycle. Hence, merocyanine *1* in the excited state has a nearly neutral structure. To put it differently, the electronic excitation is accompanied by a drastic decrease in the dipole molecule moment.

The second group primarily involves intraionic dyes in which, unlike compound *1*, the ground and excited states are characterized by neutral and bipolar structures, respectively [15]. An example of these dyes is merocyanine *2* (Fig. 2).

Unlike merocyanine *1*, the dipole moment of merocyanine *2* considerably increases upon light absorption.

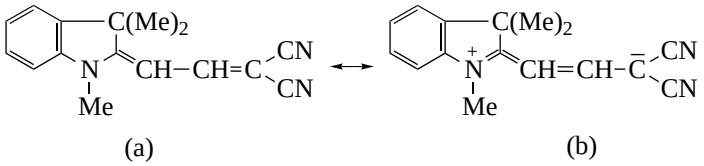

2

Fig. 2. Structural formulas of merocyanine *2* in (a) the ground and (b) excited states.

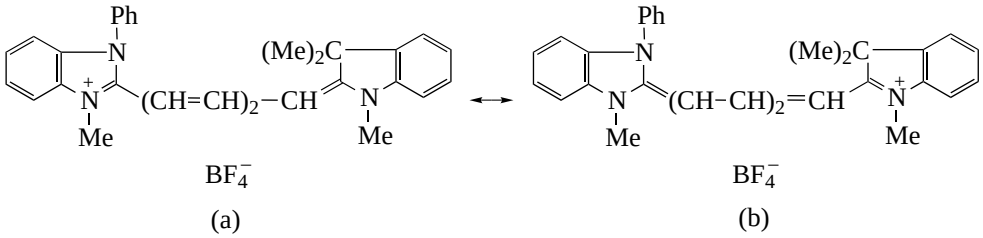

3

Fig. 3. Structural formulas of cationic asymmetric polymethine dye *3* in (a) the ground and (b) excited states.

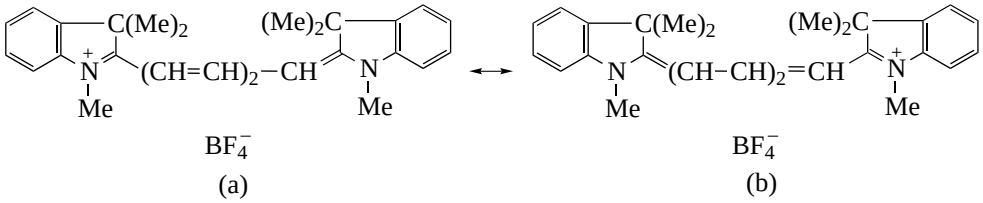

4

Fig. 4. Structural formulas of cationic symmetric polymethine dye *4* in (a) the ground and (b) excited states.

Asymmetric ionic dyes, for example, dye *3* (Fig. 3), also fall into the second group.

A dye molecule consists of two separate counterions. Light is absorbed by a chromophore of the organic counterion. Unlike merocyanines *1* and *2*, chromophores of ionic dyes are charged in both the ground and excited states (see structures in Figs. 3a, 3b). The total charges of cationic (colored cation) and anionic (colored anion) dyes are equal to +1 and –1, respectively. These charges are retained in both the ground and excited states. However, in the case of asymmetric dyes, particular charges are nonuniformly distributed in the ions. For example, as can be seen from the structural formula of cationic asymmetric polymethine dye *3*, the positive charge in the ground state is predominantly localized on a more electron-donating benzimidazole heterocycle. By contrast, this charge in the excited state is predominantly localized on the indole heterocycle. The boundary structures of asymmetric dye *3* (Figs. 3a, 3b) have a similar cationic form, whereas the structures of merocyanines *1* and *2* in the ground and excited states differ radically (one structure is bipolar and the other structure is neutral). Therefore, the change in dipole moment upon excitation of asymmetric dyes of type *3* is less than that of merocyanines.

Symmetric ionic (cationic and anionic) dyes belong to the third group. Unlike asymmetric polymethine dyes, they are characterized by a symmetric distribution of charge among the terminal heterocycles of a colored chromophore. This is explained by the fact that symmetric dyes have identical terminal groups, as is the case in dye *4* (Fig. 4). More rigorous quantum-chemical calculations demonstrate that the structures of dyes of type *4* in the ground and excited states (Figs. 4a, 4b) are not equivalent, even though both states exhibit a symmetric charge distribution [14]. The difference between

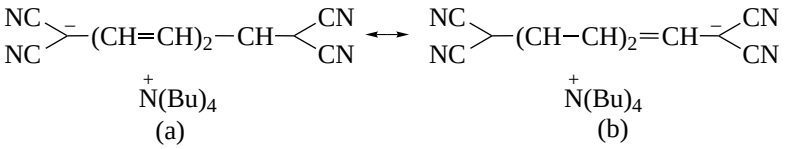

5

Fig. 5. Structural formulas of anionic symmetric polymethine dye *5* in (a) the ground and (b) excited states.

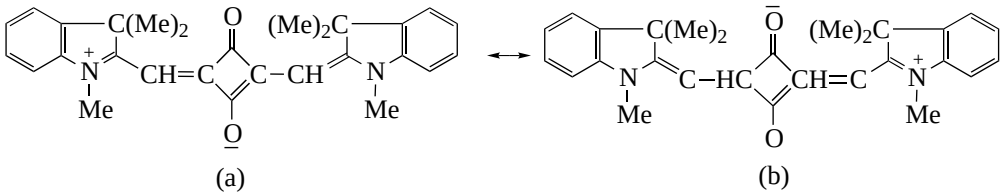

6

Fig. 6. Structural formulas of symmetric squaraine *6* in (a) the ground and (b) excited states.

the structures shown in Figs. 4a and 4b is caused by changes in the numerical values of charges on particular atoms upon excitation. Similar tendencies in the charge distribution are characteristic of symmetric anionic dyes of type *5* (Fig. 5).

The third group of dyes also includes the symmetric squaraine-type dyes. They are a variety of intraionic dyes, which, unlike merocyanines, have bipolar structures in both the ground and excited states. A representative of this dye group is squaraine *6* (Fig. 6).

The samples were prepared in the form of structures with a free surface: glass substrate–conducting layer $SnO_2 : In_2O_3$–polymer film. We used PEPC, poly(styrene) (PS), and poly(vinyl butyral) (PVB) films with a dye content of 1 wt %. The polymer films were obtained by drying polymer solutions with a dye in 1,2-dichloroethane, which were spread over the surfaces of glass substrates with $SnO_2 : In_2O_3$ layers. The thickness of the dried films was 1.5–2 μm.

The absorption coefficient of the prepared polymer films and its change in an external electric field were measured on a KSVU-23 spectrometric computer system. Initially, the absorption coefficient κ_0 of the polymer film without an external electric field was determined at the chosen wavelength λ. Then, the polymer film was charged in a corona discharge, the variation in the absorption coefficient with time was recorded to the attainment of its new quasi-stationary value, and the absorption coefficient κ_E in the external electric field E was determined. These values were used to calculate the change in the absorption coefficient in the external electric field: $\delta\kappa = \kappa_E - \kappa_0$. The polymer film was charged in a corona discharge with a special electronic device. The electric field strength E in the film was determined from the difference in potential between the free surface and the $SnO_2 : In_2O_3$ conducting layer. The obtained E values varied in the range $(6–10) \times 10^7$ V/m. The absorption coefficients and $\delta\kappa$ were measured in the light wavelength range 400–1000 nm, in which the optical absorption is observed in dyes and is absent in PEPC, PS, and PVB. The measurements were performed for unpolarized and linearly polarized light at different polarization angles. In the latter case, ahead of the entrance slit of the monochromator, an additional polarizer (with a variable polarization direction) was put in the light beam passed from the light source through a polarizer and the studied sample. The experiments were carried out at the temperature $T = 293$ K.

3. RESULTS

For all samples studied, the external electric field affects the optical absorption spectra of the PEPC, PS, and PVB films containing dyes (Figs. 7–9). After the application of an electric field, this effect manifests itself in the appearance of maxima and minima in the $\delta\kappa(\lambda)$ dependence in the light wavelength range that corresponds to the absorption maximum of dyes. When the electric field is switched off, the absorption spectrum completely regains its initial form. It is proved that the replacement of the PEPC polymer matrix with the PS and PVB matrices leads to a change in the wavelength λ of the absorption maximum of the dye due to the change in the refractive index and the permittivity of the polymers [14]; however, this replacement does not affect the sequence of maxima and minima in the $\delta\kappa(\lambda)$ dependence. The sequences of maxima and minima are also identical in the $\delta\kappa(\lambda)$ dependences mea-

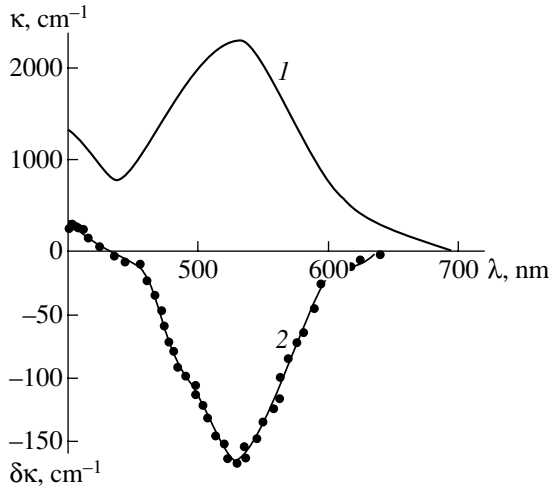

Fig. 7. Wavelength dependences of (*1*) the absorption coefficient and (*2*) its change in the electric field for PEPC films with dye *1*. Dye content is 1 wt %, $E = 8 \times 10^7$ V/m.

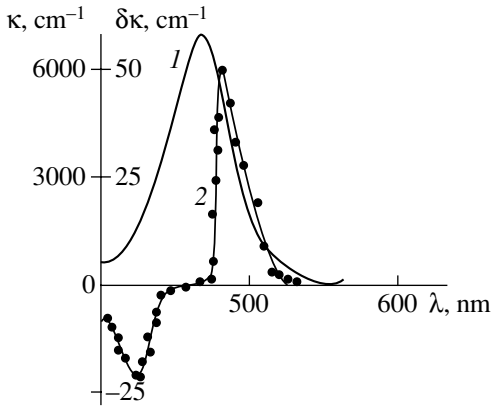

Fig. 8. Wavelength dependences of (*1*) the absorption coefficient and (*2*) its change in the electric field for PEPC films with dye *2*. Dye content is 1 wt %, $E = 8 \times 10^7$ V/m.

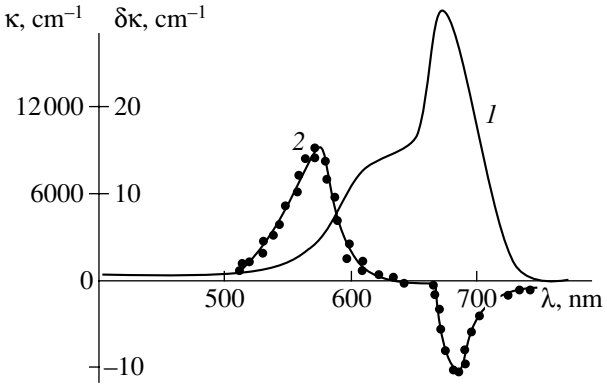

Fig. 9. Wavelength dependences of (*1*) the absorption coefficient and (*2*) its change in the electric field for PEPC films with dye *4*. Dye content is 1 wt %, $E = 8 \times 10^7$ V/m.

sured for the samples with polymer films containing dyes of the same group. The magnitudes of $\delta\kappa$ increase with an increase in strength of the external electric field but remain independent of the polarization of incident and passed (through the sample) light. After the application of an external electric field, the absorption coefficient changes with the rate of film surface charging for a time of no longer than 0.2 s for polymer films with dyes of the second (dyes *2*, *3*) and third (dyes *4–6*) groups and for a time of more than 20 s for polymer films with dyes of the first group (dye *1*).

The difference of the polymer films with dyes of the first group (dye *1*) from the films with dyes of the second (dyes *2*, *3*) and third (dyes *4–6*) groups also lies in the fact that the κ coefficient for the former films in an external electric field decreases over the entire wavelength range corresponding to the long-wavelength absorption maximum. Specifically, as follows from the dependences $\kappa(\lambda)$ and $\delta\kappa(\lambda)$ for the PEPC films with dye *1* (Fig. 7), the location of the minimum in the $\delta\kappa(\lambda)$ dependence coincides with that of the maximum in the $\kappa(\lambda)$ dependence.

In the case of polymer films with dyes *2* and *3* (second group), as the light wavelength decreases (beginning with the long-wavelength absorption edge), the $\delta\kappa(\lambda)$ dependence exhibits first a maximum and then a minimum. This sequence of the extrema in the $\delta\kappa(\lambda)$ dependence for the PEPC films containing a dye of the second group is displayed in Fig. 8. Note that the dependence under consideration changes sign near the light wavelengths that correspond to the absorption maximum of the dye, and the difference in locations of the maximum and the minimum in the $\delta\kappa(\lambda)$ dependence is approximately equal to 40 nm (~0.35 eV).

For the third group (dyes *4–6*), with a decrease in the light wavelength (beginning with the long-wavelength absorption edge), the $\delta\kappa(\lambda)$ dependence shows first a minimum and then a maximum (Fig. 9). It should also be noted that the $\delta\kappa(\lambda)$ dependence changes sign near the light wavelengths that correspond to the absorption maximum of the dye, and the difference in locations of the minimum and the maximum in this dependence is about 110 nm (~0.49 eV).

4. DISCUSSION

For all three groups of dyes, the absorption spectra completely regain their initial shape after switching off the electric field. The spectra are regularly reproduced after each application of the field. Consequently, the spectral effects described are unrelated to the decomposition of the dyes. It can be assumed that the changes observed in the absorption spectra of the polymer films with dyes in an external electric field are caused by several factors.

A decrease in the absorption coefficient of the polymer films with an increase in the electric field strength can be explained by the increase in the concentration of

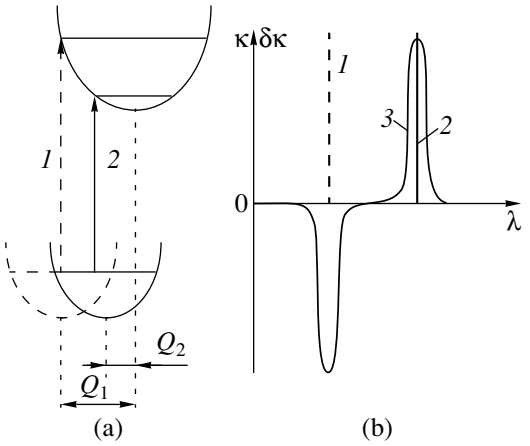

Fig. 10. (a) Energy diagrams and electron transitions in a molecule of dyes of the second group and (b) the dependences $\kappa(\lambda)$ and $\delta\kappa(\lambda)$ for these transitions.

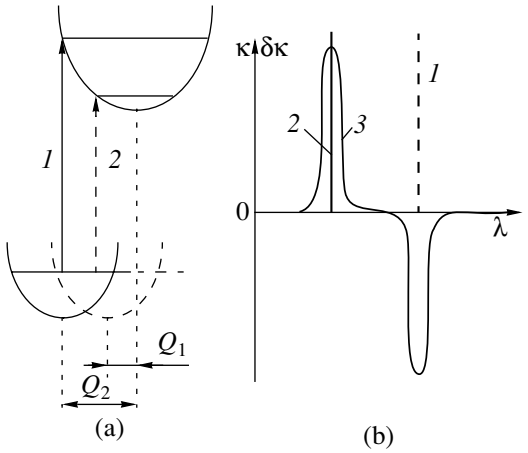

Fig. 11. (a) Energy diagrams and electron transitions in a molecule of dyes of the third group and (b) the dependences $\kappa(\lambda)$ and $\delta\kappa(\lambda)$ for these transitions.

charge carriers due to photogeneration of electron–hole pairs and their separation in the electric field as a result of the charge transfer between molecules. This should bring about a change in the charge state of dye molecules, a decrease in the intensity of the absorption band of the dye, and the appearance of absorption bands associated with radicals of the dye and molecules involved in the charge carrier transfer. However, the effect of electric field on the absorption spectra of the dyes is observed not only in the PEPC films (characterized by photogeneration and a transfer of charge carriers) but also in the PS and PVB films in which photoconductivity is absent. Moreover, the maxima in the $\delta\kappa(\lambda)$ dependences for the PEPC films with different dyes are observed at different light wavelengths; hence, these maxima cannot be identified with the absorption maxima of carbazole cation radicals formed upon photogeneration and a transfer of holes.

The second possible reason for the change in the absorption spectra is the splitting of the electron transition energies in the electric field (Stark effect). However, the dependences $\delta\kappa(\lambda)$ for the studied samples with dyes of the first group exhibit only a minimum in the range corresponding to the absorption band of the dye. Any maxima that would be characteristic of the Stark effect [16] are absent. In the case of samples with dyes of the second and third groups, the location of the minimum in the $\delta\kappa(\lambda)$ dependence does not coincide with the location of the maximum in the $\kappa(\lambda)$ dependence and the considerable energy separation between the maxima and minima in the $\delta\kappa(\lambda)$ dependences (Figs. 8, 9, curves *2*) is larger than that expected for the Stark effect in the electric fields used [16]. Furthermore, the absorption spectra are unaffected by the polarization of the incident light. Therefore, even though the effects under consideration are associated with the polarizabilities of dye molecules in an electric field, this phenomenon calls for more detailed investigation.

We assume that the change in the absorption spectra of the polymer films with dyes in an electric field is primarily determined by the polarization of electron shells of dye molecules. However, in the case of dye molecules with a large dipole moment, the observed effect can also be caused by the change in the molecular orientation.

The dyes of the first group in the ground state have a pronounced bipolar structure and are most strongly affected by the external electric field. The mechanism of this effect can be explained by the increase in the differences between the structures in the ground and excited states, which is accompanied by a broadening of the absorption band and a decrease in its intensity [14]. Moreover, molecules of these dyes are prone to reorientation in the electric field. For this reason, they are characterized by a decrease in the absorption coefficient over the entire spectral range of the long-wavelength absorption maximum. Note also that the large duration of change in κ after switching on the electric field can be associated with the rotational mobility of dye molecules in the polymer matrix. The mechanism of this phenomenon is similar to the Freédericksz effect [12, 13].

For dyes of the second and third groups, the time of variations in the absorption spectra after switching on the electric field is short and can be determined by the polarization of electron shells of dye molecules. This mechanism consists in redistributing the electron density among terminal parts of the π-conjugated system. Therefore, the features in the $\delta\kappa(\lambda)$ dependences are brought about by the electronic structure and the symmetry of dye molecules. The latter circumstance can be explained using energy diagrams for the ground and excited states of a dye molecule.

For molecules of dyes of the second group, the electron transitions from the ground to the first excited state prior to (transition *1*) and after the application of an electric field (transition *2*) are depicted by vertical arrows in Fig. 10a. In the electric field, the electron density is redistributed compared to the initial equilibrium distribution over nuclei of the atoms forming the molecule. As a result, the initial asymmetric distribution of the electron density among terminal parts of the molecule is averaged throughout the molecular structure, which can be represented as the averaging of the electron density over regions near atomic nuclei. Consequently, the potential energy minimum of the ground state becomes closer to that of the excited state. The differences between the locations of the potential energy minima in the ground and excited states are designated by the generalized coordinates Q_1 (without the electric field) and Q_2 (with the electric field) (Fig. 10a). Figure 10b schematically shows the absorption lines *1* and *2* (in the absence and in the presence of the electric field, respectively), which correspond to transitions *1* and *2* in Fig. 10a, and the expected change $\delta\kappa(\lambda)$ (curve *3*) in the absorption spectrum of the asymmetric polymethine dye in the electric field. Note that the sequence of the maximum and minimum in the $\delta\kappa(\lambda)$ dependence in Fig. 10b agrees with that for polymer films with dyes of the second group (Fig. 8).

The symmetric dyes of the third group are characterized by a uniform distribution of the electron density among terminal parts of the π-conjugated system of the molecule in the ground state. The application of an external electric field results in the breaking of this symmetry due to the redistribution of the electron density along the electric field lines. As a consequence, the potential energy minimum of the ground state moves away from that of the excited state. For this situation, the electron transitions from the ground to the excited state in the absence (transition *1*) and in the presence (transition *2*) of the electric field are displayed in Fig. 11a. The absorption lines *1* and *2* of electron transitions (without and with the electric field, respectively) and the expected change $\delta\kappa(\lambda)$ (curve *3*) in the absorption spectrum of the symmetric polymethine dye in the electric field are depicted in Fig. 11b. It should also be noted that the sequence of the maximum and minimum in the $\delta\kappa(\lambda)$ dependence in Fig. 11b is in agreement with that for the polymer films with symmetric dyes of the third group (Fig. 9).

5. CONCLUSION

Thus, changes in the absorption spectra of the films containing dyes of all three groups are observed in the range of the long-wavelength absorption maximum of the dye under the influence of an external electric field. These changes can be explained by the spatial redistribution of the electron density in the electric field. Consequently, the external electric field induces the anisotropy in the distribution of dipole moments of electron transitions inside the dye molecules. Upon photogeneration, this can result in the predominant transfer of charge carriers from dye molecules to the amorphous molecular semiconductor along the electric field lines. Therefore, it should be expected that, in doped amorphous molecular semiconductors, an increase in strength of the external electric field can result in an increase in the quantum yield of electron–hole pair photogeneration due to the induced anisotropy of the photogeneration centers themselves.

REFERENCES

1. N. G. Kuvshinskiĭ, N. A. Davidenko, and V. M. Komko, *Physics of Amorphous Molecular Semiconductors* (Lybid', Kiev, 1994).
2. M. Pope and C. E. Swenberg, *Processes in Organic Crystals* (Clarendon, Oxford, 1982).
3. L. Onsager, Phys. Rev. **54** (5), 554 (1938).
4. V. M. Gol'danskiĭ, L. I. Trakhtenberg, and V. N. Flerov, *Tunneling Phenomena in Chemical Physics* (Nauka, Moscow, 1986).
5. K. I. Zamaraev, R. Khaĭrutdinov, and V. P. Zhdanov, *Electron Tunneling in Chemistry* (Nauka, Moscow, 1985).
6. N. A. Davidenko and G. N. Kuvshinsky, J. Inf. Rec. Mater. **21**, 612 (1994).
7. N. A. Davidenko and A. A. Ishchenko, Chem. Phys. **247**, 237 (1999).
8. N. A. Davidenko, A. K. Kadashchuk, N. G. Kuvshinsky, *et al.*, J. Inf. Recording **24**, 327 (1996).
9. A. K. Kadashchuk, N. I. Ostapenko, N. A. Davidenko, *et al.*, Fiz. Tverd. Tela (St. Petersburg) **39** (7), 1183 (1997) [Phys. Solid State **39**, 1047 (1997)].
10. N. A. Davidenko, A. A. Ishchenko, A. K. Kadashchuk, *et al.*, Fiz. Tverd. Tela (St. Petersburg) **41** (2), 203 (1999) [Phys. Solid State **41**, 179 (1999)].
11. N. A. Davidenko and A. A. Ishchenko, Zh. Nauchn. Prikl. Fotogr. **44** (5), 56 (1999).
12. L. M. Blinov, *Electro-Optical and Magneto-Optical Properties of Liquid Crystals* (Nauka, Moscow, 1978; Wiley, New York, 1983).
13. S. Kielich, *Molecular Nonlinear Optics* (Warsaw, 1977; Nauka, Moscow, 1981), translated from Polish.
14. A. A. Ishchenko, *Structure and Spectral–Luminescent Properties of Polymethine Dyes* (Naukova Dumka, Kiev, 1994).
15. Ch. Reichardt, Chem. Rev. **94** (8), 2319 (1994).
16. L. D. Landau and E. M. Lifshitz, *Course of Theoretical Physics*, Vol. 3: *Quantum Mechanics: Non-Relativistic Theory* (Nauka, Moscow, 1989, 4th ed.; Pergamon, New York, 1977, 3rd ed.).

Translated by O. Borovik-Romanova

Physics of the Solid State, Vol. 43, No. 8, 2001, pp. 1433–1437. Translated from Fizika Tverdogo Tela, Vol. 43, No. 8, 2001, pp. 1376–1380.

SEMICONDUCTORS AND DIELECTRICS

A Possible Spectrum of Positron States in Porous Silicon

V. I. Grafutin*, E. P. Prokop'ev*, S. P. Timoshenkov, G. G. Myasishcheva*, and Yu. V. Funtikov***

** Institute of Theoretical and Experimental Physics, ul. Bol'shaya Cheremushkinskaya 25, Moscow, 117259 Russia*

*** Moscow Institute of Electronic Engineering (Technological University), Moscow, 103498 Russia*

e-mail: grafutin@vitep5.itep.ru

Received June 15, 2000; in final form, November 28, 2000

Abstract—A kinetic scheme of transformations and annihilation decays of positron and positronium states is considered in the bulk of a crystal in the crystal skeleton, and on the surface and in the bulk of pores of porous silicon. Formulas relating the intensities of temporal components of annihilation decay to the rates of decays and transformations of positron and positronium states in the pore volume are derived. The rate of interaction with the pore surface, accompanied by the formation of the surface state of a positronium atom, is estimated at 10^7–10^8 s^{-1}, while the estimated value for the pore radius is ≈2 nm. © *2001 MAIK "Nauka/Interperiodica".*

1. INTRODUCTION

Porous silicon, obtained by anodizing silicon single crystals in acidic alcoholic solutions of HF, is widely used in the manufacture of semiconducting devices, light-emitting devices, and micromechanical instruments and devices [1]. The structure and properties of porous silicon (specific surface and specific monocrystalline structure) depend primarily on the conditions of anodizing and thermal treatment. The properties of porous silicon, including defects of the open volume type, are often studied by using the positron annihilation technique [1–6].

Earlier investigations proved [1] that porous silicon contains a component with a lifetime varying between 400 and 600 ps. The intensity of this component depends strongly on the anodizing conditions, annealing temperature, and the properties of porous silicon. Itoh *et al.* [4] discovered a long-lived temporal component with a lifetime of several tens of nanoseconds whose intensity was determined by its pore size. The presence of this component is usually attributed to the formation of orthopositronium (ortho-Ps) in the porous layer. The authors of [4] also measured the narrow peak associated with the decay of parapositronium (para-Ps). They calculated [5] the mean pore radius from the measured lifetimes of ortho-Ps, which was found to be ~1 nm. Suzuki *et al.* [2] probed a porous silicon layer 10 μm thick with a monochromatic positron beam and concluded that positronium is formed on the pore surface. The intensity and lifetime of the positronium component strongly depended on the sample temperature and the annealing temperature. Shantarovich *et al.* [3] used methods of angular and temporal spectrometry to obtain information on the number and size of pores in porous silicon on a polycrystalline substrate. It is shown that the size distribution for pores has a peak of the order of 10^{19} cm^{-3} for a radius of approximately 7 Å. The distribution is asymmetric and extends towards larger radii. Knights *et al.* [6] studied porous silicon using a monochromatic beam of slow positrons. They observed large values of the shape parameter for the Doppler broadening of the annihilation line (DBAL), corresponding to positron annihilation in the porous layer and to para-Ps decay. The thickness of the porous layer calculated taking into account its density is in satisfactory agreement with the results of ellipsometric measurements. Experiments [6] proved that a SiO_2 layer of considerable thickness exists on the pore surface.

It should be noted that in the publications mentioned above, a detailed analysis of positron and positronium states in the bulk of pores is presented, but these states were not investigated in the substrate crystal and in the crystal skeleton. In the present paper, we will carry out such an analysis in order to systematize the properties and clarify the problem as a whole. In other words, we will study the kinetics of transformations and annihilation decays of positron and positronium states typical of materials with a developed surface [7–14].

2. POSITRON AND POSITRONIUM STATES IN POROUS SILICON

The theory of positron states in porous systems with a developed surface [15–19] and in perfect silicon crystals [20] has been considered by many authors. The concepts developed in these publications (especially in [14, 15, 20]) can also be applied to porous silicon alongside the possible concepts of positron states in defect-free silicon crystals [20]. We will consider porous silicon as a system consisting of two subsystems: (1) the bulk of the monocrystalline substrate

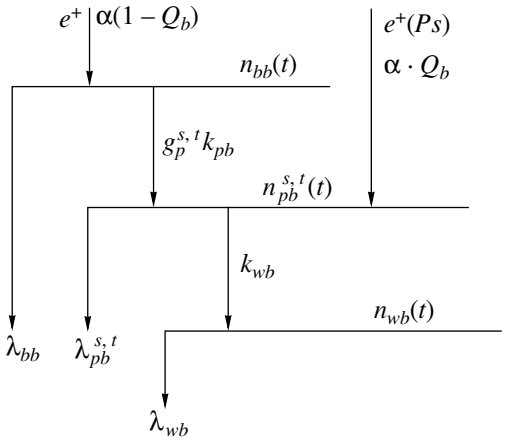

Fig. 1. Kinetic diagram of transformations and annihilation decay of positron and positronium states in a silicon crystal and in the crystal skeleton of porous silicon.

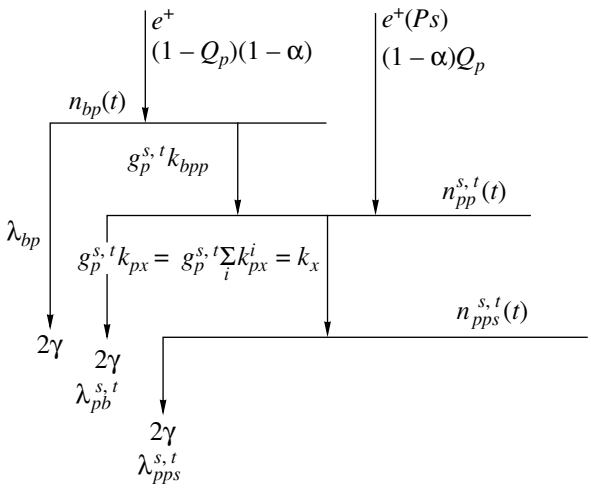

Fig. 2. Kinetic diagram of transformations and annihilation decay of positron and positronium states in porous silicon.

and of the crystal skeleton of pore walls and (2) the surface and bulk of a porous oxidized surface layer coated with SiO_2 [2, 4, 5], as well as the bulk of pores. According to the results of our earlier publications [19, 20], quasi-free positrons and Ps atoms being converted into Wheeler complexes $Ps^-(e^-e^+e^-)$ at free charge carriers can be observed in the general case [21] in the bulk of monocrystalline silicon and the crystal skeleton of porous silicon at the initial instant of time. According to [1–7], positrons and positronium in the bulk of pores and the surface states of Ps atoms were observed in a porous layer. Let us consider the conditions for the formation and properties of these states in degased *n*-type semiconductors [14] in a consistent manner in order to exclude the effects of interaction between ortho-Ps and oxygen molecules from the atmosphere. We assume that the pore surface is coated with a SiO_2 layer, so that normal positronium is formed on the surface of the semiconducting oxide (in contrast to quasi-positronium in the bulk of the crystal). In this case, a high Ps yield is possible in porous silicon as follows from the conditions for the formation of the Ps atom and for its dynamic stability [19].

The properties of positron and positronium states in the bulk of a silicon single crystal were considered in [20]. Special attention was paid to Wheeler complexes and quasi-free positrons, whose annihilation in semiconducting Si single crystals limits the lifetime to a value of $\tau_b \approx 2.24 \times 10^{-10}$ s in the bulk, which satisfactorily agrees with the experimental value $\tau_1 \approx (2.22 \pm 0.02) \times 10^{-10}$ s. Positrons and positronium emitted from the surface of the oxide layer of pores interact with the pore surface. Proceeding from the experimental data [1–7] and the concepts of positron and positronium states in porous silicon described above, we assume that the main types of states existing at a certain instant *t* are free quasi-positrons in the bulk of the monocrystalline layer and in the crystal skeleton of porous silicon with a concentration $n_{bb}(t)$. The fraction of free quasi-positrons is equal to $\alpha(1 - Q_b)$, where α is the fraction of positrons annihilated in the bulk of the crystal and Q_b is the positronium yield in the bulk of the crystal during the slowing down of positrons. Free quasi-positrons either annihilate in the two-quantum manner at a rate λ_{bb} or undergo transitions to positronium states with a concentration $n_{pb}^{s,t}(t)$ at rates $g_p^{s,t}k_{pb}$ {pb} ($g_p^{s,t}$ are the statistical weights of parapositronium (s) and orthopositronium (*t*): $g_p^s = 1/4$ and $g_p^t = 3/4$) with decay rates $\lambda_{pb}^{s,t}$. In the bulk of the crystal, positronium can be converted at free charge carriers into Wheeler complexes $n_{wb}(t)$ at a rate k_{wb}; they decay in a two-quantum manner with the rate constant λ_{wb}. The diagram of annihilation decays and transformations of positron and positronium states is presented in Fig. 1.

Figure 2 shows the diagram of transformations and annihilation decays of positron and positronium states in the bulk of pores and on the surface of porous silicon. The main types of positron and positronium states in this case are positron states with concentration $n_{bp}(t)$ [whose share is $(1 - \alpha)(1 - Q_p)$] and positronium states with concentration $n_{pp}^{s,t}(t)$ [whose share is $(1 - \alpha)Q_p$] in the bulk of pores, where $1 - \alpha$ is the relative number of positrons annihilated in the bulk of pores and on the surface of porous silicon and Q_p is the positronium yield in the bulk of pores and on the surface of porous silicon during the slowing down of positrons. Free positrons with concentration $n_{bp}(t)$ interact with the pore surface at a rate $g_p^{s,t}k_{bpp}$ and form Ps atoms with concentration $n_{pp}^{s,t}(t)$ or are annihilated in the two-quantum manner as a result of collisions at rates λ_{bp}. In

turn, Ps atoms of concentration $n_{pps}^{s,t}(t)$ interact with the pore surface and either form surface states of Ps atoms with concentration $n_{pps}^{s,t}(t)$ at rates $g_p^{s,t}k_{px} = g_p^{s,t}\sum_i k_{px}^i = k_x$ (k_{px}^i is the rate of the i-type interaction) or decay at rates $\lambda_{pp}^{s,t}$ as a result of collisions with the surface. The surface states of Ps atoms decay at rates $\lambda_{pps}^{s,t}$.

3. KINETICS OF TRANSFORMATIONS AND ANNIHILATION DECAYS OF POSITRON AND POSITRONIUM STATES IN POROUS SILICON

Taking into account the positron and positronium states considered above (Figs. 1, 2), we can write a system of kinetic equations for their transformations and annihilation decays as follows [22, 23].

For the processes in the bulk of the crystal and in the crystal skeleton of pores, we have

$$\frac{dn_{bb}}{dt} = -(\lambda_{bb} + k_{bp})n_{bb} = -\mu_{bb}n_{bb}, \quad (1)$$

$$\frac{dn_{pb}^{s,t}}{dt} = g_p^{s,t}k_{bp}n_{bb} - (\lambda_{pb}^{s,t} + k_{wb})n_{pb}^{s,t} = g_p^{s,t}k_{bp}n_{bb} - \mu_{pbb}^{s,t}n_{pb}^{s,t}, \quad (2)$$

$$\frac{dn_{wb}}{dt} = g_p^{s,t}k_{wb}n_{pb}^{s,t} - \lambda_{wb}n_{wb}. \quad (3)$$

The system of equations (1)–(3) for the bulk of the crystal and for the crystal skeleton of pores is supplemented with the initial conditions for $t = 0$:

$$n_{bb}(0) = \alpha(1-Q_b)n_0, \quad n_{pb}^s(0) + n_{pb}^t(0) = \alpha Q_b n_0,$$
$$n_{pb}^s(0) = \frac{1}{4}\alpha Q_b n_0, \quad n_{pb}^t(0) = \frac{3}{4}\alpha Q_b n_0, \quad (4)$$
$$n_{wb}(0) = 0.$$

For the most probable processes in the bulk of pores in porous silicon and on its surface, we have

$$\frac{dn_{bp}}{dt} = -(\lambda_{bp} + k_{bpp})n_{bp} = -\mu_{bp}n_{bp}, \quad (5)$$

$$\frac{dn_{pp}^s}{dt} = g_p^s k_{bpp}n_{bp} - g_p^s(\lambda_{pp}^s + k_{px})n_{pp}^s = g_p^s k_{bpp}n_{bp} - g_p^s\mu_{ppx}^s n_{pp}^s, \quad (6)$$

$$\frac{dn_{pp}^t}{dt} = g_p^t k_{bpp}n_{bp} - g_p^t(\lambda_{pp}^t + k_{px})n_{pp}^t = g_p^t k_{bpp}n_{bp} - g_p^t\mu_{ppx}^t n_{pp}^t, \quad (7)$$

$$\frac{dn_{pps}^s}{dt} = g_p^s k_x n_{pps}^s - \lambda_{pps}^s n_{pps}^s, \quad (8)$$

$$\frac{dn_{pps}^t}{dt} = g_p^t k_x n_{pps}^t - \lambda_{pps}^t n_{pps}^t. \quad (9)$$

The system of equations (5)–(9) is supplemented with the initial conditions

$$n_{bp}(0) = (1-\alpha)(1-Q_p)n_0,$$
$$n_{pp}^s(0) + n_{pp}^t(0) = (1-\alpha)Q_p n_0,$$
$$n_{pp}^s(0) = \frac{1}{4}(1-\alpha)Q_p n_0, \quad n_{pp}^t(0) = \frac{3}{4}(1-\alpha)Q_p n_0, \quad (10)$$
$$n_{pps}^s(0) = n_{pps}^t(0) = 0.$$

According to the results of our early publications [22, 23], the observed time spectrum for the system of equations (1)–(3) is determined by four components,

$$n_b(t) = -\frac{1}{\alpha n_0}\frac{dn_b}{dt} = \mu_{bb}I_{bp}\exp(-\mu_{bb}t) + \mu_{pbb}^{s,t}I_{pb}^{s,t}\exp(-\mu_{pbb}^{s,t}) + \lambda_{wb}I_{wb}\exp(-\lambda_{wb}), \quad (11)$$

where I_i^j are the intensities of the τ_i^j components in the time annihilation spectra; i.e.,

$$\tau_i^j = 1/\mu_i^j.$$

Solving the system of equations (1)–(3) with the initial conditions (4), we obtain from Eq. (11) the following values of I_i^j, i.e., the decay constants μ_i^j and λ_i^j for various τ_i^j components in the time annihilation spectra:

$$I_{bb} = \alpha(1-Q_b)\left(1 - g_p^s\frac{k_{bp}}{\mu_{bb} - \lambda_{pb}^s} - g_p^t\frac{k_{bp}}{\mu_{bb} - \lambda_{pb}^t}\right), \quad \frac{1}{\tau_{bb}} = \mu_{bb} = \lambda_{bb} + k_{bp}, \quad (12)$$

$$I_{pb}^s = g_p^s\alpha Q_b\left(1 - \frac{k_{wb}}{\mu_{pbb}^s - \lambda_{wb}}\right) + \alpha(1-Q_b)g_p^s\frac{k_{bp}}{\mu_{bb} - \lambda_{pb}^s}, \quad \frac{1}{\tau_{pbb}^s} = \mu_{pbb}^s = \lambda_{pb}^s + k_{wb}, \quad (13)$$

$$I_{pb}^t = g_p^t\alpha Q_b\left(1 - \frac{k_{wb}}{\mu_{pbb}^t - \lambda_{wb}}\right) + \alpha(1-Q_b)g_p^t\frac{k_{bp}}{\mu_{bb} - \lambda_{pb}^t}, \quad \frac{1}{\tau_{pbb}^t} = \mu_{pbb}^t = \lambda_{pb}^t + k_{wb}, \quad (14)$$

$$I_{wb} = g_p^s \alpha Q_b \frac{k_{wb}}{\mu_{pbb}^s - \lambda_{wb}} + g_p^t Q_b \frac{k_{wb}}{\mu_{pbb}^t - \lambda_{wb}}, \qquad \lambda_{wb} = \frac{1}{\tau_{wb}}. \tag{15}$$

In the case described by the system of equations (5)–(9), the observed time spectrum in the bulk of porous silicon and on the pore surface contains five components:

$$\begin{aligned} n_p(t) &= -\frac{1}{(1-\alpha)n_0}\frac{dn_p}{dt} = \mu_{bp} I_{bp} \exp(-\mu_{bp} t) \\ &+ \mu_{ppx}^s I_{pp}^s \exp(-\mu_{ppx}^s t) + \mu_{ppx}^t I_{pp}^t \exp(-\mu_{ppx}^t t) \\ &+ \lambda_{pps}^s I_{pps}^s \exp(-\lambda_{psx}^s t) + \lambda_{pps}^t I_{pps}^t \exp(-\lambda_{pps}^t t). \end{aligned} \tag{16}$$

Solving the system of equations (5)–(9) with the initial conditions (10), we determine from Eq. (16) the following values of I_i^j, as well as the decay rates μ_i^j and λ_i^j for various τ_i^j components in the time annihilation spectra:

$$I_{pb} = (1-\alpha)(1-Q_p)\left(1 - g_p^s \frac{k_{bpp}}{\mu_{pp}^s} - g_p^t \frac{k_{bpp}}{\mu_{pp}^t}\right), \qquad \frac{1}{\tau_{bp}} = \mu_{bp} = \lambda_{bp} + k_{bp}, \tag{17}$$

$$I_{pp}^s = g_p^s (1-\alpha) Q_p \left(1 - \frac{k_x}{\mu_{ppx}^s - \lambda_{pps}^s}\right) + (1-\alpha)(1-Q_p) g_p^s \frac{k_{bpp}}{\mu_{bp} - \lambda_{pp}^s}, \qquad \frac{1}{\tau_{ppx}^s} = \mu_{ppx}^s = \lambda_{pp}^s + k_{px}, \tag{18}$$

$$I_{pp}^t = g_p^t (1-\alpha) Q_p \left(1 - \frac{k_x}{\mu_{ppx}^t - \lambda_{pps}^t}\right) + (1-\alpha)(1-Q_p) g_p^t \frac{k_{bpp}}{\mu_{bp} - \lambda_{pp}^t}, \qquad \frac{1}{\tau_{ppx}^t} = \mu_{ppx}^t = \lambda_{pp}^t + k_{px}, \tag{19}$$

$$I_{pps}^s = g_p^s (1-\alpha) Q_p \frac{k_x}{\mu_{ppx}^s - \lambda_{pps}^s}, \quad \frac{1}{\tau_{ppx}^s} = \lambda_{pps}^s, \tag{20}$$

$$I_{pps}^t = g_p^t (1-\alpha) Q_p \frac{k_x}{\mu_{ppx}^t - \lambda_{pps}^t}, \quad \frac{1}{\tau_{pps}^t} = \lambda_{pps}^t. \tag{21}$$

Thus, in accordance with Eqs. (12)–(15) and (17)–(21), the time annihilation spectrum for porous silicon is determined by nine components with lifetimes τ_i^j. At the same time, most experiments on annihilation [1–7] prove that the time spectrum can be resolved into three components: $\tau_1(I_1)$, $\tau_2(I_2)$, and $\tau_3(I_3)$. According to Itoh *et al.* [5], the values of these components for some porous silicon samples are $\tau_1 \approx 230$ ps ($I_1 = 47$–91%), $\tau_2 \approx 580$–1030 ps ($I_2 = 3$–7%), while the values of $\tau_3(I_3)$ considerably depend on the method of sample preparation. For instance, $\tau_3 = 25800$–36300 ps ($I_3 = 6$–18%) for samples obtained for a current density of ~ 100 mA/cm^2, while for samples obtained for a current density of ~10 mA/cm^2, these parameters are $\tau_3 = 4500$–5300 ps ($I_3 = 1$–2%). It is found that the curves describing the angular distribution of annihilation photons contain a narrow component I_N and that the parameter S of the Doppler broadening spectra is smaller than the value of S for bulk silicon.

Consequently, proceeding from these experimental data and in accordance with our earlier results [22, 23], we can single out in Eqs. (12)–(15) and (17)–(21) three groups of lifetimes: τ_M, $\tau_3 = \tau_{pps}^t = 1/\lambda_{pps}^t$, and $\tau_2 = \tau_{ppx}^t = 1/\mu_{ppx}^t$, which are given by

$$\tau_1 = \tau_M = \frac{\tau_b I_b + \tau_{bp} I_{bp} + \tau_{pps}^s I_{pps}^s + \tau_{pp}^s I_{pp}^s}{I_b + I_{bp} + I_{pps}^s + I_{pp}^s}, \tag{22}$$

where τ_b is the bulk lifetime in perfect silicon crystals and I_b is defined as

$$I_b \equiv \alpha = I_{bb} + I_{pb}^s + I_{pb}^t + I_w. \tag{23}$$

In accordance with what has been said above, the long-lived components $\tau_3(I_3)$ and $\tau_2(I_2)$ in the bulk of porous silicon are given by

$$\tau_3 = 1/\lambda_3 = \tau_{pps}^t = 1/\lambda_{pps}^t, \tag{24}$$

$$I_3 = I_{pps}^t = g_p^t (1-\alpha) Q_p \frac{k_x}{\mu_{ppx}^t - \lambda_{pps}^t}, \tag{25}$$

$$\tau_2 = 1/\lambda_2 = \tau_{ppx}^t = 1/\mu_{ppx}^t = 1/(\lambda_{pp}^t + k_x), \tag{26}$$

where

$$\lambda_{pp}^t = \lambda_{pp0}^t + \lambda_p. \tag{27}$$

Here, $\lambda_{pp0}^t = 0.714 \times 10^7$ s^{-1} is the 3γ annihilation rate of ortho-Ps in the bulk of a pore, which is, in general, a function of the pore size for small radii [9]; λ_p is the rate of pick-off annihilation of ortho-Ps due to a collision with a pore wall; and $k_x = g_p^{s,t} k_{px} = g_p^{s,t} \sum_i k_{px}^i$ is the rate of interaction of ortho-Ps with the pore surface, which involves the rates of ortho–para Ps conversion at

surface paramagnetic centers. The intensity I_2 is given by

$$I_2 = I_{pp}^t = g_p^t(1-\alpha)Q_p\left(1-\frac{k_x}{\mu_{ppx}^t-\lambda_{pps}^t}\right) + (1-\alpha)(1-Q_p)\frac{k_{bpp}}{\mu_{bp}-\lambda_{pps}^t}. \quad (28)$$

Expressions (25) and (28) for $k_{bpp} \longrightarrow 0$ lead to

$$I_2 + I_3 = g_p^t(1-\alpha)Q_p. \quad (29)$$

Substituting this expression into Eq. (25), we obtain

$$\frac{I_3}{I_2+I_3} = \frac{k_x}{\mu_{ppx}^t-\lambda_{pps}^t} = \frac{k_x}{\lambda_2-\lambda_3}, \quad (30)$$

or

$$k_x = (\lambda_2-\lambda_3)\frac{I_3}{I_2+I_3}. \quad (31)$$

Thus, it becomes possible to determine the interaction rates of ortho-Ps with the surface, accompanied by the formation of the Ps surface state, directly from the experimental data on $\tau_3(I_3)$ and $\tau_2(I_2)$. Proceeding from Eqs. (24) and (27), the rate $\lambda_2 = 1/\tau_2$ can be written in the form

$$\lambda_2 = \lambda_{pp0}^t + \lambda_p + k_x, \quad (32)$$

where λ_p and k_x are the rate of annihilation and the rate of formation of the Ps surface state, respectively. The quantum-mechanical calculations of $\lambda_2 = 1/\tau_2$ carried out in [9] allowed us to establish the relation between λ_2 and the pore radius R_0 with an approximate average experimental value $\bar{r}_{\text{pore}}$:

$$\lambda_2 = 2[1 - R/R_0 + (2\pi)^{-1}\sin(2\pi R/R_0)], \quad (33)$$

where

$$R = R_0 - R_W, \quad R_W = 1.656\ \text{Å}.$$

Here, R_W is the effective size of the positronium annihilation region in the pore walls.

This enabled us to use formulas (31) and (33) to estimate, on the basis of the experimental data [2, 5], the values $k_x \approx 10^7$–10^8 s^{-1} and $\bar{r}_{\text{pore}} \approx 2$ nm, which are in accordance with the results obtained by other authors [2]. Thus, the value ≈2 nm of the pore radius following from Eq. (33) corresponds to $\lambda_2 \approx 10^9$ s^{-1}. Comparing this value with $k_x \approx 10^8$ s^{-1}, we may conclude that the chemical interaction of orthopositronium in a pore reduces the lifetime by approximately 10%.

REFERENCES

1. R. M. de la Cruz and R. Pareja, in *Positron Annihilation*, Ed. by L. Dorikens-Vanpraet, M. Dorikens, and D. Segers (World Scientific, Singapore, 1989), p. 702.
2. R. Suzuki, T. Mikado, H. Ohgaki, *et al.*, Phys. Rev. B **49** (24), 17484 (1994).
3. V. P. Shantarovich, I. B. Kevdina, Yu. A. Novikov, *et al.*, Fiz. Tverd. Tela (St. Petersburg) **38** (9), 2686 (1996) [Phys. Solid State **38**, 1473 (1996)].
4. Y. Itoh, H. Murakami, and A. Kinoshita, Appl. Phys. Lett. **63** (20), 2798 (1993).
5. Y. Itoh, H. Murakami, and A. Kinoshita, Hyperfine Interact. **84** (1), 121 (1994).
6. A. P. Knights, G. Kowalski, A. S. Saleh, *et al.*, J. Appl. Phys. **78** (7), 4411 (1995).
7. Y. C. Yean, Microchem. J. **42** (1), 72 (1990).
8. R. B. Gregory, J. Appl. Phys. **70** (9), 4665 (1991).
9. E. P. Prokop'ev, in *Proceedings of the 47th International Conference on Nuclear Spectroscopy and Atomic Nuclear Structure* (Nauka, St. Petersburg, 1996), p. 377.
10. V. P. Shantarovich, Yu. P. Yampol'skiĭ, and I. B. Kevdina, Khim. Vys. Énerg. **28** (1), 53 (1990).
11. I. B. Kevdina, Yu. M. Sivergin, and V. P. Shantarovich, Khim. Vys. Énerg. **30** (2), 145 (1990).
12. V. P. Shantarovich, V. I. Kleĭner, A. Yu. Alent'ev, *et al.*, Khim. Vys. Énerg. **32** (1), 34 (1998).
13. V. P. Shantarovich, Yu. A. Novikov, and Z. K. Azamatova, Fiz. Tverd. Tela (St. Petersburg) **40** (1), 164 (1998) [Phys. Solid State **40**, 147 (1998)].
14. A. V. Goldanskii, V. A. Onishuk, and V. P. Shantarovich, Phys. Status Solidi A **108** (2), 550 (1987).
15. G. M. Bartenev, A. Z. Varisov, V. I. Gol'danski, *et al.*, Dokl. Akad. Nauk SSSR **197** (3), 510 (1971).
16. E. P. Prokop'ev, Kinet. Katal. **18** (3), 776 (1977).
17. A. O. Tatur, Author's Abstract of Candidate's Dissertation in Mathematical Physics (Moscow, 1972).
18. A. O. Tatur and A. D. Mokrushin, Fiz. Tverd. Tela (Leningrad) **14** (10), 3060 (1972) [Sov. Phys. Solid State **14**, 2617 (1972)].
19. E. P. Prokop'ev, S. P. Timoshenkov, V. I. Grafutin, G. G. Myasishcheva, and Yu. V. Funtikov, *Positronics of Ionic Crystals, Semiconductors and Metals* (Mosk. Gos. Inst. Élektron. Tekh., Moscow, 1999).
20. E. P. Prokop'ev, Khim. Fiz. **18** (5), 45 (1999).
21. J. A. Wheeler, Ann. (N.Y.) Acad. Sci. **48** (1), 219 (1946).
22. E. P. Prokop'ev, Available from TsNII "Electronics" No. P-5154 (Moscow, 1989).
23. E. P. Prokop'ev, Available from TsNII "Electronics" No. P-5172 (Moscow, (1989).

Translated by N. Wadhwa

Physics of the Solid State, Vol. 43, No. 8, 2001, pp. 1438–1441. Translated from Fizika Tverdogo Tela, Vol. 43, No. 8, 2001, pp. 1381–1384.

SEMICONDUCTORS AND DIELECTRICS

Evaluation of Band Gaps in $CuGa(S_xSe_{1-x})_2$ Solid Solutions from Calculated Total Densities of States

A. A. Lavrent'ev, B. V. Gabrel'yan, and I. Ya. Nikiforov

Don State Technical University, Rostov-on-Don, 344010 Russia

e-mail: sintez@aaanet.ru

Received September 21, 2000; in final form, December 1, 2000

Abstract—The local partial and total densities of states in $CuGa(S_xSe_{1-x})_2$ (x = 0, 0.17, 0.33, 0.50, 0.67, 0.83, and 1.0) solid solutions are calculated by the local coherent potential method within the virtual crystal approximation. The lattice parameters of the chalcopyrite solid solutions under investigation are determined in the framework of the Jaffe–Zunger theory with the use of the Pauling tetrahedral radii. It is revealed that the band gap E_g linearly depends on the sulfur concentration x in the anionic sublattice. This result is in agreement with the experimental data, but the theoretical band gaps E_g are found to be approximately 0.5 eV less than the experimental values. *© 2001 MAIK "Nauka/Interperiodica".*

1. INTRODUCTION

Solid solutions in the $CuGaS_2$–$CuGaSe_2$ system exhibit complete solubility; i.e., they can exist at any sulfur concentration x in the anionic sublattice [1]. For the most part, the properties of $CuGa(S_xSe_{1-x})_2$ solid solutions have been thoroughly investigated experimentally. In particular, their photoluminescence and reflectivity spectra were analyzed in [2, 3]. Bodnar *et al.* [4] studied the microhardness of $CuGa(S_xSe_{1-x})_2$ (and a number of other) solid solutions. Experimental and theoretical investigations into the electronic band structure of different chalcopyrites of the $A^IB^{III}C_2^{VI}$ type and their solid solutions were reported in [5–11].

In calculations, the electronic band structure of the $A^IB^{III}C_2^{VI}$-type compounds is traditionally compared with that of isoelectronic and isostructural binary compounds of the $A^{II}B^{VI}$ type. Under normal conditions, the majority of the $A^{II}B^{VI}$ binary compounds crystallize in a sphalerite (zinc blende) lattice, which can be represented as two face-centered cubic sublattices shifted relative to each other by a quarter of the principal diagonal of the cube. In this structure, the nearest environment of each anion (cation) involves four cations (anions) occupying the vertices of a regular tetrahedron. In all the $A^{II}B^{VI}$ chalcogenides, the valence band top is predominantly formed by the p electron states of the anion and the conduction band bottom is determined by the s and p states of the cation and the p and d states of the anion [12, 13].

The $CuGa(S_xSe_{1-x})_2$ solid solutions, as well as $CuGaS_2$ and $CuGaSe_2$ compounds, crystallize in a chalcopyrite lattice, which, to a first approximation, can be considered a sphalerite lattice doubled along the z axis (the crystal lattice is specified by two unit-cell parameters, namely, the parameter a along the x and y axes and the parameter $c = 2a$ along the z axis). However, unlike the sphalerite lattice, the face-centered cationic sublattice contains metals of two types; i.e., this sublattice can be separated into two sublattices, one of which contains only Cu atoms and the other is composed of Ga atoms. As a result, the perfect tetrahedral environment of C^{VI} atoms becomes disturbed. This distortion is usually specified by two parameters: the tetragonal contraction parameter, which characterizes the deviation of the lattice parameter c from $2a$ (the distortion along the z axis), and the displacement of the C^{VI} atom from the tetrahedron center in the xy plane. In all the $A^IB^{III}C_2^{VI}$ chalcogenides, the valence band top is predominantly formed by the p states of the C^{VI} nonmetal and the d states of the A^I noble metal [12, 14], whereas the conduction band bottom is determined by the s states of the B^{III} metal, the p states of the B^{III} and C^{VI} atoms, and the d states of the C^{VI} atom. A specific feature of $A^IB^{III}C_2^{VI}$ ternary compounds is that the d electron states of the noble metal are localized near the valence band top, which leads to symmetry-allowed hybridization of the p states of the C^{VI} nonmetal and the d states of the A^I noble metal (the d–s, p resonance [15]). This feature brings about a substantial decrease in the band gap of $A^IB^{III}C_2^{VI}$ ternary semiconductors as compared to the band gap of isoelectronic binary analogs of the $A^{II}B^{VI}$ type.

The lattice parameters of $A^IB^{III}C_2^{VI}$ solid solutions change according to Vegard's law [16, 17]. The available experimental data also indicate that the band gap linearly depends on the solid solution composition [1, 16] and increases with an increase in the sulfur content, which is consistent with the change in color of these crystals from light green for $CuGaS_2$ to black for $CuGaSe_2$ [17].

1063-7834/01/4308-1438$21.00

2. CALCULATION TECHNIQUE

The crystal muffin-tin potential was calculated according to the scheme proposed by Vol'f *et al.* [18]. Within this approach, the crystal charge density is determined from the overlapped atomic wave functions of the components of the compound under investigation. Then, this density is used to construct both the exchange and Coulomb components of the crystal potential. The electrostatic potential of the sublattices (the Madelung potential) should also be taken into account. The exchange component of the potential is calculated within the X_α-approximation.

The local coherent potential method was developed by Gyorffy [19] for calculating the local partial densities of states in disordered substitutional solid solutions. This approach was repeatedly used in our earlier works in calculations for pure compounds and different solid solutions [12–14, 20]. The basic equations of this method were described, for example, in [12].

The solid solutions were simulated by effective scatterers in the virtual crystal approximation. The metal sublattices were composed of real scatterers, and the anionic sublattice consisted of effective scatterers with

$$t_l^{\text{eff}}(E) = xt_l^{\text{S}}(E) + (1-x)t_l^{\text{Se}}(E), \qquad (1)$$

Here, t_l^{S} and t_l^{Se} are the single-site t scattering matrices for sulfur and selenium, respectively. In order to calculate the local partial densities of states for sulfur, we constructed a cluster centered at the sulfur atom. The coordination spheres of the cluster were filled with metal atoms and effective scatterers (instead of the sulfur and selenium atoms). For each type of atoms in the compound, we constructed a particular cluster and calculated the total density of states according to the formula

$$n_{\text{tot}}(E) = \sum_l n_l^{\text{Cu}}(E) + \sum_l n_l^{\text{Ga}}(E) + 2\left(x\sum_l n_l^{\text{S}}(E) + (1-x)\sum_l n_l^{\text{Se}}(E)\right). \qquad (2)$$

Jaffe and Zunger [21] proposed a theory for calculating all lattice parameters of any chalcopyrite from the atomic radii of its constituent elements. This approach makes it possible to calculate the electronic band structure of a particular compound without invoking a need for additional experimental information. This method is indispensable in the case when experimental data on the lattice parameters of chalcopyrite compounds are unavailable. In the present work, the lattice parameters of all the studied solid solutions (including $CuGaS_2$ and $CuGaSe_2$ compounds) were calculated according to the Jaffe–Zunger theory with the use of the Pauling tetrahedral covalent radii r_{tet}^i. By designating the lengths of bonds between the corresponding atoms in the $A^{\text{I}}B^{\text{III}}C_2^{\text{VI}}$ compounds as R_{AC} and R_{BC}, we calculated the parameters of chalcopyrite from the following relationships [21]:

$$R_{\text{AC}} = r_{\text{tet}}^{\text{A}} + r_{\text{tet}}^{\text{C}}, \quad R_{\text{BC}} = r_{\text{tet}}^{\text{B}} + r_{\text{tet}}^{\text{C}},$$
$$a = \sqrt{\frac{12a^2}{2\beta + \alpha - \sqrt{(2\beta+\alpha)^2 - 18\alpha^2}}},$$
$$\eta = \sqrt{\frac{8(\beta-\alpha)}{3a^2}}, \qquad (3)$$
$$u = \frac{1}{2} - \frac{1}{4}\sqrt{2\eta^2 - 1},$$

where $\alpha = R_{\text{AC}}^2 - R_{\text{BC}}^2$ and $\beta = R_{\text{AC}}^2 + R_{\text{BC}}^2$.

The calculated parameters are linearly dependent on the sulfur concentration in the anionic sublattice and exceed the experimental values by approximately 0.1 Å.

In all the calculations, the clusters contained approximately 150 atoms.

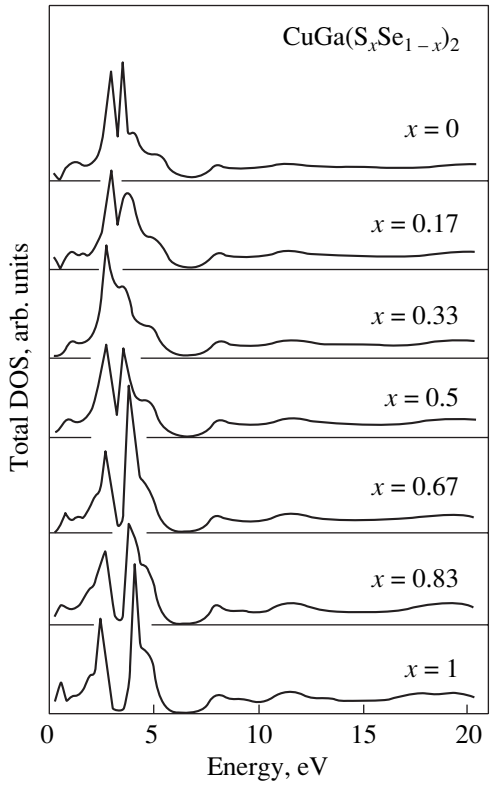

Fig. 1. Calculated total densities of states in $CuGa(S_xSe_{1-x})_2$ solid solutions for clusters containing approximately 150 atoms.

3. RESULTS AND DISCUSSION

Figure 1 shows the calculated total densities of states in the $CuGa(S_xSe_{1-x})_2$ solid solutions at sulfur concentrations x = 0, 0.17, 0.33, 0.50, 0.67, 0.83, and

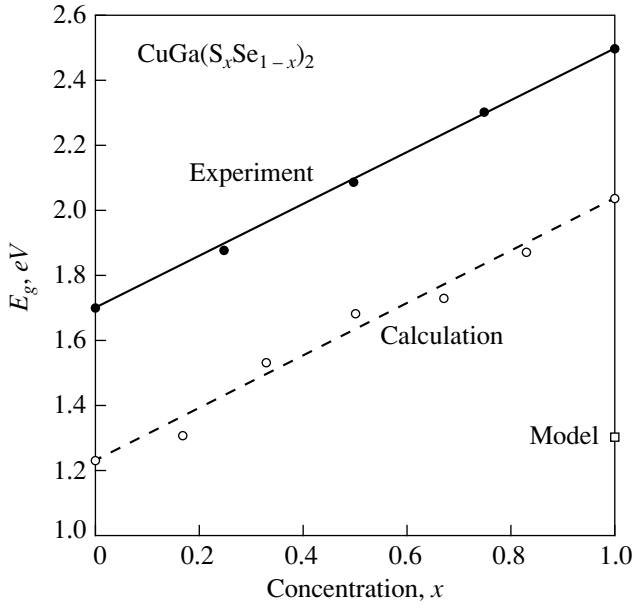

Fig. 2. Dependences of the band gap E_g on the sulfur concentration in the anionic sublattice of CuGa(S$_x$Se$_{1-x}$)$_2$ solid solutions. The experimental data are taken from [22].

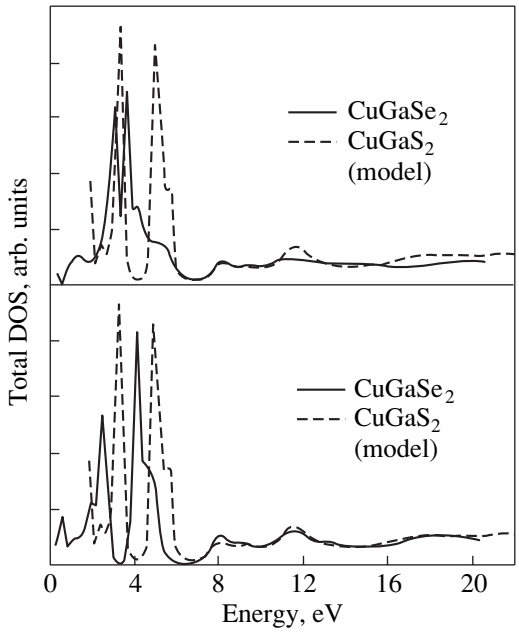

Fig. 3. Calculated total densities of states in $CuGaSe_2$ and $CuGaS_2$. Dashed lines are the total densities of states in $CuGaS_2$ with the lattice parameters characteristic of $CuGaSe_2$.

1.0 in the anionic sublattice. As follows from the calculations, the substitution of sulfur for selenium does not lead to the formation of new levels in the band gap but results in a gradual energy shift of the valence band top and the conduction band bottom. In this case, the valence band top shifts to the low-energy range, whereas the conduction band bottom is displaced toward the high-energy range. As a consequence, the band gap increases with an increase in the sulfur concentration.

The dependence $E_g(x)$ of the band gap on the solid solution composition (see Fig. 2, table) was determined from the total densities of states for solid solutions with different concentrations x. This dependence exhibits a linear behavior, which is in agreement with the experimental data. At first glance, it would seem that this result is trivial, because the crystallographic parameters change according to Vegard's law and the linear combination of the single-site scattering matrices of sulfur and selenium in the virtual crystal approximation is used instead of the single-site scattering matrices themselves. However, this is not the case. In our recent work [13], the electronic band structure of isostructural and isoelectronic binary analogs of CuGa(S$_x$Se$_{1-x}$)$_2$ solid solutions, namely, the ZnS$_x$Se$_{1-x}$ solid solutions, was calculated by the local coherent potential method within the virtual crystal approximation. It was proved that there is a substantial quadratic contribution to the dependence $E_g(x)$ [13]. In the present work, we qualitatively determined how the change in the Cu–S (or Cu–Se) distance affects the electronic band structure of the compound (this is the main problem associated with the virtual crystal approximation for which the difference between the Cu–S and Cu–Se bond lengths is ignored). In addition, we carried out model calculations of the electronic band structure of $CuGaS_2$ with the use of the lattice parameters characteristic of $CuGaSe_2$ compounds. Figure 3 shows the calculated total densities of states in comparison with the total densities of states in "true" $CuGaS_2$ and $CuGaSe_2$. It can be seen that the change-over from the crystallographic parameters of the $CuGaS_2$ compound to those of $CuGaSe_2$ leads to a shift of the valence band top and the conduction band bottom toward each other in such a way that the band gap of model $CuGaS_2$ coincides with the band gap of $CuGaSe_2$. Note that the shape of the total density of states in the valence band is virtually identical for both true and model $CuGaS_2$ but essentially differs for $CuGaS_2$ and $CuGaSe_2$.

Calculated and experimental band gaps E_g (eV) in CuGa(S$_x$Se$_{1-x}$)$_2$ solid solutions

Concentration x	Calculation	Experiment [22]
0.00	1.23	1.70
0.17	1.31	–
0.25	–	1.87
0.33	1.53	–
0.50	1.68	2.08
0.67	1.73	–
0.75	–	2.29
0.83	1.88	–
1.00	2.04	2.50

As can be seen from Fig. 2, the theoretical band gaps E_g are less than the experimental values. According to the results of model calculations, this discrepancy can be explained by the difference between the used and experimental lattice parameters of the studied chalcopyrites. Indeed, the band gaps E_g, which were estimated from the calculated total densities of states for $CuGaS_2$ and $CuGaSe_2$, proved to be closer to the experimental values of E_g. However, as follows from the data reported, for example, in review [21], there is a considerable scatter in the lattice parameters of $CuGaSe_2$ and, especially, $CuGaS_2$. In this case, the choice of the lattice parameters becomes ambiguous. We were primarily interested in the trend of the $E_g(x)$ curve. In this respect, the above scheme for calculating the lattice parameters of the studied chalcopyrites and their solid solutions should lead only to the same systematic absolute error in determination of E_g, which is clearly seen in Fig. 2.

The differences in the band gaps E_g are virtually identical (0.8 eV) for the ZnS_xSe_{1-x} [13] and $CuGa(S_xSe_{1-x})_2$ solid solutions at the sulfur concentrations $x = 0$ and 1. However, the absolute value of E_g for ZnS is equal to 3.8 eV, whereas E_g for $CuGaS_2$ is 2.5 eV; i.e., the latter value is 1.3 eV lower. The absolute value of E_g for ZnSe is approximately equal to 2.8 eV, whereas E_g for $CuGaSe_2$ is 1.7 eV; i.e., the latter value is 1.1 eV lower. The largest deviation in the $E_g(x)$ dependence for ZnS_xSe_{1-x} from a straight line is approximately equal to 0.1 eV, which is one order of magnitude less than the change in E_g. Therefore, the behavior of E_g in solid solutions of ternary chalcogenides is primarily affected by the same factors that lead to a decrease in E_g compared to that in their binary analogs. This factor is the *p–d* repulsive interaction (*d–s*, *p* resonance). The effect of the *p–d* repulsive interaction on the E_g band gap is proportional to the change in the densities of the S *p* and Se *p* states near the valence band top, which vary linearly with a change in the concentration. We believe that this factor is responsible for the linear behavior of E_g in the $CuGa(S_xSe_{1-x})_2$ solid solutions.

REFERENCES

1. M. Quintero, C. Rincon, and P. Grima, J. Appl. Phys. **65** (7), 2739 (1989).
2. S. Tanaka, S. Kawami, H. Kolayashi, and H. Sasakura, Phys. Chem. Solids **38** (6), 680 (1977).
3. B. K. Vainshtein, V. M. Fridkin, and V. L. Indembot, *Modern Crystallography* (Nauka, Moscow, 1979; Springer-Verlag, Berlin, 1982), Vol. 2.
4. I. V. Bodnar, B. V. Korzum, and A. P. Chernyakova, Phys. Status Solidi A **101**, 409 (1987).
5. J. L. Shay and B. Tell, Surf. Sci. **37**, 748 (1973).
6. J. E. Jaffe and A. Zunger, Phys. Rev. B **28** (10), 5822 (1983).
7. A. A. Lavrentyev, A. N. Gusatinskii, M. A. Blokhin, *et al.*, J. Phys. C **20**, 3445 (1987).
8. L. K. Samanta, D. K. Ghosh, and G. C. Bhar, Phys. Rev. B **33** (6), 4145 (1986).
9. V. F. Agekyan, D. Radzhab, and A. Yu. Serov, Fiz. Tverd. Tela (Leningrad) **32** (2), 622 (1990) [Sov. Phys. Solid State **32**, 365 (1990)].
10. V. F. Agekyan, N. V. Orekhova, D. Rajab, and A. Yu. Serov, Fiz. Tverd. Tela (St. Petersburg) **34** (7), 2272 (1992) [Sov. Phys. Solid State **34**, 1215 (1992)].
11. Yu. A. Khazitarkhanov, L. M. Suslikov, Z. P. Gal'mashi, and V. Yu. Slivka, Kvantovaya Élektron. (Kiev) **44**, 24 (1993).
12. A. A. Lavrent'ev, I. Ya. Nikiforov, A. B. Kolpachev, and B. V. Gabrel'yan, Fiz. Tverd. Tela (St. Petersburg) **38** (8), 2347 (1996) [Phys. Solid State **38**, 1291 (1996)].
13. B. V. Gabrel'yan, A. A. Lavrent'ev, and I. Ya. Nikiforov, Zh. Strukt. Khim. **41** (3), 498 (2000).
14. A. A. Lavrent'ev, B. V. Gabrel'yan, and I. Ya. Nikiforov, Zh. Strukt. Khim. **41** (3), 515 (2000).
15. E. P. Domashevskaya and V. A. Terekhov, Phys. Status Solidi B **105** (2), 121 (1981).
16. M. Robbins, J. C. Phillips, and V. B. Lambrecht, J. Phys. Chem. Solids **34**, 1205 (1973).
17. I. V. Bodnar', Yu. V. Voroshilov, and A. I. Lukomskiĭ, Neorg. Mater. **13** (5), 921 (1977).
18. G. V. Vol'f, V. V. Dyakin, and V. P. Shirokovskiĭ, Fiz. Met. Metalloved. **38** (5), 949 (1974).
19. B. L. Gyorffy, Phys. Rev. B **5** (6), 2382 (1972).
20. B. V. Gabrel'yan, A. A. Lavrent'ev, and I. Ya. Nikiforov, Fiz. Tverd. Tela (St. Petersburg) **41** (1), 41 (1999) [Phys. Solid State **41**, 35 (1999)].
21. J. E. Jaffe and A. Zunger, Phys. Rev. B **29** (4), 1882 (1984).
22. L. K. Samanta, D. K. Ghosh, and G. C. Bhar, Phys. Rev. B **35** (9), 4519 (1987).

Translated by O. Borovik-Romanova

Physics of the Solid State, Vol. 43, No. 8, 2001, pp. 1442–1444. Translated from Fizika Tverdogo Tela, Vol. 43, No. 8, 2001, pp. 1385–1387.

SEMICONDUCTORS AND DIELECTRICS

Properties of Bismuth Selenide Intercalated with Lithium from a Solution of *n*-C_4H_9Li

I. I. Grigorchak, V. V. Netyaga, S. V. Gavrilyuk, B. P. Bakhmatyuk, and Z. D. Kovalyuk

Institute of Material Sciences (Chernovtsy Branch), National Academy of Sciences of Ukraine, ul. Vilde 5, Chernovtsy, 58001 Ukraine

e-mail: chimsp@unicom.cv.ua

Received January 10, 2001

Abstract—The lithium-selective intercalation of bismuth selenide (Bi_2Se_3) samples is accomplished by treating them in a solution of *n*-butyllithium (*n*-C_4H_9Li) in hexane. It is found that, upon incorporation of lithium atoms, the interlayer spacing increases and the resistivity in the direction normal to the layers ($\rho_\perp$) increases by a factor of more than two. The dependence $\rho_\perp(x)$ acquires the form of an oscillating function of the degree of guest "load" (the intercalant content) and the frequency-independent portion of the $\rho_\perp$ curve (100 mHz $\le \omega \le$ 1 MHz) substantially decreases upon completion of the process. © *2001 MAIK "Nauka/Interperiodica".*

1. INTRODUCTION

At present, there is no doubt that intercalation is a promising method of nanotechnology for materials with a strongly anisotropic character of chemical bonding. Among these materials are solid phases characterized by a wide variety of electronic structures. Semiconductor compounds have attracted the particular attention of researchers owing to the high sensitivity of their characteristics to different-type guest components. For complete understanding of the nature of guest–host systems, specifically intercalates, which are essentially the compounds of a process, it is necessary to reveal their characteristic properties upon preparation using different methods. In our earlier works [1–3], we considered the problems of electrochemical lithium intercalation of bismuth selenide Bi_2Se_3, which is one of the most interesting (in fundamental and applied aspects) semiconductor materials with a layered crystal structure. The purpose of the present study was to elucidate the main features of lithium-selective intercalation of bismuth selenide.

2. EXPERIMENTAL TECHNIQUE

Crystals of bismuth selenide were prepared by the Bridgman technique from the initial material with a stoichiometric composition of components. The *n*-type conductivity in these crystals is provided primarily by background impurities and structural defects.

The intercalation was accomplished by treating the Bi_2Se_3 samples with a 24 wt % solution of *n*-butyllithium (*n*-C_4H_9Li) in hexane. All the procedures were carried out in a dry inert atmosphere at 20°C.

3. RESULTS AND DISCUSSION

Figure 1 shows variations in the dc resistivity in the direction normal to the layers (along the crystallographic axis *c*), which was measured in the course of intercalation. It is seen that incorporation of lithium atoms leads to an increase in the resistivity in the direction normal to the layers by a factor of more than two. In this case, the $\rho_\perp$ curve has the form of an oscillating function of the degree of guest load (the intercalant content). This behavior of the measured resistivity can be explained by the following.

The delocalization of the wave functions along the *c* axis can be judged from the properties of transfer processes in the initial matrix [4]. Note that a random field of the introduced intercalant can be dominant in scattering processes and the variation in field fluctuations during intercalation can determine the character of the change in the electrical conductivity for a monotonic or weak dependence of the free-carrier concentration on

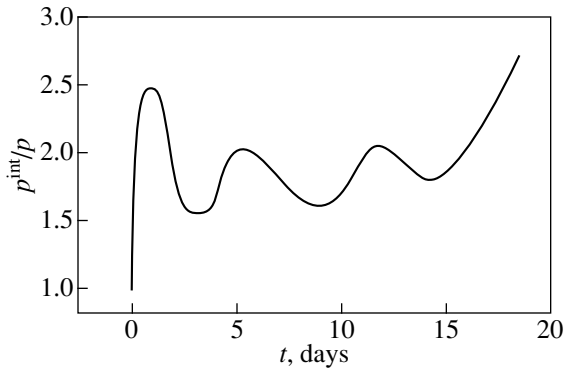

Fig. 1. Variation in the resistivity of Bi_2Se_3 in the direction normal to the layers in the course of intercalation.

1063-7834/01/4308-1442$21.00 © 2001 MAIK "Nauka/Interperiodica"

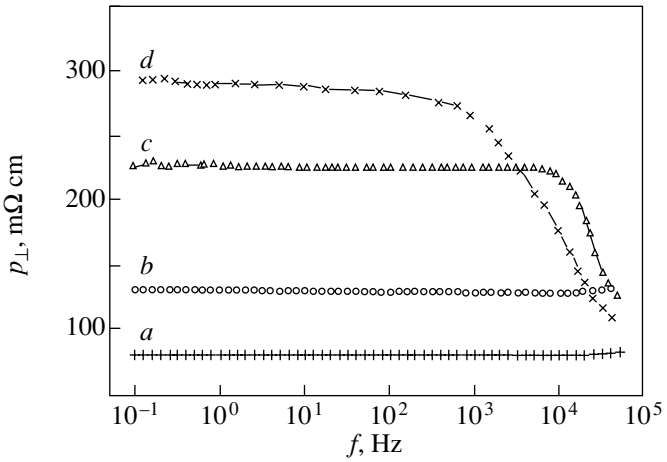

Fig. 2. Frequency dependences of the resistivity in the direction normal to the layers of Bi_2Se_3 (*a*, *b*) before and (*c*, *d*) after intercalation at temperatures of (*a*, *d*) –40°C and (*b*, *c*) +60°C.

the degree of intercalation. Let us assume that this field is a Gaussian smooth field. In this case, the scattering probability is determined by the characteristics of a random field that modifies the density of states. According to [5], the electrical conductivity σ becomes proportional to the square of the density of states at the Fermi level:

$$\sigma \sim \rho^2(F), \tag{1}$$

As was shown in [6], the magnitude of σ is inversely proportional to the mean square of the random-field fluctuations. Consequently, the strictly periodic minima of the electrical conductivity can be attributed to the processes of ordering in every fourth (the first minimum), then in every second, and finally in all van der Waals gaps (i.e., these minima correspond to the completion of the formation of four, two, and one echelons, respectively, according to the echeloning mechanism). This interpretation stems from the fact that the random-field fluctuations are minimum in magnitude in the aforementioned instances and increase in intermediate phases. The monotonic character of these local minima indicates the compensating effect of guest particles. Below the Fermi level, these particles give rise to a larger number of electron states as compared to the number of carried-in electrons, thus changing the energy topology of the impurity centers.

After completion of the intercalation process, the equilibrium (relative to lithium) electrode potential of the samples, which were washed with a large amount of hexane and dried under similar conditions, considerably (by a factor of ~10) decreased compared to the initial values and the lattice parameter *c* increased by 0.032 Å, even though the symmetry remained virtually the same. All these findings, together with the data of

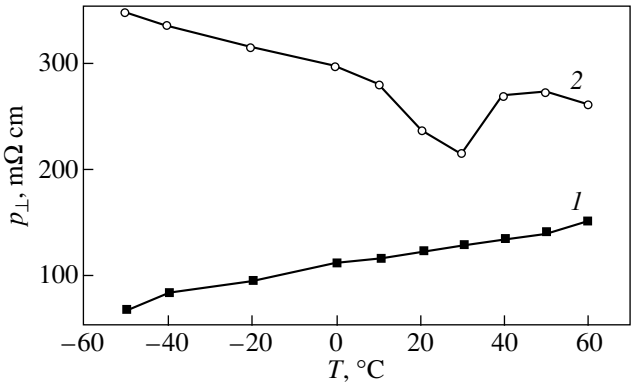

Fig. 3. Temperature dependences of the resistivity in the direction normal to the layers (*1*) before and (*2*) after lithium intercalation from *n*-butyllithium.

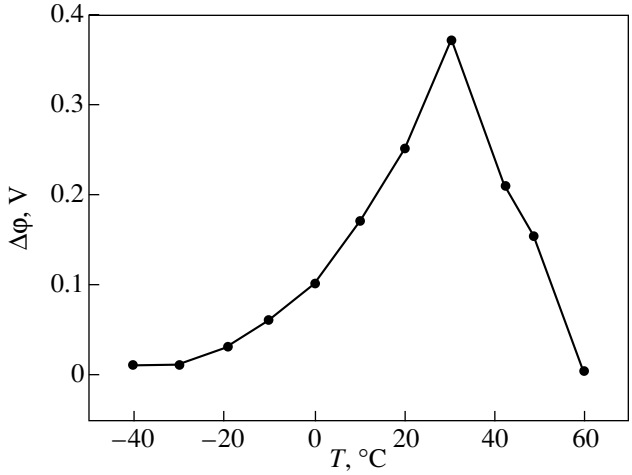

Fig. 4. Temperature dependence of the difference in potential between the surfaces of Bi_2Se_3 samples intercalated with Li from *n*-butyllithium.

flame photometry, allowed us to write the equation for the intercalation reaction in the following form:

$$Bi_2Se_3 + x(n\text{-}C_4H_9Li) = Li_xBi_2Se_3 + x/2C_8H_{18},$$

where x is the degree of guest load, which is proportional to the treatment time.

In order to elucidate the kinetic features of current carriers in the resultant intercalates, the frequency and temperature dependences of the complex electrical conductivity were investigated using a Shlumberger SI 1255 amplitude–frequency analyzer. The frequency ranged from 100 mHz to 1 MHz, and the amplitude of the measurement was chosen to be minimum in the linear portion of the current–voltage characteristic. Figure 2 depicts the frequency dependences of the resistivity in the direction normal to the layers of Bi_2Se_3 prior to and after intercalation at two different temperatures. The most important feature of these dependences is as follows: upon intercalation, the frequency-independent portions of the $\rho_\perp$ curves decrease and the descending portions appear in the frequency range 10^3–4×10^5 Hz. The observed changes can be explained by the activation of impurity centers (localized below the Fermi level at this temperature) that are formed or undergo redistribution due to intercalation. Note that, as the temperature decreases, the frequency-independent region should become narrower and a simultaneous increase in the ρ resistivity should occur, which is clearly seen in Fig. 2. The temperature dependence of the electrical resistivity (Fig. 3) suggests that the crossover from metallic to pronounced semiconductor conductivity of bismuth selenide occurs as the result of intercalation. The latter circumstance also indicates that the Fermi level decreases.

An interesting feature of the results obtained is the appearance of a singularity in the thermal coefficient of the electrical resistance at a temperature close to 30°C, which, as a rule, is associated with the softening of the phonon spectrum [7, 8]. This suggests that the material under investigation can acquire pyroelectric properties [8, 9]. Actually, when monitoring the equipotential surfaces of the samples normal to the c axis, we revealed a difference in electric potential $\Delta\varphi$ in the closing stages. This difference did not disappear even when the corresponding contacts were short circuited for one month. The results of measuring the dependence $\Delta\varphi(T)$ (Fig. 4) showed that the maximum of this dependence coincides with the minimum of the $\rho_\perp(T)$ curve measured after intercalation.

The polarized state arises from a distribution of guest components over the regions of van der Waals bonds which leads to the formation of a concentration gradient of electron trapping centers along the c axis. It is assumed that intercalation is accompanied by electron trapping in these centers and the formation of either actual-charge layers or quasi-dipoles attached to the layers [10, 11]. The thermionic discharge of this state brings about the formation of the gradient $\Delta\varphi$. Therefore, the pyroelectric states (nonlinear polarization) are induced by intercalation in the centrosymmetric Bi_2Se_3 crystal. Phenomenologically, this process is determined by the displacement of the generated quasi-dipoles from the center and their localization in tetrahedral sites of the van der Waals gap. On the microscopic level, they can be attributed to the impurity Jahn–Teller pseudoeffect [9, 12].

ACKNOWLEDGMENTS

This work was supported by the Science and Technology Center in Ukraine, project no. 591.

REFERENCES

1. I. I. Grigorchak, Z. D. Kovalyuk, I. D. Koz'mik, *et al.*, in *Proceedings of the 7th All-Union Conference "Chemistry, Physics, and Technical Applications of Chalcogenides," Uzhgorod, 1988*, Part 3, p. 144.
2. I. D. Koz'mik, É. G. Krigan, I. I. Grigorchak, *et al.*, in *Proceedings of the 6th All-Union Conference on Physicochemical Principles of Semiconductor Materials Doping* (Nauka, Moscow, 1988), p. 147.
3. S. V. Gavrilyuk, I. I. Grigortchak, Z. D. Kovalyuk, and B. P. Bakhmatyuk, in *Proceedings of the International School–Conference on Physical Problems in Material Science of Semiconductors, Chernivtsi, Ukraine, 1995*, p. 109.
4. B. M. Gol'tsman, V. A. Kudinov, and I. A. Smirnov, *Semiconducting Thermoelectric Materials Based on Bi_2Te_3* (Nauka, Moscow, 1972).
5. V. L. Bonch-Bruevich, I. P. Zvyagin, R. Kapper, A. G. Mironov, and R. Énderlaĭn, *The Electron Theory of Disordered Semiconductors* (Nauka, Moscow, 1981).
6. I. I. Grigorchak, B. A. Lukiyanets, and Z. D. Kovalyuk, Ukr. Fiz. Zh. **26**, 1165 (1981).
7. N. B. Brandt, V. V. Avdeev, S. G. Iskov, *et al.*, Zh. Éksp. Teor. Fiz. **91**, 1121 (1986) [Sov. Phys. JETP **64**, 663 (1986)].
8. V. M. Fridkin, *Photoferroelectrics* (Nauka, Moscow, 1976; Springer-Verlag, Berlin, 1979).
9. *Electrets*, Ed. by G. M. Sessler (Springer-Verlag, Berlin, 1980; Mir, Moscow, 1983).
10. I. V. Mintyanskiĭ, I. I. Grigorchak, Z. D. Kovalyuk, and S. V. Gavrilyuk, Fiz. Tverd. Tela (Leningrad) **28**, 1263 (1986) [Sov. Phys. Solid State **28**, 713 (1986)].
11. I. I. Grigorchak, Z. D. Kovalyuk, and I. V. Mintyanskiĭ, Fiz. Tverd. Tela (Leningrad) **31** (2), 222 (1989) [Sov. Phys. Solid State **31**, 302 (1989)].
12. B. A. Lykiyanets, K. D. Tovstyuk, V. V. Boichuk, and K. K. Danilevich-Tovstyuk, Phys. Status Solidi B **124** (2), 693 (1984).

Translated by N. Korovin

Physics of the Solid State, Vol. 43, No. 8, 2001, pp. 1445–1448. Translated from Fizika Tverdogo Tela, Vol. 43, No. 8, 2001, pp. 1388–1391.

SEMICONDUCTORS AND DIELECTRICS

Specific Features of the Electronic Band Structure and X-ray Spectra of Boron Nitride in Sphalerite and Wurtzite Modifications

T. P. Zhdanova, V. V. Ilyasov, and I. Ya. Nikiforov

Don State Technical University, Rostov-on-Don, 344010 Russia

e-mail: root@sintez.rnd.su

Received January 24, 2001

Abstract—The electronic band structure of boron nitride compounds with crystal lattices of the sphalerite (*c*-BN) and wurtzite (*w*-BN) types is calculated by the local coherent potential method in the cluster muffin-tin approximation within the framework of the multiple scattering theory. The local partial densities of 2*p* states for boron and nitrogen in *c*-BN and *w*-BN modifications are compared with the experimental boron and nitrogen *K* x-ray emission spectra and band-structure calculations. A comparison of the total densities of states in *c*-BN and *w*-BN with the x-ray photoelectron spectra and the band calculations has revealed both similarities and differences in the electronic structures of these modifications. The fine structure in the vicinity of the valence band top of boron nitride in different crystal modifications is theoretically calculated for the first time. The specific features of the electronic structure and the x-ray spectra of boron nitride in different modifications are discussed. *© 2001 MAIK "Nauka/Interperiodica".*

1. INTRODUCTION

Progress in crystal growing technologies and increased interest in wide-gap semiconductor crystal materials (different polytypes of BN, SiC, GaN, etc.) have been stimulated by their potential use in optoelectronic high-temperature devices. It is known that boron nitride can be synthesized in two modifications of the sphalerite (*c*-BN) and wurtzite (*w*-BN) types. There is experimental evidence [1] that, within the limits of experimental error, the x-ray photoelectron spectra of valence electrons, as well as the IR transmission spectra, coincide for both crystal modifications, even though their spectra for boron exhibit certain differences [2]. However, theoretical calculations of the densities of electron states of the valence band top in the crystal modifications under investigation gave different (quantitative and qualitative) results. Nemoshkalenko and Aleshin [3] analyzed the experimental boron and nitrogen *K* x-ray emission spectra and interpreted the x-ray spectra of cubic boron nitride (*c*-BN) crystals. Moreover, they revealed that the x-ray emission spectra exhibit van Hove singularities. Xu and Ching [4] calculated the electronic structure, the charge-density distributions, and the total energies in cubic, hexagonal, and wurtzite-type boron nitrides by using the method of orthogonalized linear combination of atomic orbitals (OLCAO) and discussed the problems concerning the relative stability and possible occurrence of phase transitions between these states. The x-ray spectra of boron nitride were also presented in [4], but without being interpreted. The present work is a continuation of our theoretical investigations into the electronic band structure of *c*-BN and *w*-BN modifications within a unified approach. The purpose of this work was to elucidate the specific features of the fine structure of the valence band top in *c*-BN and *w*-BN crystal modifications [5].

In the calculations presented in this paper, we used the local coherent potential method in the cluster approximation, which was proposed by Gyorffy [6, 7], within the framework of the multiple scattering theory. This method, as applied to cubic boron nitride, was described in detail in our earlier work [8].

2. CALCULATION TECHNIQUE

The electronic band structure of the boron nitride crystal modifications under investigation (see table) was calculated within a unified approach using the local coherent potential method. The crystal potential of boron nitride was constructed in the muffin-tin approximation as the sum of the Coulomb potential, the exchange component, and the Madelung potential. The contributions of neighboring atoms to the electron density and the Coulomb potential of fifteen coordination spheres were also included in the calculation. The wurtzite crystal structure was considered as consisting of four built-in hexagonal unit cells. For simplicity, the ratio between the lattice parameters was taken to be equal to $c/a = 1.633$ instead of $c/a = 1.67$ [5]. In this case, two nearest coordination spheres (containing three and one atoms, respectively) are combined into a single sphere, which drastically simplifies the calculation without a severe loss in accuracy. The Madelung potential was calculated by the Ewald method and

1063-7834/01/4308-1445$21.00

Crystal chemical characteristics and crystal potentials of the studied compounds

Characteristic	Lattice type			
	sphalerite		wurtzite	
	B	N	B	N
Unit cell parameter, nm	0.3615		a = 0.2550 c/a = 1.633	
Coordination number	4		4	
Number of atoms per unit cell	8		4	
Radius of the muffin-tin sphere, au	1.449	1.449	1.279	1.279
Radius of the Wigner–Seitz sphere, au	2.12	2.12	1.898	1.279
Number of valence electrons in the muffin-tin sphere	2.97	5.19	2.71	4.72
Potential between the muffin-tin spheres	0.0098544		–0.12366	
Charge density between the muffin-tin spheres	0.070609		0.1149	

accounted for the electrostatic contribution made by different sublattices to the crystal potential, that is,

$$\varphi_{11} = \varphi_{22} = -4.5849q/a, \quad \varphi_{12} = \varphi_{21} = -0.80194q/a$$

for boron nitride (sphalerite-type lattice) and

$$\varphi_{11} = \varphi_{22} = -3.242q/a, \quad \varphi_{12} = \varphi_{21} = -0.91568q/a$$

for boron nitride (wurtzite-type lattice), where φ_{ii} is the potential produced by the ith boron (i = 1) or nitrogen (i = 2) atom at atoms of the ith sublattice and φ_{ij} is the potential produced by atoms of the ith sublattice at atoms of the jth sublattice. The exchange component of the potential was determined in the Slater approximation with the exchange correction α = 2/3. The crystal muffin-tin potentials were used in solving the Schrödinger radial equation at l = 0.1 (for light elements such as boron and nitrogen, the d electron states were disregarded) in the energy range from 0.02 to 1.5 Ry. The local partial densities of states for boron and nitrogen in boron nitride were calculated with a cluster containing 35 atoms in four coordination spheres for c-BN and 33 atoms in five coordination spheres for w-BN according to the relationship [5]

$$n_l^A(E) = -\frac{\sqrt{E}}{\pi}\int_0^{r_{ws}}\{R_l^A(r, E)r\}^2 dr\frac{\mathrm{Im}\,\mathrm{Tr}\,T^{00, A}_{lm, l1m1}}{\mathrm{Im}\,t_l^A(E)}, \quad (1)$$

where l is the orbital quantum number, $R_l^A(r)$ stands for the radial wave functions of the A-type atom in the cluster, and $T^{00, A}_{lm, l1m1}$ is the matrix element of the scattering operator. The total density of states (TDOS) of valence electrons per unit cell for one spin projection was determined as the sum of the local densities of states (LDOS) according to the formula

$$N(E) = \sum_{l=0}^{1} n_l^{\mathrm{B}}(E) + \sum_{l=0}^{1} n_l^{\mathrm{N}}(E). \quad (2)$$

3. RESULTS AND DISCUSSION

Figure 1 shows the total densities of states of valence electrons in boron nitride polytypes, which were calculated in the present work, in comparison with the experimental x-ray photoelectron spectrum [2] and the theoretical TDOS curves calculated using the orthogonalized plane wave (OPW) [3] and OLCAO [4] methods. Analysis of the data presented in Fig. 1 revealed the nature of the specific features in the spectra under consideration. In particular, the origin of the B peak is explained by the s–p-hybridized states of boron and the peak itself contains a substantial contribution from the p states of nitrogen. This peak (singularity) is observed in the calculated TDOS curves (the B' and B'' peaks). The C peak at an energy of 0.25 Ry is associated with the B p and N p states and coincides in energy with the X_5 state of the van Hove singularity. The high-energy peak D (0.5 Ry) is attributed only to the nitrogen electron states with the p symmetry and corresponds to the L_3 state. According to our calculation, the valence band top of cubic boron nitride c-BN contains a set of localized electron states; in other words, the valence band top in c-BN has a fine structure. For the w-BN modification, the fine structure of the valence band top is less pronounced and the densities of electron states of the valence band top are less than those in c-BN. The latter statement is in agreement with the band-structure calculations performed by Xu and Ching [4].

The calculated local partial densities of boron p states for cubic and wurtzite-type boron nitrides in comparison with the experimental boron K x-ray emission spectra [2] are displayed in Fig. 2. Comparison of the experimental and theoretical energy spectra was performed with respect to the principal maximum. This allowed us to reveal the specific features of the fine structure and to elucidate their nature in the high-energy and low-energy ranges of the boron x-ray emission spectra of boron nitride. The low-energy peak A, which is observed in the experimental x-ray emission

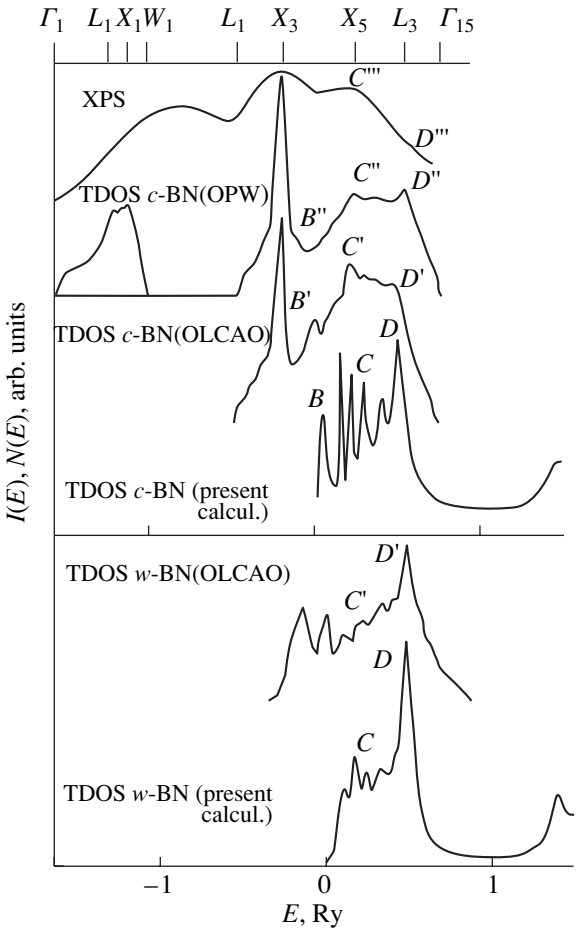

Fig. 1. Experimental x-ray photoelectron spectrum (XPS) [2] and the total densities of states (TDOS) of valence electrons according to OPW [3], OLCAO [4], and our calculations for cubic (*c*-BN) and wurtzite-type (*w*-BN) boron nitrides, respectively.

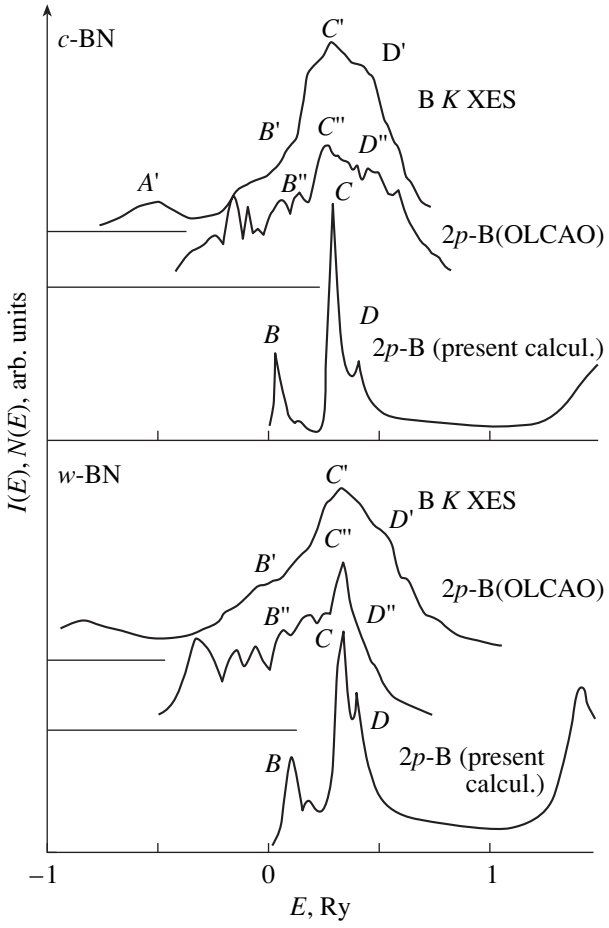

Fig. 2. Experimental boron *K* x-ray emission spectra (B *K* XES) [2] and the local partial densities of boron 2*p* states according to OLCAO [4] and our calculations for cubic (*c*-BN) and wurtzite-type (*w*-BN) boron nitrides, respectively.

spectra, can be attributed to the quasi-core 2*s* electrons of boron. The *B* peak in the theoretical curves of the local partial density of boron 2*p* states corresponds to both the *B*" peak in the LDOS curves calculated using the OLCAO method and the *B*' shoulder in the experimental spectra. This peak can be considered a manifestation of the hybridization of the boron 2*p* and nitrogen 2*p* states at energies of 0.10 and 0.05 Ry for boron nitride crystal modifications of the wurtzite (*w*-BN) and sphalerite (*c*-BN) types, respectively. Compared to the experimental spectra, the principal maximum *C* in the theoretical LDOS curves exhibits a finer structure, which is also seen in the LDOS curves calculated using the OLCAO method. According to the assumption made by Fomichev [9], the high-energy shoulders *D*' and *D*" (which correspond to the *D* peak at energies of 0.42 and 0.4 Ry for *c*-BN and *w*-BN, respectively) can be associated with the emission of boron in which impurities occur in the boron nitride samples under investigation. However, our calculations demonstrate that this peak can be due to the transfer of boron *p* electrons into the high-energy region. It should be noted that the height of the *D* peak is smaller than that of the principal maximum by a factor of three for cubic boron nitride and only by a factor of 1.3 for wurtzite-type boron nitride. The difference between the energies of the *C* and *D* peaks for *w*-BN is one-half the difference in their locations in the spectra of *c*-BN. It is quite possible that this feature of boron in *w*-BN is associated with the increase in the band gap [5].

The calculated local partial densities of nitrogen 2*p* states for *c*-BN and *w*-BN modifications in comparison with the experimental nitrogen *K* x-ray emission spectrum [3] for cubic boron nitride are shown in Fig. 3. Comparison of the experimental and theoretical energy spectra was performed with respect to the high-energy peak *D*. Analysis of the data presented in Fig. 3 revealed the nature of some features in the nitrogen *K* x-ray emission band. Specifically, the difference between the energies of the *C* and *D* peaks in the experimental and theoretical spectra is equal to 0.24 Ry (3.26 eV). The energy locations of these peaks in the experimental nitrogen *K*

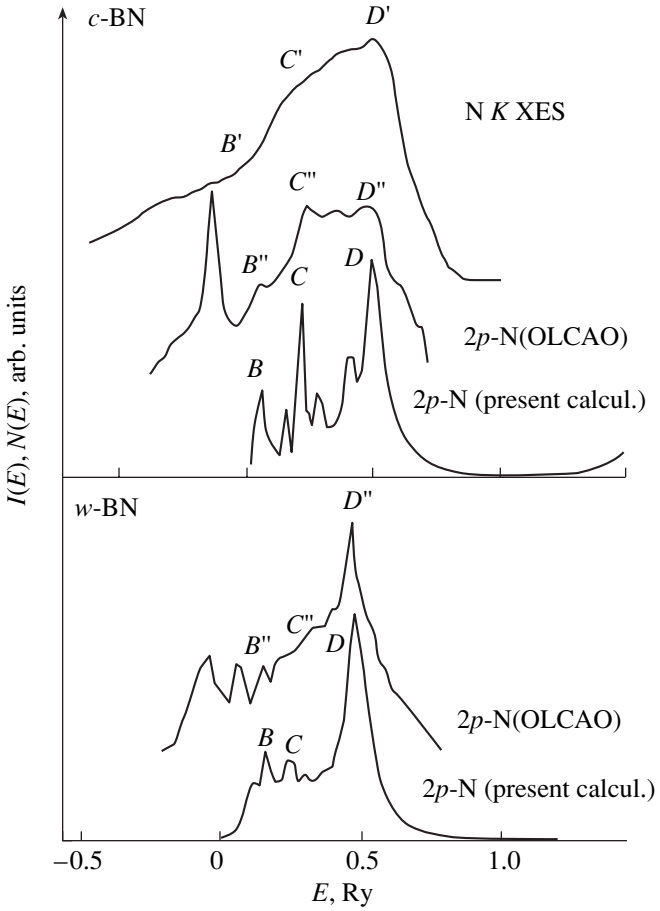

Fig. 3. Experimental nitrogen *K* x-ray emission spectrum (N *K* XES) [3] for cubic boron nitride and the local partial densities of nitrogen 2*p* states according to OLCAO [4] and our calculations for cubic (*c*-BN) and wurtzite-type (*w*-BN) boron nitrides, respectively.

x-ray emission spectrum and the calculated LDOS curves coincide to within 0.5 eV. The *C*' shoulder in the experimental *K* emission band and the *C*" peak in the LDOS curves calculated with the OLCAO method are attributed to the nitrogen localized electron states at energies of 0.24 and 0.25 Ry for *c*-BN and *w*-BN, respectively. The height of the *C* peak is smaller than that of the *D* peak by a factor of 1.3 for cubic boron nitride and almost by a factor of three for wurtzite-type boron nitride.

Comparison of our results and the data obtained by the OLCAO method [4] shows that the calculations we performed using the local coherent potential method in the cluster approximation reveal the fine structure of the boron *K* spectrum in the vicinity of the valence band top in greater detail. It follows from this comparison that the results of our calculations are in better qualitative agreement with the experimental boron *K* emission spectra [2]. In conclusion, it should be noted that the local coherent potential method (in the cluster approximation), as applied to the class of wurtzite-like compounds, allowed us to elucidate the nature of the fine structure of the boron and nitrogen *K* emission spectra in the high-energy region of the valence band.

REFERENCES

1. V. P. Elyutin, I. V. Blinov, I. I. Goryunova, *et al.*, Neorg. Mater. **26** (5), 978 (1990).
2. Y. Muramatsu, H. Kouzuki, M. Motoyama, *et al.*, in *Photon Factory Activity Report* (National Laboratory for High Energy Physics, Oho-machi, 1994–1995).
3. V. V. Nemoshkalenko and V. G. Aleshin, Fiz. Tverd. Tela (Leningrad) **12** (1), 59 (1970) [Sov. Phys. Solid State **12**, 46 (1970)].
4. Yong-Nian Xu and W. Y. Ching, Phys. Rev. B **44** (15), 7787 (1991).
5. T. P. Zhdanova, V. V. Ilyasov, and I. Ya. Nikiforov, Zh. Strukt. Khim. **39** (6), 1083 (1998).
6. B. L. Gyorffy, Phys. Rev. B **5** (6), 2382 (1972).
7. B. L. Gyorffy, J. Phys. (Paris) **35** (5), C4–75 (1974).
8. V. V. Ilyasov, N. Yu. Safontseva, and I. Ya. Nikiforov, Fiz. Tverd. Tela (St. Petersburg) **36** (2), 451 (1994) [Phys. Solid State **36**, 247 (1994)].
9. V. A. Fomichev, Izv. Akad. Nauk SSSR, Ser. Fiz. **31** (6), 957 (1967).

Translated by O. Borovik-Romanova

Physics of the Solid State, Vol. 43, No. 8, 2001, pp. 1449–1453. Translated from Fizika Tverdogo Tela, Vol. 43, No. 8, 2001, pp. 1392–1395.

SEMICONDUCTORS AND DIELECTRICS

Weak Localization of Inelastically Reflected Electrons under Auger Emission Conditions

V. V. Doubov and V. V. Korablev

St. Petersburg State Technical University, Politekhnicheskaya ul. 29, St. Petersburg, 194251 Russia

e-mail: quark@stu.neva.ru

Received November 24, 2000

Abstract—A new type of weak localization of electrons emerging during electron emission is considered. It is manifested in singularities of the angular spectra of particles reflected inelastically from a solid and causing Auger ionization of the atoms. The orientational dependences in this case appear as a result of interference of two types of processes. In one case, an electron from the primary beam penetrates the solid, undergoes inelastic scattering, ionizes an atom, and is then scattered elastically through a large angle, after which it leaves the solid. In the other case, elastic scattering of an electron precedes its inelastic scattering due to the Auger ionization of an atom. The azimuthal angular dependences of currents created by inelastically reflected electrons contain information on new processes of weak localization of particles. © *2001 MAIK "Nauka/Interperiodica".*

1. INTRODUCTION

In this work, we analyze the coherence effects emerging during the emission of Auger electrons from a solid. Such an emission takes place when crystalline samples, both ordered (single crystals) and disordered, are bombarded by electrons with intermediate energies (ranging from a few hundred electronvolts to several kiloelectronvolts).

A new type of weak localization emerges as a result of the interference of electronic waves undergoing both elastic and inelastic scattering. In contrast to traditional weak localization of the Anderson type, such localization takes place when localized electrons undergo elastic scattering in combination with inelastic scattering. In the traditional Anderson-type localization, the role of inelastic processes is subordinate and negative since inelastic scattering usually violates coherent processes. However, a new type of weak localization of electrons emerges in inelastic scattering of particles.

The new type of weak localization leads to the emergence of a certain type of angular dependences for the recorded intensities of particles which experience, along with elastic scattering, inelastic scattering in a disordered medium. These angular dependences are not connected with the angular dependences of elementary scattering processes (e.g., with the angular dependence of the scattering cross section of atoms). The possibility of this localization was established earlier by Libenson *et al.* [1] using a model in which elastic collisions were reduced to multiple small-angle scattering and single Born elastic scattering through a large angle.

Subsequently, it was proved [2] that multiple elastic electron collisions resulting in scattering through arbitrary angles do not affect weak localization of the new type, although such collisions are incoherent and generally lead to complete or partial smoothing of orientational coherent effects. The effect of the surface on the angular dependences of the scattering probability of electrons reflected from a disordered semi-infinite medium was also investigated under quantum-transport conditions, when the ratio of the angle of incidence of electrons on the surface and the angle of their emission from the surface is arbitrary.

The theoretical results obtained made it possible to detect processes of a new type of weak localization in experiments on the interaction between electrons and disordered solids.

Such experiments include the observation of the angular spectra of electrons in the case of Auger emission [3, 4]. The experimental technique associated with the recording of the azimuthal dependences alone [4, 5] in angular spectra is the most convenient for studying the new type of weak localization [1, 2].

Weak localization of the new type can be observed for electrons belonging to various groups scattered both elastically and inelastically in a solid. These can be Auger electrons emitted by a solid or electrons from the primary beam that have experienced both elastic scattering from atoms of the solid (including large-angle scattering) and inelastic scattering, for example, at the initial stage of generation of Auger electrons. In this work, we will mainly consider the electrons participating in the latter type of processes accompanying Auger emission.

1063-7834/01/4308-1449$21.00

2. THE WAVE FUNCTION OF AN ELECTRON SCATTERED INELASTICALLY IN A DISORDERED SOLID

The system under investigation consists of a semi-infinite disordered solid occupying the half-space $z > 0$ (the z axis is normal to the surface of the solid) and an external intermediate-energy electron interacting with the solid.

In experiments on Auger emission, variations of the intensity of the emitted Auger electrons are usually studied as a function of various parameters, such as the energy and the angle of incidence of primary electrons on the sample and the angle of emission of Auger electrons.

We will concentrate our studies on the electrons from the primary beam that penetrate into the crystal and experience both elastic scattering in it (including large-angle scattering) and inelastic scattering due to primary Auger ionization of an atom; after this, they leave the solid.

Previous investigations [1, 2] of the new type of weak localization of electrons proved that angular azimuthal dependences of the intensities of scattered electrons are essential in detecting the effects associated with such localization. It is these azimuthal dependences (applied to the Auger electrons emitted from the solid) that are recorded in experiments on Auger emission devoted to analyzing the anisotropy of the yield [4, 5]. We will prove here that the new type of weak localization of electrons scattered in disordered media can be manifested in the azimuthal dependences of the intensities of electrons undergoing inelastic reflection. We denote by $\psi(\mathbf{r}, \mathbf{R})$ the wave function of the system comprising a solid and an electron from the primary beam scattered from it. Here, $\mathbf{r}$ is the coordinate of the external electron and $\mathbf{R}$ is the set of coordinates of particles in the medium. The wave function $\psi(\mathbf{r}, \mathbf{R})$ satisfies the equation

$$\Delta\psi(\mathbf{r}, \mathbf{R}) + \frac{2m}{\hbar^2}[E - U(\mathbf{r}) - U(\mathbf{r}, \mathbf{R}) - U(\mathbf{R})]\psi(\mathbf{r}, \mathbf{R}) = 0. \quad (1)$$

Here, the Laplace operator Δ contains second derivatives with respect to all components of the radius vectors of the projectile particle $\mathbf{r}$ and of the particles of the medium $\mathbf{R}$. The quantity $U(\mathbf{r})$ is the total potential of randomly arranged scattering centers from which the external particle is scattered elastically. Potential $U(\mathbf{R})$ describes the interaction of particles of the medium. The quantity $U(\mathbf{r}, \mathbf{R})$ is the potential energy of interaction between the external particle and the particles of the medium.

The wave function $\psi(\mathbf{r}, \mathbf{R})$ of the given system can be expanded into a complete orthonormal set of the wave functions $\Phi_n(\mathbf{R})$ of the particles of the medium:

$$\psi(\mathbf{r}, \mathbf{R}) = \Sigma_n \psi_n(\mathbf{r})\Phi_n(\mathbf{R}). \quad (2)$$

The wave functions $\Phi_n(\mathbf{R})$ describing the state of particles of the scattering medium satisfy the equation

$$\Delta_{\mathbf{R}}\Phi_n(\mathbf{R}) + \frac{2m}{\hbar^2}[\varepsilon_n - U(\mathbf{R})]\Phi_n(\mathbf{R}) = 0, \quad (3)$$

where ε_n is the energy of the medium.

The solution to these equations in the zeroth approximation in the interaction of the external particle with the particles of the disordered solid has the form

$$\psi(\mathbf{r}, \mathbf{R}) = \psi_0(\mathbf{r})\Phi_0(\mathbf{R}). \quad (4)$$

Function $\Phi_0(\mathbf{R})$ is the wave function of particles of the solid in the ground (unexcited) state.

Function $\psi_0(\mathbf{r})$ is the unperturbed wave function of the external electron. If we disregard the interaction of the external electron with the particles of the medium, this function has the form of a plane wave with wave vector $\mathbf{k}_0$, where $|\mathbf{k}_0| = \sqrt{2mE/\hbar^2}$. However, it is convenient to write this function, which describes the motion of an electron from the external primary beam in a medium with randomly arranged scattering centers, while taking averaged electron–electron interactions into account. First of all, we will take into account the decrease in energy (and wave vector) of the particle due to its interaction with the average crystalline potential U_0 of the disordered medium (surface potential barrier) in the wave function component describing the motion of the external electron within the solid (i.e., for $z > 0$). Consequently, the wave function $\psi_0(\mathbf{r})$ in the medium should have the form of a plane wave with wave vector $\mathbf{k}$, where $|\mathbf{k}| = \sqrt{2mE/\hbar^2}$.

In addition, we will take into account the decay of the wave function $\psi_0(\mathbf{r})$ caused by inelastic interaction of the external electron with the solid during the motion of the particle in the half-space $z > 0$. The inelastic scattering with an extended potential in the region $z < 0$ in the vicinity of the crystal surface (i.e., outside the solid) can be neglected [6].

The inclusion of the effect of inelastic processes on the motion of the external electron in a solid within the model of optical potential U_{opt} [7] leads to the emergence of a exponentially decaying multiplicative factor of the form $\exp(-\kappa z/\cos\theta)$ in the wave function $\psi_0(\mathbf{r})$ of the external particle in the region $z > 0$ (κ is the decay coefficient defined, as usual, through the imaginary part U_i of the optical potential U_{opt} and θ is the angle of incidence of the primary beam on the surface of the solid).

After presenting the solution of equations in the zeroth approximation in this way, we consider, to the first order of perturbation theory, the scattering of the external electron by particles of the medium in the case of generation of an Auger emission.

We will write the first-order correction $\psi^{(1)}(\mathbf{r}, \mathbf{R})$ to the unperturbed wave function $\psi_0(\mathbf{r}, \mathbf{R})$ in the form of an expansion similar to expansion (2):

$$\psi^{(1)}(\mathbf{r}, \mathbf{R}) = \Sigma_n \psi_n^{(1)}(\mathbf{r})\Phi_n(\mathbf{R}), \tag{5}$$

where the orthogonal functions $\Phi_n(\mathbf{R})$ describe excited states of the medium.

The first-order equation of perturbation theory for the crystalline region $z > 0$ has the form

$$\begin{aligned}&\Delta\Sigma_n\psi_n^{(1)}(\mathbf{r})\Phi_n(\mathbf{R})\\ &+\frac{2m}{\hbar^2}[E - U(\mathbf{R}) - U_{\text{opt}}]\Sigma_n\psi_n^{(1)}(\mathbf{r})\Phi_n(\mathbf{R})\\ &= \frac{2m}{\hbar^2}[U(\mathbf{r}) + U(\mathbf{r}, \mathbf{R})]\psi_0(\mathbf{r})\Phi_0(\mathbf{R}).\end{aligned} \tag{6}$$

Multiplying this equation by $\Phi_n^*(\mathbf{R})$ and integrating over the coordinates of all particles of the medium, we obtain the following equation for the first-order correction $\psi_n^{(1)}(\mathbf{r})$ of perturbation theory to the required wave function of the primary particle:

$$\begin{aligned}&\Delta\psi_n^{(1)}(\mathbf{r}) + \frac{2m}{\hbar^2}[E - \varepsilon_n - U_{\text{opt}}]\psi_n^{(1)}(\mathbf{r})\\ &= \frac{2m}{\hbar^2}[U(\mathbf{r})\delta_{on} + \int d\mathbf{R}\Phi_n^*(\mathbf{R})U(\mathbf{r}, \mathbf{R})\Phi_i(\mathbf{r})].\end{aligned} \tag{7}$$

The solution to this equation can be written in terms of its Green's function $G(\mathbf{r}, \mathbf{r}')$. Using the notation introduced earlier [2] to characterize the amplitude of inelastic interaction of an external electron with particles of a disordered polycrystal,

$$T(\mathbf{r}, i \longrightarrow n) = \int d\mathbf{R}\Phi_n^*(\mathbf{R})U(\mathbf{r}, \mathbf{R})\Phi_0(\mathbf{R}), \tag{8}$$

we can write the solution to Eq. (7) in the form

$$\begin{aligned}&\psi_n^{(1)}(\mathbf{r})\\ &= \frac{2m}{\hbar^2}\int d\mathbf{r}' G(\mathbf{r}, \mathbf{r}')[U(\mathbf{r})\delta_{on} + T(\mathbf{r}', i \longrightarrow n)]\psi_0(\mathbf{r}).\end{aligned} \tag{9}$$

Here, $G(\mathbf{r}, \mathbf{r}')$ is the Green's function for Eq. (7), which satisfies the following equation in the half-space $z > 0$ occupied by the medium:

$$\Delta G(\mathbf{r}, \mathbf{r}') + \frac{2m}{\hbar^2}[E - \varepsilon_n - U_{\text{opt}}]G(\mathbf{r}, \mathbf{r}') = \delta(\mathbf{r} - \mathbf{r}'). \tag{10}$$

The next correction $\psi_n^{(2)}(\mathbf{r})$ to the wave function of the external electron undergoing inelastic scattering can be written by analogy with the first-order correction (9) and has the following form in the crystalline region:

$$\begin{aligned}\psi_n^{(2)}(\mathbf{r}) &= \frac{2m}{\hbar^2}\int d\mathbf{r}' G(\mathbf{r}, \mathbf{r}')[U(\mathbf{r})\psi_f^{(1)}(\mathbf{r})\\ &+ \Sigma_n T(\mathbf{r}', n \longrightarrow f)\psi_n^{(1)}(\mathbf{r})].\end{aligned} \tag{11}$$

In subsequent (including computer) calculations, the wave function of an electron experiencing elastic and inelastic scattering in a solid will be determined to the first or second approximation using formulas (9) and (11). In turn, the wave function of the electron makes it possible to write expressions for the intensity of electrons scattered by the solid. This intensity is a quantity measured in the experiments.

Higher (than second-order) corrections do not introduce any basically new (at least orientational) effects. At the same time, the corrections calculated above made it possible to reveal the new type of weak localization effects for inelastically scattered electrons.

The intensity of inelastically scattered electrons is determined by the density matrix

$$\rho_n(\mathbf{r}, \mathbf{r}') = \langle\psi_n(\mathbf{r})\psi_n^*(\mathbf{r}')\rangle. \tag{12}$$

The angle brackets on the right-hand side of Eq. (12) signify averaging over the distribution of scattering centers.

The calculations are simplified when the factor TT^* can be taken out of the angle brackets. This is the case in the approximation used by us here. The effect of the inelastic channel on itself should be (if necessary) taken into account in higher orders of perturbation theory. In the problem under investigation, there are no sound reasons for the inclusion of higher-order corrections.

The current created by inelastically reflected electrons also contains the products $U(\mathbf{r})U^*(\mathbf{r})$. Since we have singled out the optical component U_{opt} among the potentials, the potential $U(\mathbf{r})$ is a superposition of randomly arranged atomic cores from which an electron is scattered elastically through large angles.

The current of electrons scattered inelastically from the solid is determined by the asymptotic forms of expressions (9) and (11). It was proved earlier [1, 2] that the new type of weak localization effect is manifested in the intensities of electrons experiencing inelastic scattering and elastic incoherent scattering simultaneously. The group of such electrons can be singled out experimentally. In the derived formulas, we are interested in the intensity of this group of electrons.

The angular spectra of reflected particles are determined by the integral with respect to the coordinates along the axes perpendicular to the z axis:

$$\int d\boldsymbol{\rho} d\boldsymbol{\rho}' \boldsymbol{\rho}(\mathbf{r}, \mathbf{r}')e^{-i\mathbf{k}_\parallel(\boldsymbol{\rho} - \boldsymbol{\rho}')}. \tag{13}$$

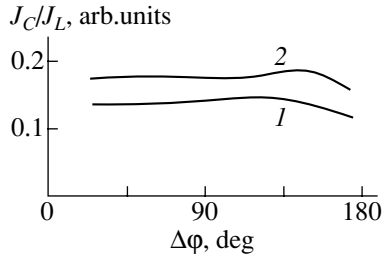

Fig. 1. Angular dependence of the degree of coherence J_C/J_L on the difference Δφ between the azimuthal angles for $E/\Delta E = 10$, $E/U_i = 120$, and θ = θ' = (*1*) 45° and (*2*) 60°.

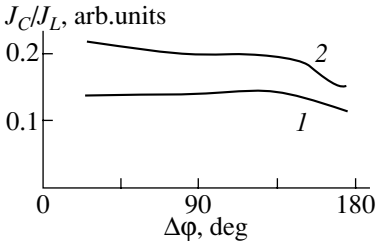

Fig. 2. Angular dependence of the degree of coherence J_C/J_L on the difference Δφ between the azimuthal angles for $E/\Delta E = 10$, $E/U_i = 120$, and θ = θ' = (*1*) 45° and (*2*) 60°.

The asymptotic form of the Green's function, which determines the asymptotic form of the wave functions (9) and (11), is given by

$$G(\mathbf{r}, \mathbf{r}') = -\frac{e^{ik'r}}{4\pi r}\langle \psi_0^*(\mathbf{r}')\rangle \qquad (14)$$

and depends on the wave vector **k**' of a reflected electron.

The wave function (11) determining the required current created by electrons inelastically reflected from a disordered solid contains a sum that can be written in the operator representation as follows:

$$\hat{G}\{\hat{U}\hat{G}[\hat{U} + \hat{T}] + \Sigma_n \hat{T}\hat{G}[\hat{U} + \hat{T}]\}. \qquad (15)$$

The group of electrons whose current includes the new-type weak localization effects we are interested in is described by terms of the form

$$\hat{G}\{\hat{U}\hat{G}\hat{T} + \Sigma_n \hat{T}\hat{G}\hat{U}\}, \qquad (16)$$

which will be considered below.

The intensity of electrons reflected inelastically from the solid is determined by the squared modulus of the sum in Eq. (16). Equations (8), (9), (11), and (13) and the asymptotic form in Eq. (14) make it possible to calculate the required intensity.

Proceeding from the assumptions made by us earlier, we single out two components in the total current J of reflected electrons, J_L and J_C. The former current J_L is determined by the sum of the squared moduli of the first and second terms in Eq. (16). Current J_C contains cross terms of the squared modulus of expression (16). The ratio of the currents J_C and J_L is usually referred to as the degree of coherence.

The angular dependences of the two components (J_L and J_C) of the total current J can be different. According to the results of computer calculations, this situation is observed in our case. Consequently, the degree of coherence depends on the azimuthal angle of emission of electrons. The origin of this dependence is associated, among other things, with the new type of weak localization of electrons observed during their motion in the disordered solid.

The above theoretical analysis and computer calculations make it possible to study the orientational effects that emerge in the case of inelastic reflection of electrons from disordered solids under Auger emission conditions. An analysis shows that the quantity J_C/J_L depends on the angles. We consider the situation when the polar angles of incidence of the primary electron beam on the solid and of the emission of an inelastically scattered electron to vacuum are fixed.

We analyzed the dependence of the degree of coherence J_C/J_L on the difference between the azimuthal angles of incidence and emission of particles. This azimuthal dependence turns out to be nonmonotonic; the curves usually display a peak at an angle difference Δϕ close to $2\pi/3$ followed by a dip for values of Δϕ close to π.

The angular dependences turn out to be very sensitive to the parameters of the problem under investigation. These parameters include, above all, the crystal parameters, as well as the parameters of the wave function of an electron penetrating the solid and the value of energy ΔE transferred by an external particle to the medium.

Figures 1 and 2 show the calculated dependences of the degree of coherence J_C/J_L on the difference Δϕ of the azimuthal angles for various values of parameters. The sensitivity of the angular spectra to the values of parameters U_0 and U_i of the optical potential and to the energy loss ΔE is worth noting. The dependences $J_C/J_L(\Delta\phi)$ are presented for various values of the abovementioned parameters and for two fixed values of the polar angles θ and θ' of the wave vectors **k** and **k**', equal to $\pi/4$ and $\pi/3$.

Figure 1 shows that as the ratio E/U_i increases for preset values of parameter $E/\Delta E$, the effect is manifested more and more clearly on the angular dependences of J_C/J_L. The effect under investigation is also manifested more clearly for large values of the polar angles θ and θ' (Fig. 2).

The above analysis leads to the conclusion that the new type of weak electron localization effect can be detected in the case of inelastic reflection of particles under Auger emission conditions. The characteristics of

the recorded spectra can be used for determining the parameters of the solid, as well as for studying the elementary acts of interaction of particles in the solid.

REFERENCES

1. B. N. Libenson, K. Yu. Platonov, and V. V. Rumyantsev, Zh. Éksp. Teor. Fiz. **101** (2), 614 (1992) [Sov. Phys. JETP **74**, 326 (1992)].
2. V. V. Rumyantsev and V. V. Doubov, Phys. Rev. B **49** (13), 8643 (1994).
3. R. Baudoing, I. Blank, and C. Gauvert, Surf. Sci. **128** (1), 22 (1983).
4. M. V. Gomoyunova and I. I. Pronin, Poverkhnost, No. 7, 44 (1982).
5. J. D. Place and M. Prutton, Surf. Sci. **82** (4), 315 (1979).
6. V. V. Doubov, Fiz. Tverd. Tela (Leningrad) **33** (8), 2241 (1991) [Sov. Phys. Solid State **33**, 1263 (1991)].
7. A. Howie and R. M. Stern, Z. Naturforsch. A **27**, 382 (1972).

Translated by N. Wadhwa

Physics of the Solid State, Vol. 43, No. 8, 2001, pp. 1454–1463. Translated from Fizika Tverdogo Tela, Vol. 43, No. 8, 2001, pp. 1396–1404.

SEMICONDUCTORS AND DIELECTRICS

Electron Excitations in LiB_3O_5 Crystals with Defects: Low-Temperature Time-Resolved Luminescence VUV Spectroscopy

I. N. Ogorodnikov*, V. A. Pustovarov*, M. Kirm, A. V. Kruzhalov*, and L. I. Isaenko*****

** Ural State Technical University, ul. Mira 19, Yekaterinburg, 620002 Russia*

*** II Institut für Experimentalphysik der Universität Hamburg, Hamburg, D-22761 Germany*

**** Institute of Single Crystals, Siberian Division, Russian Academy of Sciences, Novosibirsk, 630058 Russia*

e-mail: ogo@dpt.ustu.ru

Received December 15, 2000

Abstract—The dynamics of electron excitations and luminescence of LiB_3O_5 (LBO) single crystals was studied using low-temperature luminescence vacuum ultraviolet spectroscopy with a subnanosecond time resolution under photoexcitation with synchrotron radiation. The kinetics of the photoluminescence (PL) decay, the time-resolved PL emission spectra, and the time-resolved PL excitation spectra of LBO were measured at 7 and 290 K, respectively. The PL emission bands peaking at 2.7 eV and 3.3 eV were attributed to the radiative transitions of electronic excitations connected with lattice defects of LBO. The intrinsic PL emission bands at 3.6 and 4.2 eV were associated with the radiative annihilation of two kinds of self-trapped electron excitations in LBO. The processes responsible for the formation of localized electron excitations in LBO were discussed and compared with those taking place in wide-gap oxides. © *2001 MAIK "Nauka/Interperiodica"*.

1. INTRODUCTION

In cubic alkali-halide crystals with substantially ionic bonds, self-trapped excitons (STEs) of several types are known to exist [1, 2]. The process of self-trapping of excitons in low-symmetry crystals with complex crystallographic structures differs substantially from that in alkali-halide crystals. It is well known [2, 3] that the luminescence of STEs in alkali-halide crystals is excited both upon optical production of excitons and in the range of band-to-band transitions upon recombination of an electron with an immobile self-trapped hole. The energy spectrum of exciton states in complex oxides can completely or partly overlap with states of the electron–hole continuum. This means that direct excitons in such systems are metastable with respect to the temperature-independent self-ionization, which actively manifests itself even at low temperatures. Indeed, it was experimentally established for $Y_3Al_5O_{12}$(YAG) and $YAlO_3$ crystals [4] that a significant part of electron excitations is due to mixed exciton and electron–hole levels, which form the initial state for the subsequent branching between the various channels of STE formation.

In a number of oxide crystals, bands of intrinsic luminescence with properties characteristic of STE luminescence were revealed (Table 1). The large half-width and the Stokes shift of the bands indicate their relation to the annihilation of localized electron excitations formed after an equilibrium distribution of the luminescence centers over vibronic states is reached. Two types of luminescence bands are distinguished. Band I (Table 1) does not manifest itself in recombination processes such as thermostimulated luminescence (TSL) even at low temperatures. In contrast to alkali-halide crystals, this type of exciton self-trapping in complex oxides is not accompanied by the self-trapping of the corresponding hole component [4]. The relatively large oscillator strength (about 0.1 per electron), the high quantum efficiency of photoluminescence (PL), the absence of structure in the excitation spectrum of PL in the region of the optical transparency of the crystal, and a number of other properties exclude the relation of these luminescence modes to any impurity or lattice defects [4, 9]. This PL does not become frozen upon cooling; its excitation spectrum is completely located in the fundamental absorption band of the crystal and correlates with the region of exciton-related features in the reflectance spectrum.

Along with the above luminescence mode, a band of intrinsic luminescence of another type (band II in Table 1) was identified in complex oxides; the excitation of this band is substantially determined by recombination processes. Band II is observed in the spectra of TSL, PL, x-ray luminescence, and cathodoluminescence in a wide range of temperatures, including relatively low temperatures (5–10 K). In various crystals, the luminescence processes of this type not only have similar excitation spectra located in the fundamental absorption range but also exhibit similar temperature dependences. This indicates the identical mechanism of excitation of the PL of this type related to the formation of the same primary

Table 1. Parameters of the intrinsic-luminescence bands in some oxides

Crystal	Band I		Band II			Reference
	E_m, eV	μ	E_m, eV	μ	T_m, K	
BeO	6.7	0.360	4.9	0.540	290	[5]
Al_2O_3	7.5	0.162	3.8	0.587	250	[6]
$YAlO_3$	5.9	0.263	4.2	0.447	245	[4]
$Y_3Al_5O_{12}$	4.9	0.300	4.2	0.373	220	[4]
$KTiOPO_4$	2.1	0.475	2.85	0.337	–	[7]
LiB_3O_5	3.6	0.550	4.2	0.533	240	[8]

Note: E_m is the position of the maximum of luminescence and $\mu = (E_{ex} - E_m)/E_{ex}$ is the relative Stokes shift, where E_{ex} is the position of the maximum of the photoexcitation band and T_m is the temperature of the maximum quantum efficiency of luminescence in band II.

electron excitations. The main channel of energy transformation in this case is due to the recombination of charge carriers [10]. Upon excitation in the range of exciton absorption, energy transfer is observed along with the accumulation of charge carriers at traps responsible for the TSL, even at 5 K. In other words, the region of exciton absorption overlaps with the region of excitation of other states responsible for luminescence of the recombination type. Using two-photon optical spectroscopy, these states were identified as the states of electron–hole continuum [11]. Note that the excitation of such luminescence can hardly be distinguished from recombination processes involving intrinsic or impurity lattice defects that cause luminescence bands of similar spectral composition [9, 10]. Convincing experimental evidence for the existence of the recombination channel in the excitation of intrinsic luminescence of Al_2O_3 was obtained only recently [12].

Though important from the practical viewpoint, the borates of alkali and alkaline-earth metals have been studied insufficiently in this respect. Thus, in LiB_3O_5 (LBO), $Li_2B_4O_7$, and $CsLiB_6O_{10}$ crystals, we identified luminescence bands of STEs that were similar in their properties, located in the same energy range (3.4–3.7 eV), did not manifest themselves in the TSL spectra, and were excited at the long-wavelength edge of the fundamental absorption band in the tentative region of photoproduction of unrelaxed excitons [8, 13]. This agrees well with the above-considered properties of the luminescence of STE (band I) in complex oxides. In addition, in the unactivated LiB_3O_5 crystals, other luminescence bands were revealed, which partly overlapped with the spectrum of luminescence of STEs and can manifest themselves both in the TSL and upon excitation in the fundamental absorption range. Some of these bands are characterized by a set of properties that permit one to also regard them as related to the intrinsic luminescence of the crystal.

This work is a continuation of the investigation that was started in [8, 13] and is devoted to studying the dynamics of electron excitations and luminescence in LiB_3O_5 crystals by low-temperature time-resolved optical vacuum-ultraviolet spectroscopy.

2. EXPERIMENTAL TECHNIQUE

We used unactivated crystals of lithium triborate LiB_3O_5; the technology of growing such crystals was described in [8, 14]. Samples with dimensions of $8 \times 8 \times 1$ mm had polished plane-parallel laser finished surfaces. The major planes of the samples were perpendicular to the crystallographic axis *Z*.

Measurements were performed on a SUPERLUMI experimental station of the laboratory Hamburger Synchrotronstrahlungslabor (HASYLAB) at DESY, Hamburg [15], at 7 and 290 K. A detailed description of the technique, experimental procedure, and experimental conditions were given in our previous works [8, 13]. In this work, the repetition period of exciting pulses of the synchrotron radiation of a DORIS storage ring was 480 ns. The time-resolved photoexcitation spectra of PL were recorded simultaneously in two independent time windows; the parameters of each window (the window width Δt and the delay with respect to the excitation pulse δt) were optimized in concrete measurements with allowance for the decay kinetics. The primary monochromator with a diffraction lattice covered with platinum had a spectral resolution of 0.32 nm. The luminescence in the visible and ultraviolet ranges was recorded using a 0.5-m monochromator (Czerny–Turner scheme) and an XP2020Q photomultiplier. The luminescence excitation spectra were normalized using sodium salicylate. The kinetics of the luminescence decay was analyzed using the convolution method with allowance for the instrumental profile of the excitation pulse (FWHM ≈ 350 ps).

3. EXPERIMENTAL RESULTS

The excitation of LBO in the region of the optical transparency of the crystal using photons with an energy $E_{ex} = 6.3$ eV at low temperatures yields a wideband PL in the range of 2.3–4.0 eV (Figs. 1–3).

The kinetics of the PL of LBO under these conditions is represented by an exponential component with a time constant $\tau = 8.3$ ns, which can be reliably recorded at 7 K in a dynamic range of intensities of

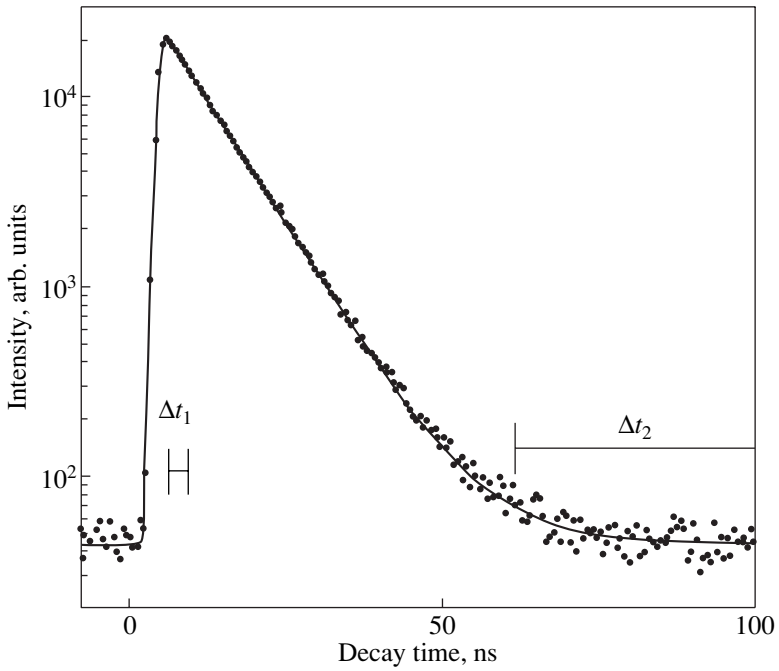

Fig. 1. Kinetics of PL decay in LBO at 7 K in the band E_m = 3.33 eV for the energy of exciting photons E_{ex} = 6.3 eV. Positions of the time windows Δt_1 and Δt_2 are indicated.

about three decades (Fig. 1). Note that at 290 K this PL has not been recorded. No other components of the decay kinetics of the low-temperature PL of LBO in the range of decay times below 500 ns upon excitation in the region of the optical transparency were revealed.

To investigate time-resolved PL emission spectra and time-resolved PL excitation spectra, time windows Δt_1 (δt_1 = 2.1 ns, Δt_1 = 5.9 ns) and Δt_2 (δt_2 = 62 ns, Δt_2 = 332 ns) were chosen, as is shown in Fig. 1. Into the first time window, the fast component with τ = 8.3 ns falls predominantly (the contribution from the pedestal, i.e., from the decay component with τ > 500 ns, is less than 0.3%), whereas the contribution to the second window Δt_2 is mainly caused by the pedestal.

Figure 2 displays PL excitation spectra measured in these time windows. As follows from Fig. 2, no excitation bands were revealed at 290 K in the region of optical transparency of LBO (E_{ex} < 7.5 eV). At the same time, at 7 K, the excitation spectrum of the fast component (window Δt_1) exhibits a wide band (FWHM = 0.53 eV) with a maximum at 6.25 eV (Fig. 2c). In its intensity, this band competes with the main PL excitation band of LBO in the exciton region at 7.9–8.0 eV. However, the efficiency of excitation of the slow component (window Δt_2) in the region of this band is insignificant (Fig. 2).

Table 2. Parameters of the defect-related photoluminescence bands of LBO measured at T = 7 K and E_{ex} = 6.3 eV

Parameter	Δt_1		Δt_2	Total	
E_m, eV	2.72	3.45	3.36	2.71	3.35
FWHM, eV	0.87	1.78	1.23	0.88	1.24
S, %	60	40	100	11	89

Note: E_m and FWHM are the position of the maxima and the full widths at half-maximum of bands in the luminescence spectra measured in time windows Δt_1 and Δt_2 (the positions of the windows are shown in Figs. 1, 2) or in the PL spectra measured without time resolution (Total); S is the percentage contribution of elementary bands to the PL spectrum.

Figure 3 shows the PL spectra of an LBO crystal at 7 K excited by photons with an energy of 6.3 eV. The PL spectrum of the slow component (pedestal) is represented by a wide Gaussian band with a maximum at 3.3 eV (Table 2). The PL spectrum measured in the time window Δt_1 contains two bands at 2.7 and 3.4 eV. In the band located at 3.4 eV, about 40% of the light sum of PL is emitted (Table 2), whereas the contribution of the pedestal to the time window Δt_1 does not exceed 0.3%. The total PL spectrum (without time resolution) consists of two bands at 2.7 and 3.3 eV, but the contribution of the short-wavelength band to this spectrum reaches 89% (Table 2). These estimates show that at 7 K, the spectrum of the fast component of PL with τ = 8.3 ns contains both bands (at 2.7 and 3.4 eV), whereas the spectrum of the pedestal (slow components) exhibits only one band at 3.3 eV.

When the LBO crystals are excited at 7 K by photons with energies above the fundamental absorption edge, the kinetics of the PL decay is represented by two fast components with time constants τ_1 < 1 ns and τ_2 = 8.8 ns. However, the major part of the light sum (85–98%) is accumulated in the pedestal. A comparison of the time-resolved PL emission spectra (Fig. 4) and

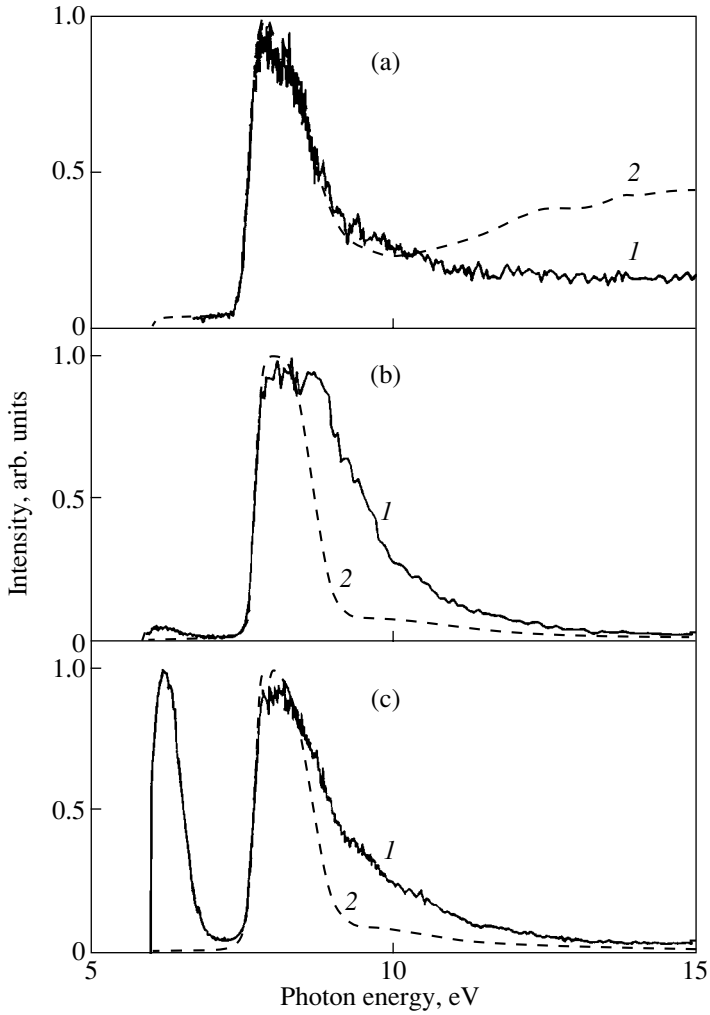

Fig. 2. Normalized PL excitation spectra of the LBO crystal at (a) 290 and (b, c) 7 K in the luminescence bands located at (a, c) 3.5 and (b) 4.2 eV in time windows (*1*) δt_1 = 2.1 ns, Δt_1 = 5.9 ns and (*2*) δt_2 = 62 ns, Δt_2 = 332 ns.

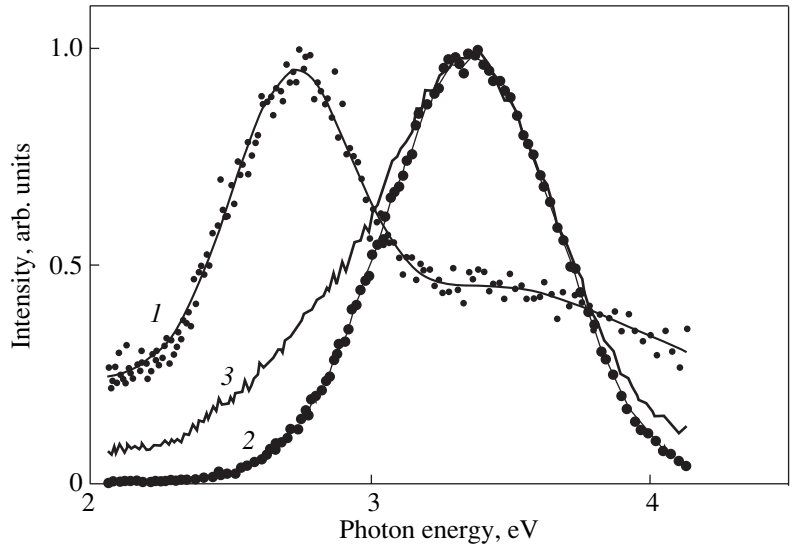

Fig. 3. Photoluminescence emission spectra of the LBO crystal at T = 7 K and E_{ex} = 6.3 eV, measured in time windows (*1*) δt_1 = 2.1 ns, Δt_1 = 5.9 ns and (*2*) δt_2 = 62 ns, Δt_2 = 332 ns; (*3*) PL spectra measured without time resolution.

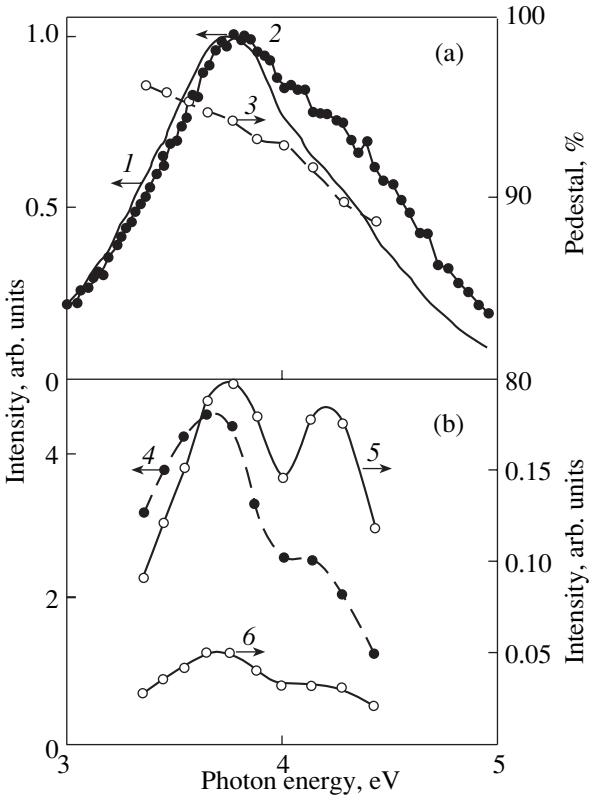

Fig. 4. (a) Photoluminescence emission spectra of LBO at $T = 7$ K and $E_{ex} = 8.8$ eV, measured in time windows (*1*) $\delta t_2 = 21.3$ ns, $\Delta t_2 = 111$ ns and (2) $\delta t_1 = 1.2$ ns, $\Delta t_1 = 5.6$ ns. (b) Spectral dependences of the kinetic parameters of PL: (*3*) percentage contribution of the pedestal to the total light yield, (*4*) total light yield under the PL decay curve, (*5*) specific light yield of the component with $\tau = 8.8$ ns, and (*6*) specific light yield of the component with $\tau < 1$ ns.

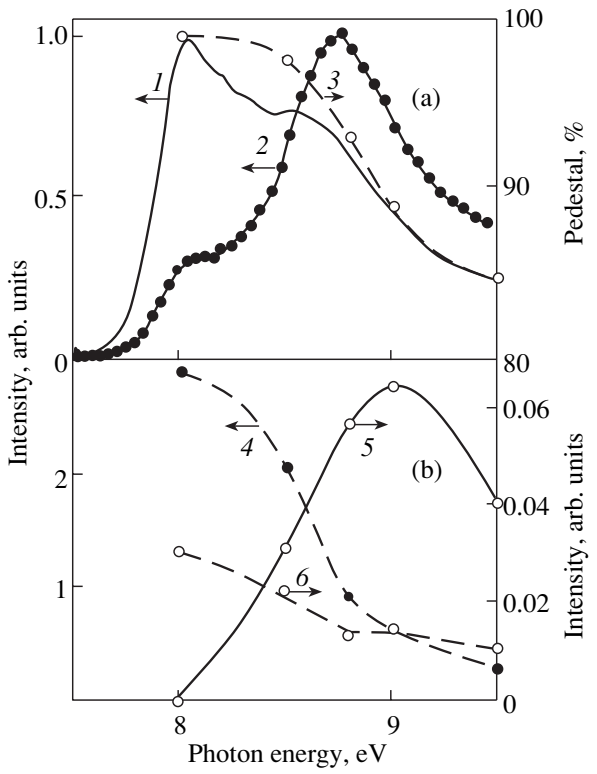

Fig. 5. (a) Photoluminescence excitation spectra of LBO at $T = 7$ K and $E_{ex} = 4.2$ eV, measured in time windows (*1*) $\delta t_2 = 21.3$ ns, $\Delta t_2 = 111$ ns and (2) $\delta t_1 = 1.2$ ns, $\Delta t_1 = 5.6$ ns. (b) Spectral dependences of the kinetic parameters of PL: (*3*) percentage contribution of the pedestal to the total light yield, (*4*) total light yield under the PL decay curve, (*5*) specific light yield of the component with $\tau = 8.8$ ns, and (*6*) specific light yield of the component with $\tau < 1$ ns.

time-resolved PL excitation spectra (Fig. 2) shows that each of them contains no less than two overlapping bands caused by the fast decay components. To clarify the contribution of fast components to these bands, we studied the kinetics of PL in various spectral points at various energies of the exciting photons. When measuring each curve, the number of photons striking the crystal was always the same. Based on an analysis of these curves, we constructed spectral dependences of the parameters of the PL kinetics (Figs. 4, 5). As follows from Fig. 4, at $E_{ex} = 8.8$ eV, the spectral dependence of the light yield of slow components (pedestal) has a distinct maximum at 3.7 eV and a shoulder at 4.2 eV. The spectrum of the light yield of the fast component with $\tau_1 < 1$ ns has a similar character, whereas in the spectrum of the light yield of the second fast component (with $\tau_2 = 8.8$ ns), the amplitudes of both bands (at 3.7 and 4.2 eV) are almost identical. This means that the observed monotonic decrease in the contribution of the pedestal (slow components) to the total light yield under the curve of the PL decay (Fig. 4) is caused by the corresponding increase in the contribution of the second fast component with $\tau_2 = 8.8$ ns.

In the region of the fundamental band of LBO, the PL excitation spectrum at 7 K is represented by two main overlapping bands at 7.9–8.5 and 8.5–9.2 eV peaking at 7.9 and 8.75 eV, respectively (Figs. 2, 5). An analysis of the contributions of various decay components to these bands (Fig. 5) shows that in the spectrum of PL excitation at $E_m = 4.2$ eV, the fast component $\tau_1 <$ 1 ns and the pedestal mainly contribute to the first excitation band at 7.9 eV. The second excitation band at 8.75–9.2 eV is mainly due to the second fast component $\tau_2 = 8.8$ ns. As follows from the time-resolved excitation spectra (Fig. 5), the second fast component is excited inefficiently at the edge of the fundamental band but dominates in the energy range $E_{ex} > 8.5$ eV and yields a maximum contribution to the light sum at 9.0 eV. As the energy E_{ex} increases further, the intensity of this maximum decreases (Figs. 2, 5). In the energy range of 7.9–9.5 eV, the contribution from the pedestal decreases, which is due to the corresponding increase in the contribution from the second fast component $\tau_2 =$ 8.8 ns.

4. DISCUSSION

The photoluminescence of the LBO crystal begins at photon energies above 7.5 eV [14, 16]. In this connection, the PL bands at 2.7 and 3.3 eV that are efficiently excited in the region of the optical transparency of the crystal by photons with an energy of about 6.3 eV should be regarded as being caused by the luminescence of intrinsic or impurity lattice defects of LBO. The exponential law of decay of the main component of the PL kinetics indicates the intracenter character of the luminescence process. Previously, we found a wide band of optical absorption of LBO at 6.2 eV, which manifests itself at 80 K after irradiation of the LBO crystal with a 200-keV electron beam [17, 18]. The stimulation of the optical absorption into this band by irradiating the crystal with an ArF laser at room temperature leads to the excitation of PL at 3.3 eV [19].

The determination of the nature of these defects in LBO requires special experimental investigations. At present, we can only suggest general considerations about it. It was established in [20] using high-resolution infrared spectroscopy that during heat treatment of LBO crystals, some changes occur in the nearest neighborhood of Li–O bonds because of the migration of vacancies and interstitial atoms. In [21], we computationally analyzed the possibility of capturing electrons in LBO at free (broken) orbitals of boron atoms that are directed toward an oxygen vacancy. The calculated data predict the possibility of forming local levels of the ground and excited states of defects in the forbidden energy band of LBO. The tentative characteristics of these defects are qualitatively similar to those of F^+ color centers in some oxide crystals [22]. In this connection, we may assume that the PL of the LBO crystals at 3.3 eV is due to color centers that are characterized by the optical absorption band at 6.2 eV. On the other hand, we cannot exclude the possibility of forming defects based on some uncontrolled cation impurities. For example, for the paramagnetic O^- center in LBO, the problem of the mechanism of stabilization of the hole at a regular oxygen ion still remains unsolved to date [23]. A similar center in Al_2O_3:Sc represents a hole at an oxygen ion stabilized by an impurity atom of scandium [12, 24]. However, in any case, the established spectral–kinetic and luminescence–optical characteristics of this color center in LBO permit its use as a luminescence probe for studying the dynamics of electron excitations.

The excitation of an LBO crystal at 7 K by photons with energies above the fundamental absorption edge leads to the appearance of intrinsic luminescence in a band located at 3.6–3.7 eV, which significantly overlaps with the band of PL of defects. This may be one more cause for the apparent efficient excitation of PL at 3.3 eV in the region of the fundamental absorption edge of LBO at low temperatures (Fig. 2). In reality, an analysis of the spectra (Fig. 2) and kinetics of PL indicates that the contribution of color centers to the PL of LBO upon its excitation in the region of the fundamental absorption edge is insignificant, which implies a low efficiency of the exciton mechanism of energy transport to color centers. This situation is typical of crystals of complex oxides (e.g., YAG [25]), in which the contribution of the exciton mechanism to the energy transfer becomes actual only at high concentrations of activators, when the probability of the formation of excitons in the immediate vicinity of these centers increases. Otherwise, a competitive channel of energy transformation (related to exciton self-trapping) dominates. With a further increase in the energy of exciting photons, the excitation of color centers by hot photoelectrons can occur in the region of band-to-band transitions. Indeed, in the spectrum of the fast component of PL near 3.3 eV, a hump is observed, whose intensity increases with increasing energy of the exciting photons [8].

Now, we discuss the results that concern the bands of intrinsic luminescence of LBO excited only in the fundamental absorption band of the crystal. An analysis of the time-resolved excitation spectra of luminescence of LBO revealed the existence of a fine structure in these spectra near the fundamental absorption edge (Figs. 4, 5). It is obvious that the different PL excitation bands have different natures. The band at 7.9 eV was ascribed to the optical production of molecular excitons (ME) in LBO [8]. The self-trapping of MEs and the subsequent radiative annihilation of STEs lead to the PL at 3.6–3.8 eV. The efficiency of excitation of this PL is highest just in the long-wavelength portion of the expected region of production of free excitons in LBO (7.9–8.5 eV), where the optical absorption coefficient is $10–10^4$ cm^{-1}. In contrast to alkali-halide crystals, no luminescence band of the given STEs was revealed in the TSL spectra (15–300 K) of LBO. The efficiency of excitation of this band in the region of band-to-band transitions in LBO is smaller by a factor of about 40 than in the exciton region. The

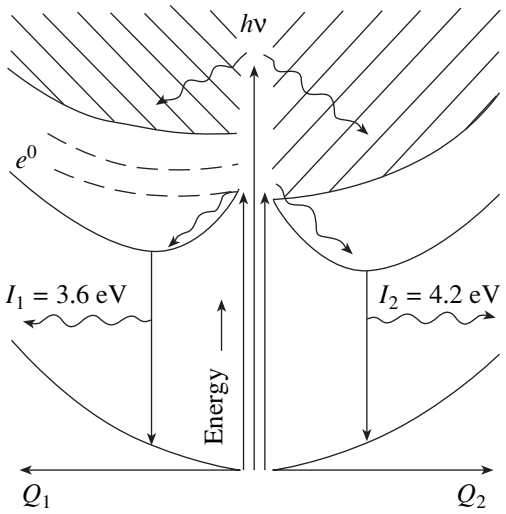

Fig. 6. Adiabatic curves of potential energy of STE in LBO crystals.

difference in the properties of this luminescence and the luminescence of STEs in alkali-halide crystals reflects the fundamental difference in the processes of self-trapping in these two types of crystals.

In the short-wavelength part of the tentative region of production of free excitons in LBO (8.5–9.2 eV), an efficient excitation of PL at 4.2 eV occurs at 7 K. This PL is not excited in the region of the crystal transparency; its excitation band partly overlaps with the main excitation band of PL in LBO at 8.0 eV and is shifted with respect to it toward the short-wavelength region by about 1 eV (Fig. 5). In the region of production of electron–hole pairs, the efficiency of excitation of this PL at 7 K is much smaller. By the totality of its properties, the PL band at 4.2 eV can be referred to the intrinsic emission of LBO caused by the annihilation of localized electron excitations. However, their nature, as well as the nature of primary electron excitations formed by photons with energies of 8.5–9.2 eV, differ from those characteristic of the preceding case.

In complex oxides, two alternative mechanisms of the formation of STEs are distinguished. The first is related to the optical production of excitons (exciton mechanism) and its subsequent relaxation into a self-trapped state. The second mechanism is connected with the formation of STEs through the relaxation of electron excitations from the lower states of the electron–hole continuum (recombination mechanism) [4, 9]. In many cases, these mechanisms can lead to substantially different final stages of relaxation (different configurations of STEs), thereby causing the appearance of different luminescence bands (bands I and II in Table 1). The causes for the formation of different configurations of STEs in complex oxides are connected with the significant nonuniformity of the electron structure of the valence band (VB). It is well known that in low-symmetry crystal fields, there occurs a complete splitting of the 2*p* states of oxygen that form the upper states of the VB in oxides [26]. The nonbonding orbitals (π orbitals) occupy the uppermost position, form the top of the VB, and determine the dynamics of relaxed holes. In the upper, rather narrow subband of the VB (UVB) with a weak dispersion, the holes are characterized by a relatively large translational mass [9, 27]. As a result of covalent effects, the lower subband of the valence band (LVB) has a large width and large dispersion and is responsible for the significant covalent contribution to the oxygen–metal chemical bond. It was shown by two-photon spectroscopy [25] that in YAG crystals, the situation with two types of electron excitations resembles to a certain extent the case of the overlap of the energy states of direct excitons with the edge of band-to-band transitions (the lower state of the electron–hole continuum), as is the case, e.g., in crystals of silver halides [2]. Such an overlap of states is responsible, in particular, for the instability of excitons with respect to self-ionization. Comparing these data with experimental results (Figs. 2–5), we can assume that, at 7 K, photons with energies of 8.5–9.2 eV form in LBO electron excitations which are closely related to the lower states of the electron–hole continuum. In our opinion, the self-trapping of these electron excitations at 7 K leads to the formation in LBO of STEs of another configuration. The radiative annihilation of such STEs causes the luminescence of LBO at 4.2 eV.

Figure 6 displays a simplified scheme of the processes of excitation and relaxation of electron excitations in LBO. The different configurational coordinates (Q_1 and Q_2) in this figure correspond to the different ways of lattice relaxation upon the formation of two types of electron excitations. As follows from the model under consideration, the molecular exciton e^0 produced by photoexcitation in the immediate vicinity of the fundamental absorption edge or as a result of relaxation from highly excited states then relaxes into a self-trapped state (configurational coordinate Q_1). It was shown in [8] that the molecular exciton e^0 in LBO is formed with the participation of states of the LVB. The self-trapping of the hole component of the molecular exciton is improbable because of the small translational mass of holes in the LVB. However, the Sumi's theory [28] predicts that although an electron or a hole cannot be self-trapped separately, such self-trapping is probable for an exciton as a whole if the deformations produced by an electron and a hole are added. Such an STE should have a small radius and a large translational mass and is called a "self-shrunk exciton" (SSE). Since the formation of an SSE requires a synchronous deformation of the lattice by the electron and the hole, no SSEs are usually formed in recombination processes. It was shown only recently that the formation of SCEs upon recombination of an electron and a hole is possible in Al_2O_3 at high densities of excitations (above 10^{18} cm^{-3}) [12]. It was supposed [12] that the majority of the observed bands of intrinsic luminescence in complex oxides (band I in Table 1) belong to SSEs. In this connection, it is reasonable to suppose that the molecular excitons e^0 in LBO (Fig. 6) become self-trapped via this mechanism into the SSE state whose radiative annihilation causes luminescence at 3.6–3.8 eV.

The lowest-energy band-to-band transitions should occur from the states of nonbonding oxygen orbitals of the upper valence subband that form the top of the valence band. As is shown in Fig. 6, it is these transitions that cause the manifestation of recombination processes in the energy region of photoproduction of molecular excitons. The hole of the upper valence subband has a relatively large translational mass and can pass into the state of a polaron of small radius, which suits the role of the hole core of the STE well. The vibrational relaxation from the lower states of the electron–hole continuum that contains the holes of the upper valence subband can lead to the formation of an self-trapped electron excitation (configurational coordinate Q_2) whose radiative annihilation causes the luminescence of LBO at 4.2 eV. It is assumed that a similar mechanism is realized in some other complex oxides (band II in Table 1). At low temperatures, the intensity of this band is relatively small; however, it does not become frozen even at 4 K. Using one-photon

and two-photon optical spectroscopy, it was shown for some complex oxides [11] that the interaction between exciton states and the lowest states of the electron–hole continuum is very weak; therefore, either type of electron excitation can arise independently. The possibility of the simultaneous observation of both branches of relaxation is due to the competition of the processes of fast self-trapping and relatively slow self-ionization. It was shown in [29] that for a relatively large region of the Sumi diagram, two types of self-trapping can coexist: SSE and STE, whose core is a self-trapped hole belonging to the upper subband of the valence band. The physical processes that lead to the formation of these types of STEs are substantially different, which is reflected in the complex character of the temperature dependences of the luminescence intensity and in the differences in the excitation spectra and decay kinetics.

In contrast to alkali-halide crystals and SiO_2, long searches for the existence of a self-trapped hole in complex oxides (such as Al_2O_3, BeO) were unsuccessful. In the close-packed oxygen sublattice of such compounds, the holes in the polaron state can migrate even at 4 K, since the related lattice polarization appears to be insufficient to provide for self-trapping. Moreover, in Al_2O_3 crystals with a defect concentration of about 10 ppm, the holes are localized just near various impurity atoms and weak lattice distortions [12]. It can be assumed that in complex oxides, the self-trapping of a hole occurs only if the hole is part of an electron–hole pair formed upon recombination of an electron and a relaxed hole of the upper valence subband. In contrast to the situation with the formation of an SSE, the hole in the upper valence band has a large translational mass and can serve as the core of an STE. We assume that it is the radiative annihilation of such an STE that is responsible for the luminescence band at 4.2 K in LBO. As was established in [12], the cross section for the recombination of mobile electron and hole is small, but in a local region where small inhomogeneities exist (weak lattice distortions or point defects that do not produce electron or hole traps), the recombination cross section can increase by several orders of magnitude. Thus in Al_2O_3, the recombination cross section near a defect (Sc^{3+}) that does not form a trap is higher by three orders of magnitude than the corresponding cross section for the defect-free region [12]. It is obvious that if charge carriers of only one sign are localized at defects (as, e.g., in the case of TSL), the probability for recombination increases even greater. If in this case the defects have no activator luminescence bands, localized electron excitations can be formed whose parameters are close to those for the STEs of the recombination type and quite weakly depend on the parameters of the defect. Indeed, the spectrum of the main peaks of TSL in LBO (130 and 240 K) is concentrated in the 4.2-eV band [30]. A similar phenomenon was observed previously in BeO, where the thermostimulated electron and hole recombination with the participation of various defects that have no activator PL bands leads to luminescence at 4.9 eV (band II in Table 2) [5,31,32].

The kinetic energy of the components of an electron–hole pair produced at 7 K by photons with an energy close to E_g is small. This implies a large probability of recombination in geminate (genetically related) pairs with subsequent formation of STEs according to the above-described mechanism. With increasing exciting-photon energy, the components of the electron–hole pair acquire a kinetic energy sufficient for them to leave their "birthplace" (to "fly away"). The band electron and the band hole that are formed as a result of such flying away at 7 K immediately become localized at traps. Therefore, it is only the lowest-energy band-to-band transitions from the levels of the upper valence subband (at the top of the valence band) that can lead in LBO to the formation of electron excitations whose self-trapping yields STEs of the recombination type. It is this mechanism that, in our opinion, is responsible for the excitation band at 9.0 eV (Fig. 5).

As the temperature of the LBO crystal increases to above 240 K, thermostimulated delocalization of charge carriers from traps occurs; these charge carriers give an additional contribution to the recombination process. The natural consequences are an increase in the intensity of the PL band at 4.2 eV and an increase in the efficiency of excitation of this band by photons with energies exceeding E_g (Fig. 2). The kinetics of PL decay under these conditions is determined by the processes of thermostimulated delocalization of charge carriers and is characterized by a time constant in the microsecond or millisecond range [33, 34].

An analysis of spectral dependences of the parameters of the PL kinetics (Fig. 4) shows that the decay component with τ = 8.8 ns manifests itself in both bands of intrinsic PL of LBO, although its relative contribution to these bands changes. Since the interference of the STE and SSE states is improbable [29], this component can be related to the process of branching between the states of primary electron excitations that are responsible for the corresponding STE and SSE. It is well known [11] that the interaction between the exciton state of the molecular exciton and the lowest states of the electron–hole continuum is very weak, but with increasing excitation energy, their interaction increases sharply. In our case, the energy of photon excitation E_{ex} = 8.8 eV lies in the region of the maximum of the short-wavelength excitation band (Fig. 5). According to the model under consideration, this maximum should lie much higher than the onset of band-to-band transitions into the states of the electron–hole continuum that includes holes of the upper valence subband. In this connection, it is reasonable to relate the τ = 8.8-ns PL decay component located at 4.2 eV to the process of interaction (scattering) between the molecular exciton states and electron–hole continuum of the upper subband of the valence band.

CONCLUSION

Thus, an analysis of the results of vacuum ultraviolet luminescence low-temperature time-resolved spectroscopy permitted us to distinguish photoluminescence (PL) bands of LiB_3O_5 (LBO) that are related to defects (2.7 and 3.3 eV) and the bands of intrinsic luminescence of the LBO crystal caused by radiative annihilation of two types of self-trapped excitons (STEs). The luminescence band at 3.6 eV (band I) is related to the annihilation of self-shrunk excitons (SSEs), which is a result of the self-trapping of a molecular exciton (ME) with a hole component in the lower subband of the valence band (LVB). A self-trapped exciton of another type is formed upon the self-trapping of primary electron excitations produced by the recombination of a mobile electron and a heavy hole in the upper valence subband (UVB). The probability of such a process is extremely low, but under certain circumstances it can increase by several orders of magnitude: (a) in the case of geminate (genetically related) electron–hole pairs produced by photons near the onset of band-to-band transitions, (b) in the presence of small inhomogeneities (weak lattice distortions and defects that do not produce traps), and (c) in thermostimulated recombination processes involving defects that have no activator photoluminescence bands. The radiative annihilation of self-trapped excitons of recombination type in LBO results in a photoluminescence at 4.2 eV (band II). The decay component of this photoluminescence with τ = 8.8 ns is ascribed to the process of interaction (scattering) between the molecular exciton states and the states of the electron–hole continuum involving holes of the upper subband of the valence band.

ACKNOWLEDGMENTS

This work was supported in part by the Russian Foundation for Basic Research (project no. 02-16206), the Ministry of Education of the Russian Federation (project no. 992886), and the Deutscher Akademischer Austauschdienst (DAAD) and Deutsche Forscgungsgemeinschaft (DFG) (grant no. ZI-159/4-1). We are also grateful to G. Zimmerer (Hamburg Universität) for his permanent attention to our work and assistance.

REFERENCES

1. Ch. Lushchik, in *Excitons*, Ed. by E. I. Rashba and M. D. Sturge (North-Holland, Amsterdam, 1982), Vol. 2, p. 505.
2. A. S. Song and R. T. Williams, *Self-Trapped Excitons* (Springer-Verlag, Berlin, 1996).
3. Ch. B. Lushchik and A. Ch. Lushchik, *Electron Excitation Decay with Defect Formation* (Nauka, Moscow, 1989).
4. V. Mürk, Mater. Sci. Forum **239–241**, 537 (1997).
5. I. Ogorodnikov and A. Kruzhalov, Mater. Sci. Forum **239–241**, 51 (1997).
6. A. I. Kuznetsov, B. R. Namozov, and V. V. Myurk, Izv. Akad. Nauk Ést. SSR, Fiz., Mat. **36** (2), 193 (1987).
7. P.-P. Proulx, V. Denks, A. Dudelzak, *et al.*, Nucl. Instrum. Methods Phys. Res. B **141**, 477 (1998).
8. I. N. Ogorodnikov, V. A. Pustovarov, A. V. Kruzhalov, *et al.*, Fiz. Tverd. Tela (St. Petersburg) **42** (3), 454 (2000) [Phys. Solid State **42**, 464 (2000)].
9. A. I. Kuznetsov, V. N. Abramov, V. V. Mürk, and B. R. Namozov, Tr. Inst. Fiz. Akad. Nauk Ést. SSR **63**, 19 (1989).
10. V. Mürk, B. Namozov, and N. Yaroshevich, Radiat. Meas. **24** (4), 371 (1995).
11. V. Mürk, A. Kuznetsov, B. Namozov, and K. Ismailov, Nucl. Instrum. Methods Phys. Res. B **91**, 327 (1994).
12. M. Kirm, G. Zimmerer, E. Feldbach, *et al.*, Phys. Rev. B **60** (1), 502 (1999).
13. I. N. Ogorodnikov, V. A. Pustovarov, A. V. Kruzhalov, *et al.*, Fiz. Tverd. Tela (St. Petersburg) **42** (10), 1800 (2000) [Phys. Solid State **42**, 1846 (2000)].
14. I. N. Ogorodnikov, E. A. Radzhabov, L. I. Isaenko, and A. V. Kruzhalov, Fiz. Tverd. Tela (St. Petersburg) **41** (2), 223 (1999) [Phys. Solid State **41**, 197 (1999)].
15. G. Zimmerer, Nucl. Instrum. Methods Phys. Res. A **308** (1-2), 178 (1991).
16. I. Ogorodnikov, E. Radzhabov, L. Isaenko, and A. Kruzhalov, in *Excitonic Processes in Condensed Matter*, Ed. by R. T. Williams and W. M. Yen (The Electrochemical Society, Pennington, 1998); Proc.-Electrochem. Soc. **PV98-25**, 426 (1998).
17. I. N. Ogorodnikov, A. V. Porotnikov, S. V. Kudyakov, *et al.*, Fiz. Tverd. Tela (St. Petersburg) **39** (9), 1535 (1997) [Phys. Solid State **39**, 1366 (1997)].
18. I. Ogorodnikov, A. Kruzhalov, A. Porotnikov, and V. Yakovlev, J. Lumin. **76-77**, 464 (1998).
19. R. Kink, M. Kink, I. Kink, *et al.*, in *Max-Lab Activity Report* (Max-Lab, Lund, 1998), p. 134.
20. A. A. Khodyakov, M. Kh. Dzhafarov, L. N. Kurilenko, *et al.*, Zh. Fiz. Khim. **9**, 2561 (1991).
21. A. Yu. Kuznetsov, A. B. Sobolev, I. N. Ogorodnikov, and A. V. Kruzhalov, Fiz. Tverd. Tela (St. Petersburg) **36** (12), 3530 (1994) [Phys. Solid State **36**, 1876 (1994)].
22. A. B. Sobolev, Fiz. Tverd. Tela (St. Petersburg) **36** (10), 2926 (1994) [Phys. Solid State **36**, 1557 (1994)].
23. A. V. Porotnikov, I. N. Ogorodnikov, S. V. Kudyakov, *et al.*, Fiz. Tverd. Tela (St. Petersburg) **39** (8), 1380 (1997) [Phys. Solid State **39**, 1224 (1997)].
24. B. R. Namozov, V. V. Mürk, R. I. Zakharchenya, and M. P. Korobkov, Fiz. Tverd. Tela (St. Petersburg) **40** (4), 653 (1998) [Phys. Solid State **40**, 599 (1998)].
25. V. Mürk and N. Yaroshevich, Phys. Status Solidi B **181**, K37 (1994).
26. R. Evarestov, A. Ermoshkin, and V. Lovchikov, Phys. Status Solidi B **99**, 387 (1980).
27. V. G. Krongauz, O. Ya. Manashirov, and V. B. Mikhitar'yan, Pis'ma Zh. Tekh. Fiz. **15** (12), 79 (1989) [Sov. Tech. Phys. Lett. **15**, 488 (1989)].
28. A. Sumi, J. Phys. Soc. Jpn. **43** (4), 1286 (1977).

29. A. I. Kuznetsov, V. N. Abramov, V. V. Mürk, and B. R. Namozov, Fiz. Tverd. Tela (Leningrad) **33** (7), 2000 (1991) [Sov. Phys. Solid State **33**, 1126 (1991)].

30. I. Ogorodnikov, L. Isaenko, A. Kruzhalov, and A. Porotnikov, Radiat. Meas. (2001) (in press).

31. I. N. Ogorodnikov, V. Yu. Ivanov, and A. V. Kruzhalov, Fiz. Tverd. Tela (St. Petersburg) **36** (11), 3287 (1994) [Phys. Solid State **36**, 1748 (1994)].

32. I. Ogorognikov, V. Ivanov, and A. Kruzhalov, Radiat. Meas. **24** (4), 417 (1995).

33. I. N. Ogorodnikov, A. V. Porotnikov, A. V. Kruzhalov, and V. B. Yakovlev, Fiz. Tverd. Tela (St. Petersburg) **40** (11), 2008 (1998) [Phys. Solid State **40**, 1817 (1998)].

34. I. Ogorognikov, A. Kruzhalov, A. Porotnikov, and V. Yakovlev, Radiat. Eff. Defects Solids **150** (1–4), 299 (1999).

Translated by S. Gorin

Physics of the Solid State, Vol. 43, No. 8, 2001, pp. 1464–1467. Translated from Fizika Tverdogo Tela, Vol. 43, No. 8, 2001, pp. 1405–1408.

SEMICONDUCTORS AND DIELECTRICS

Pyroelectric Properties of Lithium Triborate in the Temperature Range from 4.2 to 300 K

S. Matyjasik* and Yu. V. Shaldin**

**International Laboratory of Strong Magnetic Fields and Low Temperatures, 53529 Wroclaw, Poland*

***Shubnikov Institute of Crystallography, Russian Academy of Sciences, Leninskiĭ pr. 59, Moscow, 117333 Russia*

e-mail: griamo@aha.ru

Received January 9, 2001

Abstract—Temperature dependences of pyroelectric coefficients γ^T and γ^S corresponding to the mechanically free (T) and clamped (S) states of a lithium triborate (LBO) sample are studied and found to be nonmonotonic. It is proposed that the anomalies are associated with an increase in anharmonism of the lithium sublattice of LBO long before its transition to the superionic state. The spontaneous polarization at $T = 200$ K is estimated to be 0.25 C/m^2. In the structural motif, the mesotetrahedra responsible for the emergence of spontaneous polarization of LBO are singled out. © *2001 MAIK "Nauka/Interperiodica".*

1. INTRODUCTION

The interest in lithium triborate (LiB_3O_5) is due to the peculiar combination of its physical properties. In view of its high nonlinear (quadratic) susceptibility and broad transparency region (from 4.6 to 7.9 eV) [1, 2], this substance belongs to the class of pyroelectrics and can go over to the superionic state [3] at high temperatures.

Lithium triborate (which will be henceforth referred to as LBO) crystals belong to the orthorhombic system (space group $Pna2_1$). Traditionally, its structure is formed by plane BO_3 triangles and BO_4 tetrahedra combined into a 3D skeleton through common oxygen ions [4]. Lithium ions are localized in the voids of the skeleton and lie along the 2_1 symmetry axis, which corresponds to the orientation of the spontaneous polarization. It was found [3] that the so-called through channels in the structure are also oriented along this direction. An analysis of the features of the LBO structure and the experimentally established ionic-type conduction at $T > 400$ K indicate the possibility of ionic transport of Li along the direction of the spontaneous polarization. A natural question arising in this connection concerns the possibility of experimental estimation of the temperature from which the instability of the lithium sublattice starts manifesting itself. The answer to this question obviously stems from analyzing the manifestations of the pyroelectric effect, since the enhancement of the anharmonism in the lithium sublattice (long before its transition to the superionic state) must affect the total dipole moment of the LBO structure in the $\langle 001 \rangle$ direction. This is of practical importance since it could provide preliminary information on the possible temperature dependence of the nonlinear (quadratic) susceptibility of a pyroelectric possessing some coefficients directly connected with spontaneous polarization [5]. The spontaneous polarization of a pyroelectric can be estimated from the results of optical and pyroelectric measurements.

This work is devoted to analysis of the pyroelectric properties of mechanically free and clamped lithium triborate crystals and to determining the features of the LBO structure responsible for the pyroelectric effect and, hence, for the spontaneous polarization of the crystal.

2. EXPERIMENTAL TECHNIQUE

LBO crystals grown from solution in melt belong to the linear pyroelectric class (point group $mm2$).[1] A square billet cut from an initial boule was oriented and polished to fit the size $8.0 \times 8.06 \times 1.53$ mm. The deviation in the orientation relative to the 2_1 axis did not exceed 30′. The electrode material deposited on the (001) faces was of silver paste, thus providing a good ohmic contact with the sample. The sample intended for temperature measurements was mounted in a helium cryostat in a special crystal holder. The sample temperature was monitored using a Cemox-1050-SD thermometer. A quasi-continuous temperature regime was set using a Keithly-220 programmed power supply, which made it possible to select (taking into account the time constant of the measuring system) the required rate of continuous variation of the temperature. The charge generated by the sample was measured as a function of T using a Keithly-617 programmed electrometer. The resistance of the sample with current leads was of the order of 10^{12} Ω at ~300 K. In our experiments, two versions of sample connection were realized: (a) mechanically free (the sample was hang-

[1] The results of dilatometric measurements [6] and the results presented below also confirm this fact.

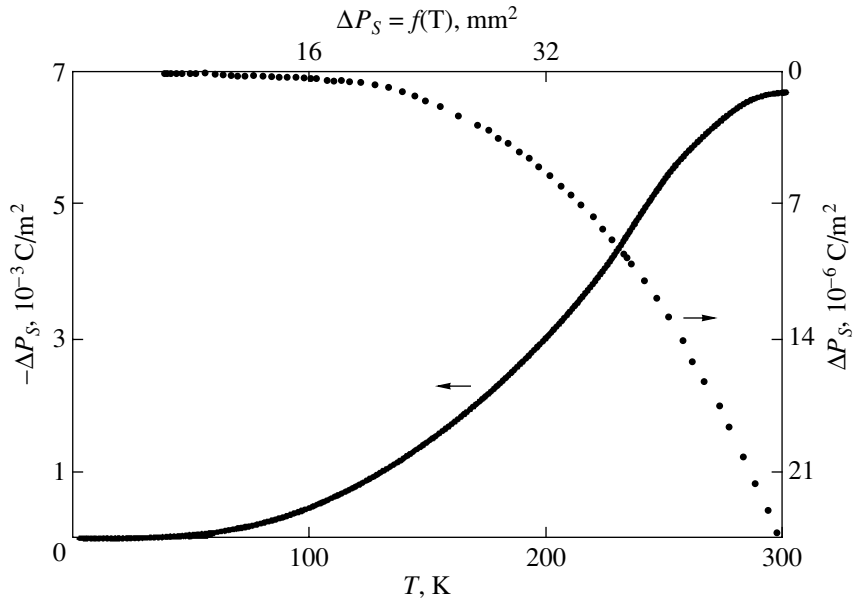

Fig. 1. Temperature dependence of the change in the spontaneous polarization of a mechanically free LBO crystal; $S = 65\text{mm}^2$.

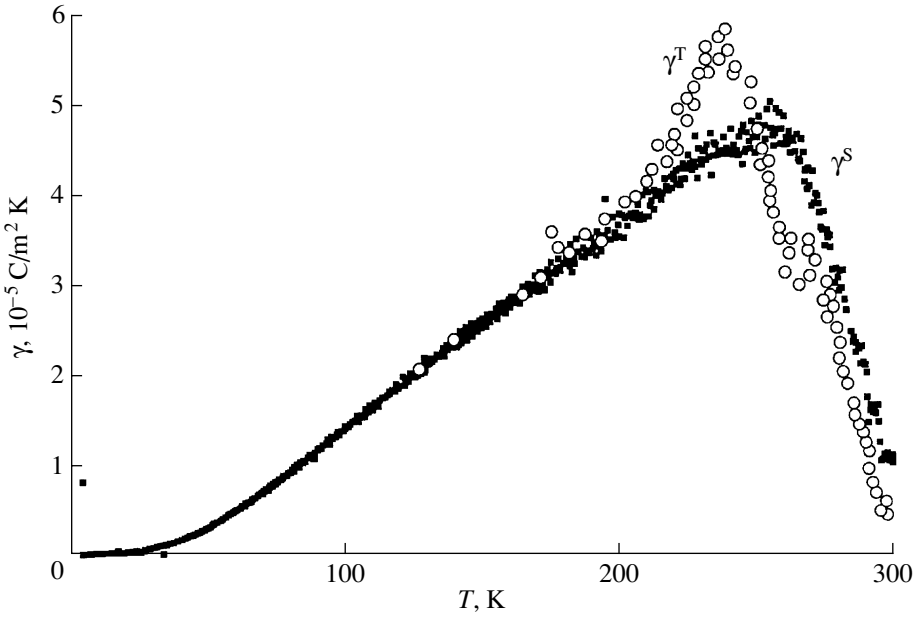

Fig. 2. Temperature dependence of the pyroelectric effect for a mechanically free (γ^T) and clamped (γ^S) LBO crystal; $S = 65\text{mm}^2$.

ing on current leads) and (b) mechanically clamped (the sample was pressed between bulk electrodes). The results of measurements of the spontaneous polarization ΔP_S presented in Fig. 1 indicate the high quality of the samples (no anomalies are observed in the liquid-helium temperature region) and good reproducibility of the experimental data (the experimental points for sample heating and cooling coincide).

3. RESULTS AND DISCUSSION

The results of measurements of the pyroelectric coefficients γ^T and γ^S for the above states of the sample are presented in Fig. 2.[2] The temperature dependences of γ^T and γ^S coincide to within the measurement error in

[2] The choice of the sign of the pyroelectric coefficients is dictated by the obvious condition $\partial P_S/\partial T < 0$.

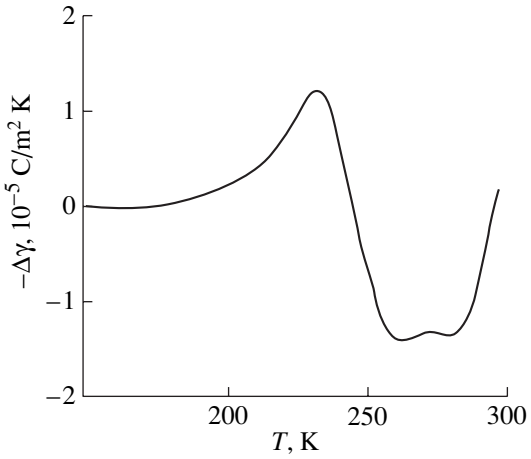

Fig. 3. Temperature dependence of the contribution from the secondary pyroelectric effect $\Delta\gamma$ to the pyroelectric coefficient γ^T for an LBO crystal.

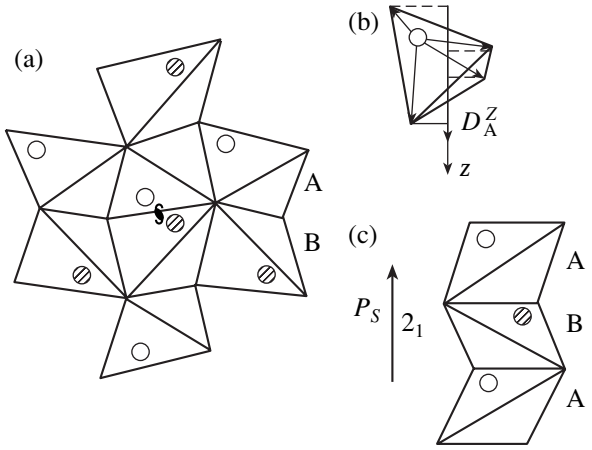

Fig. 4. Atomic structure of pyroelectric LBO presented as a combination of mesotetrahedra of A and B types: (a) projection of the LBO structure on the (*x*, *y*) plane; hatched and light circles are lithium atoms with coordinates $z = 0.9545$ and 0.4545, respectively; (b) a mesotetrahedron and its resultant dipole moment D_A; and (c) projection of a layer in the structure on the (*y*, *z*) plane.

the low-temperature range and diverge starting from 200 K. According to Cady [7], their difference is determined by the contribution from the secondary pyroelectric effect,

$$\Delta\gamma(T) = \gamma^T - \gamma^S = e_{311}g_{11} + e_{322}g_{22} + e_{333}g_{33},$$

and is expressed in terms of the piezoelectric moduli e_{ijk} and the linear expansion coefficients g_{ii} of LBO. The $\Delta\gamma(T)$ dependence obtained by us is presented in Fig. 3. The lack of information on the piezoelectric effect in LBO does not allow us to compare the experimental data with the phenomenological theory. Taking into account the linear-expansion anisotropy data [6], we can state that the $e_{ijl}(T)$ dependences are monotonic for LBO crystals in this temperature range. The temperature dependence of the secondary pyroelectric effect in lithium triborate is rather peculiar: the sign of $\Delta\gamma$ coincides with the sign of the primary pyroelectric effect up to 245 K and is then reversed in the interval from 245 to 295 K; then, the contribution of the secondary effect exhibits a strong tendency toward growth, which can indicate a decrease in the primary pyroelectric effect in LBO. The reliability of the obtained results indirectly confirms the data on the temperature dependence of the LBO lattice parameters in the temperature range from 0 to 800°C [6]: $\partial c/\partial T < 0$, where *c* is the lattice constant along the 2_1 axis.

The data on the pyroelectric effect in LBO at temperatures above 200 K are of special interest. In spite of the fact that the resistivity of LBO in this temperature interval exceeds 10^{22} Ω cm, the temperature dependences of γ^T and γ^S deviate from the standard behavior typical of the pyroelectric effect in high-resistivity pyroelectrics. We interpret this result as a manifestation of strong anharmonism of lithium atoms relative to the entire skeleton of lithium triborate. Consequently, we can state that the emergence of ionic transport at $T >$ 400 K is preceded by an enhancement of anharmonism of the lithium sublattice in the crystallographic direction ⟨001⟩. In order to explain the phenomenon observed, we should analyze the structure of LBO in more detail. For this purpose, we use the crystallographic approach [8], which makes it possible to single out a set of noncentrosymmetric invariants describing the deviation of the crystal from central symmetry.

In our opinion, the LBO structure can be presented as a combination of A- and B-type mesotetrahedra formed by the PO_4 group and Li atoms, whose probable position is displaced towards an apex of the mesotetrahedra (Fig. 4a). Such an asymmetric position of lithium atoms is determined by local crystal fields, whose effect decreases upon heating, and mesotetrahedra gradually become equivalent.

According to the results of structural studies [4], the tetrahedra in question are strongly deformed and their local symmetry corresponds to the *I* group. In the packing in the LBO structure, mesotetrahedra (for example, of type A) must possess a dipole moment D_A in the direction coinciding with the symmetry axis (Fig. 4b). It can easily be verified that the dipole moment of the next mesotetrahedron has the opposite orientation and $D_A \neq D_B$ in accordance with the symmetry conditions. Thus, infinitely long chains extended along the polar direction are formed and each of them has translational symmetry along the axis. The mesotetrahedra form two sublattices, each of which possesses a spontaneous dipole moment. These moments only determine the spontaneous polarization P_S(A) and P_S(B) of the sublattices. It can easily be proved that their invariance is preserved only if they are oriented along the 2_1 axis and differ not only in magnitude but also in sign. In this case, their difference is equal to the spontaneous polar-

Spontaneous polarizations for some Li-based compounds

Compound	P_S, C/m^2
LiB_3O_5	0.27
$LiTaO_3$ [10]	0.50
$LiIO_3$ [11]	1.5

ization P_S, which can be estimated experimentally in the case of ferroelectrics.

It is well known [9] that direct measurements of the spontaneous polarization in linear pyroelectrics are very difficult and that experiments provide information only on the temperature variation of P_S. If, however, information on the pyroelectric coefficient, birefringence Δn [8], and the temperature variation of Δn (i.e., $\partial\Delta n/\partial T$) is available, we can estimate P_S as [8]

$$P_S \cong (2\Delta n\gamma)/(\partial\Delta n/\partial T).$$

All the initial data and the results of calculations are compiled in the table. It is beyond doubt that the spontaneous polarization of this type of lithium compounds is much higher than in other compounds, including ferroelectrics. In our opinion, this fact should be attributed to the high anharmonicity of the Li–BO_4, Li–IO_3, and Li–TaO_3 groups constituting the mesotetrahedra of these compounds (see, for example, [12]). In turn, the purely crystallographic packing sequences of mesotetrahedra in general and in lithium compounds in particular can differ considerably. For example, the apexes of the mesotetrahedra in LiO_3 and $LiTaO_3$ single crystals, whose local symmetry corresponds to point group *3m*, are aligned along the highest symmetry axis of the point symmetry group of the crystal. It follows from Fig. 4c that a different situation is observed for LBO: the apexes of mesotetrahedra are oriented along irrational directions. This packing is not exceptional and is observed, for example, in crystals of the KH_2PO_4 type. Thus, it is clear why the spontaneous polarization and, hence, the pyroelectric coefficient are largest in trigonal crystals (see table).

ACKNOWLEDGMENTS

The authors are grateful to A.M. Yurkin for providing an LBO singe crystal for the experiments.

REFERENCES

1. Shujic Lin, Zhaogang Sun, Bochang Wu, and Chuahgtian Chen, J. Appl. Phys. **67** (2), 634 (1990).
2. V. G. Dmitriev, G. G. Gurzadyan, and D. N. Kogosyan, *Handbook of Nonlinear Optical Crystals* (Springer-Verlag, New York, 1994), Vol. 64.
3. S. F. Radaev, N. I. Sorokin, and V. I. Simonov, Fiz. Tverd. Tela (Leningrad) **33** (12), 3597 (1991) [Sov. Phys. Solid State **33**, 2024 (1991)].
4. H. Konig and R. Hoppe, Z. Anorg. Allg. Chem. **139**, 71 (1978).
5. V. DiDomenico and S. Wemple, J. Appl. Phys. **40** (1), 720 (1969).
6. Lin Wei, Dai Guinging, Huang Qingzxhan, *et al.*, J. Phys. D **23**, 1073 (1990).
7. W. G. Cady, *Piezoelectricity* (McGraw-Hill, New York, 1946; Inostrannaya Literatura, Moscow, 1949), p. 817.
8. Yu. V. Shaldin, Fiz. Tverd. Tela (Leningrad) **19** (6), 1580 (1977) [Sov. Phys. Solid State **19**, 922 (1977)].
9. I. S. Zheludev, *Fundamentals of Ferroelectricity* (Atomizdat, Moscow, 1973), p. 465.
10. A. Glass, Phys. Rev. **172** (1), 565 (1968).
11. R. Poprawski, Yu. Shaldin, and S. Matyjasik, Phys. Status Solidi A **90**, 167 (1985).
12. Yu. V. Shaldin, Opt. Spektrosk. **72** (4), 913 (1992) [Opt. Spectrosc. **72**, 492 (1992)].

Translated by N. Wadhwa

Physics of the Solid State, Vol. 43, No. 8, 2001, pp. 1468–1475. Translated from Fizika Tverdogo Tela, Vol. 43, No. 8, 2001, pp. 1409–1415.

SEMICONDUCTORS AND DIELECTRICS

Anomalies of Elastic Properties of Layered Materials

L. A. Kulakova

Ioffe Physicotechnical Institute, Russian Academy of Sciences, Politekhnicheskaya ul. 26, St. Petersburg, 194021 Russia
e-mail: L.Kulakova@shuvpop.ioffe.rssi.ru

Received January 25, 2001

Abstract—Acoustic investigations of layered crystals $KY(MoO_4)_2$ and glassy alloys $Si_{20}Te_{80}$ (with inclusions of nanocrystallites) are performed with the purpose of elucidating the character of binding forces in layered materials. The absorption and velocity of sound, as well as the spatial evolution of the spectrum of acoustic fluxes in various directions in wide ranges of temperatures (90–300 K), frequencies (14–1800 MHz), and intensities (0.04–100 W/cm^2) of sound, are measured. Acoustooptical and pulse-echo methods were used for the measurements. A theoretical analysis of the data obtained has revealed anomalously large values of the nonlinear elastic coefficients and anharmonicity constants of longitudinal phonon modes that are determined by the anharmonicity of binding forces across the layers and at boundaries with nanocrystallites. It is shown that the anisotropy of the mechanical strength of layered crystals is to a large extent determined by the anharmonicity of binding forces. *© 2001 MAIK "Nauka/Interperiodica".*

1. INTRODUCTION

The investigation of physical properties of layered materials is of as a great importance now as ever. Most suitable natural objects for such investigations are layered crystals possessing a strongly pronounced anisotropy of mechanical strength. The presence of anisotropy manifests itself in thermal, optical, and other properties of these crystals [1] so vividly that one is permitted to speak of a two-dimensional character of physical phenomena in these crystals.

When studying the influence of mechanical anisotropy on the photoelastic effect in layered crystals of GaSe [2] and $KY(MoO_4)_2$, a high anisotropy of photoelasticity was revealed [3]: the corresponding photoelastic moduli differed by about an order of magnitude. On the other hand, the authors of [2] showed that the layered structure of GaSe crystals led to a two-dimensionalization of the exciton wave function.

The problem of the character of binding forces that determine the specific properties of layered crystals has not yet been completely solved. The previous investigations of elastic properties of such crystals [4, 5] showed that the significant anisotropy of mechanical strength does not lead to equally strong anisotropy of linear binding forces. Thus, the ratios of second-order elastic moduli [6] (that are determined by the binding forces) along and perpendicular to layers in layered crystals differ only slightly from the ratio of the corresponding moduli in crystals that do not possess mechanical strength anisotropy. For example, $C_{11}/C_{33} \approx 3$ for clearly pronounced layered GaSe crystals [4] and $C_{33}/C_{11} \approx 2.3$ for Te crystals. This suggests that a decrease in the binding forces is not the main cause of the significant decrease in mechanical strength in the corresponding directions of layered crystals.

Naturally, a question arises as to how the ways in which the nonlinear elastic properties, which are determined by the anharmonicity of binding forces and, in turn, determine the magnitudes of the third-order elastic moduli [6], change in layered crystals. In view of the experimental difficulties related to the difficulty of growing crystals of high quality and sufficiently large dimensions, as well as to some difficulties of methodical character, only a restricted number of works are available at present that are devoted to investigation of the anharmonicity of binding forces in layered crystals [5, 7, 8]. To calculate the Grüneisen constant γ [9] that characterizes the anharmonicity of binding forces, changes in the ultrasound velocity or shifts of Raman scattering lines under the effect of hydrostatic pressure were used in the above works. The calculations based on such measurements yield values of an order of 1 to 10 for γ of longitudinal phonon modes propagating across the layers. However, in view of the existence of surface inhomogeneities characteristic of layered crystals due to the splitting of layers in the course of the preparation of crystals, the method with the use of hydrostatic pressure can give noticeable errors. As to the investigations of elastic nonlinearities in layered crystals by the direct measurements of the spatial generation of higher harmonics of a corresponding ultrasonic wave, no such works have been performed as yet.

This work is devoted to the investigation of the anharmonicity of binding forces in layered materials by the acoustooptical method, which permits one to follow in detail the spatial evolution of the spectrum of an ultrasonic wave introduced from outside and, consequently, to measure (to a sufficient accuracy) nonlinear elastic coefficients and to obtain the anharmonicity constants of the corresponding phonon modes. As the object of investigation, we used not only layered crys-

1063-7834/01/4308-1468$21.00

tals but also an isotropic alloy containing nanocrystallites as inclusions. The investigation performed showed that the nonlinear elastic properties at the boundaries of such crystallites exhibit some features that are characteristic of layered crystals.

2. EXPERIMENTAL TECHNIQUE

For the investigations, we used layered crystals of $KY(MoO_4)_2$. They possess high optical transparency, uniform optical properties, and acoustooptical efficiency [3] in the visible range and are excellent objects for studying nonlinear acoustic properties by the acoustooptical method. The crystals have a rhombohedral symmetry (D_{2h}) and exhibit perfect cleavage on planes *XZ* and less perfect cleavage on planes *XY* [10].

We used single crystals prepared in the Institute of Inorganic Chemistry, Siberian Division, Russian Academy of Sciences. Optically uniform crystals $4 \times 4 \times 10$ mm in dimensions were oriented along crystallographic axes. The faces perpendicular to the layers were subjected to fine polishing; those parallel to the layers were prepared by cleaving in such a way as to remove the damaged surface layer.

The glassy isotropic alloy $Si_{20}Te_{80}$ with inclusions of tellurium nanocrystallites turned out to be an interesting model object, in which the role of layers was played by crystallite boundaries. The $Si_{20}Te_{80}$ glasses were obtained by B.T. Melekh in the Ioffe Physicotechnical Institute, Russian Academy of Sciences. The alloys were quenched in icy water or in air. The x-ray diffraction analysis [11] showed that these quenching modes yielded an amorphous alloy and an alloy containing nanocrystallites of Te (about 100 Å in size), respectively. Samples $4 \times 4 \times 6$ mm in size were prepared by cutting (with cooling) and subsequent fine grinding and optical polishing.

In acoustooptical measurements, the method of Bragg diffraction of light on an acoustic wave was used. The light source was an He–Ne laser ($\lambda = 0.63$ μm for $KY(MoO_4)_2$ and $\lambda = 3.39$ μm for $Si_{20}Te_{80}$).

As photodetectors, a FÉU-62 photomultiplier ($\lambda = 0.63$ μm) and an InSb-based photodiode cooled with liquid nitrogen ($\lambda = 3.39$ μm) were used.

The ultrasound was excited by resonance piezoelectric transducers made of lithium niobate and a piezoelectric ceramic; they were glued to a corresponding face of a sample using a Nonaq Stopcock. Both fundamental frequencies of the transducers ($f = 30$ and 14 MHz) and higher harmonics were used.

Data on the sound velocity were obtained using the ultrasonic pulse-echo-overlap technique [12]. The accuracy of relative measurements was about 0.01% in this case.

RESULTS AND DISCUSSION

It was revealed upon investigation of the acoustic properties of $KY(MoO_4)_2$ crystals [3] that, as in GaSe crystals, the anisotropy of the binding forces ($C_{11}/C_{22} \approx 10/3$) in them differs only a little from that of conventional crystals. Note also the relatively small magnitude of absorption for all types of waves (Fig. 1). This is especially surprising for both longitudinal and shear waves propagating along the *Y* axis (perpendicular to the plane of basic layers). Because of the low interlayer mechanical strength, one could expect a greater viscosity and, consequently, absorption of elastic waves in these crystals. However, the absorption of sound waves exhibits no anomalies; both qualitatively and quantitatively it corresponds to the Akhiezer's absorption [13] $\alpha^{anh} \sim f^2\bar{\gamma}^2$, which is determined by the interaction of sound with thermal phonons.

Let us dwell in more detail on the results of the investigation of absorption of the longitudinal sound propagating perpendicular to the layers. Data on the absorption for this wave (Fig. 1) were obtained under conditions of very small sound intensity ($P < 0.1$ W/cm^2). With increasing intensity, the absorption begins to grow; a sharp dependence of the absorption coefficient on the sound intensity is seen to occur (Fig. 2) and higher harmonics appear and grow in the spectrum of the acoustic flow (Fig. 3). The picture of the spatial evolution of the spectrum of the acoustic flux is given for a lower frequency ($f_1 = 390$ MHz), since with decreasing frequency, a greater number of harmonics can be observed due to the recording of a greater number of diffraction orders. It is obvious that, with increasing sound inten-

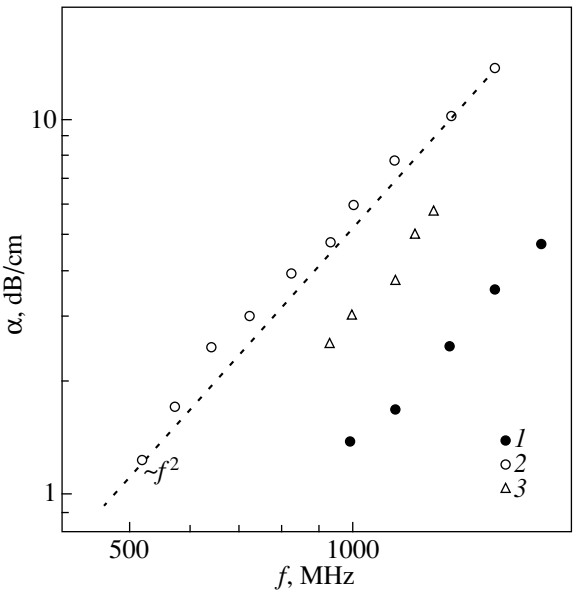

Fig. 1. Frequency dependences of linear absorption coefficients: (*1*), (*2*) longitudinal waves in the *X* and *Y* directions, respectively; (*3*) transverse wave propagating along the *Y* direction and polarized along the *X* axis.

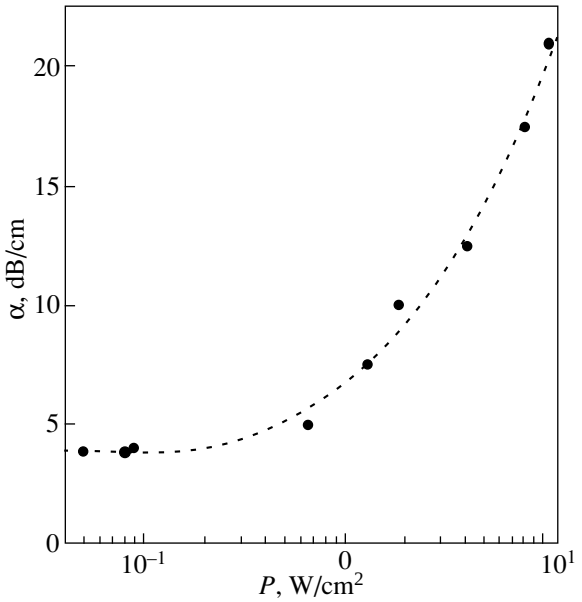

Fig. 2. Variation of the absorption coefficient as a function of the sound intensity for a longitudinal wave propagating perpendicular to the layers (along the *Y* axis). f = 800 MHz.

sity, the absorption coefficient to be measured is determined not only by the lattice absorption of sound at the frequency of the introduced signal but also by the energy transfer into higher harmonics. All this indicates the substantially nonlinear regime of propagating this type of wave. At the same time, upon the propagation of longitudinal waves along the *Z* and *X* axes (Fig. 4) at higher intensities of the fundamental wave, only a second-harmonic generation can be observed. The sharp anisotropy of the anharmonicity of binding forces is shown most vividly in Fig. 5, where the intensities P_k of the fundamental components of longitudinal waves propagating along the crystallographic axes at which the generation of only second harmonic is observed (regime of weak nonlinearity) are compared. The P_k values were obtained from the acoustooptical data on the intensities of diffracted light I_k using the known relationship $I_k = 1/2 I_0 M_2 P_k (\pi d/(\lambda \cos\theta_i^k))^2$ (where I_0 is the intensity of light transmitted directly through the sample, d is the width of the acoustic beam, θ_i^k is the optimum Bragg angle of incidence for the corresponding kth component, and M_2 is the acoustooptical Q-factor) and values of M_2 (see table). It is seen from Fig. 5 that the second harmonic grows to a noticeable level in the direction of the *Y* axis (perpendicular to the basic layers) already at a sound intensity $P_1^Y \approx 4$ W/cm², whereas along the layer, the growth of the second harmonic is only revealed when the intensity increases by more than an order of magnitude ($P_1^X \approx 100$ W/cm²).

The data shown in Fig. 5, which were obtained under conditions of weak nonlinearity (when the displacement amplitude u_1 of the component of the fundamental frequency still does not change because of the energy transfer into higher harmonics) were used to

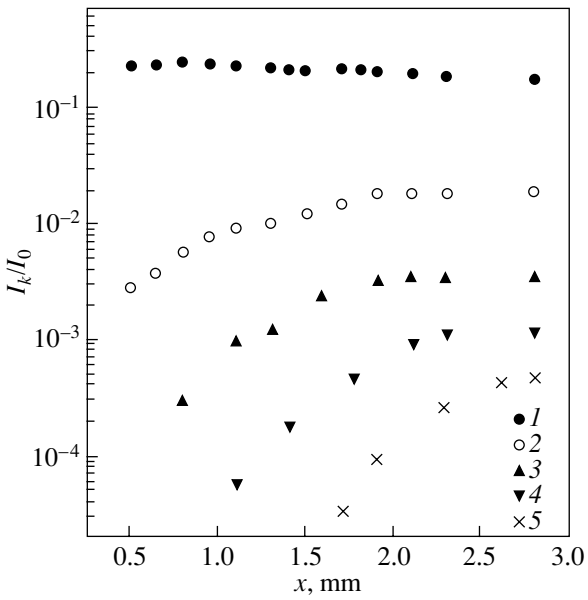

Fig. 3. Spatial evolution of the spectrum of an acoustic flux propagating perpendicular to the layers (along the *Y* axis): (*1*)–(*5*) corresponding harmonics. f_1 = 390 MHz.

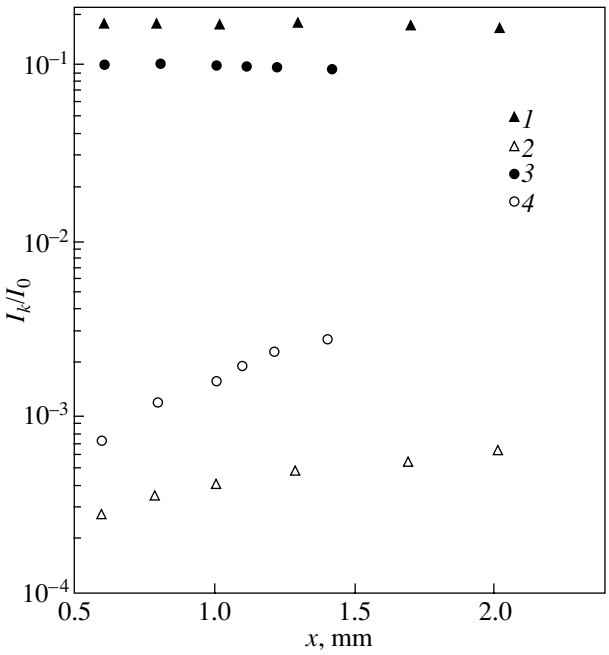

Fig. 4. Spatial evolution of the spectrum of acoustic flows propagating along the basic layers: (*1*), (*2*) along the *X* axis; (*3*), (*4*) along the *Z* axis; (*1*), (*3*) the fundamental components; and (*2*), (*4*) second harmonics. f_1 = 390 MHz.

Elastic parameters of layered crystals $KY(MoO_4)_2$, alloy $Si_{20}Te_{80}$, and some other crystals

Material	i	M_2, 10^{-18} s^3 g^{-1}	v_i, 10^5 cm s^{-1}	Γ_i	γ_l^i	$\bar{\gamma}$	C_{ii}, 10^{12} dyn cm^{-2}	C_{iii}, 10^{12} dyn cm^{-2}
$KY(MoO_4)_2$	1	0.5 [3]	5.08	4	2		1.006	–7
	2	21 [3]	2.87	40	20	1.3	0.321	–13.8
	3	1.93 [3]	3.6	9	4.5		0.505	–5.5
$Si_{20}Te_{80}$, amorphous	1	2800	2.03	3	1.5	1.4	0.027	–1.4
$Si_{20}Te_{80}$, with crystallites	1	2800	2.03	30	15	1.4	0.207	–6.8
$LiNbO_3$ [14]	1		6.57	8.1	4.05		2.002	–22
$PbMoO_4$ [14]	3		3.7	13	6.5		0.8	–13

calculate the nonlinear elastic coefficient Γ for all three crystallographic directions. In this case, with allowance for sound attenuation determined by the linear acoustic absorption of the material, the displacement amplitude of the second harmonic u_2 is described by the following expression [15]:

$$u_2 = \Gamma k_1^2 u_1^2 [\exp(-2\alpha_1 x) - \exp(-\alpha_2 x)]/8(\alpha_2 - 2\alpha_1), \quad (1)$$

where x is the distance along the sample in which the growth of the second harmonic is measured; $k_1 = 2\pi f_1/v$; v is the sound velocity; and α_1 and α_2 are the amplitude coefficients of sound absorption at the frequency of the fundamental component and second harmonic, respectively. Taking into account the smallness of absorption in $KY(MoO_4)_2$ crystals, we obtain from Eq. (1)

$$u_2 = \Gamma k_1^2 u_1^2 x/8. \quad (2)$$

When processing the data shown in Fig. 5, we used for calculating Γ the change $\Delta u_2 = u_2(x) - u_2(x_0)$ in a distance $\Delta x = x - x_0$ (where x_0 is the point nearest to the edge of the sample, which is taken as the origin for counting along x) rather than the value of u_2 itself. This was done to eliminate possible nonlinear contributions that can arise because of some anharmonicity of the input signal. This procedure is correct if these contributions are sufficiently small, such that they cannot influence the fundamental component.

The calculation based on Eq. (2) using data of Fig. 5 (with $f_1 = 390$ MHz and values of v given in the table) yields an anomalously large value $\Gamma_Y = 40$ for the direction perpendicular to the basic layers. Such a value of the nonlinear coefficient was not observed, according to [14], in any of the known materials. For comparison, the table also lists the values of Γ for crystals that possess the greatest elastic nonlinearity [14]. A value that is smaller by an order of magnitude was obtained for the nonlinear coefficient ($\Gamma_X \approx 4$) for the direction of the perfect cleavage; in the Z direction, an intermediate value was determined ($\Gamma_Z \approx 9$).

It is known [9, p. 313; 16] that, for longitudinal waves that propagate along the crystallographic axes, we have $\Gamma_i = -(3 + C_{iii}/C_{ii})$, $\gamma_l^i = \Gamma_i/2$. Using these relationships in combination with the values of Γ_i obtained above and the second-order elastic moduli C_{ii} given in the table, we can calculate the third-order elastic moduli C_{iii} and the Grüneisen constants γ_l^i of the corresponding longitudinal phonon modes. As follows from the results of these calculations (see table), the anharmonicity constants γ_l^2 of the longitudinal phonon modes propagating across the layer are one order of magnitude larger than the γ_l^1 constants responsible for the anharmonicity of the intralayer longitudinal modes.

As was indicated above, the linear absorption of sound waves both qualitatively and quantitatively corresponds to the Akhiezer's absorption, which is determined by the interaction of sound with thermal

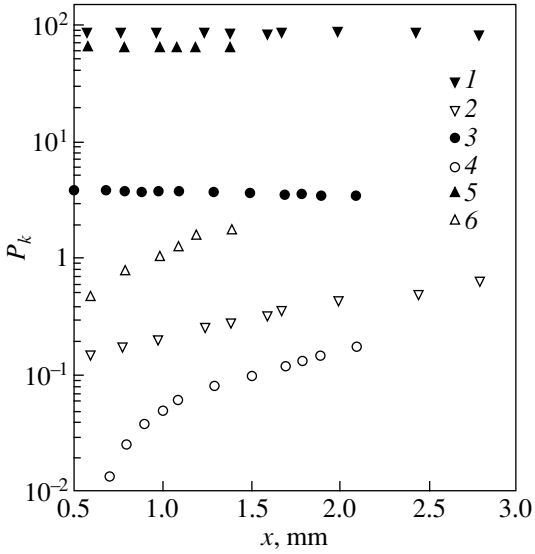

Fig. 5. Second-harmonic generation along the crystallographic axes under the condition of weak nonlinearity: (*1*), (*2*) along the *X* axis; (*3*), (*4*) along the *Y* axis; (*5*), (*6*) along the *Z* axis; (*1*), (*3*), (*5*) fundamental components; and (*2*), (*4*), (*6*) second harmonics.

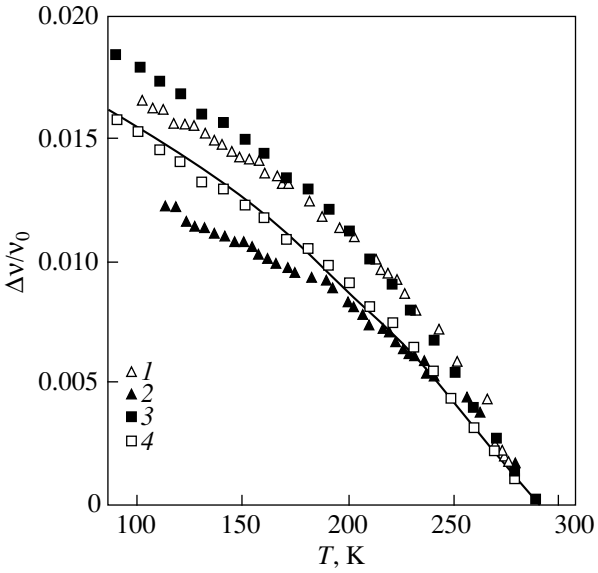

Fig. 6. Temperature dependence of the sound velocity: (*1*), (*2*) transverse waves propagating along the *X* axis and polarized along the *Y* and *Z* axes, respectively; (*3*) longitudinal wave propagating along the *Y* axis; (*4*) change in the velocity of longitudinal sound in the direction perpendicular to the layers due to the temperature dependence of the second-order elastic moduli. The solid line is the calculation according to Eq. (3).

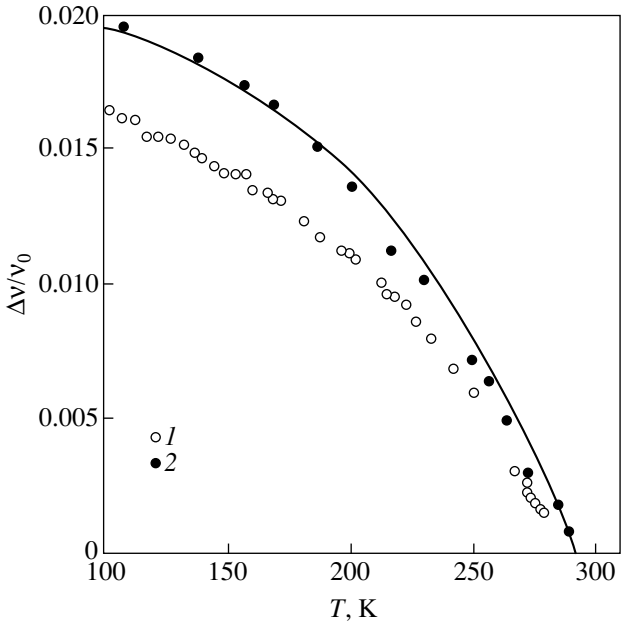

Fig. 7. Temperature dependences of the velocity of transverse waves (with identical deformations): (*1*), (*2*) propagating along the *X* and *Y* axes and polarized along the *Y* and *X* axes, respectively. The solid line is the result of summation of $\Delta v/v_0$ for S_{12} and of the contribution of the thermal linear expansion in the direction perpendicular to the layers.

phonons. On the other hand, it exhibits no anomalously large anharmonicity of interlayer binding forces that was revealed in our work; the absorption coefficients of the corresponding longitudinal and transverse waves have values that are characteristic of crystals with small lattice absorption.

In order to clarify the possible influence of the anharmonicity of interlayer binding forces on the sound velocity *v*, we measured temperature dependences of $\Delta v/v = (v(T) - v(T_0))/vT_0$, where $T_0 = 292$ K (Fig. 6). Both for the transverse and longitudinal waves, these dependences in the crystals studied have a rather traditional appearance. Note, however, a somewhat steeper (than in the case of transverse waves) dependence for longitudinal waves that propagate perpendicular to the layers.

Usually, the contribution of linear expansion of crystals to the change (to be measured) in time for which sound propagates through the sample due to the change in its length with temperature is negligible in comparison with the change in the sound velocity caused by the temperature dependence of second-order elastic moduli. In our case, this rule can be violated because of the anomalously large anharmonicity of the interlayer binding forces. Indeed, the above-measured $\Delta v(T)/v$ dependences (Fig. 7) for transverse waves with identical deformation ($S_{12} = S_{21}$) but different directions of propagation, i.e., along the layers (*X* direction, S_{12}) and perpendicular to the layers (*Y* direction, S_{21}), distinctly reveal an additional contribution to $\Delta v(T)/v$ for S_{21}, which can be reasonably ascribed to the difference in the linear expansion in the directions perpendicular and parallel to the layers.

Let us estimate the magnitude of this contribution. Because of the linear expansion, the quantity $(\Delta v(T)/v)_L$ is numerically equal to the relative change in length of the sample $\Delta L(T)/L_0$ upon cooling; taking into account that the linear thermal expansion coefficient α_L changes with temperature in the same manner as the heat capacity C_p [9], we can write $(\Delta v(T)/v)_L = \alpha_L \Delta T = \alpha_L(T_0)(T/T_0)^n(T_0 - T)$. Summing this contribution with the quantity $\Delta v(T)/v$ for S_{12} and performing a necessary fitting, we obtain good agreement (solid curve in Fig. 7) with experimental data for $\Delta v(T)/v$ for S_{21} at $n = 0.7$ and $\alpha_L(T_0) = 3 \times 10^{-5}$ ($I_0 = 292$ K). If we make the natural assumption that $\alpha_L^X \ll \alpha_L^Y$, then it follows from the above estimates that, first, $\alpha_L^Y = 3 \times 10^{-5}$ at room temperature and, second, that $C_p \sim T^{0.7}$ in the crystals studied. It is obvious that the contribution $(\Delta v(T)/v)_L$ is the same for longitudinal and transverse waves propagating in the same direction. Therefore, subtracting the thus-calculated quantity $(\Delta v(T)/v)_L$ from the $\Delta v(T)/v$ for longitudinal waves (curve *3* in Fig. 6), we obtain the temperature change in the velocity of the longitudinal sound caused by the temperature dependence of the second-order elastic moduli due to the anharmonicity of the phonon modes (curve *4* in

Fig. 6). Since this change is determined by the known relationship [17]

$$\frac{(\Delta v)^{\text{anh}}}{v(T_0)} = \frac{\bar{\gamma}^2}{3v^2(T_0)}[T_0 C_p(T_0) - TC_p(T)], \qquad (3)$$

we can estimate the averaged Grüneisen constant $\bar{\gamma}$ of the phonon modes that interact with the sound wave. Using Eq. (3) for fitting with $C_p \sim T^{0.7}$ (as follows from our estimates of thermal expansion), $C_p(T_0) = 0.177$ cal/(g K), as in GaSe crystals, and, under the assumption that $\bar{\gamma}$ is temperature independent, we obtain a sufficiently traditional value (typical of majority of materials) $\bar{\gamma} \approx 1.3$. Thus, the large anharmonicity of the binding forces in the directions transverse to the layers exerts no substantial effect on the averaged anharmonicity constant; this explains the small magnitude of sound absorption, which is determined [17] by the same parameter $\bar{\gamma}$.

The investigations of the acoustic properties of $Si_{20}Te_{80}$ alloys with various degrees of structural perfection showed that the appearance of crystallites in the glass network does not change the absorption (Fig. 8), sound velocity, or acoustooptical Q-factor (which has a record value among the materials for IR engineering) within the measurement error (see table). Regarding the nonlinear properties, the situation is quite different.

In order to study the influence of structural changes that occur in $Si_{20}Te_{80}$ glasses on the anharmonicity of binding forces, we performed measurements of the spatial evolution (along the direction of propagation of the longitudinal sound wave) of the spectrum of acoustic flux in amorphous samples and in samples containing nanocrystalline inclusions. It is seen from the results of these measurements (Fig. 9) that in the samples with nanocrystallites, there occurs a significant spatial growth of the second harmonic (curves *4*, *6*), which indicates the existence of a significant elastic nonlinearity. Nothing similar is observed in amorphous samples (Fig. 9): as the intensity of sound of the fundamental frequency increases at the input (curve *1*), the intensity of the second harmonic (curve *2*) first remains almost unaltered, then a weak falloff is observed. Such a behavior is explained by a very insignificant growth of the second harmonic, which is compensated by the linear absorption of sound at the frequency of the second harmonic. Using these data, we can calculate the nonlinear elastic coefficient Γ. Taking into account that the acoustic absorption linearly changes with frequency (Fig. 8), to estimate Γ with a sufficient accuracy, we can use the following approximation that results from Eq. (1) under the condition $(\alpha_1 x)^2 \ll 1$:

$$u_2 = \Gamma k_1^2 u_1^2 x(1 - 2\alpha_1 x + 2\alpha_1^2 x^2)/8. \qquad (4)$$

When processing the data shown in Fig. 9 for calculating Γ, we used the above-given relationships between P_k and u_k and, as before, the change in u_2 ($\Delta u_2 = u_2(x) - u_2(x_0)$) within a distance $\Delta x = x - x_0$ rather than the quantity u_2 itself.

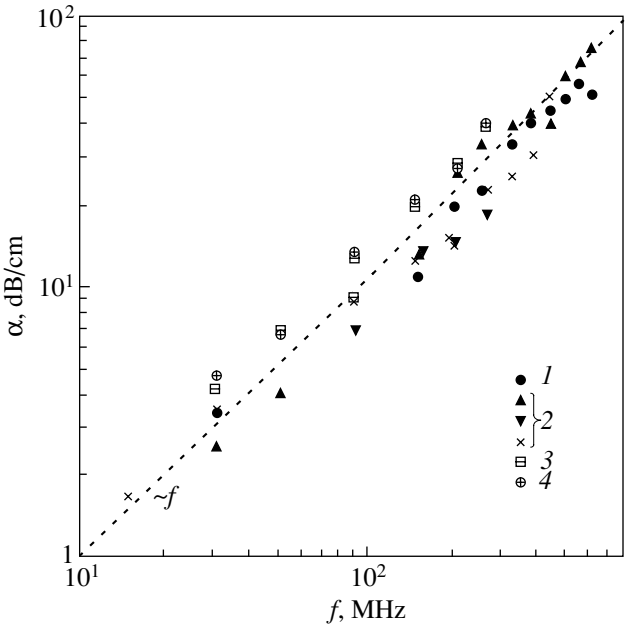

Fig. 8. Frequency dependences of the absorption coefficients of (*1*), (*2*) longitudinal and (*3*), (*4*) transverse sound: (*1*), (*3*) amorphous samples and (*2*), (*4*) samples with nanocrystallites.

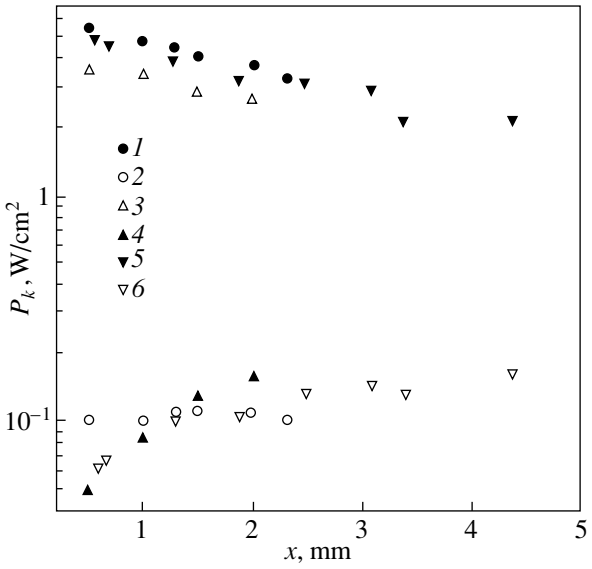

Fig. 9. Changes in the intensities of the components of (*1*), (*3*), (*5*) the fundamental frequency P_1 and (*2*), (*4*), (*6*) of the second harmonic P_2 depending on the distance from the input transducer: (*1*), (*2*) amorphous samples and (*3*)–(*6*) sample with nanocrystallites.

The calculation performed on the basis of Eq. (4) using the data of Fig. 9 with $f_1 = 90$ MHz, $d = 2$ mm, $\alpha_1 = 10$ dB/cm, and $(M_2)_{12} = 2800 \times 10^{-18}$ s^3 g^{-1} (our data for the light polarization perpendicular to the

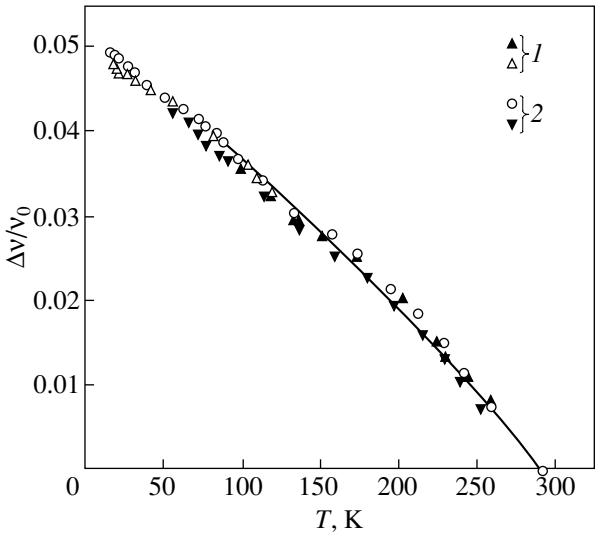

Fig. 10. Temperature dependence of the velocity of longitudinal sound (f = 14 MHz) in the $Si_{20}Te_{80}$ alloy: (*1*) amorphous samples; (*2*) samples with nanocrystallites. The solid line is the calculated dependence of the contribution of phonon modes.

sound wave vector) yields a traditional value of $\Gamma \approx 3$ for the amorphous samples and an anomalously large value $\Gamma \approx 30$ for the glasses with nanocrystallites. This yields $\gamma_l^n \approx 15$ for nanocrystalline samples and $\gamma_l^a = 1.4$ for amorphous samples.

The investigation of the temperature dependences of the sound velocity in $Si_{20}Te_{80}$ glasses showed that $\Delta v(T)/v$ (Fig. 10) both qualitatively and on the order of magnitude resembles the dependence characteristic of crystals, which is determined by the anharmonicity of thermal phonon modes. The appearance of crystallites does not change either the magnitude or shape of this dependence. Let us estimate $\bar{\gamma}$ from these data. Since, according to estimates based on our data on the linear thermal expansion coefficient for the alloy under consideration ($\alpha_L = 29 \times 10^{-6}$ K^{-1}), the contribution to the measured change in the sound velocity that is caused by the thermal expansion effect upon cooling is smaller by an order of magnitude than $\Delta v/v$, we neglect this contribution. A calculation according to Eq. (3) using the data on the temperature dependence of heat capacity $C_p(T)$ taken from [11] and under the assumption that $\bar{\gamma}$ is temperature-independent is displayed in the solid curve in Fig. 10. The averaged value of the Grüneisen constant obtained from this calculation is $\bar{\gamma} = 1.45$, which is characteristic of most crystals and glasses. Comparing these values of $\bar{\gamma}$ with the values given above for γ_l, we can state that $\gamma_l^a \approx \bar{\gamma} \approx 1.4$ is indeed a characteristic of anharmonicity of the phonon system and does not depend to a significant extent on the system of nanocrystallites under consideration. The large value of $\gamma_l^n \approx 15$ that was obtained in nanocrystalline samples is caused, in our opinion, by the anharmonicity of binding forces at the boundaries of nanocrystallites, which leads to the generation of the second harmonic of the sound wave but yields only an insignificant contribution to the averaged Grüneisen parameter. This result speaks in favor of the analogous character of binding forces at the boundaries of nanocrystallites in amorphous alloys and between layers in layered crystals.

4. CONCLUSION

Thus, the results of investigations performed in this work show that the sharp anisotropy of mechanical strength of layered crystals is a consequence of the anomalously high anharmonicity of binding forces acting between layers, which determines the anomalously large magnitude of the nonlinear elastic coefficient and the anharmonicity constant (Grüneisen constant) of the longitudinal phonon mode that propagates perpendicular to the layers.

Another consequence of the large anharmonicity of binding forces is a noticeable growth of the linear thermal expansion coefficient in the direction perpendicular to the layers.

Changes in the nonlinear elastic properties analogous to those occurring in layered crystals are also observed in the amorphous $Si_{20}Te_{80}$ alloy in the presence of fine crystallites in the glass network. The character of binding forces at glass–crystallite boundaries changes; the anharmonicity of the binding forces increases, which is reflect in the active generation of the second acoustic harmonic. This effect can be used for the diagnostics of the presence of crystallites in amorphous alloys.

The large value of the anharmonicity constant of the longitudinal phonon mode that propagates perpendicular to the layers does not substantially change the anharmonicity constant averaged over the ensemble of thermal phonons in either layered crystals or in the alloy with crystallites.

ACKNOWLEDGMENTS

This work was supported in part by the Russian Foundation for Basic Research, project nos. 95-02-04093-a and 98-02-18305. I am also grateful to A.A. Pavlov, who kindly supplied me with single crystals of $KY(MoO_4)_2$, to B.T. Melekh for the preparation of the $Si_{20}Te_{80}$ alloy, and to Yu.V. Ilisavskiĭ for fruitful discussions.

REFERENCES

1. G. L. Belen'kiĭ and V. B. Stopachinskiĭ, Usp. Fiz. Nauk **140** (2), 233 (1983) [Sov. Phys. Usp. **26**, 497 (1983)].
2. N. S. Averkiev, Yu. V. Ilisavskiĭ, and L. A. Kulakova, Fiz. Tverd. Tela (St. Petersburg) **38** (12), 3556 (1996) [Phys.

Solid State **38** (12), 1938 (1996)]; Fiz. Tverd. Tela (St. Petersburg) **38**, 3570 (1996) [Phys. Solid State **38**, 1945 (1996)].

3. L. A. Kulakova, Fiz. Tverd. Tela (St. Petersburg) **42** (1), 51 (2000) [Phys. Solid State **42**, 55 (2000)].
4. G. I. Abutalybov, Yu. V. Ilisavskiĭ, and V. L. Okulov, Fiz. Tverd. Tela (Leningrad) **28** (5), 1580 (1986) [Sov. Phys. Solid State **28**, 896 (1986)].
5. M. Gatulle and M. Fisher, Phys. Status Solidi B **121** (1), 59 (1984).
6. K. Brugger, Phys. Rev. **133**, A1611 (1964).
7. Yu. V. Ilisavskiĭ, V. L. Okulov, T. E. Svechnikova, and S. N. Chizhevskaya, Fiz. Tekh. Poluprovodn. (Leningrad) **20** (11), 2115 (1986) [Sov. Phys. Semicond. **20**, 1321 (1986)].
8. E. A. Vinogradov, G. N. Zhizhin, N. N. Mel'nik, *et al.*, Fiz. Tverd. Tela (Leningrad) **22** (3), 742 (1980) [Sov. Phys. Solid State **22**, 434 (1980)].
9. *Physical Acoustics: Principles and Methods*, Vol. 3, Part B: *Lattice Dynamics*, Ed. by W. P. Mason (Academic, New York, 1965; Mir, Moscow, 1968).
10. R. F. Klevtsov and S. V. Borisov, Dokl. Akad. Nauk SSSR **177** (6), 1333 (1967) [Sov. Phys. Dokl. **12**, 1095 (1968)].
11. L. A. Kulakova, B. T. Melekh, É. Z. Yakhkind, *et al.*, Fiz. Khim. Stekla **27**, 3 (2001).
12. E. Papadakis, J. Acoust. Soc. Am. **12** (5), 1045 (1967).
13. A. Akhiezer, Zh. Éksp. Teor. Fiz. **8**, 1318 (1938).
14. O. B. Gusev and V. V. Kludzin, *Acousto-Optical Changes* (Leningr. Gos. Univ., Leningrad, 1987), p. 52.
15. E. G. Lean and C. G. Powell, Appl. Phys. Lett. **19** (9), 356 (1971).
16. L. K. Zarembo and V. A. Krasil'nikov, Usp. Fiz. Nauk **102** (4), 549 (1970) [Sov. Phys. Usp. **13**, 778 (1970)].
17. Yu. V. Ilisavskiĭ, L. A. Kulakova, and V. V. Tikhonov, Fiz. Tverd. Tela (Leningrad) **31** (8), 153 (1989) [Sov. Phys. Solid State **31**, 1363 (1989)].

Translated by S. Gorin

Physics of the Solid State, Vol. 43, No. 8, 2001, pp. 1476–1477. Translated from Fizika Tverdogo Tela, Vol. 43, No. 8, 2001, pp. 1416–1417.

DEFECTS, DISLOCATIONS, AND PHYSICS OF STRENGTH

Effect of a Constant Magnetic Field and a Pulse Electric Current on the Mean Linear Density of Twinning Dislocations in Bismuth Crystals

A. I. Pinchook and S. D. Shavrey

Mozyr' State Pedagogical Institute, Mozyr', 247760 Belarus

e-mail: al.pinchook@tut.by

Received December 29, 2000

Abstract—Bismuth crystals are studied under the joint action of a pulse electric current and a constant magnetic field. It is shown that the combined effect of a constant magnetic field and pulse current leads to a substantial decrease in the mean linear density of twinning dislocations piled up at the boundaries of wedge twins. The decrease in the mean linear density of twinning dislocations is accompanied by a decrease in the microhardness of the samples. © *2001 MAIK "Nauka/Interperiodica".*

1. INTRODUCTION

The effect of external electric and magnetic fields on the plasticity and the strength of metals has been extensively studied over the last few decades. However, the physical mechanisms of these processes call for further investigations [1]. According to the concept proposed by Roshchupkin and Bataronov [2], electric current pulses and other external energy effects can play the role of an initiator of "discharging" dislocation pileups. In this case, a strain jump occurs at the expense of the energy of internal stresses accumulated in the course of the preliminary plastic deformation.

For experimental verification of this theory, it is necessary to consider the behavior of single dislocation pileups in the studied metal during its plastic deformation. This is dictated by the space–time inhomogeneity of plastic deformation [3]. Since twinning dislocations are piled up at the matrix–twin interfaces [4], the wedge twins that are formed upon pressing a diamond indenter into the (111) cleavage surface of bismuth crystals are convenient model objects.

In essence, the experiment is as follows. The authors revealed that, in the absence of external fields, the mean linear density of twinning dislocations ρ remains constant (within the limits of experimental error) with an increase in the indenter loading that brings about the twin growth. In the case when the joint effect of current pulses and constant magnetic field leads to a considerable jump in the strain and manifests itself as an initiator of discharging twinning dislocation pileups, the ρ value should decrease.

2. SAMPLE PREPARATION AND EXPERIMENTAL TECHNIQUE

We studied bismuth single crystals grown by the Bridgman technique from a chemically pure starting material. A smooth surface suitable to our investigations without being further treated was obtained by cleaving the bismuth single crystal along the (111) cleavage plane. The samples were prepared in the form of rectangular prisms $10 \times 5 \times 5$ mm in size. The microhardness measurements were carried out with a PMT-3 tester. For magnetic measurements, the studied sample was placed in a specially devised setup, which made it possible to exclude instrumental effects arising in response to a constant magnetic field applied to the sample. Particular attention was given to the rigidity of the elements used to mount the sample to the experimental setup and the rigidity of the setup itself.

The diamond indenter was pressed into the (111) cleavage surface of bismuth single crystals in a constant magnetic field. We examined the wedge twins belonging to the $\{110\}\langle001\rangle$ system. The vectors of load **P**, current density **j**, and magnetic induction **B** were oriented along the three mutually normal directions. The vectors **j** and **B** lay in the (111) cleavage plane. An electric current pulse with the duration $t_{imp} = 4 \times 10^{-4}$ s was passed through the sample after pressing (for 20 s) the diamond indenter into the (111) plane. The current pulse density was varied in the range $j_{imp} = 0$–70 A/mm^2. The induction B of the constant magnetic field in the sample was equal to 0.2 T. The load P on the indenter rod was constant ($P = 0.14$ N). The experimental error was no more than 3%.

The mean linear density of twinning dislocations at the twin–matrix interfaces was calculated by the for-

1063-7834/01/4308-1476$21.00

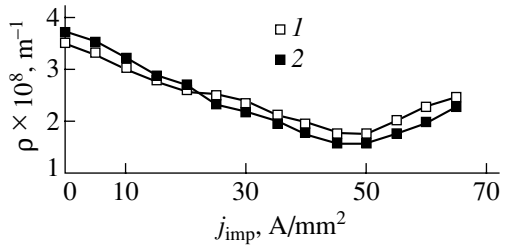

Fig. 1. Dependences of the mean linear density of twinning dislocations ρ on the pulse current density j_{imp} at $B = 0.2$ T and $P = 0.14$ N: (*1*) the positive charge induced by the Hall polarization of the sample on the (111) cleavage plane and (*2*) the negative charge on the same plane.

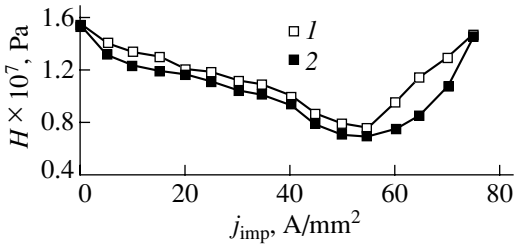

Fig. 2. Dependences of the microhardness H on the pulse current density j_{imp} at $B = 0.2$ T and $P = 0.14$ N. Curves *1* and *2* correspond to the same charges as in Fig. 1.

mula $\rho = h/La$, where a is the lattice parameter in the direction normal to the motion of twinning dislocations, h is the width of the wedge twin at the mouth, and L is the twin length. The experimental setup and the measurement technique were described in more detail in [5].

3. EXPERIMENTAL RESULTS

First, it should be noted that the strain jump and the change in ρ occur only under the joint action of the indenter load, constant magnetic field, and current pulses. The effect observed does not manifest itself in the absence of any one of these three factors. In this case, the strain jump implies an increase in the length and the width of wedge twins at their mouth [6–8].

Figure 1 shows the dependences of the mean linear density of twinning dislocations ρ on the pulse current density j_{imp}. It is seen from Fig. 1 that the ρ density substantially decreases (approximately by a factor of two) in response to external fields. Since the ratio L/h is the distance between twinning dislocations (in terms of interatomic distances) [4], it can be concluded from Fig. 1 that the mean distance between dislocations significantly increases and the repulsive forces between twinning dislocations of the same sign decrease. Within the energy approach, this experimental result implies that the growth of a twin lamella, i.e., the elongation of the wedge twin, occurs as a result of the decrease in energy of local elastic stress accumulated during preliminary plastic deformation.

A comparison of Figs. 1 and 2 demonstrates that the density ρ and the microhardness H are the mutually related parameters. A decrease in ρ is accompanied by an enhancement of twinning, which, in turn, can be one of the reasons for the decrease in H.

The electroplastic effect in bismuth crystals manifests itself when the pulse current density reaches the threshold value $j_{imp} = 50$ A/mm^2 [9]. This effect occurs with an increase in ρ and H. The physical mechanism of this phenomenon remains unclear.

REFERENCES

1. Yu. I. Golovin, Izv. Vyssh. Uchebn. Zaved., Chern. Metall., No. 8, 67 (1993).
2. A. M. Roshchupkin and I. L. Bataronov, Izv. Vyssh. Uchebn. Zaved., Fiz., No. 3, 57 (1996).
3. V. I. Likhtman, E. D. Shchukin, and P. A. Rebinder, *Physicochemical Mechanics of Metals* (Akad. Nauk SSSR, Moscow, 1962).
4. A. M. Kosevich and V. S. Boĭko, Usp. Fiz. Nauk **104** (2), 201 (1971) [Sov. Phys. Usp. **14**, 286 (1971)].
5. A. I. Pinchook and V. S. Savenko, J. Appl. Phys. **86** (5), 2479 (1999).
6. V. S. Savenko, A. I. Pinchook, V. V. Ponaryadov, and V. B. Zlotnik, Vestn. Beloruss. Univ., Ser. 1, No. 2, 27 (1995).
7. V. S. Savenko, A. I. Pinchook, V. B. Zlotnik, and S. D. Shavrey, Z. Metallkd., No. 7, 498 (1998).
8. A. I. Pinchook, V. S. Savenko, and S. D. Shavrey, Izv. Akad. Nauk, Ser. Fiz. **61** (5), 932 (1997).
9. V. S. Savenko, V. I. Spitsyn, and O. A. Troitskiĭ, Dokl. Akad. Nauk SSSR **283** (5), 1181 (1985) [Sov. Phys. Dokl. **30**, 716 (1985)].

Translated by N. Korovin

Physics of the Solid State, Vol. 43, No. 8, 2001, pp. 1478–1482. Translated from Fizika Tverdogo Tela, Vol. 43, No. 8, 2001, pp. 1418–1422.

DEFECTS, DISLOCATIONS, AND PHYSICS OF STRENGTH

Step Deformation of Solid Amorphous Polymers

N. N. Peschanskaya

Ioffe Physicotechnical Institute, Russian Academy of Sciences, Politekhnicheskaya ul. 26, St. Petersburg, 194021 Russia
e-mail: yak@pav.ioffe.rssi.ru

Received December 6, 2000; in final form, December 18, 2000

Abstract—The variation of step deformation kinetics in solids is studied as a function of morphological factors. Oscillations of creep rate at micrometer increments of the amount of deformation, which reflect the step nature of the process, are investigated from an interferogram. It is shown that the plasticization of polymethyl methacrylate by dibutyl phthalate blurs the steps, while their height varies insignificantly. The results are explained using the concept of the netlike structure of amorphous polymers. The data obtained confirm the universal nature of jumps as a mode of evolution of deformation in various solids. The jumps reflect the cooperative nature of motion of kinetic units, and the regular variation of the characteristics of the jumps lends support to the definition of creep as a process of structural self-organization. *© 2001 MAIK "Nauka/Interperiodica".*

1. INTRODUCTION

Step or jumplike deformation was discovered long ago, but it was initially regarded as a peculiar phenomenon or even as a methodological error. Subsequently, the formation of sharp localized shear bands in crystals and metals deformed at liquid-helium temperatures was studied in detail [1, 2]. Abrupt constrictions of samples subjected to extension (or swelling under compression), which are referred to as necks [3, 4], should also be attributed to jumplike processes. The above-mentioned localized deformations correspond to increments of millimeters or tenths of a millimeter in sample length and are observed in the form of stress drops on a stress–strain curve under active loading at a constant rate.

The concepts of structure and deformation levels and of structural levels of deformation [5], which are common for different bodies, are generally accepted in the literature. The main features of the structure and deformation of real bodies include heterogeneity, inhomogeneity, and localization. The localization of deformation reflects its jumplike evolution at various levels: generation and motion of dislocations (slip lines and bands) in crystals. Polymers (especially in the case of film extension) display silver cracks (shear lines and bands at an angle of 45° to the sample axis). In the theories describing the deformation of solids (including polymers), images of local defects in the form of dislocations and disclinations are also used [6]. In accordance with the prevailing ideas, creep in solids induced by a constant load is a process of structural self-organization, while macrodeformation is ensured by microdeformation of deeper levels. However, traditional methods that record creep level out the structural heterogeneity and the localization of deformation revealed by other methods and support the idea of a monotonic process with a smoothly varying rate studied as an average quantity characterizing random regions of the macrolevel deformation. This contradiction can be removed by improving the resolution of the method of rate measurement. The application of an interferometer in the material-creep recording circuit has made it possible to study the kinetics (rate) of the process on a scale of deformation increments as small as fractions of a micrometer (i.e., on a deeper, mesoscopic level of deformation and structure) and to reveal the nonmonotonic variation of rate (deformation jumps) as a common typical feature of the process [7–13].

The assumptions that jumplike deformation emerges due to strong and weak interactions between polymer molecules, which are overcome in deformation, and that the scale of jumps is determined by the size of ordered inhomogeneities typical of the given level were made in our first publication [8]. Correlations [8–10] and experiments on model polyethylene fibers and films [11–13] of the fibril structure confirm these assumptions. Since creep jumps are also typical of amorphous polymers, the presence of ordered structural inhomogeneities on the order of micrometers should be presumed for these materials. It is well known that information on the morphology of amorphous media is contradictory, but the concept of the netlike structure of amorphous polymers, which is formed by the physical nodes between segments of neighboring chains, can be regarded as generally accepted. The term physical nodes is applied at present not only to strong solitary (hydrogen or polar) interactions but also to regular stacking of parts of adjacent molecules that can be of fluctuation origin [14]. The overcoming of the resistance offered by nodes corresponds to a low velocity in a step, while the slip of molecules between the nodes corresponds to a higher velocity. In other words, we assume that the deformation step height is approximately equal to the separation between strong nodes.

1063-7834/01/4308-1478$21.00

The investigation of the relation between the characteristics of creep jumps and morphological parameters is at the initial stage, and the complexity of the problem is seen especially clearly as applied to amorphous polymers. For this reason, an analysis of the kinetics of small deformations in polymer materials with various chemical and supermolecular structures, as well as with various compositions, is essential to understanding the nature of cooperative jumplike deformation. One of the most effective methods of changing the deformation properties of polymers is plasticization, i.e., the introduction of molecules of low-molecular substances into a polymer. Plasticizer molecules normally increase the molecular mobility in a polymer, lower its glass-formation temperature, and improve the plasticity of the material.

In this work, we consider the effect of plasticization on the step deformation of polymethyl methacrylate.

2. SAMPLES AND EXPERIMENTAL TECHNIQUE

We studied creep during the compression of samples 2 mm in diameter and 6 mm in height made of both initial polymethyl methacrylate (PMMA) and that plasticized by dibutyl phthalate (DBP). The DBP content was approximately 30 wt %. Compression is preferable for the study of deformations because extension leads to the formation of classical cracks, thus complicating analysis of the step deformation.

During creep, deformation was recorded with the help of a laser interferometer [7], one mirror of which was rigidly fixed to a movable clamp and traced the sample deformation. The interferometric recording of the process in the form of beats (Fig. 1) makes it possible to carry out a more detailed analysis of the creep rate from the signal frequency. Each beat in Fig. 1 corresponds to a deformation increment of 0.3 μm. The relative strain rate is defined by the formula $\dot{\varepsilon} = \lambda\nu/2l_0$, where $\lambda = 0.63$ μm is the lasing wavelength, ν is the frequency of beats on the interferogram, and l_0 is the sample length.

The smallest strain increment that can be used for determining the strain rate with a fairly high accuracy (~1%) is equal to half the increment for a beat (0.15 μm), which amounts to 0.0025% for a sample length of 6 mm. Figure 1 shows an example of a periodic variation of the beat frequency, i.e., of the creep rate for PMMA. Since the periodicity of the strain rate is not always manifested as clearly, the strain-rate nonmonotonicity was usually investigated by measuring it on sequential increments of deformation of 0.3 μm within arbitrary intervals at various temporal stages of creep. The dependence of the strain rate for sequential increments of 0.3 μm was then plotted as a function of their number. This dependence demonstrated that the strain-rate spread is not accidental [8]. Oscillations of the strain rate near a mean value correspond to deformation jumps: the period L of oscillations is the height

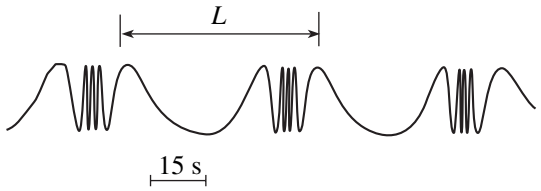

Fig. 1. Interferogram of jumplike creep in PMMA. One beat corresponds to a deformation increment of 0.3 μm; the strain rate is proportional to the beat frequency. The period of strain-rate variation corresponds to the height of a deformation jump (here, $L = 1.5$ μm), and the ratio of the maximum to the minimum strain rate within a period corresponds to the sharpness of the jump h.

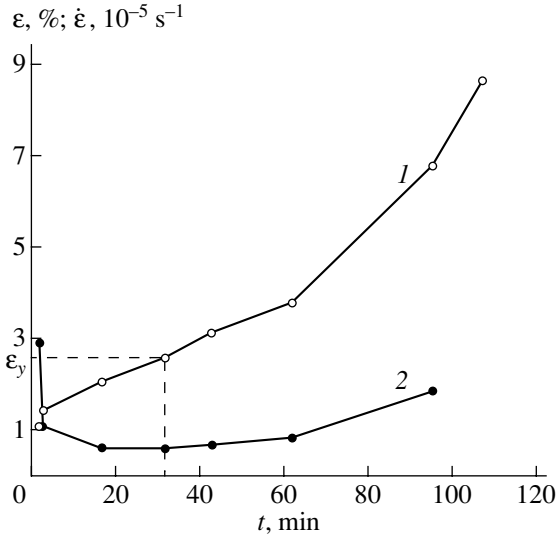

Fig. 2. Dependences of (*1*) the strain on time and (*2*) the average creep rate on strain for PMMA + DBP under a stress $\sigma = 13.3$ MPa. The minimum strain rate corresponds to a strain of 2.6%.

of a deformation step, and the ratio of the maximum to the minimum strain rate over the same oscillation period characterizes the sharpness of the deformation step $h = \dot{\varepsilon}_{max}/\dot{\varepsilon}_{min}$ [8–13]. The values of L and h are usually averaged over several strain-rate oscillations.

3. DISCUSSION OF RESULTS

Under the action of a constant stress, the strain ε first increases with a decreasing rate $\dot{\varepsilon}$ and, after assuming a certain value ε_y (yield point), the strain rate passes through a minimum and starts increasing (Fig. 2). Below ε_y, plastic shear occurs in local microscopic volumes which do not interact with one another and the macroscopic deformation is reversible in time. In the vicinity of ε_y, shear lines forming an angle of 45° with the sample axis appear and are responsible for strong macroscopic localization of the deformation in the form of a constriction in the case of extension and bulg-

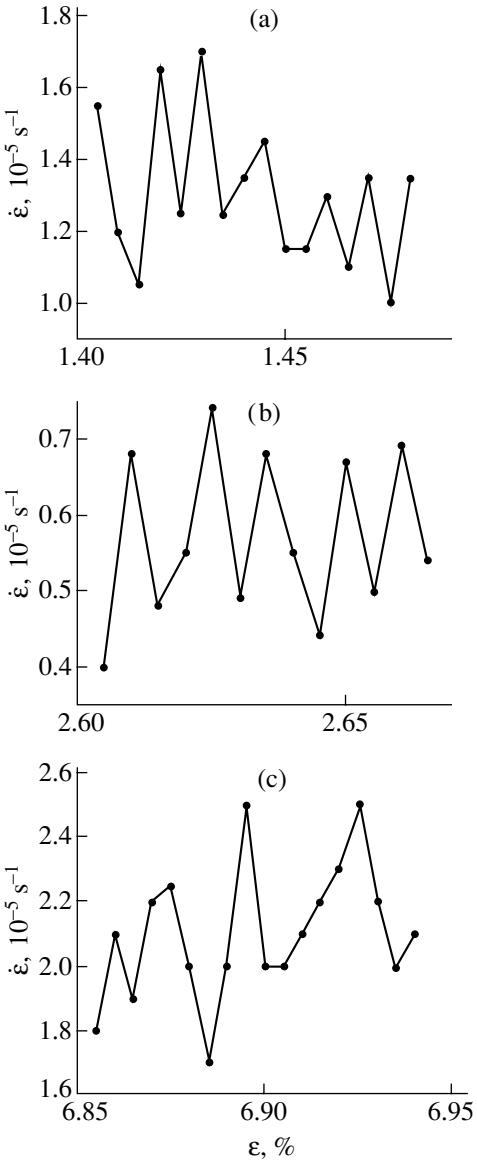

Fig. 3. Strain-rate variation with sequential deformation increments of 0.3 μm in different regions of the creep curve for PMMA + DBP under a stress σ = 13.3 MPa. Average jump parameters *L*, μm, and *h* are (a) 0.75 and 1.25; (b) 0.75, 1.6, and (c) 1.2 and 1.25, respectively.

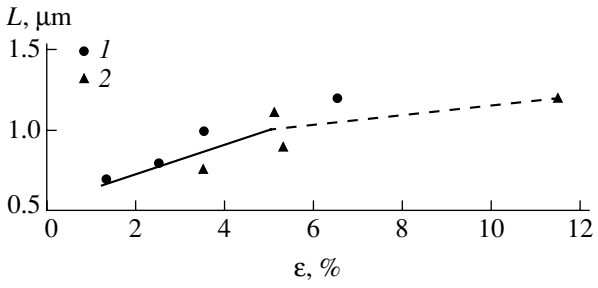

Fig. 4. Periods of strain-rate oscillations (*L*) at the initial creep stage for (*1*) PMMA + DBP and (*2*) PMMA; σ = (*1*) 13.3 and (*2*) 70 MPa.

ing or bending (macroscopic shear) of the sample during compression. Irreversible deformation and the rearrangement of the initial structure begin, and the boundaries of the localized deformation move along the sample length. The irreversible change in the sample shape corresponds to an increase in the strain rate and to the orientation of the polymer structure on various levels.

Micrometer-size deformation steps in amorphous polymers appear even at the first stage (below ε_y), and then sharper and larger jumps are formed, which sometimes have a more complex structure [8–13]. It is assumed that the parameters of jumps at the initial stage more clearly reflect the heterogeneity in the initial stacking of molecular chains. For this reason, the correlation between the structural and jump parameters was usually considered at the characteristic point ε_y of unstable equilibrium of the initial structure.

Let us analyze the change in the jump parameters near ε_y for PMMA with DBP and then compare the obtained results with the data for PMMA in a similar deformation region. Figure 2 shows an $\varepsilon(t)$ creep curve; its point of inflection can be determined most accurately from the $\dot{\varepsilon}(\varepsilon)$ dependence. It follows from Fig. 2 that the yield point of plasticized polymethyl methacrylate is approximately 2.6%, while pure polymethyl methacrylate at 20°C becomes plastic when the strain exceeds 10% [15]. It should be noted that the yield point ε_y depends on the creep rate (on stress) but weakly varies in the strain limits $\Delta\varepsilon = 0.5\%$ at a given temperature.

Figure 3 shows strain-rate oscillations as a function of strain for PMMA + DBP, which are manifested most clearly near the point (2.6%) corresponding to the minimum of the strain rate (Fig. 2). Constructions similar to those in Fig. 3 were used earlier to calculate the mean values of *L* and *h* for PMMA. A comparison of the values of *L* and *h* for two materials (Figs. 4, 5) proved that the heights of steps *L* for plasticized and nonplasticized PMMA are virtually identical at the initial stage of deformation and that the sharpness of jumps *h* at the yield points ε_y, which are different for these polymers, passes through peaks whose heights differ by a factor of three.

Earlier, it was assumed (and confirmed in model polymers [11–13]) that there exists a correlation between the scale of jumps and the sizes of ordered inhomogeneities (fibrils) in the direction of the applied stress. The observed correlations have much in common with the wave theory of plasticity, in which the length of plastic waves is related to the grain size in metals [16]. It is more difficult to explain the presence and scale of jumps in amorphous solids in which no clearly manifested structural inhomogeneities are observed, and the ideas concerning their nature are contradictory and ambiguous. However, from experiments, it is well known that micrometer-scale jumps in deformation correspond to a displacement of the boundary of

a macroscopic shear band with a highly oriented structure. Consequently, we can assume that, under directional stresses and strains, the segments of polymer chains in amorphous polymers are oriented along the planes in which the shear stresses are maximum (at 45° to the sample axis). The degree of local orientation of molecules in this case can be many times higher than that of the average orientation detected by instruments. Deformation can lead to the formation of ordered fibril-type structures in which molecules are oriented in shear planes. Electron micrographs of deformed amorphous polymers indicate the emergence of an inhomogeneous oriented structure [3]. Thus, the assumption that deformation itself organizes the structure that determines the jump scale is well founded. The lengths of ordered inhomogeneities in amorphous polymers can be determined from the lengths of molecules oriented under deformation (the molecular lengths are of the order of fractions of a micrometer and micrometers). It is appropriate here to mention the dislocation models of deformation that were initially applied to structures with a long-range order. Later [17, 18], hypotheses on the emergence of instability in the form of a slip dislocation loop propagating over the sample cross section under shear stresses were developed and dislocations models were also applied to amorphous polymers [19]. Taking into account the universal nature of jumplike displacements in inhomogeneous media, one can assume a jumplike nature of motion of individual dislocations and their ensembles.

The results depicted in Fig. 4 correspond to the above considerations. Indeed, if the micrometer level of jumps observed on the initial creep stage is associated with the lengths of the extended molecules, the magnitude of the jumps should not be changed by plasticization, because it does not affect the size of polymer molecules; this has been confirmed experimentally.

The effect of plasticization on the strain-rate inhomogeneity in jumps characterized by h is completely different. It can be seen from Fig. 5 that the value of h at the yield point ε_y for plasticized PMMA is much lower than that for the initial polymer. This result also agrees with the model of jumplike motion associated with nonuniformity of molecular interactions discussed in the Introduction. It is well known that the introduction of a plasticizer increases the molecular mobility in a polymer (this increase is due, among other things, to the suppression of interaction between groups of atoms in adjacent molecules). It was proved earlier [13] that the values of h for different polymers are proportional to the nonuniformity of intermolecular interaction potentials (this nonuniformity is typical of these polymers). The introduction of a plasticizer increases the distance between polymer molecules and can heavily suppress the strongest cohesive bonds playing the role of stoppers in the case of shear deformation. A decrease in the nonuniformity of potential barriers to shear reduces the difference in the strain rates within the jumps; i.e., the sharpness h of the jumps decreases

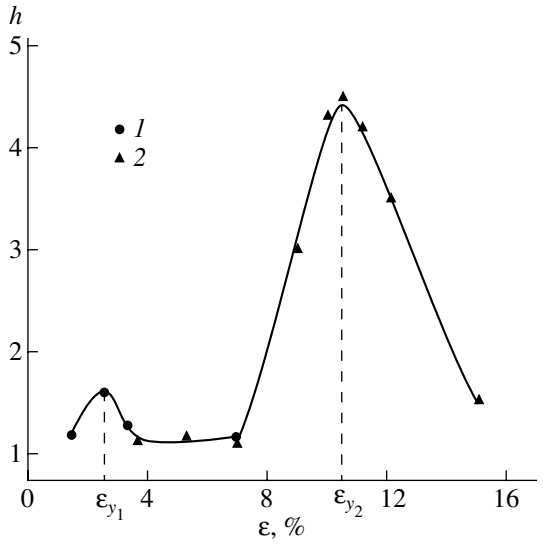

Fig. 5. Strain dependence of jump sharpness h in the vicinity of the yield points for (*1*) PMMA + DBP and (*2*) PMMA; σ = (*1*) 13.3 and (*2*) 70 MPa.

(Fig. 5). Thus, the change in the jumplike creep as a result of modification of the polymer can be explained on the basis of traditional concepts concerning the structure and kinetics of deformation of amorphous polymers.

On the other hand, step creep exhibits all features of self-organization of the structure [20]: spontaneous regular behavior in a complex system as a result of the evolution of instability; ordering of the disordered system is associated with the collective motion of the subsystems in the form of deformation jumps. Haken, one of the founders of synergetics, defined the structure as the coherent behavior of a large number of particles. Deformation jumps reflect, by definition, the cooperative (coherent) behavior of molecules; consequently, we must admit their organization during the deformation of ordered inhomogeneities that naturally develop under a constant stress. It would be more appropriate to speak of the kinetic structure of amorphous polymers manifested in the form of jumps during creep. It should be noted that collective displacements confirm the assumption [21] on the existence of stacks in amorphous polymers, as well as modern ideas concerning nanostructures [22]. Nanostructures can serve as nuclei in the formation of coarser kinetic structures, including micrometer-scale jumps of deformation.

REFERENCES

1. V. I. Startsev, V. Ya. Il'ichev, and V. V. Pustovalov, *Plasticity and Metal and Alloy Strength under Low Temperatures* (Metallurgiya, Moscow, 1975).
2. V. V. Shpeĭzman, V. I. Nikolaev, B. I. Smirnov, *et al.*, Fiz. Tverd. Tela (St. Petersburg) **42** (6), 1034 (2000) [Phys. Solid State **42**, 1066 (2000)].

3. A. A. Askadskiĭ, *Deformation of Polymers* (Khimiya, Moscow, 1973).
4. V. I. Bekichev, Vysokomol. Soedin., Ser. A **16** (8), 1745 (1974).
5. V. A. Likhachev and V. G. Malinin, Izv. Vyssh. Uchebn. Zaved., Fiz., No. 2, 121 (1990).
6. N. A. Pertsev, Prog. Colloid Polym. Sci. **92**, 52 (1992).
7. N. N. Peschanskaya, G. S. Pugachev, and P. N. Yakushev, Mekh. Polim., No. 2, 357 (1977).
8. N. N. Peschanskaya and P. N. Yakushev, Fiz. Tverd. Tela (Leningrad) **30** (7), 2196 (1988) [Sov. Phys. Solid State **30**, 1264 (1988)].
9. N. N. Peschanskaya, Vysokomol. Soedin., Ser. A **31** (6), 1182 (1989).
10. N. N. Peschanskaya, Fiz. Tverd. Tela (St. Petersburg) **35** (11), 3019 (1993) [Phys. Solid State **35**, 1484 (1993)].
11. N. N. Peschanskaya, L. P. Myasnikova, and A. B. Sinani, Fiz. Tverd. Tela (Leningrad) **33** (10), 2948 (1991) [Sov. Phys. Solid State **33**, 1665 (1991)].
12. N. N. Peschanskaya, P. N. Yakushev, L. P. Myasnikova, *et al.*, Fiz. Tverd. Tela (St. Petersburg) **38** (8), 2582 (1996) [Phys. Solid State **38**, 1416 (1996)].
13. N. N. Peschanskaya, Doctoral Dissertation (Fiz.-Tekh. Inst. im. A. F. Ioffe Ross. Akad. Nauk, St. Petersburg, 1999).
14. G. M. Bartenev and A. G. Barteneva, *Relaxation Properties of Polymers* (Khimiya, Moscow, 1992).
15. N. N. Peschanskaya, V. Yu. Surovova, and P. N. Yakushev, Fiz. Tverd. Tela (St. Petersburg) **34** (7), 2111 (1992) [Sov. Phys. Solid State **34**, 1127 (1992)].
16. V. E. Panin, L. B. Zuev, V. I. Danilov, and N. M. Mnikh, Dokl. Akad. Nauk SSSR **308** (6), 1375 (1989) [Sov. Phys. Dokl. **34**, 940 (1989)].
17. A. S. Argon, Philos. Mag. **26** (5), 1121 (1972).
18. P. B. Bowden and S. Raha, Philos. Mag. **29** (1), 149 (1974).
19. A. B. Sinani, N. N. Peschanskaya, and V. A. Stepanov, Fiz. Tverd. Tela (Leningrad) **24** (5), 1368 (1982) [Sov. Phys. Solid State **24**, 775 (1982)].
20. G. Nicolis and I. Prigogine, *Self-Organization in Non-Equilibrium Systems* (Wiley, New York, 1977; Mir, Moscow, 1979).
21. V. A. Kargin and G. M. Slonimskiĭ, *Brief Outlines on Physicochemistry of Polymers* (Khimiya, Moscow, 1967).
22. V. A. Berstein, P. N. Yakushev, L. Karabanova, *et al.*, J. Polym. Sci., Part B: Polym. Phys. **37**, 429 (1999).

Translated by N. Wadhwa

Physics of the Solid State, Vol. 43, No. 8, 2001, pp. 1483–1487. Translated from Fizika Tverdogo Tela, Vol. 43, No. 8, 2001, pp. 1423–1427.

DEFECTS, DISLOCATIONS, AND PHYSICS OF STRENGTH

Phenomenology of Wave Processes in a Localized Plastic Flow

L. B. Zuev, S. A. Barannikova, N. V. Zarikovskaya, and I. Yu. Zykov

Institute of Strength Physics and Materials Science, Siberian Division, Russian Academy of Sciences, Tomsk, 634021 Russia
e-mail: lev@zuevs.tomsk.ru

Received January 12, 2001; in final form, February 6, 2001

Abstract—The motion of localized deformation sites in mono- and polycrystallites of metals and alloys is investigated experimentally at the stages of easy slip and linear strain hardening. The wave nature of localization of deformation at these stages of plastic flow is established, and the velocity of waves and their dispersion relation are determined. The scale effect and the dependence of the localized deformation wavelength on the grain size are investigated. A qualitative interpretation of the results obtained is proposed. © *2001 MAIK "Nauka/Interperiodica".*

1. INTRODUCTION

In our earlier publications [1–3], we established that the common feature of plastic flow in solids is its localization at all deformation stages, the type of localization site distribution being determined by the strain hardening regularity for a given stage of plastic flow. The emerging localization regions are ordered in the sample being stretched, and their pattern is determined by the form of the $\theta(\varepsilon)$ dependence, where $\theta = G^{-1}d\tau/d\varepsilon$ is the strain hardening coefficient; τ and ε are the tangential stress and the shear strain in the flow, respectively; and G is the shear modulus. Of particular interest is the evolution of the deformation localization pattern at the stages of easy slip and linear strain hardening (θ = const [4]); the uniform motion of solitary (easy slip) or equidistant sites of localized plasticity (linear hardening) creates a typical wave pattern [2, 3] for which the wavelength λ and the velocity of its propagation V_w can be measured. Knowledge of their dependence on the deforming conditions and the structure of the material (e.g., grain size) is essential for establishing the nature of the phenomenon.

2. MATERIALS AND EXPERIMENTAL CONDITIONS

In this work, we present and discuss the results obtained from an analysis of the propagation of localized deformation sites at various stages of plastic flow. The velocity of propagation and the wavelength were determined for a wide class of materials. From the table, it can be seen that we analyzed the deformation of fcc, bcc, and hcp materials with different doping levels in mono- and polycrystalline states which exhibited different mechanisms of deformation (dislocation slip, twinning, and martensite transformation). The mechanical properties and the type of plastic-flow diagram were varied by changing the orientation of the tensile strain axes of monocrystalline samples. Stretching was carried out on a tension testing machine Instron-1185 at a velocity 3.35×10^{-6} m/s of its movable clamp (the relative strain rate was 6.7×10^{-5} s^{-1}). The speckle-interferometry technique used by us [3] makes it possible to calculate the component of the plastic distortion tensor, to determine the position X^* of plastic strain localization zones in a sample, and to trace the displacement of these zones during stretching (Fig. 1). As shown in the figure, the $X^*(t)$ curves can be used to estimate the wavelength λ and the period T of the wave process.

3. DYNAMICS OF MOTION OF LOCALIZED DEFORMATION SITES

The velocity V_w of plastic-deformation sites at the linear hardening stage is determined from the slope of the $X^*(t)$ curves. For all samples under investigation that have this stage, this velocity is determined primarily by the strain hardening coefficient; the dependence

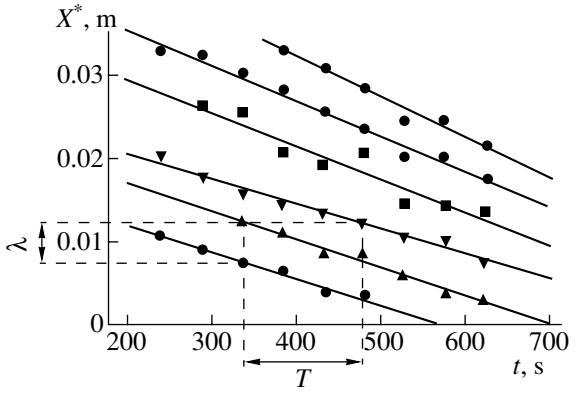

Fig. 1. Kinetics of the space–time evolution of localized plasticity sites during extension of a Cu single crystal: X^* is the coordinate of a localization site on the tensile strain axis of the sample.

1063-7834/01/4308-1483$21.00 © 2001 MAIK "Nauka/Interperiodica"

Composition, structure, and deformation mechanisms of the materials under investigation

Metal or alloy (composition, wt %)	Crystal lattice	Single crystal or polycrystal	Mechanisms of plastic deformation
Cu (99.8%)	fcc	Single crystal	D
Cu + 10% Ni + 6% Sn	fcc	"	D
Fe + 16% Cr + 12% Ni(Fe_I)	fcc	"	D
Fe + 13% Mn + 1% C(Fe_{II})	fcc	"	D
Fe + 13% Mn + 1% C(Fe_{III})	fcc	"	Tw
Ti–Ni (equiatomic composition)	bcc	"	DT
Al (99.85%)	fcc	Polycrystal	D
Zr + 2.3% Nb	hcp	"	D

Note: *D* denotes the deformation mechanism; Tw, twinning; and DT, deformation-induced transformation.

of the velocity on θ is linear and has the form (curve *2* in Fig. 2)

$$V_w = V_0 + \Omega/\theta. \quad (1)$$

Here, V_0 and Ω are constants and the correlation coefficient ρ is equal to 0.92.[1] Since the data obtained for all samples are described by the same equation, the result obtained is a proof of the universal nature of the wave processes observed at the linear hardening stage.

Let us consider the possible reason for the emergence of a dependence of the type $V_w \sim \theta^{-1}$. It can be naturally assumed that $dV_w \sim l$ (l is the length of the slip trace at the linear hardening stage). It is well known [4] that at this stage, $l = \Lambda/(\varepsilon - \varepsilon^*)$, where Λ = const and depends only on the type of the material under investigation, while the strain ε* corresponds to the onset of the linear stage of strain hardening [4]. The strain hardening coefficient at this stage is given by [4]

$$\theta \approx (nb/3\Lambda)^{1/2}, \quad (2)$$

where n is the number of dislocations with the Burgers vector b in a plane cluster [4]. Accordingly, $dV_w \sim l \sim \Lambda \sim \theta^{-2}$ and $d\theta \neq 0$ if the value of θ varies due to changes in the material; i.e.,

$$dV_w \sim nb[(\varepsilon - \varepsilon^*)\theta^2]^{-1} d\theta. \quad (3)$$

If the difference $\varepsilon - \varepsilon^*$ changes insignificantly upon a transition from one material to another [4], we can put $\varepsilon - \varepsilon^* \approx$ const for estimating Λ. It then follows from Eq. (3) that $V_w \sim \theta^{-1}$.

The velocity V_w of a localized deformation site at the easy slip stage displays a linear dependence of V_w on the strain hardening coefficient as in Eq. (1); it follows from Fig. 2, however, that the results obtained can be divided into two groups. The main reason for this division is the different value of V_0 for each of these groups: $V_0 \approx 0$ for Cu single crystals and Cu–Ni–Sn and Ti–Ni alloys (straight line *1*), while $V_0 < 0$ for γ-Fe single crystals (straight line *1*').

The wave processes in the plastic deformation of solids were discovered long ago (see, for example, [6, 7]). However, the dependence of the wave propagation velocity on the strain hardening coefficient, according to Eq. (1), differs radically from that for plastic waves ($V_p \sim \theta^{-1/2}$ [6, 7]). This difference leads to the conclusion that we observe a new type of wave process associated with plastic deformation [8], namely, plastic-flow localization waves.

4. DISPERSION RELATION FOR PLASTIC-FLOW LOCALIZATION WAVES

Experimental methods of obtaining information on the velocity of plastic-flow sites make it possible to determine the spatial (wavelength λ) and temporal (T) periods of observed wave processes (Fig. 1). It is natural to try to find the relation between these periods under the conditions when one of these quantities varies due to changes in the deformation conditions. This can be done by varying the orientation of tensile strain axes for monocrystalline samples or by varying the chemical composition of alloys. It was established (Fig. 3) that there are two groups of materials for which the relation between the wave number $k = 2\pi/\lambda$ and the frequency $\omega = 2\pi/T$ is linear (the correlation coefficients for these groups are $\rho_1 = 0.98$ and $\rho_2 = 0.88$, respectively, for the statistical significance level of relation [5] ~0.99) and has the form

$$\omega = V^*(k - k_0). \quad (4)$$

The constants are $k_0 = 512\ m^{-1}$ and $V^* = 2.15 \times 10^{-4}$ m/s for the first group and $k_0 = 333\ m^{-1}$ and $V^* = 4.8 \times 10^{-5}$ m/s for the second group.

The relation obtained can be formally regarded as the dispersion relation for the wave processes of a localized plastic flow observed at the linear hardening stage. Unfortunately, the information on the two groups of

[1] According to the estimate obtained in [5], this correlation level is statistically significant with a probability higher than 0.99.

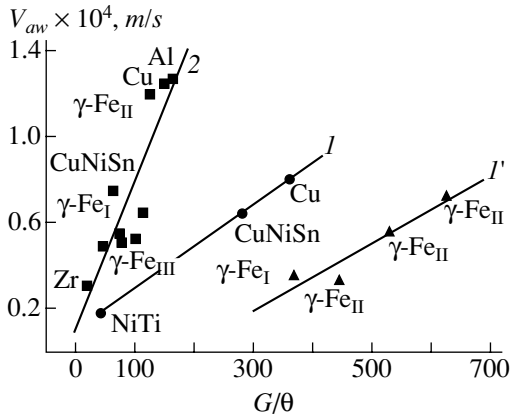

Fig. 2. Generalized dependence of the velocity of waves on the strain hardening coefficient: *1* and *1'* correspond to the easy-slip stage and *2* corresponds to the linear strain hardening stage. Large values of the strain hardening coefficient are due to growth imperfections in the crystals under investigation.

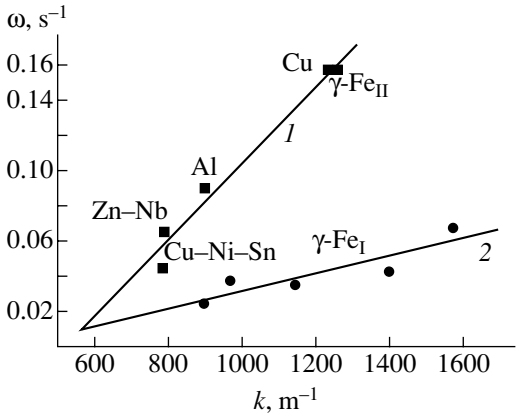

Fig. 3. Dependence $\omega(k)$ (dispersion relation) for the materials under investigation. The numbers on the curves indicate the groups of materials.

materials presented in Fig. 3 is insufficient for discussion of the reason behind the difference in the results.

The velocity of wave propagation is small and lies in the interval 10^{-5} m/s $\le V_w \le 10^{-4}$ m/s for all materials studied. This circumstance emphasizes once again that the origin of the waves under investigation differs from that of plastic waves [6, 7]. For plastic waves [6], $V_p \approx (\theta/\rho_m)^{1/2}$; therefore, since the characteristic value of the strain hardening coefficient at the linear hardening stage is $\theta_{II} \approx 3 \times 10^{-3}$ [4], we have $V_p \approx 5.5 \times 10^{-2} V_t \approx 10^2$ m/s ($V_t \approx (G/\rho_m)^{1/2}$ is the velocity of transverse elastic waves and ρ_m is the density of the medium), which is 6–7 orders of magnitude higher than the velocity of the waves considered here.

The nature of the wave processes observed during the plastic flow of solids is yet unclear. Some authors (see, for example, the review by Malygin [8]) put forth the hypothesis (on the basis of the evolution of dislocation ensembles in the course of plastic deformation) on the relation of these wave processes with the self-organization in the deformed medium. It was proved in our earlier publication [9] that the mechanisms of deformation localization can be regarded as self-oscillatory processes in an active medium. The necessary condition for the realization of such processes is the existence of an energy flux through the system, which must be reflected in the expression for the velocity of the waves under investigation. Indeed, it was proved by us earlier [10] that for measurements on the same material (single crystals of doped γ-Fe), a dependence of the Eq. (1) type on the dimensional strain hardening coefficient $\theta_\tau = d\tau/d\varepsilon$ is observed. In this case, the magnitude and dimensions (W/m^2) of the coefficient of θ_τ^{-1} correspond to the energy flux through the sample being deformed, which justifies such an interpretation.

5. SCALE EFFECT OF DEFORMATION LOCALIZATION

Analysis of the possible effect of the size of a system undergoing deformation on the parameters of plastic-deformation localization (scale effect) is important for understanding the nature of this phenomenon. The dependence between the sample length L and the localization length λ makes it possible to obtain additional information on the nature of such localization zones and the kinetics of their formation. We studied the $\lambda(L)$ dependence for samples 25, 50, 75, 100, and 125 mm in length and 5 mm in width (all samples) cut from a homogeneous 1.6 mm thick sheet of a Zr–1 wt % Nb alloy. The grain size was 5 μm in all cases. The use of a sheet material allowed us to maintain uniformity of the properties required in the experiments. The localized-deformation wavelength was determined for the tensile strain $\varepsilon_{tot} \approx 2.5\%$, which was the same for all samples.

Under these conditions, we observed a clearly manifested size effect, which obeyed the equation

$$\lambda(L) = \lambda^* + \alpha \ln L, \qquad (5)$$

where $\lambda^* = -21.4$ mm, $\alpha = 7.8$ mm, and the correlation coefficient $\rho = 0.99$ (Fig. 4). The obtained dependence can be interpreted as follows. We introduce the derivative $d\lambda/dL > 0$ characterizing the increment of the wavelength upon an increase in the sample length and assume that it is inversely proportional to the probability w of the emergence of a localization site, which is, in turn, proportional to the sample length; i.e., $d\lambda/dT \sim w^{-1} \sim L^{-1}$. Thus, $d\lambda = \alpha dL/L$, which leads to Eq. (5). The proportionality factor α in this case characterizes the scale of spatial nonuniformity of plastic deformation in the sample.

It follows from Eq. (5) that $\lambda = 0$ for $L_0 \approx 2\alpha \approx 16$ mm (Fig. 4); this is the value of L_0 that corresponds to the minimum size of the sample in which periodic patterns

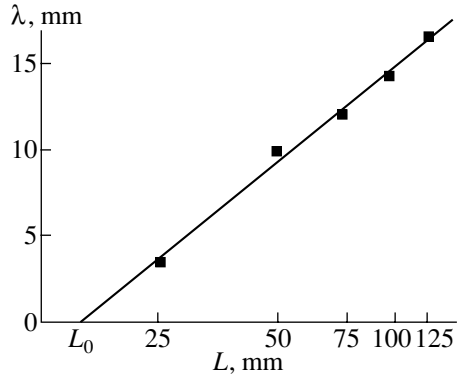

Fig. 4. Wavelength of localized deformation as a function of sample length (scale effect).

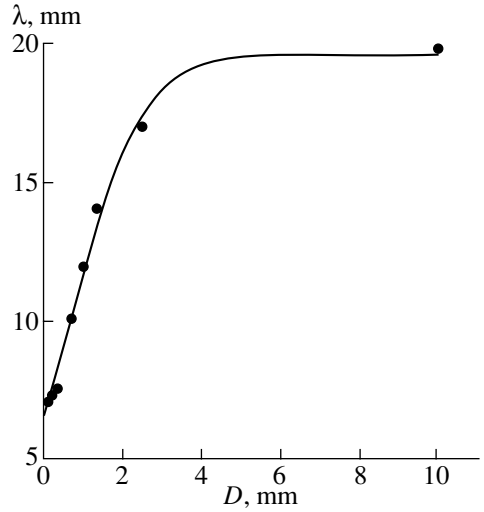

Fig. 5. Localized deformation wavelength as a function of the grain size in Al.

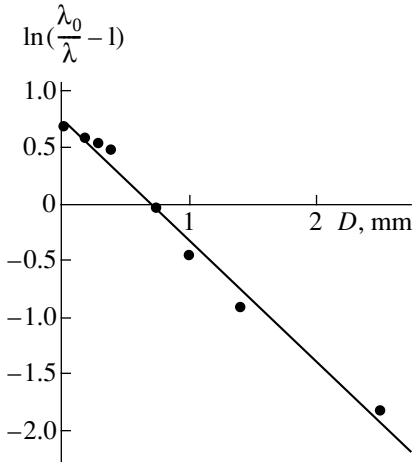

Fig. 6. Linearization of the λ(*D*) dependence in accordance with the results presented in Fig. 5.

of plastic-flow localization can still emerge. In samples whose length $L \le L_0$, we can expect that the strain distribution during extension will be uniform.[2] Among other things, this probably explains why the emergence of periodic patterns of plastic-flow localization is virtually not mentioned in the literature devoted to problems of deformation localization. The possibility of deformation localization in large samples is apparently the reason for the scale effect (the dependence of strength on size [11], which plays an important role in engineering).

6. LOCALIZED DEFORMATION WAVELENGTH

In order to explain the nature of wave processes of deformation localization, the form of the possible dependence of wavelength on grain size in alloys is of considerable importance. It is known that nearly all mechanical properties of metals and alloys are determined to a considerable extent by this natural and important parameter of the material. We studied 99.86 wt % pure aluminum samples. The grain size D was varied from 10^{-2} to 22 mm through recrystallization annealing following preliminary plastic extension. The samples had a working part of size 50×5 mm and were punched from an aluminum sheet 1 mm thick.

The experimentally established dependence of the localized deformation wavelength on the grain size is shown in Fig. 5. From these data, it follows that $\lambda \sim e^D$ for a small grain size ($D \le 50$ μm), while in the range of large sizes ($D \ge 2.5$ mm), the value of λ tends to the limit $\lambda_0 \approx 20$ mm and then remains virtually unchanged.

Let us consider the possible meaning of this type of λ(*D*) dependence. It is natural to assume that the wavelength of localized deformation increases with the grain size because of the corresponding increase in the width of the shear band during an elementary deformation act. However, for a grain size comparable to the sample cross section (5 mm), the rate of this increase must decrease. Taking into account both these circumstances, we can write the differential equation connecting λ and D in the form

$$d\lambda/dD = a\lambda - b\lambda^2 . \qquad (6)$$

Here, a and b are positive dimensional constants and the quadratic term $b\lambda^2$ on the right-hand side of Eq. (6) takes into account the slowing down of the increase in λ in the range of large D, which is associated with the limited size of the sample. Integrating Eq. (6), we arrive at the well-known equation of the logistic curve (see, for example, [12])

$$\lambda = \lambda_0/[1 + C\exp(-aD)], \qquad (7)$$

where $\lambda_0 = a/b$ and C is the dimensionless integration constant. Plotting the λ(*D*) dependence in the $\ln(\frac{\lambda_0}{\lambda} - 1)$

[2] Indeed, no deformation localization was observed in a special experiment on a sample in which $L < L_0$.

vs. D coordinates, in which its graph should be linearized (Fig. 6), we can see that Eq. (7) satisfactorily describes the experimental data obtained for the $\lambda(D)$ in a wide range of values of D.

For small grain sizes (10^{-2} mm $\le D \le 10^{-1}$ mm), we have $a\lambda \gg b\lambda^2$ and the term $b\lambda^2$ in Eq. (6) can be neglected. Then, the solution to Eq. (6) leads to the dependence $\lambda \sim \exp(aD)$ observed in this range. Contrarily, in the macroscopic size region ($D \ge 1$ mm) in which the increase in the wavelength slows down, we can assume that the relative increase in λ is proportional to the number of grains over the working length L of the sample; i.e., $d\lambda/dD \sim L/D$, which obviously leads to the relation $\lambda \sim \ln D$ typical of this region (for L = const). This was established earlier in experiments on plastic-flow localization in macrocrystalline Al [3].

A comparison of this result with the dependence of the wavelength λ on the macroscopic parameter (sample length L) (scale effect) leads to the conclusion that the logarithmic type of the dependence of λ on variable D or L in the range of their macroscopic values is fairly universal.

7. ON THE NATURE OF LARGE-SCALE NONUNIFORMITY OF PLASTIC FLOW

It was proved by us earlier [1–3] that the localized deformation sites emerging at different stages of plastic flow have a macroscopic correlation length $\lambda \approx 10$ mm, while the correlation radius corresponding to the microscopic processes responsible for plasticity is of the order of the dislocation ensemble size ($\le 10^{-2}$ mm) [14]. Explaining this difference and the matching of these scales is one of the most difficult tasks in the problem under investigation. We will solve this problem by using a model based on the following concepts. We consider the propagation of acoustic pulses emitted in each elementary act of plastic flow (see, for example, [15]). In a nonuniformly deformed medium, ultrasonic waves can be focused at a certain distance from the plasticity site acting at a given stage. To this end, the nonuniformities of dislocation structure emerging during plastic deformation should play the role of acoustic lenses. This is quite possible since the sound velocity in the medium depends on its plastic deformation [16] and the changes in this velocity are associated with local processes of plastic flow [17]. If the characteristic size (radius of curvature) of a nonuniformity is R, the focal length f of such an acoustic lens is, according to Bergman [18],

$$f \approx (1-n)^{-1}R, \qquad (8)$$

where $n = V_0/V$ is the refractive index for acoustic waves (V_0 and V are the velocities of ultrasound in undeformed and deformed media, respectively). According to estimates obtained on the basis of our earlier results [16], $n \approx 1.002$. Following Ball [19], we put $R \approx 0.01$ mm for the deformation of Al. In this case, it follows from Eq. (8) that $f \approx 5$ mm $\approx \lambda$. In other words, a new stress concentrator is generated at a distance λ from the previous concentrator in the region in which the elastic energy emitted in an elementary act of plasticity is focused. It is at this distance that the probability of the emergence of the next shear increases and a new site of localized plastic flow is formed. The values of n and R depend on the initial structure of the material and determine the corresponding rearrangements in the wave pattern of deformation localization in view of their evolution with the flow.

REFERENCES

1. L. B. Zuev, V. I. Danilov, and N. V. Kartashova, Pis'ma Zh. Éksp. Teor. Fiz. **60** (7), 538 (1994) [JETP Lett. **60**, 553 (1994)].
2. L. B. Zuev and V. I. Danilov, Fiz. Tverd. Tela (St. Petersburg) **39** (8), 1399 (1997) [Phys. Solid State **39**, 1241 (1997)].
3. L. B. Zuev and V. I. Danilov, Philos. Mag. A **79** (1), 43 (1999).
4. A. Seeger, in *Dislocations and Mechanical Properties of Crystals: Proceedings of the International Conference, 1956* (Wiley, New York, 1957; Inostrannaya Literatura, Moscow, 1960).
5. A. G. Mitropol'skiĭ, *Technique of Statistical Computing* (GIFML, Moscow, 1961).
6. H. Kolsky, *Stress Waves in Solids* (Clarendon Press, Oxford, 1953; Inostrannaya Literatura, Moscow, 1955).
7. L. M. Shestopalov, *Metal Deformation and Plasticity Waves in Metals* (Akad. Nauk SSSR, Moscow, 1958).
8. G. A. Malygin, Usp. Fiz. Nauk **169** (9), 979 (1999).
9. L. B. Zuev, Metallofiz. Noveĭshie Tekhnol. **16** (10), 31 (1994).
10. S. A. Barannikova, L. B. Zuev, and V. I. Danilov, Fiz. Tverd. Tela (St. Petersburg) **41** (7), 1222 (1999) [Phys. Solid State **41**, 1112 (1999)].
11. B. B. Chechulin, *Scale Factor and Statistical Theory of Metal Strength* (Metallurgizdat, Moscow, 1963).
12. G. Murdie, in *Mathematical Modelling*, Ed. by J. Andrews and R. McLone (Butterworths, London, 1976; Mir, Moscow, 1979).
13. V. I. Danilov, L. B. Zuev, N. M. Mnikh, *et al.*, Fiz. Met. Metalloved., No. 3, 188 (1991).
14. J. Friedel, *Dislocations* (Pergamon, Oxford, 1964; Mir, Moscow, 1967).
15. P. P. Gillis and M. A. Hamstad, Mater. Sci. Eng. **14** (1), 103 (1974).
16. L. B. Zuev, B. S. Semukhin, K. I. Bushmeliova, and N. V. Zarikovskaya, Mater. Lett. **42** (1), 97 (2000).
17. B. S. Semukhin, L. B. Zuev, and K. I. Bushmeleva, Prikl. Mekh. Tekh. Fiz. **41** (3), 197 (2000).
18. L. Bergmann, *Der Ultraschall und seine Anwendung in Wissenschaft und Technik* (Hirzel, Zürich, 1954; Inostrannaya Literatura, Moscow, 1957).
19. C. J. Ball, in *Dislocations and Mechanical Properties of Crystals: Proceedings of the International Conference, 1956* (Wiley, New York, 1957; Inostrannaya Literatura, Moscow, 1960).

Translated by N. Wadhwa

Physics of the Solid State, Vol. 43, No. 8, 2001, pp. 1488–1498. Translated from Fizika Tverdogo Tela, Vol. 43, No. 8, 2001, pp. 1428–1438.

MAGNETISM AND FERROELECTRICITY

Lattice Effects in the Bulk-Magnon Spectrum of a Finite Low-Temperature Antiferromagnet

S. V. Tarasenko

Donetsk Physicotechnical Institute, National Academy of Sciences of Ukraine, Donetsk, 83114 Ukraine

Received November 2, 2000

Abstract—For a plate of a low-temperature antiferromagnet ($T_N < T_D$, where T_N and T_D are the Néel temperature and the Debye temperature, respectively), it is shown that the effect of the lattice on the magnetic-dipole and exchange spin dynamics in magnetically ordered crystals can lead to anomalies in the spectrum of propagating bulk magnons. These anomalies are absent in the cases of an infinite magnet and of a plate of a high-temperature antiferromagnet ($T_N > T_D$). *© 2001 MAIK "Nauka/Interperiodica".*

1. INTRODUCTION

When theoretically describing spin waves in finite ferromagnets and antiferromagnets (a $2d$ thick plate), one usually takes into account only magnetic-dipole and inhomogeneous exchange interactions [1]. If one of these two interactions dominates in a finite ferromagnet, magnetostatic or exchange spin waves arise. In both cases, the spin-wave modes form a denumerable set (with mode index $\nu = 1, 2, \ldots$). However, the dispersion relations $\omega = \Omega_{m\nu}(k_\perp)$ of magnetostatic and exchange spin waves ($k_\perp$ is the wave number and ω is the frequency of a spin wave) are essentially different: the frequency depends not only on the spin-wave polarization and wave number $k_\perp$ but also on the relative orientation of the vectors **n**, **l**, **m**, and $\mathbf{k}_\perp$, where **n** is a normal to the surface of the plate and **l** and **m** are the (equilibrium) antiferromagnetism and ferromagnetism vectors, respectively. For large enough values of ν/d, dispersion of a bulk spin wave is determined fundamentally by inhomogeneous exchange interaction. For this reason, the following inequality takes place for any $k_\perp \neq 0$ ($k_\perp a \ll 1$, a is the lattice parameter) and for any magnon polarization (in the case where the exchange interaction is treated in the nearest neighbor approximation):

$$\partial\Omega_{m\nu}(k_\perp)/\partial k_\perp > 0, \quad \partial^2\Omega_{m\nu}(k_\perp)/\partial k_\perp^2 > 0. \qquad (1)$$

As ν/d is decreased, the effect of hybridization of the two types of spin–spin interaction on the structure of the bulk-magnon spectrum becomes progressively stronger and a number of anomalies appear in the dispersion relation $\nu(\Omega_{m\nu}(k_\perp))$ of mode ν of bulk dipole–exchange spin waves for $k_\perp \neq 0$. Among the anomalies in the bulk-magnon spectrum associated with dipole–exchange interaction are inflection points [$\partial^2\Omega_{m\nu}(k_\perp)/\partial k_\perp^2 = 0$], crossover points at which $\Omega_{m\nu}(k_\perp) = \Omega_{m\rho}(k_\perp)$ ($\nu \neq \rho$), and extreme points [$\partial\Omega_{m\nu}(k_\perp)/\partial k_\perp = 0$, $\partial^2\Omega_{m\nu}(k_\perp)/\partial k_\perp^2 > 0$]. At given values of ω, $k_\perp$, ν, and d, the character of these features depends on the relative orientation of **n**, $\mathbf{k}_\perp$, **m**, and **l**. For arbitrary boundary conditions, the degeneracy $\Omega_{m\nu}(k_\perp) = \Omega_{m\rho}(k_\perp)$ is lifted and the corresponding dispersion curves (without dissipation) repel each other. This situation corresponds to nonuniform spin–spin resonance. A necessary condition for a bulk dipole–exchange magnon mode (with mode index ν, frequency ω, and wave number $k_\perp$) to show the aforementioned anomalies is the fulfillment of the magnetostatic criteria (for a magnetic $2d$ thick plate) $\omega \ll c\pi\nu/d$ for $\nu \neq 0$ and $\omega \ll ck_\perp$ for $\nu = 0$, where c is the speed of light. Since magnetic dipole interaction is relativistic in nature, the optimum conditions for these anomalies to occur are realized in those magnetic crystals in which the spectrum of normal spin-wave oscillations has branches with a sufficiently low activation energy. This is the case, in particular, in magnets with weak (e.g., cubic or easy-plane type) anisotropy and near magnetic phase transitions of the soft-mode type. In all these cases, as is well known, the dimensionless parameter of linear magnon–phonon coupling ξ is of order unity [2] and, therefore, the low-frequency magnon spectrum can be adequately described only with allowance for the interaction with the elastic subsystem even in an infinite crystal away from magnetoacoustic resonance. Thus, in order for a theoretical description of low-frequency spin dynamics of a real magnetic crystal to be consistent, one should simultaneously take into account, at the least, (i) the finite size of the real magnet, (ii) nonlocal spin–spin (magnetic dipole, inhomogeneous exchange, etc.) interactions, and (iii) interaction between the spin and elastic subsystems.

The effect of the lattice on the bulk spin dynamics of a magnetic plate has been analyzed in many papers [2–5]. However, additional magnetoacoustic resonances (fast magnetoelastic waves [4]) have been the

primary object of investigation to data. These resonances occur in a magnetic film near the points at which the frequencies of bulk dipole–exchange magnons $\Omega_{m\nu}(k_\perp)$ and traveling (in the same direction) normal bulk elastic waves $\Omega_{\mathrm{ph},\rho}(k_\perp)$ are equal:

$$\Omega_{m\nu}(k_\perp) = \Omega_{\mathrm{ph},\rho}(k_\perp) \quad (\nu \neq \rho). \tag{2}$$

As for the effect of magnetoelastic interaction on the spectrum of bulk dipole–exchange magnons away from magnetoacoustic resonance, the long-wavelength spectral region of magnetoelastic waves has been the primary object of investigation to date. It is believed that the effect of the lattice on the magnon spectrum reduces to the formation of a magnetoelastic gap in the spin-wave spectrum and to a renormalization of the magnetic anisotropy constant via spontaneous striction [2, 3] and is independent of the relationship between the Debye temperature T_D and the Néel temperature T_N. At the same time, it was shown [6] that the spectra of bulk magnetoelastic waves in the short-wavelength region in high-temperature ($T_N > T_D$) and low-temperature ($T_N < T_D$) antiferromagnets (AFMs) are qualitatively different even in the infinite-crystal model. In particular, in a low-temperature AFM at $k \gg k_{m,\mathrm{ph}}$ ($k_{m,\mathrm{ph}}$ is the wave vector at which magnetoacoustic resonance takes place), the effect of the lattice on the spin dynamics can be described by elastostatics equations ($\partial\sigma_{ik}/\partial x_k = 0$, where σ_{ik} is the elastic stress tensor). This effect corresponds to the case of a free lattice (this approximation is invalid in high-temperature AFMs). In [7–10], it was shown that the linear magnon–phonon interaction in a plate of a low-temperature AFM leads to indirect spin–spin interaction of magnetic moments via the long-range field of quasi-static magnetoelastic deformations, which results in the formation of a new type of propagating exchangeless spin-wave excitations, elastostatic spin waves. Due to hybridization of the elastostatic and inhomogeneous exchange mechanisms of spin–spin interaction, traveling elastic exchange spin waves are formed in a magnetic plate. As in the case of dipole–exchange spin waves, the spectrum of bulk elastic exchange magnons depends on the relative orientation of vectors $\mathbf{k}_\perp$, $\mathbf{n}$, and $\mathbf{l}$, as well as on the mode index ν and polarization of the spin waves; however, the phonon anomalies in the spectrum of bulk exchange magnons can qualitatively differ in character from the well-known features of the spectrum of dipole–exchange spin waves. A necessary condition for the operation of the elastic exchange mechanism of dispersion of a bulk spin wave of mode index ν, frequency ω, and wave number $k_\perp$ in a magnetic plate of thickness $2d$ is the fulfillment of the elastostatic criterion

$$\begin{aligned} \omega &\ll s_t \pi\nu/d \quad \text{for} \quad \nu \neq 0, \\ \omega &\ll s_t k_\perp \quad \text{for} \quad \nu = 0. \end{aligned} \tag{3}$$

Here, s_t is the minimum phase velocity of transverse elastic vibrations propagating in the specified plane of an infinite crystal (calculated without regard for magnetoelastic interaction). Since $s_t/c \approx 10^{-5}$ (c is the speed of light), the condition in Eq. (3) for bulk magnons with mode index ν and minimum phase velocity c_m should be supplemented by the condition $s_t \gg c_m$, which is the case, e.g., in low-temperature AFMs ($T_N < T_D$). In this case, a traveling bulk spin wave will be accompanied not only by a long-range magnetic dipole field but also by a long-range field of quasi-static magnetoelastic deformations. However, in the calculations performed in [7–10], it was taken into account that the effect of magnetic dipole interaction on the magnon spectrum is decreased and, at the same time, the effect of magnetoelastic interaction is enhanced by an exchange in the exchange-collinear AFM in a magnetic field much lower than the sublattice exchange field. This makes it possible, as a first approximation, to neglect the effect of magnetic dipole interaction in comparison with the effect of magnetoelastic interaction when considering the magnon spectrum of a finite AFM in which the ferromagnetism vector $\mathbf{m}$ and the antiferromagnetism vector $\mathbf{l}$ in the ground state satisfy the inequality

$$|\mathbf{m}| \ll |\mathbf{l}|. \tag{4}$$

In the general case, in addition to elastostatic and inhomogeneous exchange interactions, there is magnetic dipole interaction in a real magnet. However, an analysis of the influence of the lattice on the bulk dipole–exchange spin dynamics of a low-temperature AFM has not yet been made in the case of $0 \leq \xi^2 \leq 1$ and the fulfillment of the elastostatic criterion in Eq. (3). The objective of this paper is to investigate the additional anomalies that are produced by the lattice under conditions (3) in the spectrum of traveling bulk dipole–exchange spin waves in a plate of an AFM with $T_N < T_D$.

2. BASIC RELATIONS

Following [8], we consider a two-sublattice AFM (the sublattice magnetizations are denoted by $\mathbf{M}_{1,2}$ with $|\mathbf{M}_1| = |\mathbf{M}_2| = M_0$) with orthorhombic magnetic [11] and elastic anisotropy. We use a phenomenological approach in which the Lagrangian of the AFM includes the interaction between the spin and elastic subsystems and is expressed in terms of the ferromagnetism vector $\mathbf{m}$ and the antiferromagnetism vector $\mathbf{l}$ in the form [6, 8]

$$\begin{aligned} L = M_0^2 \Bigg[\frac{\alpha}{2c_m^2}\left(\frac{\partial l}{\partial t}\right)^2 - \frac{\alpha}{2}(\nabla l)^2 - 0.5\beta_x l_x^2 \\ - 0.5\beta_z l_z^2 - B_{iklm} l_i l_k u_{ik} \Bigg] - c_{klm} u_{ik} u_{lm} + 0.5\rho\left(\frac{\partial \mathbf{u}}{\partial t}\right)^2, \end{aligned} \tag{5}$$

$$c^2 \equiv \alpha\delta\omega_s^2/4,$$

where u_{ik} is the elastic strain tensor; $\mathbf{m} = \mathbf{M}_1 + \mathbf{M}_2$; $\mathbf{l} = \mathbf{M}_1 - \mathbf{M}_2$; δ and α are the homogeneous and inhomogeneous exchange constants, respectively; B and c are the magnetostriction and elastic constant tensors, respec-

tively; β_x and β_z are the magnetic anisotropy constants; ρ is the density; and g is the gyromagnetic ratio.

Throughout this paper, the inequality $\omega \ll \omega_E$ is assumed to be satisfied, with ω_E being the exchange frequency. Following [6], it can be shown that, when inequality (4) takes place, both the linear and nonlinear spin dynamics of the AFM under study with magnetoelastic and magnetic dipole interactions can be described by a closed set of dynamic equations relating the antiferromagnetism vector **l**, the elastic lattice displacements **u**, and the magnetostatic potential ϕ. This reduced set is valid for any amount of deviation of the antiferromagnetism vector **l** from its equilibrium orientation. In what follows, we assume that

$$|\beta_z| \gg \beta_x > 0 \quad \beta_z < 0. \tag{6}$$

This condition is characteristic of AFMs of the easy-plane type. Under this assumption, when analyzing the magnetoacoustic effects in the case of $0 \le \xi^2 \le 1$, it is sufficient [2, 3, 6] to study only the low-frequency spin-wave dynamics of the crystal at hand ($\mathbf{l} \parallel x$) and to ignore the indirect coupling [via the magnetic dipole and magnetoelastic fields] between the high-frequency ($\tilde{l}_z \neq 0$, $\tilde{m}_y \neq 0$) and low-frequency ($l_y \neq 0$, $\tilde{m}_z \neq 0$) branches of the magnon spectrum of an infinite AFM described by Eqs. (5) and (6).[1]

The dispersion relation that describes the spectrum of normal magnetoelastic vibrations ($\tilde{l}_y \neq 0$, $\tilde{m}_z \neq 0$) of an infinite AFM described by Eqs. (5) and (6) with magnetic dipole, magnetoelastic, and exchange interactions for an arbitrary direction of $\mathbf{k}_\perp$ is found to be

$$\begin{aligned}&(\omega_m^2 - \omega^2)G\\ &- \omega_{me}^2(c_{66}k_y^2 G_{11} + k_x^2 G_{22} - 2k_x k_y G_{12}) = 0,\end{aligned} \tag{7}$$

where $G \equiv \det|\Gamma_{ik}|$, $\Gamma_{ik} \equiv \Lambda_{ik} - \rho\omega^2\delta_{ik}$ with $i, k = 1$–3; G_{ik} is the algebraic adjunct of the element (i, k) of the determinant G; $\hat{\Lambda}$ is the Christoffel tensor [12]; $\omega_0^2 \equiv c_m^2\beta_x/\alpha$; $\mathbf{k}^2 \equiv k_x^2 + k_y^2 + k_z^2$; and $\omega_m^2 \equiv \omega_0^2 + \omega_{me}^2 + c_m^2\mathbf{k}^2$. If the plane of wave propagation coincides with one of the coordinate planes, then, as follows from Eq. (7), the dispersion relations of magnetoelastic waves involving only low-frequency magnon modes ($\tilde{l}_y \neq 0$, $\tilde{m}_z \neq 0$) for $\mathbf{k} \in xz$ ($k_y = 0$) and $\mathbf{k} \in yz$ ($k_x = 0$) coincide, except for the substitution $k_x \longrightarrow k_y$ ($c_{44} \longrightarrow c_{55}$). For example, in the case of $\mathbf{k} \in xz$ ($k_y = 0$), we have

$$\begin{aligned}&(\omega_m^2 - \omega^2)(c_{66}k_x^2 + c_{44}k_z^2 - \omega^2\rho) - \xi^2 c_{66}k_x^2\omega_m^2 = 0,\\ &\xi^2 \equiv \omega_{me}^2/\omega_m^2.\end{aligned} \tag{8}$$

[1] The amplitude of small oscillations of a quantity A about its equilibrium value is designated as $\tilde{A}$.

It should be noted that a magnetoelastic wave propagating in this plane is accompanied by a quasi-static magnetic dipole field; that is, it is a magnetic-dipole active wave. In the case of $\mathbf{k} \in xy$ ($k_z = 0$), as follows from Eq. (7), the corresponding normal magnetoelastic wave is not magnetic-dipole active:

$$\begin{aligned}&(c_{11}k_x^2 + \bar{c}_{66}k_y^2 - \omega^2\rho)(\bar{c}_{66}k_x^2 + c_{22}k_y^2 - \omega^2\rho)\\ &\quad - (c_{12} + \bar{c}_{66})^2 k_x^2 k_y^2 = 0,\\ &\bar{c}_{66} \equiv c_{66}(\omega_m^2 - \omega^2 - \omega_{me}^2)(\omega_m^2 - \omega^2)^{-1}.\end{aligned} \tag{9}$$

In what follows, we restrict our consideration to the case of $\mathbf{k} \in xy$, because in this geometry, as follows from Eq. (9), the influence of the lattice on the magnon spectrum is the most significant. We note that, for an AFM described by Eq. (5), the result that a magnetoelastic wave with $\mathbf{k} \in xy$ ($\mathbf{l} \parallel x$) is not magnetic-dipole active is not associated with approximation (6). A magnetoelastic wave with $\mathbf{k} \in xy$, $\tilde{l}_y \neq 0$, and $\tilde{m}_x \neq 0$ ($\mathbf{l} \parallel x$) can become magnetic-dipole active in the presence of a Dzyaloshinski interaction of the type $D(m_x l_y - m_y l_x)$ even in the case of $\mathbf{H} = 0$. The corresponding dispersion relation for normal magnetoelastic waves has the same form as in Eqs. (7) and (9), but now we have

$$\omega_m^2 \longrightarrow \omega_{*m}^2 \equiv \omega_0^2 + \omega_D^2 k_x^2 k^{-2} + \omega_{me}^2 + c_m^2\mathbf{k}^2. \tag{10}$$

Our interest is in the spin dynamics of a finite AFM in which the magnetoelastic, magnetostatic, and inhomogeneous exchange interactions are all present. For an antiferromagnetic $2d$ thick plate, the dynamic equations must be supplemented by the corresponding boundary conditions. We assume that the normal **n** to the surface of the plate is directed along one of the coordinate axes in the xy plane. If the magnetic moments at the surface of the plate are rigidly fixed, the exchange boundary conditions have the form [13] (ζ is the coordinate along the normal **n** and $2d$ is the thickness of the plate)

$$\tilde{l}_y = 0, \quad \zeta = \pm d. \tag{11}$$

For the sake of simplicity, in both cases of $\mathbf{n} \parallel x$ and $\mathbf{n} \parallel y$ ($\mathbf{k} \in xy$), the boundary conditions for the elastic variables at both surfaces of the plate are taken to correspond to a boundary with tangential slipping [14]:

$$(\tilde{u}n) = 0, \quad [ns] = 0, \quad s_i = \sigma_{ik}n_k, \quad \zeta = \pm d. \tag{12}$$

Physically, these conditions correspond to a fully incoherent boundary [15] between two media, one of which (medium 2) is absolutely rigid. If the plate separates two superconducting half-spaces ($\zeta > d$ and $\zeta < -d$) for which the London penetration depth is λ, then the corresponding electrodynamic boundary condition for the magnetostatic potential ϕ can be written in the form

$$\partial\phi/\partial\xi + b\phi = 0, \quad b = k_\perp \tanh(k_\perp\lambda), \quad \zeta = \pm d. \tag{13}$$

3. THE SPECTRUM OF MAGNETOELASTIC WAVES IN AN ANTIFERROMAGNETIC PLATE

In order to solve the boundary-value problem formulated above, we use a method developed in [16, 17] when studying the effect of magnetic dipole interaction on the exchange magnon spectrum in a thin ferromagnetic film. For the magnetostatic equations ($\omega/c \longrightarrow 0$) with boundary conditions (13) in the case of $\mathbf{k} \in xy$ ($\mathbf{n} \parallel y$), the relation between the amplitude of the magnetostatic potential ϕ and the amplitude of oscillations of the y component of the antiferromagnetism vector $\mathbf{l}$ is determined by the Green's function:

$$\Theta(\zeta, t) \equiv \begin{cases} \cosh(k_\perp(t-d+\zeta_*)) \\ \times \cosh(k_\perp(\zeta+d+\zeta_*))/\Delta, \quad -d \le \zeta \le t \\ \cosh(k_\perp(t+d+\zeta_*)) \\ \times \cosh(k_\perp(\zeta-d+\zeta_*))\Delta, \quad t \le \zeta \le d, \end{cases}$$
$$k_\perp \tanh(\zeta_* k_\perp) = b, \quad \Delta \equiv k_\perp \sinh(2k_\perp d) \tag{14}$$

(the spatial magnetization distribution in the plate is assumed to be given). Using Eq. (14), one can eliminate the variables related to the magnetostatic potential ϕ. Therefore, it remains to solve the magnetoelastic boundary-value problem with only exchange [Eq. (11)] and elastic [Eq. (12)] boundary conditions for a set of three equations, one of which is an integro-differential equation. For both cases of $\mathbf{n} \parallel y$ and $\mathbf{n} \parallel x$ ($\mathbf{k} \in xy$), we will seek a solution to the magnetoelastic boundary-value problem in the form of an expansion in terms of the eigenfunctions of the exchange boundary-value problem in Eq. (11) (η is the coordinate along the propagation direction of a spin wave, $\kappa_\nu \equiv \pi\nu/d$, $\nu = 1, 2, \ldots$):

$$\tilde{l}_y = \sum_\nu A_\nu \sin(\kappa_\nu \zeta) \exp(i\omega t - ik_\perp \eta). \tag{15}$$

As a result, a dispersion relation describing the spectrum of bulk magnetostatic magnetoelastic vibrations of an antiferromagnetic plate with $\mathbf{k} \in xy$ ($\tilde{l}_y$, $\tilde{m}_z \neq 0$) and boundary conditions (11) and (12) is found in the form of an infinite set of linear algebraic equations for the unknown amplitudes A_ν. In particular, for $\mathbf{n} \parallel y$, this set of equations has the form

$$(W_{\nu\nu}(k_\perp) - \omega^2)A_\nu - W_{\nu\rho}(k_\perp)A_\rho = 0, \quad \nu \neq \rho, \quad \nu, \rho = 1, 2, \ldots, \tag{16}$$

$$W_{\nu\nu}(k_\perp) = \omega_0^2 + \omega_{me}^2 R_\nu + \omega_D^2 R_{\nu\nu} + c_m^2(k_\perp^2 + \kappa_\nu^2),$$
$$W_{\nu\rho}(k_\perp) = \omega_D^2 P R_{\nu\rho},$$
$$R_\nu \equiv 1 - c_{66}(\kappa_\nu^2 G_{11}^* + k_\perp G_{22}^* - 2G_{12}^* \kappa_\nu k_\perp)/(\rho G^*), \tag{17}$$

$$R_{\nu\nu} = k_\perp^2 \int_{-d}^{d} dy \sin(\kappa_\nu y) \int_{-d}^{d} dt \Theta(y, t) \sin(\kappa_\nu t),$$
$$R_{\nu\rho} = k_\perp^2 \int_{-d}^{d} dy \sin(\kappa_\rho y) \int_{-d}^{d} dt \Theta(y, t) \sin(k_\nu t).$$

Here, $G_{ik}^* \equiv G_{ik}$; $G^* \equiv G$ if $k_x = k_\perp$, $k_y = \kappa_\nu$, and $k_z = 0$. The set of equations (16) and (17) for A_ν has a nontrivial solution if its determinant is equal to zero. An analysis shows that, for $b = 0$ (a perfect superconductor or superdiamagnet [18]) and arbitrary ν, ρ, and $k_\perp$, we have $W_{\nu\rho} = 0$ if $D = 0$ (for both cases of $\mathbf{n} \parallel x$ and $\mathbf{n} \parallel y$). If $D \neq 0$, we also have $W_{\nu\rho} = 0$ for any value of ν, ρ, and $k_\perp$, but now only for $\mathbf{n} \parallel y$ ($b = 0$, $\mathbf{k} \in xy$). In all these cases, the spectrum of bulk magnetoelastic waves traveling along the antiferromagnetic plate is found from Eqs. (16) and (17) to be given by the relations

$$\omega^2 - W_{\nu\nu}(k_\perp) = 0, \quad \nu = 1, 2, \ldots \tag{18}$$

If the dimensionless magnetoelastic coupling parameter is small ($\xi^2 \ll 1$), then, to the zeroth order in ξ^2 and for any values of ν and $k_\perp$, Eqs. (17) and (18) determine two sets of dispersion relations:

$$\Omega_{m\nu}^2 = \omega_0^2 + \omega_D^2 k_x^2 \mathbf{k}^{-2} + c_m^2 \mathbf{k}^2, \tag{19}$$

$$(c_{11}k_x^2 + c_{66}k_y^2 - \omega^2\rho)(c_{66}k_x^2 + c_{22}k_y^2 - \omega^2\rho) - (c_{12} + c_{66})^2 k_x^2 k_y^2 = 0. \tag{20}$$

In Eqs. (19) and (20), $k_x = \kappa_\nu$ and $k_y = k_\perp$ for $\mathbf{n} \parallel x$ and $k_x = k_\perp$ and $k_y = \kappa_\nu$ for $\mathbf{n} \parallel y$ ($\mathbf{k} \in xy$).

Equation (19) describes the spectrum of bulk dipole–exchange modes with $\tilde{l}_y$, $\tilde{m}_z \neq 0$ traveling along the magnetic plate ($\mathbf{k} \in xy$). The spectrum of normal traveling elastic waves polarized in the sagittal plane of the plate (of an orthorhombic crystal) is given by Eq. (20) in the case of boundary conditions (12) at both surfaces of the plate.

Analysis of Eq. (19) shows that the spectrum of dipole–exchange waves with $k_\perp \neq 0$ ($\mathbf{k} \in xy$) has the following features depending on the relative orientation of the vectors $\mathbf{n}$ and $\mathbf{l}$ in the xy plane: (i) one (for $\mathbf{l} \parallel \mathbf{n}$) or two (for $\mathbf{l} \perp \mathbf{n}$) inflection points on the dispersion curve [$\partial\Omega_{m\nu}^2(k_\perp)/\partial k_\perp^2 = 0$], (ii) a maximum at a point $k_\perp \neq 0$ [$\partial\Omega_{m\nu}(k_\perp)/\partial k_\perp = 0$] for $\mathbf{n} \parallel \mathbf{l}$, and (iii) a crossover (degeneracy) point for bulk dipole–exchange waves with mode indices ν and ρ ($\nu \neq \rho$): $\Omega_{m\nu}(k_\perp) = \Omega_{m\rho}(k_\perp)$ for $b = 0$ and $\mathbf{l} \perp \mathbf{n}$. In addition, from Eqs. (16)–(20), it follows that, in the approximation in question ($\varepsilon^2 = 0$) for both cases of $\mathbf{n} \parallel y$ and $\mathbf{n} \parallel x$, the spectrum of bulk magnetoelastic vibrations in Eqs. (16) and (17) has degeneracy points of the type $\Omega_{m\nu}(k_\perp) = \Omega_{\mathrm{ph},\rho}(k_\perp)$ at some $k_\perp \neq 0$.

Thus, using the coupled-mode method, we arrived at the spectrum of bulk magnetoelastic vibrations in Eqs. (16) and (17), from which it follows that, in the general case, the off-diagonal elements $W_{\nu\rho} \neq 0$ in Eqs. (16) and (17) can be considered a perturbation on the zeroth approximation ($W_{\nu\rho} \neq 0$) given by Eqs. (18)–(20). The presence of $W_{\nu\rho} \neq 0$ leads to interaction between bulk magnetoelastic waves with mode indices ν and ρ. Therefore, if the modes with given indices ν and ρ are degenerate in Eq. (18), then for $W_{\nu\rho} \neq 0$, the crossover points will be absent and, in the vicinity of the specific crossover points determined at $W_{\nu\rho} = 0$ from Eq. (18) by the relations $\Omega_{m\nu}(k_\perp) = \Omega_{m\rho}(k_\perp)$ or $\Omega_{m\nu}(k_\perp) = \Omega_{\mathrm{ph},\rho}(k_\perp)$, the spectrum of bulk magnetoelastic vibrations can be represented [using Eq. (17)] in the form

$$(W_{\nu\nu} - \omega^2)(W_{\rho\rho} - \omega^2) - W_{\nu\rho}^2 = 0 \quad (\nu \neq \rho). \quad (21)$$

From Eqs. (19)–(21), it follows that, for a given mode ν of bulk magnetoelastic vibrations, spectra (19) and (20) will have no degenerate point at any value of $k_\perp$ if one of the following conditions is fulfilled:

$$\omega_0^2 d^2 \gg (s_l^2 - c_m^2)\pi^2\nu^2, \quad (22)$$

$$\omega_0^2 d^2 \ll (s_t^2 - c_m^2)\pi^2\nu^2. \quad (23)$$

From the point of view of the influence of the lattice on the dynamics of mode ν in the antiferromagnetic plate at hand, Eq. (22) corresponds to the frozen-lattice approximation [2] and is valid not only for high-temperature AFMs ($T_N > T_D$) for any value of d and ν but also for a low-temperature AFM ($T_N < T_D$) for those modes ν for which the ratio $\omega_0 d/\nu$ is sufficiently large. In this case, the inequality $\Omega_{m\nu}^2(k_\perp) \gg \Omega_{\mathrm{ph},\rho}^2(k_\perp)$ takes place for the spectra in Eqs. (19) and (20). As for the condition in Eq. (23), it can be fulfilled only for magnons in a low-temperature AFM, and the ratio $\omega_0 d/\nu$ in Eq. (23) must be sufficiently small in this limiting case. This corresponds to the free-lattice case [2], and for the spectra in Eqs. (19) and (20), we have $\Omega_{m\nu}^2(k_\perp) \ll \Omega_{\mathrm{ph},\rho}^2(k_\perp)$ in this case. It should be noted that, in order for different limiting cases of the magnetoelastic dynamics of a plate for $\nu \neq 0$ to be realized, it is not necessary, in contrast to the case of an infinite magnet, to choose the appropriate values of the wavelength; the limiting cases can also be achieved by varying the plate thickness in both cases of $c_m < s_t$ and $c_m > s_t$.[2]

Thus, relations (22) and (23) can be used to analyze the effect of the lattice on the spectrum of traveling bulk spin waves with $\mathbf{k} \in xy$ ($\mathbf{n} \parallel x$ or $\mathbf{n} \parallel y$) away from magnetoacoustic resonance $\Omega_{m\nu}(k_\perp) = \Omega_{\mathrm{ph},\rho}(k_\perp)$ in plates of a high-temperature and a low-temperature AFM characterized by Eqs. (11)–(13). In this case, the magnon spectrum of an antiferromagnetic plate described by Eq. (5) is determined with satisfactory accuracy by the following relation, which is derived from Eqs. (16) and (17) in both cases of $\mathbf{n} \parallel x$ and $\mathbf{n} \parallel y$:

$$\Omega_{m\nu}^2(k_\perp) = W_{\nu\nu}. \quad (24)$$

We note that, for dipole–exchange spin waves in a plate of a low-temperature AFM, neglect of the degeneracy points of the type $\Omega_{m\nu}(k_\perp) = \Omega_{\mathrm{ph},\rho}(k_\perp)$ is well founded for any values of $k_\perp$ for those lowest modes in Eq. (19) for which the excitation frequency ω satisfies the inequality

$$\omega < s_t/d. \quad (25)$$

In this case, only the zeroth mode of bulk longitudinal elastic waves (dilatation wave) can propagate along the magnetic plate at hand because of the elastic boundary conditions (12), and this mode, as is well known [2, 3], virtually does not interact with bulk spin waves in an antiferromagnetic crystal described by Eq. (5). Thus, if condition (22) or (23) is fulfilled, then from Eqs. (16) and (17) it follows that, for $\mathbf{n} \parallel x$ or $\mathbf{n} \parallel y$ ($\mathbf{k} \in xy$) and for any value of the wave number $k_\perp$, the bulk magnon spectrum calculated with allowance for magnetoelastic, magnetic-dipole, and inhomogeneous exchange interactions in an antiferromagnetic plate with boundary conditions (11)–(13) is described by the expression

$$\Omega_{m\nu}^2 = \omega_0^2 + \omega_{me}^2 + \omega_D^2 k_x^2 \mathbf{k}^{-2} + c_m^2 \mathbf{k}^2 \quad (T_N > T_D), \quad (26)$$

in the case of condition (22) and by

$$\Omega_{m\nu}^2 = \omega_0^2 + \omega_{me}^2 k_x^2 k_y^2 (p k_x^4 + q k_y^4 + 2r k_x^2 k_y^2)^{-1} + \omega_D^2 k_x^2 \mathbf{k}^{-2} + c_m^2 \mathbf{k}^2, \quad (T_N < T_D),$$
$$p \equiv c_{11}c_{66}/(c_{11}c_{22} - c_{12}^2), \quad q \equiv c_{22}c_{66}/(c_{11}c_{22} - c_{12}^2),$$
$$2r \equiv 1 - 2c_{22}c_{66}/(c_{11}c_{22} - c_{12}^2) \quad (27)$$

in the case of condition (23). In Eqs. (26) and (27), as before, $k_x = \kappa_\nu$ and $k_y = k_\perp$ for $\mathbf{n} \parallel x$ and $k_x = k_\perp$ and $k_y = \kappa_\nu$ for $\mathbf{n} \parallel y$ ($\mathbf{k} \in xy$).

In order to investigate in more detail the contributions from the non-Heisenberg spin–spin interactions to the formation of the spectrum of traveling bulk spin waves in a plate of an AFM, we will analyze Eqs. (26) and (27) in the limit of $\alpha \longrightarrow 0$. This corresponds to the exchangeless approximation, i.e., to the case where the effects of inhomogeneous exchange interaction are ignored [13].

4. SPIN DYNAMICS OF AN ANTIFERROMAGNETIC FILM IN THE EXCHANGELESS APPROXIMATION

First we consider a crystal which is elastically isotropic in the sagittal plane ($\mathbf{k}_\perp, \mathbf{n} \in xy$). In this case, as

[2] In what follows, when discussing the spin dynamics of a plate of a high-temperature or a low-temperature AFM, conditions (22) and (23) are assumed to be fulfilled, respectively.

is well known, $c_{11} = c_{22}$ and $c_{11} - c_{12} = 2c_{66}$ and from Eqs. (26) and (27) it follows that in the limit of $\alpha \longrightarrow 0$ the spectrum of exchangeless bulk magnons with $\mathbf{k} \in xy$ ($k_z = 0$) in a thin antiferromagnetic film in which $D \neq 0$, and the magnetic-dipole and elastostatic mechanisms of spin–spin interaction operate is described by the following expressions (for both cases of $\mathbf{n} \parallel y$ and $\mathbf{n} \parallel x$) depending on the relationship between the Néel temperature T_N and Debye temperature T_D:

$$\Omega_{m\nu}^2(k_\perp) = \omega_0^2 + \omega_{me}^2 + \omega_D^2 k_z^2 \mathbf{k}^{-2}, \quad (T_N > T_D), \quad (28)$$

$$\Omega_{m\nu}^2(k_\perp) = \omega_0^2 + 4\omega_{*me}^2 k_x^2 k_y^2 k^{-4} + \omega_D^2 k_x^2 \mathbf{k}^{-2}, \quad (T_N < T_D). \quad (29)$$

In Eqs. (28) and (29), $k_x = \kappa_\nu$ and $k_y = k_\perp$ for $\mathbf{n} \parallel x$, $k_x = k_\perp$ and $k_y = \kappa_\nu$ for $\mathbf{n} \parallel y$ ($\mathbf{k} \in xy$); and $\omega_{*me}^2 \equiv \omega_{me}^2(1 - c_{66}/c_{11})$. From Eqs. (28) and (29), it follows that the spectrum of exchangeless spin waves in a film of a low-temperature AFM [Eq. (29)] has additional anomalies in comparison with the spectrum in Eq. (28). These extra anomalies occur because, in this case, the magnon dispersion is caused not only by magnetic-dipole interaction but also by indirect spin–spin interaction via the long-range field of quasi-static magnetoelastic deformations. Therefore, in the exchangeless approximation, dispersion of spin waves of the type under discussion ($\tilde{l}_y \neq 0$; $\mathbf{k}_\perp$, $\mathbf{n} \in xy$) in a thin film of an orthorhombic AFM described by Eq. (5) can arise even in the case of $D = 0$ (where the mode is not magnetic-dipole-active). An analysis of Eqs. (28) and (29) in the case of $D = 0$ shows that, in the geometry chosen, for $T_N < T_D$ and under condition (23), the elastostatic spin–spin interaction leads to anomalies in the dispersion law of a traveling spin wave which are absent in the case of a high-temperature AFM, as well as in other geometries of the easy-plane-type AFM under study with $T_N < T_D$. In particular, for a given mode index ν, for both cases of $\mathbf{n} \parallel x$ and $\mathbf{n} \parallel y$, an exchangeless spin wave characterized by the spectrum in Eq. (29) is of the direct-wave type [$\partial\Omega_{m\nu}(k_\perp)/\partial k_\perp > 0$] for $k_\perp < k_{*\nu}$ and it is of the back-wave type [$\partial\Omega_{m\nu}(k_\perp)/\partial k_\perp < 0$] for $k_\perp > k_{*\nu}$; at $k_\perp = k_{*\nu} \neq 0$, we have $\partial\Omega_{m\nu}(k_\perp)/\partial k_\perp = 0$, which corresponds to a maximum on the dispersion curve of this mode of spin waves. If $\nu < \rho$, we have $\Omega_{m\nu}(k_\perp) > \Omega_{m\rho}(k_\perp)$ for $k_\perp < k_{*\nu}$ and $\Omega_{m\nu}(k_\perp) < \Omega_{m\rho}(k_\perp)$ for $k_\perp > k_{*\nu}$. In addition, in contrast to the case of the spectrum in Eq. (28), even in a thin film of a low-temperature AFM, dispersion curves described by Eq. (29) for modes ν and ρ can intersect at $k_\perp = k_{\nu\rho}$, $\Omega_{m\nu}(k_{\nu\rho}) = \Omega_{m\rho}(k_{\nu\rho})$, because of the elastostatic mechanism of dispersion of exchangeless magnons. If $\nu < \rho$, we have $k_{*\nu} < k_{\nu\rho} < k_{*\rho}$. In this case, near the crossover point $k_\perp \approx k_{\nu\rho}$, mode ν is of the direct-wave type, while mode ρ is of the back-wave type. The accumulation points of the spectrum in Eq. (29) for $D = 0$ are ω_0 in both limits of $k_\perp \longrightarrow 0$ and $k_\perp \longrightarrow \infty$; that is, in both these limits, $|\Omega_{m\nu}(k_\perp) - \Omega_{m\rho}(k_\perp)| \longrightarrow 0$. From Eq. (29), it follows that, if for $\mathbf{n} \parallel x$ or $\mathbf{n} \parallel y$ the condition $4\omega_{me*}^2 > \omega_D^2$ is fulfilled, then in the case where the elastostatic and magnetic-dipole mechanisms of indirect spin–spin interaction operate simultaneously in the crystal, the spectrum of exchangeless bulk magnons remains qualitatively the same as the spectrum in a plate of a low-temperature AFM in Eq. (29) for $D = 0$ ($\mathbf{l} \parallel x$); this was discussed above. The only difference is that for $D \neq 0$, the accumulation points at $k_\perp \longrightarrow 0$ and $k_\perp \longrightarrow \infty$ in the magnon spectrum in Eq. (29) do not coincide: $\Omega_{m\nu}(k_\perp \longrightarrow 0) < \Omega_{m\nu}(k_\perp \longrightarrow \infty)$ for $\mathbf{l} \perp \mathbf{n}$ and $\Omega_{m\nu}(k_\perp \longrightarrow 0) > \Omega_{m\nu}(k_\perp \longrightarrow \infty)$ for $\mathbf{l} \parallel \mathbf{n}$. In the case of $4\omega_{*me}^2 < \omega_D^2$, the spectrum of exchangeless bulk magnons in question is independent of the relationship between the Néel temperature and the Debye temperature of the antiferromagnetic crystal.

If we take into account the anisotropy of the elastic moduli in the sagittal plane xy ($D \neq 0$), the spectrum of exchangeless bulk magnons in a plate of an orthorhombic AFM will have the following form instead of Eq. (29) [as in Eqs. (28) and (29), we have $k_x = \kappa_\nu$ and $k_y = k_\perp$ for $\mathbf{n} \parallel x$ and $k_x = k_\perp$ and $k_y = \kappa_\nu$ for $\mathbf{n} \parallel y$ ($\mathbf{k} \in xy$)]:

$$\Omega_{m\nu}^2 = \omega_0^2 + \omega_{me}^2 k_x^2 k_y^2 (pk_x^4 + qk_y^4 + 2rk_x^2 k_y^2)^{-1} + \omega_D^2 k_x^2 \mathbf{k}^{-2}. \quad (30)$$

An analysis of Eq. (30) shows that in the case where the elastostatic and magnetic-dipole mechanisms of the formation of the spectrum of exchangeless bulk magnons with $\mathbf{k} \in xy$ ($\tilde{l}_y$, $\tilde{m}_z \neq 0$) operate simultaneously, then for $\mathbf{n} \parallel y$ or $\mathbf{n} \parallel x$, the dispersion curve of mode ν can have not only a maximum (as for $D = 0$) but also a minimum at some values of $k_\perp \neq 0$. The corresponding wavenumbers $k_{\nu\pm}$ are real positive roots of the equation $\partial\Omega_{m\nu}(k_\perp)/\partial k_\perp = 0$, where $\Omega_{m\nu}(k_\perp)$ is given by Eq. (30). In particular, a dispersion curve of bulk magnon mode ν of Eq. (30) will have such a shape if the following conditions are fulfilled:

$$\begin{aligned} q, 2r &\ll p \quad (\mathbf{n} \parallel y), \\ p, 2r &\ll q \quad (\mathbf{n} \parallel x). \end{aligned} \quad (31)$$

An analysis of expressions for $k_{\nu\pm}^2$ shows that, as $D \longrightarrow 0$, we have $k_{\nu+} \longrightarrow \infty$ and $k_{\nu-} \longrightarrow k_{*\nu}$ for $\mathbf{n} \parallel y$ and $k_{\nu-} \longrightarrow 0$ and $k_{\nu+} \longrightarrow k_{*\nu}$ for $\mathbf{n} \parallel x$.

In addition, from Eq. (30) at $\alpha \longrightarrow 0$, it follows that, in the case where the magnetic-dipole and elastostatic mechanisms of exchangeless magnon dispersion operate simultaneously in a thin film of a low-temperature AFM, two crossover points can exist at some values of $k_\perp \neq 0$ for given modes ν and ρ of exchangeless bulk spin waves described by Eq. (29). The corresponding wavenumber values $k_\pm$ can be found from the equation

$\Omega_{m\nu}(k_{\nu\rho}) = \Omega_{m\rho}(k_{\nu\rho})$ and Eq. (30). In the formal limit of $D \longrightarrow 0$ (neglecting the Dzyaloshinski interaction), we have $k_- \longrightarrow k_{\nu\rho}$ and $k_+ \longrightarrow \infty$ for $\mathbf{n} \parallel y$ and $k_+ \longrightarrow k_{\nu\rho}$ and $k_- \longrightarrow 0$ for $\mathbf{n} \parallel x$.

If the relationship between the elastic constants of a magnet is opposite to that in Eq. (30), then for both cases of $\mathbf{n} \parallel y$ and $\mathbf{n} \parallel x$, the dispersion curve of any mode ν of exchangeless magnons described by Eq. (30) will have only one extremum (maximum) at $k_\perp \neq$ and given modes ν and ρ will have only one crossover point.

For sufficiently large values of D, the dispersion curves of the same magnon mode ν in a high-temperature AFM [Eq. (28)] and a low-temperature AFM [Eq. (30)] will be similar in character for a given relative orientation of the vectors **n** and **l**.

5. EFFECTS OF INHOMOGENEOUS EXCHANGE INTERACTION

To date, when analyzing the dispersion relations (26) and (27), we ignored the effects of inhomogeneous exchange interaction ($\alpha \longrightarrow 0$). From Eq. (26), it follows that, if $\alpha \neq 0$ ($c_m \neq 0$), then in a high-temperature AFM of the easy-plane type, the spectrum $\Omega_{m\nu}(k_\perp)$ of traveling bulk spin waves with $\mathbf{k} \in xy$ ($D \neq 0$) will have a contribution from the Heisenberg nonlocal spin–spin interaction in addition to the magnetic-dipole contribution. For this reason, in the case of $\mathbf{n} \parallel y$, the dispersion curves of the two given modes ν and ρ can have two crossover points at $k_\perp \neq 0$, $\Omega_{m\nu}(k_{\nu\rho}) = \Omega_{m\rho}(k_{\nu\rho})$. These points arise in the spectrum of bulk spin waves $\Omega_{m\nu}(k_\perp)$ only when the magnetic-dipole and inhomogeneous exchange spin–spin interactions are both present in the antiferromagnetic plate with $\mathbf{n} \parallel y$ (i.e., when $D \neq 0$ and $\alpha \neq 0$). In this case, we have $\partial\Omega_{m\nu}(k_\perp)/\partial k_\perp > 0$ for any values of $k_\perp$ and ν. In the case of $\mathbf{n} \parallel x$, as follows from Eq. (26), if the magnetic-dipole and Heisenberg spin–spin interactions are both taken into account, the dispersion curve of mode ν of dipole–exchange spin waves can have a minimum at $k_\perp \neq 0$. In addition, the dispersion curve can have one and two inflection points at $k_\perp \neq 0$ in the cases of $\mathbf{n} \parallel x$ and $\mathbf{n} \parallel y$, respectively. These points can be found from Eq. (26) and the condition $\partial^2\Omega_{m\nu}(k_\perp)/\partial k_\perp^2 = 0$.

In the case of a film of a low-temperature AFM, analysis of Eq. (27) shows that even without magnetic dipole interaction [i.e., at $D = 0$ in Eq. (27)], a combination of elastostatic and Heisenberg spin–spin interactions leads to significant changes in the spectrum of bulk magnons relative to its exchangeless limit ($\alpha \longrightarrow 0$) in Eqs. (29) and (30), namely, (i) to the appearance of two crossover points of the dispersion curves of elastic–exchange spin-wave modes ν and ρ and (ii) to the appearance of two extreme points at $k_\perp \neq 0$, one of which corresponds to a maximum and the other to a minimum on the $\Omega_{m\nu}(k_\perp)$ dispersion curve described by Eq. (27). If $D \neq 0$ in Eq. (27), then the magnetic-dipole mechanism of nonlocal spin–spin interaction, together with elastostatic and Heisenberg mechanisms, produces additional anomalies in the spectrum of the spin waves with $\mathbf{k} \in xy$ ($k_z = 0$) relative to the spectrum of pure elastic–exchange magnons investigated above (i.e., for $D = 0$). Analysis shows that even in the presence of a weak inhomogeneous exchange interaction, the accumulation points at $k_\perp \longrightarrow 0$ and $k_\perp \longrightarrow \infty$ in the spectrum of exchangeless bulk spin waves [Eqs. (28)–(30)] disappear and an additional crossover point arises in their stead for modes ν and ρ. For this to be the case, the condition $\Omega_{m\nu}(k_\perp) > \Omega_{m\rho}(k_\perp)$ must be fulfilled at this point for $\nu < \rho$ in the case of $\alpha = 0$. If in the no-exchange limit [Eqs. (28)–(30)] the mode of bulk spin waves is of the back-wave type in the vicinity of the short-wavelength point of accumulation, i.e., $\partial\Omega_{m\nu}(k_\perp)/\partial k_\perp < 0$, then a minimum can appear on the corresponding dispersion curve due to inhomogeneous exchange interaction. But if in the limit of $\alpha \longrightarrow 0$ the mode of bulk spin waves in the vicinity of the short-wavelength point of accumulation is of the direct-wave type, i.e., $\partial\Omega_{m\nu}(k_\perp)/\partial k_\perp > 0$, then an additional inflection point [$\partial^2\Omega_{m\nu}(k_\perp)/\partial k_\perp^2 = 0$] can appear on the corresponding dispersion curve when inhomogeneous exchange interaction is taken into account.

An analysis of Eqs. (26) and (27) shows that, in the case of $\alpha \neq 0$, if the mode index ν is sufficiently large or the thickness of the magnetic film $2d$ is small, then the $\Omega_{m\nu}(k_\perp)$ dispersion curve described by Eqs. (26) and (27) will correspond to a mode of the direct-wave type [$\partial\Omega_{m\nu}(k_\perp)/\partial k_\perp > 0$] for any value of the wavenumber $k_\perp$; this dispersion curve has no inflection points [$\partial^2\Omega_{m\nu}(k_\perp)/\partial k_\perp^2 = 0$] and no crossover points [$\Omega_{m\nu}(k_\perp) = \Omega_{m\rho}(k_\perp)$]. In particular, for a plate of a crystal which is elastically isotropic in the sagittal plane, the condition for simultaneous existence of a maximum and a minimum ($k_\perp \neq 0$) on the $\Omega_{m\nu}(k_\perp)$ dispersion curve of mode ν of bulk magnons for the antiferromagnetic plate at hand in the case where elastostatic, magnetic-dipole, and inhomogeneous exchange interactions are all taken into account has the form $16\omega_{me*}^2 c_m^2 \kappa_\nu^2 < (4\omega_{me*}^2 + \omega_D^2)^3/27$ for $\mathbf{n} \parallel x$ and $16\omega_{me*}^2 c_m^2 \kappa_\nu^2 < (4\omega_{me*}^2 - \omega_D^2)^3/27$ for $\mathbf{n} \parallel y$.

As is well known from crystal optics [19], when analyzing the reflection and refraction of a bulk normal wave at the interface of two media, the shape of the refraction (slowness) surface of the normal wave is of primary importance. Clearly, the local geometry of the wave-vector surface of the normal bulk waves under study also significantly affects the spectrum of normal vibrations of a finite crystal, because the spatial distribution of the amplitude of normal bulk vibrations is determined by the interference of bulk waves incident on and reflected from the boundaries of the crystal. In

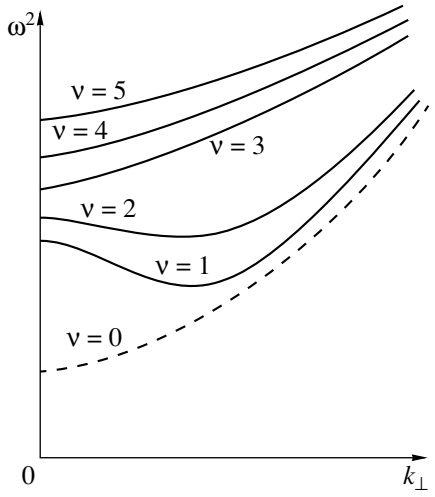

Fig. 1. Dispersion curves of dipole–exchange bulk spin waves in a plate of an elastically isotropic antiferromagnet of the easy-plane type ($T_N > T_D$), described by Eqs. (5), (6), and (11)–(13), with $\mathbf{n} \parallel \mathbf{l}$.

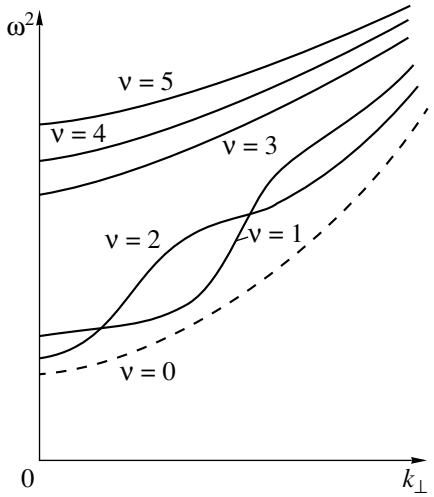

Fig. 2. Dispersion curves of dipole–exchange bulk spin waves in a plate of an elastically isotropic AFM of the easy-plane type ($T_N > T_D$), described by Eqs. (5), (6), and (11)–(13), with $\mathbf{n} \perp \mathbf{l}$.

the next section, we analyze the influence of magnetic-dipole, elastostatic, and inhomogeneous exchange interactions on the shape of the refraction surface of normal spin waves in an infinite magnet and the relationship between the local geometry of this surface and the anomalies of the bulk magnon spectrum investigated above in a thin film of a high-temperature or a low-temperature AFM.

6. THE SHAPE OF THE REFRACTION SURFACE

Since the wave vector of a spin wave described by Eqs. (26) and (27) lies in the *xy* plane, we will investigate the shape of the cross section of an isofrequency surface of the spin waves under discussion (ω = const; $\tilde{l}_y$, $\tilde{m}_z \neq 0$) in **k** space in the $k_x k_y$ sagittal plane. Using Eqs. (9) and (10) and the condition $\omega/s_t|\mathbf{k}| \longrightarrow 0$, we find that the cross section is described by the equations ($k_x^2/k^2 \equiv \cos^2\theta$, $\mathbf{k}^2 \equiv k_x^2 + k_y^2$, $\mathbf{l} \parallel x$, $D \neq 0$)

$$c_m^2\mathbf{k}^2 = \omega^2 - \omega_0^2 - \omega_D^2\cos^2\theta - \omega_{me}^2, \quad T_N > T_D, \tag{32}$$

$$\begin{gathered} c_m^2 k^2 = \omega^2 - \omega_0^2 - \omega_D^2\cos^2\theta \\ - \omega_{me}^2(1 - R(\theta)), \quad T_N < T_D, \\ R(\theta) \equiv c_{66}(\sin^2\theta\bar{\Lambda}_{11} + \cos^2\theta\bar{\Lambda}_{22} - 2\bar{\Lambda}_{12}\sin 2\theta) \\ \times (\bar{\Lambda}_{11}\bar{\Lambda}_{22} - \bar{\Lambda}_{12}^2)^{-1}. \end{gathered} \tag{33}$$

Here, $\bar{\Lambda}_{ik} \equiv \Lambda_{ik}(k_x \equiv k\cos\theta, k_y \equiv k\sin\theta)$.

An analysis of the extreme points of curves described by Eqs. (32) and (33) and a comparison with the results obtained above by analyzing the shape of dispersion curves described by Eqs. (26) and (27) shows that the appearance of crossover points or of a local extremum on the dispersion curve of mode ν of the guided magnons under study is associated with the presence of regions of $\partial\omega/\partial k_\perp = 0$ or $\partial\omega/\partial k_n = 0$ [$k_n \equiv (\mathbf{kn})$] in the cross section [described by Eqs. (32), (33)] of the refraction surface of a normal spin wave of the same polarization (in an infinite crystal) in the plane containing the vectors **n** and $\mathbf{k}_\perp$ [see Figs. 1, 2 for a high-temperature AFM described by Eqs. (5), (6) and Figs. 3, 4 for a low-temperature AFM described by Eqs. (5), (6)].[3]

As before, the directions of the vectors **n** and $\mathbf{k}_\perp$ are assumed to coincide with the coordinate axes (the *x* or *y* axis in the case at hand). In this case, the points of intersection of straight lines k_y = const or k_x = const and the refraction surface described by Eqs. (32) and (33) give information on the spectrum of the corresponding guided magnons with given wavenumber $k_\perp$, frequency ω, and mode index ν [the spectrum described by Eq. (26) or (27) in the case at hand] of a plate of an easy-plane-type AFM with $T_N > T_D$ or $T_N < T_D$. In particular, if the direction of the normal to the film surface **n** lying in the k_x, k_y plane coincides with the ordinate axis ($\mathbf{n} \parallel y$), the presence of points common to the $k_x = k_\perp$ straight line and the curve described by Eq. (32) or (33) is a necessary condition for the existence of a crossover point for dispersion curves described by Eqs. (26) and (27). The number of intersection points of the $k_x = k_\perp$ straight line and the curve of Eq. (32) or (33) determines the maximum number of spin-wave modes in Eq. (26) or (27) that can propagate along the *x* axis in

[3] In Figs. 1–4, it is assumed that $\mathbf{k} \in xy$, $W_{\nu\rho} \longrightarrow 0$ ($\nu \neq \rho$); for modes $\Omega_{m\nu}(k_\perp)$ with $\nu \geq 3$, condition (1) is assumed to be fulfilled.

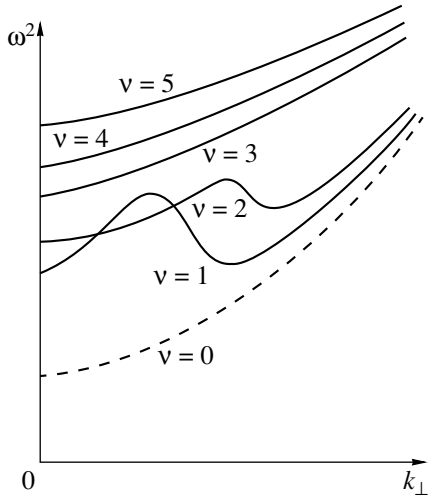

Fig. 3. Dispersion curves of dipole–exchange spin waves in a plate of an elastically isotropic AFM of the easy-plane type ($T_N < T_D$), described by Eqs. (5), (6), and (11)–(13), with $\mathbf{n} \parallel \mathbf{l}$.

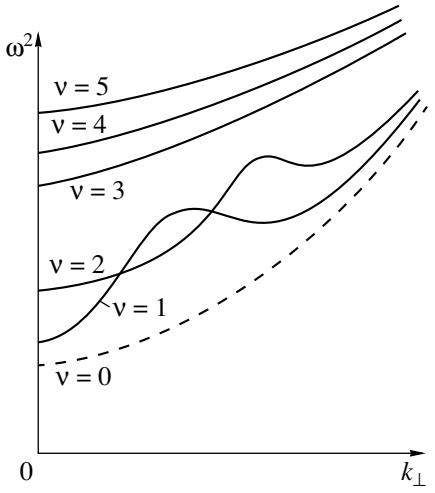

Fig. 4. Dispersion curves of dipole–exchange spin waves in a plate of an elastically isotropic AFM of the easy-plane type ($T_N < T_D$), described by Eqs. (5), (6), and (11)–(13), with $\mathbf{n} \perp \mathbf{l}$.

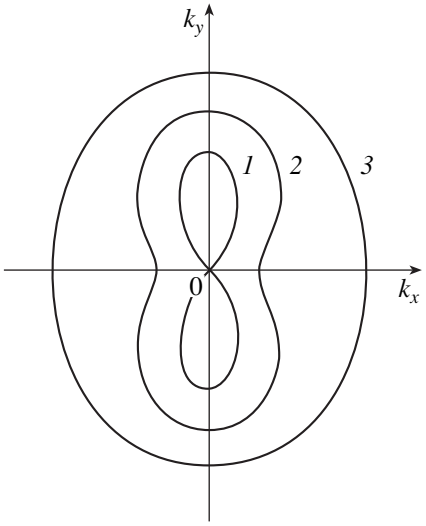

Fig. 5. Cross sections of isofrequency surfaces of a normal spin wave described by Eq. (26) by the *xy* plane for an infinite elastically isotropic AFM of the easy-plane type ($T_N > T_D$), described by Eqs. (5) and (6), with $\mathbf{l} \parallel x$: (*1*) $\omega_0^2 < \omega^2 - \omega_{me}^2 < \omega_0^2 + \omega_d^2$, (*2*) $\omega_0^2 + \omega_d^2 < \omega^2 - \omega_{me}^2 < \omega_0^2 + 2\omega_d^2$, and (*3*) $\omega_0^2 + \omega_{me}^2 + 2\omega_d^2 < \omega^2$.

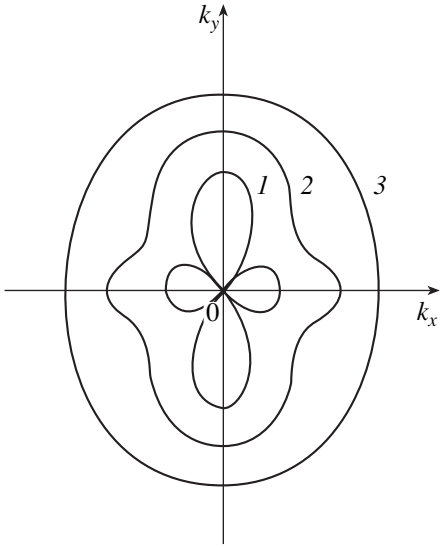

Fig. 6. Cross sections of isofrequency surfaces of a normal spin wave described by Eq. (27) by the *xy* plane for an infinite elastically isotropic AFM of the easy-plane type ($T_N < T_D$), described by Eqs. (5) and (6), with $\mathbf{l} \parallel x$: (*1*) $\omega_0^2 < \omega^2 < \omega_0^2 + \omega_{*me}^2$, (*2*) $\omega_0^2 + \omega_{*me}^2 < \omega^2 < \omega_0^2 + 5\omega_{*me}^2$, and (*3*) $\omega_0^2 + 5\omega_{*me}^2 < \omega^2$.

a $2d$ thick plate of the AFM under study and have the same wavenumber $k_\perp$ and frequency ω. In the same geometry, the points common to the curve of Eq. (32) or (33) and the $k_y = \kappa_\nu$ straight line determine the wavenumbers $k_\perp$ with which the guided magnon mode ν of the type in question and of frequency ω can propagate along a thin $2d$ thick film of the AFM under study. Since the outward normal to the refraction surface is aligned with the group velocity of the wave [14, 19], an investigation of the local geometry of the cross section of the isofrequency surface described by Eqs. (32) and (33), together with the results of analysis of Eqs. (26) and (27), allows one to determine the type (direct wave or back wave) of guided magnons corresponding to a

given region (characterized by given ω, κ_ν, and $k_\perp$) of the dispersion curve described by Eqs. (26) and (27). In particular, in the case of $\mathbf{k} \in xy$ considered in this paper, a bulk spin wave described by Eqs. (26) and (27) and propagating along a film with $\mathbf{n} \parallel y$ will be of the back-wave type if the projection of the outward normal to the refraction surface onto the x axis at the intersection point of this surface and the $k_y = \kappa_\nu$ straight line is negative; when this projection is positive, the corresponding wave with given $k_\perp$, ω, and κ_ν will be of the direct-wave type.

If this projection onto the x axis is equal to zero at some $k_\perp \neq 0$, then the dispersion curve of mode ν of bulk waves traveling along the $2d$ thick film has an extremum at the corresponding values of frequency ω and wavenumber $k_\perp$. The character of this extremum (maximum or minimum) is determined by the sign of the local curvature of the dispersion curve, described by Eqs. (32) and (33), at this point (Figs. 5, 6). In particular, the extremum is a maximum if the local curvature is negative.

In this paper, Eqs. (16) and (17) are basically investigated to the zeroth order in $W_{\nu\rho}$. However, it should be noted that if two dispersion curves intersect at the degeneracy point $\Omega_{m\nu}(k_\perp) = \Omega_{m\rho}(k_\perp)$ or $\Omega^2_{m\nu}(k_\perp) = \Omega^2_{\mathrm{ph},\rho}(k_\perp)$, one of them being of the direct-wave type and the other being of the back-wave type, then, as can be seen from Eq. (21), this degeneracy is lifted, with the consequence that two additional extreme points appear, one of which is a local maximum and the other is a local minimum of the dispersion curve.

As follows from Eqs. (23) and (27), a necessary condition for the manifestation of lattice-induced anomalies of the dispersion curve of mode ν of dipole–exchange bulk magnons in a plate of a low-temperature AFM is the fulfillment of the condition

$$\omega^2_{me},\ \omega^2_0 \gg c^2_m \pi^2 \nu^2 / d^2. \tag{34}$$

If $\omega_{me} \approx 10^9$ Hz and $c_m \approx 10^5$ cm/s [2, 3], then for $\omega_0 \ll \omega_{me}$ (near the boundary of stability of this magnon state) the anomalies investigated above will occur in a plate with $d \gg 10^{-3}\nu$ cm. It should be noted that condition (34) is fulfilled the better, the lower the Néel temperature ($T_N < T_D$).

7. CONCLUSIONS

Thus, in this paper, we determined the necessary conditions for the occurrence of earlier unknown anomalies produced by the crystal lattice in the spectrum of traveling bulk spin waves in a thin antiferromagnetic film. The existence of these anomalies depends critically not only on the finite dimensions of the crystal but also on the relationship between the Néel temperature and the Debye temperature. In this paper, the following anomalies are found to occur in the spectrum of dipole–exchange bulk magnons in the presence of magnetoelastic interaction:

(1) Even in the exchangeless approximation, the $\Omega_{m\nu}(k_\perp)$ dispersion curve of mode ν has several points $k_\perp \neq 0$ at which $\partial\Omega_{m\nu}(k_\perp)/\partial k_\perp = 0$. These points can correspond to both a local maximum and a local minimum of the dispersion curve.

(2) Crossover points at $k_\perp \neq 0$ can exist for dispersion curves of modes ν and ρ in the spectrum $\Omega_{m\nu}(k_\perp)$ of a thin antiferromagnetic film not only in the presence of inhomogeneous exchange interaction but also in the exchangeless approximation (because of hybridization of elastostatic and magnetostatic spin–spin interactions).

(3) There is a one-to-one correspondence between the local geometry of the refraction surface of normal spin waves in an infinite magnetic crystal and the structure of the spectrum of this type of waveguide waves in a thin film of the same material. There is no question that the correlation found between the shape of the refraction surface of a normal wave, the structure of the spectrum of guided waves, and their type (direct wave or back wave) also takes place for other types of normal waves in an infinite crystal (phonons, excitons, etc.).

In this paper, we considered only the case of $\mathbf{H} = 0$. It can easily be shown that in the case of $\mathbf{H} \parallel y$ and $D = 0$, all results obtained above for $\mathbf{l} \parallel x$, $(\mathbf{k}_\perp, \mathbf{n}) \in xy$, and $(\tilde{l}_y, \tilde{m}_z) \neq 0$ remain valid, except for the substitutions $\omega_D \longrightarrow \omega_H$ and $\omega_0^2 \longrightarrow \omega_0^2 + \omega_H^2$. The consequences of rotational invariance will be considered elsewhere.

ACKNOWLEDGMENTS

The author is grateful to E.P. Stefanovskiĭ, T.N. Tarasenko, and I.E. Dragunov for their encouragement and helpful discussions.

REFERENCES

1. C. Patton, Phys. Rep. **103** (5), 251 (1984).
2. E. A. Turov and V. G. Shavrov, Usp. Fiz. Nauk **140** (3), 429 (1983) [Sov. Phys. Usp. **26**, 593 (1983)].
3. I. E. Dikshteĭn, E. A. Turov, and V. G. Shavrov, in *Dynamical and Kinetic Properties of Magnetics* (Nauka, Moscow, 1986).
4. Yu. V. Gulyaev and P. E. Zil'berman, Izv. Vyssh. Uchebn. Zaved., Fiz. **31** (11), 6 (1988).
5. Yu. V. Gulyaev, I. E. Dikshteĭn, and V. G. Shavrov, Usp. Fiz. Nauk **167** (7), 735 (1997) [Phys. Usp. **40**, 701 (1997)].
6. V. I. Ozhogin and V. L. Preobrazhenskiĭ, Usp. Fiz. Nauk **155** (4), 593 (1988) [Sov. Phys. Usp. **31**, 713 (1988)].
7. S. V. Tarasenko, Pis'ma Zh. Tekh. Fiz. **14** (22), 2041 (1988) [Sov. Tech. Phys. Lett. **14**, 885 (1988)].
8. A. L. Sukstanskiĭ and S. V. Tarasenko, Zh. Éksp. Teor. Fiz. **105** (4), 928 (1994) [JETP **78**, 498 (1994)].

9. S. V. Tarasenko, Fiz. Tverd. Tela (Leningrad) **33** (10), 3021 (1991) [Sov. Phys. Solid State **33**, 1705 (1991)].

10. S. V. Tarasenko, Zh. Éksp. Teor. Fiz. **110** (10), 1411 (1996) [JETP **83**, 778 (1996)].

11. E. A. Turov, *Physical Properties of Magnetically Ordered Crystals* (Akad. Nauk SSSR, Moscow, 1963).

12. M. P. Balakirev and I. A. Gilinskiĭ, *Waves in Piezoelectric Crystals* (Nauka, Novosibirsk, 1982).

13. A. G. Gurevich and G. A. Melkov, *Magnetic Oscillations and Waves* (Nauka, Moscow, 1994).

14. V. A. Krasil'nikov and V. V. Krylov, *Introduction to Physical Acoustics* (Nauka, Moscow, 1984).

15. A. G. Khachaturyan, *The Theory of Phase Transformations and the Structure of Solids Solutions* (Nauka, Moscow, 1974).

16. O. G. Vendik and D. N. Chartorizhskiĭ, Fiz. Tverd. Tela (Leningrad) **12** (5), 1538 (1970) [Sov. Phys. Solid State **12**, 1209 (1970)].

17. B. A. Kalinikos, Izv. Vyssh. Uchebn. Zaved., Fiz. **24** (8), 42 (1981).

18. V. I. Alshits, A. N. Darinskii, and J. Lothe, Wave Motion **16**, 265 (1992).

19. Yu. I. Sirotin and M. P. Shaskolskaya, *Fundamentals of Crystal Physics* (Nauka, Moscow, 1979; Mir, Moscow, 1982).

Translated by Yu. Epifanov

Physics of the Solid State, Vol. 43, No. 8, 2001, pp. 1499–1502. Translated from Fizika Tverdogo Tela, Vol. 43, No. 8, 2001, pp. 1439–1442.

MAGNETISM AND FERROELECTRICITY

Magnetization Dynamics under Nonlinear Ferromagnetic Resonance Conditions in a (111) Film

A. M. Shutyĭ and D. I. Sementsov

Ul'yanovsk State University, ul. L'va Tolstogo 42, Ul'yanovsk, 432700 Russia

e-mail: shuty@mail.ru

Received June 28, 2000

Abstract—The equation of motion of magnetization of a garnet ferrite (111) film is solved numerically. It is shown that different regimes of the resonance precession of magnetization are realized depending on the bias and microwave fields; the regimes differ in amplitude and in the shape of their magnetization precession trajectories. In addition, bifurcations occur which lead to an abrupt change in amplitude, to bistability, and to precession with a period that is a multiple of the microwave-field period. *© 2001 MAIK "Nauka/Interperiodica".*

1. The nonlinear dynamics of magnetization in magnetically ordered crystals is of interest because of the variety of dynamic regimes of precession of the magnetization vector and the possibility of attaining large angles of uniform precession [1–4]. The latter property is of importance because magnetization precession can be useful for modulating laser radiation, the efficiency of which is determined by the precession angle [5, 6]. In [7], the features of nonlinear precession of a magnetic moment associated with its nutation in an effective field and with the frequency-doubling effect were investigated in a (111) film of a cubic crystal. The investigation was carried out in a geometry where bias fields were applied perpendicular to the film surface and for frequencies corresponding to resonance precession, i.e., to ferromagnetic resonance (FMR). It was found that, for a given microwave (MW) field characterized by its amplitude and polarization, the angle of resonance precession is large only at certain values of the bias static field and is induced by crystalline anisotropy fields. Under conditions for nonlinear FMR, the precession of the magnetic moment is accompanied by its nutation, which is dominated by the contribution from the third harmonic of the fundamental precession. Away from FMR, in the case of a linearly polarized MW field, the frequency-doubling effect is significant and the second harmonic becomes dominant. In this paper, we present the results of a numerical solution to the equations of motion of magnetization, which indicate that there are several regimes of precession: bifurcation, bistable dynamic states, and precession with a period that is a multiple of the MW field period.

2. Let the crystallographic [111] axis of a single-crystal garnet ferrite film be aligned with the *x* axis (which is taken to be normal to the film surface). The *y* and *z* axes are taken to be parallel to the $[11\bar{2}]$ and $[\bar{1}10]$ directions, respectively. The polar angle θ and azimuthal angle ψ of the magnetization **M** are reckoned from the *x* and *y* axes, respectively. The dynamic behavior of the magnetization in an external static magnetic field *H* and an MW field *h* is described by the equations of motion [8]

$$\begin{aligned} \dot{\psi} M \sin\theta &= \gamma \frac{\partial F}{\partial \theta} + \frac{\lambda}{M} \frac{1}{\sin\theta} \frac{\partial F}{\partial \psi}, \\ \dot{\theta} M &= \frac{\lambda}{M} \frac{\partial M}{\partial \theta} - \gamma \frac{1}{\sin\theta} \frac{\partial F}{\partial \psi}, \end{aligned} \tag{1}$$

where γ is the gyromagnetic ratio, λ is the damping constant, and *F* is the free-energy density. From the conditions $\partial F/\partial\theta = 0$ and $\partial F/\partial\psi = 0$, we find the equilibrium angles θ_0 and ψ_0. Using the basic parameters determining the film magnetization, we solve Eq. (1) using numerical methods for those values of the static field **H** for which the equilibrium orientation of the vector **M** is along the normal ($\theta_0 = 0$) to the film (for given values of the growth-induced and crystalline anisotropy constants, K_u and K_1, respectively). The resonance frequency equals $\omega_r = \gamma H_{\text{eff}}(0)$, where the effective field is

$$H_{\text{eff}}(0) = H - 4\pi M + \frac{2}{M}\left(K_u - \frac{2}{3}K_1\right). \tag{2}$$

The MW field is linearly polarized and lies in the *yz* plane (i.e., $\mathbf{h} \perp \mathbf{H}$).

3. The numerical solution of Eq. (1) shows the projections of the stationary trajectories of the precessing magnetic moment onto the *yz* plane for different values of the static and MW fields. The stationary magnetization precession is independent of the orientation of the MW field in the film plane and the initial phase of this field in the cases under study. In our calculations, we used the following parameters of a real garnet ferrite film $Y_{2.9}La_{0.1}Fe_{3.9}Ga_{1.1}O_{12}$: $4\pi M = 214.6$ G, $\gamma = 1.755 \times 10^7$ (Oe s)$^{-1}$, $\lambda = 3 \times 10^6$ s^{-1}, and $K_u = K_1 = -10^3$ erg/cm^3 [4]. For the bias field values in the range $H_0 < H < H_c$,

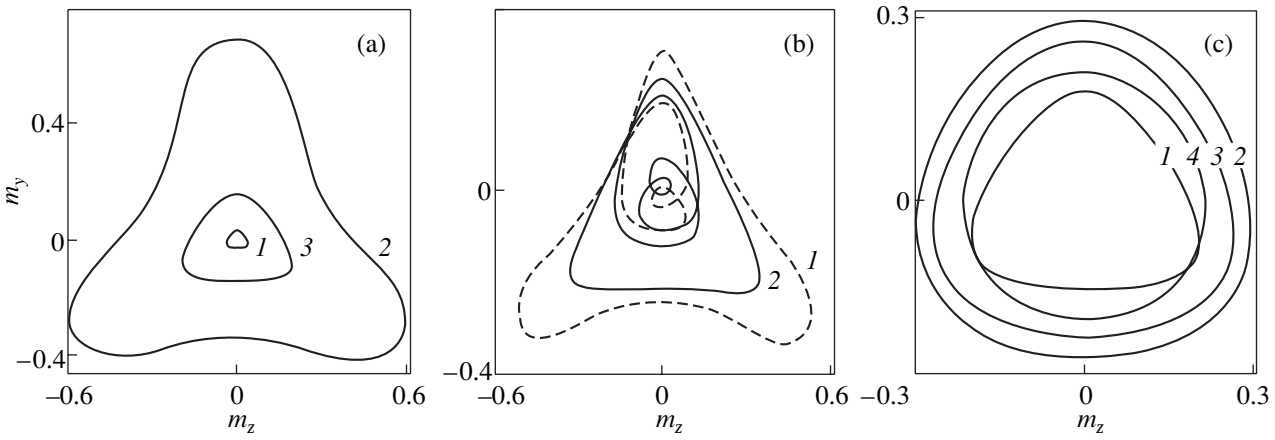

Fig. 1. Projections of stationary trajectories of precession of the magnetic moment onto the *yz* plane for various values of the bias field H = (a) (*1*) 260 and (*2*, *3*) 283.5; (b) (*1*) 280 and (*2*) 285; and (c) (*1*) 290, (*2*) 350, (*3*) 400, and (*4*) 600; and for various values of the MW field amplitude h = (a) (*1*) 0.04, (b) (*1*) 2, and, in the other cases [(a) (*2*, *3*), (b) (*2*), (c) (*1–4*)], 1.5 Oe. $m_\alpha = M_\alpha/M$, with $\alpha = y, z$.

where $H_0 \cong 254$ Oe is the minimum value corresponding to the resonance frequency $\omega_r = 0$ and $H_c \cong 275$ Oe, the axis of precession is normal to the film plane only for MW fields of amplitude $h \le 5 \times 10^{-2}$ Oe (curve *1* in Fig. 1a). As the MW field is increased, the magnetization tilts to one of the three directions that are determined by the value of the bias field and the film anisotropy precesses about this direction with an average amplitude of $\langle\phi\rangle \le 3°$. An increase in the bias field causes the magnetization to precess again about the normal to the film with the maximum amplitude; for example, for h = 1.5 Oe, the amplitude of precession is as large as $\langle\phi\rangle \cong 30°$ (curve *2* in Fig. 1a). Further, a fairly narrow range of bias fields ($\Delta H \sim 1$ Oe) follows in which dynamic bistability takes place; namely, in addition to the orbit with the maximum amplitude of precession of the magnetic moment, another stationary orbit arises with $\langle\phi\rangle \cong 10°$ (curve *3* in Fig. 1a). Which of these two dynamic states is realized depends on the parameters of the fields and magnetization (and on their fluctuations), as well as on the initial phase of the MW field. In this FMR geometry, as can be seen from the M trajectories presented, the dominant contribution to nutation of the magnetic moment comes from the third harmonic of fundamental oscillations with resonance frequency ω_r. This contribution is maximum in the regime where the precession angle $\langle\phi\rangle$ is maximum. Over very narrow ranges of bias fields ($\Delta H \sim 10^{-2}$ Oe), regimes occur in which the trajectories are complex and the period of precession is a multiple of the MW field period; i.e., $T = 2\pi l/\omega_r$, where l is an integer. The curves presented in Fig. 1b correspond to stationary periodic motions of magnetization with l = 3 (curve *1*) and 4 (curve *2*); for $H \cong 284$ Oe and h = 1.5 Oe, a regime with l = 8 can occur. With a further increase in H and the MW field amplitude $h \le 1.7$ Oe kept fixed, the precession amplitude first increases and then decreases (curves *1–4* in Fig. 1c). The trajectories more and more closely resemble circles; that is, the contribution from the higher harmonics of fundamental oscillations with the resonance frequency to magnetization nutation decreases.

Contributions from harmonics of fundamental oscillations with frequency ω_r to nutation of the magnetization **M**

H, Oe	ϕ_0, deg	ϕ_ω/ϕ_0	$\phi_{2\omega}/\phi_0$	$\phi_{3\omega}/\phi_0$
283	30.108	2.50×10^{-2}	1.38×10^{-2}	3.62×10^{-1}
300	11.463	3.20×10^{-2}	4.42×10^{-2}	1.13×10^{-1}
400	16.904	1.98×10^{-3}	1.25×10^{-2}	5.03×10^{-2}
500	15.721	1.09×10^{-3}	6.29×10^{-3}	2.89×10^{-2}
600	12.228	7.24×10^{-4}	4.94×10^{-3}	1.65×10^{-2}
700	9.629	4.13×10^{-4}	4.94×10^{-3}	1.02×10^{-2}

Figure 2 shows the time dependence of the normal component of the magnetic moment in the process of transition to a stationary orbit for the MW field amplitude h = 1.5 Oe and the bias field H equal to (a) 260 and (b) 283.5 Oe. Figure 2a corresponds to a transition to stationary precession with a small amplitude about an axis making an angle $\theta = 40.7°$ with the normal to the film. Figure 2b corresponds to a regime of dynamic bistability in which the magnetic moment precesses about the normal to the film; precession with a large amplitude (curve *1*) occurs when the initial phase of the MW field is equal to 10°, while the small stationary orbit of precession with a much smaller amplitude of nutation (curve *2*) corresponds to the zero initial phase.

In order to calculate the contributions to magnetization nutation from different harmonics of fundamental oscillations with the resonance frequency, we expand

the time-dependent precession angle $\phi(t)$ into a Fourier series:

$$\phi(t) = \sum \phi_{n\omega} \exp(i\omega n t). \quad (3)$$

The contributions from the first three harmonics are listed in the table for several values of the bias field H. It can be seen that, in a (111) film under FMR conditions, the contribution from the third harmonic is the largest of the contributions from the higher harmonics ($n > 0$) [7]. For sufficiently large values of the bias field, $H \gg H_0$, and small amplitudes of precession, the angle $\phi(t)$ is determined by the constant component $\phi_0 = \langle\phi\rangle$ with a high degree of accuracy and the higher harmonics can be ignored when describing the motion of the magnetization.

In this case, the average angle of precession ϕ_0 is approximated as

$$\cos\phi_0 = 1 - \frac{h^2}{4M^2}(|\chi|^2 + |\chi_a|^2), \quad (4)$$

where the complex diagonal ($\chi = \chi' - i\chi''$) and off-diagonal ($\chi_a = \chi_a' - i\chi_a''$) components of the high-frequency susceptibility tensor, which determines the linear relation between the MW field and the corresponding response of the magnetization, are equal to (at resonance, $\omega = \omega_r$) $\chi' = \gamma M(\lambda^2 - \gamma^2 M^2)/\omega\Delta$, $\chi'' = \gamma^2 M^2(3\lambda^2 + 2\gamma^2 M^2)/\omega\lambda\Delta$, $\chi_a' = \gamma^3 M^3/\omega\Delta$, and $\chi_a'' = 2\gamma^4 M^4/\omega\lambda\Delta$, where $\Delta = \lambda_2 + 4\gamma^2 M^2$ [8]. For example, for H = 500, 600, and 700 Oe, Eq. (4) gives $\phi_0 = 17.510°$, 12.431°, and 9.639°, respectively. Comparison of this with the data in the table shows that Eq. (4) is a close approximation in the case of high bias fields.

For MW field amplitudes in the range $1.7 \le h \le 2$ Oe, as numerical analysis shows, bifurcation occurs and precession with a sharply increased amplitude is observed; this precession is stable in the range of bias fields $H_1(h) < H < H_2(h)$, the width of which increases with h. For $h \ge 2$ Oe, the upper limit H_2 is absent; only a sharp increase in the precession amplitude is observed, and then the amplitude decreases rather smoothly. Figure 3 shows the time dependence of the normal component of the magnetic moment that moves from the initial position $\theta = 0$ and goes into a stationary orbit under the action of an MW field with an amplitude of h = 2 Oe. The bias field is taken to be near its bifurcation value H_1 (curve *1* corresponds to H = 334.44 Oe; curve *2*, to H = 334.45 Oe). As H approaches H_1, range *A* in Fig. 3 increases in length, which means that precession with an intermediate amplitude $\langle\phi\rangle$ becomes stable at $H = H_1$. Therefore, in the case of the bifurcation in question, precession of the vector **M** changes over from one stable stationary orbit to the other via a third stable state.

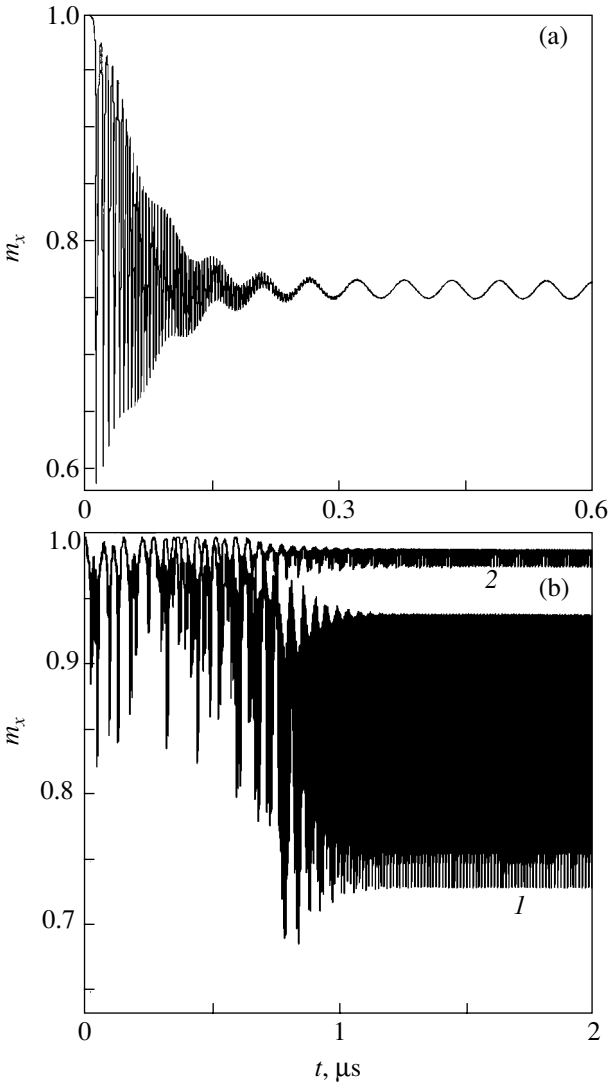

Fig. 2. Time dependence of the normal component of the magnetization **M** ($m_x = M_x/M$) which moves from its initial position $\theta = 0$ and goes (a) into a stationary precession orbit about an axis tilted with respect to the normal to the film and (b) into one of the two stationary orbits in the dynamic-bistability regime.

The dependence of the average polar angle $\langle\theta\rangle$ of the magnetic moment on the bias field H is shown in Fig. 4 for different values of the MW field amplitude. In the range $260 \le H \le 275$ Oe, the average amplitude of stationary precession is $\langle\phi\rangle \le 3°$ and its axis is not normal to the film plane. As the bias field is increased, the magnetization begins to precess about the normal to the film with a maximum amplitude ($\langle\theta\rangle \equiv \langle\phi\rangle$) and then a bistable state arises. For H > 284.5 Oe, only the orbit with a small precession amplitude remains stable; if $h <$ 1.7 Oe, the precession amplitude first increases with increasing bias field, then passes through a feebly

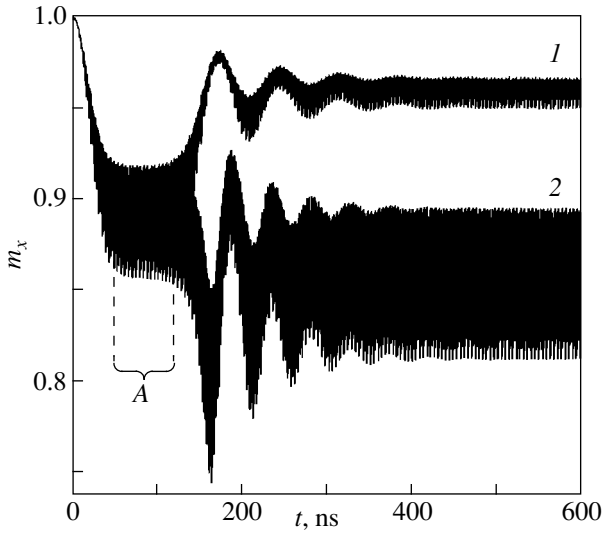

Fig. 3. Time dependence of the normal component of the magnetic moment which moves from its initial position θ = 0 and goes into a stationary precession orbit for two values of the bias field close to the bifurcation field H_1 (see text).

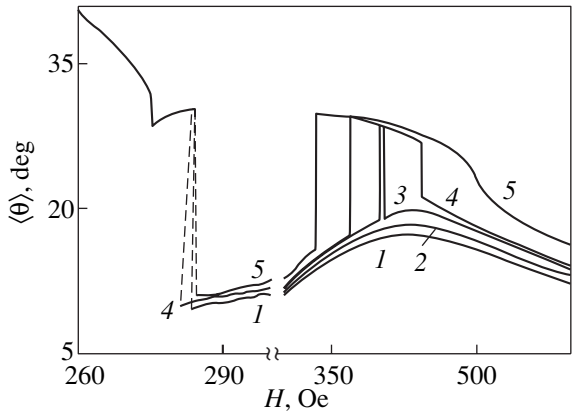

Fig. 4. Dependence of the average polar angle ⟨θ⟩ of the magnetization **M** on the bias field H for different values of the MW field amplitude h = (*1*) 1.5, (*2*) 1.6, (*3*) 1.702, (*4*) 1.75, and (*5*) 2.0 Oe; ⟨θ⟩ ≡ ⟨ϕ⟩ for $H \gtrsim 275$ Oe.

marked maximum and decreases. In the case of sufficiently large MW field amplitudes, the small orbit becomes unstable at $H = H_1(h)$ and the precession amplitude increases sharply; however, at $H > H_2(h)$ (for $h < 2$ Oe), the orbit with a small precession amplitude again becomes the only stable orbit.

The investigation performed in this paper shows that, under FMR conditions, various regimes of magnetization precession can occur in a garnet ferrite (111) film; these precession regimes differ greatly in amplitude and in the shape of their trajectories. In addition, bifurcation can arise, which leads to a sharp change in the precession amplitude, to bistable states, and to precession with a period that is a multiple of the resonant MW field period.

REFERENCES

1. G. S. Kandaurova and A. E. Sviderskiĭ, Pis'ma Zh. Éksp. Teor. Fiz. **47** (8), 410 (1988) [JETP Lett. **47**, 490 (1988)].
2. F. V. Lisovskiĭ, E. G. Mansvetova, E. P. Nikolaeva, and A. V. Nikolaev, Zh. Éksp. Teor. Fiz. **103** (1), 213 (1993) [JETP **76**, 116 (1993)].
3. S. M. Rezende and F. M. de Aguiar, Proc. IEEE **78** (6), 893 (1990).
4. B. Neite and H. Doetsch, Proc. SPIE **1018**, 115 (1989).
5. A. M. Prokhorov, G. A. Smolenskiĭ, and A. N. Ageev, Usp. Fiz. Nauk **143** (1), 33 (1984) [Sov. Phys. Usp. **27**, 339 (1984)].
6. D. I. Sementsov and A. M. Shutyĭ, Opt. Spektrosk. **84** (2), 280 (1998) [Opt. Spectrosc. **84**, 238 (1998)].
7. A. M. Shutyĭ and D. I. Sementsov, Fiz. Tverd. Tela (St. Petersburg) **42** (7), 1268 (2000) [Phys. Solid State **42**, 1306 (2000)].
8. A. G. Gurevich and G. A. Melkov, *Magnetic Oscillations and Waves* (Nauka, Moscow, 1994).

Translated by Yu. Epifanov

Physics of the Solid State, Vol. 43, No. 8, 2001, pp. 1503–1508. Translated from Fizika Tverdogo Tela, Vol. 43, No. 8, 2001, pp. 1443–1448.

MAGNETISM AND FERROELECTRICITY

Effect of Hydrogen on the Magnetic Characteristics of Nanocrystalline Iron

A. A. Novakova, O. V. Agladze, and T. Yu. Kiseleva

Moscow State University, Vorob'evy gory, Moscow, 119899 Russia

e-mail: aan@runar.phys.msu.su

Received August 14, 2000

Abstract—This paper reports the results of a complex investigation into the properties of nanocrystalline iron prepared through mechanical dispersion in a hydrogen atmosphere. Magnetic measurements reveal changes in the magnetic characteristics of iron samples obtained for different times of milling (i.e., samples with different grain sizes). The structural transformations responsible for these changes are studied by x-ray diffraction, Mössbauer spectroscopy, and thermogravimetry. It is found that incorporation of hydrogen into the boundary region between single-domain particles of consolidated nanocrystalline iron leads to an increase in the coercive force. Magnetic anisotropy induced by strains is observed. It is established that the strain-induced magnetic anisotropy affects the field dependence of the saturation magnetization of nanocrystalline iron. *© 2001 MAIK "Nauka/Interperiodica".*

1. INTRODUCTION

Research on the nanocrystalline state of matter is a topical direction of solid-state physics. This state substantially differs in atomic ordering from the polycrystalline and amorphous states [1]. Numerous experimental studies have demonstrated that a decrease in the particle size to ~10 nm results in a drastic change in the heat capacity and the magnetic, electrical, and mechanical characteristics of the material [2]. This effect is more pronounced in experiments with isolated particles. For example, ferromagnetic nanocrystalline particles are characterized by changes in their magnetic properties, such as the magnetic moment, the Curie temperature, and the coercive force.

A different situation occurs in consolidated nanocrystalline ferromagnets. Their unusual physical properties can be associated with the small sizes of their crystallites (grains) and also with the fact that the interface regions (grain boundaries) can involve from 10 to 50% of the total number of atoms. As the grain size decreases, the misorientation of nanocrystallites leads not only to a decrease in the atom density in interface regions but also to the formation of stress fields that extend from the boundaries deep into the grains. The stress fields induce displacements of atoms from their regular lattice sites and, thus, change the configuration of the nearest neighbor atoms. All these factors can bring about a change in the energy of magnetic exchange interaction because of the limiting ferromagnetic exchange length (according to different estimates, the exchange length for α-Fe is equal to 25–30 nm). Moreover, depending on the preparation conditions of the nanocrystalline samples, the chemical composition of interface regions can differ from that of crystallites. In this respect, the separation of the contributions from atoms located in grains and atoms within the interface regions to the physical effects under investigation is a central problem in the study of the consolidated nanocrystalline state. In order to solve this problem, it is necessary to obtain experimental data on the interrelation between the structural and physical properties of nanomaterials with correctly evaluated grain sizes.

In the present work, we carried out a complex investigation into the structural and magnetic characteristics of nanocrystalline iron. The iron samples were prepared using a currently efficient and widely used method—mechanical dispersion in a high-power ball mill. However, unlike the standard inert atmosphere which is commonly used for producing nanocrystalline materials, we used a hydrogen atmosphere in the mill. In our earlier work [3], we showed that the presence of hydrogen in the atmosphere during milling of the material changes the dispersion kinetics and provides the conditions for mechanical synthesis; i.e., hydrogen affects the mechanism of the phase formation in the interface regions of contacting particles.

It is known that hydrogen does not dissolve in the solid phase of iron at room temperature. Ponyatovskiĭ and his collaborates [4, 5] proved that the formation of iron hydride FeH requires a hydrogen pressure up to 7 GPa and a temperature of approximately 250°C. Iron hydride is unstable: it transforms into α-Fe with an increase in the temperature above 150 K and very easily releases hydrogen under mechanical treatment. However, the solubility of hydrogen depends not only on the gas phase pressure and temperature but also on the purity of the metal, defectiveness of its structure, and the dislocation distribution. As was shown in [6–11], hydrogen readily interacts with structural defects such

1063-7834/01/4308-1503$21.00

as microcracks, dislocations, defects clusters, and grain boundaries.

The mechanical dispersion of iron brings about the formation of numerous boundaries with a high defect content, which, in our opinion, provides favorable conditions for the incorporation of hydrogen (forming the atmosphere in the course of milling) into interface regions of nanocrystalline iron.

In this work, we examined changes in the magnetic characteristics of nanocrystalline iron samples prepared in a hydrogen atmosphere for different milling times (i.e., samples with different grain sizes) and revealed the structural transformations responsible for the observed effects.

2. EXPERIMENTAL TECHNIQUE

The nanocrystalline iron samples were prepared by mechanical dispersion of highly pure carbonyl iron (the total content of oxygen and carbon impurities was less than 0.01%) in a high-power planetary ball mill with a ball-to-iron powder mass ratio of 20 : 1. The milling was performed in a hydrogen atmosphere for 2 and 8 h. For comparison, the nanocrystalline iron samples were prepared in an inert (argon) atmosphere for the same times of milling.

X-ray structure analysis of the samples (lattice parameters, sizes of coherent-scattering regions, and lattice strains) was carried out on a Rigaku-D/MAX x-ray diffractometer (CuK_α radiation) with a monochromator.

The Mössbauer spectra were recorded in an absorption geometry on a "Mössbauer Laboratory" spectrometer (Hungary) using a ^{57}Co(Rh) gamma-ray source with an activity of 50 mCi. The spectrometer was calibrated against an α-Fe standard absorber. The spectra obtained were mathematically processed according to the UNIVEM software package.

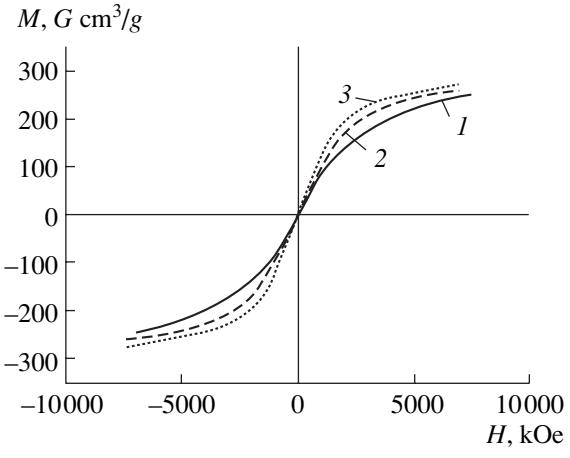

Fig. 1. Dependences of the saturation magnetization on the external field for (*1*) the initial polycrystalline iron and nanocrystalline iron milled in hydrogen for (*2*) 2 and (*3*) 8 h.

The thermoanalytical determination of the amount of adsorbed hydrogen was carried out with a NEZTSCH STA-409 thermoanalyzer, which made it possible to perform a thermogravimetric analysis of the samples. The measurements were carried out in the temperature range 20–800°C at a heating rate of 20 K/min in a dried helium atmosphere.

The coercive force and the saturation magnetization of the samples were measured using a vibrating-sample magnetic anisotropy meter, which, in the magnetometer operating mode, had a sensitivity as high as 5×10^{-8} G cm^3 in the field range ±10 kOe.

3. RESULTS AND DISCUSSION

Figure 1 shows the dependences of the saturation magnetization on the external field for the studied samples. The main magnetic parameters calculated from these dependences are given in Table 1.

It can be seen from Fig. 1 that, compared to the initial polycrystalline iron, the saturation magnetization of both nanocrystalline iron samples milled in hydrogen reaches a maximum in weaker fields. At the same time, with an increase in the milling time, the saturation magnetization σ of nanocrystalline iron milled in hydrogen (Table 1), to within the error of determination, remains identical to that of polycrystalline iron.

The coercive force H_c (characterizing the remanent magnetization of iron) is equal to 1.8 Oe for the initial carbonyl iron and increases with an increase in the milling time. After milling for 8 h, the coercive force drastically increases (by a factor of more than seven) to H_c = 13.2 Oe (Table 1). It should be noted that the coercive force for the nanocrystalline iron sample milled in an argon atmosphere for 8 h increases only by a factor of 1.5.

With the aim of interpreting the observed changes in the magnetic characteristics of the nanocrystalline iron samples prepared through mechanical dispersion in a hydrogen atmosphere, we carried out structural investigations. The x-ray diffraction patterns of all the samples studied are shown in Fig. 2. The diffraction lines of milled iron are broader and less intense compared to the lines in the diffraction pattern of the initial carbonyl iron.

The x-ray diffraction data were used to calculate the structural characteristics of nanocrystalline iron, namely, the size of coherent-scattering regions and the degree of lattice strain (Table 2). A comparison of the data presented in Table 2 shows that the size of coherent-scattering regions (in actual fact, the crystallite size) decreases to 20 and 13 nm after milling for 2 and 8 h, respectively. The mechanical dispersion of iron in a hydrogen atmosphere is accompanied by an increase in the degree of lattice strain: the strain increased by a factor of 1.5 after the 2-h milling and by a factor of 6 [to

a value of $(4.3 \pm 0.2) \times 10^{-3}$] after the 8-h milling. All these results indicate that the degree of structure imperfection increases.

Unfortunately, x-ray diffraction analysis has failed to separate the boundary and size effects in nanostructured materials. For this purpose, the structural components of nanocrystalline iron were studied by Mössbauer spectroscopy.

The Mössbauer spectra of iron in the initial state and after milling in hydrogen for 2 and 8 h are displayed in Fig. 3. The spectrum of iron in the initial state is represented by one sextet with the hyperfine magnetic splitting H_{eff} = 330 kOe, isomer shift δ = 0 mm/s, and linewidth Γ = 0.26 mm/s. These values agree with the hyperfine parameters of polycrystalline α-Fe (Fig. 3a). The spectrum of nanocrystalline iron milled in hydrogen for 2 h can be described by the sum of two sextets. One sextet (hyperfine magnetic splitting H_{eff} = 330 kOe, isomer shift δ = 0 mm/s, linewidth Γ = 0.27 mm/s, and resonance area S = 88%) corresponds to the bulk of a grain. The other sextet (H_{eff} = 320 kOe, δ = 0.11 mm/s, Γ = 0.4 mm/s, and S = 12%) is attributed to the grain boundary. As the milling time increases to 8 h, the contribution from the partial spectrum of the grain boundary increases to 16%. An increase in the area of the partial spectrum of the grain boundary is attended by changes in its parameters: the hyperfine magnetic splitting and the isomer shift decrease to 314 kOe and 0 mm/s, respectively, and the linewidth increases to 0.55 mm/s. The hyperfine Mössbauer parameters for iron prior to and after milling in a hydrogen atmosphere for different milling stages are listed in Table 3.

It is seen from Table 3 that the linewidth in the partial spectrum of the grain boundary increases to a value of $2\Gamma_{\text{exp}}$ with an increase in the milling time. This increase can be explained by the fact that Fe atoms in the interface region are separated by different distances, each characterized by its own effective magnetic field. It is this distribution of effective magnetic fields that is responsible for the broadening of the spectral lines corresponding to the grain boundary. The mean effective magnetic fields decrease to 320 and 314 kOe after milling for 2 and 8 h, respectively. This can be interpreted as follows. In the course of milling, the nearest distances between iron atoms in the interface region become larger than those in metallic iron, which is in reasonable agreement with the concept of the decrease in density of the interface region [12].

The isomer shift is another important spectral parameter that characterizes the structural state of the grain boundary. It is well known that the isomer shift in the Mössbauer spectrum is determined by the relationship

$$\delta \approx \partial R/R\{|\Psi(0)|_a^2 - |\Psi(0)|_s^2\},$$

where $|\Psi(0)|_s^2$ and $|\Psi(0)|_a^2$ are the s electron densities at the nucleus for a source and an absorber, respectively, and $\partial R/R$ determines the difference between radii of the nucleus in the excited and ground states. For the ^{57}Fe nucleus, we have $\partial R/R = -1.8 \times 10^{-3}$. Hence, an increase in the electron density at the nucleus in the sample under investigation leads to a decrease in the isomer shift δ.

Table 1. Saturation magnetizations σ and coercive forces H_c for polycrystalline carbonyl iron and nanocrystalline iron obtained in a hydrogen atmosphere

Sample	σ, G cm^3/g	H_c, Oe
Initial carbonyl Fe	240 ± 50	1.8 ± 0.2
Fe milled in H_2 for 2 h	270 ± 55	1.9 ± 0.2
Fe milled in H_2 for 8 h	270 ± 55	13.2 ± 0.2

Table 2. Structural characteristics of iron prior to and after milling in a hydrogen atmosphere (calculations from x-ray diffraction data obtained with CuK_α radiation)

Sample	D, nm	$\eta \times 10^{-3}$	a, nm
Prior to milling	42 ± 2	0.7 ± 0.2	2.867 ± 0.002
After milling in H_2 for 2 h	20 ± 2	1.2 ± 0.2	2.863 ± 0.002
After milling in H_2 for 8 h	13 ± 2	4.3 ± 0.2	2.863 ± 0.002

Note: D is the size of coherent-scattering regions, and η is the degree of lattice strain.

As follows from Table 3, the isomer shift in the partial spectrum of the grain boundary in iron milled in hydrogen for 2 h increases to 0.11 mm/s (for polycrystalline iron, δ = 0 mm/s). This agrees with the data obtained by Herr *et al.* [12], who observed an increase in the isomer shift for the grain boundary of iron nanoparticles with a decrease in the grain size. This increase can be associated with a decrease in the density of the interface region. However, in the Mössbauer spectrum of the nanocrystalline iron milled for 8 h, the isomer shift of the partial spectrum of the grain boundary unexpectedly decreases to 0 mm/s. This behavior of the isomer shift corresponds to an increase in the s electron density in the interface region and is inconsistent with

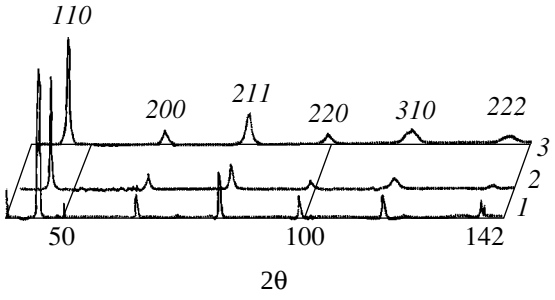

Fig. 2. X-ray diffraction patterns (CuK_α radiation) of (*1*) the initial carbonyl iron and iron prepared through mechanical dispersion in hydrogen for (*2*) 2 and (*3*) 8 h.

Table 3. Parameters of the Mössbauer spectra of carbonyl iron prior to and after milling in a hydrogen atmosphere

Sample	Partial spectrum	δ, mm/s	*H*, kOe	Δ, mm/s	Γ, mm/s	*S*, %
Prior to milling	Grain	0	330 ± 2	–	0.26 ± 0.02	100
	Boundary	–	–	–	–	–
After milling in H_2 for 2 h	Grain	0	330 ± 2	–	0.27 ± 0.02	88
	Boundary	0.11 ± 0.02	320 ± 2	–	0.40 ± 0.02	12
After milling in H_2 for 8 h	Grain	0	331 ± 2	–	0.27 ± 0.02	84
	Boundary	0	314 ± 2	–	0.55 ± 0.02	16

the concept of the decrease in density of the interface region. At the same time, this effect can be explained by the incorporation of hydrogen into the interface region.

A decrease in the crystallite size brings about an increase in the size of the interface region and the number of interface defects. Hence, it is clear that a further increase in the milling time provides more favorable conditions for hydrogen absorption. For iron samples with a grain size of 13 nm, the width of a boundary layer with a high defect content was estimated (according to the data obtained for similar materials from high-resolution electron microscopy [1]) to be as large as 1 nm. This is favorable for the capture of hydrogen by dislocation loops and three-dimensional defects in grain boundary junctions. Furthermore, the incorporation of hydrogen into the interface region during mechanical dispersion is facilitated by local pressure and temperature jumps up to 15×10^8 Pa and 10^3 K, respectively [13]. Hydrogen atoms penetrate between iron atoms located in the interface region and lose electrons to the common conduction band. This should bring about an increase in the *s* electron density at iron

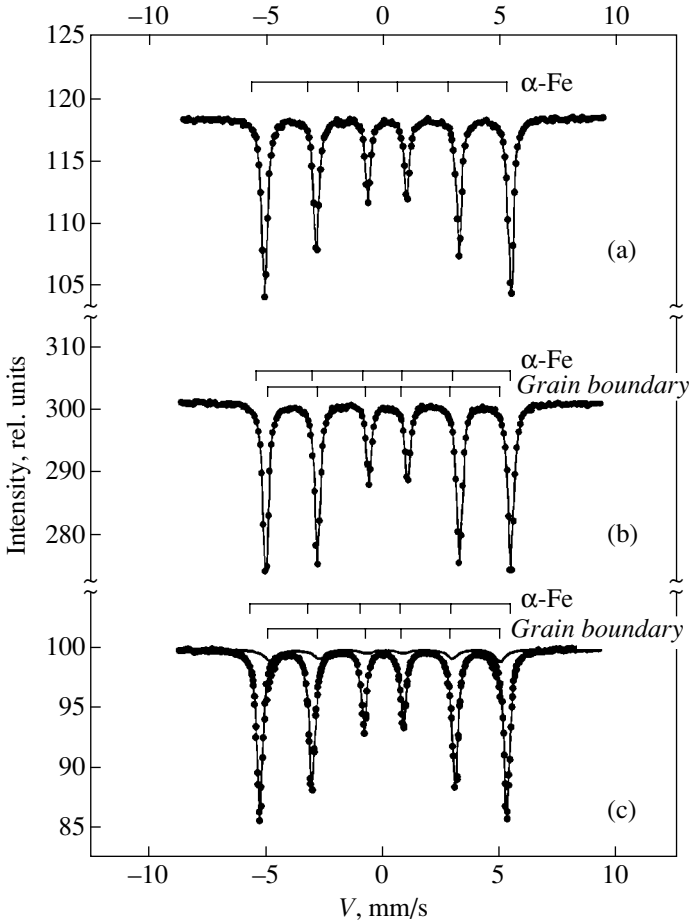

Fig. 3. Mössbauer spectra of (a) the initial carbonyl iron and carbonyl iron after milling in hydrogen for (b) 2 and (c) 8 h.

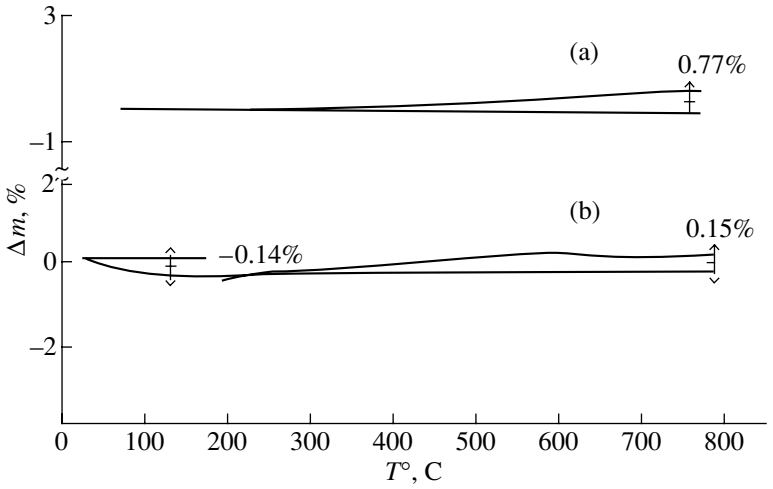

Fig. 4. Thermogravimetric curves for iron samples prepared through mechanical dispersion in hydrogen for (a) 2 and (b) 8 h.

nuclei and, correspondingly, a decrease in the isomer shift. Thus, the decrease in the isomer shift of the partial spectrum of the grain boundary in our sample is indirect evidence that, during the milling of iron in a hydrogen atmosphere for 8 h, hydrogen is incorporated into the interface region. It should be noted that, in the Mössbauer spectra of nanocrystalline iron milled in an argon atmosphere for 8 h, the isomer shift of the partial spectrum of the grain boundary does not decrease, which also corroborates our assumption.

In order to directly confirm the incorporation of hydrogen into the structure of grain boundaries in nanocrystalline iron, we carried out a thermogravimetric analysis of our samples. The temperature dependences of the weight change for the nanocrystalline iron samples are plotted in Fig. 4. For the iron sample prepared by milling for 8 h (unlike the sample after milling for 2h), the weight loss in the temperature range 100–200°C is equal to 0.14 wt %. A decrease in the weight in this temperature range is characteristic of hydrogen release (removal). The possible amount of hydrogen incorporated into the structure of grain boundaries can be theoretically estimated from our structural data: the grain size in this sample is equal to 13 nm, the grain boundary width is as large as 1 nm, and the fraction of iron atoms in the grain boundary region is ~16% of the total number of iron atoms (see the calculated Mössbauer parameters in Table 3). With due regard for the atomic weight coefficients, the calculated weight fraction of hydrogen incorporated into the grain boundaries is equal to ~0.15%, which is in good agreement with the thermogravimetric data. Thus, the thermogravimetric measurements experimentally confirmed the incorporation of hydrogen into grain boundaries in the sample for which we observed indirect indications of this incorporation, namely, a sharp increase in the degree of lattice strain and an unexpected decrease in the isomer shift in the Mössbauer spectrum of the grain boundary.

The above investigation of the nanocrystalline iron samples prepared through mechanical dispersion in a hydrogen atmosphere demonstrated that an increase in the milling time to 8 h leads to the incorporation of hydrogen into defect-rich interface regions in nanocrystalline iron samples. It is worth noting that a drastic increase in the coercive force is also observed for this sample. According to the structural data, this increase can be explained as follows. The mean grain size in this sample (13 nm) indicates that the nanocrystalline iron grains are in the single-domain state. The incorporation of hydrogen into interface regions increases their density and, thus, hinders the domain wall motion, which results in an increase in the coercive force.

Analysis of the intensity ratio of the hyperfine magnetic structure components in the Mössbauer spectra of the iron samples milled in hydrogen revealed its deviation from the ratio $I_{1.6} : I_{2.5} : I_{3.4} = 3 : 2 : 1$ (characteristic of polycrystalline iron), at which the angle θ between the directions of the mean magnetic moment and the incident gamma-ray beam is equal to 54°. Thus, the samples milled for 2 and 8 h in hydrogen are characterized by a preferential direction of the magnetic moments with respect to the direction of the gamma-ray beam (θ = 66° and 59°, respectively); i.e., these samples exhibit a magnetic texture. A comparison of these data and the microtopograms obtained by scanning electron microscopy for the samples under investigation [14] allowed us to conclude that these samples possess strain-induced magnetic anisotropy. As follows from the calculated dependence of the integrated intensity of x-ray reflections on the tangent of the diffraction angle, the direction of anisotropy coincides with the (011) direction, which is the easy magnetization axis in iron. Therefore, it is this anisotropy that leads to a change in the field dependence of the saturation magne-

tization for nanocrystalline iron (milled in a hydrogen atmosphere) as compared to that for isotropic polycrystalline iron.

ACKNOWLEDGMENTS

We would like to thank B.P. Tarasov (Institute of New Chemical Problems, Russian Academy of Sciences) for preparing the nanocrystalline iron samples.

This work was supported by the Russian Foundation for Basic Research, project no. 00-02-16603.

REFERENCES

1. H. Gleiter, Prog. Mater. Sci. **3**, 223 (1998).
2. A. I. Gusev, *Nanocrystalline Materials: Methods of Preparation and Properties* (NISO Ural. Otd. Ross. Akad. Nauk, Yekaterinburg, 1998).
3. A. A. Novakova, O. V. Agladze, B. P. Tarasov, *et al.*, Mater. Sci. Forum **269–272**, 127 (1998).
4. V. E. Antonov, I. T. Belash, V. F Degtyareva, E. G. Ponyatovskiĭ, and V. I. Shiryaev, Dokl. Akad. Nauk SSSR **252** (6), 1384 (1980) [Sov. Phys. Dokl. **25**, 490 (1980)].
5. V. E. Antonov, I. T. Belash, and E. G. Ponyatovskii, Scr. Metall. **16** (20), 203 (1982).
6. L. S. Darken and R. P. Smith, Corrosion (Houston) **5**, 1 (1949).
7. D. M. Allen-Booth and J. Newitt, Acta Metall. **22**, 171 (1974).
8. M. L. Hill and E. W. Johnson, Trans. AIME **215**, 717 (1959).
9. R. A. Oriani, Acta Metall. **18**, 147 (1970).
10. M. A. Whiteman and A. R. Triano, Phys. Status Solidi **7**, K109 (1964).
11. J. E. Newman and L. L. Shreir, J. Iron Steel Inst., London **207**, 1369 (1969).
12. U. Herr, J. Jing, R. Birringer, *et al.*, Appl. Phys. Lett. **50** (8), 472 (1987).
13. A. G. Avvakumov, *Mechanical Methods of the Activation of Chemical Processes* (Nauka, Novosibirsk, 1986).
14. A. A. Novakova, O. V. Agladze, R. S. Gvozdover, *et al.*, Poverkhnost, No. 12, 27 (2000).

Translated by O. Borovik-Romanova

Physics of the Solid State, Vol. 43, No. 8, 2001, pp. 1509–1514. Translated from Fizika Tverdogo Tela, Vol. 43, No. 8, 2001, pp. 1449–1454.

MAGNETISM AND FERROELECTRICITY

Magnetic Configurations in the Region of a Nanocontact between Ferromagnetic Bars

L. L. Savchenko*, A. K. Zvezdin, A. F. Popkov***, and K. A. Zvezdin****

**Moscow State University, Vorob'evy gory, Moscow, 119899 Russia*

***Institute of General Physics, Russian Academy of Sciences, ul. Vavilova 38, Moscow, 117942 Russia*

****Lukin Research Institute of Physical Problems, Zelenograd, Moscow, 103460 Russia*

e-mail: popkov@nonlin.msk.ru

Received September 5, 2000; in final form, December 14, 2000

Abstract—A numerical solution to the Landau–Lifshitz and magnetostatics equations is used to study the residual magnetic configurations as functions of magnetic and geometrical parameters in the region of a magnetic nanocontact between oppositely magnetized ferromagnetic electrodes in the form of bulk bars. The conditions for the emergence of antiparallel orientations of adjacent spins and the domain wall in the conducting channel are determined. © *2001 MAIK "Nauka/Interperiodica".*

1. INTRODUCTION

Interest in magnetic nanocontacts has been growing steadily owing to their possible use in controllable strong variations in conductivity induced by an external magnetic field. This was recently demonstrated in experiments with longitudinally magnetized nickel bars [1]. Peculiarities in the conduction of magnetic nanocontacts in the region of its quantization are considered in publications [2, 3], which demonstrate the significant role played by the spin distribution inside the conduction channel in the spin transport. Micromagnetic configurations of the magnetization of a cobalt nanocontact between two flattened ferromagnetic electrodes formed during magnetization reversal were simulated numerically in [4]. The work by Bobo *et al.* [5], who studied the effect of ferromagnetic microbridges in antiferromagnetically coupled layers on the hysteresis properties of a multilayered structure, is also worth mentioning. Longitudinally magnetized bars that are in contact have not been subjected to miromagnetic analysis to date. We will study the effect of the competition between the long-range magnetostatic interaction, local exchange interaction, and the energy of anisotropy on the formation of rest configurations in the contact region between two oppositely magnetized bulk bars depending on the form factor of the channel.

2. BASIC EQUATIONS

Stationary configurations of magnetization were studied by numerically solving the Cauchy problem for the Landau–Lifshitz equation:

$$\frac{\partial \mathbf{M}}{\partial t} = -\gamma^*\left(\mathbf{M}\times\left[\mathbf{H}_{\text{eff}} + \frac{\alpha}{M}(\mathbf{M}\times\mathbf{H}_{\text{eff}})\right]\right), \qquad (1)$$

where M is the magnetization vector; $\gamma^* = \gamma/(1+\alpha^2)$, with γ and α being the gyromagnetic ratio and the Gilbert damping parameter, respectively; the effective magnetic field $\mathbf{H}_{\text{eff}} = \mathbf{H} + \mathbf{H}^m + \mathbf{H}^{\text{an}} + \mathbf{H}^{\text{ex}}$ includes the external field $\mathbf{H}$; the demagnetization field

$$\mathbf{H}^m = -\nabla\left(-\int_V d\mathbf{r}'\frac{\nabla\mathbf{M}(r')}{|\mathbf{r}-\mathbf{r}'|} + \int_S d\mathbf{r}_s\frac{(\mathbf{M}\mathbf{n}_s)_s}{|\mathbf{r}-\mathbf{r}_s|}\right)$$

(r is the radius vector of the point, V and S are the volume and the surface area of the magnetic structure, and $\mathbf{n}_s$ is the normal to its boundary); the uniaxial-anisotropy field $\mathbf{H}^{\text{an}} = (2K_u/M^2)(\mathbf{M}, \mathbf{n}_u)\mathbf{n}_u$ (K_u is the anisotropy constant and $\mathbf{n}_u$ is the unit vector along the easy magnetization axis); and the nonuniform-exchange field $\mathbf{H}^{\text{ex}} = (2A/M^2)\Delta\mathbf{M}$ (A is the exchange constant and Δ is the two-dimensional Laplace operator).

The boundary condition at the lateral surfaces of the structure has the form

$$\left.\frac{\partial \mathbf{M}}{\partial \mathbf{n}_s}\right|_S = 0; \qquad (2)$$

that is, it corresponds to the free boundary conditions [6].

An important feature of the physical system under consideration is that the spins in the magnetic bars at large distances from the contact are oriented strictly along the z axis and are antiparallel; i.e., $\mathbf{M}|_{z=\mp\infty} = (0, 0, \pm M)$. In the experiments made by Garcia *et al.* [1], this was attained, for example, using coils localized at the outer ends of the bars. For this reason, it is natural to assume that the left and right rods are magnitized virtually uniformly along their entire length except along the region in the vicinity of the nanocontact. It is also

natural to assume that the characteristic length scale of the region where the magnetization is distributed nonuniformly is proportional to the cross section of the bars (this is confirmed by the results of numerical experiments). The same conclusion can be made from an analysis of numerical experiments on the magnetization reversal of long isolated bars [7]. Consequently, the entire region $|z| < L$ under investigation (where L is the length of the bar in contact) can be divided for numerical simulation into three parts: $-L < z < -z_0$, $-z_0 < z < +z_0$, and $z_0 < z < L$. The magnetization in the first and last regions is assumed to be homogeneous and equal to $\mathbf{M} = (0, 0, \pm M)$, where the upper sign corresponds to the first region and the lower sign to the last. In the calculation region $|z| < z_0$ ($z_0 \gg W$, where W is the transverse size of the bar), the magnetization is calculated by solving the Landau–Lifshitz equations with allowance for the magnetic dipole interaction and the boundary conditions $\mathbf{M}|_{\mp z_0} = (0, 0, \pm M)$. On the remaining surfaces in which a magnetization jump takes place, the abovementioned free boundary conditions corresponding to unpinned spins are used.

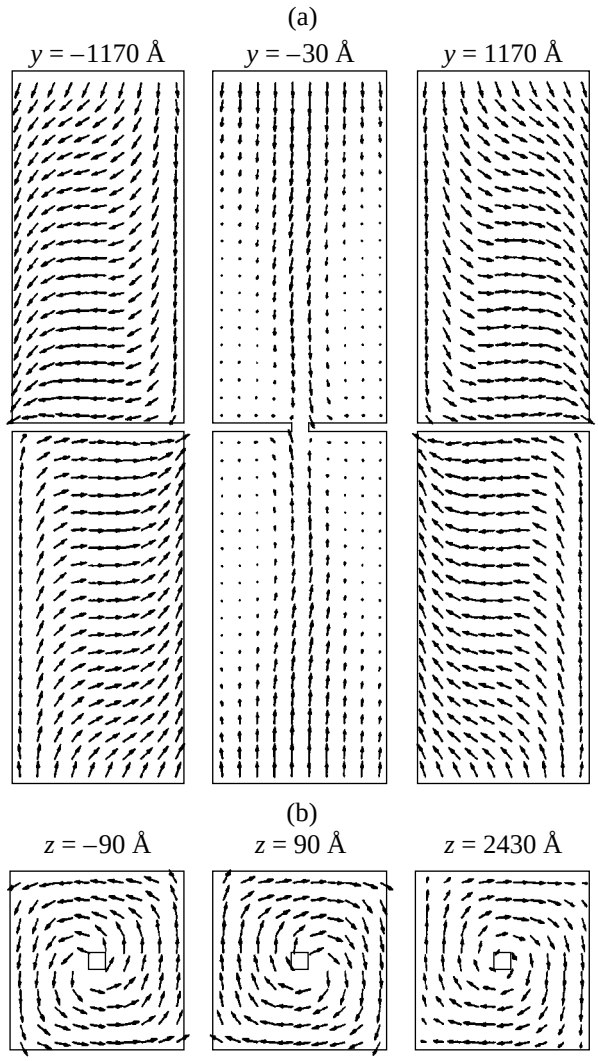

Fig. 1. Spin distribution in oppositely magnetized contacting ferromagnetic bars with a broad $24 \times 24 \times 12$-nm rectangular constriction located at the center of the contacting end faces of the ferromagnetic bars with a 240×240-nm square cross section in the case of weak anisotropy: (a) in longitudinal cross sections parallel to the *xz* plane and (b) in cross sections parallel to the *xy* plane.

The methods of numerical integration of the Landau–Lifshitz equations are described in detail in the literature and have been extensively tested (see, for example, [8–11]).

3. CONTACT BETWEEN TWO OPPOSITELY MAGNETIZED BARS

Let us consider two contacting oppositely magnetized semi-infinite bars having a square cross section of their side $W = 240$ nm, arranged along the z axis, and connected through a rectangular junction of size $w \times w \times l$. We assume that the nanocontact is formed either at the center between contacting ends, as in Figs. 1 and 2, or displaced from the center to the edge of the bars by $\Delta x = 60$ nm, as shown in Fig. 3. The size of the calculation region along the z axis is chosen such that it has the maximum possible value, $2z_0 = 960$ nm. The magnetic material parameters are assumed to be close to the permalloy parameters; i.e., $M = 800$ G, $K_u = 1000$ erg/cm^3, and $A = 10^{-6}$ erg/cm. The initial distribution is chosen in the form of two oppositely magnetized regions along the z axis separated by a line passing through the center of the contact. In order to break the symmetry of the initial distribution in the numerical integration, a small transverse magnetic field ~1 Oe is introduced. In the mesh partition, we use a $6 \times 6 \times 6$-nm cubic mesh whose characteristic size is approximately equal to the exchange length $l_{ex} = (A/2\pi M^2)^{1/2}$. Numerical calculations lead to the final steady-state configurations of the spatial spin distribution presented in Figs. 1–8.

According to the results of calculations, the volume distribution of magnetization over the electrodes of the contact is affected only slightly by introducing a magnetic constriction (except in the immediate vicinity of the nanocontact). The principal configuration mode of the spin state of the electrodes is a vortex magnetization distribution in the vicinity of the contacting ends of bars with opposite rotations of their spin (Fig. 1). This state agrees with the theory of magnetization reversal of a long bar. Indeed, it is well known [12] that the homogeneous state in an infinitely long cylinder under a magnetization reversing field becomes unstable with respect to the formation of the Brown vortex mode when the magnetization reversing field has the critical value

$$H = 2K/M + 1.08(2\pi M)(A/M^2)/R^2, \qquad (3)$$

where R is the cylinder radius. Obviously, the demagnetizing field in the vicinity of the contacting ends of

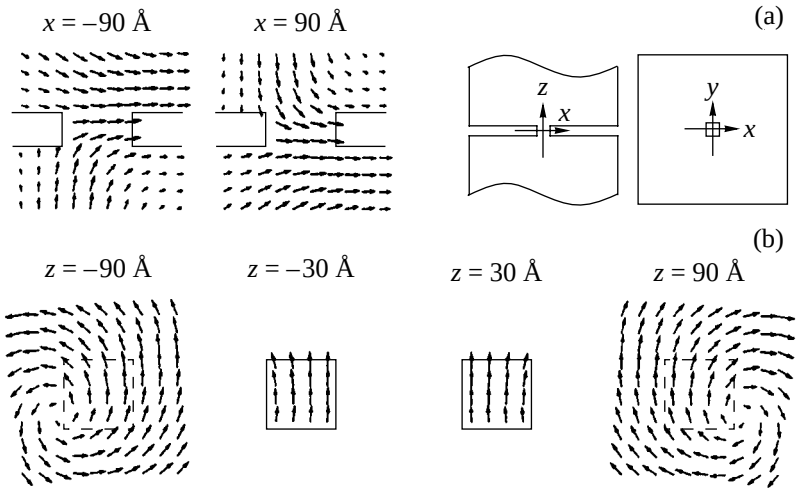

Fig. 2. Magnified fragments of the spin distribution in oppositely magnetized contacting ferromagnetic bars with a broad $24 \times 24 \times$ 12-nm rectangular constriction located at the center of the contacting end faces of the ferromagnetic bars in the case of weak anisotropy in the vicinity of the nanocontact: (a) in longitudinal cross sections parallel to the *yz* plane and (b) in cross sections parallel to the *xy* plane.

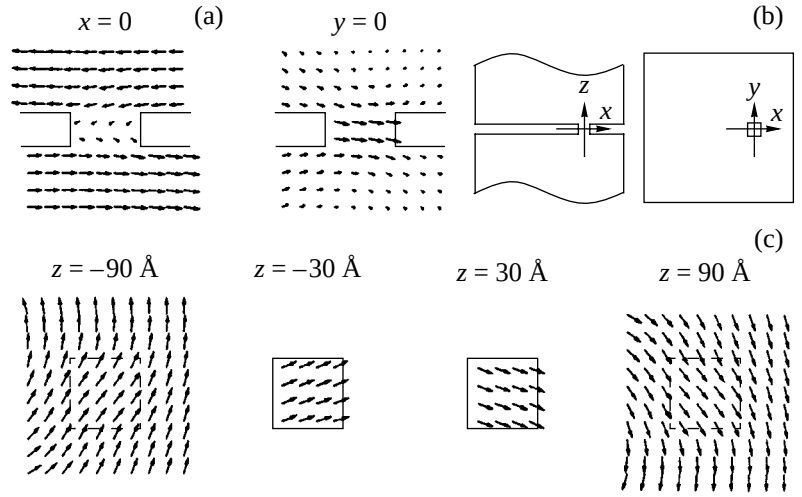

Fig. 3. Fragments of spin distributions in the *yz*, *xz*, and *xy* cross sections in the vicinity of the nanocontact between oppositely magnetized ferromagnetic bars with a broad $24 \times 24 \times 12$-nm constriction displaced by 60 nm to the edge of the cross section of the contacting bars along the *x* axis in the case of weak anisotropy. The projections of the structure under investigation on the *xz* and *xy* planes are shown on the right.

bars magnetized to saturation in opposite directions is $H = 4\pi M$. For this reason, the critical value of the anisotropy field for the formation of a vortex mode in the contacting bars is given by

$$(2K/M)_{cr} = 4\pi M(1 - 0.54(A/M^2)/R^2). \quad (4)$$

In the case of an isolated long bar of finite length, the demagnetizing field near the end at saturation is $H = 2\pi M$. Therefore, the critical anisotropy field for the formation of a vortex mode is considerably lower in this bar:

$$(2K/M)_{cr} = 2\pi M(1 - 1.08(A/M^2)/R^2). \quad (5)$$

Results of micromagnetic simulation [7] have proved that vortex magnetization distributions rotated in the same or opposite directions are formed near the ends of an isolated finite-length bar with an anisotropy lower than the critical value. In our case, vortex states with opposite rotations are preferred in the vicinity of the contact of oppositely magnetized bars because of their magnetostatic interaction.

The presence of a magnetic bridge (nanoconstriction) between the bars does not affect the distribution of most of the spins in them but changes the micromagnetic configuration in the immediate vicinity of the nanocontact. If there is a short, wide constriction at the

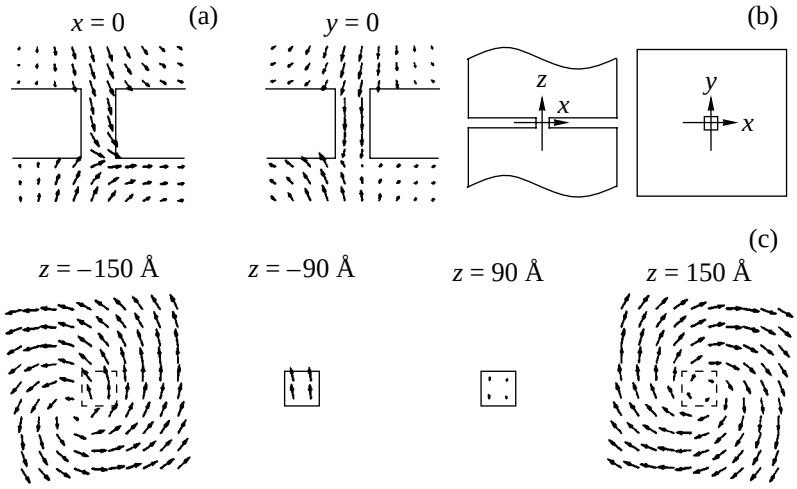

Fig. 4. Magnified fragments of the spin distribution in cross sections in the vicinity of the nanocontact between two oppositely magnetized bars with a narrow $12 \times 12 \times 24$-nm constriction located at the center.

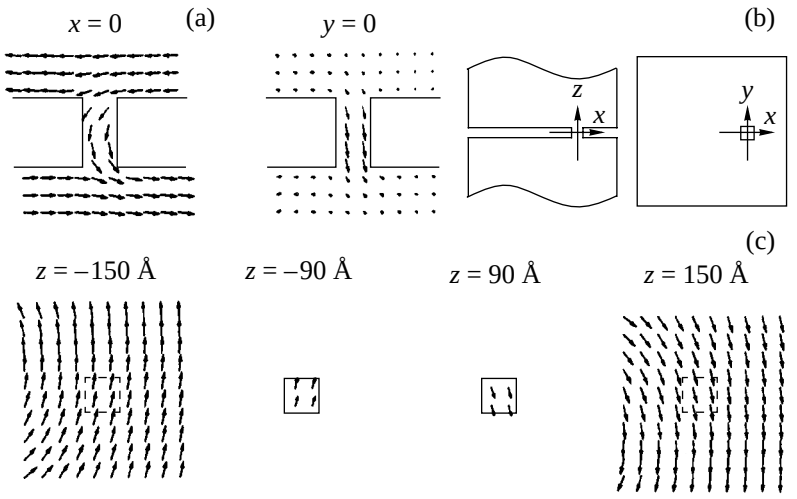

Fig. 5. Fragments of spin distributions in oppositely magnetized bars with a displaced narrow $12 \times 12 \times 24$-nm constriction in cross sections parallel to the *xy* plane.

center of the contacting end faces of the bars, the centers of the vortices are pushed apart and a blurred transition region is formed near the contact with a transverse magnetization in the contact (Fig. 2). The spin distribution along the central axis in fact resembles the spin distribution across the Néel domain wall. The asymmetry of the spin distribution along the *z* axis increases in the vicinity of the edges of the nanoconstriction. In the case of a long nanocontact located at the center of the bar cross section, an essentially asymmetric spin distribution is formed: the center of one of the vortices is drawn into the nanoconstriction so that the magnetization in the long contact is parallel to its axis up to the entrance to the other bar (Fig. 4). In this case, the center of the second vortex is displaced due to magnetostatic repulsion, so that a transition region similar to a Néel domain wall is formed in the vicinity of the entrance to the nanoconstriction.

If the nanoconstriction is located away from the center of the bar, the vortex and the antivortex in the contacting bars create transverse-magnetization zones with opposite directions of the magnetization at the entrance and exit of the nanoconstriction. This is shown in Fig. 3 for a short constriction and in Fig. 5 for a long constriction. Depending on the form factor of the constriction, the transition region has either the form of a Bloch boundary (for a broad constriction) or the form of a Néel boundary (for a narrow constriction). In both cases, the transition region is blurred at least over the length of the constriction. This is due to the low anisotropy and strong effect of long-range magnetostatic interaction. In the presence of a strong anisotropy

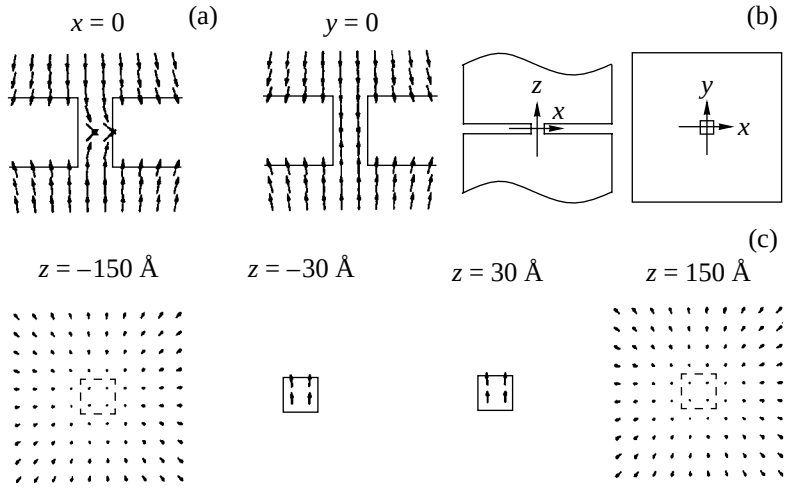

Fig. 6. Domain wall in the long nanocontact between ferromagnetic bars with a strong longitudinal anisotropy $K_u = 3 \times 10^6$ erg/cm^3.

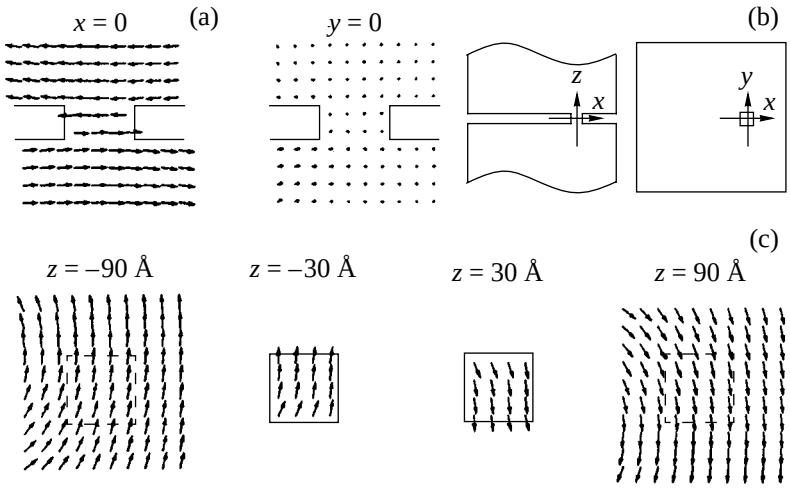

Fig. 7. Micromagnetic distributions in the vicinity of a nanocontact for the displaced broad constriction presented in Fig. 3, but with a discontinuity in the exchange interaction in the middle of the channel.

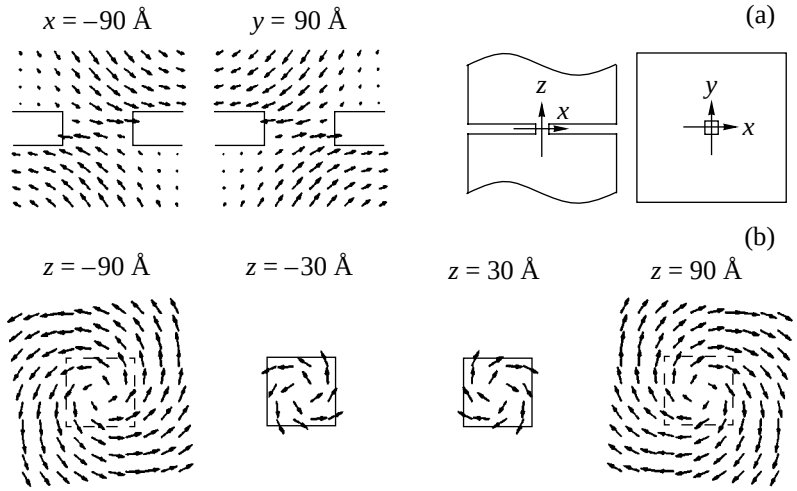

Fig. 8. Vortex states of spins in the long nanocontact presented in Fig. 2 with a discontinuity of the exchange interaction in the middle of the constriction.

($K_u = 3 \times 10^6$ erg/cm^3) with the easy axis directed along the bar axis, the vortex mode of demagnetization of the bars disappears and a head-to-head Néel type domain wall is formed in the long constriction (Fig. 6).

Let us now discuss the effect of discontinuity of the exchange interaction in the contact. Such a discontinuity appears natural in the presence of a nonmagnetic interlayer and in the case when the contact is formed mechanically. It leads to the antiferromagnetic orientation of adjacent spins in weakly anisotropic materials in short and long contacts displaced relative to the center of the bars (Fig. 7) and to the emergence of a peculiar vortex–antivortex spin structure with a discontinuity on the zero-exchange line in the contact when it is located at the center (Fig. 8).

4. CONCLUSION

Thus, the numerical analysis carried out by us shows that in a weakly anisotropic magnetic contact formed by a nanoconstriction between two oppositely magnetized rectangular bars, vortex states appear in the region of their contacting ends and a blurred transition region occurs over the entire length of the contact. Depending on the form factor of the constriction, spins are rotated along the constriction axis either across the channel analogously to a Bloch domain wall (in a short broad channel) or, as in a Néel wall, with a spin distribution in the channel parallel to its axis. The presence of a discontinuity in the exchange interaction in the constriction channel leads to the emergence of an antiferromagnetic jump of spins on the discontinuity line, and a peculiar state of the junction of oppositely rotated magnetic vortices is formed at the center of the nanocontact of the symmetric 3D structures.

The presence of strong anisotropy along the channel axis leads to the formation of a domain wall of the head-to-head type in the constriction. A transition from the asymmetric state with a domain wall displaced to the edge of the constriction to the symmetric state has the form of a first- or second-order phase transition depending on the form factor of the constriction and on the ratio of the magnetostatic energy to the uniaxial-anisotropy energy.

These peculiarities of micromagnetic states in the vicinity of a nanocontact must be taken into account in analyzing the spin transport in such structures in the conductivity quantization region.

ACKNOWLEDGMENTS

One of the authors (A. K. Z.) is grateful to N. Garcia for his hospitality and valuable discussions during the author's visit to the Institute of Physics of Small Systems and Nanotechnologies (Madrid) in 1998.

This work was supported by the Russian Foundation for Basic Research, project nos. 98-02-16469 and 00-02-17240.

REFERENCES

1. N. Garcia, M. Munoz, and Y.-W. Zhao, Phys. Rev. Lett. **82** (14), 2923 (1999).
2. H. Imamura, N. Kobayashi, S. Takahashi, and S. Maekawa, Phys. Rev. Lett. **84** (5), 1003 (2000).
3. A. K. Zvezdin and A. F. Popkov, Pis'ma Zh. Éksp. Teor. Fiz. **71** (5), 304 (2000) [JETP Lett. **71**, 209 (2000)].
4. R. P. van Garkom, S. J. C. H. Theeuwen, K. P. Wellock, *et al.*, Appl. Phys. Lett. **74** (3), 422 (1999).
5. J. F. Bobo, H. Kikuchi, O. Redon, *et al.*, Phys. Rev. B **60** (6), 4131 (1999).
6. A. G. Gurevich, in *Magnetic Resonance in Ferrites and Antiferromagnets* (Nauka, Moscow, 1973), p. 410.
7. M. E. Shabes, J. Magn. Magn. Mater. **95**, 249 (1991).
8. E. D. Boerner and H. N. Bertram, IEEE Trans. Magn. **33** (5), 3052 (1997).
9. N. Hayashi, K. Kosavisutte, and Y. Nakatani, IEEE Trans. Magn. **33** (5), 4164 (1997).
10. A. F. Popkov, L. L. Savchenko, and N. V. Vorotnikova, Pis'ma Zh. Éksp. Teor. Fiz. **69** (8), 555 (1999) [JETP Lett. **69**, 596 (1999)].
11. A. F. Popkov, L. L. Savchenko, N. V. Vorotnikova, *et al.*, J. Appl. Phys. **77** (2), 277 (2000).
12. S. Shtrikman and D. Treves, in *Magnetism*, Vol. 3: *Spin Arragements and Crystal Structure, Domains, and Micromagnetics*, Ed. by G. T. Rado and H. Shul (Academic, New York, 1963), pp. 395–414.

Translated by N. Wadhwa

Physics of the Solid State, Vol. 43, No. 8, 2001, pp. 1515–1517. Translated from Fizika Tverdogo Tela, Vol. 43, No. 8, 2001, pp. 1455–1457.

MAGNETISM AND FERROELECTRICITY

On Estimating Nanoparticle Size with the Help of the Mössbauer Effect

V. I. Nikolaev*, A. M. Shipilin, and I. N. Zakharova****

** Moscow State University, Vorob'evy gory, Moscow, 119899 Russia*

*** Yaroslavl State Technical University, Moskovskiĭ pr. 88, Yaroslavl, 150023 Russia*

e-mail: vnik@cs.msu.su

e-mail: shipilin@polytech.yaroslavl.su

Received October 16, 2000

Abstract—A method for estimating nanoparticle size by determining the distribution function $p(H_n)$ of hyperfine magnetic fields from data on the Mössbauer spectrum of ^{57}Fe nuclei is described. The idea of the method stems from the fact that, owing to the breaking of exchange bonds for surface atoms, their contribution to the total area bounded by the $p(H_n)$ curve can be singled out. The potentialities of the method are illustrated using the data obtained in experiments with nanoparticles of magnetite. © *2001 MAIK "Nauka/Interperiodica".*

The analysis of the properties of surface layers of nanoparticles is an important but complicated problem in solid-state physics. Methods of investigation into such problems should make it possible to observe the surface and bulk layers of atoms constituting nanoparticles. In this communication, we demonstrate that Mössbauer spectroscopy provides quantitative information not only on the properties of surface layers but also on the nanoparticle size.

The method proposed by us involves determining the distribution function p of a parameter of the Mössbauer spectrum of a system of ultrasmall particles. From this point of view, the most interesting object is the ^{57}Fe isotope, for which the variations of the spectral parameters associated with a change in the closest surrounding of a nucleus can be recorded reliably. In view of the high sensitivity of the hyperfine field H_n to the closest surrounding of a ^{57}Fe nucleus, the distribution function $p(H_n)$ of these fields is especially convenient for this purpose. The size of the particles can be estimated by calculating the total area $S = S_e + S_i$ that is bounded by the $p(H_n)$ curve and by separating the part S_e that corresponds to surface atoms (S_i is the contribution to S from the internal iron atoms). Indeed, assuming that the volumes of the external and internal regions are $V_e = 4\pi r^2\Delta r$ and $V_i = 4/3\pi r^3$, respectively (r is the particle radius and Δr is the thickness of the surface region), we can approximate that

$$S_e/S_i = 3\Delta r/r,$$

since $S_e/S_i = V_e/V_i$.

The object of our investigation was ultradisperse powder of magnetite obtained through the standard chemical condensation technique. According to electron microscopy data, the average size of magnetite particles was $d(=2r) \approx 7.5 \pm 0.5$ nm. The Mössbauer spectra were recorded in terms of absorption geometry. The sample thickness was ~0.15 mg^{57}Fe/cm^2, which corresponds to a thin sample [1]. The radiation source was a ^{57}Co isotope in a Cr matrix. In order to obtain the magnetic-field distribution function $p(H_n)$ at the sites of ^{57}Fe nuclei in the nanoparticle system under investigation, we used the formalism of "restoring and improving the image quality" [2] (see also [1] on this subject).

The choice of magnetite was dictated by the fact that its crystalline and magnetic structures have been studied comprehensively. In addition, the features of the Mössbauer spectrum of ^{57}Fe nuclei in bulk particles of this ferrimagnetic oxide are well known. In particular, we took into account the fact that, as the magnetite particle size d decreases, the Verwey transition temperature for them increases noticeably. For nanoparticles, it exceeds room temperature [3, 4], whereas it amounts to 119 K for bulk particles.

From Fig. 1, it can be seen that the Mössbauer spectrum of magnetite nanoparticles at room temperature has the same appearance as the spectrum for bulk magnetite particles below the Verwey point [5]. This might be a confirmation of the fact that, in accordance with [3], the Verwey transition temperature for the particles under investigation is indeed higher than room temperature. Consequently, for the internal, as well as for the external nuclei, the spectrum can be treated as a superposition of three partial spectra: two sextets which are close in their parameters and correspond to trivalent iron ions $Fe^{3+}(A)$ and $Fe^{3+}(B)$ at A and B sites and a sextet with a slightly weaker splitting from bivalent iron ions $Fe^{2+}(B)$ at B sites.

Figure 2 shows the distribution function $p(H_n)$ of the effective magnetic fields corresponding to this spec-

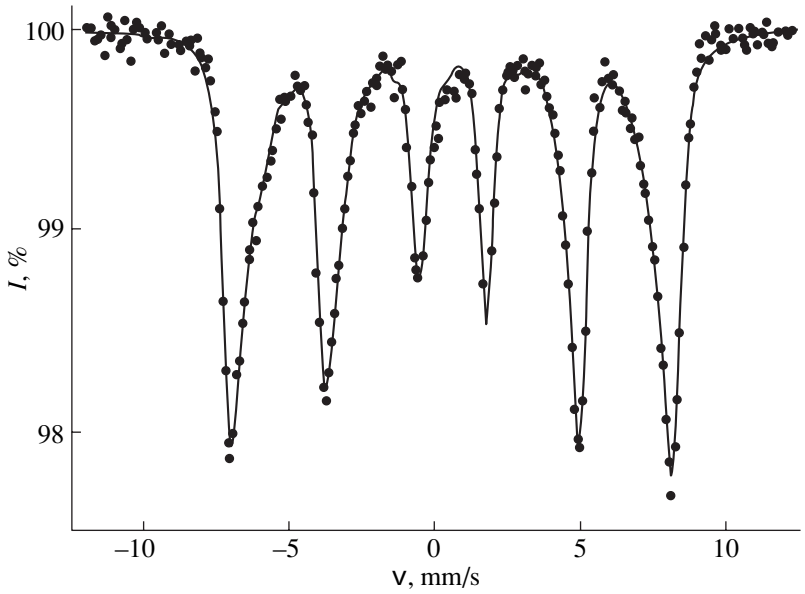

Fig. 1. Mössbauer spectrum of magnetite nanoparticles at room temperature.

trum. Four peaks can be clearly seen on the picture; they correspond to the following values of magnetic fields: H_{n1} = 407 kOe, H_{n2} = 431 kOe, H_{n3} = 456 kOe, and H_{n4} = 482 kOe. The last two fields obviously correspond to the fields for $Fe^{2+}(B)$ ions, as well as for $Fe^{3+}(A)$ and $Fe^{3+}(B)$ ions, in the internal regions.

As regards the fields H_{n1} and H_{n2}, it is natural to assume that they are analogs of H_{n3} and H_{n4} but correspond to iron ions in the surface region of a particle. Taking into account the crystalline structure of magnetite, we can attribute to the surface region two outer layers of iron ions whose surrounding differs from that of inner iron ions. The decrease in the effective magnetic fields at the sites of ^{57}Fe nuclei for surface ions $Fe^{3+}(A)$, $Fe^{3+}(B)$, and $Fe^{2+}(B)$ amounts to ~50 kOe. This decrease is associated with the different numbers of indirect exchange bonds for inner and surface iron ions, because the latter ions are deprived of a considerable part of these bonds.

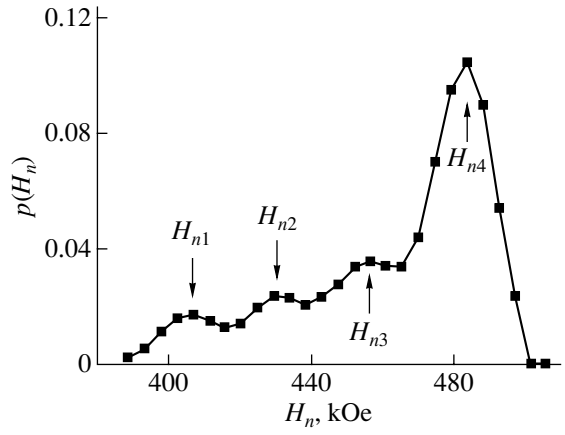

Fig. 2. Hyperfine-field distribution function $p(H_n)$ corresponding to the spectrum depicted in Fig. 1.

The contributions to the effective magnetic field from each of the indirect exchange bonds for a Fe^{3+} ion in the spinel structure were estimated in [6, 7] using the method of molecular orbitals in the approximation of a linear combination of atomic orbitals. These contributions, for the *A* and *B* sites, amounted to 8 and 12 kOe, respectively. Since twelve iron ions at the *B* sites form the closest cationic surrounding of a $Fe^{3+}(A)$ ion and six ions at the *A* sites form the nearest neighborhood for an iron ion in the *B* position, the lack of half the bonds should lead to a decrease in the effective magnetic fields by several tens of kilooersteds, which agrees with our experimental data.

The data obtained on the function $p(H_n)$ can be used to estimate the area under each peak and, hence, the ratio of the volumes V_e and V_i of the external and internal regions, respectively. According to our estimates obtained for the magnetite particles under investigation, $V_e/V_i \approx 0.3$. If we take for Δr the thickness of the surface layer as being equal to the length of the Fe–O–Fe exchange bond ($\Delta r \approx 0.4$ nm), we obtain $r \approx 4$ nm in accordance with the above equality for the S_e/S_i ratio. The agreement between the obtained results and the electron microscopy data can be regarded as quite satisfactory (taking into account the approximating nature of the calculations).

Thus, the results of our investigations show that Mössbauer spectroscopy can be used for obtaining

important information on size effects in ultrasmall magnetic particles.

REFERENCES

1. V. I. Nikolaev and V. S. Rusakov, *Mössbauer Investigations of Ferrites* (Mosk. Gos. Univ., Moscow, 1985).
2. Yu. P. Pyt'ev, Dokl. Akad. Nauk SSSR **245**, 315 (1979) [Sov. Phys. Dokl. **24**, 154 (1979)].
3. Yu. F. Krupyanskiĭ and I. P. Suzdalev, Zh. Éksp. Teor. Fiz. **67**, 736 (1974) [Sov. Phys. JETP **40**, 364 (1975)].
4. V. I. Nikolaev and A. M. Shipilin, Fiz. Tverd. Tela (St. Petersburg) **42**, 109 (2000) [Phys. Solid State **42**, 112 (2000)].
5. W. Kündig and R. S. Hargrove, Solid State Commun. **7**, 223 (1969).
6. G. A. Sawatzky, C. Boekema, and F. van der Woude, in *Proceedings of the International Conference on Magnetism, Dresden, 1971*, p. 239.
7. F. van der Woude and G. A. Sawatzky, in *Proceedings of the International Conference on Magnetism, Dresden, 1971*, p. 335.

Translated by N. Wadhwa

Physics of the Solid State, Vol. 43, No. 8, 2001, pp. 1518–1521. Translated from Fizika Tverdogo Tela, Vol. 43, No. 8, 2001, pp. 1458–1461.

MAGNETISM AND FERROELECTRICITY

Effect of Magnetostatic Pressure on the Stabilization of a Two-Phase Domain Structure in Thin Garnet Ferrite Films

Yu. A. Mamaluĭ and Yu. A. Siryuk

Donetsk State University, ul. Universitetskaya 24, Donetsk, 83055 Ukraine

Received October 18, 2000

Abstract—The coexistence of two domain phases, namely, a spiral domain and a bubble-domain lattice, is investigated experimentally in thin garnet ferrite films with uniaxial anisotropy. The condition for this coexistence is shown to be the equality of the magnetostatic pressures of the two phases. It is also shown that the possible formation of a spiral domain structure is determined by the magnetostatic pressure. © *2001 MAIK "Nauka/Interperiodica".*

A wide variety of domain structures are formed in epitaxial garnet ferrite films. These structures are determined by the physical properties of the material of the film and by the magnetic fields and temperature. Considerable recent attention has been focused on a new type of domain structure, namely, spiral domains (SDs) which arise in the presence of alternating and constant magnetic fields. These domains have different properties depending on the conditions under which they are formed. Spiral domain structures with a single arm and two arms were first observed in bulk samples of an MnAlGe alloy [1]. More recently, SDs were observed in garnet ferrite films with the easy axis normal to the film surface in alternating and constant magnetic fields [2–6]. In [2–4], spiral domains were produced from a labyrinth domain structure by applying a pulsed or an alternating magnetic field at a frequency of 100Hz–6 kHz in combination with a bias field. The spiral structure thus obtained existed only in certain ranges of frequencies and magnetic fields; it moved easily across the film and had a finite lifetime; that is, it was a dynamic domain structure. After the field was removed, the labyrinth domain structure became dominant in the film. In [5, 6], spiral domains were also formed from a labyrinth domain structure under the action of a constant magnetic field normal to the film surface. In this case, the SDs formed a stable static pattern if the external field had a certain magnitude. When the field was removed, the SDs were transformed into fields with a smaller number of turns and surrounded by a labyrinth domain structure. In [7], the SDs were stabilized by the bubble lattice (BL) surrounding them; this structure existed even in a zero magnetic field. The SDs surrounded by a BL were produced by magnetic field pulses (of the same polarity) with a repetition frequency of 200–600 Hz and an amplitude of ~60 Oe in the absence of a constant magnetic field; the pulse field was then removed. An SD thus produced in a film and surrounded by a BL could have as many turns as 10 to 30. The sense of the spin could be both clockwise and counterclockwise, and the SD diameter was 100 to 1200 μm. When an SD was destroyed through the application of a magnetic field or through an increase in temperature, a new SD, surrounded by a BL, could be produced with the same characteristics.

In this paper, we investigated the coexistence of two domain phases, a spiral domain and a BL. Faraday rotation was used to observe the domain structure. Measurements were performed on a magnetooptic setup which allowed one to apply a unipolar pulsed field and a constant field at right angles to the film at hand. Spiral domain structures were produced using the method indicated above. We investigated garnet ferrite films of different compositions and thicknesses in which a BL could be produced by a pulsed magnetic field. The films were grown through liquid-phase epitaxy on a gadolinium gallium garnet (111) substrate. The easy axis was normal to the film plane. The quality factor was Q = 1.5–2.5, and the saturation magnetization was $4\pi M_s$ = 140–280 G at room temperature.

The two domain phases are in equilibrium if the magnetostatic pressures of the BL and the SD are equal. The concept of magnetostatic pressure was introduced in [8]; this thermodynamic quantity was defined for a BL as the pressure force per unit length of the contour enclosing some area of the BL. Therefore, the magnetostatic pressure is the derivative (with the minus sign) of the BL energy with respect to the BL area. In [8], it was shown that, for a BL,

$$P = 6(2\pi M_s)^2 C\left(\frac{d}{a}\right)^4 \frac{h}{a}, \qquad (1)$$

where a is the BL parameter, d is the bubble diameter, h is the film thickness, M_s is the saturation magnetization, and C is a constant. For an equilibrium BL, we have $d/a \approx 0.74$ [9]; that is, this ratio is a constant [9] and, therefore, the BL pressure decreases with increasing a/h.

1063-7834/01/4308-1518$21.00

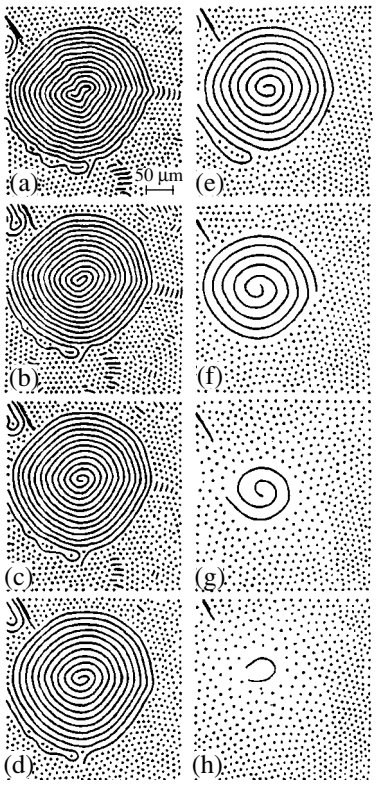

Fig. 1. Influence of a magnetic bias field on the spiral domain. H = (a) 0, (b) 60, (c) 75, (d) 90, (e) 105, (f) 112, (g) 115, and (h) 117 Oe.

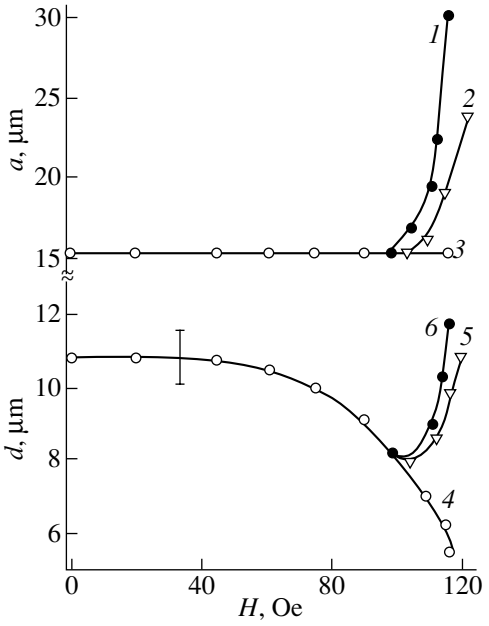

Fig. 2. Influence of a magnetic bias field on the bubble lattice parameter and on the bubble diameter measured at different distances from the spiral domain: (*1*, *6*) 30, (*2*, *5*) 90, and (*3*, *4*) 180 μm.

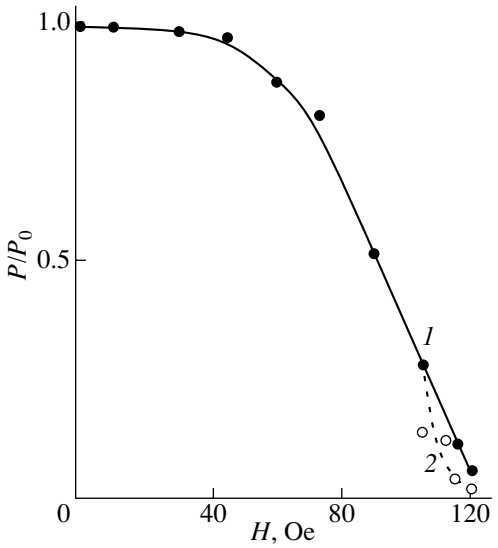

Fig. 3. Magnetostatic pressure of the bubble lattice (in relative units) as a function of bias field. The characteristics of the bubble lattice are measured at different distances from the spiral domain: (*1*) 180 and (*2*) 30 μm.

The magnetostatic pressure of an SD was calculated in [10]. It was shown that the pressure increases as the number of SD turns (or the SD radius) is increased. Therefore, an SD surrounded by a BL can be in equilibrium only where a certain relationship between the SD radius and the relative BL parameter a/h holds true.

Our investigation showed that, in the case of coexistence of two domain phases, the BL parameter a and the bubble diameter d are increased with distance from the SD (Fig. 1). The reason for this is the following. When an SD is produced by a pulsed magnetic field, the initial magnetostatic pressure of the SD is lower than the BL pressure because the SD radius is small. In the process of SD formation, its radius and the number of turns are increased; therefore, the magnetostatic pressure of the SD is also increased. The SD ceases to grow when its pressure and that of the BL become equal. The final radius and the number of turns of the SD are determined by the equilibrium characteristics of the BL. Therefore, the BL parameter and the bubble diameter are changed with distance from the SD (the number of bubbles cannot be changed). Thus, the BL which surrounds an SD is in a quasi-equilibrium state; the equilibrium BL is that produced without an SD, that is, far from the SD.

We investigated the influence of a bias magnetic field on the characteristics of an SD and the BL around it (Fig. 1). The field dependence of the BL characteristics varies with distance from the SD (Fig. 2), but the tendency for the bubble diameter d to decrease with increasing field strength persists in the region in which a remains unchanged. However, in the region in which the BL parameter a increases, the diameter d of the bubbles situated near the SD also increases. The reason for

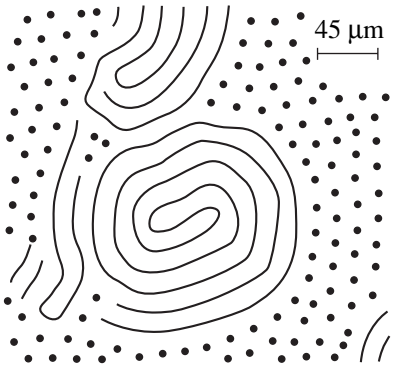

Fig. 4. Bifilar spiral domain (schematic).

the increase in the BL parameter is the expansion of the BL (rather than a decrease in the number of bubbles) with a decrease in the SD diameter in the process of equalization of the pressures of the two domain phases and the establishment of equilibrium between them. It should be noted that, although the parameters a and d increase in this range of magnetic fields, the ratio d/a remains equal to 0.74 to within the experimental error of measurement (~10%). Figure 3 shows the magnetostatic pressure of the BL calculated from the theoretical formula (1) as a function of the bias field determined from the experimental data. It can be seen that, in a certain field range, the BL pressure varies only slightly and, therefore, the SD and BL are in a quasi-equilibrium state. At a certain, critical field, the outer end of the spiral begins to move, thereby decreasing the SD pressure and disturbing the pressure balance, which is accompanied by a rearrangement of the BL. As a result, the SD disappears and only the BL remains in the film.

Examination of films of different compositions and thicknesses showed that the magnetostatic pressure of the BL not only stabilizes the SD but also determines the form of the SD structure. The SD surrounded by a BL is formed in films for which $2.0 \le a/h \le 2.7$. In the case of $a/h \le 2.0$, another type of spiral-domain structure—a bifilar spiral domain—is formed. Similar to an ordinary SD, the bifilar SD is surrounded by a BL and is in an equilibrium state in a zero magnetic field. In contrast to an SD, which has an inner and an outer end, the bifilar SD has two outer ends (Fig. 4). When a bias field is applied to the film, the bifilar SD always unrolls from its inside.

Using the experimentally measured BL characteristics for different films, we calculated the magnetostatic pressure of BLs from Eq. (1) (Fig. 5). Figure 6 shows the energy and pressure of the SD (in relative units) as a function of p/h, calculated from the formulas derived in [10], for $N = 20$ and $l/h = 0.1$ for films of different thicknesses and compositions. Here, p is the SD period, N is the number of turns in the SD, and l is the characteristic length of the film.

From Figs. 5 and 6, it is clear why different types of SD are formed depending on the ratio, a/h, that characterizes the BL. In films for which $2.0 \le a/h \le 2.7$, SDs are formed with $1.5 < p/h < 2.5$; the energy is minimum. If $a/h > 2.7$, the BL pressure is low and the pressure balance of the magnetic phases can take place only in the case of $p/h > 3.0$, where, as seen from Fig. 6, the SD

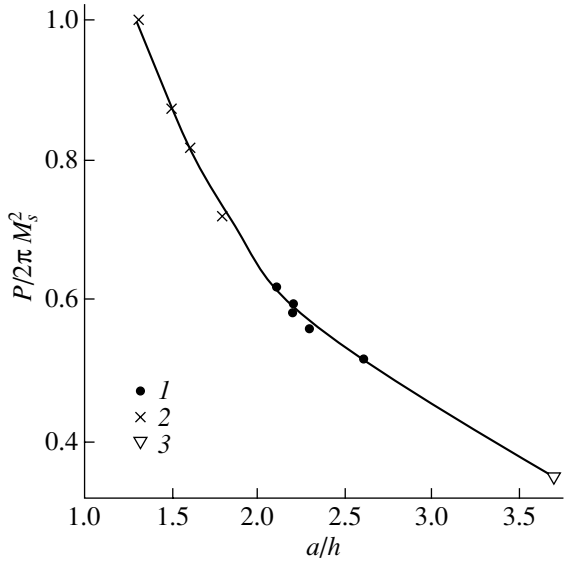

Fig. 5. Magnetostatic pressure of the bubble lattice (in relative units) as a function of the BL parameter a/h in (*1*) films in which a spiral domain is formed, (*2*) films in which a bifilar spiral domain is formed, and (*3*) a film in which no spiral domain structure is formed.

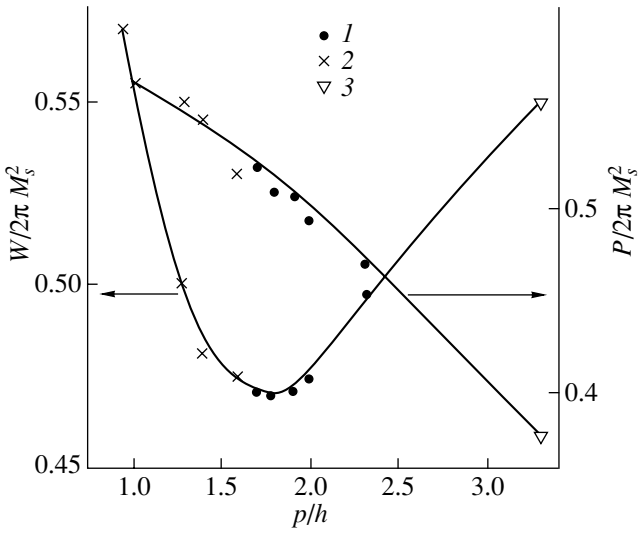

Fig. 6. Energy and the magnetostatic pressure of a spiral domain (in relative units) as a function of the spiral period p/h for (*1*) films in which a spiral domain is formed, (*2*) films in which a bifilar spiral domain is formed, and (*3*) a film in which a spiral domain structure is not stable.

does not correspond to a minimum energy and, in addition, the SD radius is too large ($R = Np/h$) for this domain structure to occur; therefore, only a BL is formed in the film.

When $a/h \leq 2.0$, the pressure of the BL produced in the film is high, such that the SD radius is fixed after its first turn is formed. In this case, the number of turns increases (up to the value at which the domain energy becomes a minimum) through the motion of the inner end of the spiral. For this reason, a bifilar SD with two outer ends is formed.

Thus, our investigations revealed that the stability of coexisting phases is determined by their magnetostatic pressure. It was also shown that the formation of a spiral domain structure and its form depend on the magnetostatic pressure of the bubble lattice.

REFERENCES

1. G. S. Kandaurova, Izv. Vyssh. Uchebn. Zaved., Fiz. **8**, 148 (1971).
2. G. S. Kandaurova and A. É. Sviderskiĭ, Pis'ma Zh. Éksp. Teor. Fiz. **47** (8), 410 (1988) [JETP Lett. **47**, 490 (1988)].
3. F. V. Lisovskiĭ and E. G. Mansvetova, Fiz. Tverd. Tela (Leningrad) **31** (5), 273 (1989) [Sov. Phys. Solid State **31**, 876 (1989)].
4. G. S. Kandaurova and Yu. V. Ivanov, Fiz. Met. Metalloved. **76** (1), 49 (1993).
5. A. P. Ges', V. V. Fedotova, A. K. Bogush, and T. A. Gorbachevskaya, Pis'ma Zh. Éksp. Teor. Fiz. **52** (9), 1079 (1990) [JETP Lett. **52**, 476 (1990)].
6. V. V. Fedotova, A. P. Ges', and T. A. Gorbachevskaya, Fiz. Tverd. Tela (St. Petersburg) **37** (9), 2835 (1995) [Phys. Solid State **37**, 1563 (1995)].
7. K. V. Lamonova, Yu. A. Mamaluĭ, and Yu. A. Siryuk, Fiz. Tekh. Vys. Davleniĭ **6** (1), 33 (1995).
8. V. G. Bar'yakhtar and Yu. I. Gorobets, *Cylindrical Magnetic Domains and Their Lattices* (Naukova Dumka, Kiev, 1988).
9. V. G. Bar'yakhtar, É. A. Zavadskiĭ, Yu. A. Mamaluĭ, and Yu. A. Siryuk, Fiz. Tverd. Tela (Leningrad) **26** (9), 2381 (1984) [Sov. Phys. Solid State **26**, 1443 (1984)].
10. J. A. Mamalui, K. V. Lamonova, and E. N. Soika, J. Phys. IV **8** (2), 393 (1988).

Translated by Yu. Epifanov

Physics of the Solid State, Vol. 43, No. 8, 2001, pp. 1522–1526. Translated from Fizika Tverdogo Tela, Vol. 43, No. 8, 2001, pp. 1462–1466.

MAGNETISM AND FERROELECTRICITY

Ferromagnetic and Spin-Wave Resonance in $Ni_{0.8}Fe_{0.2}/Dy_{1-x}Co_x$ Bilayer Films

R. S. Iskhakov*, V. Yu. Yakovchuk*, S. V. Stolyar, L. A. Chekanova*, and V. A. Seredkin***

** Kirensky Institute of Physics, Siberian Division, Russian Academy of Sciences, Akademgorodok, Krasnoyarsk, 660036 Russia*

*** Krasnoyarsk State University, Krasnoyarsk, 660041 Russia*

e-mail: rauf@iph.krasnoyarsk.su

Received November 1, 2000

Abstract—The standing spin wave spectra of $Ni_{0.8}Fe_{0.2}$(1000–3000 Å)/($Dy_{1-x}Co_x$(700 Å) bilayer exchange-biased films with two different (precompensation $Dy_{0.2}Co_{0.8}$ and postcompensation $Dy_{0.3}Co_{0.7}$) compositions of the hard magnetic layer are analyzed. Measurements are performed at room temperature. It is found that the effective magnetic layer thickness ($d_{eff} = d_0 \pm \Delta d$), which determines the wave vectors of the first modes in the spectrum, differs from the d_0 value specified in film technology. The sign of $|\Delta d| \sim 500$ Å is governed by the composition of the DyCo hard magnetic layer. © *2001 MAIK "Nauka/Interperiodica".*

1. INTRODUCTION

Intensive studies of exchange-biased films of the soft magnetic ferromagnet–hard magnetic ferrimagnet (antiferromagnet) type are stimulated by the modern demand for microelectronics [1]. In the present work, we examined the dynamic magnetic characteristics in order to determine the parameters of ferromagnetic resonance (FMR) and spin-wave resonance (SWR) in bilayer films of the compositions $Ni_{0.8}Fe_{0.2}/Dy_{0.2}Co_{0.8}$ and $Ni_{0.8}Fe_{0.2}/Dy_{0.3}Co_{0.7}$. The choice of these compositions of the rare-earth metal–transition metal amorphous ferrimagnetic alloy was made for the following reasons. It is known that DyCo amorphous alloys prepared in the form of solid solutions over a wide range of concentrations are characterized by a point of magnetic compensation. For example, the $Dy_{0.23}Co_{0.77}$ amorphous alloy is compensated at room temperature. The rare-earth metal–transition metal alloy compositions chosen for our investigations lie on different sides of the compensation point on the composition axis and, at the same time, are characterized by close magnitudes of magnetic characteristics, such as the saturation magnetization M_s= 80 G, the coercive force $H_c \sim 4$ kOe, and the perpendicular magnetic anisotropy $K = 3 \times 10^5$ erg/cm^3 [2].

Analysis of the spin wave spectra of these bilayer films revealed a very interesting effect associated with the exchange interaction between the ferromagnet–ferrimagnet layers. It was found that resonance fields of the first modes of the standing spin waves excited by microwave fields in a permalloy layer substantially depend on the chemical composition of the hard magnetic layer. The present paper reports the results of detailed investigation into this phenomenon.

2. SAMPLE PREPARATION AND EXPERIMENTAL TECHNIQUE

The NiFe/DyCo bilayer exchange-biased films were prepared by thermal evaporation under vacuum (3×10^{-6} mmHg). Cover glasses were used as substrates. The layers were deposited from three independent evaporators with a ring cathode. The permalloy layer was deposited in a constant magnetic field (20 Oe) applied along the sample plane. The thickness of the $Ni_{0.8}Fe_{0.2}$ layer was varied from 1000 to 3000 Å. The thickness of the DyCo hard magnetic layer was equal to 700 Å. Sufficiently low substrate temperatures (≤50°C), which were observed during film deposition, and the amorphous state of the hard magnetic layer (as is known, the diffusion coefficient for amorphous alloys is considerably less than that for their crystal analogues) allowed us to conclude that the studied films had a clearly defined interface between the ferromagnet–ferrimagnet layers. The magnetooptical Kerr effect in fields up to 15 kOe was used as a test technique for determining the precompensation or postcompensation composition of the hard magnetic layer. Figure 1 shows the typical magnetooptical hysteresis loops measured for the $Dy_{0.2}Co_{0.8}$ and $Dy_{0.3}Co_{0.7}$ alloy films. In order to prevent oxidation of the hard magnetic layer, a protective GeO layer was deposited onto the DyCo layer or the reversed sequence of layers DyCo/NiFe was used.

The dynamic magnetic properties of the $Ni_{0.8}Fe_{0.2}/Dy_{0.2}Co_{0.8}$ and $Ni_{0.8}Fe_{0.2}/Dy_{0.3}Co_{0.7}$ bilayer films were measured on a standard spectrometer operating in the *X* band (9.2 GHz). The FMR fields were measured at room temperature over the entire range of angles between the external field and the film plane with the aim of determining the effective magnetization

M_{eff}. The M_{eff} magnetization is defined by the relationship

$$H_{\perp}^{r} - 4\pi M_{\text{eff}} = \sqrt{H_{\parallel}^{r}(H_{\parallel}^{r} + 4\pi M_{\text{eff}})}, \quad (1)$$

where $H_{\perp}^{r}$ and $H_{\parallel}^{r}$ are the FMR fields at the appropriate geometry of the experiment.

The spin-wave resonance spectra were recorded perpendicular to the external magnetic field with respect to the plane of the studied films. For this geometry of the measurements, the resonance field H_n and the wave vector k_n of a standing spin wave are related by the following expression:

$$H_n = \omega/\gamma + 4\pi M_{\text{eff}} - \eta k_n^2, \quad (2)$$

where ω/γ is the internal field of a ferromagnet, $\eta = (2A/M_{\text{eff}})$ is the spin-wave stiffness, and A is the exchange coupling constant. As follows from the spin-wave resonance spectra (Fig. 2), the exchange boundary conditions for alternating magnetization are realized in the studied films. It is known that, in this case, the mode number n in the spin wave spectrum and the wave vector k_n of the standing spin wave are related by the formula $k_n = \pi n/d$ (where $n = 1, 2, 3, \ldots$ and d is the film thickness). By using expression (2), the numerical values of the spin-wave stiffness η were calculated from the relationship

$$\eta = (d/\pi)^2(H_i - H_j)/(n_j^2 - n_i^2). \quad (3)$$

The linewidth ΔH_n of the spin-wave mode was determined from the difference between the coordinates of extrema in the curve of the absorption spectrum derivative.

3. RESULTS

Before proceeding to the experimental results obtained for the $Ni_{0.8}Fe_{0.2}/Dy_{1-x}Co_x$ bilayer films, we recall that the $Ni_{0.8}Fe_{0.2}$ monolayer films 3000 Å thick were also prepared according to the above procedure. In the subsequent discussion, the magnetic characteristics and the spin-wave resonance spectra of the monolayer films will be used as reference data. The number of peaks observed in the spin-wave resonance spectra of these samples was greater than 10. The numerical values of the resonance fields H_n are approximated by a linear dependence in the $H_n(n^2)$ coordinates. The slope of this curve is determined by the spin-wave stiffness [see relationship (3)]. For $Ni_{81}Fe_{19}$ monolayer films, the calculated spin-wave stiffness η is equal to 20×10^{-10} Oe cm^2. The numerical values of the effective magnetization M_{eff} and the exchange coupling constant A are equal to 800 G and 0.8×10^{-6} erg/cm, respectively. The main magnetic characteristics, which were calculated for the $Ni_{0.8}Fe_{0.2}$ alloy, agree with those obtained by Rusov [3].

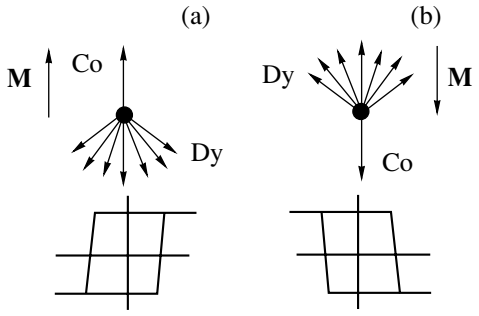

Fig. 1. A schematic representation of hypothetical local noncollinear magnetic structures of DyCo amorphous films and their typical magnetooptical hysteresis loops for (a) precompensation and (b) postcompensation alloy compositions.

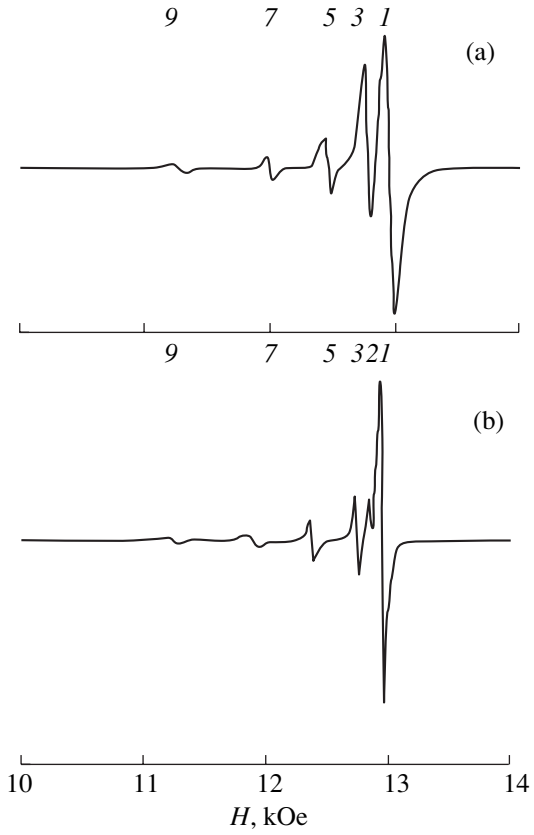

Fig. 2. Spin-wave resonance spectra of NiFe/DyCo bilayer films with (a) precompensation and (b) postcompensation hard magnetic layers.

Figure 2 shows the spin-wave resonance absorption spectra of NiFe/DyCo bilayer films, namely, the $Ni_{0.8}Fe_{0.2}/Dy_{0.2}Co_{0.8}$ film with a hard magnetic layer of the precompensation composition (Fig. 2a) and the $Ni_{0.8}Fe_{0.2}/Dy_{0.3}Co_{0.7}$ film with a hard magnetic layer of the postcompensation composition (Fig. 2b). Analysis of these spectra revealed the following features. (1) The spin-wave modes with odd and even numbers

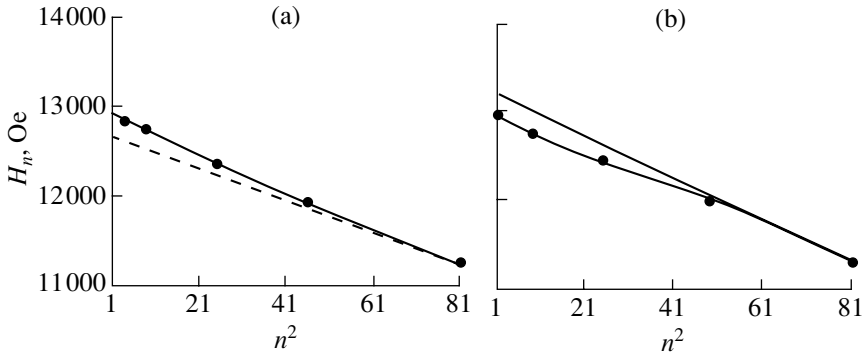

Fig. 3. Experimental dispersion dependences in the $H_n(n^2)$ coordinates for NiFe/DyCo bilayer films with (a) precompensation and (b) postcompensation hard magnetic layers.

($n = 1, 2, 3, \ldots$) are excited in the samples. (2) The intensities of even peaks are appreciably less than those of the neighboring odd peaks. (3) The intensities of even peaks in the spin-wave resonance spectra of bilayer films with a hard magnetic layer of the postcompensation composition (Fig. 2b) are considerably higher than those of the precompensation composition (Fig. 2a). The numerical values of the linewidth ΔH_1 in the spin wave spectra of these bilayer films also differ substantially. The linewidths ΔH_1 of the spin-wave resonance spectra of the studied films at different thicknesses of the permalloy layer and the effective magnetizations M_{eff} are listed in the table. From these data, it is seen that the magnetization M_{eff} of the bilayer films only slightly depends on the chemical composition of the hard magnetic layer. The deviations of the magnetization from the reference value of M_{eff} for the $Ni_{0.8}Fe_{0.2}$ alloy do not exceed 10%. At the same time, the linewidths ΔH_1 of the first mode in the spin-wave resonance spectra for the bilayer films with precompensation hard magnetic layers are twice (and more) as large as those for the films with postcompensation DyCo hard magnetic layers.

Linewidths ΔH_1 of the first mode in the spin-wave resonance spectra and effective magnetizations M_{eff} for NiFe/DyCo bilayer films

Precompensation composition of the DyCo alloy			
Parameter	NiFe (1000 Å) DyCo (700 Å)	NiFe (2000 Å) DyCo (700 Å)	NiFe (3000 Å) DyCo (700 Å)
ΔH_1, Oe	150	230	150
M_{eff}, G	724	727	800
Postcompensation composition of the DyCo alloy			
Parameter	NiFe (1500 Å) DyCo (700 Å)	NiFe (3000 Å) DyCo (700 Å)	NiFe (3000 Å) DyCo (700 Å)
ΔH_1, Oe	84	96	75
M_{eff}, G	727	810	850

Figure 3 depicts the experimental dispersion curves in the $H_n(n^2)$ coordinates for NiFe (3000 Å)/DyCo (700 Å) bilayer films with the same layer thicknesses but different (precompensation (Fig. 3a) or postcompensation (Fig. 3b)) compositions of the hard magnetic layer. The dashed line in Fig. 3 corresponds to the spin-wave stiffness $\eta \approx 20 \times 10^{-10}$ Oe cm^2, which was determined from the last modes in the spin-wave resonance spectra of these samples according to relationship (3). It should be noted that the exchange stiffness of bilayer films, which was calculated from the short-wavelength part of the spin wave spectra for both the precompensation and postcompensation alloy compositions of the hard magnetic layer, coincides with the reference value of η for the $Ni_{0.8}Fe_{0.2}$ monolayer film. However, as can be seen from Fig. 3, the resonance fields H_n of the first modes in the spin-wave resonance spectra are characterized by a systematic deviation from the reference dependence $H_n(n^2)$. In the case of bilayer films with precompensation hard magnetic layers, the measured fields H_n of the first modes in the spectrum exceed the reference values by δH_n (Fig. 3a). The opposite situation is observed in the films with postcompensation hard magnetic layers: the fields H_1, H_2, and H_3 are less than the reference values (Fig. 3b). It is also seen that an increase in the mode number n leads to a decrease in the magnitude of δH_n and, at $n = 5$, $\delta H_n \longrightarrow 0$.

As is known, the dispersion curves $H_n(n^2)$, which are calculated from the spin-wave resonance spectra of ferromagnetic films of disordered (amorphous, nanocrystalline, etc.) alloys, can exhibit specific features due to fluctuations of the magnetic parameters, the exchange interaction α [4], and the saturation magnetization M_s [5]. However, in our case, the feature observed in the $H_n(n^2)$ curve is caused by other factors. (This is evident, in particular, from a comparison of the $H_n(n^2)$ curves for the studied bilayer films and the $H_n(n^2)$ curve of the $Ni_{0.8}Fe_{0.2}$ reference film.) In our opinion, these are the interlayer exchange interaction and the orientation of

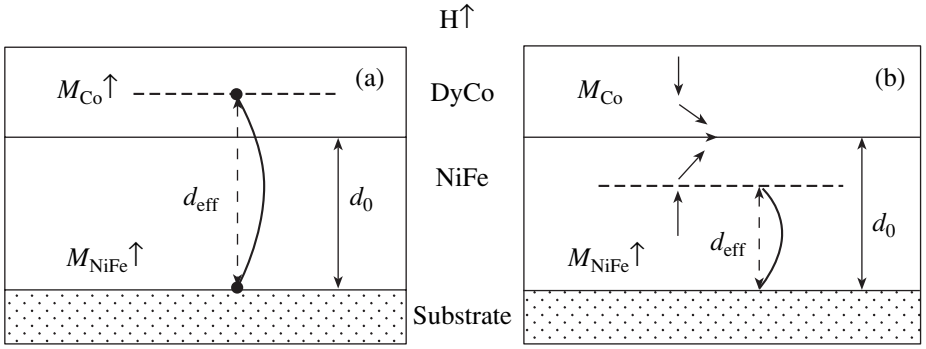

Fig. 4. Configurations of the magnetization vectors and thicknesses d_{eff} of effective magnetic layers in NiFe/DyCo bilayer films with (a) precompensation and (b) postcompensation hard magnetic layers.

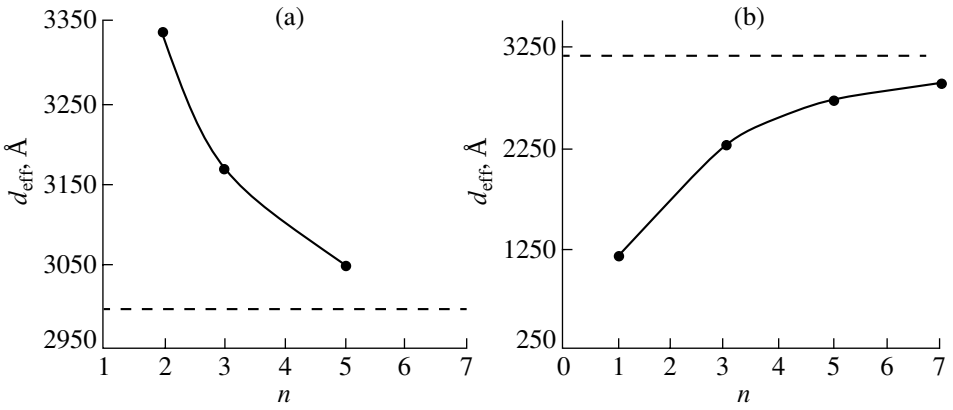

Fig. 5. Dependences of the effective magnetic thickness d_{eff} on the spin-wave mode number for NiFe/DyCo bilayer films with (a) precompensation and (b) postcompensation hard magnetic layers.

the Co sublattice magnetization in DyCo with respect to the external magnetic field **H**.

4. DISCUSSION

Let us consider the configuration of the magnetization vectors in the NiFe/DyCo bilayer films. For a bilayer film with the precompensation hard magnetic layer, the saturation magnetization vectors of the NiFe ferromagnetic alloy and the Co sublattice of the DyCo ferrimagnetic alloy are parallel to each other (Fig. 4). Owing to the exchange interaction between the local magnetic moments of the NiFe alloy and the local magnetic moments of Co atoms located near the interlayer boundary, the latter moments are involved in the precession of the net magnetization of the ferromagnetic layer under the effect of microwave fields. Hence, the exchange boundary condition for the alternating magnetization m (the Kittel condition $\mathbf{m}|_s = 0$), which specifies the node of a standing spin wave, should be met in a certain effective plane within the hard magnetic layer rather than at the interface. This is equivalent to the displacement of the standing spin wave node from the interface inside the $Dy_{0.2}Co_{0.8}$ hard magnetic alloy layer. (This situation is schematically shown in Fig. 4a). Therefore, in relationship (2), the wave vector of the first modes in the spin wave spectrum should be determined not from the formula $k_1 = \pi/d_0$ (where d_0 is the thickness of the permalloy film) but from the expression $k_1 = \pi/d_{eff}$ at $d_{eff} > d_0$ (where d_{eff} is the thickness of the effective magnetic layer for a spin wave).

The configuration of the magnetization vectors in a bilayer film with the postcompensation hard magnetic layer is depicted in Fig. 4b (see also Fig. 1b). In this case, the saturation magnetization vectors of the Co sublattice and the NiFe ferromagnetic alloy are antiparallel. The minimization of the energy (in the case of the exchange interaction Co $\longleftrightarrow$ NiFe and the uniaxial anisotropy of the DyCo hard magnetic layer) results in the formation of a transition layer between NiFe and DyCo in which spins of 3*d* metals gradually turn through an angle of π. Then, the Kittel exchange boundary condition in the interface region is replaced

by the Amenta–Rado boundary conditions $\left(\frac{\partial \mathbf{m}}{\partial \mathbf{n}}\right)_s = 0$, where **n** is the normal to the ferromagnet surface. This is confirmed by the increase in intensity of even peaks in the spin-wave resonance spectrum. Note that this configuration of free surface spins is realized in a certain effective plane inside the NiFe soft magnetic layer. This means that the thickness of the effective magnetic layer d_{eff}, which determines the wave vectors of the first spin-wave modes $k_1 = \pi/d_{\text{eff}}$), must satisfy the condition $d_{\text{eff}} < d_0$.

Numerical estimates of d_{eff} can be obtained using the relationship

$$\delta H_n/(\pi n)^2 = \eta[d_{\text{eff}}^{-2} - d_0^{-2}], \quad (4)$$

which is derived from formulas (2) and (3). The calculated dependences of the effective magnetic thickness d_{eff} on the spin-wave mode number for the studied bilayer films with precompensation and postcompensation hard magnetic layers are shown in Figs. 5a and 5b, respectively. It can be seen that, as the mode number n increases (the external magnetic field decreases), $d_{\text{eff}} = (d_0 \pm \Delta d)$ tends to d_0. Since $\Delta d \sim [(A + MH)/K]^{-0.5}$ (where K is the effective surface anisotropy constant for a layer of thickness Δd), a decrease in Δd with a decrease in the external magnetic field is quite reasonable. It is also important that the short-wavelength part of the spin-wave resonance spectrum depends only slightly on the type of exchange boundary conditions involved.

In conclusion, it should be noted that researchers dealing with the dynamic characteristics of thin metallic ferromagnetic films, apparently, rather frequently encounter the phenomenon described in the present work. Actually, thin metallic films prepared using different techniques undergo oxidation and, hence, are coated with ferrimagnetic (antiferromagnetic) oxides bound to the main ferromagnetic materials of these films through exchange interaction. For this reason, the deviations of the first peaks in the spin-wave resonance spectra from the dispersion dependence for spin waves are frequently observed. As a rule, the locations of these peaks are not included in subsequent analysis of the spin wave spectrum or their use leads to incorrect determination of the exchange coupling constant.

ACKNOWLEDGMENTS

We are grateful to S.A. Karpenko for helpful discussions.

REFERENCES

1. V. A. Seredkin, G. I. Frolov, and V. Yu. Yakovchuk, Pis'ma Zh. Tekh. Fiz. **9** (23), 1446 (1983) [Sov. Tech. Phys. Lett. **9**, 621 (1983)].
2. K. Handrich and S. Kobe, *Amorphe Ferro- und Ferrimagnetika* (Physik-Verlag, Weinheim, 1980; Mir, Moscow, 1982).
3. G. I. Rusov, Fiz. Tverd. Tela (Leningrad) **9**, 196 (1967) [Sov. Phys. Solid State **9**, 146 (1967)].
4. V. A. Ignatchenko, R. S. Iskhakov, L. A. Chekanova, and N. S. Chistyakov, Zh. Éksp. Teor. Fiz. **75** (2), 653 (1978) [Sov. Phys. JETP **48**, 328 (1978)].
5. R. S. Iskhakov, M. M. Brushtunov, and A. S. Chekanov, Fiz. Tverd. Tela (Leningrad) **29**, 1214 (1987) [Sov. Phys. Solid State **29**, 692 (1987)].

Translated by O. Borovik-Romanova

Physics of the Solid State, Vol. 43, No. 8, 2001, pp. 1527–1532. Translated from Fizika Tverdogo Tela, Vol. 43, No. 8, 2001, pp. 1467–1471.

MAGNETISM AND FERROELECTRICITY

Magnetoacoustic Activity of Rhombohedral Antiferromagnets

I. F. Mirsaev

Institute of Metal Physics, Ural Division, Russian Academy of Sciences, ul. S. Kovalevskoĭ 18, Yekaterinburg, 620219 Russia

e-mail: pilyugin@imp.uran.ru

Received November 2, 2000

Abstract—A quantitative theory of magnetic acoustic birefringence in rhombohedral antiferromagnets is developed. It is shown that acoustic activity and the Faraday effect associated with it are determined by the joint action of piezomagnetism and magnetostriction. The effect is estimated quantitatively, and the method of experimental determination of the piezomagnetic constant is indicated. The conditions for the transformation of linear polarization into circular polarization and for the rotation of linear polarization through 90° are determined.

1. INTRODUCTION

The magnetoelastic (ME) interaction of spin oscillations and elastic vibrations in antiferromagnets (AFMs) changes their elastic moduli [1, 2]. These changes are described by the dynamic ME contribution $\Delta C_{\alpha\beta}$ to the effective elastic moduli $C_{\alpha\beta} \longrightarrow C^{\text{ef}}_{\alpha\beta} = C_{\alpha\beta} + \Delta C_{\alpha\beta}$ and are manifested in various magnetoacoustic effects. For instance, the symmetric component $\Delta C^s_{\alpha\beta}$ of this tensor is responsible for the emergence of linear acoustic birefringence (Voigt's effect or the Cotton–Mouton acoustic effect) in AFMs due to the difference in the phase velocities of normal transverse elastic waves [2–4]. The antisymmetric component $\Delta C^a_{\alpha\beta}$ determines the antiferromagnetic (AF) acoustic activity (or AF gyrotropy of the medium), which is related to the circular birefringence (Faraday's acoustic effect) associated with the difference in the phase velocities of circularly polarized waves [2]. In the general case, when both symmetric ($\Delta C^s_{\alpha\beta}$) and antisymmetric ($\Delta C^a_{\alpha\beta}$) components of the moduli $\Delta C_{\alpha\beta} = \Delta C^a_{\alpha\beta} + \Delta C^s_{\alpha\beta}$ differ from zero, superposition of the linear and circular birefringence effects takes place. As a result, linearly polarized modes are transformed into elliptically polarized modes and linear birefringence is converted into elliptical birefringence.

A detailed symmetry analysis of these effects was carried out by Turov [2, 3], and a quantitative theory of the Cotton–Mouton effect in AFMs was developed in [4].

In the present work, the AF acoustic activity of trigonal AFMs (α-Fe_2O_3, $FeBO_3$, $MnCO_3$, etc.) and its influence on the acoustic birefringence effect are analyzed. In contrast to [2–4], the elastic moduli $\Delta C^s_{\alpha\beta}$ and $\Delta C^a_{\alpha\beta}$ responsible for these effects are calculated using the coupled equations of ME dynamics (the Landau–Lifshitz equations and the dynamic elasticity equations). These equations make it possible to derive more general formulas applicable in a wider frequency range. The main point is that piezomagnetism must be taken into account along with magnetostriction while calculating the antisymmetric moduli $\Delta C^a_{\alpha\beta}$. It is the combined action of these effects that leads to the emergence of the moduli $\Delta C^a_{\alpha\beta}$ and, hence, the AF acoustic activity.

2. EQUILIBRIUM STATE

We consider easy-plane AFMs with the exchange-type magnetic structure $\bar{1}(+)3_z(+)2_x(-)$ [2] ($MnCO_3$, $FeBO_3$, and α-Fe_2O_3 at $T > T_M$, where $T_M = 260$ K is the Morin temperature). We write the thermodynamic potential density in the form

$$\Phi = 2M_0\left\{H_E m^2 - H_D[\mathbf{ml}]_z + \frac{1}{2}H_A l_z^2 - \mathbf{mH}\right\} + B_{ijkl}l_i l_j e_{kl} + \Pi_{ijkl}m_i l_j e_{kl} + \Delta\Pi_{ijkl}m_i l_j \omega_{kl} + \frac{1}{2}C_{ijkl}e_{ij}e_{kl}. \quad (1)$$

Here, $\mathbf{l} = (\mathbf{M}_1 - \mathbf{M}_2)/2M_0$ and $\mathbf{m} = (\mathbf{M}_1 + \mathbf{M}_2)/2M_0$ are the relative vectors of antiferromagnetism and ferromagnetism, respectively; M_0 is the magnetization of the sublattices, $|\mathbf{M}_1| = |\mathbf{M}_2| = M_0$ and, hence, $m^2 + l^2 = 1$ and $\mathbf{ml} = 1$; H and H_E are the external and the exchange fields, respectively (the nonuniform exchange associated with derivatives $\partial\mathbf{l}/\partial x_i$ is disregarded here as inapplicable to the wavelengths under investigation); H_D and H_A are the Dzyaloshinski and magnetic anisotropy

fields, respectively; $e_{ij} = (u_{ij} + u_{ji})/2$ is the strain tensor; $u_{ij} = \partial u_j/\partial x_i$, where **u** is the elastic displacement; B_{ijkl} and Π_{ijkl} [2, 5] are the ME and piezomagnetic constants, respectively; and C_{ijkl} are the elastic moduli.

In Eq. (1), the tensor

$$\Delta\Pi_{ijkl} = 2M_0H_D\{\delta_{ik}(\delta_{jx}\delta_{ly} - \delta_{jy}\delta_{lx}) + \delta_{jk}(\delta_{iy}\delta_{lx} - \delta_{ix}\delta_{ly})\} \quad (2)$$

describes the renormalization of piezomagnetic constants, which is associated with rotational invariance of the Dzyaloshinski interaction energy that takes local rotations of a volume element $\omega_{ik} = (u_{ki} - u_{ik})/2$ into account [2]. Insignificant renormalizations of the elastic moduli ($\Delta\hat{C} \sim \hat{B}$) and of the ME constants ($\Delta\hat{B} \sim M_0H_A$) associated with ω_{ik} are omitted as small corrections.

We assume that the external magnetic field **H** is applied in the basal plane. In this case, the equilibrium vectors $\mathbf{m}_0 \parallel \mathbf{H}$ and $\mathbf{l}_0 \perp \mathbf{H}$ also lie in this plane. Anisotropy in the basal plane is assumed to be fairly weak and is neglected.

In the subsequent analysis, it is convenient to treat the direction of the **H** forming angle φ_H with the binary symmetry axis **2**(–) as a new axis **X**. In this case, $\mathbf{X} \parallel \mathbf{H} \parallel \mathbf{m}_0$, $\mathbf{Y} \parallel \mathbf{l}_0$, and $\mathbf{Z} \parallel \mathbf{3}$, where **3** is the trigonal axis.

The conditions $\partial\Phi_0/\partial m_0 = 0$ and $\partial\Phi_0/\partial e_{ij}^0 = 0$ for the minimum of the ground-state energy imply that the equilibrium values of magnetization m_0 and strain e_{ij}^0 can be determined from the equalities

$$m_0 = \frac{H + H_D}{2H_E}, \quad (3)$$

$$e_{ij}^0 = -S_{ijkl}(B_{yykl} + \Pi_{xykl}m_0), \quad (4)$$

where $\hat{S} = \hat{C}^{-1}$ is the elastic compliance tensor.

It should be noted that Eqs. (3) and (4) are written in the approximation $m_0^2 \ll l_0^2$, $l_0^2 = 1 - m_0^2 \approx 1$ adopted by us; this approximation is valid for $H, H_D \ll H_E$.

3. AMPLITUDES OF COUPLED STATES

Let us now establish the ME relation between the amplitudes of spin oscillations and elastic vibrations. For this purpose, we use the Landau–Lifshitz equations [6]

$$\dot{\tilde{\mathbf{m}}} = \gamma\left\{\left[\mathbf{m}\frac{\partial\Phi}{\partial\mathbf{m}}\right] + \left[\mathbf{l}\frac{\partial\Phi}{\partial\mathbf{l}}\right]\right\},$$
$$\dot{\tilde{l}} = \gamma\left\{\left[\mathbf{m}\frac{\partial\Phi}{\partial\mathbf{l}}\right] + \left[\mathbf{l}\frac{\partial\Phi}{\partial\mathbf{m}}\right]\right\}. \quad (5)$$

Here, $\tilde{\mathbf{l}} = \mathbf{l} - \mathbf{l}_0$ and $\tilde{\mathbf{m}} = \mathbf{m} - \mathbf{m}_0$ are the deviations of these vectors from equilibrium values and γ is the magnetomechanical ratio.

We assume that the dynamic quantities $\tilde{u}_{ik} = u_{ik} - u_{ik}^0$, $\tilde{m}_i$, and $\tilde{l}_i$ vary according to the law $\exp[i(\mathbf{kx} - \omega t)]$, where ω and **k** are the frequency and the wave vector of ME waves, respectively. Substituting Eq. (1) for Φ into Eq. (5), we obtain

$$\tilde{l}_x = \frac{\gamma^2[H_1A_{ik} + i(\omega/\gamma)\Gamma_{ik}]}{2m_0M_0(\omega^2 - \omega_f^2)}\tilde{u}_{ik},$$
$$\tilde{m}_z = \frac{\gamma^2[H_2\Gamma_{ik} - i(\omega/\gamma)A_{ik}]}{2M_0(\omega^2 - \omega_f^2)}\tilde{u}_{ik}, \quad (6)$$
$$\tilde{m}_y = -m_0\tilde{l}_x.$$

Here, $\omega = \omega_{AFMR}$ is the frequency of the quasi-ferromagnetic branch of the AF resonance:

$$\omega_f = \gamma H_f,$$
$$H_f = (H_1H_2)^{1/2} = [H(H + H_D) + 2H_EH_{me}^0]^{1/2}, \quad (7)$$
$$H_1 = H + H_D, \quad H_2 = H + H_{me}^0/m_0,$$

where

$$H_{me}^0 = (e_{ik}^0/M_0) \times [(B_{xxik} - B_{yyik}) - m_0(\Pi_{xyik} - \Pi_{yxik})] \quad (8)$$

is the effective ME spontaneous striction field. The remaining notation used in Eq. (6) is as follows:

$$A_{ik} = 2B_{xyik} + m_0(\Pi_{xxik} - \Pi_{yyik}),$$
$$\Gamma_{ik} = m_0[\Pi_{zyik} + M_0H_D(\delta_{iz}\delta_{kx} - \delta_{ix}\delta_{kz})]. \quad (9)$$

The high-frequency spin oscillations of $\tilde{m}_x$, $\tilde{l}_y$, and $\tilde{l}_z$ corresponding to the antiferromagnetic mode with activation frequency $\omega_a \gg \omega_f$ are not considered due to their relatively weak coupling with elastic deformations, which does not make a significant contribution to the elastic moduli ($\Delta\hat{C}(\omega_a) \ll \Delta\hat{C}(\omega_f)$) [1].

4. DYNAMIC ELASTIC MODULI

In the continuum model, the equations of motion for the elastic displacement **u** in an AFM have the form [1, 2]

$$\rho\ddot{u}_i = \frac{\partial\tau_{ik}}{\partial x_k}, \quad \tau_{ik} = \frac{\partial\Phi}{\partial u_{ki}}, \quad (10)$$

where ρ is the density of the material and τ_{ik} is the Piola–Kirchhoff stress tensor [7]. In accordance with

Eqs. (1) and (10), we have

$$\tau_{ik} = C_{ikpq}u_{pq} + B_{pqik}l_p l_q + \left[\Pi_{pqik} + \frac{1}{2}(\Delta\Pi_{pqik} - \Delta\Pi_{pqki})\right]m_p l_q. \quad (11)$$

Using the ME coupling relations (6) in this expression and assuming that $\tilde{m}_x = \tilde{l}_y = \tilde{l}_z = 0$, we present the dynamic component of tensor $\hat{\tau}$ in the form

$$\tilde{\tau}_{ik} = C^{\text{ef}}_{kimn}\tilde{u}_{mn}, \qquad C^{\text{ef}}_{kimn} = C_{kimn} + \Delta C_{kimn}. \quad (12)$$

Here, C^{ef}_{kimn} is the tensor of second-order effective elastic moduli and $\Delta\hat{C}$ is the dynamic contribution to the elastic moduli associated with the ME interaction of elastic waves with spin oscillations of the quasi-ferromagnetic mode. These moduli can be represented as the sum of the symmetric (s) and antisymmetric (a) components:

$$\Delta C_{kimn} = \Delta C^s_{kimn} + \Delta C^a_{kimn}, \quad (13)$$

$$\Delta C^s_{kimn} = \frac{\gamma^2(H_1 A_{ki}A_{mn} + H_2\Gamma_{ki}\Gamma_{mn})}{2m_0M_0(\omega^2 - \omega_f^2)}, \quad (14)$$

$$\Delta C^a_{kimn} = \frac{i\omega\gamma(A_{ki}\Gamma_{mn} + \Gamma_{ki}A_{mn})}{2m_0M_0(\omega^2 - \omega_f^2)}. \quad (15)$$

It should be recalled that Eqs. (14) and (15) for $\Delta\hat{C}$ are written in the rotated reference frame associated with the direction of field **H**.

5. NORMAL VIBRATIONAL MODES

We suppose that an elastic displacement wave $\mathbf{u} = \mathbf{u}_0\exp[i(\mathbf{kx} - \omega t)]$ propagates along the trigonal axis $\mathbf{k} \parallel \mathbf{3} \parallel \mathbf{Z}$ of a crystal at right angles to the magnetic field $\mathbf{H} \parallel \mathbf{m}_0 \parallel \mathbf{X}$ and to the antiferromagnetism vector $\mathbf{l}_0 \parallel \mathbf{Y}$. In this case, the ME contribution to the effective elastic moduli is described by the tensor ΔC_{zizn}. In the low-frequency range ($\omega^2 \ll \omega_f^2$), the ΔC_{zizn} components in Eqs. (13)–(15) have the form

$$\Delta C_{44} = -\tilde{B}_{14}U\sin^2 3\varphi_H, \quad \Delta C_{55} = -\tilde{B}_{14}U\cos^2 3\varphi_H, \quad \Delta C^s_{54} = \frac{1}{2}\tilde{B}_{14}U\sin 6\varphi_H, \quad (16)$$

$$\Delta C^a_{54} = -\Delta C^a_{45} = i\frac{\omega}{2\omega_E}\tilde{\Pi}U\sin 3\varphi_H,$$

where the following compact notation for pairs of indices is used: $1 \equiv xx$, $4 \equiv zy$, and $5 \equiv zx$. In Eq. (16), $\tilde{B}_{14} = B^0_{14} + m_0\Pi^0_{15}$ is the ME constant renormalized in order to take piezomagnetism into account, $U = 4H_E\tilde{B}_{14}/M_0H_f^2$ is the exchange enhancement factor [5], $\omega_E = 2\gamma H_E$ is the exchange frequency, and $\tilde{\Pi} = (\Pi^0_{zxyz} - H_DM_0)$ is the renormalized piezomagnetic constant that takes the rotation-invariant theory correction with H_D into account. Here, B^0_{14} and Π^0_{15} are the components of the initial tensors B^0_{ijkl} and Π^0_{ijkl} of magnetoelastic and piezomagnetic constants, respectively, in the initial (unturned) reference frame $X_0Y_0Z_0$ with axes $\mathbf{X}_0 \parallel \mathbf{2}$, $\mathbf{Y}_0 \perp \mathbf{X}_0$, and $\mathbf{Z}_0 \parallel \mathbf{C}$.

An analysis of the equations of motion (10) together with Eqs. (12) and (16) shows that for $\mathbf{k} \parallel \mathbf{3} \parallel \mathbf{Z}$, the longitudinal wave u_z does not interact with the magnetic subsystem and splits from the transverse vibrational modes u_x and u_y. Consequently, we can put $u_z = 0$. The propagation of transverse waves can be described more conveniently if we pass to the principal coordinate axes $\boldsymbol{\xi}$ and $\boldsymbol{\eta}$ in the basal plane:

$$\xi = x\cos\Psi + y\sin\psi, \qquad \eta = -x\sin\psi + y\cos\psi, \quad (17)$$

where the angle ψ determined from the requirement $\Delta C^s_{z\xi z\eta} = 0$ satisfies the condition

$$\tan 2\psi = \frac{2\Delta C^s_{54}}{\Delta C_{55} - \Delta C_{44}} = -\tan 6\varphi_H. \quad (18)$$

The coordinate transformation (17) corresponds to an additional rotation of the coordinate axes **X** and **Y** about the **Z** axis through the angle $\psi = \pi p/2 - 3\varphi_H$, where p is an integer. Consequently, the $\boldsymbol{\xi}$ axis forms the angle $\varphi_\xi = \pi p/2 - 2\varphi_H$ with the binary symmetry axis **2**.

In the coordinate system $\xi\eta Z$, the equations of motion (10) written taking into account Eqs. (12) and (16) have the form

$$(\rho\omega^2 - C_1k^2)u_\xi - i\Delta C^a k^2 u_\eta = 0, \qquad i\Delta C^a k^2 u_\xi + (\rho\omega^2 - C_2k^2)u_\eta = 0, \quad (19)$$

where

$$C_1 \equiv C_{z\xi z\xi} = C_{44} - \tilde{B}_{14}U, \quad C_2 \equiv C_{z\eta z\eta} = C_{44}, \quad \Delta C^a = \left|\Delta C^a_{z\xi z\eta}\right| = \left|\Delta C^a_{54}\right|. \quad (20)$$

In accordance with Eq. (19), transverse elastic waves are characterized by two vibrational modes

with the wave numbers

$$k_{1,2} = \frac{\omega}{v_{1,2}},$$

$$v_{1,2} = \left\{\frac{1}{2\rho}[C_1 + C_2 \pm (C_1 - C_2)(1 + \tan^2 2\alpha)]^{1/2}\right\}^{1/2}, \quad (21)$$

where $v_{1,2}$ are the phase velocities of acoustic waves and α is the angle defined from the equalities

$$\tan 2\alpha = 2A,$$
$$A \equiv \frac{\Delta C^a}{C_2 - C_2} = -\frac{\omega}{2\omega}\frac{\tilde{\Pi}}{\tilde{B}_{14}}\sin 2\varphi_H. \quad (22)$$

It follows from Eq. (19) that, for $\Delta C^a = 0$, the normal modes are the vibrations u_ξ and u_η linearly polarized along the $\boldsymbol{\xi}$ and $\boldsymbol{\eta}$ axes: $\mathbf{u}_\xi \parallel \boldsymbol{\xi}$ and $\mathbf{u}_\eta \parallel \boldsymbol{\eta}$. However, the presence of acoustic activity (of components $\Delta C^a_{54} = -\Delta C^a_{45}$) leads to mixing of these modes. In this case, the normal vibrations $w_n = wn_0 \exp[i(k_n z - \omega t)]$ ($n = 1, 2$) are connected with u_ξ and u_η through the relations

$$w_1 = u_\xi \cos\alpha + iu_\eta \sin\alpha,$$
$$w_2 = u_\xi \sin\alpha - iu_\eta \cos\alpha. \quad (23)$$

It hence follows that the total displacement is described by

$$\mathbf{u} = \mathbf{u}_\xi + \mathbf{u}_\eta = \mathbf{u}_{10}\exp(i\varphi_1) + \mathbf{u}_{20}\exp(i\varphi_2,)$$
$$\mathbf{u}_{10} = w_{10}(\mathbf{e}_\xi \cos\alpha - i\mathbf{e}_\eta \sin\alpha),$$
$$\mathbf{u}_{20} = w_{20}(\mathbf{e}_\xi \sin\alpha + i\mathbf{e}_\eta \cos\alpha), \quad (24)$$
$$w_{10} = u_{\xi 0}\cos\alpha + iu_{\eta 0}\sin\alpha,$$
$$w_{20} = u_{\xi 0}\sin\alpha - iu_{\eta 0}\cos\alpha,$$

where $\varphi_{1,2} = k_{1,2}z - \omega t$, $u_{\xi 0} = u_\xi(0)$ and $u_{\eta 0} = u_\eta(0)$ are the displacement components at the front face of the sample, and $\mathbf{e}_\xi$ and $\mathbf{e}_\eta$ are the unit vectors of the reference frame along the $\boldsymbol{\xi}$ and $\boldsymbol{\eta}$ axes, respectively.

Thus, the displacement wave $\mathbf{u} = \mathbf{u}_\xi + \mathbf{u}_\eta$ is a superposition of two elliptically polarized normal vibrations $\mathbf{u}_1 = \mathbf{u}_{10}\exp(i\varphi_1)$ and $\mathbf{u}_2 = \mathbf{u}_{20}\exp(i\varphi_2)$. The polarization ellipses lie in the $\xi\eta$ plane perpendicular to the wave vector $\mathbf{k}$. The major axis of the ellipse is parallel to the ξ axis for wave $\mathbf{u}_1$ and to the $\boldsymbol{\eta}$ axis for wave $\mathbf{u}_2$. The ellipticity ξ and polarization of these normal modes are characterized by the quantity $\tan\alpha \approx A$ ($|A| \ll 1$) from Eq. (22):

$$\left(\frac{u_\eta}{u_\xi}\right)_1 = \left(\frac{u_\xi}{u_\eta}\right)_2 = -i\tan\alpha \approx -iA,$$
$$\varepsilon = |\tan\alpha| \approx |A|; \quad (25)$$

this quantity has a maximum value when the magnetic field $\mathbf{H}$ is oriented at the angle $\varphi_H = \pi p/6$ to the symmetry axis **2**.

6. FARADAY EFFECT FOR ELLIPTIC VIBRATIONAL MODES

Let us now determine the ellipticity and rotation of the polarization vector of the resultant wave $\mathbf{u} = \mathbf{u}_\xi + \mathbf{u}_\eta$, which are associated with the AF corrections $\Delta\hat{C} = \Delta\hat{C}^s + \Delta\hat{C}^a$ to the effective elastic moduli. We suppose that a transverse wave at the entrance ($z = 0$) has a polarization $\mathbf{u}_0$ forming an angle φ_0 with the ξ axis. Taking into account Eq. (23), elastic vibrations u_ξ and u_η can be written in the form

$$u_\xi = R_\xi \cos(\omega t - \theta_1),$$
$$u_\eta = R_\eta \cos(\omega t - \theta_2). \quad (26)$$

Here, R_ξ and R_η are the amplitudes of acoustic vibrations given by

$$R_\xi = u_0 \cos\varphi_0 \cos 2\alpha \sin(\Delta k z/2)\,\mathrm{cosec}\,\Phi_1,$$
$$R_\eta = u_0 \sin\varphi_0 \cos 2\alpha \sin(\Delta k z/2)\,\mathrm{cosec}\,\Phi_2, \quad (27)$$

where $\Delta k = k_1 - k_2$ and the angles Φ_1 and Φ_2 are determined from the relations

$$\tan\Phi_1 = \cos 2\alpha[\cot(\Delta k z/2) - \tan\varphi_0 \sin 2\alpha]^{-1},$$
$$\tan\Phi_2 = \cos 2\alpha[\cot(\Delta k z/2) + \cot\varphi_0 \sin 2\alpha]^{-1}. \quad (28)$$

The effect of antisymmetric moduli $\Delta\hat{C}^a$ on the wave velocity $v_{1,2}$ in Eq. (21) is manifested only in the quadratic approximation through the parameter $|A| \ll 1$ given by Eq. (22) and can be disregarded in the first approximation. In this case, the difference in the wave numbers is defined as

$$\Delta k = k_0 \frac{\tilde{B}_{14}}{2C_{44}} U, \quad k_0 = \omega(\rho/C_{44})^{1/2}. \quad (29)$$

The phases of vibrations (26) can be calculated using the formulas

$$\theta_1 = \Phi_1 + (k_1 + k_2)z/2,$$
$$\theta_2 = -\Phi_2 + (k_1 + k_2)z/2. \quad (30)$$

Owing to the phase shift $\Delta\theta = \theta_1 - \theta_2$ between vibrations u_ξ and u_η, the tip of the resultant displacement vector $\mathbf{u}(z, t) = \mathbf{u}_\xi + \mathbf{u}_\eta$ at the exit ($z = d$) describes an ellipse [8]. The major axis of this ellipse forms an angle φ with the $\boldsymbol{\xi}$ axis, where φ is defined by the formula

$$\tan 2\varphi = \frac{2R_\xi R_\eta \cos(\theta_1 - \theta_2)}{R_\xi^2 - R_\eta^2}, \quad (31)$$

while the lengths of the semimajor and semiminor axes of the ellipse are

$$r_{1,2} = \frac{\sqrt{2}}{2}\{R_\xi^2 + R_\eta^2 \pm [(R_\xi^2 + R_\eta^2)^2 - 4R_\xi^2 R_\eta^2 \sin^2(\theta_1 - \theta_2)]^{1/2}\}^{1/2}. \quad (32)$$

The intensities of elastic waves at the exit ($z = d$) polarized parallel ($I_\parallel$) and perpendicular ($I_\perp$) to the initial polarization $\mathbf{u}_0$ are defined as

$$I_\parallel = u_0^2 - I_\perp,$$
$$I_\perp = u_\perp^2 = u_0^2(\sin^2 2\varphi_0 + \sin^2 2\alpha \cos^2 2\varphi_0)\sin^2(\Delta k d/2), \quad (33)$$

where $u_\perp$ is the amplitude of the wave polarized orthogonal to $\mathbf{u}_0$.

Let us now consider the case when an elastic wave $\mathbf{u}_0$ is polarized at the entrance ($z = 0$) along the ξ axis ($\varphi_0 = 0$) or the $\boldsymbol{\eta}$ axis ($\varphi_0 = \pi/2$). Taking into account the relation $|\alpha| \approx |A| \ll 1$ in Eqs. (31) and (32), we find that the angle of inclination of the ellipse in this case is defined as

$$\varphi = A \sin \Delta k d, \quad (34)$$

while the ellipticity is given by

$$\varepsilon = r_2/r_1 = 2|A| \sin^2(\Delta k d/2). \quad (35)$$

The amplitude of the wave polarized perpendicular to $\mathbf{u}_0$ is defined, in accordance with Eq. (33), by the relation

$$u_\perp = 2u_0|A \sin(\Delta k d/2)|. \quad (36)$$

Formulas (34) and (35) are completely identical to the corresponding expressions employed in optics [9]. It follows hence that, in this case, the effect of Faraday rotation of the polarization vector (major axis of the ellipse) and ellipticity are due to the superimposition of acoustic activity ($\Delta\hat{C}^a \neq 0$) on the linear birefringence ($\Delta\hat{C}^s \neq 0$).

7. COTTON–MOUTON EFFECT IN ANTIFERROMAGNETS

Linear birefringence can be observed in pure form for the orientation of the magnetic field $\mathbf{H}$ at an angle $\varphi_H = \pi p/3$ (p is an integer) to the binary symmetry axis **2**. In this case, $\Delta C^a = |\Delta C_{54}^a| = 0$ in Eq. (16) and, in accordance with Eq. (19), the normal vibrations are $\mathbf{u}_\xi \parallel \boldsymbol{\xi}$ and $\mathbf{u}_\eta \parallel \boldsymbol{\eta}$. These vibrations are linearly polarized at the entrance along the principal axes $\boldsymbol{\xi}$ and $\boldsymbol{\eta}$ which coincide with the axes $\mathbf{X} \parallel \mathbf{H}$ and $\mathbf{Y} \parallel \mathbf{I}_0$, respectively ($\boldsymbol{\xi} \parallel \mathbf{X}$, $\boldsymbol{\eta} \parallel \mathbf{Y}$). The wave of the total displacement $\mathbf{u} = \mathbf{u}_\xi + \mathbf{u}_\eta$ at the exit ($z = d$) is again polarized elliptically. Taking into account that $R_\xi = \cos\varphi_0$, $R_\eta = \sin\varphi_0$, and $\theta_1 - \theta_2 = \Delta k z$ in Eqs. (31) and (32), we obtain the angle of inclination φ and the length of the semiaxes $r_{1,2}$ of this ellipse:

$$\tan 2\varphi = \tan 2\varphi_0 \cos \Delta k d, \quad (37)$$

$$r_{1,2} = \frac{u_0\sqrt{2}}{2}\{1 \pm (1 - \sin^2 2\varphi_0 \sin^2 \Delta k d)^{1/2}\}^{1/2}. \quad (38)$$

We now apply Eqs. (37) and (38) to specific cases.

(1) If a wave is polarized at the entrance along the $\boldsymbol{\xi}$ or $\boldsymbol{\eta}$ axis ($\varphi_0 = 0$ or $\varphi_0 = \pi/2$), it becomes linearly polarized at the exit, preserving its initial direction of polarization.

(2) A linearly polarized wave entering the crystal at an arbitrary angle φ_0 remains linearly polarized at the exit if the following condition is fulfilled:

$$|\Delta k d| = (2p + 1)\pi \quad (p \text{ is an integer}). \quad (39)$$

In this case, the rotation of vector $\mathbf{u}(d)$ relative to its initial direction $\mathbf{u}_0$ forms the angle $\Delta\varphi = \varphi - \varphi_0 = -2\varphi_0$ (to within $+\pi$). In particular, for $\varphi_0 = \pi/4$, the rotation of linear polarization amounts to 90°.

(3) Let us now suppose that $\mathbf{u}_0$ is directed along the bisector of the angle between $\boldsymbol{\xi}$ and $\boldsymbol{\eta}$ ($\varphi_0 = \pi/4$). In accordance with Eqs. (37) and (38), the polarization becomes elliptical:

$$r_1 = u_0|\cos(\Delta k d/2)|,$$
$$r_2 = u_0|\sin(\Delta k d/2)|. \quad (40)$$

The ellipticity is thus given by

$$\varepsilon = (r_2/r_1) = |\tan(\Delta k d/2)|. \quad (41)$$

Here, an interesting special case can take place when polarization becomes circular. Indeed, for

$$|\Delta k d| = (2p + 1)\pi/2, \quad (42)$$

we obtain $r_1 = r_2 = u_0\sqrt{2}/2$, $\varepsilon = 1$ from Eqs. (40) and (41).

8. DISCUSSION OF RESULTS

The acoustic activity of rhombohedral AFMs with $\mathbf{k} \parallel \mathbf{3} \parallel \mathbf{Z}$ is associated with the antisymmetric elastic moduli $\Delta C_{54}^a = -\Delta C_{45}^a$ determined by the ME interaction. These components lead to mixing of various elastic modes of vibrations and conversion of linearly polarized acoustic modes into elliptically polarized modes, while linear birefringence is transformed into elliptical birefringence. The axes of the ellipse are rotated during wave propagation, which is manifested as the Faraday rotation of the wave polarization vector. In contrast to circular birefringence, for which the Faraday angle $\varphi = \Delta k d/2$increases linearly without limit with the distance d traversed by the wave, for elliptic polarization, it is an oscillating function of d in accordance with Eq. (34) and does not exceed $|A|$ given by Eq. (22). It was mentioned above that in this case, the

linear and circular birefringence effects are superimposed: the first factors (A) in Eqs. (34)–(36) are associated with acoustic activity (antisymmetric components $\Delta\hat{C}^a$), while the second factors are connected with linear birefringence (symmetric components $\Delta\hat{C}^s$).

Since the Faraday angle φ, ellipticity ε, and amplitude $u_\perp$ are bounded by the parameter $A \propto \omega/\omega_E = \omega/2\gamma H_E$, AFMs with a weaker exchange field H_E are preferable for experimental investigations of elliptic birefringence associated with acoustic activity. In this respect, manganese carbonate $MnCO_3$ with $H_E = 3.2 \times 10^5$ Oe is the most favorable material [5]. For this material, the value of the quantity A lies in the interval 10^{-5}–10^{-3} (for the sound frequency $\omega/2\pi = 10^8$–10^{10} Hz), $\varphi_H = \pi/6$, and $\tilde{\Pi}/\tilde{B}_{14} \approx 1$. For AFMs with a stronger exchange field, such as $FeBO_3$ ($H_E = 2.86 \times 10^6$ Oe [10]) and α-Fe_2O_3 ($H_E = 9.2 \times 10^6$ Oe [1]), parameter A is an order of magnitude higher.

It should be noted that the equality $\tilde{\Pi}/\tilde{B}_{14} \approx 1$ is approximate and is used in view of the absence of experimental data on the piezomagnetic constant $\tilde{\Pi}$. The latter can be determined from Eq. (22) after establishing the experimental value of parameter A from the measurements of the Faraday angle in Eq. (34) or amplitude $u_\perp$ in Eq. (36) in the case when the external magnetic field **H** is oriented at an angle $\varphi_H = \pi/6$.

Finally, the important cases of conversion of linear polarization into circular polarization and the rotation of linear polarization through 90° require the fulfillment of equalities (42) and (39), respectively, which can be achieved by varying the value of d or H. For example, in the case of $FeBO_3$ for which $M_0 = 506$ G, $H_E = 2.86 \times 10^6$ Oe, $H_D = 9.93 \times 10^4$ Oe, $2H_E H^0_{me} = 4.25 \times 10^6$ Oe, $B^0_{14} = 1.41 \times 10^7$ erg/cm^3, $C_{44} = 9.2 \times 10^{11}$ erg/cm^3, and $\rho = 4.28$ g/cm^3 [10], we find that condition (42) for circular polarization holds for $d \approx 1$ mm if the sound frequency $\omega/2\pi = 200$ MHz and the field $H = 4$ kOe. For weaker fields H, the value of d decreases; in particular, $d \approx 0.1$ mm for $H = 400$ Oe.

ACKNOWLEDGMENTS

The author is grateful to E.A. Turov and V.V. Nikolaev for their interest in this work.

This research was supported by the Russian Foundation for Basic Research, project no. 99-02-16268.

REFERENCES

1. V. I. Ozhogin and V. L. Preobrazhenskiĭ, Zh. Éksp. Teor. Fiz. **73** (3), 988 (1977) [Sov. Phys. JETP **46**, 523 (1977)]; Usp. Fiz. Nauk **155** (4), 593 (1988) [Sov. Phys. Usp. **31**, 713 (1988)].
2. E. A. Turov, *Kinetic, Optical and Acoustical Properties of Antiferromagnetics* (Ural. Otd. Akad. Nauk SSSR, Sverdlovsk, 1990).
3. E. A. Turov, Zh. Éksp. Teor. Fiz. **92** (5), 1886 (1987) [Sov. Phys. JETP **65**, 1060 (1987)].
4. E. A. Turov, Zh. Éksp. Teor. Fiz. **95** (6), 2140 (1989) [Sov. Phys. JETP **68**, 1238 (1989)].
5. E. A. Turov, A. V. Kolchanov, V. V. Men'shenin, I. F. Mirsaev, and V. V. Nikolaev, *Symmetry and Physical Properties of Antiferromagnetics* (Fizmatlit, Moscow, 2001) (in press).
6. E. A. Turov, A. V. Kolchanov, V. V. Men'shenin, *et al.*, Usp. Fiz. Nauk **168** (12), 1303 (1998) [Sov. Phys. Usp. **41**, 1191 (1998)].
7. *Physical Acoustics: Principles and Methods*, Vol. 1, Part A: *Methods and Devices*, Ed. by W. P. Mason (Academic, New York, 1964; Mir, Moscow, 1966).
8. J. W. Tucker and V. W. Rampton, *Microwave Ultrasonics in Solid State Physics* (North-Holland, Amsterdam, 1972; Mir, Moscow, 1975).
9. P. Coeuer and D. Challeton, Solid State Commun. **8** (17), 1345 (1970).
10. V. V. Tarakanov and V. I. Khizhnyĭ, Fiz. Nizk. Temp. **22** (7), 752 (1996) [Low Temp. Phys. **22**, 578 (1996)].

Translated by N. Wadhwa

Physics of the Solid State, Vol. 43, No. 8, 2001, pp. 1533–1537. Translated from Fizika Tverdogo Tela, Vol. 43, No. 8, 2001, pp. 1472–1477.

MAGNETISM AND FERROELECTRICITY

Anomalies of Magnetoelastic Properties and Insulator–Metal Phase Transitions Induced by a Magnetic Field in Substituted Praseodymium Manganites

Yu. F. Popov*, A. M. Kadomtseva*, G. P. Vorob'ev*, K. I. Kamilov*, V. Yu. Ivanov, A. A. Mukhin**, and A. M. Balbashov*****

** Moscow State University, Vorob'evy gory, Moscow, 119899 Russia*

*** General Physics Institute, Russian Academy of Sciences, ul. Vavilova 38, Moscow, 117942 Russia*

**** Moscow Power Institute, ul. Krasnokazarmennaya 14, Moscow, 105835 Russia*

e-mail: popov@phys.msu.su

Received November 29, 2000

Abstract—The magnetostriction of $Pr_{0.6}Ca_{0.4}MnO_3$ and $Pr_{0.65}Ca_{0.28}Sr_{0.07}MnO_3$ manganite crystals is investigated in pulsed magnetic fields up to 250 kOe. The field-induced phase transitions from the charge-ordered antiferromagnetic (paramagnetic) state to the metallic ferromagnetic state are studied. It is found that these transitions are accompanied by abrupt negative jumps in the longitudinal and transverse magnetostrictions and a strong hysteresis at low temperatures. The threshold fields of transitions are determined, and the *H–T* phase diagrams are constructed. © *2001 MAIK "Nauka/Interperiodica".*

1. INTRODUCTION

Considerable interest expressed by researchers in manganites of the $R_{1-x}A_xMnO_3$ (*R* is a rare-earth ion and *A* is Ca^{2+} or Sr^{2+} ion) system is stimulated by the unusual interrelation between their magnetic, kinetic, and structural properties. These are the giant magnetoresistance effect and many other interesting phenomena associated, for example, with the charge and orbital ordering and its strong dependence on the external magnetic field (see, for example, the review by Tokura and Tomioka [1]). The charge ordering of Mn^{3+} and Mn^{4+} ions, as a rule, occurs in manganites with a distorted perovskite structure (i.e., at a small tolerance factor) and a narrow conduction band and is more pronounced, for example, in the $Pr_{1-x}Ca_xMnO_3$ system in the range $0.3 \le x \le 0.75$ [2]. As the temperature decreases, manganites in this system undergo a charge and orbital ordering at $T_{CO} \sim 220$–240 K, an antiferromagnetic ordering at the Néel temperature $T_N \sim 150$–170 K, and a transition to the noncollinear (canted) state with a nonzero ferromagnetic moment at lower temperatures [2, 3]. Moreover, these manganites possess semiconductor properties over the entire temperature range, unlike manganites in the classical system $La_{1-x}Sr_xMnO_3$, in which, at $x > 0.16$, the crossover from a semiconductor-type to metallic conductivity (the dielectric–metal spontaneous transition) is observed at the ferromagnetic ordering temperature [4]. A similar dielectric–metal transition can also be induced in $Pr_{1-x}Ca_xMnO_3$ in a strong magnetic field [3, 5, 6], which is attended by the suppression of the charge ordering, a drastic stepwise decrease in the electrical resistivity (by a factor of 10^{10} in some compounds [7]), and a jump in the magnetization. The threshold field of the dielectric–metal transition is maximum for the compound with $x = 0.5$: its magnitude is approximately equal to 25 T at a temperature of ~4 K and monotonically decreases to zero as the temperature increases to $T = T_{CO}$ [6]. A decrease in the concentration results in a substantial decrease in the threshold field of the dielectric–metal transition at low temperatures and its nonmonotonic temperature dependence at $x \le 0.4$ (i.e., this field first increases with an increase in the temperature and then becomes zero at T_{CO} [1, 3, 6]). The phase transition is also accompanied by strong magnetoelastic anomalies, which manifest themselves in the magnetostriction jumps observed in $Pr_{1-x}Ca_xMnO_3$ at $x = 0.33$ (polycrystals) [7] and $x = 0.45$ (single crystals) [6]. This indicates a strong coupling of the crystal lattice with the magnetic and electronic subsystems, which can be useful in studying the field-induced phase transitions and specific features of the interaction between different subsystems in these compounds.

In the present work, we investigated anomalies in the magnetoelastic properties of $Pr_{0.6}Ca_{0.4}MnO_3$ and $Pr_{0.65}Ca_{0.28}Sr_{0.07}MnO_3$ single crystals upon dielectric–metal phase transitions induced by a magnetic field. The results obtained were used for the construction of the *H–T* phase diagrams. The choice of the latter compound, which is characterized by a lower degree of distortion of the perovskite structure, was made for the following reasons. It is expedient to enhance considerably the tendency to transition to the metallic ferromagnetic

phase. This leads to a decrease in the field of the induced phase transition and makes it possible to elucidate the behavior of this system virtually on the verge of a metal–dielectric spontaneous transition. The occurrence of this transition is confirmed by recent investigations of the magnetic and kinetic properties and neutron diffraction in (PrCaSr)MnO_3 [8, 9].

2. EXPERIMENTAL TECHNIQUE

Single crystals of the compositions under investigation were grown by zone melting with optical heating. The magnetostriction was measured with a piezoelectric quartz sensor at temperatures of 10–300 K in pulsed magnetic fields up to 250 kOe (with a pulse duration of an order of 20 ms). In addition to the magnetostriction investigations, the magnetization $M(T, H)$ and the resistivity $\rho(T, H)$ were measured in static magnetic fields $H \le 13$ kOe at $T = 4.2$–300 K.

3. RESULTS AND DISCUSSION

3.1. The temperature dependences of the resistivity in a zero magnetic field and the magnetization in a field of 10 kOe for the $Pr_{0.6}Ca_{0.4}MnO_3$ crystal are depicted in Fig. 1. As is clearly seen from this figure, the crystal undergoes phase transitions to the charge-ordered state at $T_{CO} = 240$ K and to the antiferromagnetic state at $T_N = 170$ K. The charge and antiferromagnetic ordering at these temperatures was revealed by Jirak *et al.* [2]. According to Tomioka *et al.* [3], the observed increase in the magnetization in the low-temperature range is associated with the transition to the canted antiferromagnetic state; however, the crystal remains an insulator.

Similar dependences $\rho(T, H)$ and $M(T, H)$ were obtained for the $Pr_{0.65}Ca_{0.28}Sr_{0.07}MnO_3$ crystal ($T_{CO} = 210$ K and $T_N = 160$ K) (Fig. 2). Note that the cooling of this crystal in a field of 10 kOe leads to the transition from the antiferromagnetic charge-ordered state to the ferromagnetic state in the low-temperature range, in which the resistivity decreases drastically (Fig. 2) and the magnetization increases as compared to that of the sample cooled in a zero field. The doping with Sr^{2+} ions in these compounds results in an increase in the tolerance factor, which enhances the tendency toward the transition to the ferromagnetic state and, thus, suppresses the charge ordering [8, 9].

3.2. Let us now consider the results of investigations into the magnetoelastic properties of praseodymium manganite crystals upon insulator–metal phase transitions induced by pulsed magnetic fields.

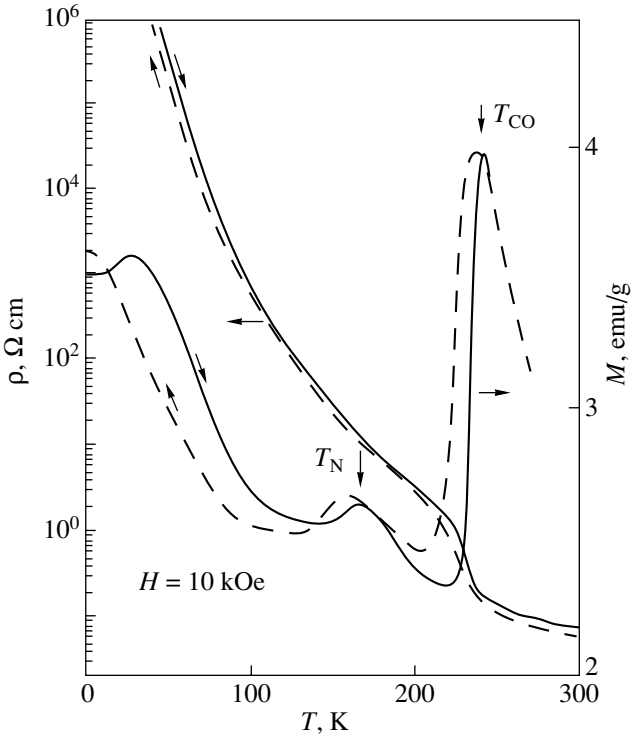

Fig. 1. Temperature dependences of the resistivity measured in a zero magnetic field (left axis) and the magnetization in a field of 10 kOe (right axis) for the $Pr_{0.6}Ca_{0.4}MnO_3$ crystal upon cooling and heating. Vertical arrows indicate the Néel point and the charge ordering temperature.

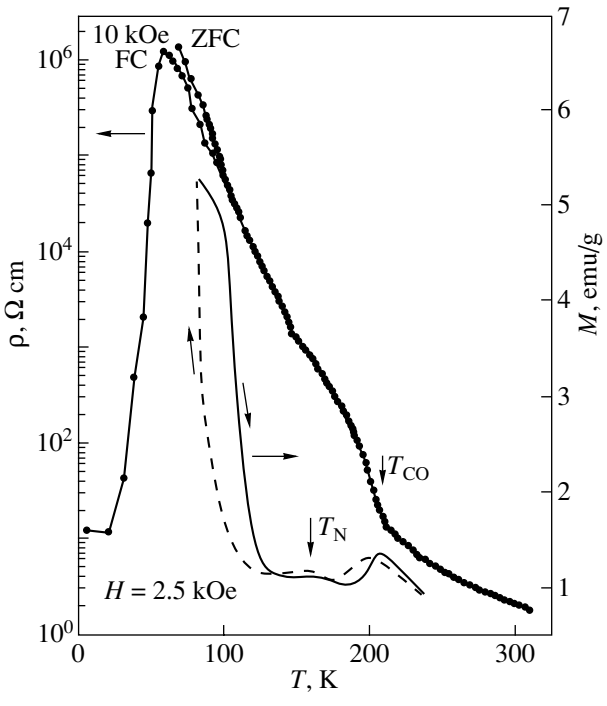

Fig. 2. Temperature dependences of the resistivity measured upon cooling in a zero magnetic field and at 10 kOe (left axis) and the magnetization in a field of 2.5 kOe (right axis) for the $Pr_{0.65}Ca_{0.28}Sr_{0.07}MnO_3$ crystal.

Figure 3 shows the field dependences of the longitudinal and transverse magnetostrictions of the $Pr_{0.6}Ca_{0.4}MnO_3$ crystal, which, as was noted above, undergoes antiferromagnetic and charge ordering at 170 and 240 K, respectively. It is seen that the longitudinal and transverse magnetostrictions at temperatures below the charge ordering point exhibit jumps in sufficiently strong magnetic fields. These jumps can be attributed to the first-order phase transitions from the antiferromagnetic charge-ordered state to the ferromagnetic metallic state, which are accompanied by suppression of the charge ordering. At low temperatures, these transitions are characterized by a considerable field hysteresis. For example, at $T = 10$ K, the magnetostrictions $\lambda_\parallel$ and $\lambda_\perp$ retain their high-field magnitudes with a decrease in the magnetic field to zero and only then relax to their initial values. Most likely, this effect has a dynamic nature and can be caused by the time delay of the measured strains with respect to the field. However, as the temperature increases, the hysteresis substantially decreases and approaches a value of ~20 kOe, which was obtained by static measurements of the conductivity [3]. It should be noted that the jumps in the longitudinal and transverse magnetostrictions are identical in sign. This indicates a considerable volume magnetostriction ($\lambda_V = \lambda_\parallel + 2\lambda_\perp \sim -1.8 \times 10^{-3}$). As the charge ordering temperature is approached, the magnetostriction jumps decrease, become less pronounced, and disappear at $T \geq T_{CO}$.

Reasoning from the experimental field dependences of the magnetostriction, we determined the critical fields of the phase transitions and constructed the *H–T* phase diagram for the $Pr_{0.6}Ca_{0.4}MnO_3$ compound (Fig. 4a). The characteristic features of this diagram are an increase in the field of the phase transition with an increase in temperature and a rather large region of the coexistence of two phases which is responsible for the pronounced hysteresis upon phase transition. Near the charge ordering point T_{CO}, the threshold field increases more slowly, then begins to decrease, and becomes zero at $T = T_{CO}$. Unfortunately, the threshold fields near T_{CO} are difficult to determine with sufficient reliability due to smearing of the field dependences of the magnetostriction. However, Tomioka *et al.* [3] studied the conductivity of $Pr_{1-x}Ca_xMnO_3$ in static magnetic fields and observed a similar behavior of the threshold field in the vicinity of T_{CO} [3]. By and large, the results obtained in [3] are in good agreement with the phase diagram obtained from our magnetostriction measurements in pulsed fields. A small difference is observed for the boundary of the ferromagnetic metallic phase at low temperatures (the lower line in Fig. 4a), which reaches zero field at a finite temperature in our case and at $T \longrightarrow 0$ in [3]. As was already mentioned, this can be explained by the manifestation of relaxation processes in the course of measurements in pulsed magnetic fields.

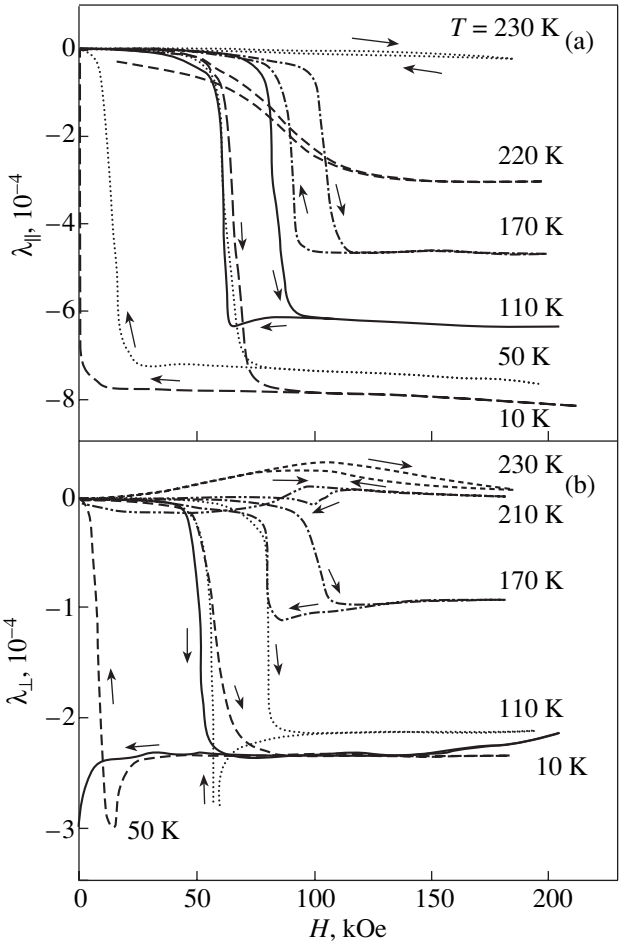

Fig. 3. Dependences of (a) longitudinal and (b) transverse magnetostrictions on the magnetic field for the $Pr_{0.6}Ca_{0.4}MnO_3$ crystal.

A similar behavior of the magnetostriction in a magnetic field is observed for the $Pr_{0.65}Ca_{0.28}Sr_{0.07}MnO_3$ single crystal ($T_N = 160$ K and $T_{CO} = 210$ K) (Fig. 5). In this case, the field dependence of the magnetostriction also exhibits negative jumps in $\lambda_\parallel$ and $\lambda_\perp$ due to the suppression of the charge ordering upon phase transition. At the same time, the magnetostriction of this compound at low temperatures shows specific features associated with a lower stability of charge ordering against the phase transition to the ferromagnetic metallic state in an external magnetic field. At $T < 60$ K, the high-field ferromagnetic metallic state remains stable after removal of the external magnetic field. This manifests itself in the fact that the initial behavior of the magnetostriction with a negative jump is not reproduced in subsequent measurements and the magnetostriction in an external magnetic field is positive. Actually, this means that both phases can coexist at low temperatures and the real state of the crystal essentially depends on its prehistory. Consequently, when the system in a strong magnetic field undergoes a crossover

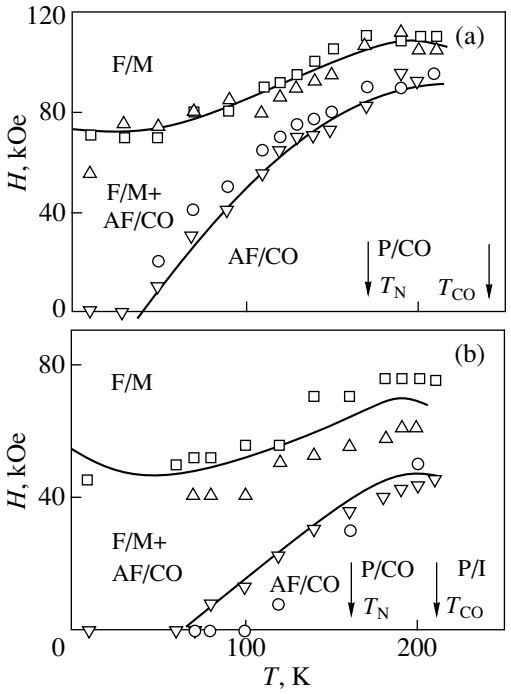

Fig. 4. *H–T* phase diagrams obtained from the dependences $\lambda_{\parallel}(H, T)$ (squares and circles) and $\lambda_{\perp}(H, T)$ (triangles) for the (a) $Pr_{0.6}Ca_{0.4}MnO_3$ and (b) $Pr_{0.65}Ca_{0.28}Sr_{0.07}MnO_3$ crystals. Designations: F/M is the ferromagnetic metallic state, AF/CO is the antiferromagnetic charge-ordered state, P/CO is the paramagnetic charge-ordered state, and P/I is the paramagnetic nonmetallic state.

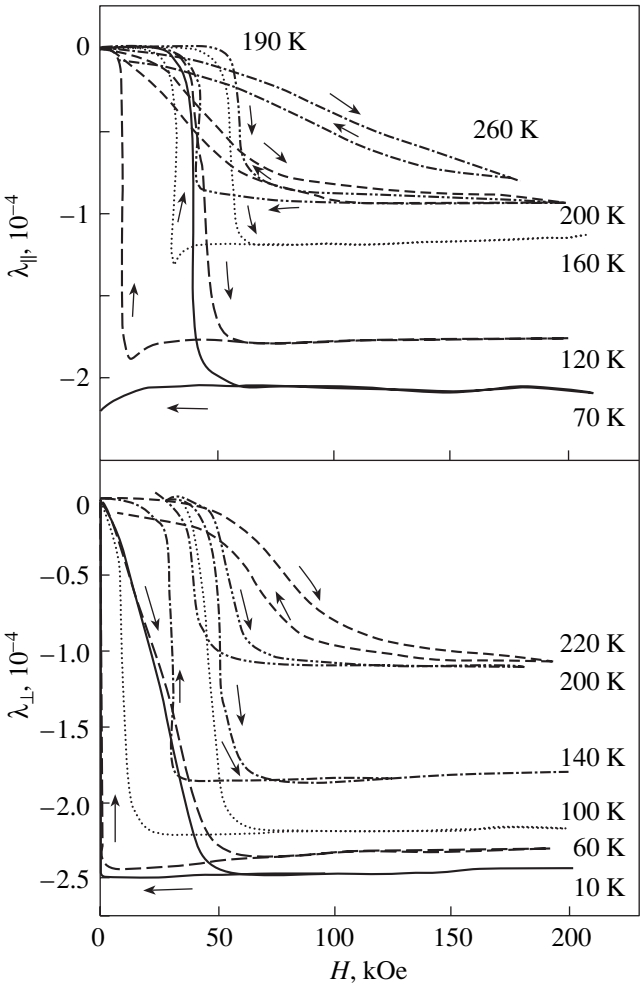

Fig. 5. Dependences of the longitudinal and transverse magnetostrictions on the magnetic field for the $Pr_{0.65}Ca_{0.28}Sr_{0.07}MnO_3$ crystal.

from the antiferromagnetic charge-ordered state to the ferromagnetic metallic state at $T < 60$ K, the initial state can be regained only after heating of the sample to temperatures above 90–100 K in a zero magnetic field. This behavior of the magnetostriction agrees well with observations of the magnetization and conductivity of this compound in static magnetic fields, according to which its initial state can also be restored by heating of the sample to 90–100 K. As for the $Pr_{0.6}Ca_{0.4}MnO_3$ compound, the jumps in the magnetostriction at high temperatures are observed with an increase and a decrease in the magnetic field, which indicates a reversible transition and a decrease in the hysteresis.

The *H–T* phase diagram constructed from the field dependences of the magnetostriction for $Pr_{0.65}Ca_{0.28}Sr_{0.07}MnO_3$ is shown in Fig. 4b. For the most part, this diagram correlates with that for $Pr_{0.6}Ca_{0.4}MnO_3$. The distinctive feature of this phase diagram is that the field of the thermodynamic phase transition in $Pr_{0.65}Ca_{0.28}Sr_{0.07}MnO_3$ is very weak and, possibly, becomes zero at low temperatures. This indicates the occurrence of a spontaneous transition from the charge-ordered state to the ferromagnetic metallic state. It should be noted that a similar *H–T* phase diagram was obtained for $Pr_{0.7}Ca_{0.3}MnO_3$ [3].

The temperature dependences of the magnetostriction of the $Pr_{0.6}Ca_{0.4}MnO_3$ crystal at a fixed magnetic field $H = 120$ kOe are depicted in Fig. 6. It can be seen that the temperature dependence of the transverse magnetostriction exhibits a small anomaly in the vicinity of the antiferromagnetic ordering point and the change of sign in the paramagnetic range. Analysis of the longitudinal magnetostriction demonstrates that the magnitude of induced strains monotonically decreases as the charge ordering temperature T_{CO} is approached and no noticeable anomalies occur at the Néel point T_N. This suggests that the crystal deformation is caused by suppression, predominantly, of the charge (orbital) ordering and, to a lesser extent, of the antiferromagnetic ordering. Above the charge ordering temperature, the induced magnetostriction is virtually absent.

3.3. Now, we discuss the mechanism of the phase transitions observed in magnetic fields. It can be assumed that this mechanism is governed by a strong dependence of the exchange interaction on the orbital

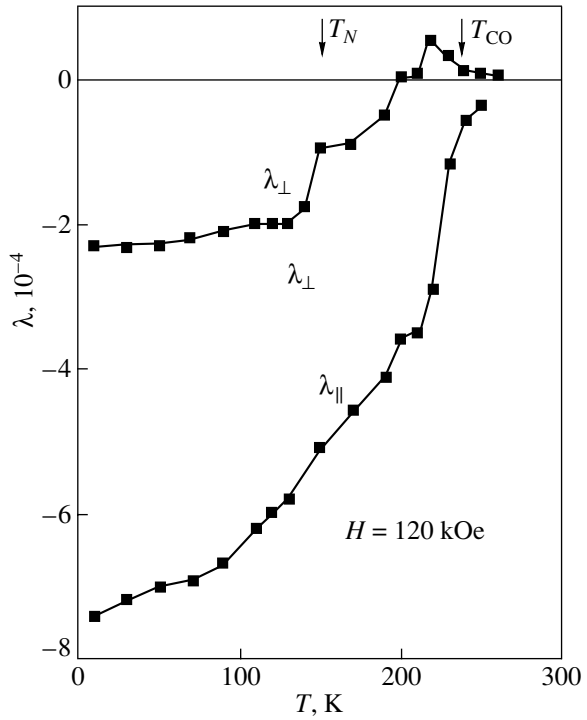

Fig. 6. Temperature dependences of the magnetostriction for the $Pr_{0.6}Ca_{0.4}MnO_3$ crystal in a fixed magnetic field of 120 kOe.

and charge ordering in the system. This is confirmed by the considerable magnetization anomaly observed at the charge (orbital) ordering point (Figs. 1, 2). Specifically, a substantial decrease in the magnetization below the T_{CO} temperature indicates suppression of the ferromagnetic exchange and enhancement of the antiferromagnetic interaction in the manganese subsystem. In actual fact, this implies that the Curie paramagnetic temperature Θ and the Curie constant C (in the expression for the paramagnetic susceptibility $\chi = C/(T - \Theta)$) depend on the order parameter characterizing the charge and orbital ordering. A change in the C constant at the T_{CO} point can mean a change in the number of manganese ions forming magnetic clusters that determine the effective magnetic moment in the Curie–Weiss law. Hence, it follows that the suppression of the charge ordering immediately produces a gain in the Zeeman energy and should be accompanied by an increase (a jump) in the magnetization even in the paramagnetic phase at $T < T_{CO}$. The above assumption is also confirmed by the considerable volume magnetostriction observed in the magnetic fields, which is usually explained by the dependence of the exchange interaction on the interatomic distance. Note that the induced magnetostriction of $Pr_{0.6}Ca_{0.4}MnO_3$ is appreciably higher than that of $Pr_{0.65}Ca_{0.28}Sr_{0.07}MnO_3$. To a certain measure, this reflects the degree of local distortions that occur in the charge-ordered (orbitally ordered) state and disappear upon transition of the system to the ferromagnetic metallic state, which is attended by delocalization of the e_g electrons and an increase in the double exchange.

The behavior of the magnetostriction upon phase transitions in the studied crystals is in good agreement with the data obtained by de Teresa *et al.* [10], who also observed a negative volume magnetostriction upon similar field-induced transitions in $Pr_{0.67}Ca_{0.33}MnO_3$ polycrystals.

4. CONCLUSION

Thus, the performed investigation of the substituted praseodymium manganites revealed clear correlations between their electrical, magnetic, and magnetostriction properties due to strong spin–charge–lattice coupling. These correlations make it possible to study efficiently various phase transformations of these compounds in magnetic fields on the basis of anomalies in their magnetoelastic properties.

ACKNOWLEDGMENTS

This work was supported by the Russian Foundation for Basic Research (project no. 00-02-16500), the International Association of Assistance for the promotion of cooperation with scientists from the New Independent States of the former Soviet Union (project no. 97-30850), and the Ministry of Science and Technology of the Russian Federation (project no. 97-0-07.3-153).

REFERENCES

1. Y. Tokura and Y. Tomioka, J. Magn. Magn. Mater. **200**, 1 (1999).
2. Z. Jirak, S. Krupicka, Z. Zimsa, *et al.*, J. Magn. Magn. Mater. **53**, 153 (1985).
3. Y. Tomioka, A. Asamitsu, H. Kuwahara, *et al.*, Phys. Rev. B **53**, R1689 (1996).
4. A. Urushibura, Y. Moritomo, T. Arima, *et al.*, Phys. Rev. B **51**, 14103 (1995).
5. H. Yoshizawa, H. Kawano, Y. Tomioka, and Y. Tokura, J. Phys. Soc. Jpn. **65**, 1043 (1996).
6. M. Tokunaga, N. Miura, Y. Tomioka, and Y. Tokura, Phys. Rev. B **57**, 5259 (1998).
7. A. Maignan, Ch. Simon, V. Caignaert, and R. Raveau, Solid State Commun. **96**, 623 (1995).
8. Y. Tomioka, A. Asamitsu, H. Kuwahara, and Y. Tokura, J. Phys. Soc. Jpn. **66**, 302 (1997).
9. M. R. Lees, J. Barratt, G. Balakrishnan, *et al.*, Phys. Rev. B **58**, 8694 (1998).
10. J. M. de Teresa, M. R. Ibarra, C. Marquina, *et al.*, Phys. Rev. B **54**, R12689 (1996).

Translated by O. Borovik-Romanova

Physics of the Solid State, Vol. 43, No. 8, 2001, pp. 1538–1542. Translated from Fizika Tverdogo Tela, Vol. 43, No. 8, 2001, pp. 1478–1481.

MAGNETISM AND FERROELECTRICITY

Domain Structure in Centroantisymmetric Antiferromagnets

A. A. Khalfina, M. Kh. Kharrasov, and M. A. Shamsutdinov

Bashkortostan State University, ul. Frunze 32, Ufa, Bashkortostan, 450074 Russia

Received November 30, 2000

Abstract—The domain structure of an antiferromagnet whose magnetic-symmetry group contains a center of antisymmetry is studied theoretically. The magnetoelectric effect and weak ferromagnetism are shown to coexist in a domain wall. It is established that when the inhomogeneous magnetic moment interacts with a sufficiently strong magnetic field $\mathbf{H} \parallel \mathbf{C}_3$, a multidomain state with an odd number of 180° domain walls becomes energetically favorable. The critical field for the transition from a single-domain state to a multidomain state is found. It is shown that domain reversal occurs when the magnetic field **H** is reversed. © *2001 MAIK "Nauka/Interperiodica".*

Antiferromagnetic ordering can cause a crystal to cease to be invariant under time reversal. In this case, the center of symmetry I of the crystal-symmetry group becomes a center of antisymmetry I^-; that is, below the Néel temperature, the crystal possesses a centroantisymmetric (CAS) structure. Since the symmetry element I^- interchanges the magnetic sublattices with one another, the free energy can contain invariants linear in the ferromagnetism vector **m**, antiferromagnetism vector **l**, and their first-order spatial derivatives, such as $l_\alpha m_\beta p_\gamma$ and $m_\alpha \partial l_\beta / \partial r_\gamma$; this leads to additional interactions [1, 2]. The term $l_\alpha m_\beta p_\gamma$ (p is the electric polarization) is responsible for the linear magnetoelectric (ME) effect discovered by Astrov [3]. Shavrov [2] analyzed the possible occurrence of the ME effect in various types of antiferromagnetic structures and calculated the spectrum of spin waves with allowance for the ME interaction. In [4–6], it was shown that the ME interaction drastically affects the acoustic and other dynamic properties of magnetoelectrics. Inhomogeneous invariants lead to the occurrence of a variety of antiferromagnetic structures: helicoidal structures [7] and long-wavelength and modulated magnetic structures [8–10]. The early studies of domain-wall structures in CAS antiferromagnets were performed by Farztdinov [11], who showed that 180° domain walls can be of two types, parallel ($S_\parallel^z$) and perpendicular ($S_\perp^z$) to the symmetry axis C_3 of the crystal. The CAS antiferromagnets are of interest because the parameters of their domain structure can be varied by using both magnetic and electric fields. In this paper, we theoretically investigate the domain structure of CAS antiferromagnets in external magnetic and electric fields with allowance for the invariants indicated above. It is shown that the linear inhomogeneous exchange interaction $\mathbf{m}\partial\mathbf{l}/\partial z$ radically alters the properties of the domain structure of a CAS antiferromagnet in a magnetic field $\mathbf{H} \parallel \mathbf{C}_3$.

As an example of a magnetoelectric medium, we consider CAS antiferromagnets with a magnetic symmetry $3_z^+ 2_x^- I^-$ [4], in particular, Cr_2O_3, which is a two-sublattice antiferromagnet of the easy-axis type. We will describe an antiferromagnet in terms of dimensionless vectors of ferromagnetism $\mathbf{m} = (\mathbf{M}_1 + \mathbf{M}_2)/2M_0$ and antiferromagnetism $\mathbf{l} = (\mathbf{M}_1 - \mathbf{M}_2)/2M_0$ ($|\mathbf{M}_1| = |\mathbf{M}_2| = M_0$, where $\mathbf{M}_1$, $\mathbf{M}_2$ are the sublattice magnetization vectors) and electric polarization **p**.

The free energy density is taken in the form

$$F = F_m + F_{mp} + F_p,$$

which includes the magnetic, magnetoelectric, and electric-polarization energies. In the case of $\mathbf{ml} = 0$ and $\mathbf{m}^2 + \mathbf{l}^2 = 1$, these energies can be written as [2, 5, 11]

$$F_m = \frac{1}{2}A\left(\frac{\partial \mathbf{l}}{\partial x_i}\right)^2 + D\mathbf{m}\frac{\partial \mathbf{l}}{\partial z} + \frac{1}{2}B\mathbf{m}^2 + \frac{1}{2}a(l_x^2 + l_y^2) + \frac{1}{2}a_1(l_x^2 + l_y^2)^2 - 2M_0\mathbf{mH},$$

$$F_{mp} = -2M_0\gamma_{ijk}l_i m_j p_k,$$

$$F_p = \frac{1}{2}\kappa_\perp^{-1}(p_x^2 + p_y^2) + \frac{1}{2}\kappa_z^{-1}p_z^2 - \mathbf{pE}.$$

Here, $B \sim 4M_0^2\chi^{-1}$ is the homogeneous exchange constant; χ is the transverse antiferromagnetic susceptibility; $A \sim Ba_0^2$ and $D \sim Ba_0$ are the quadratic and linear inhomogeneous exchange constants, respectively; a_0 is the crystal lattice parameter; a and a_1 are the magnetic anisotropy constants; **H** is an external magnetic field; $\hat{\gamma}$ is the ME interaction tensor; $\kappa_\perp$ and κ_z are components of the electric polarizability tensor; and **E** is the electric field. In the expression for F_m, we neglected the inhomogeneous-exchange anisotropy and the six-order

anisotropy constants as they are insignificant in the phenomena under study.

Minimizing the free energy with respect to **p** and **m** in the case of $H \ll H_E = B/4M_0$, we obtain

$$F = \frac{1}{2}A\left[\left(\frac{\partial \mathbf{l}}{\partial x_i}\right)^2 - \frac{D^2}{AB}\left(\frac{\partial \mathbf{l}}{\partial z}\right)^2\right] + \frac{D}{2H_E}\left(\mathbf{H} + \mathbf{H}_p, \frac{\partial \mathbf{l}}{\partial z}\right) + \frac{1}{2}\chi[(\mathbf{H} + \mathbf{H}_p, \mathbf{l})^2 - (\mathbf{H} + \mathbf{H}_p)^2] + \frac{1}{2}a(l_x^2 + l_y^2) + \frac{1}{2}a_1(l_x^2 + l_y^2)^2. \quad (1)$$

Here,

$$\mathbf{H}_p = [(\gamma_1 l_y + \gamma_3 l_z)E_x + \gamma_1 l_x E_y, \gamma_1 l_x E_x + (\gamma_3 l_z - \gamma_1 l_y)E_y, \gamma_2(E_x l_x + E_y l_y) - \gamma_0 E_z l_z],$$

where γ_i are the ME interaction constants [5].

The magnetization vector in this case is given by

$$\mathbf{M} = \chi\left[\mathbf{H} + \mathbf{H}_p - (\mathbf{H} + \mathbf{H}_p, \mathbf{l})\mathbf{l} - \frac{D}{2M_0}\frac{\partial \mathbf{l}}{\partial z}\right]. \quad (2)$$

As can be seen from Eq. (2), CAS antiferromagnet has a week ferromagnetic moment even in zero fields ($\mathbf{H} = \mathbf{E} = 0$) in the case of an inhomogeneous distribution of the antiferromagnetism vector **l**. Therefore, in contrast to the homogeneous state, in which the ME effect and weak ferromagnetism cannot coexist [2], this does not occur in an inhomogeneous state. An inhomogeneous **l** distribution along the *z* axis takes place if the crystal has a domain structure with domain walls (DWs) perpendicular to the symmetry axis C_3. The magnetization has a maximum in the region where the gradient of **l** is maximum, i.e., in the transition layer between two adjacent domains. The presence of an inhomogeneous weak ferromagnetic moment in transition layers can lead to unusual behavior of the domain structure of CAS antiferromagnets in an external magnetic field. Before investigating the characteristics of the domain structure, we discuss the possible coexistence of centrosymmetric phases in fields $\mathbf{H} \parallel \mathbf{E} \parallel z$. By minimizing expression (1) in the case of a homogeneous state, we find that if

$$a - \chi H^2 - \alpha_\parallel^2 \chi^{-1} E^2 \pm 2\alpha_\parallel EH > 0, \quad (3)$$

then the phase with $\theta = k\pi$ ($k = 0, 1, 2, \ldots$) is stable, where θ is the polar angle of vector **l** determined from the *z* axis. In Eq. (3), the plus sign corresponds to the state $\mathbf{l} \uparrow\uparrow \mathbf{H} \parallel z$ ($k = 2n$, $n = 0, 1, 2, \ldots$) and the minus sign corresponds to the $\mathbf{l} \uparrow\downarrow \mathbf{H}$ state ($k = 2n + 1$). These states have the same energy. The regions of stability of phases $\mathbf{l} \uparrow\uparrow \mathbf{H}$ and $\mathbf{l} \uparrow\downarrow \mathbf{H}$ can overlap. In the region where the conditions for stability of different phases are fulfilled, a 180° domain structure can exist.

In the case of $E = 0$, another centrosymmetric phase with $\theta = (2k + 1)\pi/2$ $\mathbf{l} \perp \mathbf{H}$ exists if

$$a - \chi H^2 + 2a_1 < 0.$$

When $a_1 < 0$, the regions of stability of states with $\mathbf{l} \parallel z$ and $\mathbf{l} \perp z$ overlap. In this case, as is well known, the sublattices flop over at $H = H_c = \sqrt{(a + a_1)/\chi}$ ($E = 0$); that is, the vector $\mathbf{l} \parallel z$ flops over into the basal plane, this process being a first-order phase transition. According to [12], the spin-flop reorientation of **l** in Cr_2O_3 is a first-order transition. For this reason, the fourth-order anisotropy constant a_1 is taken to be negative in what follows.

Now, we will investigate the inhomogeneous states in fields $\mathbf{H} \uparrow\uparrow \mathbf{E} \parallel z$. An inhomogeneity is taken to be a planar DW separating two phases (domains) with oppositely directed **l**. The DW width is assumed to be much smaller than the widths of the domains. We will investigate the characteristics of $S_\perp^z$ DWs perpendicular to the C_3 axis.

From Eq. (1), it follows that the energy density of an $S_\perp^z$ DW has the form

$$F = \frac{1}{2}A^*\left(\frac{d\theta}{dz}\right)^2 + g(\theta) - g_1(\theta)\frac{d\theta}{dz},$$
$$2g(\theta) = (a^* + 2\alpha_\parallel HE\cos\theta + a_1^*\sin^2\theta)\sin^2\theta, \quad (4)$$
$$g_1(\theta) = (D/2H_E)(H - \gamma_0\kappa_z E\cos\theta)\sin\theta,$$

where $A^* = A(1 - \mu^2)$, $\mu = D/\sqrt{BA}$ is the dimensionless inhomogeneous linear exchange constant, $\alpha_\parallel = \gamma_0\kappa_z\chi/2M_0$ is the longitudinal component of the ME susceptibility tensor, and

$$a^* = a - \chi H^2 - \alpha_\parallel^2\chi^{-1}E^2, \quad a_1^* = a_1 + \alpha_\parallel^2\chi^{-1}E^2.$$

Equation (4) differs from the expression found for the energy density of centrosymmetric antiferromagnets. First, the exchange constant is renormalized by the inhomogeneous exchange which is linear in $\partial\mathbf{l}/\partial z$. Second, the energy density has an additional term $g_1(\theta)\theta_z'$, which describes the interaction energy between the inhomogeneous magnetization **M** and the fields **H** and **E** in the DW volume. The case of $A^* < 0$ corresponds to a modulated magnetic structure [10]. In what follows, we assume that $0 < \mu < 1$ and, hence, $A^* > 0$.

A solution to the Euler equation for the problem in question,

$$A^*\frac{d^2\theta}{dz^2} - \frac{dg\theta}{d\theta} = 0, \quad (5)$$

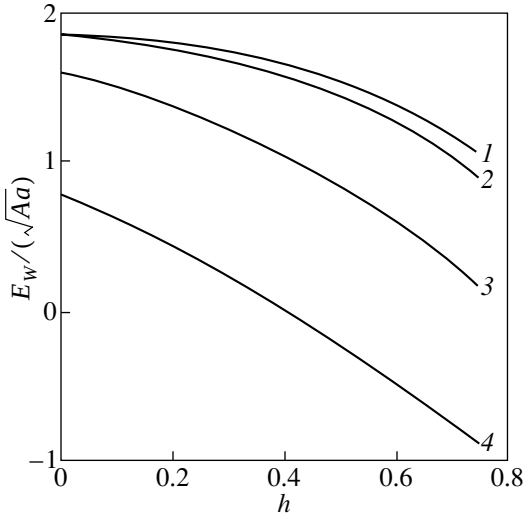

Fig. 1. Dependence of the energy of an $S_\perp^z$ domain wall on the magnetic field for $q = 0.5$, $e = 0$, and different values of μ: (*1*) 0, (*2*) 0.1, (*3*) 0.5, and (*4*) 0.9.

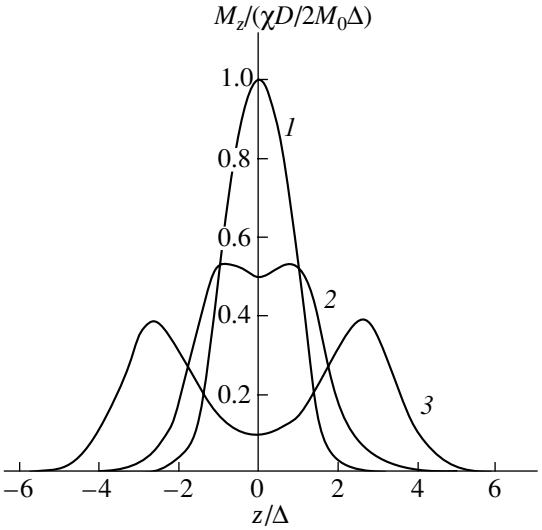

Fig. 2. Dependence of the contribution from the invariant $\mathbf{m}\partial\mathbf{l}/\partial z$ to the magnetization on the coordinate z/Δ ($\Delta = \sqrt{A^*/|a_1|}$) for $a^*/|a_1|$ = (*1*) 2, (*2*) 1.25, and (*3*) 1.01.

with boundary conditions $\theta(-\infty) = \theta(\infty) = \pi$ and $\theta_z'(\pm\infty) = 0$ has the form

$$\frac{z}{\delta} = \int_{\pi/2}^{0} \frac{d\theta}{\sin\theta\sqrt{(q^2-e^2)\cos^2\theta + 2eh\cos\theta + 1 - h^2 - q^2}}. \quad (6)$$

Here, $q^2 = a_1/a$, $e = \alpha_\parallel E/\chi H_a$, $h = H/H_a$, $H_a = \sqrt{a/\chi}$, and $\delta = \delta_0\sqrt{1-\mu^2}$ is the characteristic DW width in a CAS antiferromagnet, with $\delta_0 = \sqrt{A/a}$ being the DW width in a centrosymmetric antiferromagnet.

From Eqs. (4) and (6), the DW energy is found to be

$$E_W^\perp - \sqrt{Aa}(f - 2\mu h), \quad (7)$$

$$f = \frac{\sqrt{(1-\mu^2)}}{2(q^2-e^2)}\Bigg[(q^2-e^2+eh)\sqrt{1-(h-e)^2} + (q^2-e^2-eh)\sqrt{1-(h+e^2)} + \frac{(q^2(1-h^2-q^2+e^2)-e^2)}{\sqrt{q^2-e^2}} \times \ln\frac{\sqrt{(q^2-e^2)[1-(h-e)^2]} + q^2 - e^2 + eh}{\sqrt{(q^2-e^2)[1-(h+e)^2]} - q^2 + e^2 + eh}\Bigg]. \quad (8)$$

Equations (2)–(8) are derived without regard for the magnetostatic interaction. The magnetostatic energy of the $S_\perp^z$ DW is

$$\Delta E_m = 2\pi\int M_z^2 dz.$$

For $H_E \gg 4\pi M_0$, which is easily satisfied in antiferromagnets ($\chi \sim 10^{-3}$), the magnetostatic energy is much smaller than the total energy and its influence on the $\theta(z)$ dependence is negligible. Indeed, for $H = E = 0$, $a_1 = 0$, and $0 < \mu < 0.9$, we have

$$\frac{\Delta E_m}{|\Delta E_W|} = \frac{1}{3}\frac{4\pi M_0}{H_E}\frac{\mu^2}{\left|1-\mu^2-\sqrt{1-\mu^2}\right|} \ll 1. \quad (9)$$

Here, $\Delta E_W = E_W^\perp - E_W^\perp(\mu = 0) < 0$ is the contribution from the invariant $\mathbf{m}(\partial\mathbf{l}/\partial z)$ to the DW energy; $E_W^\perp(\mu = 0) \approx E_W^\parallel$, where $E_W^\parallel$ is the energy of the $S_\parallel^z$ DW. The negative values of ΔE_W indicate that the $S_\perp^z$ DW does not become energetically unfavorable in comparison with the $S_\parallel^z$ DW due to its inhomogeneous linear exchange being present in a wide range of parameter μ; this contradicts what was believed earlier [11].

The results of numerical calculations using Eq. (7) are presented in Fig. 1 for an inhomogeneous exchange constant and magnetic field varied in wide ranges. The magnetic-field dependence of the DW energy is transformed to a linear dependence with increasing μ, which is due to the longitudinal component of the DW magnetization $M_z = -\chi(D/2M_0)(\partial\mathbf{l}_z/\partial z)$ for $H = E = 0$. For $2M_0 \sim 10^2$–10^3 G and $D/B\delta \sim 10^{-3}$–10^{-2}, we have $M_{z\max} = 2M_0(D/B\delta) \sim 0.1$–$10$ G. The maximum value of magnetization due to invariant $\mathbf{m}\partial\mathbf{l}/\partial z$ decreases with increasing the external magnetic field (Fig. 2). How-

ever, the total magnetization in the DW volume $\int M_z dz = 4M_0 D/B \sim 10^{-5}$–$10^{-}$ G remains unchanged. For this reason, the DW width does not depend on g_1, which characterizes the contribution from invariant $\mathbf{m}\partial\mathbf{l}/\partial z$ to the Zeeman energy of the DW in Eq. (4).

The components M_z in adjacent DWs are opposite in sign (Fig. 3). Therefore, if the last term in Eq. (7) is negative in a DW, then it is positive in the next DW. If the number of DWs is even ($N = 2n$, $n = 1, 2, 3, \ldots$), the contribution from the last term in Eq. (7) to the total energy of the DWs is zero. In the case of an odd number of DWs ($N = 2n - 1$), the contribution from the last term in Eq. (7) to the total energy is nonzero and two types of domain structures are possible, with their total DW energy being equal to

$$E_{2n-1}^{(\mp)} = \sqrt{Aa}[(2n-1)f \mp 2\mu h]. \quad (10)$$

The minus sign corresponds to a structure of type *A* (Fig. 3a); the plus sign, to a structure of type *B* (Fig. 3b). In the former case, the total DW energy vanishes at a certain value H_{cr} of the magnetic field and, with a further increase in the magnetic field, a multidomain structure of type *A* becomes energetically favorable. In this case, the maximum number of DWs is

$$N_{\max} = \frac{2\mu h}{f}. \quad (11)$$

A two-domain structure (with a single DW) is the most favorable. For a given number of DWs, Eq. (11) determines the critical parameters for a transition to the multidomain state. As can be seen from Fig. 4, the critical field required for the transition to a multidomain state decreases with increasing the parameter $\mu = D/\sqrt{AB}$, which characterizes the inhomogeneous linear exchange.

When the direction of **H**/*z* is reversed, *h* should be replaced by –*h* in Eq. (7). In this case, the domain structure of type *B* has a minimum energy. Therefore, by reversing the direction of the magnetic field in the case of $H > H_{cr}$, a domain structure of type *A* can be converted into a structure of type *B* and vice versa. No data on the constant *D* are available for Cr_2O_3; therefore, the parameter μ cannot be determined. The critical field H_{cr} for domain-structure conversion depends heavily on μ. For small values of μ, the field H_{cr} is close to the field H_c above which the sublattices flop over; however, for large values of μ, domain-structure conversion occurs in fields much lower than H_c (Fig. 4). Therefore, the value of the inhomogeneous linear exchange constant can be determined from experimental data on domain reversal in a magnetic field.

The electric field **E** ∥ **H** ∥ *z* affects the DW energy only slightly because of the smallness of the ME susceptibility. At the same time, the electric field can drastically affect the DW dynamics and, hence, the process of domain reversal for other orientations of **H** and **E**. Domain reversal was observed experimentally in Cr_2O_3 in the case of **E** ∥ **H** and magnetic fields much lower than H_c and directed at an angle to the C_3 axis [13]. However, this problem is a subject for separate investigation.

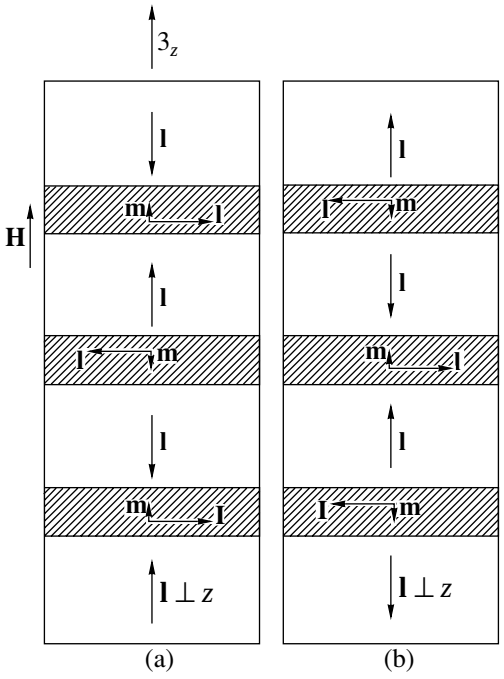

Fig. 3. Domain structure of (a) type *A* and (b) type *B* for $N = 3$ (schematic).

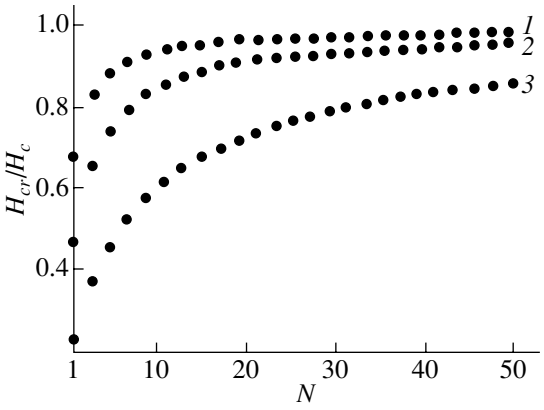

Fig. 4. Critical field for a transition to a multidomain state as a function of the number of domains *N* for different values of μ: (*1*) 0.1, (*2*) 0.5, and (*3*) 0.9.

REFERENCES

1. E. A. Turov, *Kinetic, Optical and Acoustical Properties of Antiferromagnetics* (Ural. Otd. Akad. Nauk SSSR, Sverdlovsk, 1990).

2. V. G. Shavrov, Zh. Éksp. Teor. Fiz. **48** (5), 1419 (1965) [Sov. Phys. JETP **21**, 948 (1965)].
3. D. N. Astrov, Zh. Éksp. Teor. Fiz. **40** (4), 1035 (1961) [Sov. Phys. JETP **13**, 729 (1961)].
4. E. A. Turov, Zh. Éksp. Teor. Fiz. **104** (5), 3886 (1993) [JETP **77**, 868 (1993)].
5. E. A. Turov, V. V. Men'shenin, and V. V. Nikolaev, Zh. Éksp. Teor. Fiz. **104** (6), 4157 (1993) [JETP **77**, 1014 (1993)].
6. M. Kh. Kharrasov and A. U. Abullin, Dokl. Akad. Nauk **336** (3), 335 (1994) [Phys. Dokl. **39**, 346 (1994)].
7. I. E. Dzyaloshinskiĭ, Zh. Éksp. Teor. Fiz. **46** (4), 1420 (1964) [Sov. Phys. JETP **19**, 960 (1964)]; Zh. Éksp. Teor. Fiz. **47** (3), 992 (1964) [Sov. Phys. JETP **20**, 665 (1964)].
8. V. G. Bar'yakhtar and D. A. Yablonskiĭ, Fiz. Tverd. Tela (Leningrad) **24** (8), 2522 (1982) [Sov. Phys. Solid State **24**, 1435 (1982)].
9. E. P. Stefanovskiĭ, Fiz. Nizk. Temp. **13** (7), 740 (1987) [Sov. J. Low Temp. Phys. **13**, 424 (1987)].
10. A. B. Borisov and V. V. Kiselev, Fiz. Tverd. Tela (Leningrad) **32** (1), 212 (1990) [Sov. Phys. Solid State **32**, 119 (1990)].
11. M. M. Farztdinov, *Physics of Magnetic Domains in Antiferromagnetics and Ferrites* (Nauka, Moscow, 1981).
12. M. Fiebig, D. Frohlich, and H.-J. Thiele, Phys. Rev. B **54** (18), R12681 (1996).
13. T. J. Martin, Phys. Lett. **17** (2), 83 (1965).

Translated by Yu. Epifanov

Physics of the Solid State, Vol. 43, No. 8, 2001, pp. 1543–1548. Translated from Fizika Tverdogo Tela, Vol. 43, No. 8, 2001, pp. 1482–1487.

MAGNETISM AND FERROELECTRICITY

Structural Self-Organization and the Formation of Perpendicular Magnetic Anisotropy in $Co_{50}Pd_{50}$ Nanocrystalline Films

L. I. Kveglis, S. M. Jarkov, and I. V. Staroverova

Kirensky Institute of Physics, Siberian Division, Russian Academy of Sciences, Akademgorodok, Krasnoyarsk, 660036 Russia
e-mail: jarkov@iph.krasnoyarsk.su

Received December 4, 2000

Abstract—The correlation of the atomic-order structure and the energy density of perpendicular magnetic anisotropy in $Co_{50}Pd_{50}$ films is investigated. Structural models for nanocrystalline $Co_{50}Pd_{50}$ films are proposed. It is shown that processes of structural self-organization in the films form nontrivial atomic-order structures. These structures can exist owing to high elastic stresses, which apparently ensure the emergence of strong magnetic anisotropy ($K_\perp \sim 10^6$ erg/cm^3). © *2001 MAIK "Nauka/Interperiodica".*

1. INTRODUCTION

The existence of strong magnetic anisotropy perpendicular to the plane of a structurally disordered film has been studied by many authors engaged in research involving amorphous and nanocrystalline films. The strong dependence of the perpendicular magnetic anisotropy (PMA) constant on the technological conditions of preparation and processing of samples complicates unambiguous interpretation of the PMA origin. The possible mechanisms of PMA formation, which were analyzed comprehensively in [1], are determined by the atomic-order structure and chemical composition of the film. The main reasons behind the emergence of PMA in films are crystallographic anisotropy, anisotropy of the columnar structure, magnetostriction anisotropy, anisotropy of the local atomic ordering, surface anisotropy, and exchange anisotropy between multilayers (in the case of multilayered films). Connection of the columnar and fractal structures formed perpendicularly to the film plane with PMA exceeding the shape anisotropy of the film is visually demonstrated in [2–4]. However, the mechanisms and kinetics of formation of such structures remain unclear. In our previous publications [5–8], we proved that a local atomic order is formed in nanocrystalline films of transition metal alloys ($Dy_{23}Co_{77}$, $Co_{10}Pd_{90}$, and $Co_{50}Pd_{50}$) during preparation. We proposed that, in the case of Dy–Co alloys, PMA carriers are highly anisotropic clusters of the $DyCo_5$ type [6], while such carriers for Co–Pd alloys are clusters of the $L1_0$ and ε' phases, which are oriented so that the easy magnetization axis is perpendicular to the plane of the film [7, 8]. However, these phases were not always observed in the Co–Pd films. In some cases, PMA also took place without these phases [7] and the observed structure did not correspond to the phase equilibrium diagram.

Considerable deviations from equilibrium during the preparation of nanocrystalline materials lead to the formation of atomic structures that often do not conform to the equilibrium bulk state or to known metastable states of the given material. Away from the equilibrium state, an insignificant variation of the system parameter can result in a radical change in the physical properties of the substance [9]. The number and structure of defects in a nanocrystalline material differ qualitatively from those in mono- and polycrystalline materials; for this reason, the nanocrystalline state cannot be regarded simply as a monocrystalline state with a large number of defects [10]. Thus, the atomic structure of nanoparticles can be described in the framework of classical crystallography only for certain cases. The description of the atomic structure of the nanocrystalline state requires the application of nontraditional approaches.

One of such approaches is the Voronoĭ–Delone method developed for noncrystalline materials [11]. This method involves simulation of spatial structures with the help of Voronoĭ polyhedra. A Voronoĭ polyhedron is the direct geometrical image of the nearest atomic surrounding. The special significance of Voronoĭ polyhedra is that they are convenient structural elements for use in studying spatial structural motifs.

The above idea was developed further by Bulienkov *et al.* [12–14], who described the atomic structure of materials with amorphous, nanocrystalline, and quasicrystalline discontinuous structures as an aggregate of crystalline modules. This concept is introduced in order to explain the mechanisms of self-organization of crystals and other structures with short-range and long-range order. This connects the energy of interatomic interaction and the geometry of the structure formation both on local and global levels. A crystalline module as

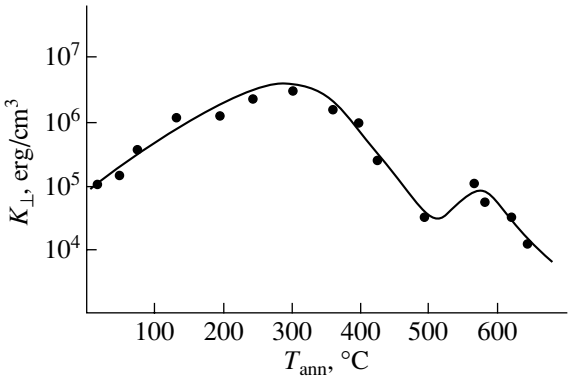

Fig. 1. Dependence of the perpendicular magnetic anisotropy constant $K_\perp$ of a $Co_{50}Pd_{50}$ film on the annealing temperature T_{ann}.

a closed three-dimensional loop is repeated periodically in space and either fills the space entirely or embraces all the atoms of the structure through its apexes, depending on the crystal symmetry. For example, a module of a face-centered cubic (fcc) lattice has the form of a primitive cell with fcc structure (in the form of a rhombohedron) and consists of an octahedron and two tetrahedra. Such an approach considerably extends the set of module polyhedra forming an atomically ordered structure as compared to the Fedorov groups and provides new opportunities to explain the unique physical properties of nanocrystalline materials.

The experiments on electron diffraction carried out by us earlier on Dy–Co and Co–Pd films [5–8] and the evolution of the concepts concerning the formation of the atomic structure in a structurally disordered material [11–14] led to the formulation of the following problems.

(1) The construction of structural models of short-range atomic ordering using the approaches described in [11–14] from an analysis of the electron diffraction patterns obtained for $Co_{50}Pd_{50}$ films with high PMA ($K_\perp \sim 10^6$ erg/cm^3).

(2) The revision of the reasons behind the formation of PMA in the $Co_{50}Pd_{50}$ films under investigation on the basis of these structural models.

2. SAMPLE PREPARATION AND EXPERIMENTAL TECHNIQUE

In this work, we present the results of an investigation of the structure and magnetic properties of Co–Pd nanocrystalline films with equiatomic composition (50 at. % Co and 50 at. % Pd) in the initial state, as well as those subjected to thermal treatment in vacuum. The films were obtained by thermal sputtering–explosion in a vacuum of 10^{-5} Torr and through magnetron sputtering in a vacuum of 10^{-6} Torr on various substrates (glass, crystalline and amorphous silicon, fused quartz, NaCl, MgO, and LiF). The microscopic structure and the phase composition of the films were studied using PREM-200 and JEM-100C transmission electron microscopes. The chemical composition of the films was monitored using x-ray fluorescence analysis. The PMA constant $K_\perp$ was determined by the torque method at room temperature in fields of strengths up to 17 kOe.

3. RESULTS

The PMA constant of the films in the initial state was $K_\perp \sim 10^5$ erg/cm^3 (Fig. 1). Electron diffraction patterns obtained from these films were in the form of a diffuse halo. Electron microscopic studies revealed that the films are composed of particles ≈20–30 Å in size. It was found that dendrite crystallization occurred in the films under the action of an electron beam in a transmission electron microscope or during annealing in a vacuum of 10^{-5} Torr at temperature T_{ann} = 260–300°C. Figure 2a shows an electron microscope image of a region of dendrite grown in a nanocrystalline film. The velocity of the crystallization front determined visually from the electron-microscopic studies was up to 1 cm/s. After the completion of dendrite crystallization, no coarsening of the size of particles constituting the film was observed (as compared to the initial state). Figure 2b shows a magnified fragment of the pattern presented in Fig. 2a with the interface between the initial nanocrystalline phase (on the right) producing a diffuse halo on the electron diffraction pattern and the newly formed crystalline phase (on the left). An electron diffraction pattern of this region is given in Fig. 2c. The electron microscope image (Fig. 2b) demonstrates clearly that the film consists of particles of the same size. The electron diffraction pattern (Fig. 2c) obtained from crystallized regions (Figs. 2a, 2b) has a set of reflection points which do not correspond to any known structures of Co–Pd alloys. According to its phase equilibrium diagram, a Co–Pd alloy crystallizes into an fcc lattice with parameter a = 3.75 Å [15].

The electron diffraction pattern (Fig. 2c) clearly demonstrates considerable radial blurring for diffraction reflections at small angles, while groups of reflection points are observed instead of a single reflection at large angles. Such a pattern is not typical of film-type single crystals and indicates that, in this case, the film consists of microcrystallites coherently oriented relative to one another. The diffraction reflections observed on the electron diffraction pattern (Fig. 2c) correspond to the interplanar distances for atomic planes of the (111) and (620) types in the fcc structure with the lattice parameter a = 3.75 Å. Such a set of reflections can be observed on an electron diffraction pattern for the fcc lattice orientation with the [134] zone axis. However, in Fig. 2c, there are two extra reflections of the (111) type, as well as superstructure reflections for an fcc lattice, such as a group of reflections of the (3/2 1/2 0), (310), and (9/2 3/2 0) types. The intensities of these

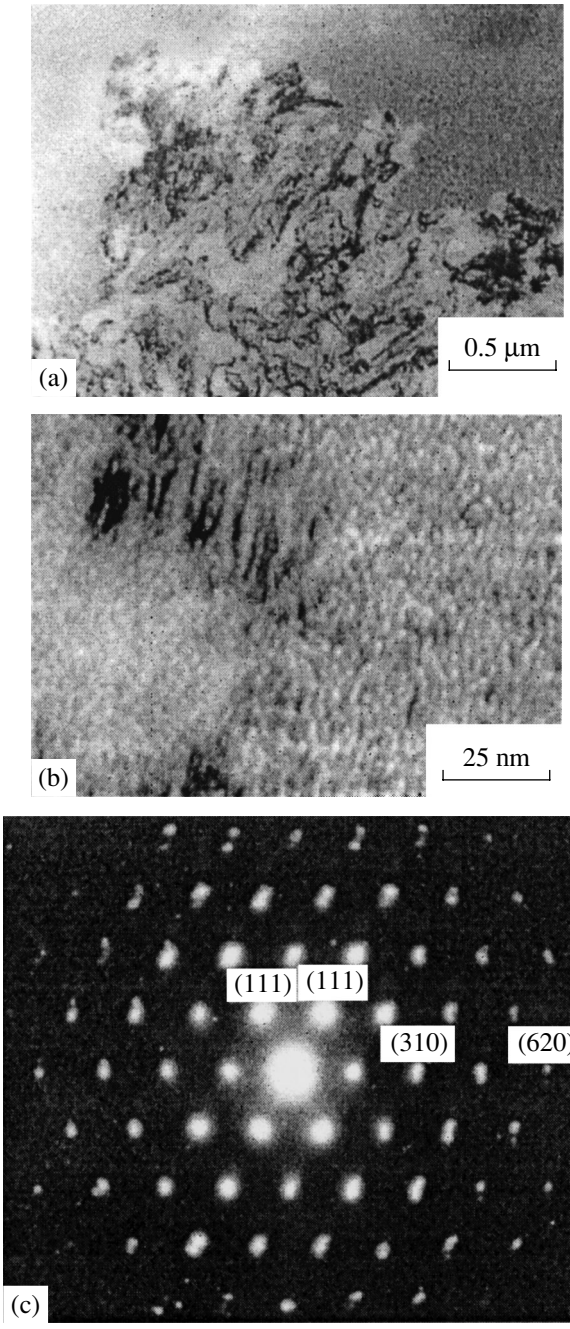

Fig. 2. (a, b) Electron microscope images of the crystallization front in a structurally disordered $Co_{50}Pd_{50}$ film after annealing (T_{ann} = 260°C) with various magnifications and (c) the electron microdiffraction pattern from a crystallized region of the film.

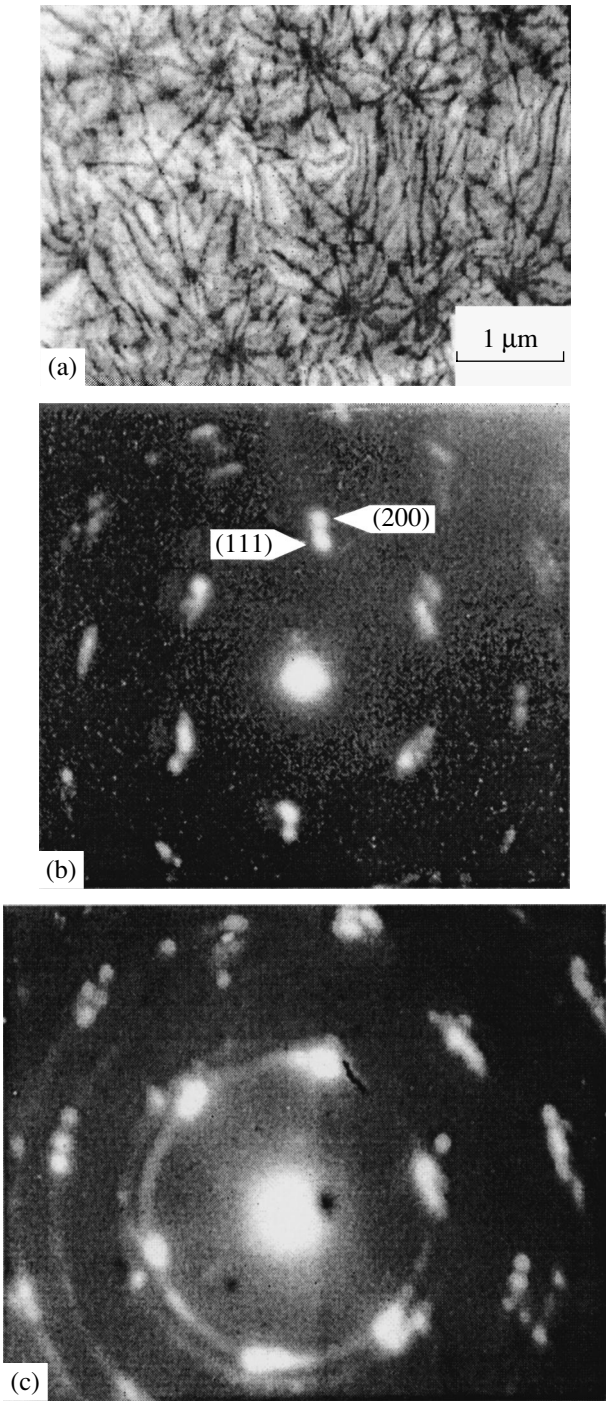

Fig. 3. (a) The electron microscope image with flexural loops and (b, c) electron microdiffraction patterns obtained from various regions of the $Co_{50}Pd_{50}$ film after annealing at T_{ann} = 320°C.

superstructure reflections are much higher than the intensity of a structure reflection of the (620) type. It should be emphasized that on the electron diffraction pattern (Fig. 3a), the angle between vectors of the [111] and [310] types is ≈60°–64°, whereas this angle must be equal to 68.58° in a cubic lattice.

After annealing at T_{ann} > 300°C, the dendrite structure in the films began to disintegrate. An electron microscope image obtained for such a film is a continuous network of intersecting flexural extinction loops (Fig. 3a). An electron diffraction pattern obtained for a disintegrating dendrite is presented in Fig. 3b. This pat-

tern is also not typical. There are groups of reflections corresponding to the atomic (111) and (200) planes of the fcc structure (a = 3.75 Å) according to the interplanar distances. In this case, the [111] and [200] vectors are almost parallel to each other, which is impossible in principle for a single cubic crystal. It should be noted that the electron diffraction pattern presented in Fig. 3b was obtained by the method of microdiffraction from a region ≈0.5 μm in diameter. Such a pattern is typical of the films under study, but a film as a whole is not a single coherently oriented ensemble forming an electron diffraction pattern with regular reflection points. Electron diffraction patterns obtained from other regions of the film can have the form of a disordered set of reflection points. Moreover, for the same sample, there exist regions in which a structure of the type presented in Fig. 3b begins to be rearranged into a polycrystalline fcc structure (Fig. 3c).

Further annealing (T_{ann} = 500°C) leads to the formation of atomically ordered phases typical of Co–Pd alloys [8, 16]: the $L1_0$ phase with a tetragonal face centered lattice and the ε' phase with a hexagonal close-packed (hcp) lattice. A distinguishing feature of all electron diffraction patterns obtained was that diffraction reflections from the $L1_0$ and ε' phases were always observed simultaneously and were oriented coherently with one another [7, 8]. After annealing at $T_{ann} \geq 650$°C, the films displayed only equilibrium polycrystalline fcc structures (a = 3.75 Å).

The PMA constant $K_\perp$ (Fig. 1) increased during annealing to 6×10^6 erg/cm^3 as a result of the formation of the dendrite structure (T_{ann} = 260–300°C) and then decreased to $5 \times (10^5$–$10^4)$ erg/cm^3 upon disintegration of this structure (T_{ann} = 300–500°C). After the formation of the atomically ordered $L1_0$ and ε' phases (T_{ann} = 560°C), the value of $K_\perp$ increased to 10^5 erg/cm^3. Further annealing (T_{ann} = 560°C) led to the formation of a polycrystalline fcc structure and a monotonic decrease in the value of the PMA constant. Our investigations did not reveal any fundamental difference in the atomic structure and magnetic properties for $Co_{50}Pd_{50}$ films obtained by different methods on different substrates.

4. DISCUSSION

As was mentioned above, the electron diffraction patterns obtained from $Co_{50}Pd_{50}$ films after dendrite crystallization did not correspond to any of the known phases of Co–Pd alloys. Attempts to interpret the electron diffraction pattern in Fig. 2c from the viewpoint of densely packed structures proved to be futile. For instance, the electron diffraction pattern from an hcp structure with the $[01\bar{1}1]$ zone axis resembles that in Fig. 2c. However, in order to form such an electron diffraction pattern, an hcp lattice with parameters a = 2.69 Å and c = 5.87 Å would be required. First, such a structure is unknown for Co–Pd alloys and, second, many high-intensity reflections observed on the electron diffraction pattern in Fig. 2c (e.g., $[\bar{1}\bar{1}21]$, $[2\bar{1}\bar{1}1]$) correspond to a superstructure for an hcp lattice. In this case, special attention should be paid to the value of the ratio (c/a) ≈ 2.18. It is well known that metals form close-packed crystalline structures; i.e., the ratio c/a for an hcp lattice in the ideal case must be equal to 1.633. Crystallization in the films under investigation occurs at high rates. For this reason, the electron diffraction pattern depicted in Fig. 2c cannot be attributed to atomic ordering, since the time is obviously insufficient for ordering to occur. A possible explanation of the formation of electron diffraction patterns that are not typical of Co–Pd alloys is the formation of intermetallic compounds. However, this assumption is also groundless since, first, the diffraction reflections corresponding to large interplanar distances that are necessarily observed for intermetallides are absent on the electron diffraction patterns and, second, the formation of intermetallides requires a large amount of impurities, while the concentration of impurities in the films obtained by magnetron sputtering in a vacuum of 10^{-6} Torr does not exceed 1 at. %. The films obtained by the method of thermal sputtering–explosion cannot also contain a large amount of impurities. Attempts to explain the observed electron diffraction patterns using the effect of twinning of known structures did not lead to positive results either. All that has been said above also respectively refers to the electron diffraction pattern presented in Fig. 3b. We considered another possibility for the formation of the electron diffraction pattern in Fig. 3b on the basis of coherent mutual orientation of microcrystallites with different orientations relative to the substrate (i.e., through superposition of the electron diffraction patterns obtained for different orientations). It was found that this electron diffraction pattern cannot be formed in this way.

In order to explain the formation of the atomic order and to interpret the electron diffraction patterns obtained from the films under investigation, we proceeded from the assumptions developed in [11–14]. However, in contrast to those publications, we employed, instead of Voronoĭ polyhedra or Bulienkov crystalline modules, assemblies of modules consisting of octahedra and tetrahedra, which can be used for describing close-packed structures of metals. A common feature between our approach with the Voronoĭ–Delone methods and the Bulienkov method is that the module assemblies fill the space through percolation rather than through translations.

Here, we propose schemes of module assemblies that help to explain the formation of the electron diffraction patterns (Figs. 2c, 3b) obtained from $Co_{50}Pd_{50}$ films. Figures 4a and 4b show module assemblies that help to explain the formation of the electron diffraction patterns in Figs. 2c and 3b. The modules are connected

through common faces, where the atoms are located at the sites. The indices on the vectors in Figs. 4a and 4b denote the serial numbers of such modules. Such assemblies can be repeated in space in various ways, e.g., in the form of a Boerdijk spiral [11, 17] supplemented with octahedra by analogy with the intergrowth rods described in [13]. These assemblies can rearrange themselves from the hcp to the fcc structure. The proposed module assemblies help to explain the possible formation of planar atomic networks in dendritic structures, which create conditions for electron diffraction and the emergence of diffraction reflection points on electron diffraction patterns. Such planar atomic networks with a high local density of atoms are responsible for the emergence of high-intensity superstructure reflections on the electron diffraction patterns. The module assemblies proposed by us also help to explain the formation of nonstandard angles on the electron diffraction patterns. The filling of 3D space with module assemblies occurs through their fitting with one another through common faces. As a result, a fractal (dendrite) structure is formed in which all vectors genetically present in the module assembly are preserved. The structures formed from such assemblies (see Figs. 4a, 4b) can obviously be regarded as quasi-crystalline. In such a structure, atoms are arranged in a quasi-periodic sequence. In spite of the fact that such a structure does not possess translational symmetry, a system of reflection points is formed on the electron diffraction pattern for a certain orientation of this structure [18, 19].

The formation of the electron diffraction pattern presented in Fig. 2c can be explained by a scheme of module assembly consisting of three modules (see Fig. 4a). Each module, in turn, is formed by a tetrahedron and an octahedron. The assembly is organized so that three tetrahedra are connected through common faces. In Fig. 4a, the tetrahedron of the second module is indicated by dashed lines and is behind the plane of the figure. The [111] vectors do not lie in the plane of the figure, and the scheme shows the projections of these vectors. The [310] vectors of the first and third modules have a common point and are almost antiparallel. The disorientation angle amounts to ≈4.5° and is manifested on the electron diffraction pattern in Fig. 2c in the form of a splitting of the (310)-type reflections. The angle formed by the [111] vectors of the first and third modules in the assembly is ≈56°; this angle is observed in the experimental electron diffraction pattern (Fig. 2c).

Figure 4b shows a scheme that enables us to interpret the electron diffraction pattern in Fig. 3b obtained from a dendrite undergoing destruction. The scheme is a system of three fcc modules (denoted by Roman numerals in the figure) supplemented with tetrahedra. The (110) planes of the modules coincide with the plane of the figure. The (111) plane of the tetrahedron at the center of the system also coincides with the plane of the figure. This tetrahedron is connected with each fcc module through another tetrahedron. According to this scheme, the [111] vector of the first module in such

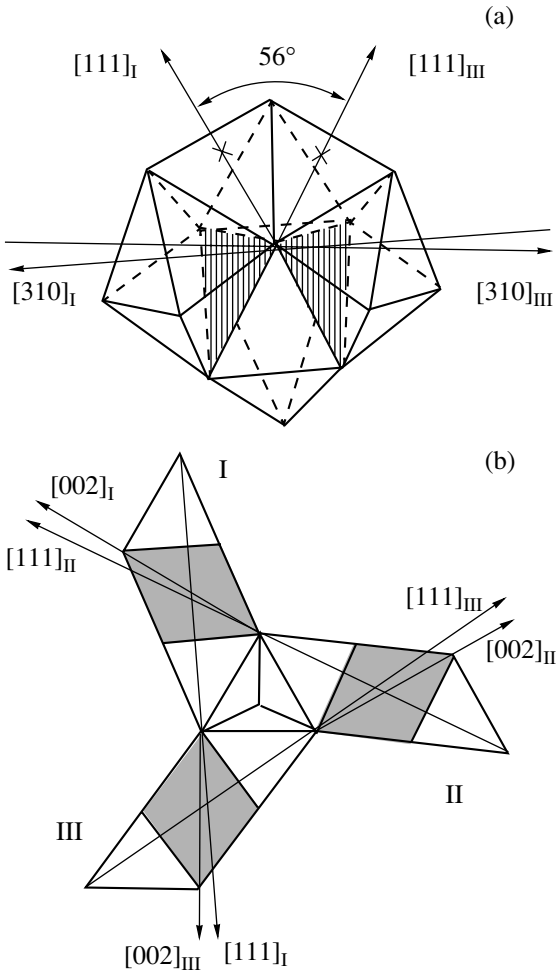

Fig. 4. (a, b) Diagrams of module assemblies explaining the formation of the electron diffraction patterns presented in Figs. 2c and 3b, respectively. The indices correspond to the fcc structure.

a module assembly is almost parallel to the [002] vector of the third module, the mismatching angle between the vectors being ≈5.3°. This explains the disorientation of vectors of the [111] and [200] types that is observed in the electron diffraction pattern in Fig. 3b.

An analysis of the dendrite crystallization rate in our films and of the observed morphological instabilities of the crystallization front and the fact that dendrite crystallization does not result in an increase in the size of particles constituting the film as compared to the initial state lead one to the conclusion that the crystallization in the investigated films is a diffusionless (i.e., kinetic) process. As a rule, such a crystallization is explosive and is accompanied by the formation of a liquid zone (having a size of ~20 Å) at the crystallization front [20]. The velocity of this front is so high that nanoparticles go over to a liquidlike state (so-called virtual melting [21] or quasi-melting [22]). The liquid interlayer ensures the conditions for the fitting of nanoparticles with one another. The morphology of dendrites formed

in this case is determined by the internal structure of nanoparticles. Their structure, in turn, is a result of module self-organization, which is reduced to a combination of module assemblies through common faces. In this case, nonideal filling of space takes place. The mismatching angle between the faces of adjacent module assemblies can be as large as several degrees. As a result, considerable stresses appear in the material. These stresses are partly removed by the displacements of atomic complexes, discontinuities, and cracks. The presence of internal stresses in the films under investigation is confirmed by the observation of tension bars in electron diffraction patterns and flexural loops in electron microscope images (Fig. 3a). Considering that Co–Pd alloys have a high magnetostriction, we can assume that magnetostriction makes a significant contribution to the formation of large values of the PMA constant in the initial state, as well as in the presence of a dendrite structure. The destruction of the dendrite quasi-crystalline structure leads to the formation of atomically ordered highly anisotropic $L1_0$ and ε' phases. The coherent orientation of these phases is ensured by the common elements of the structure (tetrahedra and octahedra). The value of the PMA constant in this case is determined by the crystallographic anisotropy of the $L1_0$ and ε' phases.

Thus, the interpretation of the electron diffraction patterns and the analysis of the peculiarities in the growth of dendrite structures in nanocrystalline $Co_{50}Pd_{50}$ films allowed us to construct a model of the nearest atomic surrounding in $Co_{50}Pd_{50}$ films with a high value of the PMA constant. It is shown that the main contribution to the magnetic anisotropy perpendicular to the film surface comes from the effects associated with the structural organization of crystalline modules.

ACKNOWLEDGMENTS

The authors are grateful to V.N. Matveev for providing the samples obtained using magnetron sputtering, to G.V. Bondarenko for analyzing the chemical composition of the films using the x-ray fluorescence method, and to N.A. Bulienkov, V.A. Petrov, and V.C. Gouliaev for useful discussions and valuable remarks.

This work was supported by the Russian Foundation for Basic Research (project no. 00-02-17358a), and by the Krasnoyarsk Krai Science Foundation.

REFERENCES

1. W. H. Meiklejohn, Proc. IEEE **74** (11), 1570 (1986).
2. H. J. Leamy and A. G. Dirks, J. Appl. Phys. **49** (6), 3430 (1978).
3. H. J. Leamy and A. G. Dirks, J. Appl. Phys. **50** (4), 2871 (1979).
4. T. Suzuki, Jpn. J. Appl. Phys. **23** (5), 585 (1984).
5. L. I. Vershinina-Kveglis, V. S. Zhigalov, A. V. Zhuravlev, and G. I. Frolov, Fiz. Met. Metalloved., No. 4, 62 (1991).
6. A. S. Avilov, L. I. Vershinina-Kveglis, S. V. Orekhov, *et al.*, Izv. Akad. Nauk SSSR, Ser. Fiz. **55** (8), 1609 (1991).
7. L. I. Vershinina-Kveglis, V. A. Petrov, and T. G. Popova, Fiz. Met. Metalloved. **58** (5), 980 (1984).
8. L. I. Vershinina-Kveglis, V. S. Zhigalov, I. V. Staroverova, *et al.*, Fiz. Tverd. Tela (Leningrad) **33** (5), 1409 (1991) [Sov. Phys. Solid State **33**, 793 (1991)].
9. I. Prigogine, *The End of Certainty. Time, Chaos and the New Laws of Nature* (The Free Press, New York, 1997).
10. H. Gleiter, Acta Mater. **48** (1), 1 (2000).
11. N. N. Medvedev, *Voronoĭ–Delone Method in Research of Noncrystalline Systems Structure* (Novosibirsk, 2000).
12. N. A. Bulienkov, Vestn. Nizhegor. Univ., Ser. Fiz. Tverd. Tela **1**, 19 (1998).
13. N. A. Bulienkov and V. S. Kraposhin, Pis'ma Zh. Tekh. Fiz. **19** (23), 1 (1993) [Tech. Phys. Lett. **19**, 739 (1993)].
14. P. V. An and N. A. Bulienkov, Mater. Sci. Res. **6** (1), 22 (2000).
15. R. M. Bozorth, *Ferromagnetism* (Van Nostrand, New York, 1951; Inostrannaya Literatura, Moscow, 1956).
16. V. Matsuo, J. Phys. Soc. Jpn. **32** (4), 972 (1972).
17. A. H. Boerdijk, Philips Res. Rep. **7**, 303 (1952).
18. D. Levine and P. J. Steinhardt, Phys. Rev. Lett. **53** (26), 2477 (1984).
19. G. M. Zaslavskiĭ, R. Z. Sagdeev, D. A. Usikov, and A. A. Chernikov, Usp. Fiz. Nauk **156** (2), 193 (1988) [Sov. Phys. Usp. **31**, 887 (1988)].
20. V. A. Shklovskiĭ and V. M. Kuz'menko, Usp. Fiz. Nauk **157** (2), 311 (1989) [Sov. Phys. Usp. **32**, 163 (1989)].
21. V. S. Ivanova, A. S. Balankin, I. Zh. Bunin, and A. A. Oksogoev, *Synergetics and Fractals in Material Science* (Nauka, Moscow, 1994).
22. P. M. Ajayan and L. D. Marks, Phys. Rev. Lett. **63** (3), 279 (1989).

Translated by N. Wadhwa

Physics of the Solid State, Vol. 43, No. 8, 2001, pp. 1549–1551. Translated from Fizika Tverdogo Tela, Vol. 43, No. 8, 2001, pp. 1488–1490.

MAGNETISM AND FERROELECTRICITY

Anisotropy of Optical Absorption of α-MnS Single Crystal

I. S. Edelman, O. B. Romanova, L. I. Ryabinkina, G. M. Abramova, and V. V. Markov

Kirensky Institute of Physics, Siberian Division, Russian Academy of Sciences, Akademgorodok, Krasnoyarsk, 660036 Russia

e-mail: ise@iph.krasnoyarsk.su

Received August 29, 2000; in final form, December 18, 2000

Abstract—The optical absorption spectra of an α-MnS single crystal and their temperature behavior in the range from 86 to 300 K are investigated for the (100) plane in the energy range from 8×10^3 to 22×10^3 cm^{-1} for the first time. Comparison of these spectra with those for the (111) plane reveals an essential absorption anisotropy in unpolarized light. The anisotropy is manifested in a much stronger splitting of the lowest energy band for the (100) plane in comparison with that for the (111) plane. With decreasing temperature, the splitting becomes smaller. Possible mechanisms for the anisotropy revealed are proposed. © *2001 MAIK "Nauka/Interperiodica".*

The discovery of colossal magnetoresistance in $Fe_xMn_{1-x}S$ solid solutions [1] revived interest in investigating the physical properties of manganese monosulfide, which is the base component of these substances. An α-MnS single crystal possesses an NaCl-type face-centered cubic lattice which undergoes a rhombohedral distortion along the cube diagonal in the (111) plane with decreasing temperature. The structural transition in α-MnS is observed at $T_s = 162 \pm 2$ K [2]; the antiferromagnet–paramagnet phase transition occurs at $T_N = 150$ K [3]. In the paramagnetic phase, the α-MnS monosulfide is a *p*-type semiconductor with a conductivity activation energy $E_a = 0.3$ eV. A sharp change in the activation energy is observed in the antiferromagnetic region: E_a is virtually zero at $T < 150$ K, and the resistivity ρ is 10^8 Ω cm [3, 4]. Optical measurements have been carried out for an α-MnS single crystal in the (111) plane [2, 5]. Three absorption peaks associated with single-ion transitions in Mn^{2+} were revealed, and a blue shift of the fundamental absorption edge was observed with decreasing temperature.

The absorption spectra of an α-MnS single crystal produced by saturation of liquid manganese with sulfur were investigated in this work.

Two α-MnS single-crystal plates parallel to the (111) and (100) planes were produced for optical measurements. The plates were about 40 μm thick, and their area was about 2 × 2 mm. Measurements were conducted in a gas-flow quartz cryostat at temperatures from 86 to 300 K with an accuracy of ±1 K within the energy range 8×10^3–22×10^3 cm^{-1}.

Figure 1 shows the optical absorption spectra obtained for the (111) and (100) planes of the α-MnS single crystal at room temperature. Figure 2 shows the spectra for these planes at three different temperatures. An essential difference between these spectra can be seen in Fig. 2. The spectra for the (111) plane (curve *1* in Fig. 1; Fig. 2a) are, in general, identical to those obtained in [2, 5]. Two maxima corresponding to the electron transitions of the Mn^{2+} ions are observed: the *A* peak ($^6A_{1g} \longrightarrow {}^4T_{1g}(^4G)$) and *B* peak ($^6A_{1g} \longrightarrow {}^4T_{2g}(^4G)$). A third maximum, *C* ($^6A_{1g} \longrightarrow {}^4A_{1g}, {}^4E_g(^4G)$), was also observed in [2]; we could record only its long-wavelength edge. Probably, this is because our samples were thicker than those used in [2, 5]. For the same reason, we could not reveal the fundamental absorption edge either.

The shape of the spectrum does not change with a decrease in temperature, the energy of peak *A* (*E* =

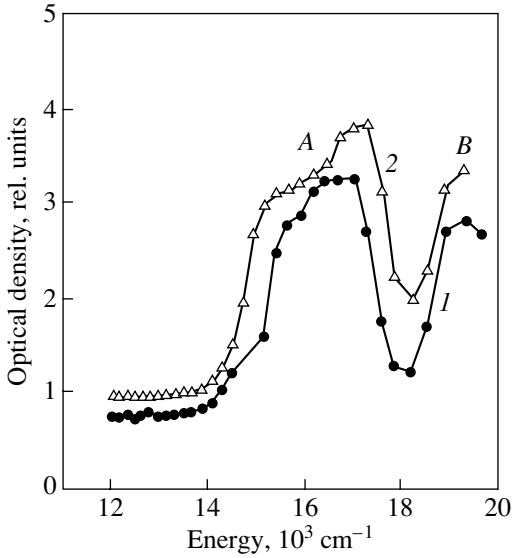

Fig. 1. Optical density $D = \ln(I_0/I)$ for an α-MnS single crystal at $T = 300$ K (I_0 and I are the intensities of incident and transmitted light, respectively). The light beam is perpendicular to (*1*) the (111) plane and (*2*) the (100) plane.

1063-7834/01/4308-1549$21.00 © 2001 MAIK "Nauka/Interperiodica"

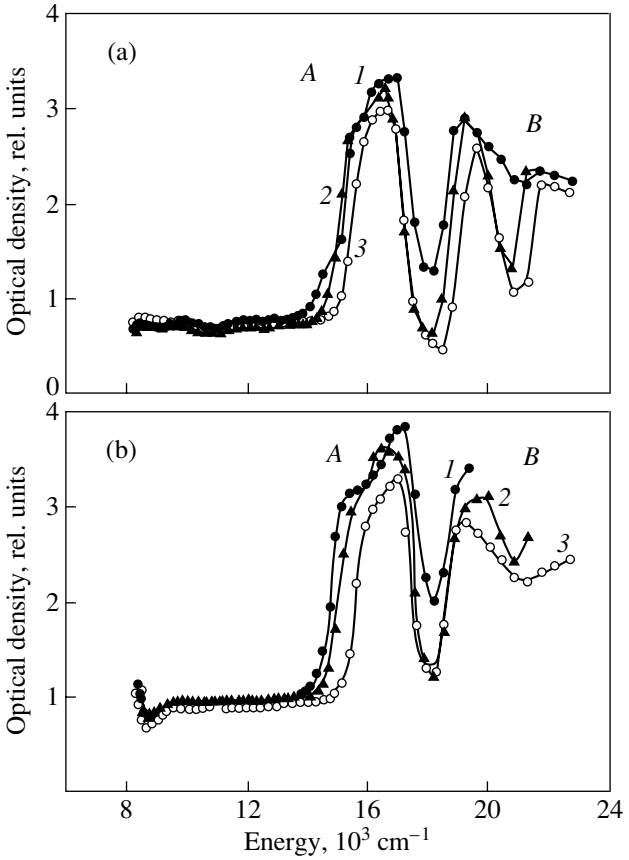

Fig. 2. Spectra of the optical density of an α-MnS single crystal at (*1*) 300, (*2*) 160, and (*3*) 86 K. The light beam is perpendicular to (a) the (111) plane and (b) the (100) plane.

16667 cm^{-1}) changes only insignificantly, and the energy of peak *B* (E = 19608 cm^{-1} at T = 300 K) increases slightly. The intensity of both peaks decreases.

Figures 1 (curve 2) and 2b show the absorption spectra for the (100) plane. Optical investigations have not yet been carried out for this plane. A wide band is observed at energies from 14×10^3 to 18×10^3 cm^{-1}; it is split into at least two components. It should be noted that negligible splitting of band *A* is also observed for the (111) plane. With decreasing temperature, the split components become closer to each other. In this case, the low-energy component undergoes a substantially larger shift to the high-energy side. The amplitudes and widths of both components decrease. At the minimum temperature used, band *A* remains appreciably asymmetric for the (100) plane, while for the (111) plane, the band asymmetry almost vanishes. At low temperatures, the spectral position of band *A* for the (100) plane corresponds to the position of band *A* for the (111) plane. For this reason, the high-energy component of the band can be attributed to the transition ${}^6A_{1g} \longrightarrow {}^4T_{1g}({}^4G)$ in the Mn^{2+} ion. The low-energy component, which undergoes a shift to higher energies with a decrease in temperature, can be associated either with the splitting of the ${}^6A_{1g} \longrightarrow {}^4T_{1g}({}^4G)$ band or with electron excitations of another nature.

In the energy range (18–20) $\times 10^3$ cm^{-1}, the band corresponding to band *B* in the spectrum for the (111) plane does not appear at room temperature. (In this energy range, the sensitivity of the photodetector decreases in comparison with the energy of approximately 16×10^3 cm^{-1}, where band *A* is observed.) Band *B* is observed beginning from $T \approx 160$ K. For the (100) plane, the intensity of the absorption bands is noticeably larger than for the (111) plane. In the window region near 18×10^3 cm^{-1}, the absorption is significantly larger for the (100) plane. Perhaps, due to these two circumstances, there is a difference between the colors of the crystals cut from the same block along different planes. In contrast to the green color typical to the (111) plane of the α-MnS crystal, the α-MnS single crystal cut in the (100) plane looks yellow. The energy of peak *B* observed for the (100) plane corresponds to the energy of peak *B* in the spectrum for the (111) plane only at low temperatures.

Thus, anisotropy of the optical absorption in unpolarized light is observed in the α-MnS single crystal. The difference in the splitting of the low-energy absorption band and in the intensities of the bands for the (100) and (111) planes are the most striking manifestations of this anisotropy.

The anisotropy revealed and the splitting of the low-energy band can be explained in a different manner. The splitting can be associated with the dynamic Jahn–Teller effect [6–8]. On the other hand, the formation of a magnetic polaron due to the exchange interaction between the charge carriers and electrons of the *d* shell of the Mn^{2+} ion (*c–l* exchange) [9] can be supposed; this exchange is observed in $Cd_xMn_{1-x}Te$ [10, 11]. At $T = 0$, according to [9], the spin-polaron state coincides with the band state, while at finite temperatures, they become essentially different. With increasing temperature, the spin-polaron band shifts to the high-energy side; the shift in the paramagnetic state can be as large as 60% of the shift in the magnetically ordered state and can be equal to ~0.1 eV [9]. To explain the anisotropy itself, it is necessary to take into account the characteristic features of the band structure of the crystal and its change at phase transitions. Additional measurements are being carried out to interpret the anomalies more clearly.

ACKNOWLEDGMENTS

This work was supported in part by the Russian Foundation for Basic Research, project no. 00-02-81059 Bel. 2000a.

REFERENCES

1. G. A. Petrakovskiĭ, L. I. Ryabinkina, G. M. Abramova, *et al.*, Pis'ma Zh. Éksp. Teor. Fiz. **69** (12), 895 (1999) [JETP Lett. **69**, 949 (1999)].
2. A. V. Malakhovskiĭ, T. P. Morozova, V. N. Zabluda, and L. I. Ryabinkina, Fiz. Tverd. Tela (Leningrad) **32** (4), 1012 (1990) [Sov. Phys. Solid State **32**, 596 (1990)].
3. L. I. Ryabinkina and G. V. Loseva, Phys. Status Solidi A **80**, K179 (1983).
4. H. H. Heikens, C. F. van Bruggen, and C. J. Haas, J. Phys. Chem. Solids **39** (8), 833 (1978).
5. D. R. Huffman and R. L. Wild, Phys. Rev. **156** (3), 989 (1967).
6. I. B. Bersuker, *Electron Structure and Properties of Coordination Compounds* (Khimiya, Leningrad, 1976).
7. M. D. Sturge, Solid State Phys. **20**, 92 (1967).
8. T. E. Freeman and G. D. Jones, Phys. Rev. **182** (2), 411 (1969).
9. É. L. Nagaev, *Physics of Magnetic Semiconductors* (Nauka, Moscow, 1979).
10. I. A. Merkulov, Fiz. Tverd. Tela (St. Petersburg) **42** (1), 126 (2000) [Phys. Solid State **42**, 132 (2000)].
11. D. R. Yakovlev and K. V. Kavokin, Comments Condens. Matter Phys. **18** (2), 51 (1996).

Translated by A. Pushnov

Physics of the Solid State, Vol. 43, No. 8, 2001, pp. 1552–1555. Translated from Fizika Tverdogo Tela, Vol. 43, No. 8, 2001, pp. 1491–1495.

MAGNETISM AND FERROELECTRICITY

The Ground State of a Strongly Correlated Fermion System in a Magnetic Field

Yu. B. Kudasov

All-Russian Research Institute of Experimental Physics, Sarov, Nizhni Novgorod oblast, 607180 Russia

e-mail: kudasov@ntc.vniief.ru

Received December 28, 2000

Abstract—A new variational method is used to investigate the ground state of the Hubbard model with a half-filled band for a one-dimensional chain, a planar square lattice, and a simple cubic lattice. A metamagnetic transition is found to occur in a one-dimensional chain and a simple square lattice. A simple cubic lattice does not undergo the metamagnetic transition. © *2001 MAIK "Nauka/Interperiodica".*

1. In [1, 2], a new variational method was developed for calculating the ground-state energy of a strongly correlated fermion system. This method allows one to take into account the well-defined short-range order in the metallic phase. The paramagnetic and antiferromagnetic phases of the Hubbard model with a half-filled band have been investigated using this method, and it was found that, in the case where the interaction in the system has an intermediate strength (the Coulomb energy is of the order of the band width), the short-range order significantly affects the ground-state energy of the system. Recently, many papers have been published on the experimental study of the short-range order in strongly correlated systems (see, e.g., [3]); among them are systems placed in a strong magnetic field [4, 5]. Therefore, it is of interest to generalize the results of [1, 2] to the case of systems in magnetic fields.

In this paper, a variational technique is used to calculate the ground-state energy for the Hubbard model with the Hamiltonian

$$H = t\sum_{\langle ij\rangle,\sigma}(a^+_{i\sigma}a_{j\sigma} + \text{H.c.}) + U\sum_i n_{i\uparrow}n_{i\downarrow} - mh, \quad (1)$$

where $a^+_{i\sigma}$ and $a_{i\sigma}$ are the creation and annihilation operators, respectively, for a fermion of spin $\sigma = \uparrow, \downarrow$ at the site i; $\langle ij\rangle$ indicates summation only over nearest neighbors; $n_{i\sigma} = a^+_{i\sigma}a_{i\sigma}$; $m = \langle n_{i\uparrow}\rangle - \langle n_{i\downarrow}\rangle$ is the magnetic moment; t is the charge-transfer energy; U is the correlation energy; and h is the magnetic field. The energy band is assumed to be half-filled; i.e., $\langle n_{i\uparrow}\rangle + \langle n_{i\downarrow}\rangle = 1$. Calculations are carried out for a one-dimensional (1D) chain, a planar (2D) square lattice, and a simple cubic 3D lattice.

2. In [1], it was shown that, in order for short-range correlations to be taken into account, the Gutzwiller trial function [6, 7] should be generalized to the form

$$|\psi\rangle = \prod_\lambda g_\lambda^{P_\lambda}|\varphi_0\rangle, \quad (2)$$

where the product includes the Gutzwiller factor and, in addition, a set of projection operators P_λ for all possible configurations of a lattice site and its two nearest neighbor sites. The real parameters g_i lie in the range $[0, \infty)$ and enable one to vary the amplitudes of different configurations of the pair of neighbor sites and, therefore, to change the short-range order. The initial N-particle wave function $|\varphi_0\rangle$ describes noncorrelated electrons and, for example, for electrons whose states are confined by the Fermi surface, has the form

$$\prod_{\mathbf{k}<V_{F\uparrow}} a^+_{\mathbf{k}\uparrow}\prod_{\mathbf{k}<V_{F\downarrow}} a^+_{\mathbf{k}\downarrow}|0\rangle, \quad (3)$$

where $\mathbf{k}$ is the wave vector of a fermion and $V_{F\sigma}$ is the volume of the region (in momentum space) bounded by the Fermi surface of fermions of spin σ.

We will construct a trial function for the paramagnetic phase of the half-filled band with an arbitrary total angular momentum. There are four projection operators that separate the different states of a lattice site. Our interest is in the projection operators for doubly occupied states:

$$\hat{X} = \sum_i n_{i\uparrow}n_{i\downarrow}.$$

In addition, there are ten projection operators for the states of the nearest neighbor pairs, for example,

$$\hat{Y}_1 = \sum_{\langle ij\rangle}(1-n_{i\uparrow})(1-n_{i\downarrow})(1-n_{j\uparrow})(1-n_{j\downarrow}),$$
$$\hat{Y}_2 = \sum_{\langle ij\rangle} n_{i\uparrow}n_{i\downarrow}n_{j\uparrow}n_{j\downarrow} \quad (4)$$

1063-7834/01/4308-1552$21.00

(see table). In comparison with the case of zero total angular momentum [1, 2], the degeneracy of the operators $\hat{Y}_\lambda$ is partially lifted.

We will consider the case of lattices in which the total number of pairs of nearest neighbor sites is $zL/2$, where z is the number of nearest neighbors of a site and L is the total number of lattice sites. The normalized eigenvalues of operators (3) and (4) are defined by

$$\begin{aligned} x|\Phi\rangle &= L^{-1}\hat{X}|\Phi\rangle, \\ y_\lambda|\Phi\rangle &= (zL/2)^{-1}\hat{Y}_\lambda|\Phi\rangle. \end{aligned} \tag{5}$$

The eigenvalues are subject to the normalization conditions [8]

$$\sum_\lambda x_\lambda = 1, \quad \sum_\lambda \beta_\lambda y_\lambda = 1, \tag{6}$$

where β_λ is the degeneracy, and to the self-consistency conditions [8]

$$\begin{aligned} y_1 + y_3 + y_4 + y_5 &= x, \\ y_2 + y_3 + y_8 + y_9 &= x, \\ y_4 + y_6 + y_7 + y_8 &= 1/2 + m/2 - x, \\ y_5 + y_7 + y_9 + y_{10} &= 1/2 - m/2 - x. \end{aligned} \tag{7}$$

The half-filled band has electron–hole symmetry, which leads to the additional conditions

$$y_1 = y_2, \quad y_4 = y_5, \quad y_8 = y_9. \tag{8}$$

We take m, x, y_3, y_4, y_5, and y_7 as independent parameters; the other parameters are expressed through them as

$$\begin{aligned} y_2 &= x - y_3 - y_4 - y_5, \\ y_6 &= 1/2 + m/2 - x - y_7 - 2y_4, \\ y_{10} &= 1/2 - m/2 - x - y_7 - 2y_5. \end{aligned} \tag{9}$$

With allowance for the degeneracy, the trial function can be taken in the form

$$|\psi(m)\rangle = g_0^{\hat{X}} g_3^{\beta_3\hat{Y}_3} g_4^{4\beta_4\hat{Y}_4} g_5^{2\beta_5\hat{Y}_5} g_7^{\beta_7\hat{Y}_7}|\varphi_0(m)\rangle. \tag{10}$$

It should be noted that all configurations involved in the configuration expansion of the initial wave function have the same total spin. Therefore, the operator in the right-hand side of Eq. (10) does not change the magnetic moment; that is, the initial wave function and the trial wave function have the same magnetic moment.

3. We calculate the norm of the trial wave function. This norm can be written as

$$\begin{aligned} \langle\psi|\psi\rangle &= A(m) \sum_{\{x, y_3, y_4, y_5, y_7\}} W_{\{x, y_3, y_4, y_5, y_7, m\}} \\ &\times g_0^{2Lx} g_3^{2zLy_3} g_4^{4zLy_4} g_5^{4zLy_5} g_7^{2zLy_7} \\ &= A(m) \sum_{\{x, y_3, y_4, y_5, y_7\}} R_{\{x, y_3, y_4, y_5, y_7, m\}}. \end{aligned} \tag{11}$$

Projection operators for different states of a pair of lattice sites and the configurations corresponding to them

Operator	Configuration		Degeneracy
	site	site	
$\hat{Y}_1$			1
$\hat{Y}_2$	↑↓	↑↓	1
$\hat{Y}_3$	↑↓		2
$\hat{Y}_4$	↑		2
$\hat{Y}_5$	↓		2
$\hat{Y}_6$	↑	↑	1
$\hat{Y}_7$	↑	↓	2
$\hat{Y}_8$	↑↓	↑	2
$\hat{Y}_9$	↑↓	↓	2
$\hat{Y}_{10}$	↓	↓	1

The summation in Eq. (11) is performed over all sets $\{x, y_3, y_4, y_5, y_7\}$. The coefficient $W_{\{x, y_3, y_4, y_5, y_7, m\}}$ is the number of configurations that correspond to the set $\{x, y_3, y_4, y_5, y_7\}$ for a given value of m. The normalization factor $A(m)$ depends on the total spin. This factor need not be calculated separately, because it will be automatically taken into account in the normalized density matrix. The norm in Eq. (11) can be calculated only approximately if there are closed paths in the lattice. For this purpose, as in [2], we employ the Kikuchi pseudoensemble method [9]. In the limiting case of an infinite number of particles ($L \longrightarrow \infty$), as usual [1, 2, 7], one can keep only the largest terms in the series in Eq. (11). In order to find the maximum of the function R, it is convenient to calculate the maximum of its logarithm. For this purpose, the factorials involved in R are transformed using Stirling's approximation and only the leading terms are kept in the logarithm of the expression thus obtained. The result is

$$\begin{aligned} L^{-1}\ln W &= (z-1)[2x\ln x + (1/2 + m/2 - x) \\ &\times \ln(1/2 + m/2 - x) + (1/2 - m/2 - x) \\ &\times \ln(1/2 - m/2 - x)] - \frac{z}{2}(2y_2\ln y_2 \\ &+ 2y_3\ln y_3 + 4y_4\ln y_4 + 4y_5\ln y_5 \\ &+ y_6\ln y_6 + 2y_7\ln y_7 + y_{10}\ln y_{10}). \end{aligned} \tag{12}$$

Here and henceforth, we use the notation y_2, y_6, and y_{10} for the corresponding expressions in Eq. (9). The necessary conditions for expression (12) to be maximum are the equations [1, 2] $\partial(\ln R)/\partial\eta_\lambda = 0$, where $\eta_\lambda = x$,

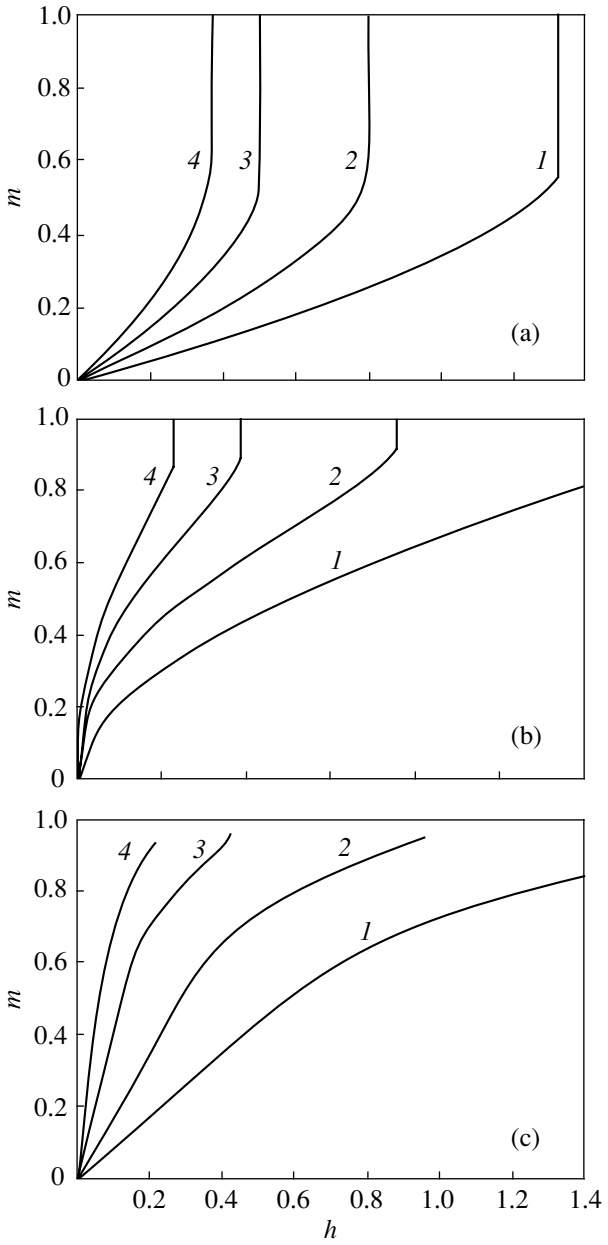

Fig. 1. Magnetic moment as a function of the magnetic field for different values of the correlation energy $I = U/8\varepsilon_0(0)$: I = (*1*) 0.4, (*2*) 0.6, (*3*) 0.8, and (*4*) 1; (a) a 1D chain, (b) a planar square lattice, and (c) a simple cubic lattice.

y_3, y_4, y_5, y_7. Using these equations, g_λ can be expressed through x and y_λ, which gives

$$g_0 = \left(\frac{(1/2 + m/2 - x)(1/2 - m/2 - x)}{x^2}\right)^{(z-1)/2}\left(\frac{y_2^2}{y_6 y_{10}}\right)^{z/4},$$

$$g_3 = \sqrt{\frac{y_3}{y_2}}, \quad g_4 = \sqrt{\frac{y_4}{\sqrt{y_6 y_2}}}, \tag{13}$$

$$g_5 = \sqrt{\frac{y_5}{\sqrt{y_{10} y_2}}}, \quad g_7 = \sqrt{\frac{y_7}{\sqrt{y_6 y_{10}}}}.$$

In order to find the ground-state energy for Hamiltonian (1), one should calculate the first-order density matrix ρ for the state described by the trial function:

$$\rho = L^{-1}\frac{\langle\psi|\sum_{\langle ij\rangle,\sigma}(a^+_{i\sigma}a_{j\sigma} + \text{H.c.})|\psi\rangle}{\langle\psi|\psi\rangle}. \tag{14}$$

A technique for calculating the density matrix is detailed in [2]: ρ can be separated into two parts, $\rho = \rho_{band} + \rho_{inter}$, where the first term describes the motion of the fermion in the Hubbard subbands and the second term is responsible for transitions between the subbands. Calculations give

$$\rho_{band} = 4y_4\left[\frac{L_1^2}{x(1/2 + m/2 - x)}\right]^{z-1} + 4y_5\left[\frac{L_2^2}{x(1/2 - m/2 - x)}\right]^{z-1}, \tag{15}$$

$$\rho_{inter} = 8\sqrt{y_3 y_7}\left(\frac{L_1 L_2}{x\sqrt{(1/2 + m/2 - x)(1/2 - m/2 - x)}}\right),$$

where

$$L_1 = \sqrt{y_2 y_4} + \sqrt{y_3 y_4} + \sqrt{y_4 y_6} + \sqrt{y_5 y_7},$$
$$L_2 = \sqrt{y_2 y_5} + \sqrt{y_3 y_5} + \sqrt{y_4 y_7} + \sqrt{y_5 y_{10}}.$$

The total energy of the system of correlated fermions can be represented in the same form as in [6]:

$$E = \frac{1}{L}\frac{\langle\psi|H|\psi\rangle}{\langle\psi|\psi\rangle} = q(m)\varepsilon_0(m) + xU. \tag{16}$$

Here, $q = \rho(m)/\rho_0(m)$, where $\rho_0(m)$ is the density matrix of noncorrelated fermions ($U = 0$) of a given spin and $\varepsilon_0(m)$ is the spin-dependent average energy of noncorrelated fermions. It is easy to verify that this normalization gives the correct value for the total energy of the system of an arbitrary spin in the case of $U = 0$; therefore, the normalization factor in Eq. (11) is automatically taken into account.

4. We calculated the ground-state energy of the paramagnetic phase for the following three systems: (a) a linear homogeneous chain ($z = 2$) with a dispersion law $\varepsilon_{\mathbf{k}} = -2\cos k_x$, (b) a planar square lattice ($z = 4$) with $\varepsilon_{\mathbf{k}} = -2[\cos k_x + \cos k_y]$, and (c) a simple cubic lattice ($z = 6$) with $\varepsilon_{\mathbf{k}} = -2[\cos k_x + \cos k_y + \cos k_z]$. The average energy of a fermion (per site) in the absence of correlation is defined as

$$\varepsilon_0(m) = \frac{1}{V_{BZ}}\int_{BZ}\varepsilon_{\mathbf{k}\sigma}\theta(\varepsilon_{F,\sigma} - \varepsilon_{\mathbf{k}\sigma})d\mathbf{k}, \tag{17}$$

where $\varepsilon_{F,\sigma} = -\varepsilon_{F-\sigma}$, the integration is performed over the Brillouin zone (BZ), V_{BZ} is the BZ volume, and $\theta(x) = 0$ for $x < 0$ and $\theta(x) = 1$ for $x > 0$. The energies of

fermions differing in spin are equal because the band is half-filled.

The ground-state energy is calculated by minimizing the total energy of the fermion system with respect to the variables m, x, y_3, y_4, y_5, and y_7. Figure 1 shows the dependence of the magnetic moment on the magnetic field. For a planar square lattice, problems arise when minimization is performed in a narrow range near $m = 0$. In this range, the energy of the fermion system virtually does not depend on the magnetic moment. From Fig. 1b, it can be seen that the magnetic susceptibility becomes high. This behavior is associated with a van Hove singularity located at the center of the energy spectrum of the square lattice. The density of states diverges logarithmically at this point [10]; that is, the magnetic susceptibility tends to infinity. The singularity becomes even slightly stronger in the presence of correlations (Fig. 1b). If the energy spectrum is approximated by the elliptic Hubbard band [7], which has no singular points, problems with minimization do not arise. We also investigated the case of an infinite-dimensional lattice. For this purpose, we calculated the ground-state energy of lattices with $z = 10$, 20, and 40 and with the energy spectrum of a $z/2$-dimensional hypercubic lattice taken as the initial spectrum. The result rapidly converges to the Gutzwiller solution [7] with increasing z, which is due to the weakening of spatial correlations with increasing lattice dimensions.

In the calculations discussed above, we ignored the splitting of the fermion spectrum into Landau levels. The results obtained for the case of large values of U (as large as the band width and greater) are of most interest. In this case, the effective masses of carriers are large (they are proportional to $\propto q^{-1}$) and the splitting of the spectrum into Landau levels ($\Delta\varepsilon \propto q$) is negligible. In principle, the splitting can be taken into account through the function $\varepsilon_0(m)$.

From Fig. 1, it can be seen that the metamagnetic transition occurs at large U for a 1D chain and a planar square lattice. In the case of a simple cubic lattice, the metamagnetic transition does not occur up to $I = 1$. Thus, the energy spectrum and the lattice dimensionality determine the occurrence of the metamagnetic transition in a strongly correlated system and, therefore, the conclusion regarding this transition inferred for an infinite lattice [6] does not necessarily hold for real lattices.

ACKNOWLEDGMENTS

The author is grateful to Prof. J. Brooks and to V. Levis for their encouragement.

This work was supported by the International Scientific and Technical Center, project no. 829.

REFERENCES

1. Yu. B. Kudasov, Phys. Lett. A **245**, 153 (1998).
2. Yu. B. Kudasov, Zh. Éksp. Teor. Fiz. **117** (3), 624 (2000) [JETP **90**, 544 (2000)].
3. W. Bao, C. Broholm, G. Aeppli, *et al.*, J. Magn. Magn. Mater. **177–181**, 283 (1998).
4. Yu. B. Kudasov, A. G. Volkov, A. A. Povzner, *et al.*, Zh. Éksp. Teor. Fiz. **116** (11), 1770 (1999) [JETP **89**, 960 (1999)].
5. G. Aeppli, E. Bucher, and T. E. Mason, in *Physical Phenomena at High Magnetic Fields*, Ed. by E. Manousakis *et al.* (Addison–Wesley, Redwood City, 1992), p. 175.
6. M. C. Gutzwiller, Phys. Rev. **137** (6A), 1726 (1965).
7. D. Vollhardt, Rev. Mod. Phys. **56** (1), 99 (1984).
8. J. M. Ziman, *Models of Disorder: the Theoretical Physics of Homogeneously Disordered Systems* (Cambridge Univ. Press, Cambridge, 1979; Mir, Moscow, 1982).
9. R. Kikuchi and S. G. Brush, J. Chem. Phys. **47**, 195 (1967).
10. P. Fazekas, *Lecture Notes on Electron Correlation and Magnetism* (World Scientific, Singapore, 1999).

Translated by Yu. Epifanov

Physics of the Solid State, Vol. 43, No. 8, 2001, pp. 1556–1562. Translated from Fizika Tverdogo Tela, Vol. 43, No. 8, 2001, pp. 1496–1502.

MAGNETISM AND FERROELECTRICITY

Distortion of a Matrix Structure and the Cluster Formation in $Mn_xZn_yFe_zO_4$ Ferrite Single Crystals

Z. A. Samoĭlenko, V. P. Pashchenko, V. S. Abramov, and N. N. Ivakhnenko

Donetsk Physicotechnical Institute, National Academy of Sciences of Ukraine, Donetsk, 83114 Ukraine

Received January 15, 2001

Abstract—The evolution of the hard and soft modes in the crystal structure of $Mn_xZn_yFe_zO_4$ manganese–zinc spinel ferrites is investigated theoretically and experimentally (x-ray structure analysis and magnetic measurements). It is shown that tetragonal and rhombohedral distortions of the cubic structure and fluctuations of the soft mode are accompanied by the formation of clusters in the form of quasi-two-dimensional fragments (50–200 and 400–1200 Å), which involve families of γ-Mn_2O_3, γ-Mn_3O_4, and α-Fe_2O_3 oxide planes inherently bound to the spinel matrix. © *2001 MAIK "Nauka/Interperiodica".*

1. INTRODUCTION

Manganese–zinc ferrites are extensively used in electronic technology [1]. They find application in color TV sets as transformer cores and in magnetic video tape recorder heads. A distinguishing feature of these ferrites is that they contain several types of cations which occupy different crystallographic positions and have a variable valence (Mn_A^{2+}, Mn_B^{3+}, $Fe_{A,B}^{3+}$, and Fe_B^{2+}) [2]. Changes in the valence of cations and their crystallographic positions in tetrahedral (A) and octahedral (B) sites of a spinel structure favor deviation from stoichiometry and the defect formation. This can give rise to localized and delocalized distortions and bring about distortions of the long-range order in multicomponent solid solutions [3]. In our earlier works [4, 5], we showed that these distortions are predominantly concentrated in high-index planes in a crystal, extend over regions containing from tens to hundreds of unit cells, and manifest themselves as large-scale fluctuations of the order parameter [6]. In order to predict the properties of these materials, it is necessary to elucidate the physical nature and regularities of the evolution of their atomic structure due to partial disordering and the related rearrangement (cluster formation) of solid solution components and to gain a better insight into the influence of this complex structure on the magnetic characteristics of compounds.

The majority of experimental investigations into structural disordering of this type have dealt with polycrystalline objects. In this respect, of special interest is the study of single-crystal samples. In the present work, the weakly distorted matrix and strongly distorted cluster structures of manganese–zinc ferrite single crystals were investigated by diffuse x-ray scattering for the first time.

2. EXPERIMENTAL TECHNIQUE

In the experiments, we used the photomethod (long-wavelength CrK_α radiation, V filter), which is sensitive in the recording of low-intensity x-ray scattering. With the aim of providing identical conditions for diffraction and recording of radiation scattered from different crystallographic planes, single-crystal samples were reduced to powder. The ferrites to be studied differed in the concentration ratio of chemical elements forming the cation sublattice in the spinel structure.

The molar formulas for real structures of manganese–zinc ferrites were calculated with due regard for the crystallographic features of spinel ferrites, specified cation ratios, electroneutrality condition, nonstoichiometry, and differences between x-ray and hydrostatic densities of the samples under investigation. The physical properties, including the electromagnetic parameters characterizing the quality of these manganese–zinc ferrites, were determined according to the universally accepted techniques [7, 8].

The compositions, real structures, x-ray and hydrostatic densities ρ, and lattice parameters *a* are given in Table 1. The lattice defectiveness (the presence of vacancies in cationic ($V^{(c)}$) and anionic ($V^{(a)}$) sublattices of manganese–zinc ferrites) was evaluated from a comparison between the x-ray and hydrostatic densities. The Mn^{3+} content was obtained from the ^{55}Mn NMR data [9]. The Fe^{2+} content was determined with due regard for the concentration of anion vacancies $V^{(a)}$ and the electron exchange $Mn^{2+} + Fe^{3+} \longleftrightarrow Mn^{3+} + Fe^{2+}$.

The mesoscopic defectiveness of the crystal structure was evaluated by examining the features of x-ray scattering from samples with different crystal chemical structures (Table 1).

1063-7834/01/4308-1556$21.00 © 2001 MAIK "Nauka/Interperiodica"

Table 1. Compositions, real crystal chemical structures, and physical properties of $Mn_xZn_yFe_zO_4$ ferrite single crystals

Sample	Crystal chemical structure of Mn–Zn spinel ferrite	Density ρ, g/cm^3		Lattice parameter *a*, Å
		x-ray	hydrostatic	
5	$(Mn^{2+}_{0.38}Zn^{2+}_{0.32}Fe^{3+}_{0.24}V^{(k)}_{0.06})[Mn^{3+}_{0.06}Fe^{2+}_{0.06}Fe^{3+}_{1.88}]O^{2-}_{3.99}V^{(a)}_{0.01}$	5.030	5.021	8.462
6	$(Mn^{2+}_{0.52}Zn^{2+}_{0.32}Fe^{3+}_{0.02}V^{(k)}_{0.14})[Mn^{3+}_{0.03}Fe^{2+}_{0.03}Fe^{3+}_{1.94}]O^{2-}_{3.96}V^{(a)}_{0.04}$	5.062	4.926	8.458
1	$(Mn^{2+}_{0.25}Zn^{2+}_{0.47}Fe^{3+}_{0.19}V^{(k)}_{0.09})[Fe^{3+}_{2.00}]O^{2-}_{3.99}V^{(a)}_{0.01}$	5.097	5.086	8.440
7	$(Mn^{2+}_{0.55}Zn^{2+}_{0.40}V^{(k)}_{0.05})[Mn^{3+}_{0.04}Fe^{2+}_{0.04}Fe^{3+}_{1.92}]O^{2-}_{3.93}V^{(a)}_{0.07}$	5.125	5.030	8.475
3	$(Mn^{2+}_{0.45}Zn^{2+}_{0.48}V^{(k)}_{0.07})[Mn^{3+}_{0.14}Fe^{2+}_{0.14}Fe^{3+}_{1.72}]O^{2-}_{3.96}V^{(a)}_{0.04}$	5.140	5.028	8.463

3. RESULTS AND DISCUSSION

As can be seen from Fig. 1, the diffraction patterns of the $Mn_xZn_yFe_zO_4$ ferrite single crystals are superpositions of the contributions from x-ray scattering of different types: (a) diffuse small-angle scattering, which leads to an increase in the background; (b) coherent Debye scattering, which is responsible for the appearance of lines at intermediate and large diffraction angles; (c) incoherent Compton scattering (with a change in the x-ray wavelength), which enhances the background at large angles; and (d) diffuse (coherent and incoherent) scattering, which additionally increases the background and gives rise to background intensity fluctuations in the form of diffuse maxima.

According to the coherent Debye scattering data, the long-range order of a ferrite material corresponds to a perovskite structure of the *Fd*3*m* type. The studied structure exhibits some features that show themselves in an enhancement of diffuse small-angle scattering and a change in the fine structure of the background intensity in the range $\theta > 54°$.

It can be stated that ions in the ferrite samples are displaced from regular lattice sites due to structural imperfections. By interacting with x-rays, these ions participate in two processes of x-ray scattering. The first process is the coherent scattering brought about by the retention of periodicity in crystal regions with defect ionic packing, which results in the appearance of low-intensity diffuse Debye maxima. The second process is the incoherent x-ray scattering caused by an incomplete absence of x-ray waves upon interference due to the disturbance of perfect periodicity in the arrangement of scattering centers. This is responsible for the background component whose intensity increases with an increase in the angle.

The background intensity monotonically increases in the case when manganese and iron ions are isolated from each other. As the concentration of manganese and iron ions increases, their effect on the solid solution becomes stronger. This manifests itself in the formation of a new ordering in the matrix spinel structure, which was observed earlier in [4, 10, 11]. The new structural formations inherently bound to the matrix structure are referred to as clusters [4, 12]. X-rays are incoherently (disorder) and coherently (order) scattered by clusters. The linear size of the clusters can be estimated from the width of diffuse maxima by using the Kitaigorodsky technique [13]. The location of the diffuse maxima is determined by the conventional Debye diffraction of x-rays by clusters and follows the relationship $2d\sin\theta = n\lambda$, which makes it possible to interpret their crystallographic structure (Figs. 1–3) [4, 5, 11, 13].

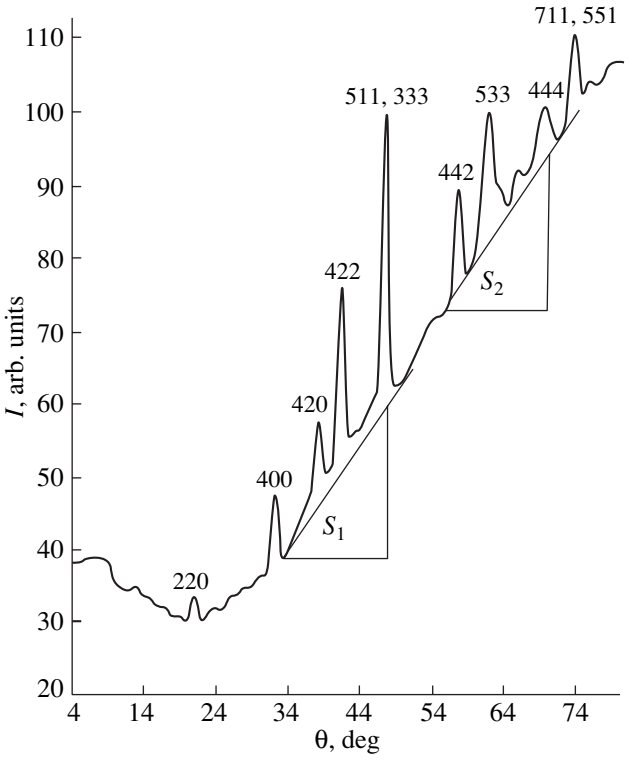

Fig. 1. Diffraction pattern (CrK_α) of sample *7*.

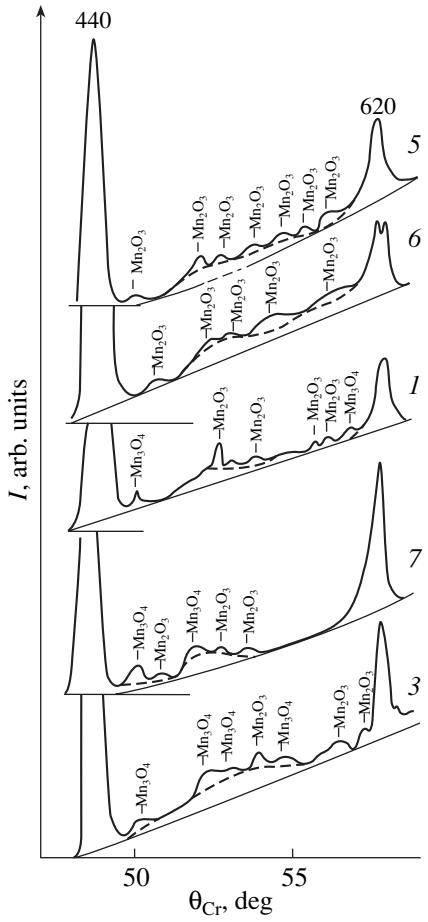

Fig. 2. Diffraction patterns with background fluctuations for $Mn_xZn_yFe_zO_4$ ferrites in the angle range 49°–60°. Here and in Figs. 3–7, numerals near the curves correspond to the sample numbers (Tables 1, 2).

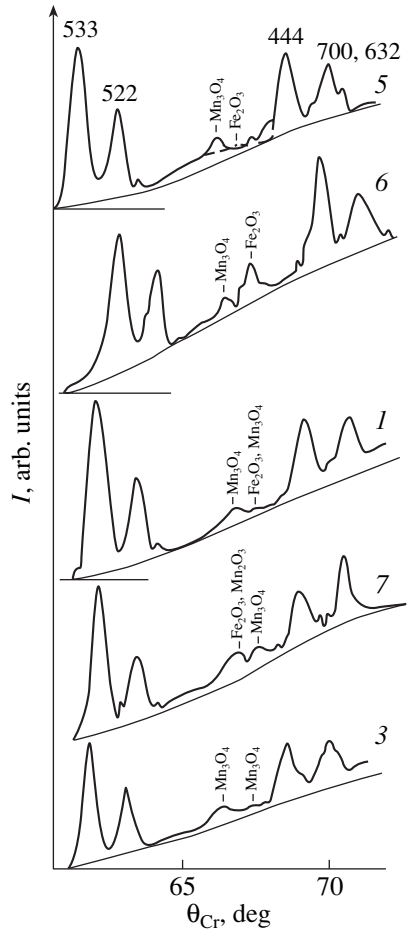

Fig. 3. Diffraction patterns with background fluctuations for $Mn_xZn_yFe_zO_4$ ferrites in the angle range 60°–73°.

According to the above approach, we estimated the integrated intensities of incoherent scattering for equal θ intervals at small θ angles, which correspond to scattering by individual centers displaced from regular lattice sites (Fig. 1, portion S_1), and at large θ angles when a further increase in the intensity is governed by a mesoscopic interaction of the components upon cluster formation (Fig. 1, portion S_2)]. As is seen from Fig. 4, the S_1 and S_2 curves obtained for different samples are similar in character. This suggests that the chemical composition of the solid solution similarly affects both the fundamental harder matrix mode of the structure [manifests itself in $S_1 = f(\rho)$] and the softer mode [manifests itself in $S_2 = f(\rho)$] responsible for the smaller-scale atomic ordering in the form of clusters in the solid solution. It is worth noting that S_1 and S_2 should be measured from the diffraction curve constructed over the entire diffraction angle range, because the use of separate portions of the curves is incorrect. In this case, the magnitudes of the intensity of incoherent x-ray scattering from the hard mode of the structure, for the most part, are less than those from the soft mode; i.e., $S_1 < S_2$.

It should be noted that samples whose structural state is characterized by displacements of ions from regular lattice sites (maximum S_1, S_2) have the closest packing of ions in the unit cell. This is confirmed by the location of a minimum in the dependence of the lattice parameter $a = f(\rho)$, which is observed at $\rho = 5.097$ g/cm^3 (Table 1, sample *1*).

In our opinion, the density ρ can serve as a representative parameter for the studied materials that are characterized by high-defect structural state (vacancies, variable-valence ions, and cluster structure). In this case, the change in density should reflect the change in structural and magnetic orders with due regard for the ion mass. From this viewpoint, the parameter ρ is not universal for all types of solid solutions. The choice of the density as an independent variable was made for the following reasons. The *a* parameter of the main undistorted lattice only weakly depends on the density (Fig. 5, curve I). At the same time, the density depen-

dences of the integrated incoherent scattering intensity (S_1 and S_2) (Fig. 4) are similar to the density dependences of the lattice parameter for the distorted structure (Fig. 5, curves II–VII). The experimentally observed minimum in the dependence $a(\rho)$ (Fig. 5) lies in the range that corresponds to bell-shaped portions in the dependences T_C, σ_s, and $B_s = f(\rho)$ (Fig. 6). The descending portions in these dependences correlate with the extrema observed in the dependences of the lattice parameters for the distorted structure (Fig. 5, curves II–VII). This implies that the structure of the distorted lattice is loose and amorphous and that amorphous–crystalline clusters can exist in the samples under investigation. Analysis of the dependences of the size of amorphous (m_a) and amorphous–crystalline (m_c) clusters (Fig. 7) and the dependences of the integrated intensities I_c and I_a of diffuse x-ray scattering by different clusters (Fig. 8) on the x-ray density of samples demonstrates that a considerable increase in the density results in the formation of states in which an increase in the density is attended by a decrease in the long-range order. In turn, a decrease in the coherence in the structure leads to a decrease in the magnetic ordering. The maximum magnetic parameters correspond to the minimum incoherent scattering intensity, i.e., to an increase in the long-range order (Figs. 4, 6).

Analysis of the locations of diffuse maxima (Figs. 2, 3) revealed that the clusters are formed by planar fragments of Mn_2O_3, Mn_3O_4, and Fe_2O_3 binary oxides. In the density range that corresponds to the maximum magnetic parameters (T_C, σ_s, and B_s), the cluster structure is determined by the interaction of trivalent iron and manganese ions with oxygen ions: $Fe_2^{3+}O_3^{2-}$ (Fe_2O_3), $Mn_1^{2+}Mn_1^{4+}O_3^{2-}$ (Mn_2O_3), and $Mn_1^{2+}Mn_2^{3+}O_4^{2-}$ and $Mn_2^{2+}Mn_1^{4+}O_4^{2-}$ (Mn_3O_4). In the range to the left of the maximum (Fig. 6), the clusters are formed by Fe^{3+} and Mn^{3+} ions (with a predominance of Mn^{3+} ions) and oxygen ions (Fig. 8). In the range to the right of the maximum, the cluster structure involves Fe^{3+}, Mn^{3+}, Mn^{2+}, and O^{2-} ions (Fig. 8). Therefore, the magnetic properties of the materials studied are substantially affected by the regions of mesoscopic atomic order (structural clusters), i.e., by the differences in ion composition responsible for the magnetic properties of clusters.

A comparison of the dependences of the lattice parameters $[a, b, c] = f(\rho)$ for the matrix ($Fd3m$) structure [calculated for the (622) and (444) planes with allowance made for split lines] (Fig. 5) and the dependences of the scattering intensity $I_c = f(\rho)$ for clusters in the range of large angles (Fig. 8) revealed the following features.

(1) The minimum a_{min} at $\rho = 5.062$ g/cm^3 for the parameters of the distorted structure is attributed to the α-Fe_2O_3 (204) clusters formed by Fe^{3+} ions, cation

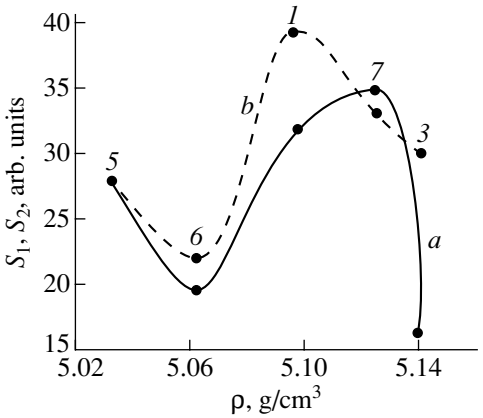

Fig. 4. Dependences of the integrated scattering intensities (*a*) S_1 and (*b*) S_2 on the sample density. Angle ranges: (*a*) 30°–50° and (*b*) 50°–70°.

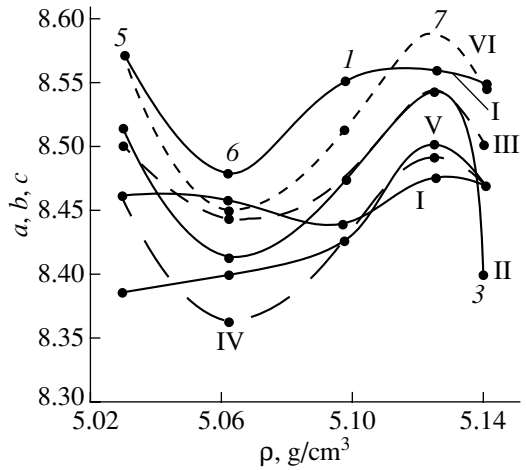

Fig. 5. Dependences of the lattice parameters of matrix structure $[a, b, c] = f(\rho)$ for the (622) and (444) planes: (I) a for undistorted lattice and (II) a_{622}, (III) a_{444}, (IV) b_{622}, (V) b_{444}, (VI) c_{622}, and (VII) c_{444} for distorted lattice.

vacancies, and oxygen (Fig. 8). The maximum concentration of these clusters corresponds to the maximum intensity $I_c(Fe_2O_3)$ of the diffuse scattering in the range 60°–70° (Fig. 8).

(2) For a solid solution with $\rho = 5.125$ g/cm^3, which corresponds to the maxima in the dependences of the lattice parameters $(a, b, c) = f(\rho)$for the distorted matrix (Fig. 5), the structure is characterized by a maximum concentration of γ-Mn_2O_3, α-Fe_2O_3, and γ-Mn_3O_4 clusters (Fig. 8). In this case, the γ-Mn_2O_3, γ-Mn_3O_4, and α-Fe_2O_3 oxides have tetragonal, orthorhombic, and rhombohedral structures, respectively, which reflects the orthorhombic ($a \neq b \neq c$) and rhombohedral ($\alpha \neq 90°$) distortions of the matrix structure.

(3) For a moderately distorted matrix lattice ($\rho = 5.097$ g/cm^3), the cluster structure exhibits a maximum

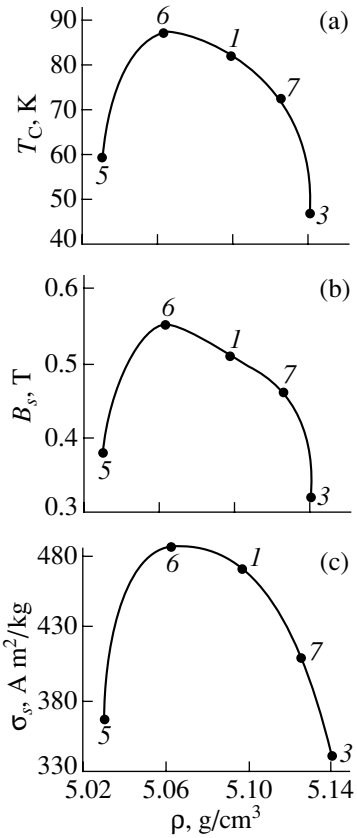

Fig. 6. Dependences of the magnetic properties on the x-ray density of the samples: (a) the specific saturation magnetization σ_s, (b) the magnetic induction B_s, and (c) the Curie temperature T_C.

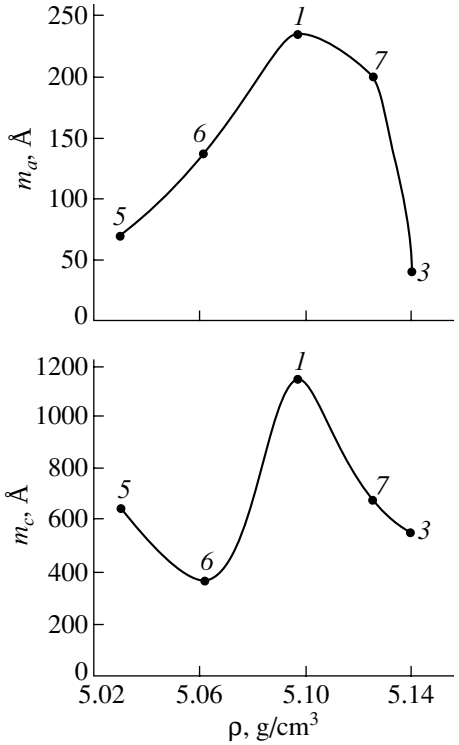

Fig. 7. Dependences of the cluster size on the x-ray density.

concentration of γ-Mn_3O_4 clusters (the orthorhombic type).

(4) In the sample with ρ = 5.14 g/cm^3, the concentration of clusters with bivalent and trivalent manganese ions increases drastically (Fig. 8).

(5) Analysis of the cluster sizes in the structure (Fig. 7) shows that the maximum mesoscopic ordering is observed for the group of samples with ρ = 5.062–5.125 g/cm^3 (first group), whereas the cluster sizes for samples with the lowest and highest densities ρ = 5.03 and 5.14 g/cm^3 (second group) are small: 140 Å ≤ m_a ≤ 230 Å for the first group and $m_a \approx 60$ Å for the second group. The small sizes of the clusters (Fig. 7) reflect their weaker effect on the physical properties of the samples. An increase in the cluster size is associated with an increase in the energy of the fluctuations. As a consequence, the larger the cluster size, the greater the deviation from the matrix structure [6, 14].

(6) The specific features in the atomic structures of the matrix and clusters manifest themselves in nonlinear dependences of the magnetic properties on the sample composition (Fig. 6).

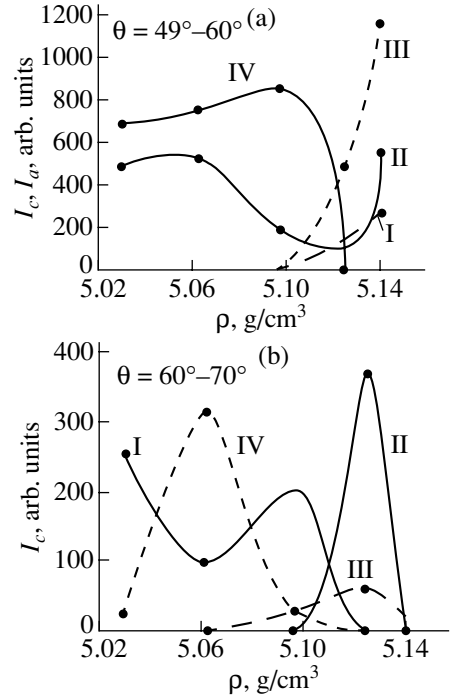

Fig. 8. Dependences of the scattering intensity for different clusters on the x-ray density of the samples in the θ ranges (a) 49°–60° and (b) 60°–70°: (a) (I) $I_c(Mn_3O_4)$, (II) $I_c(Mn_2O_3)$, (III) $I_a(Mn_3O_4)$, and (IV) $I_a(Mn_2O_3)$ and (b) (I) $I_c(20\bar{2})(Mn_3O_4)$, (II) $I_c(20\bar{2})(Mn_2O_3)$ and $I_c(20\bar{2})(Fe_2O_3)$, (III) $I_c(204)(Mn_3O_4)$, and (IV) $I_c(204)(Fe_2O_3)$. Subscripts *c* and *a* refer to crystalline and amorphous clusters, respectively.

Table 2. Mode states and cluster and structural parameters

Sample	Mode	Charge state	Magnetic state		Cluster size m, Å		Curie temperature T_C, K	
			F	η	m_{exp}	m_{theor}	T_{exp}	T_{theor}
5	O	$[_2O^-–_4Mn^+]–_3Mn^{2+}(3)–[_2O^-–_4Mn^+]$	4	–1			369	369
	m	$_4Mn^{2+}–_1Mn^{3+}–_4Mn^{2+}$	3	–1				
	O	$[_2O^-–_4Mn^+]–_1Mn^{3+}–[_2O^-–_4Mn^+]$	1	0.5	616	615.8		
	m	$[_2O^-–_4Mn^+]–_1Mn^{3+}–[_2O^-–_4Mn^+]$	2	–1				
6	O	$[_2O^-–_4Mn^+]–_1Mn^{3+}–[_2O^-–_4Mn^+]$	5	–1			486	486
	m	$_3Mn^+–_1Mn^{3+}–_3Mn^+$	9/2	2				
	O	$[_2O^-–_4Mn^+]–_1Mn^{3+}–[_2O^-–_4Mn^+]$	1	–1	197	197.1		
	m	$_4Zn^+–_1Mn^+–_4Zn^+$	5	–1				
1	O	$[_2O^-–_4Mn^+]–_1Mn^{3+}–[_2O^-–_4Mn^+]$	5	–1			470	469
	m	$_2Mn^+–_1Mn^{3+}–_2Mn^+$	7/2	–1				
	O	$[_2O^-–_4Mn^+]–_1Mn^{3+}–[_2O^-–_4Mn^+]$	1	0.5	677	677.8		
	m	$[_2O^-–_4Mn^+]–_1Mn^{3+}–[_2O^-–_4Mn^+]$	1	–1				
7	O	$[_2O^-–_4Mn^+]–_2Mn^{3+}–[_2O^-–_4Mn^+]$	5	–1			409	409
	m	$[_2O^-–_4Mn^+]–_2Mn^{3+}–[_2O^-–_4Mn^+]$	4	0.5				
	O	$[_2O^-–_4Mn^+]–_1Mn^{3+}–[_2O^-–_4Mn^+]$	1	–0.5	647	647		
	m	$[_2O^-–_4Mn^+]–_1Mn^{3+}–[_2O^-–_4Mn^+]$	2	–0.5				
3	O	$[_2O^-–_4Mn^+]–_2Mn^{3+}–[_2O^-–_4Mn^+]$	2	–1			341	340
	m	$[_1O^-–_4Mn^+]–_3Mn^{2+}–[_1O^-–_4Mn^+]$	4	–1				
	O	$_3Mn^{4+}–_1Mn^{3+}–_3Mn^{4+}$	4	–0.5	524	524		
	m	$_4Mn^{3+}–_1Mn^{3+}–_4Mn^{3+}$	7/2	–0.5				

The maximum values of the Curie temperature T_C, the magnetic induction B_s at 107 K, and the specific saturation magnetization σ_s are observed for the samples with the most distorted matrix structure and a more pronounced new ordering in the atomic structure of large-sized clusters, which shows itself in clear diffuse maxima in the diffraction patterns.

The amorphous clusters in samples *1* and *7* are two or three times larger than those in samples *3* and *5*. This is clearly seen from the dependence $m_a(\rho)$ for amorphous clusters in Fig. 7. As a result, the amorphous clusters in samples *1* and *7* make a greater contribution to the magnetic order of the structure. In the case of crystalline clusters, sample *1* is characterized by a maximum mesoscopic ordering, i.e., by the largest cluster sizes (Fig. 7). By assuming that the magnetic order favors atomic crystallographic ordering, it could be expected that this sample possesses high magnetic characteristics, which was actually observed in the experiment.

Judging from the $m_{a,c}(\rho)$ dependences, the maximum magnetic characteristics for sample *6* are unrelated to the mesoscopic ordering. Most probably, they are determined by the specific features of the long-range order in the matrix structure, which manifests itself in its anisotropy and leads to the splitting of the (620) reflection (Fig. 3). This indicates that tetragonal elements are formed in the cubic structure (a lowering of the symmetry).

Moreover, in the present work, we performed theoretical analysis of the cluster structure in $Mn_xZn_yFe_zO_4$ samples within the model concepts developed in [15, 16]. The results of this analysis and the experimental parameters are compared in Table 2. The designations of the charge and magnetic states of ions (complexes) in quasi-one-dimensional chains for the fundamental and soft modes correspond to those used in [15, 16]. Here, F is the quantum number of the total angular momentum of magnetic ions (complexes), which are exchange-coupled through diamagnetic ions (complexes) into chains, and η is the parameter describing the directionality of valence bonds. The quantum number of the magnetic state for diamagnetic complexes is given in parentheses, and the magnetic complexes are presented in square brackets.

The interaction between the fundamental and soft modes leads to their coupling with subsequent formation of quasi-two-dimensional structures (clusters). In the framework of this model, we calculated the sizes of clusters (amorphous and amorphous–crystalline) and the Curie temperatures (the phase transition temperature below which the magnetic ordering occurs; near this temperature, the transitions from a long-range order to a short-range order and then to paramagnetic

behavior can take place). The phase transition is smeared [17], which is determined by the local predominance of the short-range order due to disturbance of the long-range order. This transition is spatially inhomogeneous, because it entails a set of different magnetic configurations. For example, in samples *1* and *6*, the fundamental modes *O* are identical, whereas the soft modes *m* differ from each other (Table 2). This means that the phase transition is governed by different magnetic configurations arising from different canted states of identical main antiferromagnetic structures (by analogy with the Dzyaloshinski–Moriya weak ferromagnetism). The samples differ in the sets of magnetic configurations of the fundamental (*O*) and soft (*m*) modes (responsible for the Curie temperature, i.e., the magnetic ordering) and cluster sizes determined by the fundamental and soft modes (see Table 2 for particular samples).

4. CONCLUSIONS

The main results obtained in the above investigation can be summarized as follows.

(1) The real spinel structure of $Mn_xZn_yFe_zO_4$ ferrites is characterized by local distortions of the tetragonal, orthorhombic, and rhombohedral types in the families of high-index planes.

(2) The distortion of the rigid matrix structure is accompanied by the excitation of the soft mode in the structure and the formation of mesoscopic clusters enriched with manganese and (or) iron ions.

(3) The experimental data are in agreement with the results of calculations performed in the framework of the model concepts. Within these models, it is assumed that real samples differ in their sets of magnetic configurations of the interacting fundamental and soft modes of quasi-two-dimensional structures (clusters), which leads to variations in the physical parameters.

REFERENCES

1. V. I. Arkharov, V. P. Pashchenko, N. V. Suntsov, *et al.*, Dokl. Akad. Nauk SSSR **268** (1), 84 (1983) [Sov. Phys. Dokl. **28**, 48 (1983)].
2. V. P. Pashchenko, A. M. Nesterov, Ya. G. Drigibka, *et al.*, Poroshk. Metall., Nos. 5–6, 89 (1994).
3. V. P. Pashchenko, E. G. Darovkikh, G. A. Potapov, *et al.*, Neorg. Mater. **30** (4), 547 (1994).
4. V. P. Pashchenko, A. M. Nesterov, V. I. Arkharov, *et al.*, Dokl. Akad. Nauk SSSR **318** (2), 371 (1991).
5. V. I. Arkharov, Z. A. Samoĭlenko, V. P. Pashchenko, and A. M. Nesterov, Neorg. Mater. **29** (6), 827 (1993).
6. M.A. Krivoglaz. *Electronic Structure and Electronic Properties of Metals and Alloys* (Nauka, Kiev, 1988), p. 3.
7. J. Smit and H. P. J. Wijn, *Ferrites* (Wiley, New York, 1959; Inostrannaya Literatura, Moscow, 1962).
8. M. T. Varshavskiĭ, V. P. Pashchenko, A. N. Men', N. V. Suntsov, and A. G. Miloslavskiĭ, *Defect Structure and Physicochemical Properties of Spinel Ferrites* (Nauka, Moscow, 1988).
9. V. Ya. Mitrofanov, V. P. Pashchenko, V. K. Prokopenko, *et al.*, Fiz. Tverd. Tela (St. Petersburg) **37** (2), 123 (1995) [Phys. Solid State **37**, 662 (1995)].
10. B. M. Smirnov, Usp. Fiz. Nauk **162** (1), 119 (1992) [Sov. Phys. Usp. **35**, 37 (1992)].
11. V. D. Okunev, Z. A. Samoilenko, O. Abaloshev, *et al.*, Appl. Phys. Lett. **75**, 1949 (1999).
12. V. D. Okunev, Z. A. Samoilenko, V. M. Svistunov, *et al.*, J. Appl. Phys. **85** (10), 7282 (1999).
13. L. I. Kitaĭgorodsky, *X-ray Structure Analysis of Fine-Crystalline and Amorphous Solids* (Nauka, Moscow, 1952).
14. V. K. Malinovsky, Fiz. Tverd. Tela (St. Petersburg) **41** (5), 805 (1999) [Phys. Solid State **41**, 725 (1999)].
15. V. S. Abramov, V. P. Pashenko, S. I. Khartsev, and O. P. Cherenkov, Funct. Mater. **6** (1), 64 (1999).
16. V. I. Abramov and A. I. Linnik, Fiz. Tekh. Vys. Davleniĭ **8** (3), 90 (1998).
17. V. Ya. Shur, G. G. Lomakin, V. P. Kuminov, *et al.*, Fiz. Tverd. Tela (St. Petersburg) **41** (3), 505 (1999) [Phys. Solid State **41**, 453 (1999)].

Translated by O. Borovik-Romanova

Physics of the Solid State, Vol. 43, No. 8, 2001, pp. 1563–1566. Translated from Fizika Tverdogo Tela, Vol. 43, No. 8, 2001, pp. 1503–1506.

MAGNETISM AND FERROELECTRICITY

Generation of Pairs of Antiferromagnetic Vortices and Their Dynamics at a Domain Wall in Yttrium Orthoferrite

M. V. Chetkin and Yu. N. Kurbatova

Moscow State University, Vorob'evy gory, Moscow, 119899 Russia

Received November 23, 2000; in final form, February 1, 2001

Abstract—The stable generation of pairs of antiferromagnetic vortices at a domain wall moving at a velocity of 12 km/s is investigated at the instant it passes through a defect in a thin plate of yttrium orthoferrite. The velocities of a vortex and an antivortex moving in opposite directions along the domain wall and being accompanied by solitary flexural waves are ±16 km/s. The total velocity of antiferromagnetic vortices is close to the maximum velocity of the domain wall, 20 km/s. Such a high velocity can only be due to the action of a quite large gyroscopic force. An external dc magnetic field (±400 Oe) applied along the *b* axis of the orthoferrite affects this velocity insignificantly. The effective magnetic field that violates the Lorentz invariance of the dynamics considerably exceeds this value. © *2001 MAIK "Nauka/Interperiodica"*.

1. INTRODUCTION

The possible existence of ferromagnetic vortices follows from the Landau–Lifshitz equation describing the motion of a magnetic moment [1, 2]. For experimental observation of static magnetic vortices in domain walls (DWs) of garnet-ferrite films, the method of dark-field anisotropic diffraction of light [3] is developed. The action of gyroscopic forces on magnetic vortices in domain walls of garnet ferrites was predicted in [4]. The dynamics, pair collisions, and the soliton-like behavior of magnetic vortices in domains walls of garnet-ferrite films were studied in [5, 6] on the basis of detection of the solitary flexural waves accompanying these vortices. Theoretical predictions of the possible existence of antiferromagnetic vortices in domain walls at low temperatures were made in [7, 8] for orthoferrites and in [9] for easy-plane antiferromagnets.

The first experimental observations of solitary flexural waves in domain walls of yttrium orthoferrite at room temperature were described in our earlier publications [10, 11]. Strong local slowing down of a domain wall moving initially at a supersonic velocity of 12 km/s with the help of a decelerating magnetic field of a solitary wire crossing the domain wall was used to generate waves. It is well known that a nonhysteretic transition from the sound velocity to a supersonic velocity and back, as described by Maxwell's rule [12], takes place for a domain wall of the Néel type at the end of the region of constancy of a DW velocity equal to the velocity of transverse sound. The solitary flexural waves that accompany antiferromagnetic vortices were studied in [13, 14].

2. EXPERIMENTAL RESULTS

In this paper, we present the results of investigating the generation of solitary flexural wave pairs in domain walls of yttrium orthoferrite moving initially with a supersonic velocity and analyze their dynamics in the presence of an external magnetic field along the *b* axis of the crystal. The results confirm the law of topological-charge conservation for an antiferromagnetic vortex–antivortex pair accompanied by solitary flexural waves during their generation. The analysis of the dynamics in the presence of magnetic fields perpendicular to the weak-ferromagnetism axis of orthoferrite carried out by us here is important in understanding the origin of the forces that drive antiferromagnetic vortices. The experiments on the generation of antiferromagnetic vortices in a thin 30-μm yttrium orthoferrite plate at room temperature were carried out using the method of high-speed double-exposure photography in the same manner as in our previous works. The plate was cut at right angles to the optical axis. The normal to the plate forms an angle of 52° with the weak-ferromagnetism *c* axis. The magnetic field produced by the two coils, which had an inner diameter of 1.5 mm and were applied over the sample through a thin cover glass, had, in addition to the component along the *c* axis, a component along the *b* axis of approximately the same magnitude. This component is important for violating the Lorentz invariance of the DW dynamics in orthoferrites and can lead to the emergence of a nonzero gyroscopic force driving antiferromagnetic vortices along the domain wall. Estimates of the topological charges of antiferromagnetic vortices accompanied by solitary flexural waves, which were obtained from experimental data [13, 14] and theoretical calculations [15], are found to match. Figure 1 shows a high-speed

1063-7834/01/4308-1563$21.00

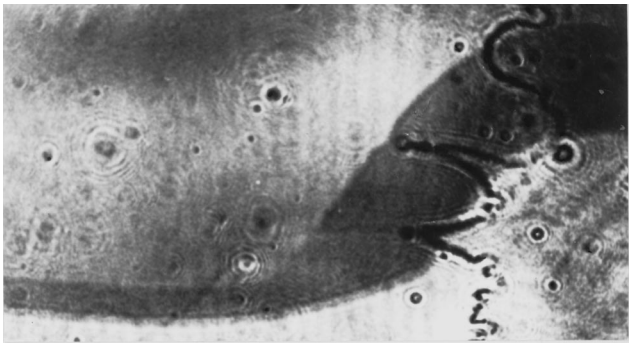

Fig. 1. Double-exposure high-speed photograph of a generated pair of solitary flexural waves accompanying a vortex–antivortex pair in the second (upper) position of an ascending domain wall in an yttrium orthoferrite plate. The dark band is the region crossed by the domain wall during the time between two light pulses.

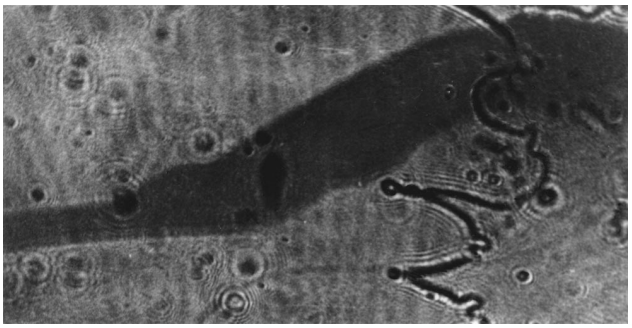

Fig. 2. Double-exposure high-speed photograph of a generated pair of two solitary flexural waves moving in opposite directions and accompanying the antiferromagnetic vortex and antivortex in a domain wall moving at a velocity of 12 km/s in a yttrium orthoferrite plate.

double-exposure photograph of an ascending domain wall in an yttrium orthoferrite plate. The first position of the domain wall (transition from the light to dark region) is shown in the lower part of the photograph. The second position of the domain wall corresponds to the transition from the dark to the light region. The dark band is the region traversed by the domain wall during the time between two light pulses. In the left part of the figure, the domain wall is almost rectilinear and moves at a velocity of 4 km/s. In the right part of the photograph, a transition to a supersonic velocity of 12 km/s takes place. In the first position, solitary flexural waves are not yet observed at the domain wall. In the second position of the domain wall in Fig. 1, a singularity consisting of two rectilinear intersecting segments, which, in accordance with Fig. 2, are the fronts of solitary flexural waves moving in opposite directions, is clearly manifested. The generation of a pair of solitary flexural waves is very stable. Every time the domain wall intersects the position marked by the arrow in Fig. 1 at a velocity of 12–13 km/s, a pair of solitary flexural waves is generated (Figs. 1, 2). Solitary flexural waves as a single entity lag behind the domain wall and have sharp leading fronts and extended trailing fronts. Figure 2 can be used to determine the velocity of waves along the domain wall. They move in opposite directions at the same speed, 16 km/s. The external magnetic field driving the domain wall as a single entity can only decelerate solitary waves. The only possible reason for the motion of solitary flexural waves along the domain wall is a gyroscopic force acting on the antiferromagnetic vortices and antivortices accompanied by these waves. In accordance with Figs. 1 and 2, the generation of a pair of solitary waves proves the validity of the topological-charge conservation law in the case of generation of antiferromagnetic vortices at a domain wall moving with a supersonic velocity in yttrium orthoferrite. For the light pulse of duration 250 ps used, no local deceleration of the part of the domain wall near a defect is observed and only the generation of a pair of solitary waves can be seen. The quasi-static advance of the domain wall clearly indicates the presence of a defect retarding the domain wall in the region of the generation of a pair of solitary flexural waves. The dynamics of domain walls in orthoferrites can be described in terms of the quasi-relativistic Lorentz-invariant σ model with the maximum velocity equal to the velocity of spin waves in the linear region of their dispersion relation [6, 16]. For a DW velocity of 12 km/s, the total velocity of each of these solitary waves is close to the limiting velocity and is equal to 19.5 ± 0.5 km/s. Such a velocity can apparently be due to a strong gyroscopic force acting on the antiferromagnetic vortices. In a magnetic field directed along the *b* axis of orthoferrite, the Lorentz invariance of the DW dynamics can be violated, as shown in [17, 18]. In accordance with the results of those works, the gyroscopic force acting along the domain wall in this case is proportional to the magnetic field applied along the *b* axis of orthoferrite. These results are applicable to velocities much smaller than the maximum velocity. In this connection, it would be interesting to study the dynamics of solitary flexural waves in magnetic fields directed along the *b* axis of the crystal. The time dependence of distances traversed by these two waves along a domain wall in a magnetic field of ±400 Oe is presented in Fig. 3. The velocity of vortices along the domain wall is close to 16 km/s. The difference in the velocities in these two cases does not exceed 5–7%, so that the effective field destroying the Lorentz invariance of the DW dynamics and generating the gyroscopic force is much stronger than that used by us. For more accurate determination of the magnitude of this field, a similar experiment must be made in stronger magnetic fields applied along the *b* axis. If the magnetic sublattices of orthoferrite are not equivalent, a gyroscopic force proportional to the Dzyaloshinski field and not to h_b can be generated [6]. The change in the magnetic anisotropy in the vicinity of a defect can

be of considerable importance in generating an antiferromagnetic vortex–antivortex pair.

3. DISCUSSION OF RESULTS

The central part of an antiferromagnetic vortex moving under the action of a gyroscopic force must contain an antiferromagnetic phase G_y [13, 14]. This phase is known to exist in dysprosium orthoferrite at low temperatures. In the yttrium orthoferrite under investigation, the phase transition $G_zF_x \longrightarrow G_y$ occurs at room temperature in an unstable supersonic domain wall decelerated by a local defect or by a magnetic field of a solitary conductor. In accordance with Figs. 1 and 2, the formation of two solitary waves proceeds similarly in magnetic fields directed along the *b* axis and in opposite fields. This means that the sign of the gyroscopic force does not change in these two cases. The pulsed magnetic field along the *b* axis created by a coil and driving the domain wall at a velocity of 12 km/s was 120 Oe. If the gyroscopic force changed its sign upon reversal of the magnetic field along the *b* axis, the generated solitary waves would move in opposite directions and annihilate each other. This follows from our earlier publications [11, 13, 14], in which antiferromagnetic vortices were generated during local deceleration of a domain wall, moving at a supersonic velocity by using a magnetic field of solitary wires crossing the domain wall. The total velocity of antiferromagnetic vortices in the domain wall of yttrium orthoferrite moving at a velocity of 12 km/s is close to the limiting velocity, 20 km/s, for the solitary flexural waves of all amplitudes observed. A theory describing the dynamics of antiferromagnetic vortices in orthoferrites, valid up to the limiting velocity *c* of their motion, has not been developed to date. The above experimental results show that the effective magnetic field destroying the Lorentz invariance of the dynamics is much stronger than the dc magnetic field along the *b* axis used by us and than the *b* component of the pulsed magnetic field produced by the coil driving the domain wall in the orthoferrite. This follows from the rather weak dependence of the velocity of antiferromagnetic vortices on the magnetic field along this axis.

Static analysis of the symmetry of domain walls moving by inertia in orthoferrites was carried out in [6, 19]. In the dynamics of *ac*-type boundaries, the m_b component of the weak ferromagnetic moment along the *b* axis differs from zero (it is proportional to V/c). A similar result also holds for domain walls driven by a magnetic field. This means that the gyroscopic force may be proportional to V^2/c^2. Under our experimental conditions, the value of this quantity is not small and is equal to 0.36. The inclusion of this force requires a special analysis, which is beyond the approximation $V \ll c$ adopted in all existing publications [15, 17, 18]. Analysis of the structure of moving domain walls has been carried out only for homogeneous domain walls of the *ac* and *ab* types. For studying the symmetry of domain walls with antiferromagnetic vortices, invariants of higher orders than those for homogeneous domain walls must be taken into account.

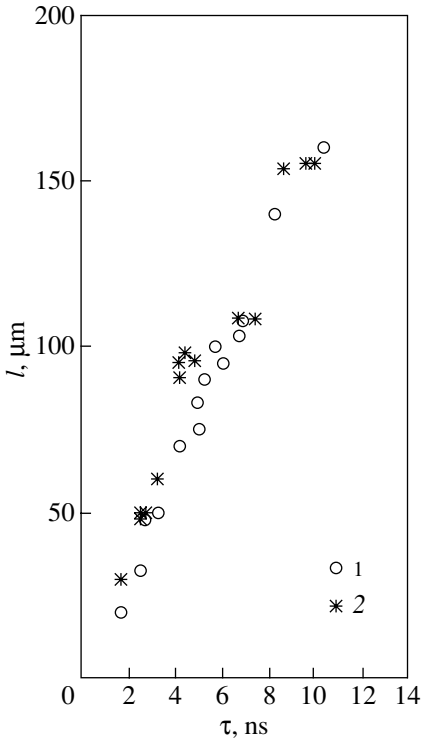

Fig. 3. Time dependence of distances traversed by the antiferromagnetic vortex and antivortex in a magnetic field of 400 Oe directed (*1*) along and (*2*) opposite to the *b* axis in an yttrium orthoferrite plate.

ACKNOWLEDGMENTS

The authors are grateful to A.M. Balbashov for providing the single crystals and to A.F. Popkov and S.S. Krotov for their valuable remarks on the results.

This work was supported by the Russian Foundation for Basic Research, project no. 98-02-16440.

REFERENCES

1. R. K. Dodd, J. C. Eilbeck, J. D. Gibbon, and H. C. Morris, *Solitons and Nonlinear Wave Equations* (Academic, New York, 1983).
2. E. Y. Vedmedenko, H. P. Oepen, and A. Ghazdli, Phys. Rev. Lett. **84** (25), 5884 (2000).
3. A. Thiaville, Ben Youssef, Y. Nakatany, and J. Miltat, J. Appl. Phys. **69**, 6090 (1991).
4. A. V. Nikiforov and É. B. Sonin, Pis'ma Zh. Éksp. Teor. Fiz. **40** (4), 325 (1984) [JETP Lett. **40**, 1119 (1984)].
5. M. V. Chetkin, I. V. Parygina, and L. L. Savchenko, Zh. Éksp. Teor. Fiz. **110** (6), 1873 (1996) [JETP **83**, 1031 (1996)].

6. V. G. Bar'jakhtar, M. V. Chetkin, B. A. Ivanov, and S. N. Gadetskiy, *Springer Tracts in Modern Physics*, Vol. 129: *Dynamics of Topological Magnetic Solitons. Experiment and Theory* (Springer-Verlag, Berlin, 1994).
7. M. M. Farztdinov, M. A. Shamsutdinov, and A. A. Khalfina, Fiz. Tverd. Tela (Leningrad) **21** (5), 1522 (1979) [Sov. Phys. Solid State **21**, 878 (1979)].
8. A. P. Malozemov and J. C. Slonchzewski, *Magnetic Domain Walls in Babbles Materials* (Academic, New York, 1979).
9. S. Komineas and N. Papanicolaou, Nonlinearity **11**, 265 (1998).
10. M. V. Chetkin, Yu. N. Kurbatova, and A. I. Akhutkina, J. Appl. Phys. **79** (8), 6132 (1996).
11. M. V. Chetkin, Yu. N. Kurbatova, and V. N. Filatov, Pis'ma Zh. Éksp. Teor. Fiz. **65** (10), 760 (1997) [JETP Lett. **65**, 797 (1997)].
12. S. V. Gomonov, A. K. Zvezdin, and M. V. Chetkin, Zh. Éksp. Teor. Fiz. **94** (1), 133 (1988) [Sov. Phys. JETP **67**, 2250 (1988)].
13. M. V. Chetkin, Yu. N. Kurbatova, and T. B. Shapaeva, Zh. Éksp. Teor. Fiz. **115** (6), 2160 (1999) [JETP **88**, 1179 (1999)].
14. M. V. Chetkin and Yu. N. Kurbatova, Phys. Lett. A **260**, 108 (1999).
15. A. K. Zvezdin, Kratk. Soobshch. Fiz., No. 6, 28 (1999).
16. A. K. Zvezdin, Pis'ma Zh. Éksp. Teor. Fiz. **29** (10), 605 (1979) [JETP Lett. **29**, 553 (1979)].
17. Yu. V. Melekhov and O. A. Perekhod, Fiz. Tverd. Tela (Leningrad) **26** (3), 924 (1984) [Sov. Phys. Solid State **26**, 564 (1984)].
18. M. M. Farztdinov, M. A. Shamsutdinov, and E. G. Ekomasov, Fiz. Tverd. Tela (Leningrad) **30** (6), 1866 (1988) [Sov. Phys. Solid State **30**, 1076 (1988)].
19. N. Papanicolaou, Phys. Rev. B **55** (18), 12290 (1997).

Translated by N. Wadhwa

Physics of the Solid State, Vol. 43, No. 8, 2001, pp. 1567–1571. Translated from Fizika Tverdogo Tela, Vol. 43, No. 8, 2001, pp. 1507–1511.

MAGNETISM AND FERROELECTRICITY

Saturation Magnetization Distribution in the Vicinity of a Grain Boundary in a Plate of a Triaxial Silicon-Iron-Type Ferromagnet

L. M. Sheiko and A. V. Sadovoĭ

Zaporozh'e State University, Zaporozh'e, 690063 Ukraine

e-mail: sheiko@zsu.zaporizhzhe.ua

Received October 10, 2000; in final form, February 8, 2001

Abstract—The one-dimensional saturation magnetization distribution $\mathbf{M}_S(x)$ in the vicinity of grain boundaries (GBs) is studied in $(01\bar{1})$ plates of soft magnetic alloys of the Fe–3% Si type in the framework of the theory of micromagnetism. The mechanisms of the emergence of spatial inhomogeneities of the saturation magnetization near planar GBs are discussed. Calculations show that macroscopic regions $\Delta x \approx 10$ mm in extent arise near GBs because of the μ* effect. This result is supported by the experimental data. © *2001 MAIK "Nauka/Interperiodica".*

1. INTRODUCTION

Grain boundaries (GBs) are the most typical defects of crystals [1–3]. They play an important part in the formation of the domain structure and magnetic properties of polycrystalline ferromagnets [2, 4–7]. The effect of GBs on the magnetic properties is particularly great in fine-grained and nanocrystalline materials [2, 7–10], in which the relative volume of GBs can be as large as 10–20% of that of the bulk phase. One of the mechanisms of the GB influence is associated with the magnetostatic field $\mathbf{H}^m(\mathbf{r})$ [which is referred to as the demagnetizing field $\mathbf{H}^d$ inside the magnet and as the stray field $\mathbf{H}^s$ outside it] produced by GBs [4, 5, 11–13]. Because $\mathbf{H}^m(\mathbf{r})$ is inhomogeneous, the total field $\mathbf{H}^i(\mathbf{r}) = \mathbf{H}^e + \mathbf{H}^m(\mathbf{r})$ (where $\mathbf{H}^e$ is a uniform external field), as well as the magnetic induction $\mathbf{B}$ and specific electromagnetic energy loss P_{sp} in grains, is also inhomogeneous [14–16]. In [11, 12, 15], the distributions of the magnetization $\mathbf{M}$ and of the stray field $\mathbf{H}^s$ near GBs were studied experimentally in plates of an Fe–3% Si alloy, the surfaces of which were approximately parallel to the crystallographic $(01\bar{1})$ plane. This paper is devoted to a theoretical investigation of the spatial inhomogeneities of the saturation magnetization $\mathbf{M}_S$ and the reasons for their occurrence near a planar GB that separates regions with differently oriented ⟨100⟩ axes in a plate of a soft magnetic material of the silicon-iron type.

2. MODEL AND BASIC RELATIONS

We consider a $2h$ thick plate (infinite along the x_1 and x_3 axes) of a triaxial silicon-iron-type ferromagnet with magnetocrystalline anisotropy constant $K_1 > 0$. The x_2 axis of the rectangular coordinate system $\{x_1, x_2, x_3\}$ is normal to the plate surface. The plate contains a planar GB separating regions 1 and 2. In these regions, the $(01\bar{1})$ planes are parallel to the plate surface (the x_1x_3 plane), but the easy magnetization directions (EDs) ⟨100⟩ make angles α_1^0 and α_2^0 with the x_1 axis, respectively. The plane of the GB coincides with the yz plane of a rectangular coordinate system $\{x, y, z\}$ whose axes x and z lie in the plate plane and make an angle γ with the x_1 and x_3 axes, respectively. The x_2 and y axes coincide, and the x axis is aligned with the normal $\mathbf{n}$ to the GB (Fig. 1). When an external uniform field $\mathbf{H}^e$ is applied along the x_1 axis, crystals 1 and 2 are magnetized to saturation ($M = M_S$). Since the plate and the GB in it are infinite along the z axis, we can assume that the magnetization $\mathbf{M}$ is independent of the coordinate z. We also assume that the magnetization lies in the plate plane ($M_y = 0$) and is uniform across the plate thickness; that is, it is also independent of the coordinate y. In

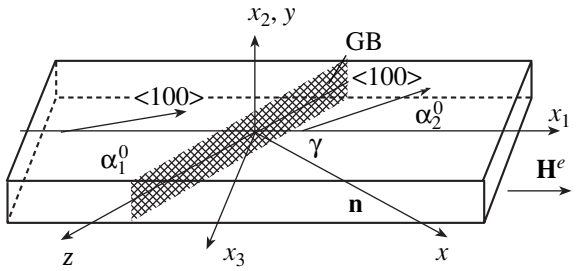

Fig. 1. Geometry of the problem.

other words, we consider the case of the one-dimensional magnetization distribution,

$$\mathbf{M}(x) = M_S[\cos\theta(x)\mathbf{e}_x + \sin\theta(x)\mathbf{e}_z], \quad (1)$$

where θ is the angle between $\mathbf{M}$ and the normal $\mathbf{n}$ and $\mathbf{e}_x$ and $\mathbf{e}_z$ are the unit vectors along the corresponding axes; the condition $M^2(x) = M_S^2 = \text{const}$ is fulfilled automatically.

The equilibrium distributions $\mathbf{M}(x)$ and $\theta(x)$ can be found as a stationary (as $t \longrightarrow \infty$) solution to the Landau–Lifshitz equation [17, 18]:

$$\frac{\partial \mathbf{M}}{\partial t} = -g \cdot \mu_0 \mathbf{M} \times \mathbf{H}^{\text{eff}} + \frac{\alpha_D}{M_S}\mathbf{M} \times \frac{\partial \mathbf{M}}{\partial t}. \quad (2)$$

Here, g is the gyromagnetic ratio and α_D is the damping constant. The effective magnetic field $\mathbf{H}^{\text{eff}}$ can be written as

$$\mathbf{H}^{\text{eff}} = \mathbf{H}_{\text{exc}}^{\text{eff}} + \mathbf{H}_k^{\text{eff}} + \mathbf{H}_h^{\text{eff}} + \mathbf{H}_m^{\text{eff}} = -\frac{1}{\mu_0}\left(\frac{\delta f_{\text{exc}}}{\delta \mathbf{M}} + \frac{\delta f_k}{\delta \mathbf{M}} + \frac{\delta f_h}{\delta \mathbf{M}} + \frac{\delta f_m}{\delta \mathbf{M}}\right), \quad (3)$$

where the effective exchange field $\mathbf{H}_{\text{exc}}^{\text{eff}}$, effective magnetocrystalline anisotropy field $\mathbf{H}_k^{\text{eff}}$, external magnetic field $\mathbf{H}_h^{\text{eff}}$, and effective magnetostatic field $\mathbf{H}_m^{\text{eff}}$ can be found as derivatives of the corresponding energy densities f_{exc}, f_k, f_h, and f_m with respect to the magnetization $\mathbf{M}$. The total free-energy density f, which is the sum of the exchange (f_{exc}), magnetocrystalline-anisotropy (f_k), and magnetostatic (f_m) energy densities and of the interaction energy density f_h between the magnetization and external field, has the form

$$f = A\left(\frac{d\theta}{dx}\right)^2 + \frac{1}{4}K_1[\sin^2 2(\theta - \alpha_{1,2}^0 - \gamma) + \sin^4(\theta - \alpha_{1,2}^0 - \gamma)] - \mu_0 M_S \cos\theta H^e - \frac{1}{2}\mu_0 M_S \cos\theta H_x^m, \quad (4)$$

where A is the exchange constant. The magnetostatic field $\mathbf{H}^m$ can be found from the well-known formula [17, 18]

$$\mathbf{H}^m = \frac{1}{4\pi}M_S \nabla \iint \frac{d\cos\theta}{dx'} \ln\left|(x-x')^2 + (y-y')^2\right| dx'dy'. \quad (5)$$

One of the major difficulties in solving such problems in the theory of micromagnetism [17–19] is the determination of the energy density f_m and the corresponding effective magnetostatic field $\mathbf{H}_m^{\text{eff}}$ [see Eq. (3)]. According to Eq. (1), $M_y = 0$; therefore, f_m is independent of $f_m(M_y)$ and we have

$$H_{my}^{\text{eff}}(x, z) = -\frac{1}{\mu_0}\frac{\delta f_m}{\delta M_y} = 0. \quad (6)$$

Using the standard methods [8, 17–19], the two other components of the field $\mathbf{H}_m^{\text{eff}}$ are found to be

$$H_{mx}^{\text{eff}}(x, z) = \frac{1}{2\pi}M_S \int_{-\infty}^{+\infty} \frac{\partial \cos\theta}{\partial x'}\left\{-2\arctan\frac{2h}{(x-x')} + \frac{(x-x')}{2h}\ln\left|1 + \frac{4h^2}{(x-x')}\right|\right\}dx', \quad (7)$$

$$H_{mz}^{\text{eff}}(x, z) = -\tan\theta H_{mx}^{\text{eff}}(x, z). \quad (8)$$

Here, x and x' are the coordinates of the source and of the point of observation of the magnetostatic field, respectively. The effective fields $\mathbf{H}_{\text{exc}}^{\text{eff}}$, $\mathbf{H}_k^{\text{eff}}$, and $\mathbf{H}_h^{\text{eff}}$ are easily found using Eqs. (3) and (4). Thus, Eq. (2) takes the form

$$\frac{\partial \theta}{\partial \tau} = -\frac{2\alpha_D}{1+\alpha_D^2}\left\{-\frac{2A}{\mu_0 M_S^2}\frac{d^2\theta}{dx^2} + \frac{K_1}{2\mu_0 M_S^2} \times [\sin 4(\theta - \alpha_{1,2}^0 - \gamma) + \sin^2(\theta - \alpha_{1,2}^0 - \gamma) \times \sin 2(\theta - \alpha_{1,2}^2 - \gamma)] + \frac{1}{M_S}H^e \sin(\theta - \gamma) + \frac{1}{2}\sin\theta(x)\int_{-\infty}^{+\infty}\frac{d\cos\theta(x')}{dx'}\left[-2\arctan\frac{2h}{x-x'} + \frac{x-x'}{2h}\ln\left|1 + \frac{4h^2}{(x-x')^2}\right|\right]dx'\right\}, \quad (9)$$

where $\tau = g\mu_0 M_S t$ is the dimensionless time. The expression in the curly brackets on the right-hand side of Eq. (9) is the total torque $L = (1/\mu_0 M_S^2)\delta f/\delta\theta$ (in relative units) provided by the effective field $\mathbf{H}^{\text{eff}}$; the terms in this expression are (in order) the torques associated with exchange interaction (L_{exc}), magnetocrystalline anisotropy (L_k), external field (L_h), and magnetostatic field (L_m), respectively. The integro-differential equation (9), which describes the process of the establishment of the equilibrium $\mathbf{M}(x)$ distribution, can be solved only by numerical methods. For calculations, we chose a finite region (D) $-a \le x \le a$ with $a \gg h$. This region is covered by a net x_i with N cells. The spacings of the net points along the x axis, $\Delta x_i = x_i - x_{i-1}$, were small enough for the angles θ_i (defining the $\mathbf{M}_S$ direction) to be considered constant within a cell. Outside region D ($|x| > a$), the magnetization is assumed to be

constant. Clearly, this last assumption introduces some error into the calculations of $\theta(x)$, because $\mathbf{H}^m$ exists in all space; however, this error can be made small by taking sufficiently large values for a. Using the net approximation and the finite-difference method, Eq. (9) is reduced to the form

$$\frac{\partial\theta_i}{\partial\tau} = -\frac{2\alpha_D}{1+\alpha_D^2}\left\{-\frac{2A}{\mu_0 M_S^2}\frac{\theta_{i+1}^n - 2\theta_i^n + \theta_{i-1}^n}{\Delta x_i^2} + \frac{K_1}{2\mu_0 M_S^2}[\sin 4(\theta_i^n - \alpha_i^0 - \gamma) + \sin^2(\theta_i^n - \alpha_i^0 - \gamma)\sin 2(\theta_i^n - \alpha_i^0 - \gamma)] + \frac{1}{M_S}H^e \sin(\theta_i^n - \gamma) + \frac{1}{2\pi}\sin\theta_i^n \sum_j \frac{\cos\theta_i^n - \cos\theta_j^n}{\Delta x_j} G_{ij}\right\}, \quad (10)$$

where the function G_{ij} is defined as

$$G_{ij} = 2(x_i - x_j)\arctan\frac{2h}{x_i - x_j} - \frac{(x_i - x_j)^2}{4h} \times \ln\left|1 + \frac{4h^2}{(x_i - x_j)^2}\right| + h\ln\left|\frac{4h^2 + (x_i - x_j)^2}{4h^2 + (x_i - x_{j-1})^2}\right| - 2(x_i - x_{j-1})\arctan\frac{2h}{x_i - x_{j-1}} + \frac{(x_i - x_{j-1})^2}{4h}\ln\left|1 + \frac{4h^2}{(x_i - x_{j-1})^2}\right|. \quad (11)$$

Equation (10) is solved numerically using the iterative technique [8, 19]. The initial distribution of angles θ_i^0 (at time $\tau = 0$) is assumed to correspond to the orientation of $\mathbf{M}_S$ along the $\langle 100\rangle$ axis in each of the adjacent crystals 1 and 2. Each subsequent distribution $\theta_i^{(n)}$ in the nth iterative cycle is calculated from the following formula using the angles $\theta_i^{(n-1)}$ obtained in the previous iterative cycle:

$$\theta_i^n = \theta_i^{(n-1)} + \frac{\partial\theta_i^{(n-1)}}{\partial\tau}(\tau_n - \tau_{n-1}). \quad (12)$$

The procedure is terminated (at some time τ_n) once the quantity $\varepsilon = \max\{L_i/(|L_i^{\text{exc}}| + |L_i^k| + |L_i^h| + |L_i^m|)\}$ becomes smaller than 10^{-3}.

3. RESULTS AND DISCUSSION

Figures 2–6 show the results of calculations for a $2h = 0.25$ mm thick plate of an Fe–3% Si alloy ($A = 1.76\times10^{-6}$ J/m, $K_1 = 3.4\times10^4$ J/m^3, $M_S = 1.59\times10^6$ A/m)

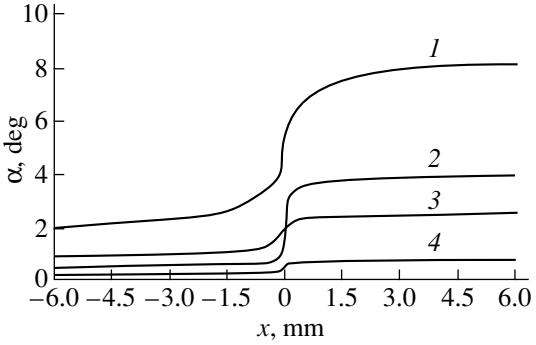

Fig. 2. Variations in the angle $\alpha(x)$ characterizing the orientation of the saturation magnetization $\mathbf{M}_S$ in the vicinity of the GB (corresponding to $x = 0$) in a silicon-iron plate with $\alpha_1^0 = 2^0$, $\alpha_2^0 = 10°$, and $\gamma = 20°$ for various values of the external uniform field H^e: (*1*) 6, (*2*) 50, (*3*) 100, and (*4*) 500 kA/m.

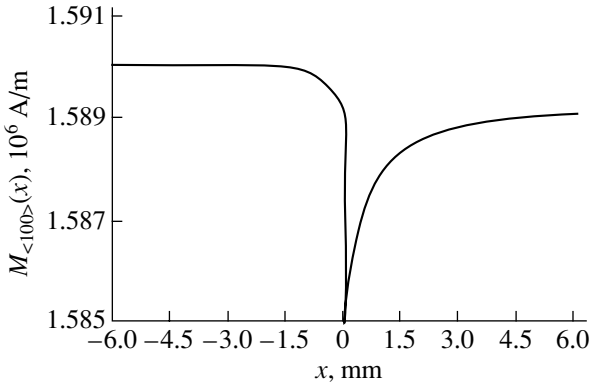

Fig. 3. Variations in the projection of the vector $\mathbf{M}_S$ onto the $\langle 100\rangle$ axis in the material under study in an external field $H^e = 6$ kA/m.

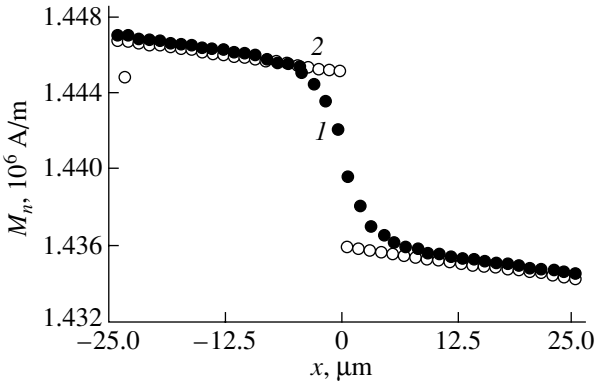

Fig. 4. Variations in the normal magnetization component $M_n(x)$ in the vicinity of the GB for $H^e = 6$ kA/m calculated (*1*) with allowance for the exchange energy f_{exc} and (*2*) without f_{exc}.

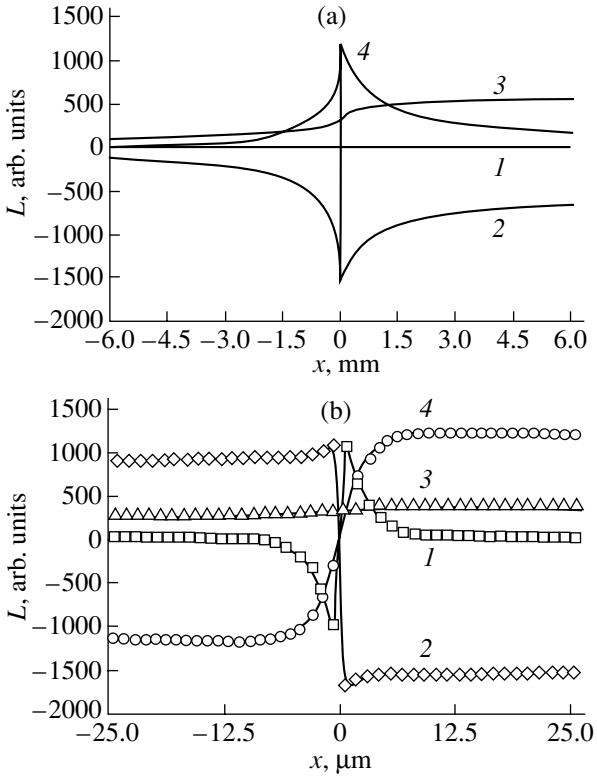

Fig. 5. Torque curves for (a) $-6 < x < 6$ mm and (b) $-25 < x < 25$ μm: (*1*) exchange $L_{exc}(x)$, (*2*) magnetocrystalline-anisotropy $L_k(x)$, and (*3*) external-field $L_h(x)$ and (*4*) magnetostatic-field $L_m(x)$ torque components.

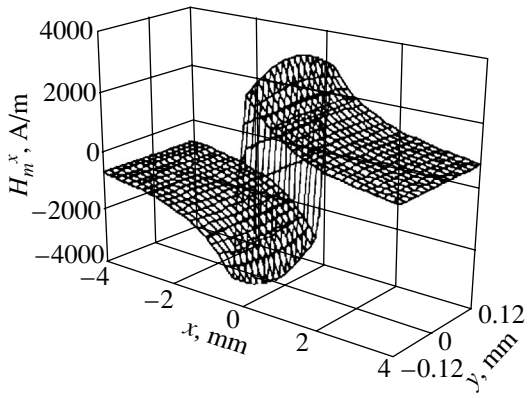

Fig. 6. Spatial distribution of the $H_x^m(x, y)$ component of the magnetostatic field $\mathbf{H}^m$ in the vicinity of the GB in the plate under study for $H^e = 6$ kA/m.

for angles $\alpha_1^0 = 2°$, $\alpha_2^0 = 10°$, and $\gamma = 20°$ (the width of the calculation region is taken to be $2a = 12$ mm for this plate). Figure 2 conveniently shows the angle $\alpha(x) = \theta(x) - \gamma$ between $\mathbf{M}$ and $\mathbf{H}^e$ (the x_1 axis) and not the $\theta(x)$ dependence. Most of the results discussed here correspond to the case of the external field $H^e = 6$ kA/m. In this case, under the action of the field $\mathbf{H}^e$, the magnetization $\mathbf{M}_S$ is oriented along a fixed direction close to the ⟨100⟩ axis in each crystal in regions far from the GB. For this reason, in the regions $x \le -5$ and $x \ge 5$ mm, the values of the angle $\alpha(x)$ are close to α_1^0 and α_2^0, respectively (Fig. 2, curve *1*), and the projection $M_{\langle 100\rangle}$ of the vector $\mathbf{M}_S$ onto the ⟨100⟩ axis (Fig. 3) is close to the saturation magnetization value ($M_{\langle 100\rangle} \approx M_S = 1.59 \times 10^6$ A/m) at distances Δx larger than 5 mm from the GB. As the GB is approached, the departure of the vector $\mathbf{M}_S$ from the corresponding ⟨100⟩ axis progressively increases; that is, the projection $M_{\langle 100\rangle}$ decreases as $x \longrightarrow 0$ (Fig. 3). For this reason, the discontinuity of the normal magnetization component M_n at the GB (i.e., at $x = 0$) disappears, $\Delta M_n = 0$ (Fig. 4). It should be noted that this behavior of the magnetization $\mathbf{M}$ near GBs was observed experimentally in plates of silicon iron [11, 12, 15]. From Figs. 2 (curve *1*), 3, and 4, it can be seen that the vector $\mathbf{M}_S$ deviates from the ⟨100⟩ direction most sharply in the immediate vicinity of the GB ($|x| \le 10$ μm, region I). At large distances from the GB (10 μm $< |x| \le 5$ mm, region II), the magnetization distribution $\mathbf{M}(x)$ becomes significantly less inhomogeneous and, for $|x| > 5$ mm (region III), it is virtually homogeneous in the case of the external-field strengths under discussion ($H^e = 6$ kA/m, Figs. 2, 3). The reason for such an $\mathbf{M}(x)$ distribution becomes clear from Fig. 5, which shows the L_{exc} L_k, L_h, and L_m torque curves (in equilibrium, the total torque L is equal to zero). In region I, the rotation of the vector $\mathbf{M}_S$, which results in the disappearance of the discontinuity ΔM_n at the GB (Fig. 4), is basically due to the short-range exchange torque L_{exc} (Fig. 5a, curve *1*). In the region $|x| > 10$ μm, the contribution from L_{exc} to the total torque L becomes negligible in comparison with the magnetostatic-field torque L_m (Fig. 5, curve *4*). This last torque, combined with L_h (Fig. 5, curve *3*), balances the magnetocrystalline anisotropy torque L_k (Fig. 5, curve *2*), which tends to hold the vector $\mathbf{M}_S$ in the ⟨100⟩ easy magnetization direction. Therefore, in a macroscopic region of width Δx of the order of 10 mm on both sides of the GB (region II), which is the greater part of the inhomogeneous $\mathbf{M}$ distribution region around the GB, the inhomogeneous deviation of the atomic magnetic moments from the ⟨100⟩ axis is caused by the magnetostatic field H^m (Fig. 6); i.e., it is the μ* effect [5, 15]. At large distances from the GB (in region III, in which $L_m < L_h$ and $L_m(x)$ depends on x only slightly), the weakly inhomogeneous $\alpha(x)$ distribution (Fig. 2, curve *1*) is basically caused by the torque L_h due to the uniform external field $\mathbf{H}^e$ (Fig. 5, curve 3). As the field $\mathbf{H}^e$ is increased, the perturbations $\delta\mathbf{M}$ of the magnetization $\mathbf{M}$ gradually decrease in the vicinity of the GB and, in fields $H^e >$ 500 kA/m, are almost completely suppressed (Fig. 2),

with the atomic magnetic moments being aligned with the field $\mathbf{H}^e$.

In closing, we note that the equilibrium magnetization distribution $\mathbf{M}(x)$ in the vicinity of the planar GB investigated here in a polycrystalline silicon-iron-type ferromagnet is similar to the structure of domain walls to some extent [18]: in both cases, the vector $\mathbf{M}_S$ is smoothly rotated from one fixed direction to another. However, unlike domain walls whose typical width is $\delta \approx 10^{-5}$–10^{-4} mm, the region of the inhomogeneous $\mathbf{M}$ distribution in the vicinity of a grain boundary has macroscopic dimensions ($\Delta x \approx 10$ mm) in soft magnetic materials, because the long-range magnetostatic field $\mathbf{H}^m$ plays a decisive role in the latter case. The results obtained in this paper agree in a qualitative manner with the relevant experimental data [15].

4. CONCLUSIONS

The main results of this paper are the following.

(1) A stationary solution to the Landau–Lifshitz equation (for $t \longrightarrow \infty$) is found. This solution describes the one-dimensional distribution of the saturation magnetization $\mathbf{M}(x)$ in the vicinity of a planar GB in a plate of a triaxial silicon-iron-type ferromagnet placed in an external magnetic field $\mathbf{H}^e$. The GB is a $(01\bar{1})$ interface between crystallites which differ in the orientation of the $\langle 100 \rangle$ easy magnetization direction.

(2) The normal magnetization component does not undergo a discontinuous change ($\Delta M_n = 0$) at the GB; the magnetization $\mathbf{M}$ rotates smoothly in the vicinity of the GB, which is due to the exchange torque L_{exc}.

(3) In macroscopic regions $\Delta x \approx 10$ mm wide near the GB, which are the greater part of the region in which the $\mathbf{M}$ distribution is inhomogeneous, the perturbations $\delta\mathbf{M}$ are due to the μ^* effect, i.e., to the departure of the atomic magnetic moments from the easy magnetization direction under the action of the magnetostatic field $\mathbf{H}^m$ arising from the GB.

REFERENCES

1. D. McLean, *Grain Boundaries in Metals* (Clarendon Press, Oxford, 1957; Metallurgiya, Moscow, 1973).
2. A. I. Mitsek and V. N. Pushkar', *Real Crystals with Magnetic Order* (Naukova Dumka, Kiev, 1978).
3. V. Randle, *The Measurement of Grain Boundary Geometry* (Inst. of Physics Publ., Bristol, 1993).
4. J. Goodenough, Phys. Rev. **95**, 917 (1954).
5. S. Chikasumi, *The Physics of Ferromagnetism: Magnetic Characteristics and Engineering Applications* (Syokabo, Tokyo, 1984; Mir, Moscow, 1987), translated from Japanese.
6. V. A. Zaĭkova, I. E. Startseva, and B. N. Fillipov, *Domain Structure and Magnetic Properties of Electrotechnical Steel* (Nauka, Moscow, 1992).
7. R. Fischer and H. Kronmuller, J. Magn. Magn. Mater. **184**, 166 (1998).
8. V. Rave and K. Ramstoch, J. Magn. Magn. Mater. **171**, 69 (1997).
9. G. Herzer, J. Magn. Magn. Mater. **157–158**, 133 (1996).
10. G. Herzer and L. K. Varga, J. Magn. Magn. Mater. **215–216**, 506 (2000).
11. L. Sheiko, G. Brekharya, S. Gaiduk, and A. Sadovoy, J. Magn. Magn. Mater. **196–197**, 813 (1999).
12. L. Sheiko, G. Brekharya, A. Sadovoy, *et al.*, J. Phys. D **32**, 2851 (1999).
13. L. Sheiko, G. Brekharya, A. Sadovoy, *et al.*, J. Magn. Magn. Mater. **215–216**, 24 (2000).
14. M. Enokizono, I. Tanabe, and T. Kubota, J. Magn. Magn. Mater. **196–197**, 338 (1999).
15. L. Sheiko, G. Brekharya, O. Kulyk, and A. Sadovoy, J. Magn. Magn. Mater. **215–216**, 86 (2000).
16. K. Senda, M. Ishida, and K. Sato, Electr. Eng. Jpn. **126** (4), 1 (1999).
17. V. G. Bar'yakhtar and Yu. I. Gorobets, *Cylindrical Magnetic Domains and Their Lattices* (Naukova Dumka, Kiev, 1988).
18. A. Hubert and R. Schafer, *Magnetic Domains* (Springer-Verlag, Berlin, 1998).
19. B. N. Filipov and L. G. Korzunin, Fiz. Tverd. Tela (St. Petersburg) **38** (8), 2442 (1996) [Phys. Solid State **38**, 1343 (1996)].

Translated by Yu. Epifanov

Physics of the Solid State, Vol. 43, No. 8, 2001, pp. 1572–1575. Translated from Fizika Tverdogo Tela, Vol. 43, No. 8, 2001, pp. 1512–1215.

MAGNETISM AND FERROELECTRICITY

Features of High-Frequency Ultrasound Propagation in the Temperature Range of Structural and Magnetic Phase Transitions in $La_{1-x}Sr_xMnO_3$ ($x = 0.175$) Manganite

Kh. G. Bogdanova*, A. R. Bulatov*, V. A. Golenishchev-Kutuzov, and M. M. Shakirzyanov***

** Zavoĭskiĭ Physicotechnical Institute, Russian Academy of Sciences, Sibirskiĭ trakt 10/7, Kazan 29, 420029 Tatarstan, Russia*

*** Kazan State Energy Research Institute, Kazan, 420066 Tatarstan, Russia*

e-mail: acustica@dionis.kfti.knc.ru

Received December 5, 2000; in final form, February 8, 2001

Abstract—The propagation of ultrasonic waves at a frequency of 770 MHz in a $La_{0.825}Sr_{0.175}MnO_3$ single crystal is investigated in the temperature range 350–150 K. It is found that the velocity, attenuation, and mode composition of ultrasonic waves change at temperatures of 315–280 and 220 K. These changes correlate with the structural and magnetic phase transitions and can be explained in terms of the Jahn–Teller distortions of the crystal lattice. © *2001 MAIK "Nauka/Interperiodica"*.

1. INTRODUCTION

Different models proposed for the explanation of a giant magnetoresistance in perovskite-like manganites, for example, the ferromagnetic–antiferromagnetic phase separation [1] and double exchange [2, 3] models, do not offer unambiguous interpretation of the experimental data. As was shown in theoretical studies (see, for example, the review by Loktev and Pogorelov [4]), this situation can be improved with the inclusion of a strong Jahn–Teller effect for Mn^{3+} ions.

Investigations of the Jahn–Teller phase transitions in ferroelectrics and magnets by ultrasonic spectroscopy [5] have demonstrated that this method can provide important information on the specific features of crystal and magnetic structures of manganites. The high efficiency of acoustical measurements was confirmed by the first experiments performed at frequencies of ~1 MHz, which revealed changes in the ultrasonic wave velocity due to structural or magnetic phase transitions [6–8].

2. EXPERIMENTAL TECHNIQUE

We carried out a detailed acoustical investigation involving measurement of the velocity and attenuation of ultrasound at frequencies three orders of magnitude higher than those used previously. The choice of the $La_{1-x}Sr_xMnO_3$ ($x = 0.175$) manganite as the object of investigation was made for the following reasons: according to the phase diagram (see Fig. 1 in [4]), this compound undergoes a number of structural and magnetic phase transitions and exhibits a giant magnetoresistance over a rather wide range of temperatures. Moreover, the transport and magnetic properties of this manganite have already been studied in a number of works. A single crystal of $La_{0.825}Sr_{0.175}MnO_3$ was grown by zone melting with an optical beam. The sample was prepared in the form of a rectangular parallelepiped ($4.85 \times 8.2 \times 7.9$ mm in size) with faces perpendicular to the [100], [010], and [001] axes to an accuracy of 0.5°. According to x-ray diffraction analysis, the sample had a single-phase composition. The ultrasonic measurements were performed on an ultrasonic spectrometer [9] operating at a frequency of 770 MHz. The longitudinal ultrasonic wave was initiated in the form of narrow acoustic pulses ($\tau_p = 1$ μs) and propagated along the [100] axis of the sample. The temperature of the sample placed in a nitrogen-flow cryostat could be changed stepwise from 350 to 150 K and in the opposite direction. At each temperature, the sample was held until a homogeneous temperature distribution over the sample was attained.

3. RESULTS

The ultrasonic measurements revealed a number of temperature anomalies in the velocity v and the attenuation coefficient α of ultrasonic waves (Figs. 1, 2). First, an increase in the velocity v_l and a decrease in the attenuation coefficient α_l of the longitudinal acoustic waves are observed in the range 325–305 K. A further decrease in temperature from 305 to 285 K leads to a drastic increase in α_l and a decrease in v_l. At $T = 285$ K, the longitudinal mode almost completely disappears.

A new acoustic mode appears in the temperature range of ~315 K (Fig. 3). This mode corresponds to transverse acoustic waves with a velocity v_t. The longitudinal and transverse modes are separated in time in

the second receiving piezoelectric transducer due to the difference between the velocities v_l and v_t. The amplitude of the transverse mode gradually increases with a decrease in temperature in the range ~315–285 K (Fig. 3). At $T = 280$ K, the v_t velocity increases sharply. With a further decrease in temperature from 275 to 230 K, the values of v_t and α_t remain virtually constant. However, at $T = 220$ K, the v_t velocity again increases and the α_t attenuation coefficient decreases. It should be noted that the transverse mode is observed over the entire temperature range (~315–150 K). In the ranges of temperature anomalies in the velocity and the attenuation coefficient, the temperature hysteresis is equal to 8–10 K.

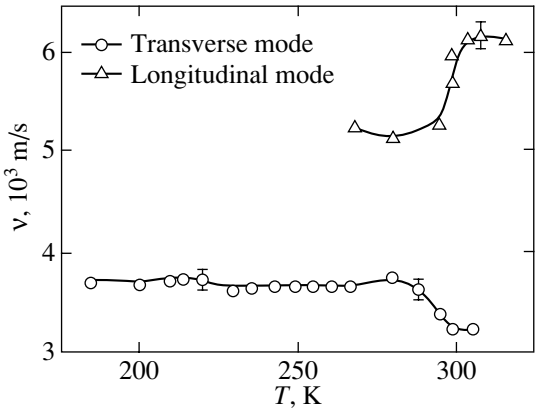

Fig. 1. Temperature dependences of the ultrasonic wave velocity.

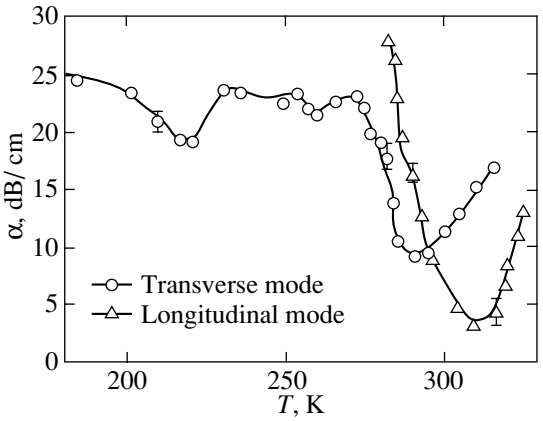

Fig. 2. Temperature dependences of the attenuation coefficient of ultrasonic waves.

4. DISCUSSION

The discussion of the results obtained will be based on the experimental data and theoretical models that describe strong coupling between the magnetic and lattice subsystems in manganites. The majority of these models are presented in reviews [1, 4].

The ABO_3 perovskite should ideally have a cubic structure [4]. This structure can be represented as a combination of vertex-shared octahedra BO_3. Each octahedron is formed by the B ion located at its center and by oxygen ions in its vertices. Each ligand formed by O^{2-} ions is shared by two nearest octahedra. As a consequence, independent rigid rotations of individual octahedra are hindered [4]. Perovskites with a cubic symmetry are rarely occur. The lowering of the symmetry can be caused by the displacement of ligand ions from the equilibrium positions in a cube due to regular rotations or deformations of octahedra without a change in the location of B transition metal ions at their centers. The rotation of an octahedron about the [110] axis of a cube leads to an orthorhombic distortion ($a \neq b \neq c$ and $\alpha = \beta = \gamma = 90°$), and the rotation of an octahedron about the [111] axis brings about a rhombohedral distortion. The factors responsible for the lattice distortion in $La_{1-x}Sr_xMnO_3$ crystals can be divided into two groups: (1) the misfit of cation sizes upon the intervalent substitution $La^{3+} \longrightarrow Sr^{2+}$ and the change in the valence state of the ion with an intermediate valence $Mn^{3+} \longrightarrow Mn^{4+}$ upon doping with Sr^{2+} ions and (2) the cooperative Jahn–Teller effect for Mn^{3+} ions. In this case, the removal of the existing twofold and threefold degeneracies of the e_g and t_{2g} sublevels results in displacement of the O^{2-} ions. The strongest octahedron deformation can be observed in the (001) plane. Consequently, cubic manganite transforms into orthorhombic manganite with two Mn ions per unit cell; i.e., the unit cell is doubled [4]. The decisive role of Jahn–Teller lattice distortions manifests itself in a change in the crystal structure, depending on the degree of doping. For example, at $T > T_c$, the crystals have an orthorhombic lattice in the range $0 \le x \le 0.15$ and a rhombohedral lattice at $x \ge 0.15$. The transition to a higher symmetry cannot be explained by the first factor but is quite consistent with the Jahn–Teller effect. Actually, an increase in x should lead to a decrease in the Jahn–Teller distortion due to both the decrease in the concentration of Mn^{3+} ions upon the $Mn^{3+} \longrightarrow Mn^{4+}$ transition and the thermostimulated redistribution of charge states $2Mn^{3+} \longrightarrow Mn^{4+} + Mn^{2+}$ with an increase in the temperature. The magnetic structure of manganites below the transition is primarily determined by the degree of doping [10]. At $0 \le x \le 0.15$, the manganites have an antiferromagnetic structure. In this case, the magnetizations of the adjacent basal planes (001) are directed toward each other as the result of a weak interplanar exchange interaction. As x increases in the range 0.15–0.5, the antiferromagnetic ordering gives way to ferromagnetic ordering. This can be explained by the increase in the concentration of Mn^{4+} ions and the strong exchange interaction between Mn^{3+} and Mn^{4+} ions. Within the model of double charge exchange [2, 3], metallic conductivity at $T \le T_c$ in the range $0.15 \le x \le 0.5$ arises only

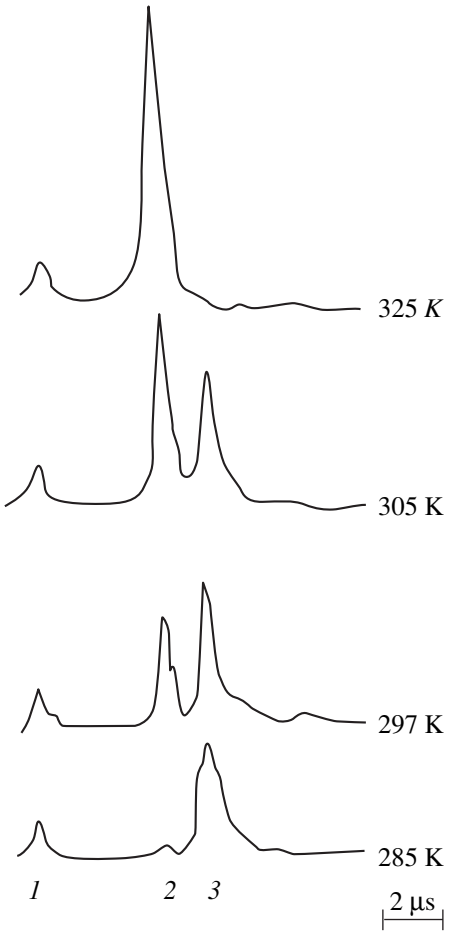

Fig. 3. Oscillograms of ultrasound pulse propagation through the sample: (*1*) exciting electromagnetic pulse, (*2*) pulse of the longitudinal acoustic mode after passage through a composite resonator, and (*3*) pulse of the transverse acoustic mode.

when the spins of the *d* shells of Mn^{3+} and Mn^{4+} ions are parallel to each other and free-carrier hopping from one ion to the next ion in the Mn^{4+}–O^{2-}–Mn^{3+} system occurs virtually without energy loss. The Jahn–Teller effect gives rise to an additional barrier to carrier motion, because each carrier hopping between the sites occupied by Mn ions results in a local change in the ion valence and, hence, a local deformation displacement of the ligands. Therefore, the carrier becomes a magnetoelastic polaron, which brings about further narrowing of the conduction band [11].

According to the Millis–Littlewood–Shraiman model [11], the collectivization of Jahn–Teller distortions of particular cells leads to a considerable increase in the electrical resistivity at temperatures above T_c. The magnetic phase transition to the ferromagnetic phase results in suppression of the Jahn–Teller distortions due to an increase in magnetization, and the resistivity decreases drastically, which is characteristic of the compounds with $x \sim 0.175$ [12]. The application of an external magnetic field up to several teslas almost completely suppresses the Jahn–Teller distortions, which gives rise to a giant magnetoresistance in the range 300–200 K at $x \sim 0.175$. We believe that the generalized model of the double exchange and Jahn–Teller distortions explains the results obtained.

In our opinion, the high velocity v_l in the temperature range 325–305 K is associated with an increase in the acoustic stiffness of the crystal in the rhombohedral phase, which agrees with the results obtained by Darling *et al.* [6]. As was shown in [11], the increase in the acoustic stiffness is caused by the decrease in the mean amplitude of octahedron rotations upon transition to the rhombohedral phase.

The drastic increase in the attenuation coefficient α_l and the decrease in the velocity v_l in the temperature range ~305–285 K can be explained by the structural phase transition from the rhombohedral to the orthorhombic phase, which is accompanied by a decrease in the acoustic stiffness of the sample. As was noted above, the decrease in the acoustic stiffness is associated with the enhancement of the Jahn–Teller effect for Mn^{3+} ions [5], whose concentration increases upon transformation of Mn^{4+} ions into Mn^{3+} ions in the studied range [4]. The temperature range of the structural phase transition corresponds to a change in the type of electrical resistivity, which was revealed earlier in [12]. The observed jumps in the velocity v_t and the attenuation coefficient α_t at $T \approx 280$ K correspond to the magnetic phase transition, which is also attended by an increase in the acoustic stiffness. The increase in the acoustic stiffness is quite consistent with the theoretical model proposed by Lee and Min [13], according to which the velocity of an acoustic wave increases and its attenuation decreases at $T < T_c$. These changes in the elastic parameters after the transition of the studied crystal to the ferromagnetic state are explained by a partial suppression of the Jahn–Teller distortions of the crystal lattice due to spontaneous deformations caused by the sample magnetization. Usually, upon similar magnetic transitions, the ultrasonic attenuation at temperatures below T_c in the absence of the Jahn–Teller effect increases as the result of scattering by magnetic domains [3]. The changes in the velocity v_t and the attenuation α_t at $T = 220$ K can be brought about by another structural transition, which is associated with further suppression of the Jahn–Teller distortions due to the increase in magnetization. The appearance of the new acoustic mode should apparently be ascribed to a strong magnetoelastic interaction. Consequently, this mode can be treated as a transverse magnetoelastic mode. This is also confirmed by the electromagnetic generation of sound at temperatures close to T_c, which was observed in [7]. A sharp decrease in the intensity of the longitudinal mode indicates the energy transfer to the magnetoelastic mode.

As follows from the above analysis of the changes in the velocity and attenuation of the longitudinal and transverse acoustic waves, the spin–phonon interaction is determined by the magnetostriction of particular unit cells rather than by the magnetostriction of the sample as a whole, because the bulk effect does not bring about changes in the transverse modes [14]. Thus, our experimental results demonstrated that the degree of deformation of unit cells in the crystal structure can be determined using ultrasonic spectroscopy.

According to the results obtained by Asamitsu *et al.* [15], the magnetic field, when applied at temperatures in the range 300–200 K, brings about an increase in the acoustic stiffness of the crystal. This indicates that the Jahn–Teller distortions of the crystal lattice are suppressed, and, as a consequence, the crystal undergoes a transition to the rhombohedral phase. Therefore, it can be assumed that, in the case of a strong exchange, the giant magnetoresistance phenomenon in the studied samples in the temperature range 300–200 K is caused by the complete suppression of Jahn–Teller lattice distortions.

ACKNOWLEDGMENTS

We are grateful to A.M. Balbashov for supplying the manganite single crystals.

This work was supported by the Russian Foundation for Basic Research, project no. 99-02-16268.

REFERENCES

1. É. L. Nagaev, Usp. Fiz. Nauk **166** (8), 833 (1996) [Phys. Usp. **39**, 781 (1996)].
2. C. Zener, Phys. Rev. **82**, 403 (1951).
3. X. Wang and A. E. Freeman, J. Magn. Magn. Mater. **171**, 103 (1997).
4. V. M. Loktev and Yu. G. Pogorelov, Fiz. Nizk. Temp. **26** (3), 231 (2000) [Low Temp. Phys. **26**, 171 (2000)].
5. L. Melcher, in *Physical Acoustic*, Ed. by W. P. Mason (Academic, New York, 1976), Part 1.
6. T. W. Darling, A. Migliori, E. G. Moshopoulon, *et al.*, Phys. Rev. B **57** (9), 5093 (1998).
7. Yu. P. Gaĭdukov, N. P. Danilova, A. A. Mukhin, and A. M. Balbashov, Pis'ma Zh. Éksp. Teor. Fiz. **68** (2), 141 (1998) [JETP Lett. **68**, 153 (1998)].
8. Yu. P. Gaĭdukov, N. P. Danilova, N. A. Vasil'eva, A. M. Balbashov, and Ya. M. Mukovskiĭ, in *Proceedings of the XVII International School–Workshop "Novel Magnetic Materials in Microelectronics"* (Mosk. Gos. Univ., Moscow, 2000), p. 799.
9. Kh. G. Bogdanova, V. A. Golenishchev-Kutuzov, V. E. Leont'ev, *et al.*, Prib. Tekh. Éksp., No. 4, 60 (1997).
10. E. O. Wollan and W. C. Kochler, Phys. Rev. **100**, 545 (1955).
11. A. I. Millis, R. B. Littlewood, and B. I. Shraiman, Phys. Rev. Lett. **74**, 5144 (1995).
12. A. Urushibara, Y. Morimoto, T. Arima, *et al.*, Phys. Rev. B **51**, 14103 (1995).
13. J. D. Lee and B. I. Min, Phys. Rev. B **55** (18), 12454 (1997).
14. H. S. Bennet and E. Pytte, Phys. Rev. **155**, 533 (1967).
15. A. Asamitsu, Y. Morimoto, Y. Tomioka, *et al.*, Nature (London) **373**, 407 (1995).

Translated by O. Borovik-Romanova

Physics of the Solid State, Vol. 43, No. 8, 2001, pp. 1576–1579. Translated from Fizika Tverdogo Tela, Vol. 43, No. 8, 2001, pp. 1516–1519.

MAGNETISM AND FERROELECTRICITY

The Contributions from Different Mechanisms of Motion of Domain Boundaries to the Effective Permittivity of Triglycine Sulfate Crystals in Moderate Low- and Infralow-Frequency Fields

A. V. Shil'nikov*, A. P. Pozdnyakov*, V. N. Nesterov*, V. A. Fedorikhin*, and L. A. Shuvalov**

**Volgograd State Architectural and Building Academy, Volgograd, 400074 Russia*

***Shubnikov Institute of Crystallography, Russian Academy of Sciences, Leninskiĭ pr. 59, Moscow, 117333 Russia*

e-mail: postmaster@vgasa.ru

Received December 20, 2000

Abstract—A study of the special features of contribution of domain boundaries to the effective permittivity ε_{eff}^{*} of a TGS crystal is made in electric fields of various frequencies and in a wide temperature range of the polar phase, up to the phase transition temperature. In considering the experimental data obtained, we classify the defects into three types depending on their interaction strength with the domain boundaries. Using the approach developed, we explain the frequency and temperature dependences of the contributions from the hysteretic and relaxation mechanisms of motion of the domain boundaries to ε_{eff}^{*}. *© 2001 MAIK "Nauka/Interperiodica".*

1. INTRODUCTION

It is well known that the study of the processes of polarization and polarization reversal in ferroelectrics plays an important role both in investigations into the fundamental properties of these materials and in considering their possible applications [1–3]. Of special importance is the determination of the character of interaction of domain walls (DWs) with defects of the crystal lattice. In earlier works on direct observation of DW motion in crystals of Rochelle salt (RS) and KDP, Mitsui and Furuichi observed continuous growth of the domains hand in hand with discontinuous growth [4, 5]. Further investigations, performed using both direct and indirect [6–8] methods, verified their hypothesis on the existence of hysteretic and relaxation mechanisms of polarization reversal. By the relaxation mechanism of the polarization reversal is meant a mechanism for which the DW motion is continuous (the resistance to their motion is analogous to viscous friction) and due to thermal activation of nuclei [9], while the polarization reversal mechanism that is associated with the jumplike DW motion is called the hysteretic mechanism (by analogy with dry friction); each jump is assumed to correspond to the switching of some macroscopic volume near the DW when the electric field attains a certain value (field-activated nucleation) [10–12].

In [7], it was noted that some information on the character of the domain contribution to the RS crystal polarization can be obtained from oscillograms of ferroelectric hysteresis loops (FHLs) in fields of various amplitudes and at different temperatures. In [11], by analyzing the amplitude dependences of the real $(\varepsilon_{eff}^{'})$ and imaginary $(\varepsilon_{eff}^{''})$ parts of the effective permittivity ε_{eff}^{*} and of the differential coefficient of electromagnetic-field energy dissipation $\gamma = \Delta\varepsilon''/\varepsilon'$ of TGS crystals, and by investigating FHLs, the DW dynamics was found to differ in character at different amplitudes of the polarization-switching field.

In further progress in studying the mechanisms of DW motion, attempts were undertaken [12–14] to classify DW motion mechanisms on the basis of dielectric spectra of the complex effective dielectric permittivity ε_{eff}^{*} and the corresponding FHL oscillograms of some model ferroelectrics (RS, TGS, KDP, and others) in electric low- (LF) and infralow-frequency (ILF) fields. Those findings formed the basis for a model [15] which allows one to quantitatively separate the contributions of different DW motion mechanisms to the LF and ILF dielectric properties of ferroelectrics and related materials by analyzing the shape of FHLs. In [16], an attempt was made to analyze the FHL parameters and quantitative contributions from different DW motion mechanisms to ε_{eff}^{*} in combination with visual observations of polarization reversal.

In this work, we studied the contribution of DWs to ε_{eff}^{*} of a TGS crystal in electric fields of various (LF and ILF) frequencies and the evolution of strong and

1063-7834/01/4308-1576$21.00

weak defects interacting with the DWs under variation in the frequency of the polarization-switching field over a wide temperature range, including the phase transition (PT) point.

2. EXPERIMENTAL TECHNIQUE AND SAMPLES

The experimental study and analysis of the main features of the contributions from relaxation and hysteretic mechanisms of DW motion to the LF and ILF permittivities ε'_{eff} and ε''_{eff} were carried out by computer processing of a family of FHLs (for details, see [17, 18]) measured with the help of an oscillograph and recorded in a sinusoidal electric field of an amplitude of $E_0 = 74$ V/cm (this is the typical polarization-switching field in which the most significant contribution of the DWs to ε^*_{eff} is observed) at frequencies $\nu = 0.05$, 0.1, 1.10, and 90 Hz in the polar phase. The contributions from the hysteretic and relaxation mechanisms of the DW motion to ε'_{eff} and ε''_{eff} of the TGS crystal were determined. The TGS crystal was in the form of a plane-parallel plate $d = 1.1$ mm thick of a Y cut with the surfaces polished to optical quality. Silver electrodes of an area of $S = 15$ mm^2 each were applied onto the surfaces of the polar cuts through the rolling of a thin foil. Measurements were taken with the use of an electronic temperature stabilizer in a feedback bridge arrangement in a quasi-steady-state temperature regime (the crystal was held at each temperature for a minimum of 30 min). The accuracy of maintaining the temperature was no worse than 0.05 K, and its measurement accuracy was to within 0.001 K.

3. EXPERIMENTAL RESULTS AND DISCUSSION

As in the case of TGS and DTGS crystals [18, 19], the shape and the size of FHLs of the TGS crystals investigated in this work essentially depend on the frequency of the polarization-switching field (with the field amplitude E_0 kept constant). In the case under consideration, the applied field is equal to $E_0 = 74$ V/cm; in this case, a sizable part of the sample volume is subjected to switching and its size depends on the frequency of the polarization-switching field (frequency dispersion of the switched crystal volume is observed). One can maintain with a fair degree of assurance that, as is the case with RS crystals [20], the DWs interact differently with defects of the crystal lattice at different frequencies (strong defects are transformed into weak defects, and/or the reverse occurs). One might also expect similar phenomena to arise when investigating the temperature dependences of the contributions from the hysteretic and relaxation mechanisms of the DW motion to ε'_{eff} and ε''_{eff} provided that the frequency and amplitude of the polarization-switching field are constant.

Let us consider the frequency dependences (Fig. 1) of the (percentage) contributions from the hysteretic (ε'_g) and relaxation (ε'_r) mechanisms of the DW motion to ε'_{eff} at temperatures of 19.1 and 35.8°C. (Notice that the $\varepsilon''_g(T, \nu)$ and $\varepsilon''_r(T, \nu)$ dependences behave in a similar way.) It can be seen that the character of the $\varepsilon'_g(\nu)$ and $\varepsilon'_r(\nu)$ dependences drastically changes in going from $T_1 = 19.1$ to $T_2 = 35.8$°C. For example, at T_1, as the frequency of the polarization-switching field increases, the contribution from the hysteretic mechanism (ε'_g) of the DW motion to ε'_{eff} first increases then passes through a flat maximum and decreases. At T_2, all things occur in a different manner (Fig. 1a). As for the contribution from the relaxation mechanism (ε'_r) of the DW motion to ε'_{eff}, it is characterized by opposite dependences (Fig. 1b) to those presented in Fig. 1a.

Let us imagine the situation that possibly occurs at temperatures $T_1 < T_2$. Here, at very low frequencies, a significant part of the weak defects interacting with the DWs are able to follow them when the latter move in an

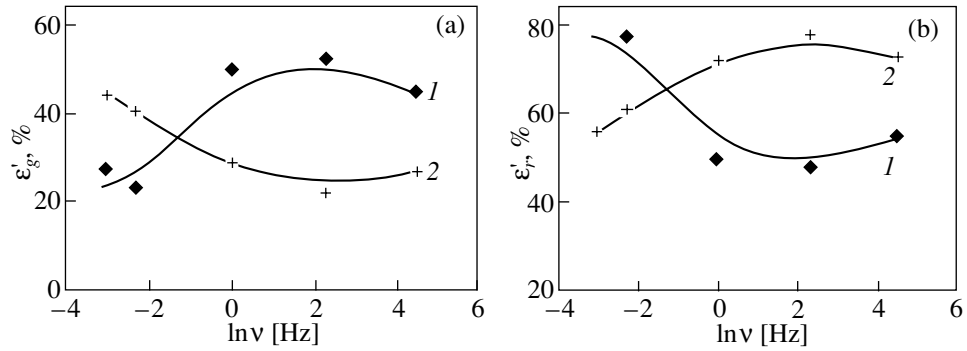

Fig. 1. Frequency dependences of the contributions (in percent) from (a) the hysteretic and (b) relaxation mechanisms of the DW motion to ε'_{eff} in a sinusoidal electric field of an amplitude of $E_0 = 74$ V/cm at temperatures (*1*) 19.1 and (*2*) 35.8°C.

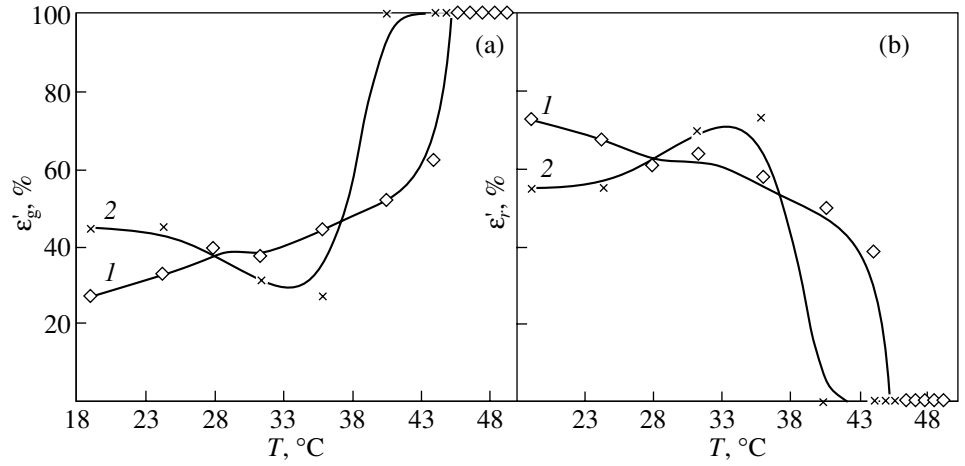

Fig. 2. Temperature dependences of the contributions (in percent) from (a) the hysteretic and (b) relaxation mechanisms of the DW motion to ε'_{eff} in a sinusoidal electric field of an amplitude of E_0 = 74 V/cm at frequencies (*1*) 0.05 and (*2*) 90 Hz.

irreversible way. In this case, such DWs move continuously (forces resisting their motion are similar to viscous friction forces) and the relative contribution from the relaxation mechanism of the DW motion to ε^*_{eff} is larger than that from the hysteretic one. As the frequency increases, some of the weak defects are transformed into moderate (intermediate) defects which are not able to follow the DWs, but, nevertheless, they do not pin the DWs which freeze them. Breaking away from these defects as from weak stoppers, the DWs move discontinuously at a given amplitude of the polarization-switching field subjected to drag forces similar to dry-friction forces. In this case, the contribution from the hysteretic DW motion mechanism to ε^*_{eff} increases at the expense of the relaxation mechanism (the relative contribution of the latter decreases). Finally, upon further increase in frequency ν, some defects grow in strength so that they become able to pin the DWs which freeze them (strong defects). If this is the case, some DWs oscillate between the neighboring strong defects that pin them [21]; their motion is reversible and their contribution to ε^*_{eff} corresponds to the relaxation mechanism. The contribution from the hysteretic DW motion mechanism to ε^*_{eff} decreases because of the increase in the contribution from the relaxation mechanism; this was observed experimentally (Fig. 1).

At $T_2 > T_1$, when thermal activation plays a more essential role, a larger part of the crystal volume is involved in the polarization-switching process (and, accordingly, a much larger number of DWs and defects interacting with them are involved). Now, some of the defects that were strong at T_1 and at the corresponding frequency ν turn into moderate defects and some of the moderate-strength defects turn into weak defects. In this case, the following process is possible at temperature T_2. As the frequency ν of the polarization-switching field increases, some of the weak defects turn into moderate defects and some of the moderate-strength defects turn into strong defects. If the second process is faster than the first, one will observe a decrease in the contribution from the hysteretic DW motion mechanism to ε^*_{eff} and an increase in the contribution from the relaxation mechanism to ε^*_{eff}. This takes place for the ε'_g and ε'_r dependences for the most part of the frequency region investigated (Figs. 1a, 1b, respectively). When the frequency ν attains a certain limiting value (which is defined by the temperature of the sample, by the quantity and quality of the defects present in it, by the amplitude of the polarization-switching field, etc.), the first process becomes faster than the second. In this case, one observes an increase in the contribution from the hysteretic mechanism and a decrease in the contribution from the relaxation mechanism to ε^*_{eff} (Figs. 1a, 1b, respectively).

In Fig. 2, the temperature dependences of the contributions to ε_{eff} (expressed in percent) from the hysteretic (ε'_g) and the relaxation (ε'_r) mechanisms of the DW motion are presented. It is clear from Fig. 2 that, far away from the PT, the relaxation DW motion is dominant (its contribution exceeds 50%) in the sample for all frequencies investigated. With increasing temperature, a redistribution between the DW motion mechanisms occurs, and on approaching the PT, the hysteretic mechanism becomes the main mechanism of the DW motion. Let us trace how the redistribution between the mechanisms can occur and how it depends on the frequency of the electric field.

As is seen from Fig. 2, there is a difference in behavior between the $\varepsilon_g(T)$ and $\varepsilon'_r(T)$ dependences for the various frequencies investigated. For example, for the

frequency $\nu = 0.05$ Hz, a continuous increase in the contribution from the hysteretic DW motion mechanism to ε'_{eff} is observed with increasing temperature (the opposite situation takes place for $\varepsilon'_r(T)$. This can be explained by the fact that, at very low frequencies of the applied field, the effective amplitude of the DW oscillations (and, accordingly, the crystal volume subjected to switching) will be large even at room temperature. In this case, some of the DWs moving in an irreversible way involve a substantial number of the moderate defects and, as a result, the DW motion is controlled by the hysteretic mechanism (the DWs experience a resistance analogous to dry friction). It is clear that with increasing temperature, the relative contribution to ε'_{eff} from the motion of these DWs is increased.

At higher frequencies ($\nu = 90$ Hz) and at relatively low temperatures, the effective amplitude of the DW oscillations is small and the motion of a significant part of the DWs is reversible; that is, it is controlled by a relaxation mechanism analogous to viscous friction. A rise in temperature leads to an increase in lability of the crystal lattice and, consequently, of the lattice defects. As a result, some of the moderate defects turn into weak defects. The latter are able to follow the DWs in the process of the sample switching [20], thereby increasing the contribution from the relaxation mechanism of the DWs to ε'_{eff}. For this reason, the increase in the contribution from the relaxation mechanism of the DW motion (reversible and irreversible relaxation DW motion) to ε'_{eff} takes place up to $T \approx 35$°C. At temperatures $T > 35$°C, the DWs move basically in an irreversible way, contributing both to the relaxation and hysteretic mechanisms of the DW motion. In this case, as the temperature increases, the role of the latter mechanism grows, because the DW oscillation amplitude increases and the moderate defects involved in the process of the DW motion increase in number.

Thus, on the basis of the experimental data obtained, we can make the conclusion that a redistribution between the hysteretic and relaxation mechanisms of the DW motion takes place, because these mechanisms are associated with defects that are modified as the temperature and the frequency of the polarization-switching field are varied. It should be emphasized that, as the PT is approached, the role of the hysteretic mechanism increases and it becomes predominant over the relaxation mechanism in the vicinity of the PT point for all frequencies investigated, because the switched volume of the TGS sample increases.

ACKNOWLEDGMENTS

This work was supported by the Russian Foundation for Basic Research and by the Ministry of Education of the Russian Federation (the Competition Center Foundation).

The authors are grateful to A.S. Sigov for useful discussions.

REFERENCES

1. L. A. Shuvalov, Izv. Akad. Nauk SSSR, Ser. Fiz. **28**, 660 (1964).
2. J. C. Burfoot, *Ferroelectrics: an Introduction to the Physical Principles* (Van Nostrand, New York, 1967; Mir, Moscow, 1970).
3. S. A. Sonin and B. V. Strukov, *An Introduction in Ferroelectricity* (Vysshaya Shkola, Moscow, 1970).
4. T. Mitsui and Y. Furuichi, Phys. Rev. **90** (2), 193 (1953).
5. T. Mitsui and Y. Furuichi, Phys. Rev. **95** (2), 558 (1954).
6. V. É. Rudyak, L. A. Shuvalov, and V. N. Kamaev, Izv. Akad. Nauk SSSR, Ser. Fiz. **29**, 943 (1965).
7. É. S. Popov, S. L. Rapoport, and A. V. Shil'nikov, Izv. Akad. Nauk SSSR, Ser. Fiz. **31**, 1199 (1967).
8. A. V. Shil'nikov, É. S. Popov, and S. L. Rapoport, Kristallografiya **14**, 1028 (1969) [Sov. Phys. Crystallogr. **14**, 890 (1969)].
9. R. C. Miller and G. Weinreich, Phys. Rev. **117**, 1460 (1954).
10. É. S. Popov and S. L. Rapoport, Kristallografiya **13** (2), 278 (1968) [Sov. Phys. Crystallogr. **13**, 216 (1968)].
11. A. V. Shil'nikov, in *Physics of Dielectrics and Semiconductors* (Volgograd, 1970), p. 95.
12. A. V. Shil'nikov, Author's Abstracts of Candidate's Dissertation (VGPI, Voronezh, 1972).
13. A. V. Shil'nikov, Author's Abstracts of Doctoral Dissertation (Inst. Fiz. Akad. Nauk Latv. SSR, Salaspils, 1988).
14. A. V. Shil'nikov, N. M. Galiyarova, S. V. Gorin, *et al.*, Izv. Akad. Nauk SSSR, Ser. Fiz. **55** (3), 578 (1991).
15. A. V. Shil'nikov, V. N. Nesterov, and A. I. Burkhanov, Ferroelectrics **175**, 145 (1996).
16. L. I. Dontsova, L. G. Bulatova, A. V. Shil'nikov, and N. A. Tikhomirova, in *Physics of Dielectrics and Semiconductors* (Volgograd, 1986), p. 165.
17. A. V. Shil'nikov, V. N. Nesterov, A. P. Pozdnyakov, *et al.*, Ferroelectrics **222**, 317 (1999).
18. A. V. Shil'nikov, A. P. Pozdnyakov, V. N. Nesterov, *et al.*, Ferroelectrics **223**, 149 (1999).
19. A. V. Shil'nikov, L. A. Shuvalov, V. A. Fedorikhin, *et al.*, Fiz. Tverd. Tela (St. Petersburg) **41** (6), 1073 (1999) [Phys. Solid State **41**, 977 (1999)].
20. R. Abe, Jpn. J. Appl. Phys. **3** (5), 243 (1964).
21. A. V. Shil'nikov, Izv. Akad. Nauk SSSR, Ser. Fiz. **51** (10), 1726 (1987).

Translated by N. Kovaleva

Physics of the Solid State, Vol. 43, No. 8, 2001, pp. 1580–1584. Translated from Fizika Tverdogo Tela, Vol. 43, No. 8, 2001, pp. 1520–1524.

MAGNETISM AND FERROELECTRICITY

Short-Lived Color and Luminescence Centers in $LiNbO_3$ Crystals Irradiated by Pulsed Electron Beams

V. Yu. Yakovlev*, E. V. Kabanova*, T. Weber, and P. Paufler****

**Tomsk Polytechnical Institute, pr. Lenina 30, Tomsk, 634034 Russia*

***Institute of Crystallography and Solid State Physics, Dresden, Germany*

e-mail: yak@list2.epd.tpu.edu.ru

Received January 18, 2001

Abstract—Data on spectra of short-lived optical absorption (SLOA) and luminescence induced in congruent crystals of lithium niobate by a pulsed electron beam (0.25 MeV, 20 ns, 15–160 mJ/cm^2) in a temperature range of 80 to 350 K are presented. Anisotropic bands with maxima at 1.6 and 4.0 eV, originating from the capture of one and two conduction electrons by an (Nb_{Nb}–Nb_{Li}) complex, respectively, and weakly polarized bands at 2.5 and 3.3 eV due to holes located at Li and Nb vacancies are identified in the structure of SLOA spectra. Cathodoluminescence (CL) of lithium niobate crystals is characterized by fast ($\tau < 4$ ns) decay and a broad spectrum, which contains the same bands as the SLOA spectra. It is shown that the change in the initial amount of defects in reduced crystals at 830 K results in an identical change in both the CL and SLOA spectra. A model which treats the luminescence as the result of radiative nonphonon transitions that accompany the thermalization of charge carriers captured into the ground state of a polaron is discussed. © *2001 MAIK "Nauka/Interperiodica".*

1. INTRODUCTION

Ferroelectric niobate crystals have found wide application in various electro- and acousto-optical devices and as a passive component in integrated optics. The properties of these crystals are determined, in many respects, by their structural defects, both those intrinsic and originating under exposure to radiation and other treatments. Therefore, a large number of papers were devoted to the study of these defects (see, e.g., review [1]). Many authors have observed changes in the light absorption by $LiNbO_3$ crystals in stationary measurement conditions after exposure to ionizing radiation [2–6] or after annealing in a reducing atmosphere (in vacuum) [7–9]. On the basis of data on optical and EPR spectra, the structure of a number of intrinsic color centers, of both electron and hole nature, was reliably determined. The origin of these centers was associated with a change in the charge state of Li and Nb vacancies due to crystal nonstochiometry and also with complexes containing antisite defects (Nb^{5+} ions) at the Li sites.

Information on the luminescence of $LiNbO_3$ crystals excited by various kinds of stationary radiation that differ in their history has been presented in many papers [1, 5, 10, 11]. Their luminescence is characterized by a low yield and a complicated spectral structure, which depends largely on the kind of exciting radiation used, the stochiometric composition [5], and the presence of structural mechanical or radiation damage [10]. The nature of the luminescence band at 2.8 eV in nonactivated crystals is usually connected with the radiative recombination of electrons and holes captured by defects [5, 11]; however, the mechanisms of the luminescence and of the influence of various external factors on its characteristics remain unexplained. The questions of possible defect formation in the anionic subsystem of the crystal and of self-localization and decay of electron excitations in the lattice regions without defects are also open.

The purpose of the present paper is to study the dynamics of formation and decay of short-lived defect states created in a lithium niobate crystal by exposure to short pulses of accelerated electrons using luminescence and optical-absorption spectrometry with nanosecond temporal resolution.

2. EXPERIMENT

We used monocrystal $LiNbO_3$ samples which were grown in the Institute of Crystallography and Solid State Physics (Dresden) and had an approximately congruent composition. The samples were cut out and polished in the form of rectangular plates of dimensions $1 \times 5 \times 8$ mm; the *z* axis of the crystal was along its long edge. Samples were put in an optical cryostat with quartz windows. The *z* axis lied in the plane of observation, and the sample was irradiated by a pulse of accelerated electrons (0.25 MeV, 20 ns, 12–150 mJ/cm^2) at a temperature in the range from 80 to 350 K.

The change in optical transmission of the sample induced by pulse irradiation was registered with the help of a high-speed spectrometer, which included a pulse source from a light probe (a flash lamp), a con-

denser system, an MDR-3 grating monochromator, and a broadband S8-12 storage oscilloscope. The temporal resolution of the spectrometer was 7 ns. The spectral sensitivity of the measuring system was calibrated with the help of standard lamps. A Rochon quartz prism was used for studying the polarization properties of the optical spectra.

3. RESULTS AND DISCUSSION

3.1. Spectra of Transient Optical Absorption

The exposure of $LiNbO_3$ crystals to radiation by a single pulse of accelerated electrons results in their coloring in a wide spectral range from 4.0 to 1.0 eV with maximum absorption at approximately 2.5 eV for all crystals (Fig. 1a). For any photon energy, the increase in optical density occurred instantaneously in terms of the duration of exciting pulses $\tau \le 4$ ns.

Analysis of the spectral structure using the Alentsev–Fock method [12] and data on stable coloring [4, 5] showed that the experimental curves can be well described by a set of Gaussians (they are shown by solid lines in Fig. 1a) with maxima at 1.6, 2.5, 3.3, and 4.0 eV. By measuring spectra in polarized light, it was found that the induced absorption is noticeably anisotropic; the spectral distribution of the absorption dichroism $d = (D_\parallel - D_\perp)/(D_\parallel + D_\perp)$ is shown in Fig. 2 ($D_\parallel$ and $D_\perp$ are the optical densities measured in the cases where the transmission plane of the analyzer is parallel and perpendicular to the z axis of the crystal, respectively). The bands at 1.6 and 4.0 eV, as follows from the data in Fig. 2, are polarized and characterized by approximately the same value of d equal to +0.25; they are likely to be associated with absorption centers with preferred orientation of the dipole moments of electron transitions along the z axis of the crystal. This conclusion is in good agreement with the assumption [8] that the band at 1.6 eV is associated with small electron polarons—electrons captured by (Nb_{Nb}–Nb_{Li}) complexes that are also directed along the z axis.

As for the band at 4.0 eV, we note that a band with similar spectral parameters was recently observed when experimentally investigating photochromic effects in reduced $LiNbO_3$ crystals [9]. According to a model suggested in [9], so-called Q bipolarons, which are formed when two electrons are captured by a defect consisting of two Nb ions at Li sites (Nb_{Nb}–Nb_{Li} complexes), are responsible for the band at 4.0 eV. However, the pronounced anisotropy of the band at 4.0 eV (Fig. 2) obviously contradicts that model. A direct comparison of the spectra from [9] with those obtained in early similar experiments [5] reveals their qualitative similarity; this suggests that ordinary bipolarons localized at (Nb_{Nb}–Nb_{Li}) complexes, which exist in large amounts in congruent crystals, are responsible for the band at 4.0 eV (and also for a number of less intensive accompanying bands distinguished by the authors of [9]). The relatively weak dichroism of the bands at 1.6 and 4.0 eV indicates that the transitions are not strictly axial. We relate this fact to the influence of the Coulomb field of the Nb vacancy, which locally compensates the charge of antisite defects in the Nb_{Li}^{4+}–V_{Nb}^{5-} complexes [1].

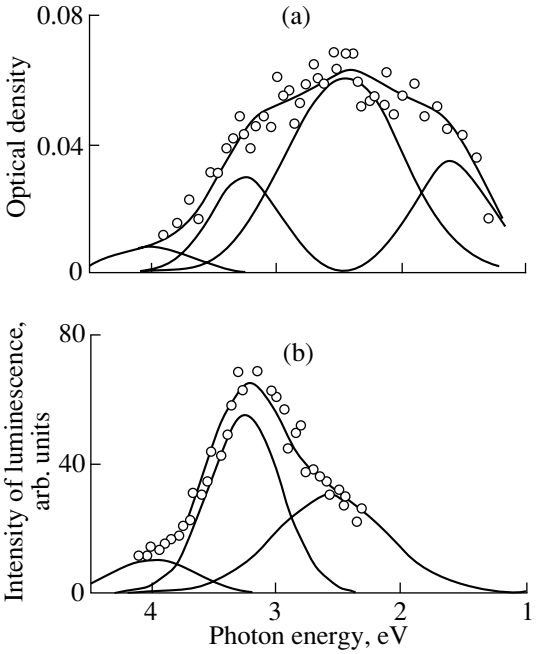

Fig. 1. Spectra of (a) SLOA and (b) CL measured at the instant of termination of pulsed electron irradiation of an $LiNbO_3$ crystal at 295 K. Points represent experimental data, and solid lines are the result of deconvolution into Gaussians.

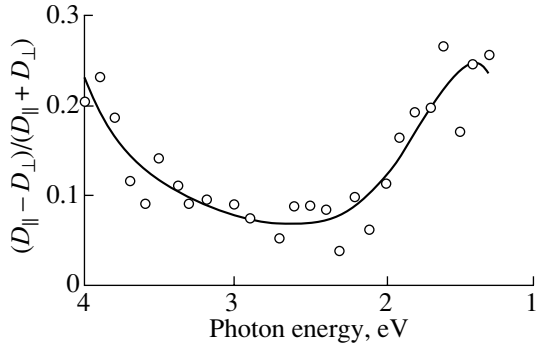

Fig. 2. Spectral distribution of dichroism of the SLOA induced by pulsed irradiation of an $LiNbO_3$ crystal at 295 K.

The parameters of the isotropic short-lived optical absorption (SLOA) bands at 2.5 and 3.3 eV coincide with the parameters of earlier distinguished bands in the spectra of samples exposed to x-ray radiation [2, 5]; therefore, it is reasonable to assume that these bands are due to hole polarons—O^- centers located near Li and Nb vacancies, respectively.

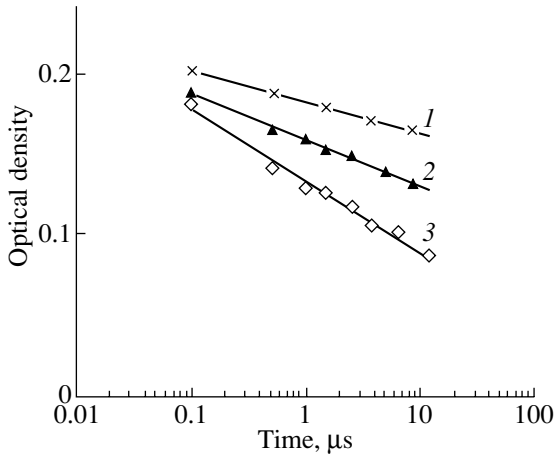

Fig. 3. Kinetic dependences of optical-density relaxation after pulsed irradiation of an $LiNbO_3$ crystal at various temperatures *T*, K: (*1*) 80, (*2*) 295, and (*3*) 350.

3.2. Kinetics of Color-Center Recombination

We observed isothermal relaxation of induced absorption after the termination of pulse irradiation at various temperatures in the range from 80 to 400 K. The relaxation ranged in duration from 10^{-8} to 10^{3} s; however, the intensity of coloring fell in time identically for various parts of the spectrum. Therefore, the shape of the spectrum did not change with time.

Figure 3 shows the optical-density decay curves at 1.6 eV after irradiation by isodose pulses at 80, 295, and 350 K. It is seen that, as the temperature is increased above 80 K, the relaxation processes become significantly faster, while the initial absorption intensity is weakly dependent on temperature. Taking into account the spectral-analysis data, this temperature behavior of the transient absorption can be interpreted as a typical consequence of the formation of color centers through the radiation-generated band carriers being captured by crystal defects. This mechanism is also supported by the character of the optical density decreasing in time, $D(t)$. The shape of the decay curves, which are close to straight lines in the $D(t)$–$\log t$ coordinates, corresponds best to the law describing, within the framework of formal kinetics, the recombination of the centers in donor–acceptor pairs through diffusion-controlled tunneling charge exchange [13]. The extrapolated lifetimes of the centers, which were found from the slope of the decay curves in the D–$(\log t/t_0)$ coordinates, varied from 0.1 ms at 350 K to 3.5 hours at 80 K.

3.3. Pulse Cathodoluminescence of $LiNbO_3$ Crystals

When a crystal was irradiated, a weak flash of fast decaying ($\tau < 4$ ns) bluish–white luminescence was observed and the shape of its oscillogram was a replica of the pulse form of the electron beam current. Lag stages of the decay were not revealed down to an intensity three orders of magnitude lower. The intensity of this luminescence in the $LiNbO_3$ crystal was very low; it was 10^{-3}–10^{-4} as large as the intensity measured in CsI under the same conditions. The luminescence spectrum excited by electrons at room temperature covers the range from 4.1 to 1.5 eV and has the form of a wide asymmetrical band with a maximum at 3.2 eV approximately for all crystals and a pronounced shoulder in the long-wavelength edge near 2.3–2.5 eV (Fig. 1b). The result of deconvolution of the spectrum into components is indicated in Fig. 1b by solid lines. It can be seen that the cathodoluminescence (CL) spectrum is satisfactorily described by a set of Gaussians centered at 4.0, 3.3, and 2.5 eV.

Luminescence with a similar spectral structure was reported to be observed in [10] for crystals excited by a continuous electron beam of 30 keV, but the authors of that work did not discuss its nature. Luminescence excited by UV light or x rays has a maximum intensity at approximately 2.8 eV, according to data from [5, 11], and is associated with recombination of electrons and holes bound to defects. When the Li/Nb ratio in the stochiometric composition was decreased, a tendency to a blue spectral shift was noted [5]. It is tempting to assume that the CL spectra observed by us are also of a recombination nature. However, the instantaneous character of the luminescence decay on the scale of the duration of exciting pulses in comparison to the lagging decrease in the induced absorption does not allow us to connect this luminescence with radiative recombination of short-lived electron and hole color centers.

3.4. Formation of Color and Luminescence Centers in Reduced $LiNbO_3$ Crystals

Direct comparison of the data from Figs. 1a and 1b shows that the SLOA and CL spectra induced by pulse irradiation are described by the same set of Gaussians. Although this result is a little unexpected, it is quite reliable and is not a consequence of any experimental error; additional information on the spectral behavior of the SLOA and CL can be obtained from the following consideration. The color centers arise in $LiNbO_3$ crystals, as mentioned before, because the charge carriers generated by irradiation are captured by existing defects of the cation sublattice and become small polarons; the optical absorption originates from photoinduced electron (hole) transitions from the localized ground state onto more or less equivalent ions surrounding the defect. The position of the photon energy absorbtion peak depends on the charge of the defects that trap the carriers [14]. Therefore, by changing the nature of defects through appropriate treatment of the crystal, one can modify the short-lived optical spectra induced by pulsed irradiation.

The results of investigating the SLOA and CL in samples reduced by annealing in vacuum (~0.1 Pa) at $T = 830$ K for 4 hours are presented in Fig. 4; the spec-

tra are measured under the same conditions as those presented in Fig. 1 for congruent crystals. A comparison of the data in Figs. 1 and 4 shows that the reduction of the crystal results in identical modifications of the SLOA and CL spectra: a decrease in the intensity of the basic bands at 3.3 and 2.5 eV and the appearance of a new band (in the high-energy region of the spectra) with its center at 3.6 and with a half-width of ~0.6 eV. In our opinion, this identity of the CL and SLOA band profiles cannot be a mere coincidence and directly indicates the existence of a specific emission mechanism of fast decaying broadband luminescence with an extremely small Stokes shift.

The change in the CL and SLOA spectra due to sample reduction by annealing might occur for the following reasons. It is agreed [1] that, during reduction by annealing, oxygen goes to the surface of the crystal, leaving electrons which are localized at the antisite defects and form bipolarons. The Li and Nb ions, on the contrary, diffuse into the volume of the crystal and occupy vacant cation positions, thereby decreasing their concentration. It is the last process that is likely to decrease the intensity of the hole bands at 3.3 and 2.5 eV in the spectra of the reduced crystals. The appearance of the band at 3.6 eV in the spectra in Fig. 4 indicates the emergence of a new deep trap for the charge carriers. According to [8], the deepest traps (antisite defects and niobium vacancies) exist in the congruent crystal lattice mainly in the form of $Nb_{Li}^{4+}-V_{Nb}^{5-}$ complexes. Taking into account that, during reduction by annealing, bipolarons are created in large quantity, it seems reasonable to connect the origin of the band at 3.6 eV with the modification of the charge state of the antisite defects in the complexes; this occurs when an antisite defect captures two conduction electrons. In the field produced by the negative charge of these electrons, the energy of the $2p^6$ states of the oxygen ions lying in the triangular bases of the two adjacent oxygen octahedrons surrounding Nb_{Li} and V_{Nb} will increase and, therefore, the hole trap will become deeper. Thus, one can suppose that the short-lived absorption band at 3.6 eV induced through the exposure of reduced crystals to irradiation is associated with the holes bound to the niobium vacancies in the $Nb_{Li}^{2+}-V_{Nb}^{5-}$ complexes.

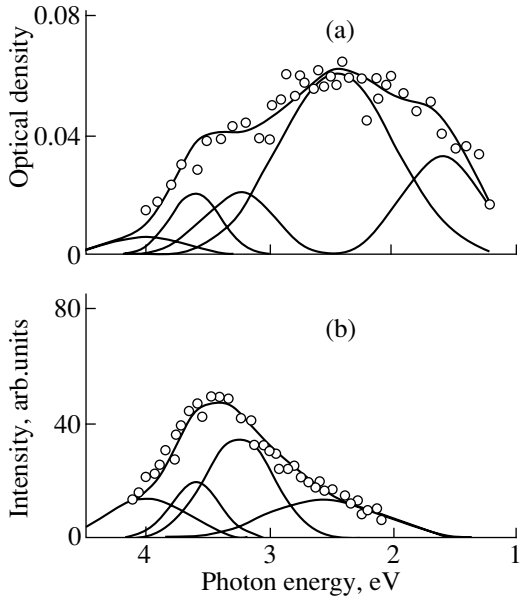

Fig. 4. Spectra of the (a) SLOA and (b) CL of a reduced $LiNbO_3$ sample.

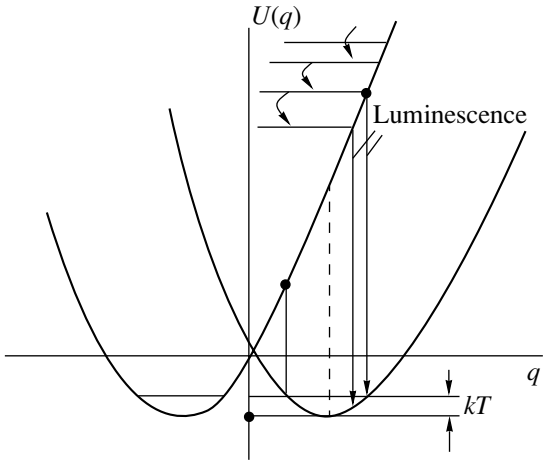

Fig. 5. Scheme of small-polaron energy relaxation after capture of a band carrier on a deep level within a two-site model.

3.5. On the Nature of Fast Decaying Luminescence in $LiNbO_3$ Crystals

The common properties characterizing the processes of formation of color centers and emission of luminescence in lithium niobate crystals, such as a weak dependence on temperature, the absence of temporal stages lagging relative to the action of exciting pulses, identical spectral parameters of the bands, and identical dependences of the spectrum profiles on the nature of defects, indicate an obvious correlation of these two processes and allow one to consider the CL in $LiNbO_3$ as a phenomenon accompanying the process of formation of color centers. Taking into account that most of the energy of the CL flash comes from the bands at 3.25 and 2.5 eV, corresponding to the optical absorption of holes located at the Nb and Li vacancies, it is reasonable to connect the origin of the CL flash with radiative band hole trapping on the split-off valence band levels of oxygen ions surrounding the vacancies.

One of the possible reasons for the similarity between the spectral characteristics of the absorption and luminescence bands is, in our opinion, nonphonon

radiative electron transitions in the process of capture of charge carriers by deep traps. This process can be described schematically in terms of configuration curves within the two-site model of small polarons [15] (Fig. 5).

Just after a band hole is trapped by one of the oxygen ions surrounding the cation vacancy into the electron ground state of the center, this ion (on the left in Fig. 5) is in a highly excited vibrational state; its relaxation is mainly nonradiative and is accompanied by the creation of phonons. However, if one of the adjacent equivalent ions O^{2-} (on the right in Fig. 5) makes a transition, due to a fluctuation, to a configuration that nearly corresponds to the thermalized state of the center, then, in accordance with the Franck–Condon principle, the hole will immediately make a transition to this stationary polaron state with emission of a photon with an energy belonging to the same set of energy values that correspond to possible (afterwards) transitions with absorption of photons. It is clear that the probability of the nonphonon radiative transitions described above is quite low; however, the luminescence efficiency in $LiNbO_3$ crystals, as noted before, is also extremely weak.

4. CONCLUSION

The results of our investigation of the spectral kinetic properties of transient optical absorption and luminescence induced in crystals of lithium niobate by pulsed electron beams of nanosecond duration allow us to make the following conclusions.

The defects produced in congruent crystals by exposure to electron pulse irradiation are electron and hole color centers–electron polarons and bipolarons and holes localized at Li and Nb vacancies; their structure is entirely determined by the stoichiometric defects of the crystals. Study of the dichroism of transient absorption showed that the formation of electron centers of both types–polarons and bipolarons (the latter centers are responsible for the absorption band at 4.0 eV)—is caused by the localization of electrons at the Nb_{Nb}–Nb_{Li} complexes oriented along the *z* axis. Optical manifestations of the processes of electron excitation decay with color-center formation and luminescence are not revealed in the lattice regions without defects.

Typical features of the luminescence excited by pulsed electron beams are low efficiency, a broadband form of the spectra, and an instantaneous character of decay in the process of irradiation by exciting pulses.

A comparison of the influence of temperature and annealing of samples in a reducing atmosphere on the characteristics of fast-decaying luminescence and transient absorption shows that there is a direct relation between the processes of photon emission and the formation of transient absorption centers. This allows us to suppose that the fast-decaying luminescence in congruent crystals of lithium niobate is caused by nonphonon radiative transitions, which accompany energy relaxation of band charge carriers captured by deep traps.

ACKNOWLEDGMENTS

This work was supported by the Russian Foundation for Basic Research, project no. 98-02-04085.

REFERENCES

1. O. F. Schirmer, O. Thiemann, and M. J. Wohlecke, Phys. Chem. Solids **52** (1), 185 (1991).
2. O. F. Schirmer and D. von der Linde, Appl. Phys. Lett. **33** (1), 35 (1978).
3. L. E. Halliburton, K. L. Sweeney, and C. Y. Chen, Nucl. Instrum. Methods Phys. Res. B **1**, 344 (1984).
4. L. Arizmendi, J. M. Cabrera, and F. J. Agulló-L'opez, J. Phys. C **17**, 515 (1984).
5. A. García-Cabañes, J. A. Sanz-García, J. M. Cabrera, *et al.*, Phys. Rev. B **37** (11), 6085 (1988).
6. J. L. Ketchum, K. L. Sweeney, L. E. Halliburton, and A. F. Armington, Phys. Lett. A **94**, 450 (1983).
7. J. Koppitz, O. F. Schirmer, and A. I. Kuznetsov, Europhys. Lett. **4**, 1055 (1987).
8. D. M. Smyth, Ferroelectrics **50**, 93 (1983).
9. I. Sh. Akhmadullin, V. A. Golinishchev-Kutuzov, and S. A. Migachev, Fiz. Tverd. Tela (St. Petersburg) **40** (6), 1109 (1998) [Phys. Solid State **40**, 1012 (1998)].
10. J. Llopis, C. Ballesteros, R. Gonzáles, and Y. Chen, J. Appl. Phys. **56** (2), 460 (1984).
11. D. M. Krol, G. Blasse, and R. C. Powell, J. Chem. Phys. **73**, 163 (1980).
12. M. V. Fok, Tr. Fiz. Inst. Akad. Nauk SSSR **59**, 3 (1972).
13. Yu. R. Zakis, L. N. Kantorovich, E. A. Kotomin, V. N. Kuzovkov, I. A. Tale, and A. L. Shlyuger, *Model of Processes in Wide-Gap Solids with Defects* (Zinatne, Riga, 1991).
14. O. F. Schirmer, Z. Phys. B **24**, 235 (1976).
15. *Polarons*, Ed. by Yu. A. Firsov (Nauka, Moscow, 1975).

Translated by O. Ivanov

Physics of the Solid State, Vol. 43, No. 8, 2001, pp. 1585–1588. Translated from Fizika Tverdogo Tela, Vol. 43, No. 8, 2001, pp. 1525–1527.

MAGNETISM AND FERROELECTRICITY

A New Monoclinic Phase and Elastic Effects in $PbZr_{1-x}Ti_xO_3$ Solid Solutions

V. Yu. Topolov and A. V. Turik

Rostov State University, ul. Zorge 5, Rostov-on-Don, 344090 Russia
e-mail: topolov@phys.md.runnet.ru
e-mail: turik@phys.md.runnet.ru

Received January 25, 2001

Abstract—The elastic matching of single- or polydomain ferroelectric phases *R*3*m*–*P*4*mm*, *Cm*–*P*4*mm*, and *R*3*m*–*Cm* and the relaxation of mechanical stresses in $PbZr_{1-x}Ti_xO_3$ solid solutions are investigated. The conditions for constancy of the optimum volume concentrations of twin domains of the *P*4*mm* and *Cm* phases in the vicinity of the morphotropic phase boundary in the *x*–*T* diagram are analyzed, and the correlation between the morphotropic boundary and interfaces, namely, the planes of zero mean strains, is discussed. © *2001 MAIK "Nauka/Interperiodica".*

Over the past few decades, the structure and properties of solid solutions of the perovskite-type oxides $PbZr_{1-x}Ti_xO_3$ (PZT) have been investigated extensively [1–3]. Particular attention is centered on the problem concerning the coexistence of ferroelectric phases in the morphotropic transition region [4–7]. Recent experimental studies [8–10] revealed a new monoclinic ferroelectric phase whose space group of symmetry *Cm* is the symmetry subgroup of the ferroelectric phases *R*3*m* and *P*4*mm*. Noheda *et al.* [10] performed precision structural investigations of a series of PZT ceramic compositions at different temperatures *T* and molar concentrations *x*, determined the phase coexistence regions, and presented a fragment of the new *x*–*T* diagram of PZT solid solutions in the vicinity of the morphotropic phase boundary (in [10], the morphotropic boundary is considered to mean the *Cm*–*P*4*mm* interface, unlike the conventional concepts [1–3]). The goal of the present work was to investigate the elastic matching of ferroelectric phases (*R*3*m*–*P*4*mm*, *Cm*–*P*4*mm*, and *R*3*m*–*Cm*) and to elucidate the role of the new phase *Cm* in the formation of heterophase structures in PZT solid solutions.

It is assumed that a mechanically free crystal or an individual crystallite of PZT ceramics undergoes a first-order phase transition between two ferroelectric phases. The axes of the Cartesian coordinate system ($X_1X_2X_3$) are oriented parallel to the crystallographic axes of a perovskite cell of PZT in the paraelectric phase *Pm*3*m*. In the chosen coordinate system, the basis vectors ($\mathbf{a}_t$; $\mathbf{b}_t$; $\mathbf{c}_t$) of the unit cells of 90° domains (the mechanical twins of the *P*4*mm* phase) are parallel to ([100], [010], [001]) and ([010], [001], [100]) and their volume concentrations are equal to n_t and $(1 - n_t)$, respectively. The *R*3*m* phase can be separated into 71° (109°) domains in which the basis vectors of unit cells ($\mathbf{a}_r$; $\mathbf{b}_r$; $\mathbf{c}_r$) are oriented at an angle ω of displacement along ([100], [010], [001]), ([100], [0$\bar{1}$0], [001]), ([$\bar{1}$00], [010], [001]), or ([$\bar{1}$00], [0$\bar{1}$0, [001]). Twin domains of the *Cm* phase with the basis vectors of unit cells ($\mathbf{a}_m$; $\mathbf{b}_m$; $\mathbf{c}_m$) and the volume concentrations n_m and $(1 - n_m)$ are assumed to be oriented (with correction for the angle of monoclinicity β of the unit cell) along ([110], [$\bar{1}$10], [001]) and ([011], [01$\bar{1}$], [100]), respectively. According to [11–14], the distortion matrices of the polydomain phases *P*4*mm* $\|N_t\|$ and *Cm* $\|N_m\|$ and the single-domain phase *R*3*m* $\|N_r\|$ can be written in the following form:

$$\|N_t\| = n_t \begin{pmatrix} \varepsilon_a & 0 & 0 \\ 0 & \varepsilon_a & 0 \\ 0 & 0 & \varepsilon_c \end{pmatrix} + (1-n_t) \begin{pmatrix} \cos\varphi_t & 0 & -\sin\varphi_t \\ 0 & 1 & 0 \\ \sin\varphi_t & 0 & \cos\varphi_t \end{pmatrix} \begin{pmatrix} \varepsilon_a & 0 & 0 \\ 0 & \varepsilon_a & 0 \\ 0 & 0 & \varepsilon_c \end{pmatrix},$$

$$\|N_m\| = n_m \begin{pmatrix} \eta_a & \eta_{ab} & \eta_{ac} \\ \eta_{ab} & \eta_b & \eta_{bc} \\ \eta_{ac} & \eta_{bc} & \eta_c \end{pmatrix} + (1-n_m) \begin{pmatrix} \cos\varphi_m & 0 & -\sin\varphi_m \\ 0 & 1 & 0 \\ \sin\varphi_m & 0 & \cos\varphi_m \end{pmatrix} \begin{pmatrix} \eta_c & -\eta_{bc} & \eta_{ac} \\ -\eta_{bc} & \eta_b & \eta_{ab} \\ -\eta_{ac} & \eta_{ab} & \eta_a \end{pmatrix},$$

1063-7834/01/4308-1585$21.00

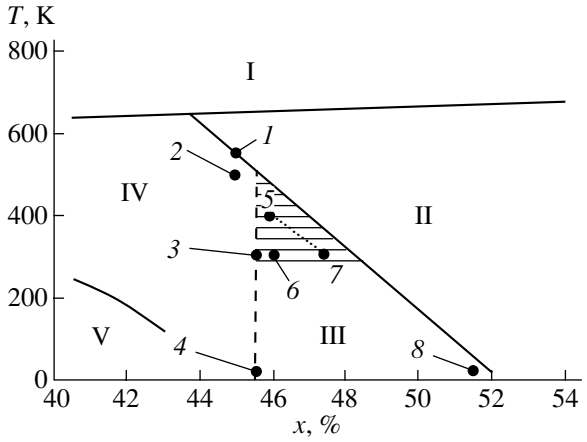

A fragment of the x–T diagram of $PbZr_{1-x}Ti_xO_3$ [10] in the vicinity of the morphotropic phase boundary. The phase-stable regions are designated by the Roman numerals I (*Pm*3*m*), II (*P*4*mm*), III (*Cm*), IV (*R*3*m*), and V (*R*3*c*). The coexistence region of the *Cm* and *P*4*mm* phases is shaded. Points *1–8* correspond to different variants of the elastic matching of ferroelectric phases presented in the table.

$$\|N_r\| = \begin{pmatrix} \mu_a & \mu & \mu \\ \mu & \mu_a & \mu \\ \mu & \mu & \mu_a \end{pmatrix}.$$

The perovskite cell distortions ε_a, ε_c (the *P*4*mm* phase), η_a, η_b, η_c, η_{ab}, η_{ac}, η_{bc} (the *Cm* phase), and μ_a, μ (the *R*3*m* phase) are represented by the unit cell parameters of these phases and the *Pm*3*m* phase. The angles of rotation $\varphi_t = \arccos[2\varepsilon_a\varepsilon_c/(\varepsilon_a^2 + \varepsilon_c^2)]$ and $\varphi_m = \arccos[2\eta_a\eta_c/(\eta_a^2 + \eta_c^2)]$ are introduced in order to account for the mutual rotation of the crystallographic axes of domains in the (X_10X_3) plane in view of the inequalities $\varepsilon_a \neq \varepsilon_c$ and $\eta_a \neq \eta_c$, respectively. Analysis of the elastic matching of the ferroelectric phases and the interphase boundaries was performed within the concepts of a zero mean strain plane (ZMSP) [11–13].[1]

As follows from the results obtained (see table), the temperature and concentration dependences of the unit cell parameters of PZT solid solutions [10] are favorable for the formation of the zero mean strain plane (points *1–5*, *7* in figure) or slightly strained interfaces (points *6*, *8* in figure). The strained interfaces can be in the form of planar [12] or conic [13] surfaces with a sufficiently small curvature. The internal mechanical stresses that arise in the case of slightly strained interfaces satisfy the condition $|\sigma_{fg}| \ll c^E_{fgij}|\xi^s_{ij}|$, where c^E_{fgij} are the elastic moduli of a single-domain ferroelectric perovskite crystal, which are measured in the electric field E = const, and ξ^s_{ij} are the spontaneous strains of the perovskite cells of the coexisting phases. As regards the interphase boundaries, namely, the planes of zero mean strain, their orientations in the $(X_1X_2X_3)$ coordinate system are determined by the Miller indices $\{0kl\}$ according to the formulas taken from [11, 12]. A very slight change in the optimum volume concentrations of twin domains $n_{t,\,\mathrm{opt}}$ and $n_{m,\,\mathrm{opt}}$ (or, correspondingly, $n'_{t,\,\mathrm{opt}}$ and $n'_{m,\,\mathrm{opt}}$) and the existence of interphase boundaries (the zero mean strain planes) with elastic matching between the single-domain phase *R*3*m* and the polydomain phase *P*4*mm* or *Cm* (see points *1–4* in table) are characteristic of a sufficiently narrow range of concentrations ($\Delta x \approx 0.01$) and a wide range of temperatures ($\Delta T > 500$ K). The separation of the *R*3*m* phase into twin domains, irrespective of their volume concentrations, virtually does not affect the results (see table): the calculated values of $n_{t,\,\mathrm{opt}}$, $n'_{t,\,\mathrm{opt}}$, $n_{m,\,\mathrm{opt}}$, and $n'_{m,\,\mathrm{opt}}$ change by less than 1%, which is explained by the smallness of the off-diagonal elements of the matrix $\|N_r\|$ as compared to its diagonal elements. The values of $n'_{t,\,\mathrm{opt}}$, which correspond to the zero mean strain plane in the matching of the *P*4*mm* and *R*3*m* phases, correlate adequately with our earlier estimates [12, 14]. These estimates were obtained from the experimental data on the unit cell parameters of the ceramic compositions PZT and PZT + 2 at. % Nd, which were synthesized by different methods.

In our opinion, the virtual constancy of the optimum volume concentrations of domains (see points *1–4* in figure and table) is due to the fact that the perovskite cell parameters of the phases *Cm* ($n_m = 1$) and *P*4*mm* ($n_t = 1$) in the studied ranges of (x, T) satisfy the conditions $\xi^s_{11,\,Cm} \approx \xi^s_{22,\,Cm} \approx \xi^s_{rr,\,P4m}$ ($r = 1, 2$) and $\beta - 90° < 0.5°$. Under these conditions, the single-domain phases *Cm* and *P*4*mm* can be elastically matched along the zero mean strain plane or slightly strained interfaces (see points *5–8* in the figure and the table) in the case when the values (x, T) correspond to the new morphotropic boundary [10]. The orientations of the zero mean strain planes, which separate the aforementioned single-domain phases, are close to $\{001\}$ in the $(X_1X_2X_3)$ coordinate system. It is interesting that the linear segment that connects points *5* and *7* (see figure) and corresponds to the interphase boundaries (i.e., the zero mean strain planes) is parallel to the *Cm*–*P*4*mm* morphotropic boundary. This correlation between the phase boundary and the plane of zero mean strains is first revealed in the present work and needs further experimental investigation. The mutual location of segment *5–7* and the *Cm*–*P*4*mm* morphotropic boundary in PZT means that the interfaces of the single-domain phases *Cm* and *P*4*mm* are slightly strained near this segment and that the internal mechanical stresses σ_{fg} are insufficient for stimulating the separation of one of these

[1] The applicability of this concept to PZT solid solutions was first proved in our earlier work [14] through an example of the elastic interaction between the *P*4*mm* and *R*3*m* polydomain phases.

Features of the elastic matching of ferroelectric phases in $PbZr_{1-x}Ti_xO_3$ solid solutions

Coexisting phases	x	T, K	Points in the figure	Optimum volume concentrations of domains for elastic matching of phases along the interphase boundaries (ZMSP)	Conditions for the existence of slightly strained interfaces (ZMSP is absent)
*P*4*mm*	0.45	550	*1*	$n_{t,\,\mathrm{opt}} = 0.691$ or $n'_{t,\,\mathrm{opt}} = 0.309$	–
*R*3*m*		500	*2*	$n_{t,\,\mathrm{opt}} = 0.698$ or $n'_{t,\,\mathrm{opt}} = 0.302$	–
*R*3*m*	0.45–0.46	300	*3*	$n_{m,\,\mathrm{opt}} = 0.700$ or $n'_{m,\,\mathrm{opt}} = 0.300$	–
Cm		20	*4*	$n_{m,\,\mathrm{opt}} = 0.724$ or $n'_{m,\,\mathrm{opt}} = 0.276$	–
*P*4*mm*	0.46	400	*5*	$n_{t,\,\mathrm{opt}} = 1$; $n_{m,\,\mathrm{opt}} = 1$ or $n'_{m,\,\mathrm{opt}} = 0$; $n'_{m,\,\mathrm{opt}} = 0$	–
Cm		300	*6*	–	$n_t \longrightarrow 1$; $n_m \longrightarrow 1$ or $n'_t \longrightarrow 0$; $n'_m \longrightarrow 0$
	0.47–0.48	300	*7*	$n_{t,\,\mathrm{opt}} = 1$; $n_{m,\,\mathrm{opt}} = 1$ or $n'_{m,\,\mathrm{opt}} = 0$; $n'_{m,\,\mathrm{opt}} = 0$	–
	0.51–0.52	20	*8*	–	$n_t \longrightarrow 1$; $n_m \longrightarrow 1$ or $n'_t \longrightarrow 0$; $n'_m \longrightarrow 0$

Note: The experimental unit-cell parameters are taken from [10]. The *R*3*m* phase is assumed to be a single-domain phase, and the corresponding basis vectors of the unit cell are taken to be oriented at an angle ω of displacement along ([100], [010], [001]).

phases into twin domains. The values of σ_{fg} vary only slightly both as the *Cm*–*P*4*mm* morphotropic boundary is approached and as the distance from it increases (see, for example, point *6* in the figure). It seems likely that this behavior of $\sigma_{fg}(x, T)$ is typical of the entire region of coexistence of the *Cm* and *P*4*mm* phases, which was experimentally determined in [10].

The data presented in the table agree with assumptions [10] on the active role of non-180-degree domains in the relaxation of mechanical stresses when the ferroelectric phases coexist in PZT. Elastic matching of two single-domain (nontwinned) phases along the zero mean strain plane (see table) rarely occurs (see, for example, [12–14]) and, most likely, is not realized in ceramic samples of PZT because of the internal mechanical stresses, composition fluctuations, etc.

It is of interest to compare the above results with the data on the elastic interaction of the *m*3*m*, *mmm*, and 2/*m* phases in a KCN ferroelectric crystal [15]. The intermediate monoclinic phase 2/*m* enhances the relaxation of internal mechanical stresses during the cooling of a three-phase crystal. Analysis of the unit cell parameters of the $(KBr)_{1-y}(KCN)_y$ crystals revealed an unusual transition from the rhombohedral–monoclinic interphase boundary, i.e., the zero mean strain plane ($y \le 0.65$), to the strained conic interface ($y \ge 0.70$) [16]. The observed change in the form of the interface agrees with the experimental data [16] on the change in the order of the phase transition: substantial internal mechanical stresses that arise as the result of an increase in y in the $(KBr)_{1-y}(KCN)_y$ crystals are accompanied by a second-order phase transition. It should also be mentioned that the y–T diagram of $(KBr)_{1-y}(KCN)_y$ [17] at $T \le 100$ K and $0.60 \le y \le 0.90$ exhibits an alternation of ferroelectric phases that is similar to the alternation of PZT ferroelectric phases in the vicinity of the morphotropic boundary (see figure). Specifically, when y increases, the ferroelectric phases become stable in the following order: rhombohedral, monoclinic, and tetragonal. The coexistence of rhombohedral and monoclinic phases, or the formation of the states which depend on the prehistory of $(KBr)_{1-y}(KCN)_y$ crystals, takes place in a limited region of the y–T diagram. The results obtained in [15–17] and the calculated data given in the table need further experimental verification: it is necessary to investigate experimentally how the domain (twin) structure of the *Cm* phase and internal mechanical stresses affect the *R*3*m*–*Cm* phase transition in PZT solid solutions.

The results obtained in this work illustrate different ways of relaxing internal stresses upon elastic matching of the ferroelectric phases in PZT solid solutions. The *Cm* phase plays an important role in stress relaxation, which is confirmed by the calculated data in the table. This study dealt with bulk crystal samples or individual crystallites for which the conditions of stress relaxation in the case of the coexistence of phases slightly differ from the corresponding conditions in ceramic samples. Nonetheless, the features of the change in the parameters of the unit cells, their spontaneous strains, and distortions in different intervals of (x, T) are the most significant factors in the formation of heterophase structures and stress relaxation in PZT solid solutions.

REFERENCES

1. B. Jaffe, W. R. Cook, and H. Jaffe, *Piezoelectric Ceramics* (Academic, New York, 1971; Mir, Moscow, 1974).
2. G. A. Smolenskiĭ, V. A. Bokov, V. A. Isupov, N. N. Kraĭnik, R. E. Pasynkov, A. I. Sokolov, and N. K. Yushin, in *Physics of Ferroelectric Phenomena* (Nauka, Leningrad, 1985), p. 357.
3. *Keramik*, Ed. by H. Schaumburg (B. G. Teubner, Stuttgart, 1994), p. 417.
4. V. A. Isupov, Fiz. Tverd. Tela (Leningrad) **22** (1), 172 (1980) [Sov. Phys. Solid State **22**, 98 (1980)].
5. W. Wersing, W. Rossner, G. Eckstein, and G. Tomandl, Silic. Ind. **50** (3–4), 41 (1985).
6. M. F. Kupriyanov, G. M. Konstantinov, and A. E. Panich, *Ferroelectric Morphotropic Transitions* (Rost. Univ., Rostov-on-Don, 1991).
7. A. V. Gorish, V. P. Dudkevich, M. F. Kupriyanov, A. E. Panich, and A. V. Turik, in *Piezoelectric Instrument Making*, Vol. 1: *Physics of Ferroelectric Ceramics* (IPRZh Radiotekhnika, Moscow, 1999), p. 159.
8. B. Noheda, J. A. Gonzalo, L. E. Cross, *et al.*, Phys. Rev. B **61** (13), 8687 (2000).
9. R. Guo, L. E. Cross, S.-E. Park, *et al.*, Phys. Rev. Lett. **84** (23), 5423 (2000).
10. B. Noheda, D. E. Cox, G. Shirane, *et al.*, Phys. Rev. B **63** (1), 14103 (2001).
11. G. Metrat, Ferroelectics **26** (1–4), 801 (1980).
12. V. Yu. Topolov and A. V. Turik, Defect Diffus. Forum A **123–124**, 31 (1995).
13. V. Yu. Topolov, L. E. Balyunis, A. V. Turik, and O. E. Fesenko, Kristallografiya **35** (3), 755 (1990) [Sov. Phys. Crystallogr. **35**, 441 (1990)].
14. V. Yu. Topolov and A. V. Turik, Izv. Sev.-Kavk. Nauchn. Tsentra Vyssh. Shk., Estestv. Nauki, No. 1, 72 (1990); Available from VINITI No. 1546-B87 (Rostov-on-Don, 1987).
15. V. Yu. Topolov, Z. Phys. B **100** (1), 27 (1996).
16. K. Knorr and A. Loidl, Phys. Rev. B **31** (8), 5387 (1985).
17. U. T. Höchli, K. Knorr, and A. Loidl, Adv. Phys. **39** (5), 405 (1990).

Translated by O. Moskalev

Physics of the Solid State, Vol. 43, No. 8, 2001, pp. 1589–1593. Translated from Fizika Tverdogo Tela, Vol. 43, No. 8, 2001, pp. 1528–1532.

LATTICE DYNAMICS AND PHASE TRANSITIONS

The Boson Peak and Nanostructure of Vitreous Benzophenone

N. A. Davydova*, V. I. Mel'nik*, K. I. Nelipovich*, Ya. Baran, and M. Drozd****

** Institute of Physics, National Academy of Sciences of Ukraine, pr. Nauki 46, Kiev, 03039 Ukraine*

*** Institute of Low Temperatures and Structural Investigations, Polish Academy of Sciences, Wroclaw, Poland*

Received November 24, 2000; in final form, January 18, 2001

Abstract—The temperature behavior of the low-frequency Raman spectra of vitreous and supercooled liquid benzophenones is investigated experimentally. The structural phase transformations are studied by differential scanning calorimetry. The results obtained suggest that the structure of glasses involves nanometer-sized fragments similar to the structural elements of the crystals. © *2001 MAIK "Nauka/Interperiodica".*

1. INTRODUCTION

Investigations into different glasses have revealed many interesting features associated with their universal properties. These properties are usually considered anomalies as compared to the properties of their crystal analogs. In particular, Raman spectra of all glasses exhibit two characteristic features irrespective of their chemical composition, namely, the boson peak and quasi-elastic light scattering, which are not observed for their crystal primogenitures [1–5]. Speculations on the nature of the boson peak have aroused considerable interest in the low-frequency vibrational excitation spectra of vitreous structures.

In the present work, we analyzed the low-frequency Raman spectra of benzophenone over a wide temperature range (12–350 K), including the glass–liquid transition temperature (T = 216.8 K) and the melting point of the crystalline benzophenone modification (T = 323.9 K). Particular attention was focused on the study of vibrational excitations near the temperature of the glass–liquid phase transition upon heating and cooling of the samples. The phase transformations of benzophenone were also studied by differential scanning calorimetry.

It is known that molecules of benzophenone $(C_6H_5)_2CO$ consist of two phenol rings C_6H_5, which are joined to each other through a carbonyl group CO. The stable crystalline modification of benzophenone (the α modification) contains four molecules per unit cell and has an orthorhombic structure [6]. At low temperatures, benzophenone can exist in the β modification. It is assumed that the β modification has a monoclinic structure.

2. EXPERIMENTAL TECHNIQUES AND RESULTS

2.1. Phase transitions in benzophenone. The phase transitions in benzophenone were thoroughly examined by differential scanning calorimetry.

Measurements were performed on a Perkin-Elmer DSC-7 instrument at a heating (cooling) rate of 20 K/min in the temperature range 143–353 K. The sample weight was 0.880 mg.

The vitreous modification of benzophenone (*X*-benzophenone) can be prepared by rapid cooling of the melt. The α and β modifications can be obtained upon transition of vitreous benzophenone to the supercooled liquid state. This is clearly seen in the thermograms shown in Fig. 1.

As is evident from the heating curve for the α modification of benzophenone (curve *1* in Fig. 1), an increase in temperature leads to a strong transition at T = 323.9 K, which corresponds to the melting point of α-benzophenone. Upon cooling, molten benzophenone undergoes a low-energy transition at T = 211.7 K (curve *2* in Fig. 1), which corresponds to the formation of the vitreous phase (*X*-benzophenone).

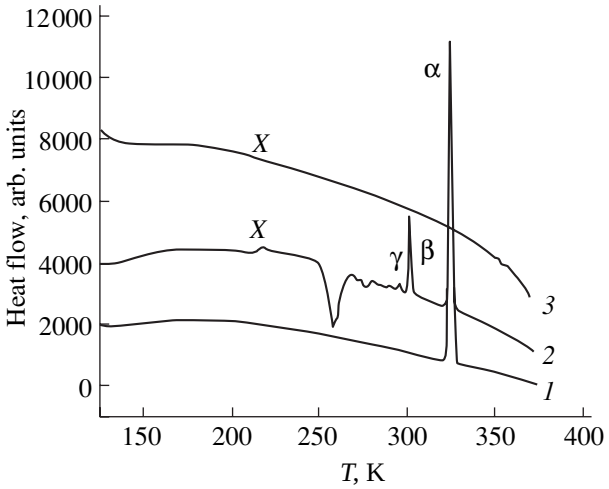

Fig. 1. Thermograms measured using differential scanning calorimetry upon (*1*) heating of crystalline benzophenone, (*2*) cooling of molten benzophenone, and (*3*) heating of vitreous benzophenone. The scanning rate is 20 K/min.

1063-7834/01/4308-1589$21.00 © 2001 MAIK "Nauka/Interperiodica"

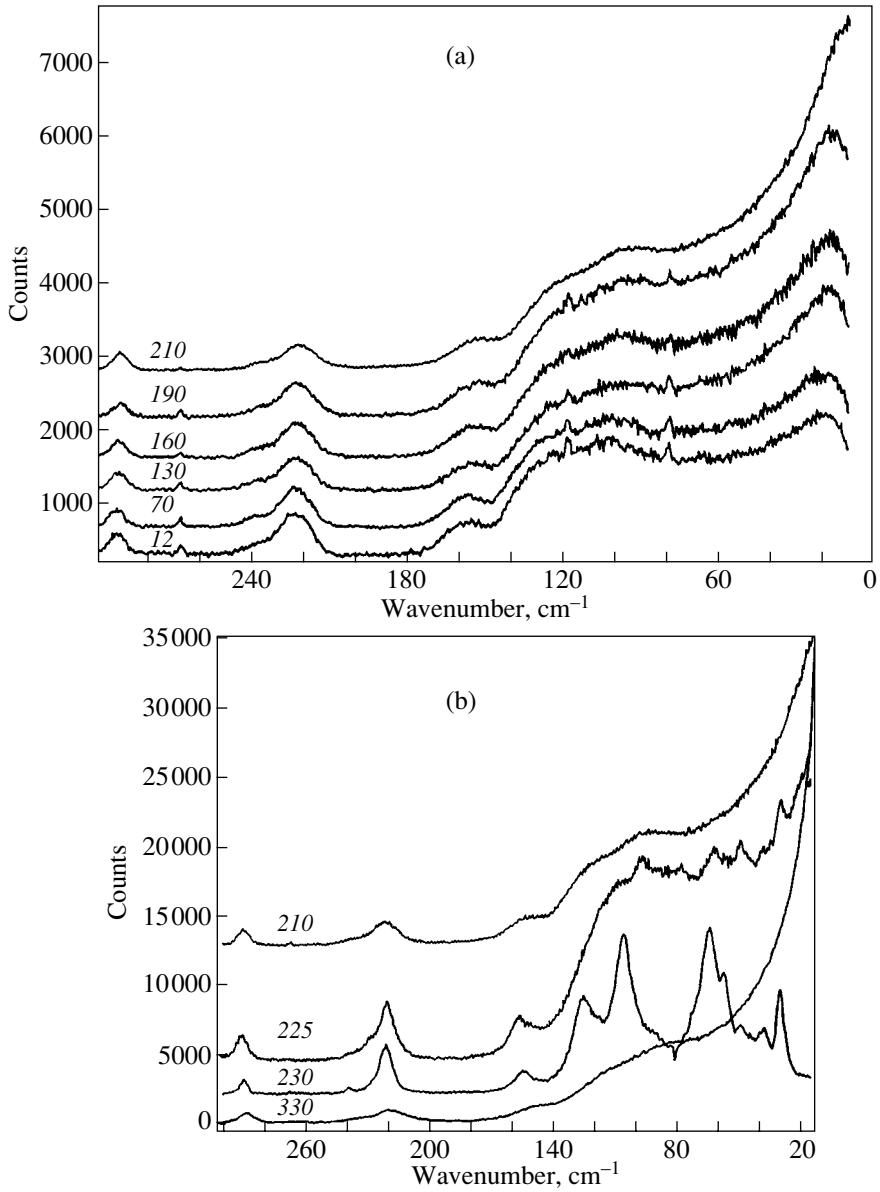

Fig. 2. Evolution of the low-frequency Raman spectra during heating of vitreous benzophenone (a) from 12 to 210 K and (b) from 210 to 330 K.

The experimental heating curve for vitreous *X*-benzophenone is also depicted in Fig. 1 (curve *3*). It is seen that curves *1* and *3* differ significantly. Curve *3* exhibits a deep exothermal minimum in the temperature range 250–263 K, which is associated with crystallization. A visual examination revealed that, in the supercooled liquid phase, continuous growth of white microcrystals occurs throughout the bulk of the sample. These microcrystals belong to the unstable β modification of benzophenone, which transforms into the α modification with an increase in temperature. This is confirmed by the data of luminescent-emission spectroscopy [7]. The first peak in curve *3* is attributed to the transformation of vitreous benzophenone into the supercooled liquid at $T = 216.8$ K. As the temperature increases, the endothermal peaks are observed at temperatures of 301 and 323.9 K (curve *3* in Fig. 1), which correspond to the melting points of the α and β modifications, respectively.

It should be noted that the crystallization of benzophenone from the supercooled liquid state is observed only in the case of heating, i.e., when the glass–liquid phase transition occurs with an increase in temperature, but the reverse reaction is not true.

2.2. Raman spectra. The Raman spectra were excited by the 514.5-nm line of an argon laser. The laser radiation power was 200 mW. The spectra were recorded on a spectrometer with a Jobin Ivon mono-

chromator in a 90° scattering geometry. The bandwidth of the spectrometer slit was equal to 2 cm^{-1}. The sample was placed in a glass capillary and mounted in a cryostat, which provided temperature variation in the range from 12 to 350 K.

The evolution of the Raman spectra of vitreous benzophenone with an increase in the temperature is shown in Fig. 2. This case corresponds to curve *3* in Fig. 1. At a temperature of 12 K, the Raman spectrum contains two lines at 17 and 100 cm^{-1} (Fig. 2a) which are not observed in the spectra of crystalline benzophenone. The former line is the so-called boson peak. The latter (broader) line is associated with molecular motions which correspond to libration optical phonons. This spectrum also exhibits two high-frequency modes of intramolecular vibrations at 223 and 290 cm^{-1}. However, in this work, we will consider the frequency range of the boson peak.

It can be seen from Fig. 2a that an increase in temperature leads to an increase in the intensity of the boson peak as compared to the libration line. At temperatures close to the glass–liquid transition point (216.8 K), the spectrum contains a contribution from quasi-elastic light scattering. The line of quasi-elastic light scattering has the shape of a broad peak that reaches a maximum at the zero frequency (the Rayleigh line) [8]. At T = 210 K, the boson peak overlaps with a strongly broadened Rayleigh line. At temperatures above the transition of vitreous benzophenone to the supercooled liquid state, the Raman spectrum changes considerably (Fig. 2b). As the temperature increases to T = 225 K, the intensity of the Rayleigh line decreases and a new structure that corresponds to the crystalline modification of benzophenone appears in the spectrum. This structure becomes more pronounced at a temperature of 230 K. At T = 330 K, the benzophenone crystal undergoes melting and only the Rayleigh line wing is observed in the spectrum.

The evolution of the Raman spectra of liquid benzophenone with a decrease in temperature from 324 to 160 K is shown in Fig. 3. This case corresponds to curve *2* in Fig. 1. A decrease in temperature leads to the appearance of a shoulder in the Rayleigh line wing (T =

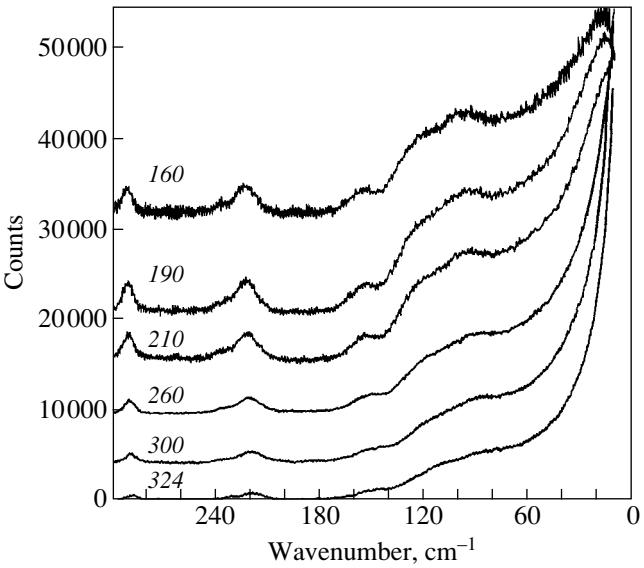

Fig. 3. Evolution of the low-frequency Raman spectra during cooling of molten benzophenone from 324 to 160 K.

210 K), which, upon further cooling, transforms into a clearly pronounced boson peak. At the same time, the intensity of the Rayleigh line substantially decreases in the frequency range 20–10 cm^{-1}. As follows from the Raman spectra and the data of differential scanning calorimetry, a decrease in the temperature of liquid benzophenone does not lead to its crystallization.

3. DISCUSSION

The universally accepted approximation for the interpretation of the Raman spectra of different glasses is the assumption that light scattering is due to disordering, and, hence, vibrations cannot be described by certain wave vectors. Consequently, all these vibrations can contribute to the scattering spectra.

According to Shuker and Gammon [9], the intensity of light scattering is proportional to the density of

Table 1. Parameters of phase transitions in benzophenone

Peak designation	Number of the curve in Fig. 1	T_{st}, K	T_{max}, K	T_f, K	Entropy, J/(g K)
X	*2*	206.6	211.7	214.6	0.36
X	*3*	213.2	216.8	218.0	1.00
α	*1*	320.7	323.9	327.9	56.48
α	*3*	321.2	323.9	328.0	74.40
β	*3*	299	301	305	16.8
γ	*3*	294.2	295.4	296.6	0.74

Note: T_{st}, T_{max}, and T_f are the temperatures of the onset, maximum, and completion of the phase transition, respectively.

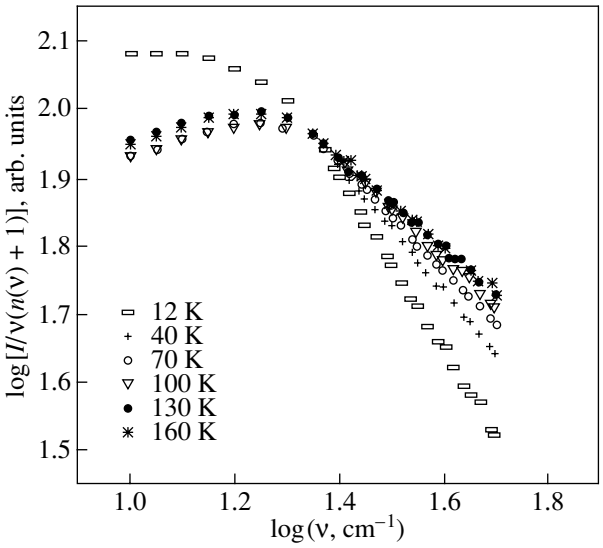

Fig. 4. Raman spectra of vitreous benzophenone (normalized to $[n(\nu) + 1]\nu$).

vibrational states $g(\nu)$ and the matrix element of coupling the vibrational modes to light $C(\nu)$; that is,

$$I_{ex} = C(\nu)g(\nu)[n(\nu) + 1]/\nu, \qquad (1)$$

where $[n(\nu) + 1] = \{1 - \exp(-h\nu/kT)\}^{-1}$ is the Bose factor and $C(\nu)$ depends on the particular mode of the permittivity modulation produced by vibrations in the medium. The theoretical predictions regarding the frequency dependence of the matrix element $C(\nu)$ are rather contradictory. The same is also true for the available experimental data. For example, Martin and Brenig [10] assumed that the frequency dependence $C(\nu)$ is described by a square law. Sokolov *et al.* [11] argued that the $C(\nu)$ is well approximated by a linear frequency dependence. Shuker and Gammon [9] postulated that $C(\nu)$ is frequency independent.

Unfortunately, the light-to-vibration coupling coefficient $C(\nu)$ cannot be precisely determined from the low-frequency Raman spectra, because the frequency dependence of the density of vibrational states $g(\nu)$ is unknown. In principle, the data on the density of vibrational states $g(\nu)$ can be obtained from analyzing the low-frequency neutron scattering spectra. However, as far as we know, data on neutron scattering in benzophenone are unavailable. For this reason, we made an attempt to determine the frequency dependence $C(\nu)$ from relationship (1) under the assumption that $g(\nu)$ can be represented by the Debye frequency dependence, i.e., $g(\nu) \sim \nu^2$.

Table 2. Exponents α at different temperatures

T, K	α
12	1.25
40	0.91
70	0.78
100	0.66
130	0.64
160	0.63

Figure 4 displays the Raman spectra of vitreous benzophenone, which were normalized to $[n(\nu) +1]\nu$. In this normalization, the slope of the curve specifies the exponent. It can be seen from Fig. 4 that, in the frequency range 20–50 cm^{-1}, where the contribution of quasi-elastic scattering is insignificant, the frequency dependence $C(\nu)$ obeys a power law; i.e., $C(\nu) \sim \nu^{\alpha}$ with the exponent α, which was found to be temperature dependent. Table 2 lists the exponents α determined from Fig. 4 for different temperatures.

It is seen from Table 2 that, as the temperature increases from 12 to 160 K, the exponent α decreases from 1.25 to 0.63 and $C(\nu)$ follows a linear frequency dependence only at a temperature of 40 K.

According to the majority of existing models, the nature of the boson peak is explained by the medium-range order in the atomic arrangement. This idea was first put forward by Martin and Brenig [10] and then developed in [2, 5, 12, 13]. At the same time, alternative models ascribe the origin of the boson peak to the presence of defects in the structure [14], fractals [15], and localized excitations in the soft potential model [16].

The results obtained in the present work suggest that a medium-range order exists in the structure of vitreous benzophenone. Analysis of the Raman spectra (Figs. 2, 3) and thermograms (Fig. 1) revealed that the crystallization of benzophenone occurs only in the case of a transition from the vitreous state to the supercooled liquid state and not from the liquid to the vitreous state. This can easily be explained by the fact that glasses involve fragments of a crystal structure which is retained within several coordination spheres; i.e., the structure of glasses can be characterized by a medium-range order. According to numerical estimates obtained from the experimental data, the characteristic medium-range order size is equal to 1–5 nm [17]. It is believed that the crystal structure plays the role of crystallization centers on the nanometer scale. This is confirmed by visual observations: the crystallization occurs uniformly throughout the bulk of the supercooled liquid. These observations also suggest that the medium-range order is retained in the supercooled liquid. It is quite reasonable that the cooling of molten benzophenone characterized by absolute disorder does not lead to crystallization.

In our opinion, the above findings are direct evidence of the existence of a nanostructure in glasses. In this case, the boson peak reflects the vibrational properties of the medium and its origin is associated with an excess density of vibrational states which appears in the absence of a long-range order. The selection rules for

the phonon wave vector **k** are violated as the result of breaking the translational symmetry, and all phonon states can contribute to light scattering.

Special mention should be made of the following interesting result. Upon heating of the studied samples from temperatures below the glass transition range to the melting point of α-benzophenone, the formation of the α phase was always preceded by the formation of the β modification. This suggests that the elements of a local structure of vitreous benzophenone are similar to the crystal structure of β-benzophenone. It seems likely that, upon rapid cooling of the melt, the formation of a monoclinic structure of the unstable β phase would be a more thermodynamically favorable process compared to the formation of the orthorhombic α phase. However, when the α modification was melted and held at room temperature for a few hours (or days), benzophenone invariably crystallized in an orthorhombic structure of the α phase.

In conclusion, we note that the structure of glasses on the medium-range order scale is the fundamental property, which, in our case, is responsible for the specific features of low-frequency Raman spectra and the features of the phase transformations in benzophenone.

REFERENCES

1. V. K. Malinovsky and A. P. Sokolov, Solid State Commun. **57** (9), 757 (1986).
2. A. P. Sokolov, Physica B (Amsterdam) **219/220**, 251 (1996).
3. M. J. Harris, S. M. Bennington, M. T. Dove, and J. M. Parker, Physica B (Amsterdam) **263/264**, 357 (1999).
4. T. Nakayama, Physica B (Amsterdam) **263/264**, 243 (1999).
5. V. K. Malinovsky, V. N. Novikov, and A. P. Sokolov, Usp. Fiz. Nauk **163** (5), 119 (1993) [Phys. Usp. **36**, 440 (1993)].
6. G. M. Lobanova, Kristallografiya **13** (6), 984 (1968) [Sov. Phys. Crystallogr. **13**, 856 (1969)].
7. V. I. Mel'nik, K. I. Nelipovich, and M. T. Shpak, Izv. Akad. Nauk SSSR, Ser. Fiz. **44** (4), 827 (1980).
8. V. Z. Gochiaev, V. K. Malinovsky, V. N. Novikov, and A. P. Sokolov, Philos. Mag. B **63** (3), 777 (1991).
9. R. Shuker and R. W. Gammon, Phys. Rev. Lett. **25** (4), 222 (1970).
10. A. J. Martin and W. Brenig, Phys. Status Solidi B **64** (1), 163 (1974).
11. A. P. Sokolov, A. Kisliuk, D. Quitmann, and E. Duval, Phys. Rev. B **48** (10), 7692 (1993).
12. V. K. Malinovsky, Fiz. Tverd. Tela (St. Petersburg) **41** (5), 805 (1999) [Phys. Solid State **41**, 725 (1999)].
13. S. Kojima, Phys. Rev. B **47** (5), 2924 (1993).
14. S. R. Elliot, Europhys. Lett. **19**, 201 (1992).
15. A. Fontana, F. Rocca, and M. P. Fontana, Phys. Rev. Lett. **58** (5), 503 (1987).
16. L. Gil, M. A. Ramos, A. Bringer, and U. Buchenau, Phys. Rev. Lett. **70** (2), 182 (1993).
17. V. K. Malinovsky, V. N. Novikov, N. V. Surovtsev, and A. P. Shebanin, Fiz. Tverd. Tela (St. Petersburg) **42** (1), 62 (2000) [Phys. Solid State **42**, 65 (2000)].

Translated by O. Borovik-Romanova

Physics of the Solid State, Vol. 43, No. 8, 2001, pp. 1594–1597. Translated from Fizika Tverdogo Tela, Vol. 43, No. 8, 2001, pp. 1533–1535.

LATTICE DYNAMICS AND PHASE TRANSITIONS

Optical and X-ray Studies of the Structural Phase Transition in Cryolite $(NH_4)_3GaF_6$

S. V. Mel'nikova*, S. V. Misyul', A. F. Bovina*, and M. L. Afanas'ev***

** Kirensky Institute of Physics, Siberian Division, Russian Academy of Sciences, Akademgorodok, Krasnoyarsk, 660036 Russia*

*** Krasnoyarsk Agricultural University, pr. Mira 88, Krasnoyarsk, 660049 Russia*

e-mail: msv@iph.krasn.ru

Received December 15, 2000

Abstract—Optical polarization and x-ray diffraction studies of powders and single-crystal plates of different cuts of an $(NH_4)_3GaF_6$ crystal are carried out in a broad temperature range, including the phase transition point. The following sequence of symmetry changes is found to occur: $O_h^5 - Fm3m$ ($Z = 4$) $\longleftrightarrow$ $C_i^1 - I\bar{1}$ ($Z = 16$).

$(NH_4)_3M^{3+}F_6$ (M^{3+}: Al, Cr, Ga, V, Fe, Sc, In) crystals with cryolite structure (the space symmetry group $Fm3m$, $Z = 4$) belong to a family of perovskite-like compounds. The three-dimensional crystalline framework of these compounds is formed by the octahedra $(NH_4)F_6$ and $M^{3+}F_6$, which are connected through their vertices, and the polyhedra between the octahedra are occupied by ammonium ions.

For most ammonium cryolites, transitions from the cubic phase are accompanied by a change in the orientation of two structural groups: $(NH_4)^+$ and $(M^{3+}F_6)$ [1]. It has been shown [2, 3] that the temperature at which the cubic phase becomes unstable depends on the M^{3+} ion size. The number of the observed phase transitions (PTs) and the sequence of symmetry changes also depend on this factor. In substances with a trivalent ion of small radius ($R_M^{3+} \le R_{Fe}^{3+}$), only one PT takes place, while in compounds with larger cations (In), two PTs are observed [3]; in $(NH_4)_3ScF_6$, three PTs occur [4, 5]. Recent studies of powders and single crystals [6] revealed the following series of symmetry changes in cryolite containing scandium: $O_h^5 - Fm3m$ ($Z = 4$) $\longleftrightarrow$ $C_{2h}^5 - P12_1/n1$ ($Z = 2$) $\longleftrightarrow$ $C_{2h}^3 - I12/m1$ ($Z = 16$) $\longleftrightarrow$ $C_i^1 - I\bar{1}$ ($Z = 16$).

The lowest symmetry phase is triclinic. Its Bravais cell is chosen to be body-centered and is four times larger in volume compared to the initial face-centered cubic cell.

For the $(NH_4)_3GaF_6$ compound containing a small trivalent cation Ga^{3+} [3], x-ray diffraction studies of powders in a temperature range including the PT have shown that the crystals have cubic symmetry $Fm3m$ ($Z = 4$) above $T_0 = 250$ K, while line splitting is observed on diffractograms below the phase transition. Superstructure reflections, which possibly indicate a change in the translation symmetry, were not detected. The diffractogram line identification was carried out for a tetragonal pseudocell with parameters $a_t \approx a_0/\sqrt{2}$ and $c_t \approx a_0$. The symmetry of the low-temperature phase was determined in [3] to be possibly triclinic $P\bar{1}$.

According to [5], all ammonium cryolites have the same symmetry of the lowest temperature phase. This conclusion was made on the basis of the similar values of the total entropy changes in the phase transitions in $(NH_4)_3GaF_6$ and $(NH_4)_3ScF_6$ and from their (P–T) diagrams.

It is well known that x-ray diffraction studies of small structure distortions should be carried out on single-crystal samples, not on powders. In [6], a complex series of changes in the symmetry of $(NH_4)_3ScF_6$ was determined by studying crystal twinning and by observing x-ray reflections from oriented single-crystal plates. In that paper, in contrast to [3], a superstructure was observed and a change in the translation symmetry was detected. The present investigation is carried out with the aim of obtaining detailed information on the symmetry of the $(NH_4)_3GaF_6$ low-temperature phase.

The $(NH_4)_3GaF_6$ compound was synthesized by means of interaction of equivalent amounts of a $GaF_3 \cdot 3H_2O$ solution in 40 vol % hydrofluoric acid (evaporated until the onset of crystallization) and of an NH_4F saturated solution. Small (2–3 mm^3) well-faceted single crystals were grown by means of slow controlled evaporation of a solution of the synthesized substance in 10 vol % HF acid by gradually lowering (over 7 days) the crystallization temperature from 333 to 293 K.

Investigations with the help of a polarizing microscope were carried out on thin crystalline platelets cut along different crystallographic directions. On cooling, a PT from the cubic phase was observed at the temperature $T_0 = 250$ K. This PT was accompanied by the formation of twins and by cracking. An extremely complicated mixed twinning structure with a nonuniform, temperature-dependent, extinction position is observed in polarized light in a very thin (<0.05 mm) sample. The domain walls are oriented along the [100] and [110] directions. In general, the twinning structure is analogous to that observed in the triclinic phase of $(NH_4)_3ScF_6$. However, in our case, the domains are smaller. Unfortunately, we were not able to obtain sufficiently large monodomain areas; for such areas, it would have been possible (as was done in [6]) to measure the temperature dependence of the orientation of the optical indicatrix precisely. However, the results obtained are sufficiently accurate for us to draw the conclusion that the following symmetry change takes place in an $(NH_4)_3GaF_6$ crystal: cubic (G_0) $\longleftrightarrow$ triclinic (G_1).

X-ray diffraction studies of $(NH_4)_3GaF_6$ crystals were carried out in a broad temperature range 100–300 K on a Dron-2.0 diffractometer equipped with a low-temperature URNT-180 attachment (CuK_α radiation, graphite monochromator). Single-crystal platelets of the $(110)_0$ and $(111)_0$ cuts, as well as powders obtained from $(NH_4)_3GaF_6$ single crystals, were used as experimental samples. Here and further on, subscripts on the symbols of planes and directions designate the crystal phase.

The set of x-ray reflections in the initial G_0 phase corresponds to cubic symmetry with a face-centered cell F [7]. The parameters of this cell at 353 K are shown in the table. Below the PT temperature T_0 = 250 K, changes in the profiles of the x-ray reflections from single-crystal plates arise and splitting of reflections on the powder diffractograms are observed (see table).

Moreover, below the phase transition temperature (the G_1 phase), a system of superstructure reflections of the ($hk0$), (hkl), and (h + 1/2, h + 1/2, h + 1/2) types is formed. Here, h is an arbitrary integer. The reflection splitting in the G_1 phase corresponds to triclinic symmetry. The formation of superstructure reflections characterized by noninteger values of index h indicates a change in the Bravais cell volume due to the PT. Figure 1 shows the temperature dependence of the integral intensity of the (5/2, 5/2, 5/2) superstructure reflection. It is evident from Fig. 1 that, in the course of the transition from the G_0 to the G_1 phase, the above-mentioned reflection arises suddenly and almost immediately reaches saturation. Since the superstructure reflection intensity characterizes shifts in the atom in the elementary cell with respect to their initial positions, we draw the conclusion that the main structural distortions in the crystal studied take place in a narrow temperature range below the PT.

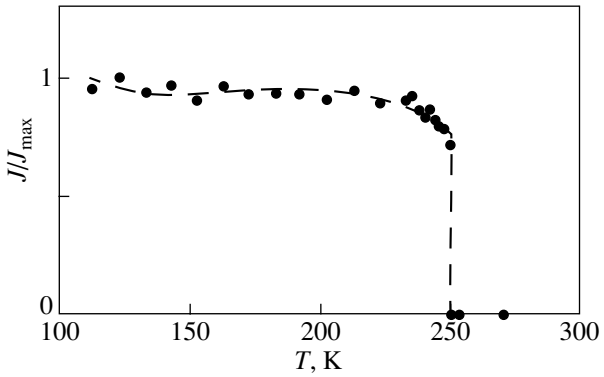

Fig. 1. Temperature dependence of the integral intensity for the (5/2, 5/2, 5/2) superstructure reflection. The reflection indices are in accordance with the parameters of the cell of the initial G_0 phase.

The temperature dependences of the linear and angular parameters of the crystal cell in the G_0 and the G_1 phases were determined from the positions of the components of the (8, 8, 0) reflection. The results of these investigations are represented in Figs. 2 and 3. It is clear from Fig. 2 that the elementary-cell parameters

Crystallographic data for $(NH_4)_3GaF_6$

	G_1	G_0
Space group	C_i^1–$I\bar{1}$	O_h^5–$Fm3m$
Z	16	4
T_{exp}, K	170	300
Bravais cell parameters		
	$-\mathbf{b}_0 + \mathbf{c}_0$	$\mathbf{a}_0$
a, Å	12.605	9.039
	$\mathbf{b}_0 + \mathbf{c}_0$	$\mathbf{b}_0$
b, Å	12.590	9.039
	$2\mathbf{a}_0$	$\mathbf{c}_0$
c, Å	18.363	9.039
α, deg	90.24	90
β, deg	89.31	90
γ, deg	89.89	90
V, Å^3	2914.118	738.514
Reflection splitting scheme		
($hh0$)		
(hhh)		
The presence of superstructure reflections	+	–

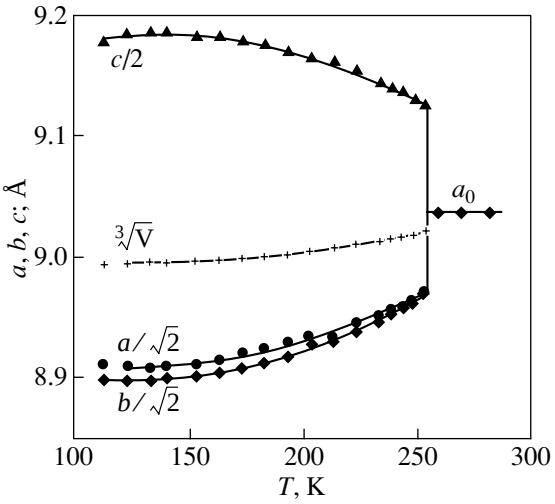

Fig. 2. Temperature dependence of the linear dimensions and volume of the Bravais cell for an $(NH_4)_3GaF_6$ crystal. The elementary-cell volume V is four times smaller in the G_1 phase.

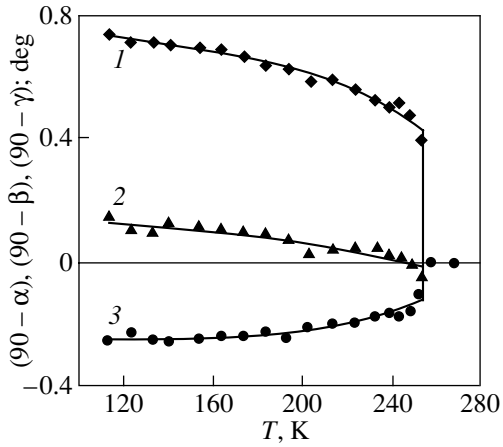

Fig. 3. Temperature dependences of the angular parameters of the Bravais cell for an $(NH_4)_3GaF_6$ crystal: (*1*) 90 – β, (*2*) 90 – γ, and (*3*) 90 – α.

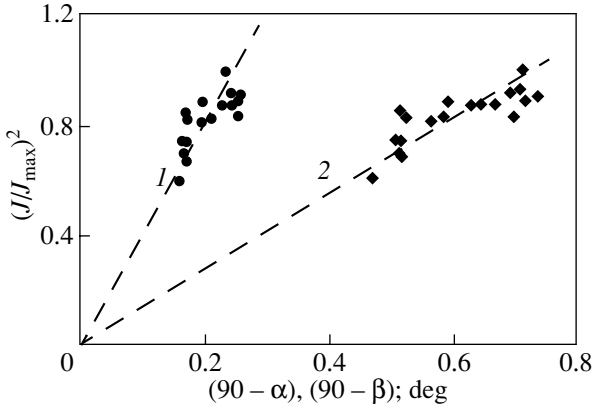

Fig. 4. Dependence of the square of the integral intensity of the (5/2, 5/2, 5/2) superstructure reflection upon distortion of the rectangular Bravais cell in the triclinic phase of the $(NH_4)_3GaF_6$ crystal: (*1*) 90 – α and (*2*) 90 – β.

are changed abruptly in the course of the transition from the cubic G_0 to the G_1 phase. However, the jump in cell volume is not large and equals approximately 0.4 percent of V_0. The linear dimensions of the triclinic cell of $(NH_4)_3GaF_6$ along the **a** and **b** directions are decreased and virtually coincide in value, while the cell parameter along the **c** axis is increased. Similar temperature dependences of the cell dimensions have been observed in scandium cryolite, whose parameters are approximately 0.2 Å greater.

The angular parameters of the Bravais cell (Fig. 3) also have many common features in these two crystals. In triclinic phases, $\beta < 90°$ and $\alpha > 90°$ and γ does not differ considerably from 90°. At $T = T_0$, the deviations of the angular parameters of the Bravais cell from the right angle (90 – α) and (90 – β) appear in a jump and then grow gradually over the whole temperature range studied. This dependence differs considerably from the behavior of the intensity of the superstructure reflections (Fig. 1).

The extinction of the structural and the superstructure reflections, as well as the splittings of the specially chosen x-ray reflections from the single-crystal plates, allowed us to determine the crystal group of the crystal. By standard definition (see [7]), the Bravais cell of the triclinic G_1 phase should be simple. However, for convenience, we took the bulk-centered cell $I\bar{1}$ ($Z = 16$). It is clear that this Bravais cell of the G_1 phase has a four times greater volume than that of the G_0 phase. However, the primitive cells of the G_0 and G_1 phases contain 1 and 8 formula units, respectively. The data on the $(NH_4)_3GaF_6$ phase symmetry and sizes and orientation of the Bravais cells are listed in the table.

Contrary to the results of [3], where the G_3 phase symmetry was determined to be $P\bar{1}$ but the Bravais cell was not chosen, our findings allow one to establish the point symmetry group and are indicative of the change in the translation symmetry. Thus, the studies carried out by us allow one to affirm that the high-temperature phases, as well as the low-temperature phases, of the two ammonium cryolites $(NH_4)_3GaF_6$ and $(NH_4)_3ScF_6$ have the same symmetry, namely, Oh^5–$Fm3m$ ($Z = 4$) and $C_i^1 - I\bar{1}$ ($Z = 16$), respectively. The former crystal is immediately converted into the triclinic phase on cooling, while the latter is transformed in three steps. Studies of the heat capacity [5] also revealed that the structural changes due to phase transitions are identical in these two crystals. The total entropy change in $(NH_4)_3ScF_6$ in the course of the three PTs is $\Sigma\Delta S_i = 20.79 \pm 1.53$ J mol^{-1} K^{-1}, while in $(NH_4)_3GaF_6$, we have $\Delta S = 23.0 \pm 1.6$ J mol^{-1} K^{-1}.

Our investigations allow one to make some conclusions regarding the possible relation between the order parameter of the phase transition and the shear deformation that appears below the phase transition. As

shown above, the changes in elementary-cell angular parameters are not proportional to the changes in superstructure reflection intensity. However, according to Fig. 4, these quantities have a quadratic relation. On this basis, one can conclude that the ferroelastic PT in $(NH_4)_3GaF_6$ is improper and that the dependence shown in Fig. 1 reflects the temperature behavior of its microscopic parameter.

ACKNOWLEDGMENTS

This work was supported by the Russian Foundation for Basic Research, project nos. 00-02-16034 and 00-15-96790.

REFERENCES

1. A. Sasaki, Y. Furukawa, and D. Nakamura, Ber. Bunsenges. Phys. Chem. **93**, 1142 (1989).
2. K. Kobayashi, T. Matsuo, H. Suga, *et al.*, Solid State Commun. **53** (8), 719 (1985).
3. A. Tressaud, S. Khairoun, L. Rabardel, *et al.*, Phys. Status Solidi A **98** (2), 407 (1986).
4. I. N. Flerov, M. V. Gorev, and T. V. Ushakova, Fiz. Tverd. Tela (St. Petersburg) **41** (3), 523 (1999) [Phys. Solid State **41**, 468 (1999)].
5. M. V. Gorev, I. N. Flerov, and A. Tressaud, J. Phys.: Condens. Matter **11**, 7493 (1999).
6. S. V. Mel'nikova, S. V. Misyul', A. F. Bovina, and M. L. Afanas'ev, Fiz. Tverd. Tela (St. Petersburg) **42** (2), 336 (2000) [Phys. Solid State **42**, 345 (2000)].
7. *International Tables for X-ray Crystallography* (The Kynoch Press, Birmingham, 1952), Vol. 1.

Translated by A. Sonin